UNIVERSIDAD DE CHILE
FACULTAD DE CIENCIAS FÍSICAS Y MATEMÁTICAS
DEPARTAMENTO DE GEOLOGÍA

GENESIS OF THE EL LACO IRON DEPOSIT UNRAVELED BY MAGNETITE GEOCHEMISTRY

TESIS PARA OPTAR AL GRADO DE DOCTOR EN CIENCIAS, MENCIÓN GEOLOGÍA

JOSÉ TOMÁS OVALLE ORTEGA

PROFESOR GUÍA:

MARTIN REICH MORALES

PROFESOR CO-GUÍA:

FERNANDO BARRA PANTOJA

MIEMBROS DE LA COMISIÓN:

DIEGO MORATA CÉSPEDES

PABLO SÁNCHEZ ALFARO

Este trabajo ha sido financiado por el Núcleo Milenio Trazadores de Metales (NMTM) NCN13_065, el Centro de Excelencia en Geotermia de los Andes (CEGA), proyecto FONDAP-CONICYT 15090013, y por el Proyecto FONDECYT #1140780

SANTIAGO DE CHILE

2021

RESUMEN

GÉNESIS DEL DEPÓSITO DE HIERRO EL LACO REVELADO POR LA GEOQUÍMICA DE MAGNETITA

La génesis de los depósitos de magnetita-apatito o *iron oxide-apatite* (IOA), fuentes históricas de hierro a nivel mundial, ha sido intensamente debatida por décadas. Gran parte de este debate se ha centrado en el depósito El Laco, ubicado en el Altiplano Chileno. Con una edad Plio-Pleistocena, este depósito representa el ejemplo más reciente y mejor preservado de este tipo de mineralización en la Tierra. Compuesto por seis cuerpos mineralizados de magnetita masiva que afloran en superficie, los depósitos de magnetita en El Laco muestran estructuras superficiales únicas las cuales se asemejan en gran medida a flujos de lava basáltica. Las hipótesis genéticas que se han propuesto para El Laco abarcan desde procesos puramente magmáticos hasta procesos puramente hidrotermales, y su génesis es considerado clave para comprender los procesos formadores de sistemas IOA.

Esta investigación tiene como objetivo dilucidar los procesos magmático-hidrotermales que conducen a la formación del depósito de hierro El Laco. El objetivo principal es identificar los procesos fisicoquímicos que controlan la precipitación de magnetita y constreñir el rol que juegan los procesos volcánicos durante la génesis de los depósitos IOA. Esta investigación combinó trabajos de campo y logueo de sondajes con una caracterización química y microtextural de detalle en muestras de magnetita. Fases de magnetita y clinopiroxeno fueron analizadas utilizando una combinación de microsonda electrónica (EPMA), ablación láser (LA-ICP-MS), y fluorescencia de rayos X mediante luz sincrotrónica (µ-XRF). El análisis de la estructura interna de muestras de magnetita fue llevado a cabo usando el método de microtomografía computarizada de rayos X de alta resolución (HRXCT).

Los resultados revelan que los cuerpos mineralizados de El Laco están formados por grandes sistemas de brechas de magnetita en profundidad que gradan a cuerpos de magnetita masiva hacia la superficie. Investigaciones mineralógicas revelan gradientes geoquímicos y texturales distintivos, que dependen de la profundidad. La magnetita de las rocas andesíticas hospedantes y de los niveles profundos de los cuerpos minerales, se caracteriza por una alta concentración de elementos traza, incluyendo Ti, V, Ni, Mn, Zn, Cr, Al, Ga, y Co en comparación con la magnetita de los niveles superiores. Por su parte, el análisis de clinopiroxenos reveló mayores contenidos de Mn y Fe en el clinopiroxeno asociado a las andesitas, y un enriquecimiento en Na y Ca en el clinopiroxeno asociado a los cuerpos minerales. Estas tendencias composicionales y microtexturales son interpretadas como reflejo de una transición desde condiciones puramente ígneas a un sistema magmático-hidrotermal dominado por fluidos en enfriamiento. Los análisis microtexturales de magnetita y clinopiroxeno son consistentes con esta hipótesis, revelando además múltiples estadios de disolución y reprecipitación mineral. Estas interpretaciones son apoyadas por observaciones de HRXCT, señalando que la mayoría de la magnetita en El Laco, y particularmente en los niveles superiores, habría precipitado a partir de fluidos hidrotermales ricos en hierro.

Los datos presentados en esta tesis apoyan un modelo genético que explica la formación del depósito El Laco por medio de una combinación de procesos magmáticos e hidrotermales que operan durante la evolución de un sistema volcánico. El modelo propuesto involucra pasos secuenciales que incluyen la segregación de magnetita ígnea, la intrusión de magmas máficos, el colapso del edificio volcánico, y la inyección y descarga en superficie de fluidos ricos en Fe de origen magmático. En resumen, las principales características observadas en El Laco son consistentes con un modelo genético en donde los cuerpos de magnetita se forman como resultado de una confluencia óptima de procesos volcánicos comunes que ocurren durante la evolución de volcanes de arco.

ABSTRACT

GENESIS OF THE EL LACO IRON DEPOSIT UNRAVELED BY MAGNETITE GEOCHEMISTRY

The genesis of iron oxide-apatite (IOA) deposits, which have been historically a major source of iron worldwide, has been highly debated for decades. Much of this long-standing debate has been centered in the Plio-Pliocene El Laco deposit in the Chilean Altiplano, which is the youngest and best preserved example of this mineralization type on Earth. With six outcropping massive magnetite orebodies hosting more than a gigaton of iron, the magnetite deposits at El Laco display unique surface structures remarkably similar to basaltic lava flows. Proposed genetic hypotheses for El Laco span the spectrum from purely magmatic to purely hydrothermal processes. Therefore, the El Laco deposit is considered key to understanding the processes that form IOA systems in volcanic settings.

This research aims to unravel the magmatic-hydrothermal processes leading to the formation of the El Laco deposit. The main goal is to identify the key physicochemical processes that control magnetite precipitation, and constrain the role of volcanic processes during iron precipitation. The research approach combined fieldwork and drill core logging with detailed microtextural and micro-chemical characterization of magnetite samples. Magnetite and pyroxene were analyzed using a combination of micro-analytical techniques, including electron probe microanalysis (EPMA), laser ablation inductively coupled plasma mass spectrometry (LA-ICP-MS), and synchrotron radiation X-ray fluorescence (μ-XRF) spectrometry. Volumetric imaging of the magnetite samples was carried out using high-resolution X-ray computed microtomography (HRXCT).

Results reveal that orebodies at El Laco are complex and vertically zoned. Generally, the orebodies are formed by large magnetite-rich breccia bodies at depth that grade to massive magnetite bodies towards surface. Mineralogical investigation of the ore bodies reveals distinct depth-dependent textural and geochemical gradients, which are consistently recorded in both magnetite and co-genetic pyroxene. Microtextural and geochemical data of magnetite reveal consistent variations with depth. Magnetite in the andesitic host rocks and from deep/intermediate levels of the ore bodies have a high concentration of trace elements including Ti, V, Ni, Mn, Zn, Cr, Al, Ga, and Co in comparison with magnetite from the upper sections of the orebodies. Clinopyroxene is present in both andesites and the ore bodies, and show similar compositional trends than those exhibited by magnetite, but Mn and Fe are higher in the former, and Na and Ca are enriched in the latter. We interpret these trends as resulting from a transition from purely igneous conditions to a fluid-dominated, cooling magmatic-hydrothermal system. Detailed microtextural analysis of magnetite and clinopyroxene from the ore bodies support this notion, revealing multiple growth stages punctuated by dissolution-reprecipitation processes. These interpretations are further supported by HRXCT volumetric imaging of massive magnetite samples from the surface outcrops that indicate that most of magnetite at El Laco, and particularly in upper levels, precipitated from cooling Fe-rich hydrothermal fluids.

The data presented in this thesis support a genetic model that explains the formation of the El Laco deposit by a combination of magmatic and hydrothermal processes operating during the evolution of the volcanic system. The proposed model involves sequential steps including igneous magnetite segregation, intrusion of mafic magma, collapse of the volcanic edifice, and injection and venting of magmatically-derived Fe-rich fluids. In summary, it is argued that the major features observed at El Laco are consistent with a genetic model wherein magnetite bodies form as result of an optimal confluence of common subaerial volcanic processes occurring during the evolution of arc volcanoes.

“Mi canto es una cadena sin comienzo ni final, y en cada eslabón se encuentra el canto de los demás”

“Nosotros somos porque existe el amor, y queremos ser mejores porque existe el amor, y el mundo gira, crea, se multiplica porque existe el amor”

VÍCTOR JARA MARTÍNEZ

AGRADECIMIENTOS

Quisiera dedicar estas palabras de agradecimiento a diversas personas que apoyaron y motivaron la realización de este trabajo, tanto de mi círculo familiar así como las personas que tuve la suerte de conocer a lo largo de mi estadía en el programa de Doctorado.

En primer lugar, quisiera agradecer a Martin Reich, por estos cinco años de constante aprendizaje en ámbitos incluso más allá de lo científico, a través de una guía cercana, basada en el soporte, motivación y un preciso balance entre la exigencia y libertad. Del mismo modo, agradezco a mis profesores co-guías Fernando Barra y Diego Morata por sus valorables contribuciones a la rigurosidad de este trabajo, y a su vez por darme la oportunidad de pertenecer al NMTM y al CEGA. Agradezco también a Pablo Sánchez, miembro de la comisión, por su contribución en la etapa final de este trabajo de tesis.

I would also like to thank my international collaboration partners that greatly supported this work: Many thanks to Adam Simon and his awesome students from the University of Michigan; Artur Deditius from Murdoch University; Margaux Le Vaillant, Belinda Godel and Louise Schoneveld from CSIRO Mineral Resources. All of you made my stay in Ann Arbor and Perth an unforgettable experience.

De una manera muy especial quiero agradecer a mi familia. A mis padres Gloria y Carlos, quienes me han brindado su apoyo e inmenso amor a lo largo de toda mi vida; a mis 3 hermanas y 4 hermanos por ser inspiración y un pilar fundamental en mi vida. Agradezco enormemente el haberme criado en un entorno cercano al mundo de la ciencia, la naturaleza, las artes, la música y la creatividad.

A mi segunda familia, los Valera Rojas, quienes me han acogido con un cariño inmenso y apoyado a lo largo de estos años. Y por su puesto, a mis compañeras de vida Carolina e Isidora, de las personas más lindas que pisan esta Tierra. Les doy las gracias por darme su amor y apoyo incondicional a lo largo de este camino, y por creer siempre en mí y alentarme a seguir adelante. Nos espera un maravilloso futuro lleno de amor.

A mis compañer@s de la oficina del NMTM, con quienes compartí diariamente muy buenos momentos y muchos litros de café acompañados de las más enriquecedoras y divertidas conversaciones, y quienes además de muy buenos consejos y conocimiento para mi investigación, me brindaron su linda amistad.

Finalmente, agradezco el apoyo financiero del Núcleo Milenio Trazadores de Metales (NMTM), del Centro de Excelencia en Geotermia de los Andes (CEGA), del Proyecto FONDECYT #1140780; de ANID por la beca de Doctorado Nacional (21170261); al Programa de Estadías Cortas de Investigación del Departamento de Postgrado y Postítulo de la Vicerrectoría de Asuntos Académicos, y a la Society of Economic Geologists por la Graduate Student Fellowship.

CONTENT

FIGURES

TABLES

CHAPTER 1: Introduction

1.1. OVERVIEW AND MOTIVATION

Discovered in the late 1950's in the Chilean Altiplano of the Central Andes, the Plio-Pleistocene El Laco iron deposit, represents the youngest and one of the most enigmatic records of iron oxide mineralization on Earth. Since the first report by Park (1961), El Laco's massive magnetite ore bodies have attracted significant attention because of their young age and their remarkable volcanic-like textures. Historically, and beyond conflicting genetic hypotheses, these characteristics have been considered as an outstanding example of volcanogenic magnetite mineralization. Therefore, and considering that El Laco represents a uniquely-preserved subaerial type of iron oxide-apatite (IOA) mineralization, the deposit has the potential to provide key information on the geological processes leading to the formation of IOA systems worldwide.

Iron oxide-apatite (IOA) deposits are historical and economically important sources for iron to our society. Also known as "Kiruna-type" deposits, IOA deposits are globally distributed over geological time ranging in age from Archean to Holocene (Williams et al., 2005; Barton, 2014). With mineralization widely dominated by magnetite with variable amounts of apatite, actinolite, pyroxene, and scapolite, and morphologies including massive, dike-like, breccias, and/or pegmatitic ore bodies, IOA deposits have been considered as the Cu-poor endmember of the iron oxide-copper-gold (IOCG) clan (Williams et al., 2005; Barton, 2014). While IOCG deposits are mostly accepted to be formed by hydrothermal processes mainly due to a lack of clear igneous correlation (Barton, 2014), the origin of IOA deposits has remained contentious by more than half a century.

Much of the long-standing debate on the genesis of IOA deposits has been centered around the enigmatic features of the El Laco massive magnetite ore bodies. Particularly, their unique volcanic textures resembling basaltic lava flows. Over the years, most studies at El Laco have attempted to explain the exact mechanism(s) for formation of the ore bodies, i.e., whether these are formed by igneous or by hydrothermal processes. With field evidence providing some support for both mechanisms — for example, lava/pyroclastic-like textures of the ore bodies, which can be also intensely brecciated, veined and hydrothermally altered — "classical" genetic models include (see section **1.3** for more details): **(1)** liquid immiscibility-based magmatic processes invoking either a hydrous Fe-Ca-P melt (Nyström and Henríquez, 1994; Naslund et al., 2002; Naranjo et al., 2010; Nyström et al., 2016; Velasco et al., 2016; Tornos et al., 2016; 2017; Broughm et al., 2017; Xie et al., 2019), or a anatectic Fe-rich carbonate-sulfate melt (Bain et al., 2021); **(2)** metasomatic replacement hydrothermal processes of andesitic volcanic rocks by magnetite precipitated from Fe-rich hydrothermal fluids sourced from magmatic or non-magmatic sources (Rhodes and Oreskes, 1995, 1999; Sillitoe and Burrows, 2002; Dare et al., 2015).

Importantly, the two classical and highly contrasting views (**1** and **2**) described above, which have prevailed for decades, have been constructed on field observations and geochemical information obtained almost exclusively from the outcropping portions of the El Laco ore bodies. Field evidence as argument of magmatic immiscibility includes magnetite displaying flow and vesicular textures, as

well as the occurrence of pyroclastic-like Fe oxide material, and vertical degassing conduits, interpreted as gas-escape chimneys (Henríquez and Martin, 1978; Nyström and Henríquez, 1994; Naslund et al., 2002). On the other hand, the metasomatic model is primarily based on the presence of widespread hydrothermal alteration at El Laco, the occurrence of altered and magnetite-veined andesite fragments in the iron ore, as well as a trace element signature of the outcropping ore bodies that overlap those of magnetite precipitated from hydrothermal fluids (Rhodes et al., 1999; Sillitoe and Burrows, 2002; Dare et al., 2015).

In the last decade, and in the light of a growing interest in the use of magnetite as a petrogenetic indicator, a third **(3)** genetic model was proposed by Knipping et al. (2015a, b) to explain the genesis of IOA systems. Although it was not specifically proposed for El Laco, but rather to explain the formation IOA deposits in the Cretaceous Iron Belt of northern Chile, this model invokes a combination of igneous and hydrothermal processes occurring during the evolution of magma systems in arc settings. Known as the *magnetite flotation model*, it involves a combination of early magmatic processes where magnetite microlites crystallized from silicate melt trigger the exsolution of a magmatic volatile phase that wets and attaches to the magnetite microlites through heterogeneous nucleation processes (e.g., Hurwitz and Navon, 1994; Edmonds, 2015). This is followed by late magmatic-hydrothermal processes of magnetite-bubble coalescence resulting in the formation of a magnetite-bearing Fe-rich suspension that separates from the silicate magma and ascends through faults, forming the deposits at different structural levels (Knipping et al., 2015a, b; 2019a, b; Simon et al., 2018; Palma et al., 2020).

However, and despite such relevant advances, the processes that led to the formation of the El Laco deposit remain poorly understood. This is due, in part, to the fact that the data reported so far only represents the uppermost and most altered portion of the deposit, i.e., the outcropping ore bodies. In fact, all previous studies have shown evidence of both hydrothermal overprinting and supergene alteration, which have obscured or modified the primary magnetite composition. The overall lack of information at depth has stimulated controversy and limited our understanding of the key processes that formed the El Laco deposit.

This research is largely motivated by this fundamental gap of geological information at El Laco. Importantly, no detailed data are available about the morphology, mineralogy and overall architecture of the mineral system at depth. As a consequence, there is a severe lack of mineralogical and geochemical information of magnetite in the deeper levels of the massive ore bodies. These data are of utmost importance to better understand the formation of El Laco and other IOA deposits, as previous studies have shown in several types of ore deposits (e.g., porphyry, skarn, Fe-Ti/V, etc.) throughout the world.

During the last decade, studies combining in-situ geochemical and microtextural approaches on magnetite from different geological environments, and particularly from magnetite-bearing deposits, have provided a framework to better understand its provenance, formation physicochemical conditions, as well as growth mechanisms and ore-forming processes (Dupuis and Beaudoin, 2011; Dare et al., 2012, 2014; Nadoll et al., 2012, 2014, 2015; Boutroy et al., 2014; Hu et al., 2014, 2015; Knipping et al., 2015b; Wen et al., 2017; Deditius et al., 2018; Palma et al., 2019; Huang and Beaudoin, 2019). These studies have demonstrated that physicochemical parameters such as temperature, pressure and oxygen fugacity control its minor and trace element budget, particularly for Ti, V, Mn, Mg, Cr, and Al. On the other hand, primary and secondary microtextural features of magnetite include exsolution lamellae, mineral inclusions and chemical zoning. Therefore,

knowledge of the main controls on elemental partitioning and the effects of re-equilibrium and post-crystallization processes are critical for robust petrogenetic interpretations.

Geochemical and microtextural information of magnetite is crucial considering the wide textural diversity recorded in the El Laco magnetite ores. These include massive magnetite and breccia bodies which are often crosscut by veins and veinlets that suggest multiple events of Fe mineralization (Rhodes et al., 1999; Sillitoe and Burrows, 2002; Naranjo et al., 2010). The textural diversity observed in magnetite at El Laco, which is also recognized in other IOA deposits, is usually attributed to superimposed iron oxide mineralization events leading to pervasive replacement, dissolution-reprecipitation processes and supergene oxidation (Huang and Beaudoin, 2019). Hence, any interpretation or genetic model proposed to explain the origin of the El Laco deposit, should be based on comprehensive geochemical studies of magnetite, from the deeper roots of the ore bodies to the outcropping portions of the system.

This research contributes directly to the understanding of the genesis of the world-class El Laco deposit by means of providing a detailed geochemical characterization of magnetite. The work presented here combined field observations, drill core logging, petrographic characterization and micro-analytical data to provide new geological, mineralogical and geochemical information of the deposit. To ensure representativeness, 251 samples were retrieved from thirteen drill cores at several depths from Laco Norte, Laco Sur, Extensión Laco Sur and Pasos Blancos. Drilling was performed by Compañía Minera del Pacífico (CMP) during an exploration program between 2007–2010. In addition, 39 samples were obtained from five outcropping massive magnetite ore bodies (Laco Norte, Laco Sur, San Vicente Alto, Rodados Negros and Cristales Grandes), and 21 volcanic rock samples were collected from the main andesitic volcanic units that host the mineralization at El Laco.

Petrographic and microtextural observations of the magnetite samples were performed using polarized light and scanning electron microscopy (SEM), which were the basis for further studies of magnetite and associated phases. Major and minor element data of magnetite and clinopyroxene were obtained using electron probe microanalysis (EPMA). Additionally, laser ablation inductively coupled mass spectrometry (LA-ICP-MS) analyses were carried out to quantify the trace element abundances in magnetite. These data were complemented with wavelength dispersive X-ray spectrometry (EPMA-WDS) and synchrotron radiation microbeam X-ray fluorescence microscopy (μ-XRF) in order to image the spatial distribution of chemical elements in the magnetite assemblages. Finally, high-resolution X-ray computed tomography (HRXCT) was carried out to study the internal structure of highly vesicular and porous massive magnetite ores that form the outcropping ore bodies. The general content of each chapter of this thesis is briefly described below.

Chapter 2 explores the deep roots of El Laco system by integrating geochemical and textural information of magnetite from drill core and surface samples. This approach revealed complex depth-dependent variations and, most notably, a systematic increase in titanium concentration of magnetite with depth. Results are consistent with an evolving system transitioning from purely magmatic at depth to magmatic-hydrothermal conditions towards the upper levels of the deposit. Based on the presented data, a new genetic model is proposed to explain the formation of the El Laco deposit, wherein magnetite bodies formed as result of an optimal confluence of common subaerial volcanic processes occurring during the evolution of the El Laco volcanic complex.

Chapter 3 deepens the analysis of ore-forming processes by integrating trace element geochemistry with detailed multi-instrumental chemical mapping of magnetite and clinopyroxene from the six ore bodies and andesite host units at El Laco. Magnetite compositions revealed distinct

trends of progressive depletion that extend from trace element-rich magnetite in the andesite to trace element-poor magnetite in the outcropping ore bodies. Such trends were also observed in chemical composition of clinopyroxene, and are interpreted along with magnetite data as record of different conditions of mineral growth, ranging from purely magmatic conditions evolving to a cooling magmatic-hydrothermal environment. These findings provide critical insights into the chemical evolution of the ore-forming magmatic-hydrothermal system as well as some key petrological constraints on the processes that took place in the magmatic system below the El Laco volcanic complex.

In *Chapter 4*, the focus was set on investigating the microtextures of the highly vesicular and porous magnetite levels that outcrop at Laco Sur. The aim was to unravel the internal structure of these complexly-textured magnetite ores, and in particular, explore the potential role of volcanic-hydrothermal processes on Fe mineralization. SEM and HRXCT data revealed the presence of abundant magnetite microparticles, including well-preserved magnetite microspheres as well as dendritic microstructures. We compared these morphologies with similar examples of spherically-shaped Fe oxide particles reported to occur in volcanic environments. Together with aqueous-phase experimental evidence of synthesis of magnetite microspheres, magnetite microstructures described at El Laco are suggestive of precipitation from Fe-rich hydrothermal fluids. The data agree with the magmatic-hydrothermal fluid model proposed in *Chapters 2* and *3* to explain the origin of El Laco, and provide new insights on the potential role of Fe colloids as agents of mineralization in volcanic systems.

In the next sections of this introductory chapter, a geological background of the El Laco volcanic complex is provided, followed by a summary of the most relevant previous studies on El Laco and the proposed genetic models. Finally, the objectives and working hypothesis are described, followed by a list of the publications and manuscripts that configure the main three chapters of this thesis. *Chapter 5* summarizes the main conclusions of this research.

1.2. GEOLOGICAL SETTING OF THE EL LACO

The El Laco iron oxide deposit is located in the Central Andes of northern Chile and 200 km eastward of the Cretaceous Chilean iron belt (Fig. 1). Hosted by a Pliocene-Pleistocene andesitic volcanic complex that bears the same name, the El Laco volcanic complex lies in the Chilean Altiplano (23°48′ S, 67°30′ W; Park, 1961; Nyström and Henríquez,1994; Tornos et al., 2017; Ovalle et al., 2018). This zone, formed on an exceptionally thick crust (58–76 km), is part of an extensive volcanic plateau, known as Altiplano-Puna volcanic complex (Fig. 1), which covered unconformably Mesozoic and Cenozoic continental sediments and a Paleozoic basement composed of Ordovician marine sedimentary rocks (Frutos and Oyarzún, 1975).

The El Laco volcanic complex comprises a composite stratovolcano system formed by several emission centers with variable preserved andesitic to dacitic lava flows, pyroclastic rocks, and volcanic breccias. These products range in age from 5.3 ± 1.9 to 1.6 ± 0.5 Ma (Naranjo et al., 2010), and are the result of a complex volcanic history, marked by several stages of extensive explosive and effusive activity, including collapse events, dome extrusions and late stages of intense hydrothermal activity. Stratigraphically, and from oldest to youngest, the major volcanic units are El Laco lower volcanic unit (lower andesites), El Laco upper volcanic unit (upper andesites), late post-ore andesite lava flows, dome-like edifices, and late volcanic breccia bodies that crosscut the older units. The majority (>90%) of the andesitic volcanic rocks are porphyritic, rarely vesicular and contain abundant

plagioclase and pyroxene phenocrysts. Magnetite is also abundant in the andesites, occurring as microphenocrysts within the andesite groundmass, large anhedral crystals (> 1 mm) and forming magnetite-(±apatite)-pyroxene glomerocrysts.

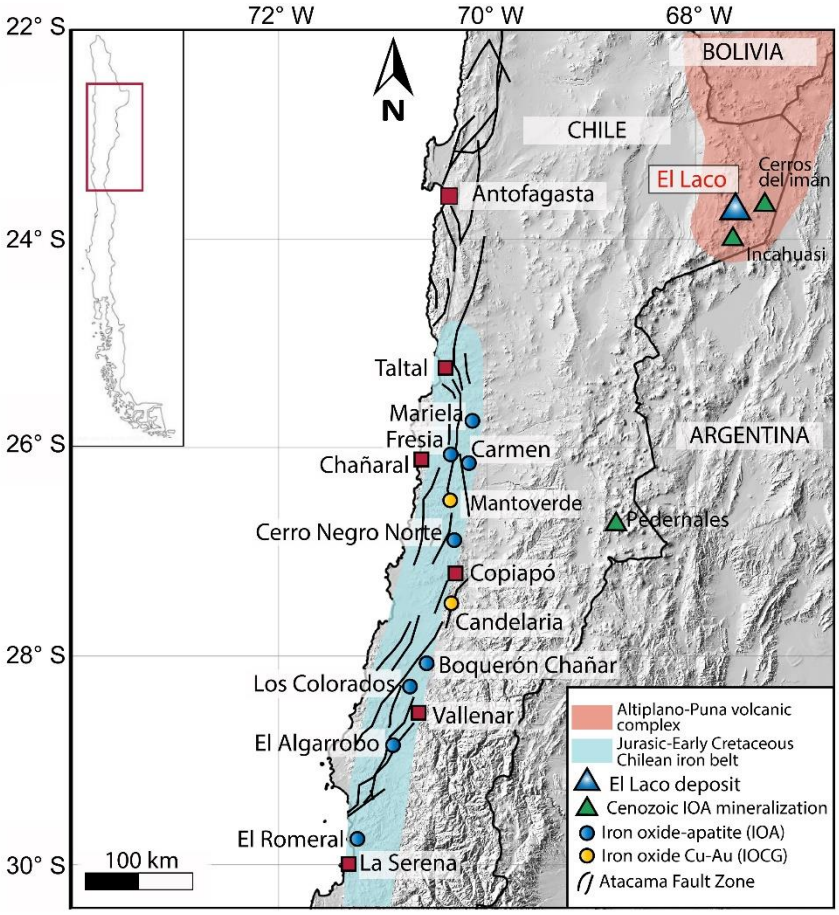

Figure 1: Location of the El Laco iron oxide deposit in the Chilean Altiplano, and other nearby Cenozoic magnetite-apatite deposits. The location of the main iron oxide-apatite (IOA) and iron oxide-cooper-gold (IOCG) deposits within the Early Cretaceous Chilean Iron Belt, is also shown.

The iron oxide mineralization (733.9 Mt at an average ore grade of 49.2% Fe; CAP Minería 2016), on the other hand, were dated at 2.0 ± 0.1 Ma (apatite fission track; Maksaev, 1988), and consists of seven massive magnetite ore bodies emplaced on the flanks of the central volcanic edifice through subvertical annular collapse structures forming secondary craters, breccia pipes and fissures. Mineralogically, the outcropping ore bodies are dominated by highly-oxidized massive magnetite with some levels showing friable iron ore material (Nyström et al., 2016). Vesicular textures as well as vertical degassing conduits and lava-like flow structures are also common in the upper sections of the magnetite ore bodies. As secondary phases, the presence of clinopyroxene, scapolite, apatite, REE phosphates and Fe phosphates are recognized. At depth, ore bodies grade to large breccia bodies and crosscutting veinlet systems (Ovalle et al., 2018). Such breccia bodies consist mainly of variably altered andesite fragments within a magnetite-rich matrix with variable amount of clinopyroxene and scapolite (Naranjo et al., 2010; Ovalle et al., 2018).

Hydrothermal alteration at El Laco is widespread both on surface and depth, and although it appears to be spatially close to the magnetite bodies, there is not always a synchronous relationship between hydrothermal alteration and iron oxide mineralization (Tornos et al., 2017). At the surface, andesitic volcanic rocks surrounding the magnetite bodies are affected by pervasive aureoles consisting of a magnetite-diopside-quartz assemblage (Vivallo et al., 1994; Rhodes et al., 1999), whereas at depth, alkalic-calcic alteration is well-developed, and comprises intense scapolitization and clinopyroxene formation, that partially to pervasively replaced andesitic fragments of the breccia bodies (Naranjo et al., 2010; Ovalle et al., 2018). Widespread andesite bleaching at El Laco is a result of a late argillic alteration, which occurs as extensive steam-heated zones marked by a penetrative replacement of andesites by clays, tridymite, cristobalite, alunite, jarosite, and minor native sulfur, forming silicic vein-like structures and irregular hydrothermal breccia bodies (Vivallo et al., 1994; Sillitoe and Burrows, 2002). Exhalative deposits at El Laco, represented by gypsum-rich mounds, are linked to discrete centers of emission spatially associated with NW-trending collapse structures, which control the recent hot spring-like geothermal activity at the El Laco volcanic complex (Vivallo et al., 1994; Rhodes and Oreskes, 1999).

1.3. PREVIOUS STUDIES AND GENETIC INTERPRETATIONS

As described in the previous section, the El Laco deposit has been extensively studied for over sixty years, with several authors proposing different models to explain its origin. Existing models can be grouped in two "classical" and inherently contrasting views i.e., the *liquid immiscibility model* and the *metasomatic replacement model*:

The liquid immiscibility model

Since the first mention in the literature (Park, 1961), the El Laco massive iron oxide ore bodies were hypothesized as surficial or shallow intrusion of "magnetite lava flows" due to their morphological similarity to aa- and pahoehoe-type vesicular basalt flows. Later, Frutos and Oyarzún (1975) reported the first compositional dataset of magnetite for El Laco deposit, revealing that outcropping ore bodies are composed by low Ti magnetite (i.e., 100 - 200 ppm) as well as low V and Cr concentrations (i.e., 300-400 and 30-100 ppm, respectively), which would be inconsistent with a primary magmatic segregation of an iron oxide melt. Comparisons with chemically similar magnetite from iron-bearing sedimentary formations led to the authors to propose a formation model based on Fe and P remobilization from anatectic melting of marine platform ferruginous-phosphatic sedimentary rocks at depth. Henríquez and Martin (1978) in turn, focused on rapid-growth textures exhibited by magnetite ore bodies at El Laco, which include dendritic, spherulitic and idiomorphic magnetite, and were interpreted as resulting of sudden supersaturation process induced by surface degassing of iron oxide melts. Later, geochronological constraints by Maksaev (1988) pointed to a Plio-Pleistocene age for El Laco ore bodies (2.1 ± 0.1 Ma), based on fission-track dating of co-genetic apatite. The obtained age is comparable with previous K-Ar dating of the andesite lava flows that host the magnetite ore bodies (2.0 ± 0.3 Ma; Gardeweg and Ramírez, 1985), indicating that the formation of the deposit was coeval with the volcanic activity in the zone.

Nyström and Henríquez (1994) and Naslund et al. (2002) presented a comparative geochemical, textural and field study of the magnetite ore bodies from E1 Laco, as well as from other well-preserved IOA deposits from the Chilean Iron Belt, and also from the Kiruna area in Sweden.

The authors interpreted the chemically similar magnetite ores from such deposits, as well as the presence of volcanic-like features, as evidence of a magmatic origin by emplacement of immiscible iron oxide melts at or near the surface. A fluid inclusion study by Broman et al. (1999), revealed the presence of high-temperature (>800 °C) hydrous saline melt inclusions hosted in ore-related pyroxene, and high-salinity aqueous fluid inclusions trapped in apatite at 400-500 °C. These results were interpreted as a record of the existence of ore magmas and magmatic fluids that evolved into hydrothermal fluids of successively lower temperature and salinity.

Later, a study by Naranjo et al. (2010) reported geological information obtained from drill core samples from the Pasos Blancos area, revealing large breccia bodies composed by altered volcanic fragments within a magnetite-clinopyroxene matrix, and associated with intense alkali-calcic alteration. These features were interpreted as formed by an extensive subvolcanic contact-metasomatic process, caused by the shallow-level emplacement of a volatile-rich iron oxide magma.

A detailed microtextural study by Nyström et al. (2016) revealed that magnetite in the pyroclastic-like Fe ores at El Laco occurs as spherules formed by aggregates of octahedral magnetite crystals, which were interpreted as a result of growth from hot magmatic gas in a volcanic plume. Velasco et al. (2016), on the other hand, reported the occurrence of Fe-rich inclusions as well as the presence of clinopyroxene, apatite and anhydrite occurring as daughter crystals within melt inclusions hosted in phenocrysts from the andesite host rocks at El Laco. These observations were interpreted as evidence of immiscible iron oxide melts that separated from a parental andesitic magma, reflecting the low Ti nature and the same mineral assemblage observed in the El Laco ores.

Works by Tornos et al. (2016, 2017) have been mostly centered in providing geological and geochemical information with main emphasis on conventional isotope data. They have reported both stable (e.g., $\delta^{18}O$, $\delta^{34}S$) and radiogenic (e.g., $^{87}Sr/^{86}Sr$ and $^{143}Nd/^{144}Nd$) isotope compositions of different types of rocks that comprise the deposit, including the massive magnetite ore bodies, magnetite veins as well as host andesite rocks. The authors support a genetic model that invokes separation, ascent, and direct crystallization of immiscible iron oxide melts. The iron oxide melts were proposed to have been physically separated from a silicate melt, triggered by assimilation of marine sedimentary rocks.

Mungall et al. (2018) reported mineralogical and chemical data of unconsolidated Fe-P-oxide materials from Laco Sur ore body. They document tephra- and bomb-like material formed dominantly by hematite, Fe-phosphate, monazite, interstitial quartz along with the occurrence of phases of hydrous shoshonitic glass, and intergrowths of Fe-P-REE oxides. The authors interpreted that these assemblages as reflect of immiscible shoshonitic and Fe-P-O melts, whose origin would be undoubtedly magmatic.

Recently, Bain et al. (2021) characterized fluid inclusions hosted in magnetite-bearing diopside-anhydrite veins from the Pasos Blancos ore body. Their results show the presence of polycrystalline fluid inclusions containing dominantly anhydrite and hematite crystals, which was interpreted to represent Fe-rich sulfate melts. Such melts would have originated by assimilation of Fe-bearing sulfate evaporitic rocks which possibly contribute to the separation of an immiscible Fe-rich liquid.

The metasomatic replacement model

A number of other studies have provided both field and geochemical evidence suggesting an origin for El Laco as formed by direct hydrothermal deposition of magnetite from Fe-rich mineralizing fluids. Despite some differences among the proposed models, this hypothesis holds that Fe-rich hydrothermal fluids metasomatically replaced the andesitic host rocks by magnetite, preserving their primary volcanic textures.

Sheets (1997) carried out the first fluid inclusion study on the El Laco deposit, documenting hydrosaline and multiphasic fluid inclusions hosted in clinopyroxene and apatite associated with magnetite. This work revealed a high-temperature (710-870 °C) early metasomatic stage, followed by a lower temperature (280-300 °C) apatite-forming stage, which took place in a hydrothermal regime dominated by boiling aqueous fluids likely sourced from a dioritic pluton at shallow depth.

Studies by Rhodes et al. (1999) and Rhodes and Oreskes (1999) focused on field mapping of the massive ore bodies (including breccia and veinlet zones), with emphasis on their alteration assemblages and textural relationships with the surrounding andesite rocks. Also, they provided chemical and stable isotope data of magnetite, diopside, apatite and quartz. The cited authors proposed that the magnetite-apatite mineralization at El Laco represents a complex and multistep hydrothermal-alteration event, in which andesite lava flows are first replaced by scapolite, followed by Ca-rich pyroxene, and finally by magnetite. The replacing hydrothermal fluids are possibly boiling Fe-rich basinal brines or fluids from nearby saline lakes.

Sillitoe and Burrows (2002) proposed a similar model, where magmatically-derived hot Fe-rich brines replaced the volcanic rocks by magnetite and developed an argillic advanced alteration above the paleowater table. They based their model on a series of field evidence that include the presence of magnetite-veined fragments of altered andesitic volcanic rocks occurring within the Laco Sur ore body, as well as the widespread steam-heated alteration observed at El Laco.

Dare et al. (2015) reported a multi-elemental data set of magnetite from El Laco determined by LA-ICP-MS method. Their results reveal that magnetite from the outcropping ore bodies has a highly depleted geochemical signature in terms of compatible elements (e.g., Cr, Zr, Hf and Sc), which is compositionally consistent with magnetite formed in hydrothermal environments, such as IOCG or porphyry-type deposits. This finding supported the previously proposed hydrothermal models of metasomatic replacement of andesitic volcanic rocks.

1.4. RESEARCH GOALS AND HYPOTHESIS

In light of these previous studies, the aim of this research was to investigate the processes that led to segregation, transport and concentration of iron in the world-class El Laco deposit. This system is an ideal location to investigate how IOA-type mineralization form in continental volcanic settings. In this research I provide a unique dataset obtained from outcrop and drill core samples, which allowed dissecting the now extinct El Laco volcanic system from the surface to the bottom.

The purpose of the research was to constrain, by focusing on magnetite geochemistry, the key ore-forming processes that controlled iron mineralization during the genesis of the El Laco deposit. The research approach involved a combination of field observations, drill core logging, and geochemical and microtextural investigation of magnetite samples. The primary goal of the study was to use magnetite geochemistry to distinguish between purely igneous and magmatic-hydrothermal

signatures, and therefore provide a more comprehensive understanding on how ore-forming processes collectively operate to produce massive IOA-type mineralization in an evolving volcanic system.

In this thesis, the following hypotheses were tested: (1) Andean IOA deposits are formed by a combination of magmatic and hydrothermal processes taking place during the evolution of arc volcanoes; the fingerprints of such processes are recorded in microtextures and the geochemistry of magnetite; (2) Variations in major, minor and trace element content of magnetite, and its associated microtextures, reflect the nature and physicochemical evolution of the mineralizing fluids; these trends correlate with key triggering mechanisms for magnetite precipitation, such as cooling, decompression and boiling; (3) The El Laco iron oxide ore bodies are genetically linked to the magmatic evolution of the hosting El Laco volcanic complex, and were formed during the Plio-Pleistocene as a result of widespread hydrothermal fluid circulation.

1.5. PUBLICATIONS RESULTING FROM THIS RESEARCH

Publications

1. **Ovalle, J.T.,** Cruz, N.L., Reich, M., Barra, F., Simon, A.C., Konecke, B.A., Rodriguez-Mustafa, M.Z., Deditius, A.P., Childress, T.M., and Morata, D. (2018) Formation of massive iron deposits linked to explosive volcanic eruptions. *Scientific Reports*, vol. 8, 14855. **(Chapter 2)**

2. **Ovalle, J.T.,** Reich, M., Barra, F., Simon, A.C., Deditius, A.P., Le Vaillant, M., Neill, O.K., Romero, R., Román, N., La Cruz, N.L., Roberts, M.P., and Morata, D. Magmatic-hydrothermal evolution of the El Laco iron deposit revealed by trace element geochemistry and high-resolution chemical mapping of magnetite assemblages (under review) - *Invited article submitted to Geochimica et Cosmochimica Acta, special issue on "Base, Precious and Critical Metals in Fluid-mineral Interactions"* **(Chapter 3)**

3. **Ovalle, J.T.,** Reich, M., Barra, F., Simon, A.C., Godel, B., Le Vaillant, M., Deditius, A.P., Palma, G., Heuser, G., Arancibia, G., and Morata, D. Fluid-assisted assembly of magnetite microparticles: evidence from the giant El Laco iron oxide deposit, Chile (to be submitted) **(Chapter 4)**

Conference Abstracts

1. **Ovalle, J.T.**, Reich, M., Barra, F., La Cruz, N.L., Simon, A.C. (2018) Origen del depósito de hierro El Laco, Chile: ¿Un resultado de volcanismo explosivo de tipo caldera? XV Chilean Geological Congress, Concepción, Chile, 18-23 November 2018.

2. **Ovalle, J.T.**, La Cruz, N.L., Reich, M., Barra, F., Simon, A.C. (2019) A new magmatic-hydrothermal genetic model for the world-class El Laco magnetite-apatite deposit, northern Chile. PDAC Meeting, Toronto, Canada, 3-6 March 2019.

3. **Ovalle, J.T.**, La Cruz, N.L., Reich, M., Barra, F., Simon, A.C. (2019) Formation of El Laco iron oxide deposit linked to explosive volcanic eruptions. SEG Conference, Santiago, Chile, 7-10 October 2019.

4. **Ovalle, J.T.,** Reich, M., Barra, F., Simon, A.C., Deditius, A.P., Le Vaillant, M., and Morata, D. (2021) Magmatic-hydrothermal evolution of the El Laco iron deposit revealed by trace element geochemistry and high-resolution chemical mapping of ore and gangue minerals. Goldschmidt Conference, Lyon, Francia, July 4–9, 2021.

1.6. OTHER PUBLICATIONS RELATED TO THIS RESEARCH

Publications

1. La Cruz, N.L., **Ovalle, J.T.**, Simon, A.C., Konecke, B.A., Barra, F., Reich, M., Leisen, M., Childress, T.M. (2020) The geochemistry of magnetite and apatite from the El Laco iron oxide – apatite deposit, Chile: Implications for ore genesis. *Economic Geology*, 115 (7): 1461–1491.

2. Childress, T.M., Simon, A.C., Reich, M., Barra, F., Bilenker, L.D., La Cruz, N.L., Bindeman, I.N., **Ovalle, J.T.** (2020) Triple oxygen, hydrogen, and iron stable isotope signatures indicate a silicate magma source and magmatic-hydrothermal genesis for magnetite ore bodies at El Laco, Chile. *Economic Geology*, 115 (7): 1519–1536.

3. Palma, G., Reich, M., Barra, F., **Ovalle, J.T.**, del Real, I., and Simon, A.C. Thermal evolution of Andean Iron Oxide-Apatite (IOA) deposits as revealed by magnetite thermometry. (in press *in Scientific Reports).*

Conference Abstracts

1. La Cruz, N.L., Konecke, B.A., **Ovalle, J.T.**, Childress, T.M., Simon, A.C., Barra, F., Reich. M. (2018) An investigation of the chemistry of magnetite and apatite from the El Laco iron oxide - apatite deposit, Chile. PDAC Meeting, Toronto, Canada, 7 March 2018.

CHAPTER 2: Formation of massive iron deposits linked to explosive volcanic eruptions

J. Tomás Ovalle[1,*], Nikita L. La Cruz[2], Martin Reich[1], Fernando Barra[1], Adam C. Simon[2], Brian Konecke[2], María A. Rodriguez-Mustafa[2], Artur P. Deditius[3], Tristan Childress[2], Diego Morata[1]

[1]*Department of Geology and Andean Geothermal Center of Excellence (CEGA), FCFM, Universidad de Chile, Plaza Ercilla 803, Santiago, Chile*

[2]*Department of Earth and Environmental Sciences, University of Michigan, 1100 North University Avenue, Ann Arbor, MI 48109-1005, USA*

[3]*School of Engineering and Information Technology, Murdoch University, Perth, WA 6150, Australia*

*Corresponding author: José Tomás Ovalle (joseovalle@ug.uchile.cl)

Published in: Scientific Reports

ABSTRACT

The genetic link between magmas and ore deposit formation is well documented by studies of fossil hydrothermal systems associated with magmatic intrusions at depth. However, the role of explosive volcanic processes as active agents of mineralization remains unexplored owing to the fact that metals and volatiles are released into the atmosphere during the eruption of arc volcanoes. Here, we draw on observations of the uniquely preserved El Laco iron deposit in the Central Andes to shed new light on the metallogenic role of explosive volcanism that operates on a global scale. The massive magnetite (Fe_3O_4) ore bodies at El Laco have surface structures remarkably similar to basaltic lava flows, stimulating controversy about their origin. A long-standing debate has endured because all proposed models were constructed based exclusively on samples collected from surface outcrops representing the uppermost and most altered portion of the deposit. We overcome this sampling bias by studying samples retrieved from several drill cores and surface outcrops. Our results reveal complex lithological, textural and geochemical variations characterized by magmatic-like features and, most notably, a systematic increase in titanium concentration of magnetite with depth that account for an evolving system transitioning from purely magmatic to magmatic-hydrothermal conditions. We conclude that El Laco, and similar deposits worldwide, formed by a synergistic combination of common magmatic processes enhanced during the evolution of caldera-related explosive volcanic systems.

2.1. INTRODUCTION

Ore deposits are normally formed by magmatic-hydrothermal processes over a range of depths within the upper crust. However, the role of subaerial volcanic processes in metallogenesis is poorly understood. In fact, volcanic eruptions preclude the formation of mineral deposits near the surface because metals and volatiles are vented during explosive events[1]. Here, we provide new evidence that supports subaerial volcanic eruptions in magmatic arcs as a viable process for the accumulation of metals at or near the surface by focusing on the world class El Laco iron deposit in the Central Andes.

The El Laco volcanic complex (ELVC) hosts world class magnetite (Fe_3O_4) deposits with remarkable volcanic and subvolcanic features. The ELVC, formed on an exceptionally thick crust (58-76 km)[2], is located at southeast margin of one of the Earth's most extensive volcanic plateaus, built during the late Miocene by an ignimbrite flare-up (Altiplano-Puna volcanic complex, APVC)[3]. In adittion, it is spatially associated with the NW–SE trending Calama–Olacapato–El Toro (COT) lineament, which is responsible for the alignment of Neogene-Quaternary volcanic activity in the region[4] (Fig. 2a). The ELVC is the product of a complex volcanic history developed from the Miocene to Pleistocene, punctuated by several volcanic events including explosive eruptions leading to stratovolcano collapse, resurgent volcanic activity, fissural emissions and late stages of intense hydrothermal activity[5-7]. These events resulted in a cluster of andesitic to dacitic volcanic structures comprising numerous NW-trending fissural emission centers and secondary craters associated with ring-shaped structures around Pico Laco. This volcanic products range in age from 5.3 ± 1.9 to 1.6 ± 0.5 Ma[7], whose structures mark the position of a collapsed ancient crater, whose resurgent magmatic activity formed Pico Laco[5].

The world-class El Laco iron deposit in the ELVC consists of six massive magnetite ore bodies that are spatially associated with the pre-existing subvertical annular collapse structures and secondary craters that form a NW-trending ellipse around Pico Laco[5,7] (Fig. 2b). Total estimated resources are 733.9 Mt at an average ore grade of 49.2 % Fe[8]. The ore bodies are interbedded between andesitic to dacitic lava flows and pyroclastic rocks, displaying different morphologies such as lava-like flows (Laco Norte, Laco Sur, and San Vicente Alto), NW-trending tabular bodies (Rodados Negros and Cristales Grandes) and dome-shaped bodies (San Vicente Bajo)[9]. The ore bodies are largely composed of magnetite with minor diopside, scapolite, apatite, REE-rich phosphates and iron phosphates, and hematite-goethite alteration formed by supergene oxidation of original magnetite.

2.2. RESULTS

2.2.1. Depth-dependent textures and geochemical gradients of magnetite

Investigation of surface and drill core samples revealed a complex lithological, textural and geochemical zoning for magnetite from the Laco Norte, Laco Sur, and Extensión Laco Sur ore bodies (Fig. 2b, and Supp. Mat. Figs. A2, A3 & A4). All magnetite ore bodies have a similar structure with massive magnetite characterized by lava-like textures up to intermediate depths (~80-90 m), followed by magnetite breccias that can extend to depths above 200 m (Fig. 3 and Supp. Mat. Figs. A2, A3, A4 & A5). Based on lithological and mineralogical characteristics, the Laco Norte ore body was divided into three main zones: shallow/surface, intermediate, and deep zones (Fig. 3). Within these zones, different types of magnetite were identified based on microtextural and geochemical criteria. EPMA analyses reveal significant surface-to-depth variations in magnetite composition (Figs. 3 & 4

a, b; Supp. Mat. Annex A, Table A6). Particularly, Ti, V, Al, and Mn concentrations in magnetite increase progressively with depth (Fig. 4b).

The shallow/surface zone (0-65 m) comprises the main part of the massive magnetite body, including its outcropping portion (Fig. 3a and Supp. Mat Fig. A2, A3 & A4). Mineralogically, it is composed of >90% modal magnetite with minor diopside and scarce apatite. The zone displays a vesicular texture, which is more common at shallower levels. Euhedral magnetite crystals cover the walls of large vesicles. Magnetite in the outcropping body is coarse-grained (Magnetite-S, >500 µm size) and shows a high degree of alteration to hematite and goethite (Fig. 3a). Iron phosphates and inclusions of monazite and thorium silicate occur in magnetite from the upper levels, particularly at grain rims, or filling both fractures and vesicles. BSE images show that Magnetite-S is characterized by abundant microporosity and pervasive replacement by hematite and goethite mostly along grain boundaries, fractures, and pores (Fig. 3a). These magnetite grains display a large compositional variability with average concentrations for Mg and Si (7522 and 4650 ppm, respectively), and low V (586 ppm) and Ti (218 ppm) contents.

At depths between ~30-65 m, the Fe-oxide mineralogy is dominated by Magnetite-Z, which is a weakly to moderately oxidized magnetite characterized by hematite formation along rims or through fractures (Fig. 3b). Late gypsum veinlets crosscut and fill open spaces in massive Magnetite-Z down to ~45 m. At depths between 40 and 65 m, Magnetite-Z forms aggregates of pristine, mostly euhedral crystals, ranging in size from ~10 to 120 µm. Magnetite-Z has a relatively high Mg content (average 7203 ppm) and is depleted in Si, Ca and Al (Appendix 1, Supp. Material); Ti and V concentrations average 1236 and 1861 ppm, respectively.

The intermediate zone (~65-145 m) is characterized by a transition from the shallow massive magnetite to a magnetite breccia body (Fig. 3). A massive magnetite level is present at ~65 m, which contains abundant coarse-grained euhedral diopside grains that vary in size from a few tens of micrometers to a few millimeters, immersed in a texturally diverse magnetite matrix (Fig. 3c). Magnetite in this diopside-rich zone displays two distinct textures. Magnetite-X occurs as pristine microcrystalline cores with grain sizes approximately 500 µm. It is replaced by Magnetite-Y via dissolution-reprecipitation processes (Fig. 3c). Magnetite-Y overgrowths Magnetite-X and is characterized by oscillatory textures, i.e., alternating inclusion-rich (trace element enriched) and inclusion-poor (trace element depleted) bands (Fig. 3c). The thickness of the individual bands varies between ~4 to 100 µm, whereas the inclusion sizes vary from 10's to 100's of nanometers to a few micrometers. This leads to significant compositional variability between Magnetite-X and –Y, about a few wt. % for Si and Mg, and 1000's ppm for Al, Ti, and Ca. Titanium-bearing silicate inclusions in Magnetite-Y increase the Ti concentration of these grains, reaching average contents of up to 3380 ppm, while Magnetite-X has lower Ti contents (2359 ppm). However, the average concentration of V is similar in both types (1802 and 1803 ppm for Magnetite-X and Magnetite-Y, respectively). A pyrite-rich magnetite zone associated with late gypsum veinlets occurs at 144 m depth. It is dominated by magnetite grains (Magnetite-γ), formed as overgrowths on inclusion-rich relict cores of magnetite-β (Fig. 3d). Magnetite-γ has a low Ti (average = 1232 ppm) and high V (average = 2547 ppm) concentrations.

The deep zone (~150-200 m) comprises a breccia body with andesite fragments replaced by fine-grained diopside within a magnetite-diopside matrix. Two types of magnetite grains are identified at different depths: Magnetite-β (152.0 m; Fig. 3e) and Magnetite-α (188.05 m; Fig. 3f). Both have similar compositions, but different textures. Magnetite-β occurs commonly as coarse-grained euhedral crystals that contain inclusion-rich cores surrounded by inclusion-free rims (Magnetite-β1;

Fig. 3e). A third (late) generation of smaller anhedral magnetite crystals (Magnetite-β2) associated with gypsum veinlets occurs at the outer rim of the inclusion-free magnetite (Fig. 3e). The Ti and V concentrations for Magnetite-β are high (average of 6144 and 2578 ppm, respectively), and similar to Magnetite-β1 (average Ti = 5970 ppm; V = 2583 ppm). In contrast, Magnetite- β2 has the lowest Ti and V contents (610 and 100 ppm, respectively). Magnetite-α forms an aggregate of titanomagnetite crystals, ~100-300 µm in size, with well-developed ilmenite exsolution lamellae and oxidation zones along grain rims and in fractures (Fig. 3f). EPMA data revealed that Magnetite-α contains the highest average contents of Ti and V at El Laco (7637 and 2631 ppm, respectively).

2.3. DISCUSSIONS

The trace element geochemistry of magnetite and its genetic interpretation have been extensively explored in a variety of mineralized systems[10,11]. These studies have used compositional differences of Al, Mn, Ti, and V in magnetite to construct discrimination diagrams that are used to differentiate between various styles of mineralization. Magnetite from surface and drill core samples at El Laco forms two distinct populations in a [Al+Mn] versus [Ti+V] diagram[11] (Fig. 4a). This plot illustrates the distinctive trend from high-temperature magnetite that progressively grades towards lower-temperature, hydrothermal compositions. The drill core data (blue circles) show a distinctive trend from igneous signatures at depth, to hydrothermal compositions towards the surface. The majority of the drill core data plot within the *Porphyry* field, which comprises magnetite crystallized from moderate- to high-temperature magmatic-hydrothermal fluids. Magnetite from the deepest drill core samples from Laco Norte and Laco Sur plot within the magmatic *Fe-Ti, V* field; i.e., their chemistry is consistent with that for magnetite that crystallized from a silicate melt[11]. On the other hand, surface samples (yellow circles) show a large dispersion, plotting in almost all fields except the magmatic field. Most surface data points plot towards low [Ti+V]; i.e., lower temperature conditions, particularly within the *IOCG-*, *BIF* fields, and even beyond the boundaries for these fields (Fig. 4a). These compositions are characteristic of growing magnetite from moderate to low-T hydrothermal fluids or magnetite that has been chemically re-equilibrated by lower temperature fluids after mineralization[11].

Figure 4b depicts the geochemical signature of the different magnetite generations identified at different depths in the drill core samples. Consistently, the deep zone magnetite grains from both Laco Norte (e.g., Magnetite-α and -β, Fig. 3e-f) and Laco Sur, extend from the purely magmatic *Fe-Ti, V* field to the *Porphyry* field (Fig. 4b). These magnetites have the highest content of Ti (up to 5.86 wt. % and average of 7082 ppm), V (up to 3900 ppm and average of 2246 ppm) and Al (up to 8200 ppm and average of 3746 ppm). The magmatic affinity of Magnetite-α is further confirmed by the well-developed ilmenite exsolution lamellae observed in these grains (Fig. 3f), which are typical of Ti-rich magnetite or titanomagnetite in magmatic Fe-Ti oxide deposits and accessory Fe-Ti oxides in igneous rocks[12-14]. Magnetite grains from intermediate depths, i.e., Magnetite-X and –Y, plot in the upper part of *Porphyry* field (Fig. 4b). Magnetite-X and –Y are more depleted in Ti and V relative to the early-crystallized Magnetite-α and –β, and configure a descending temperature trend that suggests crystallization from an evolving magmatic-hydrothermal aqueous fluid at high-temperature conditions; i.e., >500 ºC[11]. Chemical variations and microtextural relationships between Magnetite-X and –Y indicate that dissolution-reprecipitation processes played an important role during magnetite growth[15,16], resulting in precipitation of Magnetite-Y with crystallographically-controlled alternating inclusion-rich/inclusion-poor bands from a fluctuating composition hydrothermal fluid[17], leading to an increasing in the trace element concentrations in certain zones (arrow in Fig. 4b).

Magnetite grains from the upper zones are depleted in trace elements and pristine when compared with magnetite from deeper levels. They plot along the decreasing temperature trend from the lower part of the *Porphyry* field to *Kiruna* field (Fig. 4b). It is likely that Magnetite-Z has chemically equilibrated with the Fe-rich ore fluid, as evidenced by the lack of detectable porosity (Fig. 3b)[15], and homogeneous distribution of lower amounts of Al, Si, Ca, Ti and V in comparison with magnetite types -α, -β, -X and –Y; these observations are consistent with published data for surface samples[18]. Magnetite-S, representative of the Laco Norte surface samples, marks the end of the cooling trend (Fig. 4b), and its geochemical signature is consistent with published data[19].

2.3.1. The optimal pathways for iron enrichment

Our roots-to-surface study of the El Laco deposit reveals that El Laco is the product of a synergistic amalgamation of the following common igneous and magmatic-hydrothermal processes, which were enhanced during the evolution of a collapsing volcanic system (Fig. 5):

1. *Igneous magnetite segregation:*

Magnetite, clinopyroxene and plagioclase crystallized within the andesitic magma chamber beneath the ELVC as the dominant liquidus phases. Crystallization of these phases is consistent with the presence of disseminated magnetite in the hosting clinopyroxene-bearing andesites, as well as experimental phase equilibria studies of mafic to intermediate silicate magmas[20]. Dense magmatic phases such as magnetite are expected to undergo efficient gravitational settling in magma reservoirs, and form layers, cumulates, and/or disseminations (Fig. 5a)[21,22]. These primary magnetite grains correspond to those identified in the deep zone at El Laco (Fig. 3; Magnetite-α and Magnetite-β). Magnetite-α is characterized by well-developed ilmenite exsolution lamellae, a feature also found in accessory magnetite from andesites and dacites from El Laco and Lascar volcano[19], respectively.

2. *Injection of mafic magma:*

The magnetite accumulation became more efficient due to multiple events of recharge, marked by the injection of pulses of mafic magma into the ELVC hydrous andesitic magma chamber. Such processes have been documented in neighboring volcanoes[23,24], and particularly at El Laco, where observations of plagioclase-hosted melt inclusions, sieve-textured plagioclase, and chemical disequilibrium between phenocrysts and rhyodacitic groundmass from the host rock andesites, have been interpreted as reflecting mingling between felsic and mafic melts[25,26]. Open-system processes are considered an important mechanism for the upward transfer of energy and mass during magma underplating and recharge, and they can significantly contribute to both thermal rejuvenation and enrichment of transition metals and sulfur of overlying magma[27,28]. A key factor that can lead to an increase in the magnetite budget of a magma reservoir involves the injection of a crystal-bearing vapor-saturated mafic magma that intrudes into the base of an evolved crystal-rich magma chamber, wherein microlite to nanolite-sized magnetite grains and exsolved volatiles (i.e., bubbles of supercritical fluid) may be transferred, by heterogeneous nucleation processes, from the mafic intrusion into the overlying andesitic reservoir, when mixing or juxtaposition of both chemically distinct magma batches occurs (Fig. 5a)[21,22]. This mechanism has been proposed to explain the presence of magnetite-rich enclaves in arc andesites[21]. In addition, it is well known that the bubble nucleation mechanism in magmas is a predominantly heterogeneous process[29,30] where Fe-Ti oxides are considered the only viable crystalline phases that significantly impact bubble nucleation behavior in magmas. Fe-Ti oxides provide energetically favorable sites to reduce surface energy, and decrease the supersaturation

pressure required for heterogeneous nucleation[30-33]. Primary magnetite, wetted and floated by exsolved fluid bubbles within underplating and intruding mafic magma, may correspond to early-crystallized Fe-Ti oxides, fractionated from the mafic magma during its ascent through the arc crust[34-37].

The buoyant magnetite-bubble aggregates[33] that ascend through the mafic magma will form a magnetite-bearing, bubble-rich suspension at the interface between the intruding mafic magma and the overlying andesitic reservoir[21,38] (Fig. 5a). The cited authors[38] noted that the suspension layer can be transferred into the more viscous felsic magma at high gas fluxes in the mafic magma and at high viscosity ratios between both melts. In turn, if the mafic magma intrusion occurred at high injection rates, it could mix with the overlying silicic reservoir and remobilize upwards its crystal charge accumulated in the base of the magma chamber; a process consistent with numerical modeling results[39]. Hence, this mechanism would have efficiently raised the magnetite-rich cumulates from the base of the magma chamber, enhancing nucleation of exsolved fluid bubbles on remobilized magnetite crystals in suspension.

3. *Collapse of the volcanic edifice and remobilization of coalesced magnetite suspensions:*

The injection of a less evolved magma from deeper zones triggers rapid depressurization and volatile release, as commonly documented prior to explosive eruptions and collapse events[23,40-43]. At El Laco, it is well established that the ELVC morphology shows clear evidence of caldera-type collapse episodes during its volcanic history[5,26]. We argue that the collapse of the volcanic edifice played a critical role by promoting additional depressurization-derived bubble exsolution and their preferential heterogeneous nucleation on magnetite[29,30]. We propose that piston-like forces related to the collapse of the volcanic edifice promoted the efficient lateral/vertical remobilization of both a settled magnetite-rich crystal mush[41], and coalesced magnetite-rich suspensions through pre-existing ring-shaped fissures and craters[44] that form a NW-trending ellipse around Pico Laco (Figs. 2b & 5). The hydraulic injection of the accumulated magnetite and magnetite-suspension resulted in the formation of large volcanic and hydrothermal breccia bodies at depth below the ELVC (Figs. 3, 5c and Supp. Mat. Figs. A2, A3 & A4). Field observations are consistent with a Plate/Piston or Piecemeal-type collapse style[45] induced by tectonically controlled faults, which fracture the caldera or volcanic edifice floor into numerous blocks prior to eruption[46]. Therefore, we suggest that the regional NW-trending Calama–Olacapato–El Toro structural lineament could have played an important role during the collapse stage.

4. *Venting of Fe-rich hydrothermal fluids:*

During its upward migration from the magma source, the fluid component of the magnetite-bubble suspension efficiently scavenged Cl, Fe and other metals from the silicate melt[47,48]. Igneous magnetite (Magnetite-α) grains ascended in contact with the high-temperature magmatic-hydrothermal fluid from which hydrothermal magnetite precipitated over primary magnetite during cooling and decompression (Figs. 3 & 4a,b)[49-51]. High rates of magnetite nucleation and low growth rates dominated during the final ascent of the decompressing, magnetite-fluid suspension towards the surface. We argue that this Fe-rich multiphase mixture (magnetite+fluid+gas), cooled at surface temperatures, degassed extensively and sustained a rheological behavior leading to lava-like textures characteristic of the El Laco surface outcrops (Supp. Mat. Fig. A5). Evidence from numerical, experimental and empirical studies of industrial froth flotation processes shows that mineral-fluid-bubble aggregates have rheological properties similar to basaltic lava flows, i.e., both display Bingham-type behavior and exhibit similar yield stress/strength that decrease the resistance to flow[52-

[54]. Fluid circulation in the waning hydrothermal system or a late superimposed hydrothermal event is evidenced by the presence of sulfides-bearing magnetite-diopside-scapolite and late gypsum-magnetite-pyrite veinlets, which crosscut the main breccia bodies at depth (Fig. 5d), and the advanced argillic alteration at the surface[6].

2.3.2. Implications for iron metallogenesis in collapsing volcanic systems

The new mineralogical, geochemical and field evidence discussed here do not support a metasomatic replacement or a liquid immiscibility model for El Laco. The metasomatic replacement hypothesis[6,18,55] is based on field observations and geochemical data of magnetite from surface samples and although our own field observations and magnetite geochemical data from surface or near surface samples (e.g., Magnetite-Z and Magnetite-S) reflect a hydrothermal origin, magnetite from the deeper roots of El Laco is unequivocally consistent with primary magmatic compositions. The depth-dependent magmatic to magmatic-hydrothermal geochemical gradients reported in this study, as well as reported magnetite Fe-O stable isotope data[56], are consistent with magnetite crystallized both from a silicate melt and magmatic-hydrothermal fluid[56-57], precluding complete metasomatic replacement or assimilation of ferruginous sedimentary rocks[5]. On the other hand, the models that invoke shallow emplacement of iron rich melts for El Laco formation[5,7,9,25,26,58-61] are even more difficult to reconcile. These are based on field observations of "volcanic-like" textures in magnetite ore bodies and liquid immiscibility experiments[62,63], which have been critically reviewed[51,64]. The experimentally constrained $\Delta^{18}O$, defined as $\delta^{18}O_{Si\text{-}rich\text{-}melt} - \delta^{18}O_{Fe\text{-}rich\text{-}melt}$, values of 0.0 to 0.5‰[65] at magmatic temperatures disallow liquid immiscibility to explain El Laco. Published $\delta^{18}O$ values for magnetite from El Laco range from 3.5–5.5‰[58] compared with $\delta^{18}O$ values of 7 to 9‰ for silicate magmas at El Laco that would represent the conjugate Si-rich melt; the $\delta^{18}O$ for magnetite from El Laco is entirely consistent with magnetite crystallized from silicate melt or high-temperature hydrothermal fluid[56].Most importantly, recent experimental data show that during liquid immiscibility water partitions preferentially into the Si-rich melt and not into the conjugate Fe-rich melt[61], precluding its separation and ascent from a less dense high-Si conjugate melt[26].

In summary, we argue that the major features observed at El Laco are consistent with a formation model, wherein iron oxide bodies form as result of an optimal confluence of common subaerial volcanic processes occurring during the evolution of arc volcanoes, characterized by early magmatic and late magmatic-hydrothermal stages, marked by near-liquidus magnetite crystallization and periodic injections of crystal-bearing vapor-saturated mafic magma that trigger decompression and volatile exsolution. The efficient remobilization of magnetite-rich cumulates by the fluid-bubble-assisted flotation mechanism (e.g., heterogeneous nucleation) allows for the formation of a magnetite-fluid suspension that ascends from the magma chamber and is subsequently injected upward through collapse-related fissures and secondary craters on the flanks of a stratovolcano. This sequence of events results in venting of a multiphase mixture of magnetite crystals, silicate melt, fluid and gas that forms massive ore bodies and breccias at depth, and Fe-rich lava-like flows and pyroclastic deposits at the surface.

We drew on observations of modern arc volcanoes to invoke a magmatic-hydrothermal origin for this deposit, resulting from common igneous and hydrothermal processes operating in volcanic systems. Several occurrences of Fe oxide ores have been described in volcanic terrains around the world, although this evidence has been overlooked for decades. Intriguingly, numerous Fe oxide bodies are spatially associated with silicic volcanic rocks derived from explosive eruptions often in caldera-type

volcanic environments. These occurrences include Fe deposits in Mexico[66,67], Nevada[68], Chile[69], Argentina[70], South Africa[71], Iran[72], and China[73], and Fe-rich fumarolic structures in volcanic fields in Alaska[74,75], Arizona[76], Indonesia[77] and Central America[78-80]. Some of these deposits display similar structural and textural features to those described at El Laco. These include dike- and vein-like Fe oxide bodies, as well as unique volcanic-like features such as lava-like Fe-oxide flows and scoriaceous unconsolidated Fe-oxide ash, remarkably similar to the friable ore previously described at El Laco[59,60], and even Fe-oxide-bearing high-temperature fumarolic structures[66,74].

Exceptional examples of magnetite precipitation from post-volcanic fumarolic activity associated with the Novarupta-Katmai eruption of 1912 were reported at the Valley of Ten Thousand Smokes in Alaska, which is considered the world's most voluminous volcanic eruption of the 20th century, with more than ~28 km^3 of emitted silicic volcanic material[75]. Post-volcanic high-temperature fissural fumaroles developed through ignimbrites and ash-flow sheets were reported to contain abundant loosely coherent octahedral, fine-grained magnetite[74,75], similar to the octahedral magnetite crystals that cover the gas-escape chimney walls observed at Laco Sur and San Vicente Alto (Supp. Mat. Fig. A5). We support the notion that the occurrence of magnetite as pyroclastic friable material and as incrustations in high-temperature fumaroles indicate that the ascending magnetite-fluid suspension responsible for Fe transport and precipitation of magnetite, could undergo phase separation and fragmentation processes during ascent. We interpret that during ascent, the coalesced magnetite-fluid suspension could behave as an ascending magma prior to eruption. The magnetite-fluid suspension consists of large amounts of coalesced bubbles of compressible magmatic volatiles. Thus, owing to decompression, rapid expansion of the coalesced bubble populations plus some residual melt[60] may trigger the break-up of the Fe-rich suspension. The individual fragments of Fe-rich material could be ejected into the atmosphere during explosive volcanic eruptions, forming pyroclast-like unconsolidated magnetite aggregates, and resulting in the rapid growth of spherulitic magnetite agglomerates. Examples include El Laco and other iron oxide-apatite deposits from Durango and Chihuahua districts in Mexico, and magnetite-rich fumaroles such as those in the Valley of Ten Thousand Smokes[59,66,74].

Based on the global spatial and temporal distribution of iron oxide-apatite deposits[81], it is likely that the conditions of maximum efficiency for Fe enrichment will be attained in more immature arcs such as the world-class Chilean Cretaceous Iron Belt, where the crust was thinner and mafic magma fluxes were more frequent. Nevertheless, iron deposits formed in a thick crust environment and associated with more evolved magmatism, such as the pristinely preserved El Laco in the arid high Andes, may be more frequent than previously thought and exploration efforts should be set on targeting caldera-type systems in active and fossil magmatic arcs.

2.4. SAMPLES AND METHODS

Our study combined field observations and drill core logging with detailed microtextural observations and elemental micro-analysis of magnetite. We retrieved 159 samples from seven drill cores at several depths from Laco Norte, Laco Sur, Extención Laco Sur and Pasos Blancos (Fig. 2b). In addition, 39 samples were obtained from 5 outcropping massive magnetite ore bodies (Laco Norte, Laco Sur, San Vicente Alto, Rodados Negros and Cristales Grandes). Drilling was performed by Compañía Minera del Pacífico (CMP) during an exploration program between 2007 -2010.

In order to identify the textural variability of the magnetite grains from depth to surface, forty seven representative samples were selected for be inspected and imaged by using a JEOL 7800FLV field

emission-scanning electron microscope (FE-SEM) at the University of Michigan and a Model FEI Quanta 250 SEM at Universidad de Chile. Additionally, to comprehensively characterize the chemical variability of the different magnetite types throughout the deposit and at depth, 1912 electron probe microanalyses (EPMA) were obtained by using a Cameca SX-100 at the University of Michigan, USA (Electron Microbeam Analysis Laboratory, EMAL). Magnesium, Al, Si, Ca, P, Ti, V, Cr, Mn and Fe were analyzed in magnetite grains, and interference corrections were carried out for Ti concentrations since V Kβ affects the Ti Kα signal. The operating conditions employed were an accelerating voltage of 20 keV and a focused beam to avoid measuring inclusions or ilmenite exsolution lamellae in magnetite. The beam current was set to 30 nA. A counting time of 20 s was used for Fe, while counting times of 100 s (Ca, Cr, Mn), 110 s (Si, P, Mg, Al) and 120 s (Ti, V) were used for minor and trace elements. A variety of natural and synthetic oxides and silicates were used as primary standards for each element. The standards, as well as the EPMA analytical conditions used are summarized in Supplementary Material (Supplementary Table 1). The database of magnetite mineral chemistry is provided as Excel file in Supplementary Material (Annex A, Table A6). The measurements that yield values below detection limit are listed in Appendix _1 as "b.d". However, to build the [Al+Mn] versus [Ti+V] diagram, such below detection limit values, were replaced by the half of the corresponding detection limits.

2.5. REFERENCES

1. Pasteris, J.D. Mount Pinatubo volcano and 'negative' porphyry copper deposits. *Geology* **24**, 1075-1078 (1996).

2. McGlashan, N., Brown, L. & Kay, S. Crustal thickness in the central Andes from teleseismically recorded depth phase precursors. *Geophys. J. Int.* **175**, 1013-1022 (2008).

3. de Silva S. L. Altiplano-Puna volcanic complex of the central Andes. *Geology* **17**, 1102-1106 (1989).

4. Norini, G. *et al.* The Calama–Olacapato–El Toro fault system in the Puna Plateau, Central Andes: Geodynamic implications and stratovolcanoes emplacement. *Tectonophysics* **608**, 1280-1297 (2013).

5. Frutos, J. & Oyarzún, M., J. Tectonic and geochemical evidence concerning the genesis of El Laco magnetite lava flow deposits, Chile. *Econ. Geol.* **70**, 988-990 (1975).

6. Sillitoe, R.H., & Burrows, D. R. New field evidence bearing on the origin of the El Laco magnetite deposit, northern Chile. *Econ. Geol*. **97**, 1101-1109 (2002).

7. Naranjo, J. A., Henríquez, F., & Nyström, J. O. Subvolcanic contact metasomatism at El Laco Volcanic Complex, Central Andes. *Andean Geology*, **37**, 110-120 (2010).

8. CAP Minería Annual Report: http://www.capmineria.cl/wp-content/uploads/2017/03/cap_mineria_memoria_2016.pdf (2016).

9. Nyström, J. O. & Henriquez, F. Magmatic features of iron ores of the Kiruna type in Chile and Sweden; ore textures and magnetite geochemistry. *Econ. Geol.* **89,** 820–839 (1994).

10. Dupuis C. & Beaudoin G. Discriminant diagrams for iron oxide trace element fingerprinting of mineral deposit types. *Miner. Deposita* **46**, 319-335 (2011).

11. Nadoll, P., Angerer, T., Mauk, J. L., French, D. & Walshe, J. The chemistry of hydrothermal magnetite: a review. *Ore. Geol. Rev.* **61**, 1-32 (2014).

12. Frost, B. R. & Lindsley, D. H. Occurrence of Iron-Titanium Oxides in Igneous Rocks, in *Oxide Minerals: Petrologic and Magnetic Significance* (ed. Lindsley, D. H) 433-462 (Blacksburg, 1991).

13. Mücke, A. Magnetite, ilmenite and ulvite in rocks and ore deposits: petrography, microprobe analyses and genetic implications. *Miner. Petrol.* **77**, 215-234 (2003).

14. Tan, W., Peng, L., He, H., Wang, C. Y. & Liang, X. Mineralogy and origin of exsolution in Ti-rich magnetite from different magmatic Fe-Ti oxide-bearing intrusions. *The Can. Miner.* **54**, 539-553 (2016).

15. Putnis, A. Mineral replacement reactions. *Rev. Mineral. Geochem.* **70**, 87-124 (2009).

16. Hu, H. *et al.* Dissolution–reprecipitation process of magnetite from the Chengchao iron deposit: Insights into ore genesis and implication for in-situ chemical analysis of magnetite. *Ore Geol. Rev.* **57,** 393-405 (2014).

17. Deditius, A. P. *et al*. Nanogeochemistry of hydrothermal magnetite *Am. Mineral.* **173**, 46 (2018).

18. Dare, S. A. S., Barnes, S. J. & Beaudoin, G. Did the massive magnetite "lava flows" of El Laco (Chile) form by magmatic or hydrothermal processes? New constraints from magnetite composition by LA-ICP-MS. *Miner. Deposita* **50**, 607-617 (2015).

19. Broughm, S. G., Hanchar, J. M., Tornos, F., Westhues, A. & Attersley, S. Mineral chemistry of magnetite from magnetite-apatite mineralization and their host rocks: examples from Kiruna, Sweden, and El Laco, Chile. *Miner. Deposita* **53**, 1223-1244 (2017).

20. Martel, C., Pichavant, M., Holtz, F. & Scaillet, B. Effects of fO_2 and H_2O on andesite phase relations between 2 and 4 kbar: *J. Geoph. Res.* **104**, 29453-29470 (1999).

21. Edmonds, M., Brett, A., Herd, R. A., Humphreys, M. C. S. & Woods, A. Magnetite-bubble aggregates at mixing interfaces in andesite magma bodies. *Geological Society, London, Special Publications* **410**, 95–121 (2014).

22. Edmonds, M. Flotation of magmatic minerals. M. Research Focus: *Geology* **43**, 655–656 (2015).

23. Matthews, S., Sparks, R. S. J. & Gardeweg, M. C. The relationships between magma mixing and volatile behaviour at Láscar Volcano (23 22'S-67 44'W), northern Chile: Significance for the formation of copper sulphide and magnetite-apatite orebodies. Giant ore deposits II: Ontario, Queen's University, 146-181 (1995).

24. Matthews, S. J., Sparks, R. S. J. & Gardeweg, M. C. The Piedras Grandes–Soncor Eruptions, Lascar Volcano, Chile; Evolution of a Zoned Magma Chamber in the Central Andean Upper Crust. *J. Petrol.* **40**, 1891-1919 (1999).

25. Velasco, F., Tornos, F. & Hanchar, J. Immiscible iron- and silica-rich melts and magnetite geochemistry at the El Laco volcano (northern Chile): Evidence for a magmatic origin for the magnetite deposits. *Ore Geol. Rev.* **79**, 346–366 (2016).

26. Tornos F., Velasco F. & Hanchar J. M. The Magmatic to Magmatic-Hydrothermal Evolution of the El Laco Deposit (Chile) and Its Implications for the Genesis of Magnetite-Apatite Deposits. *Econ. Geol*, **112**, 1595–1628 (2017).

27. Mungall, J. E., Brenan, J. M., Godel, B., Barnes, S., & Gaillard, F. Transport of metals and sulphur in magmas by flotation of sulphide melt on vapour bubbles. *Nat. Geosci.*, **8**, 216–219 (2015).

28. Cashman, C. V., Sparks. R. J. S. & Blundy, J. D.Vertically extensive and unstable magmatic systems: A unified view of igneous processes. *Science*, **355**, Issue 6331, (2017) DOI: 10.1126/science.aag3055.

29. Knipping, J. L. *et al*. Flotation of magnetite crystals upon decompression – A formation model for Kiruna-type iron oxide-apatite deposits. In AGU Fall Meeting, New Orleans (2017). Available at: https://agu.confex.com/agu/fm17/meetingapp.cgi/Paper/209418

30. Shea, T. Bubble nucleation in magmas: A dominantly heterogeneous process? *J. Volcan. Geotherm. Res.* **343,** 155-170 (2017).

31. Hurwitz, S. & Navon, O. Bubble nucleation in rhyolitic melts: Experiments at high pressure, temperature, and water content. *Earth Planet. Sci. Let.* **122**, 267–280 (1994).

32. Gardner, J. E., & Denis, M. -H. Heterogeneous bubble nucleation on Fe-Ti oxide crystals in high-silica rhyolitic melts: *Geochim. Cosmochim. Acta*, **68**, 3587–3597 (2004).

33. Gualda, G. A. R. & Ghiorso, M. S. Magnetite scavenging and the buoyancy of bubbles in magmas. Part 2: Energetics of crystal-bubble attachment in magmas. *Contrib. Miner. Petrol.* **154,** 479-490 (2007).

34. Grove, T. L., Gerlach, D. C., Sando, T. W. & Baker, M. B. Origin of calc-alkaline series lavas at Medicine Lake volcano by fractionation, assimilation and mixing: Corrections and clarifications. *Contrib. Miner. Petrol.* **82,** 407-408 (1982).

35. Sisson, T. W. & Grove, T. L. Experimental investigation of the role of H_2O in calc-alkaline differentiation and subduction zone magmatism. *Contrib Miner. Petrol.* 113, 143-166 (1993).

36. Davidson, J. P., Turner, S., Handley, H., Macpherson, C. G. & Dosseto, A. Amphibole "sponge" in arc crust? *Geology* **35**, 787-790 (2007).

37. Zhang, J., Davidson, J. P., Humphreys, M. C. S., Macpherson, C. G. & Neill, I. Magmatic Enclaves and Andesitic Lavas from Mt. Lamington, Papua New Guinea: Implications for Recycling of Earlier-fractionated Minerals through Magma Recharge. *J. Petrol.* **56**, 2223-2256 (2015).

38. Thomas, N., Tait, S. & Koyaguchi, T. Mixing of stratified liquids by the motion of gas bubbles: application to magma mixing. *Earth and Planetary Science Letters* **115**, 161-175 (1993).

39. Bergantz, G. W., Schleicher, J. M. & Burgisser, A. Open-system dynamics and mixing in magma mushes. *Nature Geosci.* **8**, 793-796 (2015).

40. Stock, M. J., Taylor, R. N. & Gernon, T. M. Triggering of major eruptions recorded by actively forming cumulates. *Scientific Reports* **2**, 731 (2012).

41. Cashman, K. V., & Giordano, G. Calderas and magma reservoirs. *J. Volcan. Geotherm. Res.* **288**, 28-45 (2014).

42. Di Muro, A. *et al*. The shallow plumbing system of piton de la Fournaise volcano (la Reunion Island, Indian Ocean) revealed by the major 2007 caldera-forming eruption. *J. Petrol*. **55** (7), 1287-1315 (2014).

43. Kennedy, B. M. *et al*. Magma plumbing beneath collapse caldera volcanic systems. *Earth-Science Reviews* **177**, 404-424 (2018).

44. Wilson, C. & Hildreth, W. The Bishop Tuff: new insights from eruptive stratigraphy. *J. Geol.* **105**, 407–440 (1997).

45. Lipman, P.W. Subsidence of ash-flow calderas: relation to caldera size and magma chamber geometry. *Bull. Volcan*. **59**, 198-218 (1997).

46. Cole, J. W., Milner, D. M. & Spinks K. D. Calderas and caldera structures: a review. *Earth-Science Rev.* **69**, 1-26 (2005).

47. Simon, A. C., Pettke, T., Candela, P. A., Piccoli, P. M. & Heinrich, C. A. Magnetite solubility and iron transport in magmatic-hydrothermal environments. *Geochim. Cosmochim. Acta* **68**, 4905-4914 (2004).

48. Bell A. & Simon A. C. Evidence for the alteration of the $Fe^{3+}/\Sigma Fe$ of silicate melt caused by the degassing of chlorine-bearing aqueous volatiles. *Geology* **39**, 499-502 (2011).

49. Knipping, J. L. *et al*. Giant Kiruna-type deposits form by efficient flotation of magmatic magnetite suspensions. *Geology* **43**, 591-594 (2015a).

50. Knipping, J. L. *et al*. Trace elements in magnetite from massive iron oxide-apatite deposits indicate a combined formation by igneous and magmatic-hydrothermal processes. *Geochim. Cosmochim. Acta* **171**, 15-38 (2015b).

51. Simon, A. C., *et al*. Kiruna-Type Iron Oxide-Apatite (IOA) and Iron Oxide Copper-Gold (IOCG) Deposits Form by a Combination of Igneous and Magmatic-Hydrothermal Processes: Evidence from the Chilean Iron Belt. SEG Special Publication, **21** (in press). doi: 10.5382/sp.21.XX; 26 p.

52. Hulme, G. The Interpretation of Lava Flow Morphology. *Geophysical Journal International* **39,** 361-383 (1974).

53. Farrokhpay, S. The importance of rheology in mineral flotation: A review. *Minerals Eng.* **36–38,** 272-278 (2012).

54. Mader, H. M., Llewellin, E. W. & Mueller, S. P. The rheology of two-phase magmas: A review and analysis. *Journ. Volc. Geoth. Res.* **257**, 135-158 (2013).

55. Rhodes, A. L., Oreskes, N. & Sheets, R, W. Geology and REE geochemistry of the magnetite deposits at El Laco, Chile: *Econ. Geol. Spec. Pub* **7**, 299-332 (1999).

56. Bilenker, L. *et al*. Fe-O stable isotope pairs elucidate a high-temperature origin of Chilean iron oxide-apatite deposits. *Geochim. Cosmochim. Acta*, **177**, 94-104 (2016).

57. Weis, F. Oxygen and Iron Isotope Systematics of the Gränngesberg Mining District (GMD), Central Sweden. M. S. thesis, Uppsala universitet (2013). Available at: https://www.diva-portal.org/smash/get/diva2:589233/FULLTEXT01.pdf

58. Tornos, F., Velasco, F., & Hanchar, J. M. Iron-rich melts, magmatic magnetite, and superheated hydrothermal systems: The El Laco deposit, Chile. *Geology*, **44**, 427–430 (2016).

59. Nyström, J. O., Henríquez, F., Naranjo, J. A. & Naslund, H. R. Magnetite spherules in pyroclastic iron ore at El Laco, Chile. *Am. Mineral*. **101,** 587–595 (2016).

60. Mungall, J. E., Long, K., Brenan, J. M., Smythe, D. & Naslund, H. R. Immiscible shoshonitic and Fe-P-oxide melts preserved in unconsolidated tephra at El Laco volcano, Chile. *Geology* **46**, 255-258 (2018).

61. Hou, T. *et al*. Immiscible hydrous Fe–Ca–P melt and the origin of iron oxide-apatite ore deposits. *Nature Comm.* **9,** 1415 (2018).

62. Philpotts, A. R. Origin of certain iron-titanium oxide and apatite rocks. *Econ. Geol*., **62**, 303–315 (1967).

63. Lester, G. W., Clark, A. H., Kyser, T. K. & Naslund, H. R. Experiments on liquid immiscibility in silicate melts with H_2O, P, S, F and Cl: implications for natural magmas. *Contrib. Mineral. Petrol*. **166**, 329-349 (2013).

64. Lindsley, D. H. & Epler, N. Do Fe-Ti-oxide magmas exist? Probably not!. *Am. Mineral*. **102**, 2157-2169 (2017).

65. Lester, G. W., Kyser, T. K. & Clark, A. H. Oxygen isotope partitioning between immiscible silicate melts with H_2O, P and S. *Geochim. Cosmochim. Acta*, **109**, 306-311 (2013).

66. Lyons, J. I. Volcanogenic iron oxide deposits, Cerro de Mercado and vicinity Durango, Mexico. *Econ. Geol*. **83**, 1886-1906 (1988).

67. Corona-Esquivel, R., Martínez-Hernández, E., Henríquez, F., Nyström, J. O. & Tritlla, J. Palynologic evidence for iron-oxide ash fall at La Perla, an Oligocene Kiruna-type iron ore deposit in northern Mexico. *GFF* **132**, 173-181 (2010).

68. Jones, J. C. The Barth iron ore deposit. *Econ. Geol*. **8**, 247-263 (1913).

69. Grez, E., Aguilar, A., Henriquez, F. & Nystrom, J. O. Magnetita Pedernales: a new magmatic iron deposit in northern Chile. *Econ. Geol*. **86,** 1346-1349 (1991).

70. Gorustovich, S. A., Monaldi, C. R. & Salfity, J. A. Geology and metal ore deposits in the Argentine Puna, In *Cenozoic Geology of The Central Andes of Argentina*, (ed. José A. Safity & Rosa A. Marquillas) 169-187 (SCS Publisher, Salta, 2011).

71. Pirajno, F. Intrusion-related hydrothermal mineral systems, In *Hydrothermal processes and mineral systems*, (ed. Springer) 322-325 (Dordrecht, 2009).

72. Förster, H. & Knittel, U. Petrographics observations on a magnetite deposit at Mishdovan, Central Iran. *Econ. Geol.* **74**, 1485-1510 (1979).

73. Zhang, X. *et al*. Metallogenesis of the Zhibo and Chagangnuoer volcanic iron oxide deposits in the Awulale Iron Metallogenic Belt, Western Tianshan orogen, China. *Jour. Asian Earth Sciences* **113**, 151-172 (2015).

74. Keith, T. E. C. Fossil and active fumaroles in the 1912 eruptive deposits, Valley of ten thousand smokes, Alaska. *J. Volcan. Geotherm. Res.* **45,** 227–254 (1991).

75. Hildreth, W., & Fierstein, J. The Novarupta-Katmai eruption of 1912—largest eruption of the twentieth century; centennial perspectives: *U.S. Geological Survey Professional Paper* **1791**, 259 (2012).

76. Hanson, S. L., Falster, A. U. & Simmons, W. B. Mineralogy of Fumarole Deposits: At Sunset Crater Volcano National Monument Northern Arizona. *Rocks & Minerals* **83,** 534-546 (2008).

77. Symonds, R. B., Rose, W. I., Reed, M. H., Lichte, F. E. & Finnegan, D. L. Volatilization, transport and sublimation of metallic and non-metallic elements in high temperature gases at Merapi Volcano, Indonesia. *Geochim. Cosmochim. Acta* **51**, 2083-2101 (1987).

78. Stoiber, R. E. & Rose, W. I. Fumarole Incrustations at active Central American volcanoes. *Geochim. Cosmochim. Acta* **38**, 495-516 (1974).

79. Gemmell, J. B. Geochemistry of metallic trace elements in fumarolic condensates from Nicaraguan and Costa Rican volcanoes. *J. Volcan. Geother. Res.* **33**, 161-181 (1987).

80. Quisefit, J. P. *et al*. Evolution versus cooling of gaseous volcanic emissions from Momotombo Volcano, Nicaragua: Thermochemical model and observations. *Geochim. Cosmochim. Acta* **53**, 2591-2608 (1989).

81. Williams, P. J. *et al*. Iron Oxide Copper-Gold Deposits: Geology, Space-Time Distribution, and Possible Modes of Origin. *Econ. geol.* **100th Aniversary volume**, 371-405 (2005).

2.6. ACKNOWLEDGEMENTS

The authors acknowledge funding from the Millennium Science Initiative (MSI) through Millennium Nucleus for Metal Tracing along Subduction grant NC130065, as well support from FONDECYT grant #1140780 and FONDAP project15090013 “Centro de Excelencia en Geotermia de Los Andes, CEGA”. Simon acknowledges U.S. National Science Foundation (EAR 1250239 and 152439). The Society of Economic Geologists Foundation is thanked for providing funding via student grants to La Cruz and Childress and field trip funding to the University of Michigan student chapter. We thank Mario Rojo and Alejandro Mardones from Compañía Minera del Pacífico (CAP Minería) for their helpful logistical support, and for providing access to sample the deposit and drill core libraries, as well as valuable geological information. Ovalle acknowledges funding from the Society of Economic Geologists Foundation (SEGF) through Graduate Student Fellowship Program (GSF-2017).

2.7. AUTHOR CONTRIBUTIONS

Field work was carried out by J.T.O., N.L.L., M.R., F.B., A.C.S., T.M.C. and B.A.K. Drill core mapping was performed by J.T.O. Analyses were performed by J.T.O., N.L.L., B.A.K., M.A.R.-M. and T.M.C. Petrographic studies were carried out by J.T.O. and N.L.L. Preparation of figures was

performed by J.T.O. and M.R. J.T.O., M.R., F.B., A.C.S. and N.L.L. wrote the manuscript. A.P.D., M.A.R-M. and D.M. provided comments on the manuscript before submission.

2.8. FIGURES

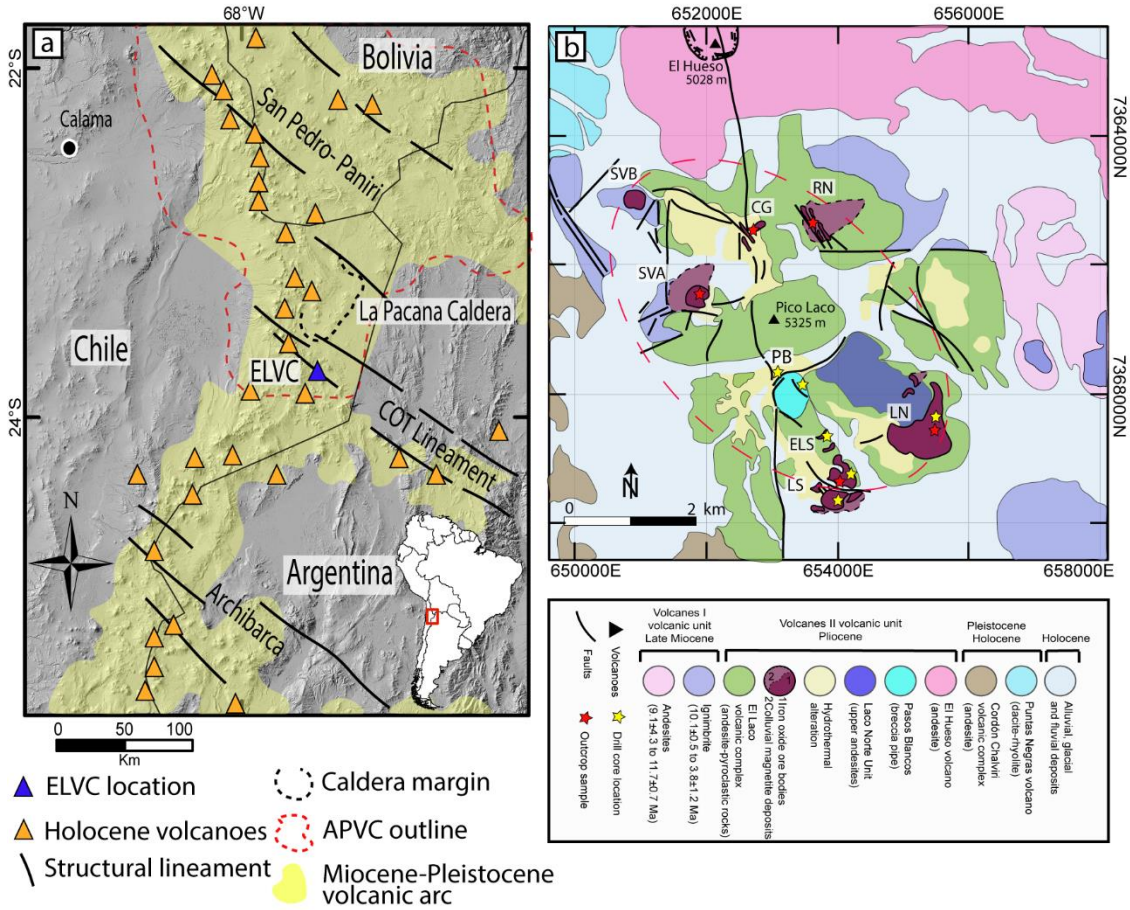

Figure 2: (a) Location of the ELVC within the main Miocene-Pleistocene volcanic arc (yellow area). The Altiplano-Puna Volcanic Complex (dashed red line) and the NW-trending structural lineaments are also shown. (b) Geologic map of the El Laco Volcanic Complex showing the location of the studied drill cores and surface samples. Based on mapping by the Compañía Minera del Pacífico (CAP Minería). LN: Laco Norte, LS: Laco Sur, ELS: Extensión Laco Sur, PB: Pasos Blancos, SVA: San Vicente Alto, SVB: San Vicente Bajo, CG: Cristales Grandes, RN: Rodados Negros. The NW-trending spatial distribution of the magnetite ore bodies is illustrated by the dashed red ellipse.

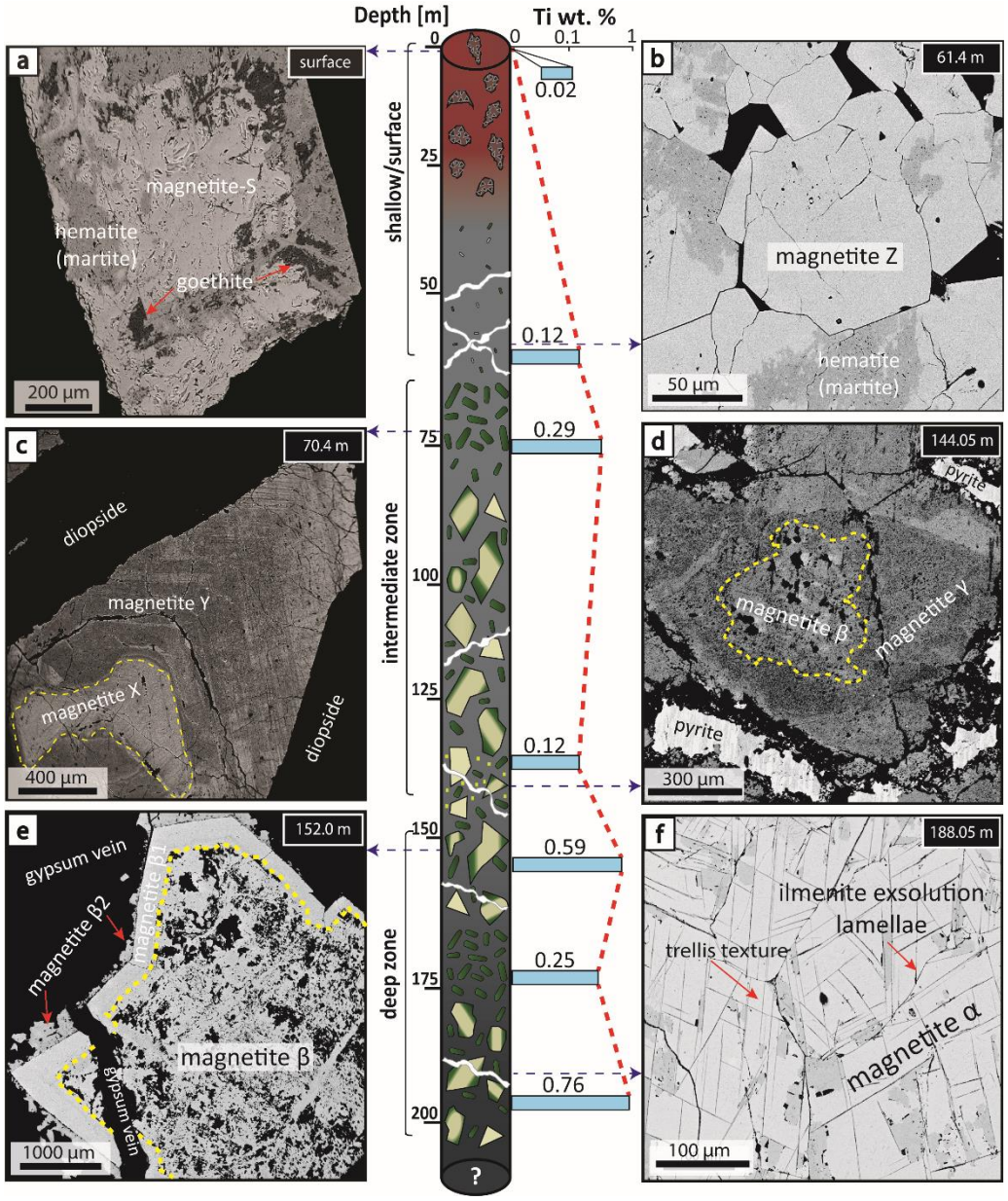

Figure 3: Schematic illustration of a representative drill core from Laco Norte (LCN-0944) showing the morphology and lithological variations of the ore bodies. The dashed red line and light blue bars indicate the average Ti concentration of the magnetite from the surface to the base of the drill core. Backscattered electron (BSE) images show the different textural types of magnetite. (**a**) Euhedral, altered and porous Magnetite-S grain from a surface sample showing pervasive replacement by hematite and goethite along grain boundaries, fractures, and pores. (**b**) Aggregate of pristine Magnetite-Z grains, weakly oxidized to hematite (sample depth 61 m). (**c**) Microcrystalline core of pristine Magnetite-X showing evidence of dissolution-reprecipitation processes. Magnetite-Y overgrowths Magnetite-X, and exhibits alternating bands of Ti-bearing inclusions, which are responsible for the increase in the magnetite Ti concentration within this zone (sample depth 70.4 m). (**d**) Ti-poor Magnetite-γ from pyrite-rich massive magnetite zone associated with gypsum veinlets. Magnetite-γ overgrowth developed on an inclusion-rich Magnetite-β core and displays sector zoning with inclusion-rich areas (sample depth 144 m). (**e**) Euhedral core of inclusion-rich Magnetite-β surrounded by a pristine inclusionfree-rim of Magnetite-β1. Both magnetite types have high Ti contents. Irregular grains of Ti-poor Magnetite-β2 associated with late crosscutting gypsum veinlets developed over Magnetite-β1 rims (sample depth: 152 m). (**f**) Aggregate of Ti-rich Magnetite-α grains showing well-developed ilmenite exsolution lamellae, which exhibit both trellis and sandwich textures (sample depth 188.05 m).

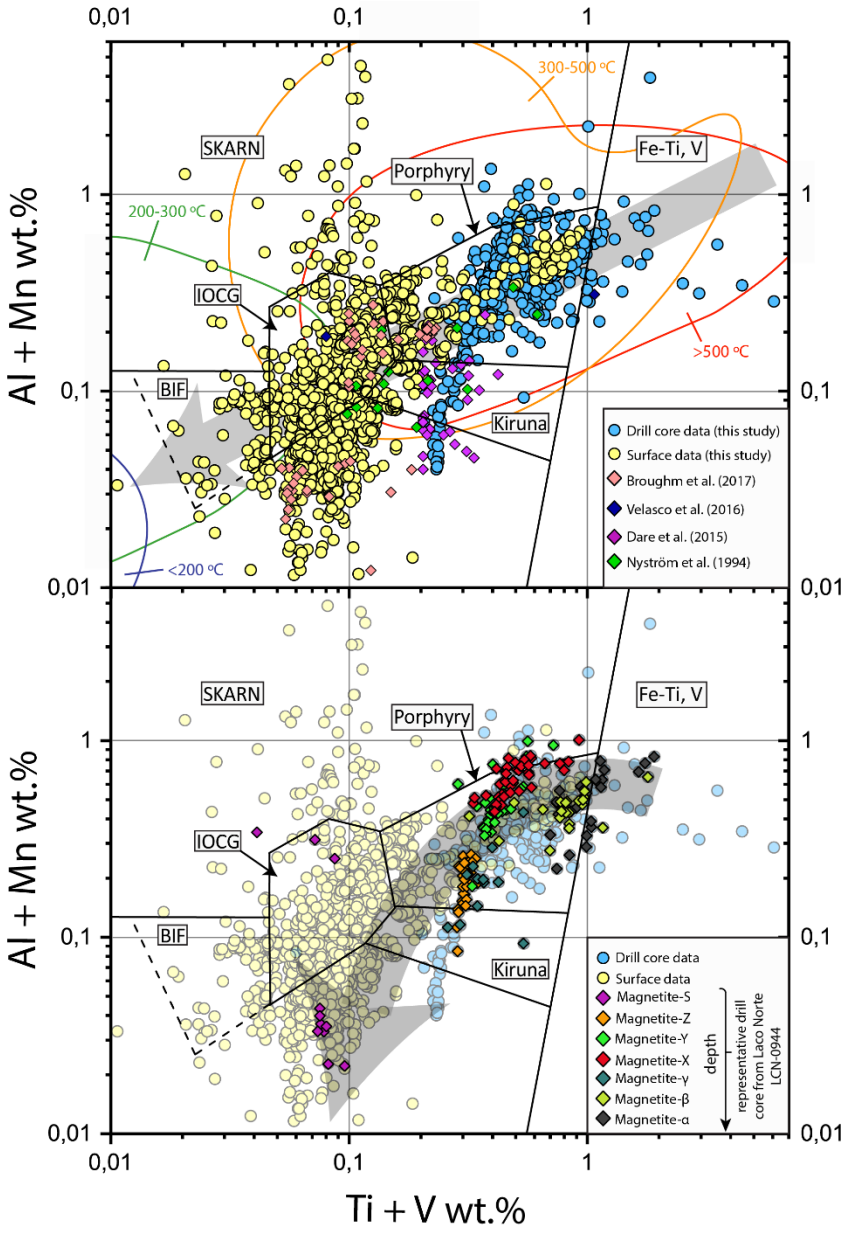

Figure 4: (**a**,**b**) [Al + Mn] versus [Ti + V] plots (in wt. %) showing the chemical variations of magnetite from El Laco. (**a**) The plot shows all EPMA data for magnetite from both drill core samples (blue circles) and surface outcrops (yellow circles) (Supp. Mat. Appendix_1). The colored diamonds correspond to magnetite data from surface samples reported in previous studies. The colored contours are from ref.11 and show estimated formation temperatures for the deposits. Magnetite from most drill core samples plot towards the high-temperature fields (*Fe-Ti, V; Porphyry* and *Kiruna fields*), whereas data points from surface samples show a larger dispersion, plotting both in the high, moderate and low temperature fields (*Porphyry*, *Skarn*, *IOCG*, *Kiruna* and *BIF fields*). This indicates a transitional cooling trend from purely magmatic conditions to magmatic-hydrothermal conditions from depth to surface, which is represented by the straight grey arrow. (**b**) The plot shows EPMA data points from the representative Laco Norte drill core in Fig. 2, illustrating the compositional variability at the grain scale from depth (Magnetite-α) to surface (Magnetite-S); note that data from previously published studies are not included in (**b**). The curved grey arrow represents a typical cooling trend.

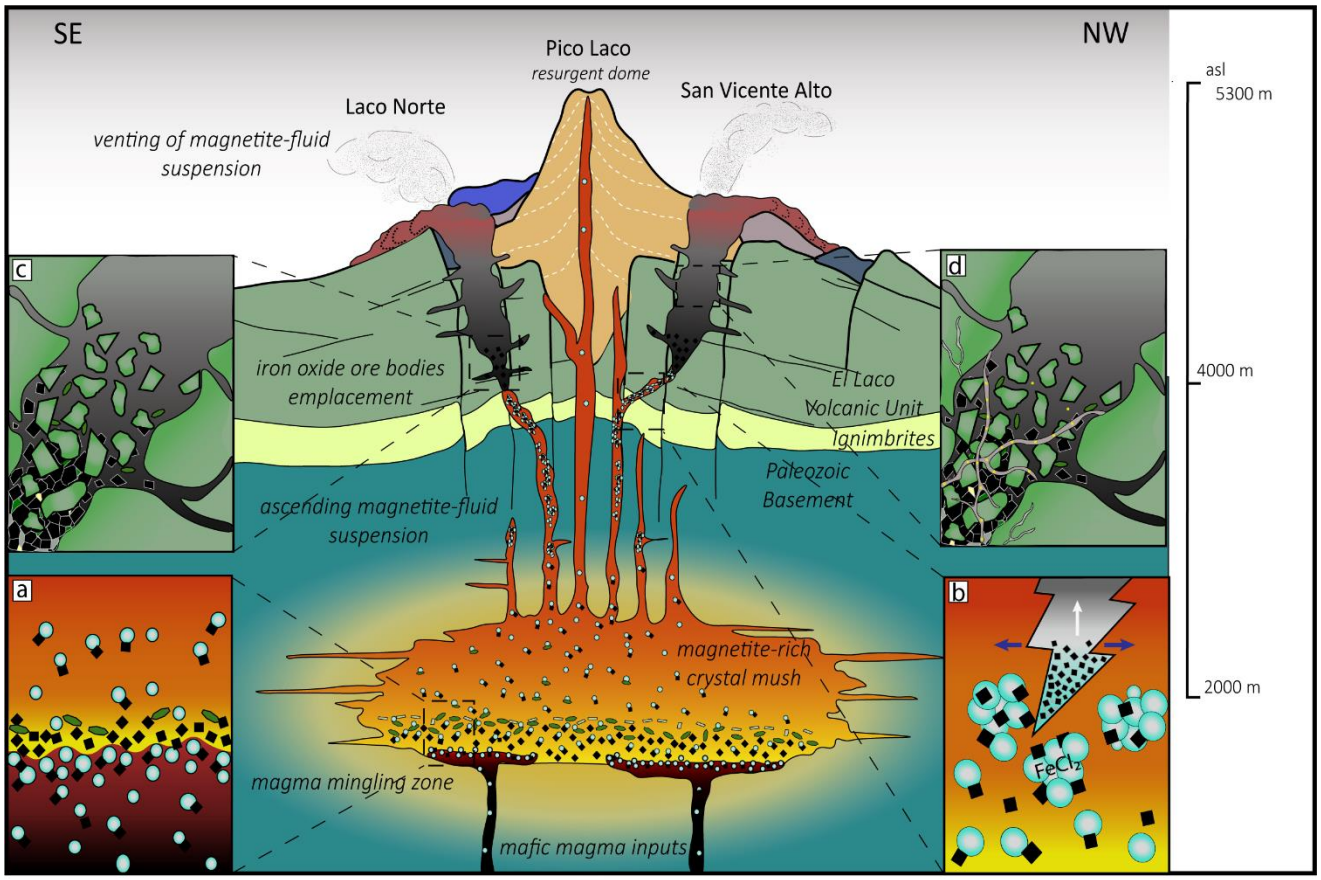

Figure 5: Proposed genetic model for the El Laco iron deposit. (**a**) Formation of a settled magnetite-rich crystal mush in an andesitic magma chamber below the ELVC. Water-saturated magnetite-bearing mafic magma underplates the andesitic magma body; exsolved bubbles nucleate on magnetite crystals from the mafic magma. Bubbles rise to form a magnetite + bubbles-rich foam at the interface, which can be transferred to the overlying magma chamber. Once the supersaturation pressure is reached, large populations of bubbles of supercritical fluid are exsolved from the andesitic reservoir, which along with the bubbles transferred by magma mingling processes, preferentially nucleate on magnetite accumulated at base of the magma chamber (Magnetite-α and -β). (**b**) Further ascent, growth, coalescence and accumulation of numerous magnetite-fluid-bubble pairs form an ascending magnetite-rich hypersaline suspension, which becomes Fe-rich by scavenging Fe from magma. (**c**) The fast and efficient hydraulic injection of the magnetite-rich suspension through fissures formed during the episode of collapse of the volcanic structure, forms large hydrothermal breccia bodies at depth, characterized by a matrix of an aggregate of remobilized primary magnetite (Magnetite-α and -β). The Fe-rich magmatic-hydrothermal fluid keeps ascending, crystallizing hydrothermal (Magnetite-X, -Y, and -Z) magnetite during progressive cooling until it reaches the surface, wherein it is cooled and exposed to atmospheric conditions forming Magnetite-S. (**d**) The final hydrothermal stage is represented by several veinlet types: (i) magnetitediopside- pyrite; (ii) scapolite-magnetite-diopside (±pyrite); (iii) diopside-pyrite; (iv) magnetite-scapolite-ilmenite- pyrite (±chalcopyrite and sphalerite); (v) gypsum-magnetite-pyrite; and (vi) gypsum-pyrite that crosscut the breccia body and the volcanic host rocks. Modified from ref.[5]

CHAPTER 3: Magmatic-hydrothermal evolution of the El Laco iron deposit revealed by trace element geochemistry and high-resolution chemical mapping of magnetite assemblages

J. Tomás Ovalle[1-2*], Martin Reich[1-2], Fernando Barra[1-2], Adam C. Simon[3], Artur P. Deditius[4], Margaux Le Vaillant[5], Owen K. Neill[3], Rurik Romero[1-2], Nelson Román[1-2], Nikita L. La Cruz[3], Malcolm P. Roberts[6], Diego Morata[1-2]

[1]*Department of Geology and Millennium Nucleus for Metal Tracing Along Subduction, FCFM, Universidad de Chile, Santiago, Plaza Ercilla 803, Chile*

[2]*Andean Geothermal Center of Excellence (CEGA), FCFM, Universidad de Chile, Plaza Ercilla 803, Santiago, Chile*

[3] *Department of Earth and Environmental Sciences, University of Michigan, 1100 North 8 University Avenue, Ann Arbor, MI 48109-1005, USA*

[4]*School of Engineering and Information Technology, Murdoch University, Murdoch, Australia*

[5]*Commonwealth Scientific and Industrial Research Organisation (CSIRO) Mineral Resources, 26 Dick Perry Ave, Kensington 6151, Western Australia*

[6]*Centre for Microscopy, Characterisation and Analysis (CMCA), The University of Western Australia, Perth, WA 6009, Australia*

*Corresponding author: José Tomás Ovalle (joseovalle@ug.uchile.cl)

Invited article submitted to Geochimica et Cosmochimica Acta, special issue on "Base, Precious and Critical Metals in Fluid-mineral Interactions"

ABSTRACT

The Plio-Pleistocene El Laco magnetite ore bodies in the Chilean Altiplano represent an unusual subvolcanic/aerial type of an iron oxide-apatite (IOA) deposit. The textures of these magnetite ore bodies have sustained a long-standing geological controversy on the origin of iron oxide deposits with models spanning the spectrum from purely igneous to magmatic-hydrothermal processes. In particular, the link between the geochemical processes taking place in the source magma and the subsequent evolution of the overlying magmatic-hydrothermal system are still not well understood. Here we address this problem by focusing on microtextural and geochemical features of iron ore and silicate gangue minerals retrieved from drill core samples from El Laco ore bodies, as well as from the andesite volcanic host rocks. We report a comprehensive geochemical dataset of magnetite assemblages at El Laco obtained using a combination of EPMA, LA-ICP-MS, and synchrotron

radiation μ-XRF methods. Microtextural and geochemical data of magnetite reveal consistent variations with depth. Magnetite in the andesitic host rocks and from deep/intermediate levels of the ore bodies have a high concentration of trace elements including Ti, V, Ni, Mn, Zn, Cr, Al, Ga, Cu and Co in comparison with magnetite from the upper sections of the ore bodies. Clinopyroxene is present in both andesites and the ore bodies, and shows similar compositional trends than those exhibited by magnetite, but Mn and Fe are higher in the former, and Na and Ca are enriched in the latter. We interpret these trends as resulting from a transition from purely igneous conditions to a fluid-dominated, cooling magmatic-hydrothermal system. Detailed microtextural analysis of magnetite and clinopyroxene from the ore bodies support this notion, revealing multiple growth stages punctuated by dissolution-reprecipitation processes. Our data further supports a genetic model that explains the formation of the El Laco iron oxide deposit through the injection, upward migration and venting of magmatically-derived Fe-rich fluids.

3.1. INTRODUCTION AND BACKGROUND

The world-renowned El Laco iron deposit in the Chilean Altiplano represents the Earth's youngest and one of the best-exposed records of iron oxide-apatite (IOA)-type mineralization genetically related to the explosive activity of a continental arc stratovolcano. Because of its well-preserved primary volcanic-like textures (e.g., flow and vesicular textures), El Laco is considered a key location to better understand the geological processes leading to the formation and evolution of IOA systems worldwide, which are an important source for iron and also host rare earth elements in apatite.

The formation of the El Laco ore bodies, beyond reasonable doubt, took place during the magmatic evolution of a continental arc volcanic system. The massive magnetite-rich ore bodies are emplaced on the flanks of a collapsed central volcanic edifice forming adventitious craters, fissural emissions, breccia pipes, and dome- and tabular-like structures, some of which are partially covered by post-ore andesitic lava flows. However, the exact mechanism for the generation of such iron oxide ore bodies has been a matter of intense scientific debate since its discovery more than half a century ago (cf. Park, 1961). Proposed genetic models for El Laco include: (1) liquid immiscibility-based magmatic processes invoking a hydrous Fe-Ca-P melt (Nyström and Henríquez, 1994; Tornos et al. 2016; Mungall et al., 2018); (2) metasomatic replacement of andesitic volcanic rocks by magnetite precipitated from Fe-rich hydrothermal fluids (Rhodes and Oreskes, 1999; Sillitoe and Burrows, 2002; Dare et al, 2015), and (3) Fe enrichment resulting from a combination of common igneous and hydrothermal processes operating in volcanic systems, enhanced during explosive events (Ovalle et al., 2018; Childress et al., 2020; La Cruz et al., 2020).

At El Laco, recent studies have recognized complex microtextural features in magnetite ores suggesting multiple events of Fe mineralization, most likely related to magmatic-hydrothermal processes (Rhodes and Oreskes, 1999; Sillitoe and Burrows, 2002; Dare et al., 2015; Nyström et al., 2016; Broughm et al., 2017; Tornos et al., 2017; Mungall et al., 2018; Ovalle et al., 2018; Xie et al., 2019; Childress et al., 2020; La Cruz et al., 2020). The textural diversity observed in magnetite at El Laco, which is also recognized in several IOA deposits worldwide, is often attributed to superimposed Fe-mineralization events leading to pervasive replacement, dissolution-reprecipitation processes and supergene oxidation (Huang and Beaudoin, 2019). Hence, any interpretation or genetic model proposed to explain the origin of El Laco, should be supported by in situ geochemical studies coupled with detailed microtextural observations.

Because magnetite is ubiquitous in ore deposits formed under diverse conditions—ranging from purely magmatic to magmatic-hydrothermal, metamorphic and sedimentary environments—its trace element signature has been used as a petrogenetic indicator in a variety of mineral systems, including magmatic Ni-Cu sulfide and Fe-Ti-V (nelsonite), porphyry copper and Fe-skarns, iron oxide-apatite (IOA) and iron oxide-copper-gold (IOCG) deposits, and banded-iron formations (Carew et al., 2006; Dupuis and Beaudoin 2011; Dare et al. 2012, 2014, 2015; Nadoll et al. 2012, 2014; Boutroy et al. 2014; Liu et al., 2015; Hu et al., 2015; Knipping et al., 2015a, b; Canil et al., 2016; Neumann et al. 2017; Xie et al. 2017; Simon et al., 2018; Ovalle et al., 2018; Huang and Beaudoin, 2019; Palma et al., 2020).

In addition to its variable trace element chemistry, magnetite is characterized by a diversity of primary and secondary microtextural features including exsolution lamellae, mineral inclusions and chemical zoning or banding. Therefore, a comprehensive knowledge of the main controls on elemental partitioning and the effects of re-equilibrium and post-crystallization processes are critical for robust petrogenetic interpretations. Most of our current knowledge of igneous magnetite and Fe-Ti oxides is based on the pioneering studies by Buddington and Lindsley (1964), Frost (1991) and Mücke (2003), and from more recent contributions focusing on Fe-Ti-V ores in layered intrusions and anorthosite massifs (Liu et al., 2015; Tan et al., 2015; 2016; He et al., 2016). Our understanding of hydrothermal magnetite, on the other hand, has improved over the last few years from detailed microtextural descriptions in Fe-skarns (Hu et al., 2014, 2015; Yin et al., 2017), BIFs (Zhang et al., 2020), IOA and IOCG deposits (Knipping et al 2015b; Heidarian et al., 2016; Deditius et al., 2018; Ovalle et al., 2018; Huang and Beaudoin, 2019; Salazar et al., 2019; Rodriguez-Mustafa et al., 2020; Palma et al., 2020), and hydrothermally altered igneous magnetite from granitic plutons (Wen et al., 2017). Most of these studies focused exclusively on the chemistry of magnetite and overlook the geochemical distribution of trace elements in other co-genetic phases. Therefore, analytical strategies should consider a combination of microtextural observations and in situ trace element analysis of magnetite and associated mineral phases in order to develop a more comprehensive understanding of the ore-forming processes.

Here, we report the results of a comprehensive study that combines elemental data and high-resolution multi-instrumental chemical mapping of magnetite and clinopyroxene from the El Laco iron oxide deposit. Our aim is to provide new insights on the magmatic-hydrothermal processes taking place during the evolution of the ore-forming system. Samples were collected from outcropping volcanic host rocks and ore bodies, as well as from representative drill cores throughout the deposit. Major, minor and trace element concentrations in magnetite were determined using electron probe microanalysis (EPMA) and laser ablation inductively coupled plasma mass spectrometry (LA-ICP-MS). The data were integrated with multi-instrumental elemental mapping of selected samples collected at different depths in the deposit, as well as samples of the andesite host rocks. This approach included wavelength dispersive X-ray spectrometry (EPMA-WDS) and high spatial resolution elemental mapping using synchrotron radiation microbeam X-ray fluorescence microscopy (μ-XRF). Specifically, multidetector arrays were used to obtain chemical images of the complex textural features at mm-scale. By applying this approach to a representative number of surface and drill core samples, we explored the chemical and textural complexities of the El Laco magnetite ores, and present a data set that is consistent with the formation of the deposit resulting from a combination of igneous and hydrothermal processes.

3.2. GEOLOGICAL SETTING

The El Laco iron oxide deposit is located in the Central Andes of northern Chile at elevations ranging between 4500 and 5300 m (Fig. 6a; Park, 1961; Nyström and Henríquez, 1994; Rhodes and Oreskes, 1995; Naslund et al., 2002; Sillitoe and Burrows, 2002; Naranjo et al., 2010; Velasco et al., 2016; Tornos et al., 2016; 2017; Ovalle et al., 2018). The deposit is hosted within the Miocene-Pliocene El Laco volcanic complex (ELVC), which covers an area of ~35-40 km2 and comprises multiple superimposed episodes of volcanic activity that led to the construction and degrading of the stratovolcano complex. Stratigraphically, and from oldest to youngest, the major volcanic units are El Laco lower volcanic unit (lower andesites), El Laco upper volcanic unit (upper andesites), late post-ore andesite lava flows, dome-like edifices, and late volcanic breccia bodies that crosscut the older units. The majority (>90%) of the andesitic volcanic rocks are porphyritic, rarely vesicular and contain abundant plagioclase and pyroxene phenocrysts. Magnetite is also abundant in the andesites, occurring as microphenocrysts within the andesite groundmass, large anhedral crystals and forming magnetite-(±apatite)-pyroxene glomerocrysts. The outcropping massive magnetite ore bodies are located around the central volcanic plug (Pico Laco), and are structurally associated with collapse-related fissures and secondary craters (Fig. 6a) (Frutos and Oyarzún, 1975; Naranjo et al., 2010; Ovalle et al., 2018). Reported K-Ar ages for the volcanic units range from 5.3 ± 1.9 to 1.6 ± 0.5 Ma (K-Ar) (Figs. 6a; b) (Naranjo et al., 2010), whereas apatite fission track dating constrained magnetite formation at 2.0 ± 0.1 Ma (Maksaev, 1988).

Based on their morphologies and surface textures, the ore bodies can be classified as stratabound (Laco Norte, Laco Sur, San Vicente Alto), dome-shaped (San Vicente Bajo), and tabular (Rodados Negros, and Cristales Grandes). In addition, drilling campaigns by CAP Minería, the propriety owner, revealed the occurrence of two additional hidden ore bodies composed of magnetite breccias and veinlets; the Extensión Laco Sur and Pasos Blancos ore bodies (Naranjo et al., 2010; Ovalle et al., 2018). Total resources for El Laco have been estimated at 733.9 Mt with an ore grade of 49.2 % Fe (CAP Minería 2016 Annual Report). The outcropping ore bodies are dominated by highly-oxidized massive magnetite with some levels showing pyroclastic-like features (Nyström et al., 2016). Degassing and lava-like flow textures are common. Besides magnetite, minor amounts of clinopyroxene, scapolite, apatite, REE phosphates and Fe phosphates are recognized in these outcropping bodies. Drill core data reported by Ovalle et al. (2018) showed that the ore bodies are vertically zoned with massive magnetite at shallow levels to breccias at depth (Fig. 6b). The breccias consist mainly of variably altered andesite fragments within a magnetite-rich matrix with variable amount of clinopyroxene and scapolite.

Widespread hydrothermal alteration is observed at surface and depth; however, despite being spatially close to the ore bodies, it is apparently unrelated to magnetite mineralization (Tornos et al., 2017). At depth in the Pasos Blancos area, alkalic-calcic alteration is well-developed, and comprises intense scapolitization and clinopyroxene formation, that partially to pervasively replaced andesitic fragments of the breccia bodies (Naranjo et al., 2010; Ovalle et al., 2018). Some of the most notable expressions of hydrothermal alteration correspond to argillic zones developed by intense leaching of the andesitic host rocks. These zones are dominated by tridymite, cristobalite, alunite and jarosite, forming silicic veins and irregular hydrothermal breccia bodies (Vivallo et al., 1994; Sillitoe and Burrows, 2002). Exhalative deposits at El Laco, represented by gypsum-rich mounds, are linked to discrete centers of emission spatially associated with NW-trending collapse structures, which control the recent hot spring-like geothermal activity at the ELVC (Vivallo et al., 1994; Rhodes and Oreskes, 1999).

3.3. SAMPLES AND METHODS

Thirty-two drill core samples were collected from six vertical and subvertical drill holes that crosscut the magnetite ore bodies at San Vicente Alto (SVA), San Vicente Bajo (SVB), Cristales Grandes (CG), Rodados Negros (RN) (Fig. 6). Additionally, twelve drill core samples from Laco Norte, Laco Sur, Extensión Laco Sur, and Pasos Blancos ore bodies, previously studied by Ovalle et al. (2018) and La Cruz et al. (2020), were further investigated. To ensure representativeness, the samples were selected considering the areal and depth distribution of magnetite ore bodies. Field work and drill core logging revealed that the ore bodies formed breccia-pipe-like structures that crosscut andesite lava flows and pyroclastic rocks (Fig. 6b). The studied drill cores show that the magnetite ore bodies comprise a shallow/surficial upper zone (Mgt-surface: ~0-30 m depth) characterized by highly vesicular massive magnetite with variable oxidation followed by large breccia bodies located at intermediate levels (Mgt-interm: ~30-150 m depth) and composed of hydrothermally-altered volcanic fragments within a magnetite-dominated matrix and variable amounts of clinopyroxene and scapolite. In some cases these breccia bodies can extend further down reaching depths of ~450 m (Mgt-deep: >150 m depth), where they occur associated with veinlets and a more intense Ca-Na alteration (Fig. 1b; Naranjo et al., 2010; Ovalle et al., 2018). The upper section of the ore bodies has been extensively studied by several authors (e.g., Dare, et al., 2015; Nystrom, et al., 2016; Ovalle et al., 2018; Mungall, et al., 2018; Childress et al., 2020; La Cruz, et al., 2020). Therefore, in this study we focused exclusively on the intermediate and deep sections.

In addition to drill core samples, we investigated the andesitic host rocks, including the underlying and overlying andesite flows that pre-date and post-date the magnetite mineralization (Fig. 6a; b). A brief summary of the characteristics of the different volcanic samples is presented in Annex B, Table B10, whereas sample photographs and images are shown in Figure B1.

Polished thin (30 µm) and thick (100 µm) sections were prepared for petrographic and SEM observation, and EPMA and LA-ICP-MS analysis. Microtextural and in situ geochemical analyses were focused primarily on magnetite. In addition, EPMA data were obtained for clinopyroxene. Synchrotron µ-XRF microscopy studies were carried out on representative samples to obtain spatially resolved geochemical data of the magnetite assemblages at the thin-section scale.

3.3.1. SEM and EPMA methods

Carbon coated polished thin sections were studied by using a FEI Quanta 250 SEM at the Andean Geothermal Center of Excellence (CEGA), Department of Geology, Universidad de Chile. The SEM was used to study textural relationships, zoning patterns, mineral inclusions, exsolutions and overgrowths. Backscattered-electron (BSE) images were obtained using an accelerating voltage of between 15 and 20 kV, a filament current of 80 µA, a beam intensity of ~1 nA, a spot size of 5µm, and a working distance of 10 mm.

Electron probe microanalyses (EPMA) of magnetite and pyroxenes were carried out at the Electron Microbeam Analysis Laboratory (EMAL), University of Michigan, USA by using a Cameca SX-100 instrument and at the Centre of Microscopy, Characterisation and Analysis (CMCA), University of Western Australia, by using a field-emission JEOL JXA8530F Plus Hyper probe. Both probes are equipped with five wavelength dispersive spectrometers (WDS), and the same analytical conditions were used on both instruments. The accelerating voltage was 20 kV, and a focused beam (~1 µm) was set to avoid hitting inclusions and/or thin exsolution lamellae. Interference corrections were carried out for Ti concentrations because V Kβ affects the Ti Kα signal. The beam current was set to 30 nA. A counting time of 20 s was used for Fe, while higher counting times were used for the other

elements: 100 s for Ca, Cr, Mn, 110 s for Si, P, Mg, Al, and 120 s for Ti and V. The same elements, plus Na, were measured in clinopyroxene, using an accelerating voltage of 15 kV, a beam current of 40 nA and a 2 µm beam size. Background corrections for all elements were made by using the Mean Atomic Number (MAN) Method of Donovan and Tingle (1996).

In addition to quantitative spot analyses, wavelength dispersive X-ray spectrometry (WDS) maps were collected at the CMCA facilities, University of Western Australia. Quantitative WDS maps of Fe, Ti, V, Si, Al, Mg, Mn, Ca, Cr, and Na were obtained on selected magnetite and pyroxene grains. Operating conditions were 40° take-off angle and a beam energy of 20 keV. The beam current was 50 nA and counting times were 20–60 ms/step. ZAF corrections were applied for all elements and interference corrections were performed for Fe Kα and V Kα because of Mn Kβ and Ti Kβ overlap, respectively. The standards used in both cases included natural and synthetic oxides and silicates.

3.3.2. LA-ICP-MS analysis

Trace element concentrations were determined on selected magnetite grains using a Teledyne-Photon Machines Analyte G2 193-nm ArF excimer laser ablation system coupled to a Thermo Fisher Scientific iCAP-Q quadrupole mass spectrometer at the CEGA Mass Spectrometry Laboratory, Department of Geology, Universidad de Chile. The analytical protocol follows the procedure described in Palma et al. (2020). Briefly, the mass spectrometer was tuned for maximum sensitivity, low-oxide formation rate (ThO/Th<0.005) and low double-charged ion formation ($^{22}M/^{44}Ca<0.0005$). Considering that He gas was used as a carrier and Ar as a plasma gas, interferences with these elements were evaluated when choosing representative isotopes for each element. Thus, although ^{56}Fe is more abundant than ^{57}Fe, the latter was measured to determine the iron content because 56Fe has an isobaric interference with ArO. Each spot involved a 60 s ablation time and 20 s background measurement using a laser repetition rate of 8 Hz, a fluence of 4.0−6.0 J/cm^2 and a 30–40 µm spot diameter. The dwell time was 0.01 s for all the monitored isotopes: ^{23}Na, ^{24}Mg, ^{27}Al, ^{29}Si, ^{31}P, 39K, ^{44}Ca, ^{45}Sc, ^{52}Cr, ^{55}Mn, ^{59}Co, ^{60}Ni, ^{63}Cu, ^{66}Zn, ^{73}Ge, ^{85}Rb, ^{88}Sr, ^{51}Y, ^{90}Zr, ^{93}Nb, ^{95}Mo, ^{107}Ag, ^{111}Cd, ^{120}Sn, ^{121}Sb, ^{138}Ba, ^{139}La, ^{140}Ce, ^{208}Pb, ^{232}Th and ^{238}U with the exception of ^{51}V, ^{49}Ti and ^{69}Ga that was 0.02 s. The concentration of Fe in magnetite, determined by EPMA, was used as the internal standard for calibration. The USGS GSE-1G reference material was used as a primary standards for magnetite analysis and the USGS GSD-1G as a secondary standard to determine analytical accuracy and precision. Thirty-seven analyses were performed on the GSD standard in which the trace element concentrations obtained present a small relative difference within 2 to 5% for most analytes with those reported by Jochum et al. (2005). The analytical precision determined using the GSD standard is within 2 to 5% for most analytes. LA-ICP-MS analyses were carried out using the sample-standard bracketing method with measurements of the GSE-1G (x 2), GSD-1G (x 1), and then 20-25 unknowns (sample), followed by measurements of GSD-1G (x 1), GSE-1G (x 2). Data reduction was performed by using the Iolite software (Paton et al., 2011), which calculates detection limits after Longerich et al. (1996). LA-ICP-MS profiles were carefully inspected for signal heterogeneities attributable to micrometer- to nanometer-sized mineral inclusions and/or exsolution lamellae within magnetite. When identified, the profiles were discarded for quantification purposes.

3.3.3. Synchrotron X-ray fluorescence microscopy

The spatial distribution of major, minor and trace elements in selected samples was determined by means of microbeam X-ray fluorescence microscopy (µ-XRF) at the Australian Synchrotron in Melbourne, Australia, using the Kirkpatrick Baez mirror microprobe end-station. Elemental maps were collected using the Maia 384 multi-detector array, which when combined with an ultra-bright

collimated synchrotron microbeam source enables 1) high spatial resolution, 2) high sensitivity to concentrations in the hundreds to thousands of ppm range, and 3) rapid data collection such that cm2 areas can be scanned in a matter of a few hours (Ryan et al., 2010; Paterson et al., 2011; Fisher et al., 2015). Data were acquired in event mode (Ryan et al., 2014) with each detected X-ray event tagged by detector number in the array and X, Y scan pixel coordinate in records tagged by accumulated flux and transit time per pixel. The data were analyzed, event by event, using the Dynamic Analysis (DA) method for real-time spectral deconvolution, which accumulates element concentration maps with the effects of spectral overlap, pileup, and background removed (Ryan et al., 2010). Maia µ-XRF data were collected following the method recently reported by Barnes et al. (2020). Thin-section-scale chemical images were first collected at high incident energies (18.5 keV) and a spatial resolution of 4 µm; then, smaller areas of interest were scanned with input beam energies below the FeKα absorption edge (7.05 keV) and a spatial resolution of 2 µm in order to achieve enhanced sensitivity for elements lighter than Fe, particularly Cr and Ti. Scan velocities of 5 mm/s were used, giving an effective dwell time of 0.4 ms per pixel. Yield corrections were calculated from the major element composition of Fe-Ti oxides and clinopyroxene. The GeoPIXE software was used to convert raw spectrometric data to element concentrations and construct chemical maps (Paterson et al., 2011; Ryan et al., 2014).

3.4. RESULTS

3.4.1. Magnetite microtextures and elemental distribution

Magnetite in the andesite host rocks

Magnetite is a ubiquitous phase in volcanic rocks at the El Laco complex. Magnetite in the andesite host rocks (Figs. 6; B1; Table B10) occurs forming clusters or glomerocrysts (~500-800 µm size) with clinopyroxene (augite), orthopyroxene (enstatite), apatite and minor plagioclase, and also as large megacrysts (Figs. 7b, c) and isolated phenocrysts. Magnetite in glomerocrysts (Mgt-glom, Figs. 7a; B1) occurs along with abundant coarse-grained plagioclase phenocrysts and minor clinopyroxene and orthopyroxene, immersed within a micro-crystalline groundmass composed of clino- and orthopyroxene, plagioclase and magnetite. Magnetite in the glomerocrysts occurs mostly as pristine grains, occasionally with apatite inclusions or display variable degrees of ilmenite oxy-exsolution (trellis and sandwich-type textures) (Figs. 7a; B1). Magnetite megacrysts (Mgt-meg; Figs. 7b, c), on the other hand, are large crystals (>5mm) and are dominantly composed of highly porous and fractured magnetite with clinopyroxene occurring towards the rims and in some cases, spatially associated with porosity (Fig. 7b). Synchrotron µ-XRF maps reveal core-to-rim normal zoning for Fe, Mn and Cr in the megacrysts, whereas Ti shows a reverse pattern (Figs. 7b, c).

Magnetite in the ore bodies

Most ore bodies at El Laco (e.g., Laco Norte, Laco Sur, San Vicente Alto, San Vicente Bajo, Rodados Negros, and Cristales Grandes) are composed by massive magnetite at surface/shallow levels to magnetite-rich hydrothermal breccias and minor veinlets at depth (Figs. 6b; B2-B3). At Pasos Blancos and Extensión Laco Sur, only breccias and veinlets were recognized in the drill holes. In all areas, the breccia bodies are formed by volcanic fragments variably altered to fine-grained clinopyroxene and scapolite, within a magnetite- and clinopyroxene-dominated matrix, as seen in µ-XRF maps (Figs. 8; B2-B4). In addition, veinlets containing mm-sized magnetite and clinopyroxene ± ilmenite crosscut the andesite fragments and the magnetite-rich matrix (Figs. 8c, d; B4-B5).

Magnetite in the deep zone (>150 m depth, Mgt-deep) is usually related to clinopyroxene and variable amounts of ilmenite, scapolite and titanite in the breccia matrix or veinlets (Figs. 8; B4-B5). Magnetite from breccias and veinlets is characterized by well-developed ilmenite exsolution lamellae and ilmenite grains (Figs. 8; B4-B5). Ilmenite exsolution domains, mostly of the trellis-type texture, occur within magnetite cores in breccias (Fig. 8a), and can be homogeneously distributed in magnetite from veinlets (Figs. 8c, d). On the other hand, ilmenite grains commonly exhibit symplectite-like textures formed by magnetite-rutile intergrowths (Figs. 8a, inset; B4c, d).

At intermediate levels (~30-150 m. depth), the magnetite-rich ore bodies consist of a massive magnetite-to-breccia body transitional zone characterized by magnetite grains (Mgt-interm) that are texturally more diverse than magnetite from the deeper levels. Mgt-interm shows abundant re-equilibrium textures, evidenced by sinuous and resorbed cores that are overgrown by oscillatory- and sector-zoned magnetite (Fig. 9a); ilmenite exsolution lamellae are also observed within the same magnetite grain (Figs. 9b; B6a). The magnetite cores show complex internal textures including cores with abundant (and often) oriented silicate inclusions (Fig. 9a) and/or oscillatory and multiple resorption textures (Fig. 9). Magnetite overgrowths, on the other hand, show oscillatory patterns defined by alternating inclusion-rich and inclusion-poor bands (Fig. 9a, b). Chemically, the overgrowths have a lower Fe content relative to the magnetite cores, but higher concentrations of Mg, Ti, Si, Al, Ca and Na (Figs. 9; B6).

The shallow/outcropping levels (0–35 m) of the El Laco deposit comprise massive magnetite bodies. Mineralogically, they are composed of >90% modal magnetite with minor diopside and scarce apatite. The zone displays a macroscopic vesicular texture, which increases towards the surface. Texturally, magnetite grains in surface samples (Mgt-surface, for further discussion) commonly meet at triple junctions forming mosaic-textured porous aggregates, which vary from pristine, to moderate to pervasive replacement by oxidation products (e.g., hematite and goethite), and are characterized by abundant microporosity. Oscillatory banding and sector zoning are also present in some cases, whereas exsolution textures are uncommon for this zone (Nystrom, et al., 2016; Ovalle et al., 2018; La Cruz et al., 2020).

3.4.2. Geochemistry of magnetite

Major and minor element composition

A statistical summary of EPMA data for each type of magnetite occurrence is presented in Table 1, whereas all data are reported in Supplementary Material Appendix 1, including previously published magnetite EPMA data from outcropping and subsurface ore bodies at El Laco (Ovalle et al., 2018) (Fig. 10). Overall, magnetite from the El Laco ore bodies exhibits a wide compositional variability as a function of depth. Elemental variations can reach up to one order of magnitude for elements such as Ti (average contents of 850, 3510, and 2780 ppm for Mgt-surface; Mgt-interm, Mgt-deep, respectively) and V (890, 2050 and 1730 ppm, respectively), and less pronounced for Al, Cr and Mn (Table 1).

Figure 10 and Table 1 show that magnetite from the host andesite (Mgt-glom and Mgt-meg) is more enriched in Ti (5.32 and 3.90 wt%, respectively) and Al (1.16 and 1.43 wt%, respectively) than magnetite from the subsurface ore bodies, with concentration levels above 1 wt% (Table 1). Mgt-interm and Mgt-deep have similar concentrations for most elements (Fig. 10), whereas magnetite from the shallow/outcropping ore bodies (Mgt-surface), has lower concentrations of minor and trace elements (Table 1). Overall, the EPMA data display a distinct trend of decreasing concentrations of

Ti, Mn and Al and V from bottom to top of the system (Figs. 10a-d), whereas Mg contents are moderately high and fairly constant (Fig. 10e).

Trace element composition

LA-ICP-MS data for magnetite from the andesite host rocks and the subsurface ore bodies are reported in the Supplementary Material Annex B, Table B14. Figure 11 shows boxplots of trace element concentrations of Ti, V, Ni, Mn, Cr, Zn, Al, Ga, Co, Cu, Mg, and Sn measured in the different types of magnetite grains; i.e., Mgt-glom, Mgt-meg, Mgt-interm and Mgt-deep. Magnetite trace element data from shallow/outcropping zones (Mgt-surface) were taken from La Cruz et al. (2020), as well as drill core data from Laco Norte, Laco Sur, Extensión Laco Sur and Pasos Blancos ore bodies. A statistical summary including minimum, maximum, average and median concentrations for each element analyzed in the different magnetite type are reported in Table 2.

Overall, LA-ICP-MS data of magnetite show similar trends to those revealed by EPMA (See Figs. 10 and 11), i.e., a progressive trend of depletion from trace element-rich magnetite in the host andesite to trace element-poor magnetite in the outcropping ore bodies (Table 2; Fig. 11). Distinct patterns are configured by decreasing concentrations of Ti, V, Ni, Mn, Zn, Cr, Al, Ga, Cu and Co, following the order: Mgt-glom (andesite) > Mgt-meg (andesite) > Mgt-deep > Mgt-interm > Mgt-surface (Fig. 11; Table 2; Suppl. Mat. Annex B, Table B14). In general, median trace element concentrations of magnetite in the andesite rocks (Mgt-glom and Mgt-meg) and in the deeper levels of the ore bodies (Mgt-deep) are up to 1-2 orders of magnitude higher than in the shallower sections. This decreasing trend is well evidenced by, for example, Ti (65,400 ppm, Mgt-glom; 59,400, Mgt-meg; 7170, Mgt-deep; 3191, Mgt-interm; 210 ppm, Mgt-surface), Cr (789 ppm, Mgt-glom; 664, Mgt-meg; 15.35, Mgt-deep; 19.0, Mgt-interm; 9.80 ppm, Mgt-surface), as well as Al, V, and Mn (Fig. 11; Table 2). Magnesium and Sn concentrations, in contrast, exhibit less compositional variability among different magnetite types (Fig. 11).

3.4.3. Microtextures and chemical composition of clinopyroxene

Clinopyroxene is a common mineral phase at El Laco, intimately associated with magnetite in both the host andesites and the outcropping and subsurface ore bodies. In the andesite host rocks, clinopyroxene occurs as phenocrysts and a groundmass-forming microlite phase. It also occurs with magnetite in glomerocrysts (Cpx-glom, Figs. 7a; B1), or is included in magnetite megacrysts porous rims (Cpx-meg, Fig. 7b). In the ore bodies, on the other hand, clinopyroxene is modally the second most abundant mineral after magnetite and its abundance increases significantly with depth (Cpx-ore). Clinopyroxene grains have variable size ranging from ~50 µm to a few millimeters and occur mostly as euhedral crystals immersed within the surrounding magnetite and can contain ilmenite inclusions (Fig. B7). No magnetite inclusions within Cpx-ore were identified throughout the studied samples.

EPMA-WDS and synchrotron µ-XRF elemental maps of clinopyroxene grains from andesite host rocks and the ore bodies reveals complex microtextural features and distinct chemistry (Fig. 12). Zoning patterns are recognized in different mineral growth areas of the grains, which vary from oscillatory to sector zonings (e.g., Fig. 12a-c). In the host andesites, the most notable features of Cpx-glom are resorbed Ti-poor cores and an intermediate (mantle) zones with oscillatory zoning that alternates Cr- and Ti-rich layers (Fig. 12a). In addition, Cpx-glom hosts Fe-Ti oxide inclusions that are distributed randomly from core to rim, whereas apatite inclusions occur forming distinct growth bands that are depleted in Ti and enriched in Ca (Fig. 12a). On the other hand, as described above for magnetite, Cpx-ore grains exhibit distinct textural patterns depending on depth (Figs. 12b, c; B7).

Cpx-ore from the deep zone has cores with high Mg (~10 wt%) and relatively low Fe and Al and Na concentrations (~2–3, <0.5, and 0.5–1.0 wt%, respectively), which also display complex internal growth patterns with relatively high Cr contents (~0.3 wt%) (Figs. 12c; B8). These cores are, in turn, overgrown by mantles with lower Mg (7–8 wt%) and higher Fe, Al and Na contents (~8, ~1.5, and 2.0–2.5 wt%, respectively), which along with Ti (~0.5–1.0 wt%), increase towards rims, with growth bands separated in some grains by highly sinuous µm-scale dissolution surfaces (right-hand grain in Fig. 7c). Cpx-ore grains from intermediate levels are Fe-rich (~4–6 wt%), but cores have low Mg (7–8 wt%) and Cr (<0.1 wt%) concentrations (Fig. 12b). Aluminum and Ti distributions reveal three clearly defined zones: cores with relatively low Al and Ti contents (<0.5 and ~1 wt%, respectively); enriched mantle zones (~1.0–1.5 and ~2.5 wt%, respectively), which grade through highly-resorbed and irregular contacts towards depleted rims (~0.1–0.3 and 0.8–1.0 wt%) in those elements, characterized by a particularly Cr-rich (~0.5 wt%) oscillatory zoning (Fig. 12b). Sodium in turn shows a core-to-rim oscillatory behavior marked by Na-poor (~0.5 wt%) cores, relatively enriched mantles (~1 wt%) and outer rims with slightly lower concentrations (~0.8 wt%). (See Figure 12 for details). The majority of Cpx-ore grains contain irregular and compositionally different zones within their cores.

Chemical data show that Cpx-glom and Cpx-meg have mostly augite compositions, whereas Cpx-ore grains have both diopside and augite compositions (Fig. 13a; Table 3; Suppl. Mat. Annex B, Table B13). Likewise, Figure 8b shows that these three varieties have a predominantly diopsidic component ranging from Di_{62} to Di_{93} in the hedenbergite (Hd), johannsenite (Jo), and diopside (Di) ternary plot expressed in terms of Fe, Mn and Ca mole fractions, respectively. Overall, Cpx-glom and Cpx-meg have higher Hedenbergite values and average contents of Fe (7.24 and 6.67 wt%, respectively), Al (1.18 and 0.95 wt%), Mn (0.23 and 0.18 wt%), and less pronounced for Ti (0.31 and 0.24 wt%) than Cpx-ore (5.16, 0.75, 0.06, and 0.16 wt%, respectively) (Fig. 13d-g; Table 3). Cpx-ore contains higher concentrations of Ca, a higher Mg# (expressed as Mg#=Mg/(Mg+Fe)) and notoriously higher Na (0.69 wt%) than Cpx-glom and Cpx-meg (both 0.26 wt%) (Fig. 13c, d; Table 3).

3.5. DISCUSSION

3.5.1. Origin of magnetite microtextures in the andesite host rocks

Magnetite in the volcanic host rocks from El Laco display different textures, including thin- and thick-scale trellis- and sandwich-type ilmenite exsolution lamellae, as well as irregular granule ilmenite domains (Mgt-glom, Figs. 7a; B1). These textures in magnetite are the result of oxy-exsolution processes, commonly observed in both extrusive and intrusive igneous rocks that experienced extensive sub-solidus re-equilibration, resulting in spinel exsolution products ranging from ulvöspinel, ilmenite to pleonaste (Frost, 1991). Oxy-exsolution occurs when the Fe_2TiO_4 component in the spinel solid solution is oxidized at a temperature above the magnetite-ulvöspinel solvus, forming ilmenite lamellae along the {111} planes of the host titanomagnetite (Buddington and Lindsley, 1964). In contrast, pleonaste and ulvöspinel exsolution lamellae tend to align along {100} planes of host magnetite (Turnock and Eugster, 1962, Price 1980, 1981). In the El Laco andesites, it is likely that the ilmenite exsolutions were formed by the oxidation of titanomagnetite (magnetite-ulvöspinelss) during progressive cooling after eruption based on their {111} plane orientation pattern and their typical sandwich-type texture reported in cooling volcanic and sub-volcanic rocks (Buddington and Lindsley, 1964).

Ilmenite lamellae have also been proposed to form as a result of either direct exsolution from cation-deficient spinel solid solution through the substitution of Fe^{2+} by Ti^{4+} at low oxygen fugacity and high-temperature conditions (Lattard, 1995), or subsolidus re-equilibration of coexisting Fe-Ti oxides (Tan et al., 2016). Nevertheless, the presence of 1) two distinctive ilmenite exsolution domains occurring simultaneously within the same magnetite grain (e.g., trellis- and granule-type, and trellis- and sandwich-type, Fig. 7a); and 2) ilmenite grains showing Fe-rich exsolutions (Fig. 7a), probably represent a more complex evolution, with multiple stages of ilmenite exsolution under fluctuating fO2 conditions, indicating that inter-oxide re-equilibration might have taken place (Tan et al., 2016).

On the other hand, magnetite megacrysts partially surrounded by discrete clinopyroxene grains were observed within the (pre-ore) Laco Norte lower andesite unit (Figs. 6; 7b). These megacrysts (Mgt-meg) show abundant porosity and fracturing particularly towards grain rims, which may be suggestive of extensive re-equilibrium and partial dissolution by reaction with either a silicate melt or fluids, or both. Mgt-meg shows a core-to-rim gradual decrease in the concentration of Fe, Mn and Cr and a reverse concentration gradient of Ti content (core: 1 wt% to rim: 6 wt%; See Fig. 7c). The increasing Ti towards the rim, correlated with decreasing Fe content in magnetite, is well documented (e.g., Ghiorso and Evans 2008; Sauerzapf et al. 2008). Previous studies interpreted the reverse zoning of Ti in magnetite-ilmenite phenocryst pairs from volcanic rocks as evidence of magma mixing and pre-eruptive heating events (Nakamura, 1995; Morgado et al., 2019). However, the rims of Mgt-meg grains are highly porous and there is no presence of ilmenite grains in direct contact with magnetite. Most importantly, synchrotron µ-XRF data reveal that the Ti reverse zoning is spatially related to Mgt-meg porosity, such that Ti concentrations increase with porosity (Fig. 7b; c). Therefore, we interpret that the Ti zoning is related to intragrain diffusion caused by reaction with high-temperature magmatic-hydrothermal fluids rather than reaction with a silicate melt. It is likely that exsolved fluids strongly promoted the partial dissolution of Mgt-meg rims and might have influenced the precipitation of interstitial clinopyroxene associated with porosity (Figs. 7b, c). Although no experimental studies of Ti or Fe diffusion in magnetite-fluid systems are currently available, evidence from magnetite-melt-based diffusion and partitioning experiments by Sievwright et al. (2020) indicate that Ti would be more susceptible to diffusive re-equilibration between magnetite and surrounding silicate melt. In contrast, the original Cr content would be best preserved in the magnetite core due to its slower diffusion rates (Sievwright et al., 2020), in agreement with observed µ-XRF for this element (Fig. 7c, lower panel).

Overall, microtextural observations and chemical data of accessory magnetite grains hosted in the El Laco andesites are indicative of an igneous origin. Textural and compositional changes of magnetite were probably caused by cooling and/or subsolidus oxidation, and are supported by the presence of abundant oxy-exsolution and zoning features. It is important to note that evidence of liquid immiscibility, e.g., 1) interstitial Fe-P melt and immiscible Si-rich conjugate (Xie et al., 2019), 2) immiscible iron-rich droplets and silicate melts within andesite-hosted melt inclusions (Velasco et al., 2016; Tornos et al., 2017), were not observed during our comprehensive inspection of the volcanic host rocks. Therefore, all magnetite in the studied andesite samples point to magnetite crystallization from a silicate melt.

3.5.2. Fluid-mediated magnetite ore formation and dissolution-reprecipitation

Magnetite from the El Laco ore bodies, on the other hand, displays complex microtextural changes with depth. At depth (Mgt-deep, >150 m depth) magnetite shows well-developed trellis-type textures,

similar to those described in accessory magnetite from the host andesites (Figs. 8; B4-B6a), although with thinner lamellae (commonly <10 µm). As above, these ilmenite lamellae are interpreted as oxy-exsolution products from primary Ti-rich magnetite (Frost, 1991; Buddington and Lindsley 1964). The assemblage of magnetite with trellis-texture and ilmenite grains, has been commonly described in igneous rocks, as well as in magmatic Fe-Ti-(V) and Ni-Cu sulfide deposits (Buddington and Lindsley, 1964; Boutroy et a., 2014; Tan et al., 2016). These authors have invoked cooling-related re-equilibrium (e.g., oxy-exsolution) formation mechanisms under magmatic conditions. This dominantly igneous-like component in the deeper portion of El Laco magnetite ores is also supported by the magnetite + rutile symplectites observed in ilmenite grains from the Mgt-deep zone (Figs. 8b; B4). This is a well-documented texture in igneous rocks that involves the breakdown of unstable minerals that are intergrown as curved or vermicular lamellae as a result of changing chemical and/or physical factors (i.e., rapid cooling, decompression, oxidation and infiltration of aqueous fluids; Moseley, 1984; Claeson, 1998; Hippertt and Valarelli, 1998; Dégi et al., 2010; Tan et al., 2015; Regan et al., 2019). Similar textures were reported for ilmenite grains from the Xinjie Fe-Ti oxide-bearing mafic-ultramafic layered intrusion in SW China (See Fig. 1a; b in Tan et al., 2016). These authors suggested that the formation of magnetite + rutile symplectite is caused by sub-solidus oxidation of the ilmenite-hematite solid solution under relatively oxidizing conditions controlled by the composition and proportion of interstitial magmatic-hydrothermal fluid (Buddington and Lindsley, 1964). Therefore, microtextures of coexisting magnetite and ilmenite in the deep levels of the El Laco ore bodies are consistent with magmatic-like conditions in the roots of the El Laco ore system, and also provide supporting evidence for the idea of more oxidizing conditions during iron mineralization.

Noteworthy is the transitional zone from deep to intermediate levels where magnetite grains (Mgt-interm, ~30–150 m depth) shows both ilmenite exsolution lamellae and dissolution-reprecipitation textures, evidencing complex growth histories and re-equilibration processes (Figs. 9a, b; B6a). Particularly, the irregular and sharp chemical contacts that separate highly-resorbed magnetite cores from oscillatory-textured overgrowths are indicative of dissolution-reprecipitation reactions assisted by fluids (Putnis, 2009) (Fig. 9a). Similar textures have been reported in samples of hydrothermally altered igneous magnetite (Wen et al., 2017), Fe-skarns and IOA-IOCG deposits (Hu et al., 2014, 2015; Heidarian et al., 2016; Yin et al., 2017; Deditius et al., 2018; Huang and Beaudoin, 2019; Palma et al., 2020). Dissolution-reprecipitation involves the break-down of a parent mineral coupled with nucleation and crystallization of a new phase at the mineral-fluid interface, resulting from the continuous interaction with hydrothermal fluids under fluctuating physicochemical conditions (Geisler et al., 2007; Putnis and Austrheim, 2013). As described, the resorbed magnetite cores are surrounded by magnetite overgrowths characterized by oscillatory and sector zoning, and the occurrence of alternating inclusion-rich and inclusion-poor bands (Fig. 9a). These textures are produced by physicochemical changes, which periodically affects the partitioning behavior of trace elements into magnetite (Shimazaki, 1998; Dare et al., 2015; Sievwright et al., 2017; Huang et al., 2018). Furthermore, fluctuating supersaturation of mineralizing fluids with respect to oxide and silicate phases can trigger the formation of bands with abundant mineral nanoparticles during progressive growth of hydrothermal magnetite (Deditius et al., 2018; Yin et al., 2019). The described textures suggest that hydrothermal fluids were responsible for modifying the primary features of magnetite in the ore bodies. Notably, some magnetite grains from the intermediate zone (Mgt-interm) display more complex textures where dissolution-reprecipitation textures and oscillatory/sector-zoned areas are overprinted by ilmenite exsolution lamellae within the same magnetite grain (Figs. 9a, b; B6a, respectively). The observed textures suggest that Ti-rich magnetite occurring at intermediate levels (Mgt-interm) precipitated from magmatic-hydrothermal fluids, whose Ti-rich nature could be associated with partial dissolution of primary titanomagnetite at depth or Ti

remobilization after ilmenite exsolution from trellis textured Mgt-deep. These complexly-textured grains underwent oxy-exsolution after dissolution-reprecipitation, probably in response to decreasing temperature and increasing fO_2 conditions under hydrothermal conditions (Frost, 1991; Lindsley, 1991) (Figs. 9b; B6a).

The precipitation of Ti-rich magnetite from magmatic-hydrothermal fluids at El Laco is further supported by the occurrence of veinlets and breccias at depth, where magnetite contains ilmenite exsolution lamellae and coexists with variable amounts of ilmenite grains (Figs. 8a-f; B4-S5). Even though these features are mostly typical of igneous magnetite (Frost and Lindsley, 1991; Mücke, 2003; Tan et al., 2016), Ti-rich magnetite, ilmenite and lamellar exsolution textures have also been reported for a number of magmatic-hydrothermal systems, including Fe-skarns (Hu et al., 2015), volcanic-hosted Fe-Cu deposits (Wang et al., 2020), IOCG systems (Huang and Beaudoin, 2019; Rodríguez-Mustafa et al., 2020), and IOA deposits (Borrok et al., 1998; Parente et al., 2019; Palma et al., 2020). Experimental evidence indicates that Ti solubility is critically dependent on fluid chemistry and is significantly favored at high temperature and relatively reducing fO_2 conditions (Frost, 1991; Lindsley, 1991; Rapp et al., 2010; Tanis et al., 2016). In addition, experimental data show that halogen-rich aqueous fluids can transport Ti as well as other HFSE. A decrease in the F and Cl concentration in the fluid would result in rutile precipitation (Audétat and Keppler, 2005; Rapp et al., 2010; Tanis et al., 2016), which is consistent with the abundant presence of Cl-bearing marialitic (Na-rich) scapolite in the Ti-rich assemblages at El Laco (Figs. 8e; B4d; B5e-g; see EDS spectrum in Fig. B8). The presence of scapolite in the breccias, replacing the rims of andesite fragments (Fig. 8e), in veinlets and alteration haloes (Figs. B4-B5), is in agreement with the involvement of high-temperature hydrothermal fluids during mineralization at El Laco. Scapolite is commonly described in (Ca-Na-Fe)-rich high-temperature alteration assemblages in ore systems including Fe-skarns (Pons et al., 2009; Hawkins et al., 2017), IOCG (Marschik and Fontbote, 2001a; Bernal et al., 2017; del Real et al., 2018; Huang et al., 2019) and IOA deposits (Bookstrom, 1997; Lupulescu et al., 2017; Rojas et al., 2018; Camprubí et al., 2019; Salazar et al., 2019). Therefore, the presence of scapolite-bearing assemblages with trellis-textured magnetite and ilmenite grains in veinlets and magnetite from the breccia matrix (Fig. 3e) support that these ores precipitated from a high-temperature Ti-rich magmatic-hydrothermal fluid under relatively reducing conditions. Subsequently, this assemblage re-equilibrated through oxy-exsolution processes in response to increasing fO2 and progressive cooling.

3.5.3. Geochemical gradients in magnetite and magmatic-hydrothermal evolution

The EPMA and LA-ICP-MS data presented here reveal a systematic decrease in trace element concentrations in magnetite (Figs. 10, 11). As described above (section 4.2), igneous magnetite in the host andesites is trace element-rich, while magnetite in the ore bodies show a progressive trend of depletion from the deeper portions towards the surface. This trend is interpreted as resulting from a combination of magmatic-hydrothermal processes operating during the formation of the El Laco ore bodies (Dare et al., 2015; Ovalle et al., 2018; La Cruz et al., 2020; Childress et al., 2020). Titanium, V, Cr, Ni, Co, Ga, Zn, Sn and depletion trends have been shown particularly relevant for Fe-rich mineral systems (Nadoll et al., 2014; Dare et al., 2015; Salazar, et al., 2019; Palma et al., 2020), and are consistent with magnetite crystallizing under high-temperature (>500 °C) that progressively grade towards lower temperature (<500 °C) hydrothermal conditions (Nadoll et al., 2014).

Trace element scatterplots and magnetite discriminant diagrams provide additional support for a progressive magmatic-to-hydrothermal transition in the El Laco system (Fig. 14). The Fe vs. V/Ti graph shows that magnetite grains from the host andesite (Mgt-glom and Mgt-meg) consistently plot

in the igneous field (Fig. 14a), whereas most magnetite grains from the ore bodies plot in the hydrothermal field (Fig. 14a). Noteworthy is a trend characterized by increasing Fe concentrations and V/Ti ratios from igneous magnetite glomerocrysts (Mgt-glom) to megacrysts (Mgt-meg) in the host andesites, to hydrothermal magnetite (Mgt-deep, Mgt-interm and Mgt-surface) (Fig. 14a). This trend is consistently observed in several plots for well-known indicator elements used to discriminate between igneous and hydrothermal magnetite, such as Ti, V, Ga, Cr, and Ni (Loberg and Horndahl, 1983; Nadoll et al., 2014; 2015; Dare et al., 2014; Knipping et al., 2015b; Salazar et al., 2019) (Fig. 14b-g). In addition, a new plot of Zn vs. Mn also shows a similar trend for the different magnetite types in El Laco (Fig. 14d).

The Ga vs. V data of magnetite in Figure 14c is consistent with previous observations that Ga and V concentrations are typically higher in igneous than in hydrothermal magnetite (Nadoll et al., 2014; Salazar et al., 2019; Palma et al., 2020). Experimental and empirical evidence indicate that redox-sensitive elements such as V are preferentially incorporated into magnetite at high temperature and more reducing conditions (Toplis and Corgne, 2002; Nadoll et al., 2014; Sievwright et al., 2017). The partitioning behavior of Ga between magnetite and silicate melt, on the other hand, is relatively insensitive to oxygen fugacity changes (D(Ga) 0.93-1.36; Sievwright et al., 2017); therefore, high concentrations of Ga in igneous magnetite suggests a temperature control (Figs. 11; 14c), and consistent with recent empirical (Liu et al., 2015; He et al., 2016; Polivchunk, 2017) and experimental studies (D(Ga) >2.49; Horn et al., 1994). Therefore, we conclude that the Ga vs. V data define a clear trend from high-temperature magmatic and highly reduced conditions (e.g., high Ga and V; Mgt-glom) that shift to lower-temperature and more oxidizing magmatic-hydrothermal conditions (e.g., lower Ga and V; Mgt-deep, -interm, -surface). Mgt-meg represents a transitional signature between the two environments (Figs. 11; 14c). Further, such highly oxidizing conditions during the formation of the magnetite-dominated El Laco mineral system are consistent with the presence of anhydrite and hematite as daughter crystals within clinopyroxene-hosted hydrosaline fluid inclusions at El Laco (Sheets, 1997; Brooman et al., 1999). However, some variability is observed caused by hydrothermal overprinting and chemical re-equilibration (Hu et al. 2014, 2015; Wen et al., 2017; Ovalle et al., 2018; Huang et al., 2018; Huang and Beaudoin, 2019), which highlights the importance of careful textural studies that must be performed before the quantitative compositional analysis of magnetite.

These geochemical trends support our mineralogical data discussed here (section 5.1). We therefore conclude that our El Laco data record the transition from magnetite crystallized from a silicate melt (Mgt-glom), to magnetite crystallizing in the presence of a silicate melt and an exsolved volatile (fluid) phase (Mgt-meg), to magnetite crystallizing under fluid-dominated (sub-solidus) hydrothermal conditions, i.e., magnetite in the ore bodies, which was also subjected to dissolution-reprecipitation processes (Mgt-deep, Mgt-interm). It is relevant to note that magnetite in the ore bodies preserves an igneous-like signature only in the deep zones of the system (Mgt-deep).

3.5.4. Supporting evidence from clinopyroxene in the andesites and ore bodies

Previous studies on El Laco deposit have reported the widespread occurrence of clinopyroxene in the host andesites (Velasco et al., 2016; Xie et al., 2018; 2019) and as the main silicate gangue mineral associated with the magnetite ore bodies (Nystrom and Henríquez, 1994; Rhodes et al., 1999; Brooman et al., 1999; Vivallo, 1991; Naranjo et al., 2010; Ovalle et al., 2018). Clinopyroxene in the andesites (Cpx-glom) is characterized by resorbed cores and an intermediate zone (mantle) with alternating Cr-rich concentric layers, which are also recorded by orthopyroxene in the same glomerocryst (Fig. 12a). This texture possibly reflects abrupt changes in the physicochemical state of the magmatic system, most likely related to eruption-triggering mafic magma recharges into a

glomerocryst-forming magma reservoir (Streck, 2008; Ubide and Kamber, 2018; Ubide et al., 2019a; Xing and Wang, 2021). On the other hand, Ti distribution in Cpx-glom grains is decoupled from Cr, with low Ti contents and high Cr bands in the cores, and a Ti-rich outermost rim (Fig. 12a). Resorbed cores with low concentrations of incompatible elements such as Ti are indicative of a recycled (antecryst) origin, whereas the oscillatory Ti-rich bands developed towards the rims may be related to kinetically-controlled growth caused by high rates of undercooling during rapid magma ascent and eruption (Ubide et al., 2019b). In addition, the occurrence of Fe-Ti oxides and apatite inclusions in the cores and rims of the Cpx-glom grains, which in some cases are associated with Cr-rich Fe-Ti oxide and Ti-poor (apatite) bands, suggests an early fractionation and episodic supersaturation conditions for these accessory phases during clinopyroxene growth.

On the other hand, clinopyroxene in the ore bodies (Cpx-ore) from the El Laco deposit is complexly zoned and has a different chemistry than igneous clinopyroxene (Figs. 12; 13; Fig. B8). Cpx-ore grains exhibit notorious core-to-rim compositional variations and microtextures including sector and oscillatory zoning, and sinuous contacts separating growth zones with highly-contrasting chemistry (Figs. 12b, c). As described for magnetite, clinopyroxene in the El Laco ore bodies also exhibit depth-dependent characteristics. In the deeper levels of the ore bodies, homogeneous (Mg-Cr)-rich and (Fe-Al-Na)-poor cores are overgrown by (Mg-Cr)-poor and (Fe-Al-Na)-rich oscillatory zones (Figs. 12c; B7a). It is likely that Cpx-ore cores grew under relatively stable (near-equilibrium) conditions, followed by a stage of rapid growth dominated by repeated pulses of hydrothermal fluids of variable composition, which formed the oscillatory zones (Wen et al., 2020). The two zones are separated by sinuous contacts (line contours in Fig. 12c), which are interpreted as evidence of dissolution-reprecipitation processes (Harlov et al., 2005; Putnis, 2009; Krause et al., 2013). Interestingly, inverse core-to-rim zonings were observed in Cpx-ore at the intermediate levels of the ore bodies. This zonation is characterized by Fe-rich and (Mg-Cr)-poor cores, (Ti-Al)-rich mantles, and oscillatory enrichments in Cr that are notably developed in the grain rims (Figs. 12b; B7b). This may indicate that the magmatic-hydrothermal fluids that formed the oscillatory-zoned rims of Cpx-ore in deep samples would have been also involved in formation of Cpx-ore cores at intermediate levels of the system.

Similar dissolution-reprecipitation textures and core-to-rim compositional zonations were recently described for hydrothermal clinopyroxene from Fe-skarn deposits (Wen et al., 2020). The cited authors suggested a transition in mineral growth mechanisms from early diffusive metasomatism by low-salinity fluids under low water/rock ratios, to later advective metasomatism by high-salinity fluids under high water/rock ratios. Those authors proposed that such abrupt shifts in water/rock ratios could be related to permeability-forming fracturing processes that promote significant depressurization of the system that, in turn, results in phase separation of the ore fluids into a dilute vapor phase and a dense brine. At El Laco, the collapse of the volcanic edifice generated subvertical ring-shaped structures and fissures that favored the rapid emplacement of the magnetite ore bodies towards the upper volcanic levels forming large breccia bodies at depth (Ovalle et al., 2018). Thus, it is likely that this breccia-forming transition from lithostatic to hydrostatic regimes would have triggered abrupt pressure drops in the system causing boiling of the magmatic-hydrothermal fluids. This hypothesis is supported by previous fluid inclusion studies that consistently suggested an evolution of ore fluids recorded by early high-temperature (750-840 °C) hydrosaline, and liquid-dominated to late lower temperature (250-400 °C) vapor-dominated and more diluted fluid inclusions within ore-related clinopyroxene and apatite, respectively (Sheets, 1997; Broman et al., 1999). The core-to-rim patterns observed in Cpx-ore for Fe and Na (Fig. 12c) may suggest an increase in salinity (e.g., NaCl content) of the mineralizing fluids, which is known to correlate with an increasing capacity

for Fe transport (Simon et al., 2004; Scholten et al., 2019). Further evidence that supports the effects of salinity on metal transport can be observed in Cpx-ore from intermediate levels. Clinopyroxene grains show a well-defined correspondence between Cr and Na in oscillatory zones, particularly towards the rims (Fig. 12b). Previous studies have shown that Cr solubility is favored in high salinity hydrothermal fluids either as $CrCl^{-4}$ or $CrCl(OH)^{0}$ complexes (Watenphul et al., 2014; Huang et al., 2019). Hence, the spatial correspondence between Cr and Na distribution in Cpx-ore may suggest growth from ore fluids with fluctuating salinity due to intermittent boiling, which tends to increase the salinity of the residual brine (Sheets, 1997; Kouzmanov and Pokrovski, 2012). These observations—in addition to the occurrence of oriented fluid inclusions hosted by magnetite (Mgt-deep) that contain halite crystals (See Suppl. Mat. Fig. B9)—are consistent with microthermometry data that suggest the involvement of high-temperature Fe-rich hydrosaline fluids that underwent extensive boiling in the near-surface volcanic environment at El Laco (Sheets, 1997; Broman et al., 1999).

Petrologic studies often use Cr zoning in igneous clinopyroxene as proxy for tracking hotter and less evolved magma injections in volcanic magma chambers (Ubide and Kamber, 2018). Therefore, it is possible that Cr zoning in ore-related clinopyroxene at El Laco may be associated with pulses of hotter hypersaline fluids from the magmatic source at depth, resulting in alternating Cr-rich band textures in Cpx-ore (Fig. 12b, c). However, due to lack of clinopyroxene data for other IOA deposits, this interpretation should be taken with caution and should motivate further studies on the subject.

In summary, clinopyroxene data at El Laco point to several stages of mineral growth, probably under highly fluctuating P-T-X_{NaCl} conditions related to a magmatic source. This is supported by different compositions of clinopyroxene grains (Cpx-glom, Cpx-meg and Cpx-ore), illustrated in Figure 13. The observed trends for clinopyroxene (Fig. 13a-h) are generally similar to those reported here for magnetite (Figs. 10; 11; 14). The compositional trends for clinopyroxene are represented by decreasing Mn and Ti concentrations as Hedenbergite values decrease, as well as by decreasing Al, and increasing Ca concentrations with increasing Mg# (Fig. 13e-h). Remarkably, the Mn and Fe vs. Na plots in Figures 13c and 13d show a well-defined transition from purely igneous (i.e., Cpx-glom) to magmatic-hydrothermal compositions (i.e., Cpx-meg and Cpx-ore). These trends can also be observed in the ternary plots (Fig. 13a, b), and are consistent with clinopyroxene data of magmatic (mafic/ultramafic layered intrusions; Cao et al., 2019) and hydrothermal end members (Fe-skarn deposits; Wen et al., 2020).

3.6. SUMMARY AND CONCLUSIONS

EPMA, LA-ICP-MS and synchrotron μ-XRF data for magnetite and clinopyroxene from El Laco reveal complex microtextural and geochemical features that provide valuable information about the origin of this enigmatic deposit. Figure 15 summarizes our findings, which point to a combination of igneous and hydrothermal processes operating in a volcanic system.

- *Igneous stage:* A remarkable feature of the andesites that host the Fe mineralization at El Laco is the abundant presence of magnetite-rich glomerocrysts (Mgt-glom), sometimes reaching up to 30% of modal abundance (Figs. 15a-c). Our data show that these magnetite grains have the highest concentrations of trace elements in the entire system, consistent with compositions typical of magnetite crystallized from a silicate melt (Fig. 14). We interpret the formation of igneous magnetite as early in the history of El Laco (Martel et al., 1999). Magnetite in glomerocrysts may have formed in situ in the magma chamber, or may have been physically entrained from lower levels in the magma

plumbing system, possibly through mafic magma recharge processes (Edmonds, et al., 2014; Ovalle et al., 2018). This conclusion is supported by multiple Cr-rich growth bands and Fe-Ti oxides and apatite inclusions observed in clinopyroxene glomerocrysts (Cpx-glom, Fig. 15c).

On the other hand, the occurrence of magnetite megacrysts (Mgt-meg; Fig. 15d) also supports the idea of a magma chamber efficiently precipitating magnetite below El Laco volcano. The reverse zoning of Ti in these magnetites, spatially associated with porosity and dissolution fronts (Fig. 7c), suggests reaction with an exsolved high-temperature fluid phase that promoted dissolution of Mgt-meg and subsequent formation of clinopyroxene within this porous rim (Fig. 15d). The coarsening of Mgt-meg via clustering of smaller magnetite and clinopyroxene along Mgt-meg's rims may have been favored by heterogeneous nucleation within the melt (Fig. 15d) (Edmonds et al., 2014; Pleše et al., 2019; Knipping et al., 2019). This is a well-documented process occurring during the evolution of silicate magmas, where early formed magnetite microlites trigger volatile saturation, forming mineral-bubble suspensions that ascend and cluster (Edmonds, 2015; Knipping et al. 2019). Experimental studies and numerical simulations have demonstrated the feasibility and efficiency of this process to segregate magnetite in magmatic systems (Hurwitz and Navon, 1994; Edmonds et al., 2014; Shea, 2017; Pleše et al., 2019). Furthermore, this process has also been proposed as a key factor controlling bubble nucleation in silicate magmas and their explosive behavior through volcanic eruptions (Burgisser et al., 2020). Textural evidence of this process has been reported in studies focusing on 3D textural observations of samples (Pleše et al., 2019; Schoneveld et al., 2020; Burgisser et al., 2020). We propose that the magnetite megacrysts (Mgt-meg) in the El Laco andesites is indicative of interaction between magnetite and exsolved fluids, considering the fact that the chemistry of both magnetite and clinopyroxene that form megacrysts is transitional between purely igneous (e.g., Mgt- and Cpx-glom) and magmatic-hydrothermal conditions (Mgt-deep and Cpx-ore) (Figs. 10, 11, 13, 14).

- *Magmatic-hydrothermal stage:* One of the key findings of this study relates to variations in both chemistry and mineral microtextures with depth. The deeper zones of the El Laco ore bodies are dominated by breccias and veinlets with both magmatic and hydrothermal characteristics (Fig. 15e; f). Magnetite in these deep breccia zones (Mgt-deep, Figs. 15e) displays oxy-exsolution textures and has high concentrations of Ti, V, Al, Ga, Ni and Cr, spanning compositions from igneous to high-temperature hydrothermal (Nadoll et al., 2014; Wen et al., 2017) (Fig. 14). Clinopyroxene grains (Cpx-ore) associated with Mgt-deep have microtextures formed under multiple stages of mineral growth. The core-to-rim increase in both Fe (and other elements) and Na in oscillatory zones of Cpx-ore, as well as the presence of dissolution-reprecipitation textures, suggest an increase in the salinity of the ore-forming fluids, similarly to processes documented in some Fe-skarns (Wen et al., 2020). The magnetite-clinopyroxene breccias found at intermediate levels of the ore bodies are characterized by complex growth histories, and decreasing concentrations of key elements (Ti, V, Al, Cr, Ni, Mn, Zn, and Ga) that indicate a more hydrothermal character (Fig. 11). Both magnetite and clinopyroxene exhibit resorbed cores with sinuous and sharp contacts, and overgrowth zones with well-developed oscillatory zoning (Fig. 15f). These textures are commonly observed in a wide range of hydrothermal environments and are indicative of dissolution-reprecipitation processes affecting primary magnetite and clinopyroxene (Deditius et al., 2018; Wen et al., 2020).

Our observations at El Laco point to an evolving system increasingly influenced by hydrothermal circulation with high fluid fluxes and fluctuating physicochemical conditions (Sheets, 1997; Deditius et al., 2018; Wen et al., 2020). Magnetite from the shallow and surficial ore zones (Mgt-surf, Fig. 15g) has a low concentration of most trace elements (Ti, Cr, V, Ni, Ga and Al) and a highly vesicular

nature. These features are consistent with previous studies suggesting that magnetite precipitated from a spent hydrothermal fluid (Nadoll et al., 2014; Knipping et al., 2015b; Dare et al., 2014; Deditius et al., 2018; La Cruz et al., 2020), which was possibly vented at the surface as a multiphase Fe-rich mixture (Ovalle et al., 2018).

We propose that the processes responsible for the compositional and microtextural variations in magnetite and clinopyroxene at El Laco were probably caused by rapid depressurization during the breccia-forming event, triggered by the de-stabilization of the volcanic edifice during explosive eruption.

3.7. ACKNOWLEDGEMENTS

Funding for this study was provided by ANID through Millennium Science Initiative Program (NCN13_065) "Millennium Nucleus for Metal Tracing Along Subduction", and by ANID-FONDAP project 15090013 "Centro de Excelencia en Geotermia de Los Andes, CEGA". The authors acknowledge the Graduate School of the Universidad de Chile for providing travel support through the Research Stay Program Grant for graduate students. We acknowledge the CSIRO Australian Resources Research Centre, Kensington for hosting J.T. Ovalle as a visiting student in Perth, Australia. The µ-XRF chemical maps presented in this study were collected on the X-ray fluorescence microscopy beamline at the Australian Synchrotron, part of ANSTO, and we thank David Paterson for his helpful technical assistance during data collection. The LA-ICP-MS analytical work was supported by ANID-FONDEQUIP instrumentation grant EQM120098. The authors also acknowledge the facilities, and the scientific and technical assistance of the Electron Microbeam Analysis Laboratory, University of Michigan, USA; and the Centre for Microscopy, Characterisation & Analyses, The University of Western Australia. Mario Rojo, Alejandro Mardones and Nino Sosa from Compañía Minera del Pacífco (CAP Minería) are thanked for their logistical support, and for providing access to the deposit and drill core libraries. Teresa Ubide is thanked for stimulating discussions about the chemical and textural data of clinopyroxene. J.T. Ovalle thanks financial support provided by ANID/Doctorado Nacional/2017-21170261, through a PhD scholarship, and by the Society of Economic Geologists Foundation (SEGF) through Graduate Student Fellowship Program (GSF-2017).

3.8. REFERENCES

1. Audétat A. and Keppler H. (2005) Solubility of rutile in subduction zone fluids, as determined by experiments in the hydrothermal diamond anvil cell. *Earth Planet. Sci. Lett.* **232**, 393–402.

2. Barnes S. J., Paterson D., Ubide T., Schoneveld L. E., Ryan C., and Le Vaillant M. (2020) Imaging trace-element zoning in pyroxenes using synchrotron XRF mapping with the Maia detector array: Benefit of low-incident energy. *Am. Mineral.* **105**, 136–140.

3. Bernal N. F., Gleeson S. A., Smith M. P., Barnes J. D., and Pan Y. (2017) Evidence of multiple halogen sources in scapolites from iron oxide-copper-gold (IOCG) deposits and regional Na-Cl metasomatic alteration, Norrbotten County, Sweden. *Chem. Geol*. **451**, 90-103.

4. Bookstrom A. A. (1977) The magnetite deposits of El Romeral, Chile. *Econ. Geol.* **72**, 1101–1130.

5. Borrok D. M., Kelser S. E., Boer R. H., and Essene E. J. (1998) The Vergenoeg magnetite-fluorite deposit, South Africa; support for a hydrothermal model for massive iron oxide deposits. *Econ. Geol.* **93**, 564–586.

6. Boutroy E., Dare S. A. S., Beaudoin G., Barnes S. J., and Lightfoot P. C. (2014) Magnetite composition in Ni-Cu-PGE deposits worldwide: Application to mineral exploration. *J. Geochem. Explor.* **145**, 64-81.

7. Broman C., Nyström J. O., Henriquez F. and Elfman M. (1999) Fluid inclusions in magnetite-apatite ore from a cooling magmatic system at El Laco, Chile: *GFF* **121**, 253–267.

8. Broughm S. G., Hanchar J. M., Tornos F., Westhues A. and Attersley S. (2017) Mineral chemistry of magnetite from magnetite-apatite mineralization and their host rocks: Examples from Kiruna, Sweden, and El Laco, Chile: *Miner. Deposita* **52**, 223–244.

9. Buddington A. F. and Lindsley D. H. (1964) Iron-titanium oxide minerals and synthetic equivalents. *J. Petrol.* **5**, 310–357.

10. Burgisser A., Arbaret L., Martel C., Forien M., and Colombier M. (2020) The role of oxides in the shallow vesiculation of ascending magmas. *J. Volcanol. Geotherm. Res.* **406**, 107072.

11. Camprubí A., Cabrera-Roa M. A., González-Partida E. and López-Martínez, M. (2019) Geochronology of Mexican mineral deposits. VIII: the Zacatepec polymetallic skarn, Oaxaca. *Bol. Soc. Geol. Mex.* **71**, 1, 207 – 218.

12. Canil D., Grondahl C., Lacourse T., and Pisiak L. (2016) Trace elements in magnetite from porphyry Cu–Mo–Au deposits in British Columbia, Canada. *Ore Geol. Rev.* **72** (1), 1116–1128.

13. Cao J., Wang X., and Tao, J. (2019) Petrogenesis of the Piqiang mafic-ultramafic layered intrusion and associated Fe-Ti-V oxide deposit in Tarim Large Igneous Province, NW China. *Int. Geol. Rev.* **61**,18, 2249-2275.

14. CAP Minería Annual Report 2016 <http://www.capmineria.cl/wp-content/uploads/2017/03/cap_mineria_memoria_2016.pdf >.

15. Carew M. J., Mark G., Oliver N. H. S. and Pearson N. (2006) Trace element geochemistry of magnetite and pyrite in Fe oxide (±Cu–Au) mineralised systems: insights into the geochemistry of ore-forming fluids. *Geochim. Cosmochim. Acta* **70**, 18, A83.

16. Childress T., Simon A. C., Reich M., Barra F., Bilenker L.D., La Cruz N. L., Bindeman I., and Ovalle J. T. (2020) Triple oxygen, hydrogen, and iron stable isotope signatures indicate a silicate magma source and magmatic-hydrothermal genesis for magnetite orebodies at El Laco, Chile: *Econ Geol.* **115**, 1519–1536.

17. Claeson D. T (1998) Coronas, reaction rims, symplectites and emplacement depth of the Rymmen gabbro, Transscandinavian Igneous Belt, southern Sweden. *Miner. Mag.* **62**, 743–757.

18. Dare S. A. S., Barnes S.-J., and Beaudoin G. (2012) Variation in trace element content of magnetite crystallized from a fractionating sulfide liquid, Sudbury, Canada: Implications for provenance discrimination: *Geochim. Cosmochim. Acta* **88**, 27–50.

19. Dare S. A. S., Barnes, S-J., Beaudoin G., Méric J., Boutroy E., and Potvin-Doucet, C. (2014) Trace elements in magnetite as petrogenetic indicators. *Miner. Deposita* **49**, 785-796.

20. Dare, S.A.S., Barnes, S.-J., and Beaudoin, G. (2015) Did the massive magnetite "lava flows" of El Laco (Chile) form by magmatic or hydrothermal processes? New constraints from magnetite composition by LA-ICP-MS: *Mineral. Deposita* **50**, 607–617.

21. Deditius A. P., Reich M., Simon A. C., Suvorova A., Knipping J., Roberts M. P., and Saunders M. (2018) Nanogeochemistry of hydrothermal magnetite. *Contrib. Miner. Petrol.* **173**, 46.

22. Dégi J., Abart R., Török K., Bali E., Wirth R., and Rhed, D. (2010) Symplectite formation during decompression induced garnet breakdown in lower crustal mafic granulite xenoliths: mechanisms and rates. *Contrib. Miner. Petrol.* **159**, 293–314.

23. del Real I., Thompson J. F. H., and Carriedo J. (2018) Lithological and structural controls on the genesis of the Candelaria-Punta del Cobre iron oxide copper gold district, Northern Chile: *Ore Geol. Rev.* **102**, 106–153.

24. Donovan J. J. and Tingle T. N. (1996) An improved mean atomic number background correction for quantitative microanalysis. *Microsc. Microanal.* **2**, 1, 1-7.

25. Dupuis C. and Beaudoin G. (2011) Discriminant diagrams for iron oxide trace element fingerprinting of mineral deposit types. *Miner. Deposita* **46**, 319-335.

26. Edmonds M. (2015) Flotation of magmatic minerals. M. Research Focus, *Geology* **43**, 655–656.

27. Edmonds M., Brett A., Herd R. A., Humphreys M. C. S., and Woods A. (2014) Magnetite-bubble aggregates at mixing interfaces in andesite magma bodies. *Geological Society, London*, Special Publications **410**, 95–121.

28. Fisher L. A., Fougerouse D., Halfpenny A., Ryan C. G., Micklethwaite S., Hough R. M., Cleverley J. S., Gee M., Paterson D., and Howard, D. (2015) Fully quantified, multi-scale element mapping of mineral system samples using the Maia detector array: recognizing chemical variation on micron to cm scales. *Miner. Deposita* **50**, 665–674.

29. Frost B. R., and Lindsley D. (1991) Oxide minerals: petrologic and magnetic significance. *Rev. Mineral. Soc. Am.* **25**, 509.

30. Frutos J., and Oyarzun M. J. (1975) Tectonic and geochemical evidence concerning the genesis of El Laco magnetite lava flow deposits, Chile. *Econ. Geol.* **70**, 988–990.

31. Geisler T., Schaltegger U., and Tomaschek F. (2007) Re-equilibration of Zircon in Aqueous Fluids and Melts. *Elements* **3**, 1, 43–50.

32. Ghiorso M. S., and Evans B. W. (2008) Thermodynamics of rhombohedral oxide solid solutions and a revision of the Fe–Ti two-oxide geothermometer and oxygen-barometer. *Am. J. Sci.* **308**, 957–1039.

33. Harlov D. E., Wirth R., and Förster H. (2005) An experimental study of dissolution–reprecipitation in fluorapatite: Fluid infiltration and the formation of monazite. *Contrib. Mineral. Petr.* **150**, 268–286.

34. Hawkins T., Smith M. P., Herrington R. J., Maslennikov V., Boyce A. J., Jeffries T., and Creaser R. A. (2017.) The geology and genesis of the iron skarns of the Turgai belt, northwestern Kazakhstan. *Ore Geol. Rev.* **85**, 216-246.

35. He H. L., Song Y. Y., Song Y. X., Du Z. S., Dai Z. H., Zhou T. and Xie W. (2016) Origin of nelsonite and Fe–Ti oxides ore of the Damiao anorthosite complex, NE China: evidence from trace element geochemistry of apatite, plagioclase, magnetite and ilmenite. *Ore Geol. Rev.* **79**, 367–381.

36. Heidarian H., Lentz D., Alirezaei S., Peighambari S., and Hall D. (2016) Using the chemical analysis of magnetite to constrain various stages in the formation and genesis of the Kiruna-type chadormalu magnetite-apatite deposit, Bafq district, Central Iran. *Miner. Petrol.* **110**, 927–942.

37. Hippertt J. F., and Valarelli J. V. (1998) Myrmekite: constraints on the available models and a new hypothesis for its formation. *Eur. J. Mineral.* **10**, 2, 317–331.

38. Horn I., Foley S. F., Jackson S. E., and Jenner G. A. (1994) Experimentally determined partitioning of high-feld strength-elements and selected transition-elements between spinel and basaltic melt. *Chem Geol.* **117**, 193–218.

39. Hu H., Li J. W., Lentz D., Ren Z., Zhao X., Deng X.D., and Hall D. (2014) Dissolution-reprecipitation process of magnetite from the Chengchao iron deposit: insights into ore genesis and implication for in-situ chemical analysis of magnetite. *Ore Geol. Rev.* **57**, 393–405.

40. Hu H., Lentz D., Li J. W., McCarron T., Zhao X. F., and Hall D., (2015) Reequilibration processes in magnetite from iron skarn deposits. *Econ. Geol.* **111**, 1–8.

41. Huang X. W. and Beaudoin G. (2019) Textures and chemical compositions of magnetite from iron oxide copper-gold (IOCG) and Kiruna-type iron oxide-apatite (IOA) deposits and their implications for ore genesis and magnetite classification schemes. *Econ. Geol.* **114**, 1–74.

42. Huang X-W., Zhou M-F., Beaudoin G., Gao J-F., Qi L., and Lyu C. (2018) Origin of the volcanic-hosted Yamansu Fe deposit, Eastern Tianshan, NW China: Constraints from pyrite Re-Os isotopes, stable isotopes, and in situ magnetite trace elements: *Miner. Deposita* **53**, 1039–1060.

43. Hurwitz S. and Navon O. (1994) Bubble nucleation in rhyolitic melts: Experiments at high pressure, temperature, and water content. *Earth Planet. Sci. Lett.* **122**, 267–280.

44. Jochum K. P., Willbold M., Raczek I., Stoll B., and Herwig K. (2005) Chemical characterisation of the USGS reference glasses GSA-1G, GSC-1G, GSD-1G, GSE-1G, BCR-2G, BHVO-2G and BIR-1G using EPMA, ID-TIMS, ID-ICP-MS and LA-ICP-MS. *Geostand. Geoanal. Res.* **29**, 285–302.

45. Knipping J. L., Bilenker L. D., Simon A. C., Reich M., Barra F., Deditius A. P. and Munizaga R. (2015a). Giant Kiruna-type deposits form by efficient flotation of magmatic magnetite suspensions. *Geology*, **43**, 591–594.

46. Knipping J. L., Bilenker L. D., Simon A. C., Reich M., Barra F., Deditius A. P., Munizaga R. (2015b) Trace elements in magnetite from massive iron oxide-apatite deposits indicate a combined formation by igneous and magmatic-hydrothermal processes. *Geochim. Cosmochim. Acta* **171**, 15-38.

47. Knipping J., Webster J. D., Simon A. C., and Holtz F. (2019) Accumulation of magnetite by flotation on bubbles during decompression of silicate magma. *Sci. Rep*. **9**, 3852.

48. Kouzmanov K. and Pokrovski G. S. (2012) Hydrothermal Controls on Metal Distribution in Porphyry Cu (-Mo-Au) Systems. Society of Economic Geologists, Inc. Special Publication **16**, 573–618.

49. Krause J., Harlov D. E., Pushkarev E. V. and Brügmann G. E. (2013) Apatite and clinopyroxene as tracers for metasomatic processes in nepheline clinopyroxenites of Uralian-Alaskantype complexes in the Ural Mountains, Russian Federation. *Geochim. Cosmochim. Acta* **121**, 503–521.

50. La Cruz N. L., Ovalle J. T., Simon A. C., Konecke B. A., Barra F., Leisen M., Reich M., and Childress T. M. (2020) The geochemistry of magnetite and apatite from the El Laco iron oxide-apatite deposit, Chile: Implications for ore genesis: *Econ. Geol.* **115**, 1461–1491.

51. Lattard D. (1995) Experimental evidence for the exsolution of ilmenite from titaniferous spinel. *Am. Mineral.* **80**, 968–981.

52. Lindsley D. H. (1991) Experimental studies of oxide minerals. *Rev. Mineral. Geochem.* **25**, 69–106.

53. Liu P-P., Zhou M-F., Chen W. T., Gao J-F., and Huang X-W. (2015) In-situ LA-ICP-MS trace elemental analyses of magnetite: Fe-Ti-(V) oxide-bearing mafic-ultramafic layered intrusions of the Emeishan large igneous province, SW China: *Ore Geol. Rev.* **65**, 853–871.

54. Loberg B. E., and Horndahl A. K. (1983) Ferride geochemistry of Swedish Precambrian iron ores. *Miner. Deposita* **18**, 487–504.

55. Longerich H. P., Günther D., and Jackson S. E. (1996) Elemental fractionation in laser ablation inductively coupled plasma mass spectrometry. *Fresenius J. Anal. Chem.* **355**, 538–542.

56. Lupulescu M. V., Hughes J. M., Chiarenzelli J. R., and Bailey D. G. (2017) Texture, Crystal Structure, and Composition of Fluorapatites from Iron Oxide-apatite (IOA) Deposits, Eastern Adirondack Mountains, New York. *Canad. Mineral.* **55**, 399–417.

57. Maksaev V., Gardeweg M., Ramírez C. F. and Zentilli M. (1988) Aplicación del método trazas de fisión a la datación de cuerpos de magnetita de El Laco e Incahuasi en el Altiplano de la Región de Antofagasta: V Congreso Geológico Chileno, Actas, 1:B1–B23.

58. Marschik R., and Fontboté L. (2001) The Candelaria-Punta del Cobre iron oxide Cu-Au (-Zn-Ag) deposits, Chile: *Econ. Geol.* **96**, 1799–1826.

59. Meinert L. D., Dipple G. M. and Nicolescu, S. (2005) World skarn deposits. In *Econ. Geol., 100th Anniversary Volume*, (eds. J. W. Hedenquist, J. F. H. Thompson, R. J. Goldfarb and J. P. Richards), 299–336.

60. Morgado E., Morgan D. J., Castruccio A., Ebmeier S. K., Parada M. A., Brahm R., Harvey Gutiérrez J. F., and Walshaw R. (2019). Old magma and a new, intrusive trigger: using diffusion chronometry to understand the rapid-onset Calbuco eruption, April 2015 (Southern Chile). *Contrib. Mineral. Petrol.* **174**, 61.

61. Moseley D. (1984) Symplectic exsolution in olivine. *Am. Mineral.* **69**, 139–153.

62. Mücke A. (2003) Magnetite, ilmenite and ulvite in rocks and ore deposits: petrography, microprobe analyses and genetic implications. *Miner. Petrol.* **77**, 215–234.

63. Mungall J. E., Long K., Brenan J. M., Smythe D. and Naslund H. R. (2018) Immiscible shoshonitic and Fe-P-oxide melts preserved in unconsolidated tephra at El Laco volcano, Chile. *Geology* **46**, 255–258.

64. Nadoll P., Mauk J. L., Hayes T. S., Koenig A. E., and Box S. E. (2012) Geochemistry of 1804 magnetite from hydrothermal ore deposits and host rocks of the Mesoproterozoic Belt Supergroup, USA. *Econ. Geol.* **107**, 1275-1292.

65. Nadoll P., Angerer T., Mauk J. L., French D., and Walshe, J. (2014) The chemistry of hydrothermal magnetite: a review. *Ore Geol. Rev.* **61**, 1-32.

66. Nakamura M. (1995) Continuous mixing of crystal mush and replenished magma in the ongoing Unzen eruption. *Geology* **23**, 807–810.

67. Naranjo J. A., Henríquez F. and Nyström J. O. (2010) Subvolcanic contact metasomatism at El Laco Volcanic Complex, Central Andes: *Andean Geology* **37**, 110–120.

68. Naslund H. R., Henriquez F., Nyström J. O., Vivallo W. and Dobbs F. M. (2002) Magmatic iron ores and associated mineralisation: Examples from the Chilean High Andes and Coastal Cordillera, in Porter, T.M., ed., Hydrothermal iron oxide copper-gold and related deposits: A global perspective: Adelaide, *PGC Publishing*, **2**, 207–226.

69. Neumann E-R., Svensen H. H., Polozov A. G., Hammer O. (2017) Formation of Si-Al-Mg-Ca-rich zoned magnetite in an end-Permian phreatomagmatic pipe in the Tunguska Basin, East Siberia. *Miner. Deposita* **52**, 1205–1222.

70. Nyström J. O. and Henriquez F. (1994) Magmatic features of iron ores of the Kiruna type in Chile and Sweden: Ore textures and magnetite geochemistry. *Econ. Geol*, **89**, 820–839.

71. Nyström, J. O., Henríquez F., Naranjo J. A., and Nasuland H. R. (2016) Magnetite spherules in pyroclastic iron ore at El Laco, Chile. *Am. Min.* **101**, 587–595.

72. Ovalle J. T., La Cruz N. L., Reich M., Barra F., Simon A. C., Konecke B. A., and Morata, D. (2018) Formation of massive iron deposits linked to explosive volcanic eruptions. *Sci. Rep.* **8**, 14855.

73. Palma G., Barra F., Reich M., Simon A. C., Romero R. (2020) A review of magnetite geochemistry of Chilean iron oxide-apatite (IOA) deposits and its implications for ore-forming processes. *Ore Geol. Rev.* **126**, 103748.

74. Parente C. V., Vieira Veríssimo C. U., Francisquini N., Perez Xavier R., Menez J., de Oliveira R., Araújo da Silva C. D., and Saraiva dos Santos T. J. (2019) Geology, petrography and mineral chemistry of iron oxide-apatite occurrences (IOA type), western sector of the neoproterozoic Santa Quiteria magmatic arc, Ceará northeast, Brazil. *Ore Geol. Rev.* **112**, 103024.

75. Park C. R. (1961) A magnetite "flow" in northern Chile: *Econ. Geol.* **56**, 431–441.

76. Paterson D., de Jonge M. D., Howard D. L., Lewis W., McKinlay J., Starritt A., Kusel M., Ryan C. G., Kirkham R., Moorhead, G., and Siddons, D. P. (2011) The X ray Fluorescence Microscopy Beamline at the Australian Synchrotron. Proceedings of the Australian Institute of Physics, **1365**, 219–222.

77. Paton C., Hellstrom J., Paul B., Woodhead J., and Hergt J., (2011) Iolite: Freeware for the visualization and processing of mass spectrometric data. *J. Anal. At. Spectrom.* **26**, 2508–2518.

78. Pleše P., Higgins M. D., Baker D. R., Lanzafame G., Kudrna Prašek M., Mancini L. and Rooyakkers S. M. (2019) Production and detachment of oxide crystal shells on bubble walls during experimental vesiculation of andesitic magmas: *Contrib. Mineral. Petr*. **174**, 21.

79. Pons J. M., Franchini M., Meinert L., Recio C., and Etcheverry R. (2009) Iron Skarns of the Vegas Peladas District, Mendoza, Argentina. *Econ. Geol*. 104,157–184.

80. Price G. D. (1980) Exsolution microstructures in titanomagnetite and their magnetic significance. *Phys. Earth Planet. Inter.* **23**, 2–12.

81. Price G. D. (1981) Subsolidus phase relations in the titanomagnetite solid solution series. *Am. Min.* **66**, 751–758.

82. Putnis A. (2009) Mineral replacement reactions: *Rev. Mineral. Geochem.* **70**, 87–124.

83. Putnis A. and Austrheim H. (2013) Mechanisms of metasomatism and metamorphism on the local mineral scale: The role of dissolution-reprecipitation during mineral re-equilibration, in *Metasomatism and the chemical transformation of rock: The role of fluids in terrestrial and extraterrestrial processes: (*eds. D.E. Harlov and H. Austrheim) Berlin-Heidelberg, Springer-Verlag, pp. 141–170.

84. Rapp J. F. Klemme S., Butler I. B., and Harley S. L. (2010) Extremely high solubility of rutile in chloride and fluoride-bearing metamorphic fluids: An experimental investigation. *Geology* **38**, 323–326.

85. Regan S., Lupulescu M., Jercinovic M., Chiarenzelli J., Williams M., Singer J., and Bailey D. (2019) Age and Origin of Monazite Symplectite in an Iron Oxide-Apatite Deposit in the

Adirondack Mountains, New York, USA: Implications for Tracking Fluid Conditions. *Minerals* **9**, 65.

86. Rhodes A. L. and Oreskes N. (1995) Magnetite deposition at El Laco, Chile: Implications for Fe-oxide formation in magmatic-hydrothermal systems: Giant Ore Deposits Workshop, 2nd, April 25-27, 1995, Queens University, Kingston, Ontario, Canada, Proceedings, pp. 582–622.

87. Rhodes A. L., Oreskes, N. and Sheets R. W. (1999) Geology and REE geochemistry of the magnetite deposits at El Laco, Chile: *Econ. Geol.* Special Publication **7**, 299–332.

88. Rodriguez-Mustafa M. A., Simon A. C., del Real I., Thompson John F. H., Bilenker L. D., Barra F., and Bindeman I. (2020) A Continuum from Iron Oxide Copper-Gold to Iron Oxide-Apatite Deposits: Evidence from Fe and O Stable Isotopes and Trace Element Chemistry of Magnetite. *Econ. Geol.* **115**, 1443–1459.

89. Rojas P., Barra F., Deditius A., Reich M., Simon A., Roberts M., and Rojo M. (2018) New contributions to the understanding of Kiruna-type iron oxide-apatite deposits revealed by magnetite ore and gangue mineral geochemistry at the El Romeral deposit. Chile. *Ore Geol. Rev.* **93**, 413–435.

90. Ryan C. G., Kirkham R., Hough R. M., Moorhead G., Siddons D. P., de Jonge M. D., Paterson D. J., De Geronimo G., Howard D. L. and Cleverley J. S. (2010) Elemental X ray imaging using the Maia detector array: The benefits and challenges of large solid-angle. Nuclear Instruments & Methods in Physics Research Section A: Accelerators Spectrometers Detectors and Associated Equipment, **619**, 37–43.

91. Ryan C. G., Siddons D. P., Kirkham R., Li, Z. Y. de Jonge M. D., Paterson D. J., Kuczewski A., Howard D. L., Dunn P.A., Falkenberg G., and others (2014) Maia X-ray fluorescence imaging: Capturing detail in complex natural samples. Journal of Physics: Conference Series, **499**, 012002.

92. Salazar E., Barra F., Reich M., Simon A., Leisen M., Palma G. and Rojo, M. (2020) Trace element geochemistry of magnetite from the Cerro Negro Norte iron oxide− apatite deposit, northern Chile. *Miner. Deposita* **55**, 409-428.

93. Sauerzapf U., Lattard D., Burchard M. and Engelmann R. (2008) The titanomagnetite–ilmenite equilibrium: new experimental data and thermo-oxybarometric application to the crystallization of basic to intermediate rocks. *J. Petrol.* **49**, 1161–1185.

94. Scholten L., Schmidt C., Lecumberri-Sanchez P., Newville M., Lanzirotti A., Sirbescu M. C. and Steele-MacInnis M. (2019) Solubility and speciation of iron in hydrothermal fluids. *Geochim. Cosmochim. Acta* **252**, 126–143.

95. Schoneveld L. E., Barnes S. J., Godel B., Le Vaillant M., Yudovskaya M. A., Kamenetsky V. and Sluzhenikin S. F. (2020) Oxide-sulfide-melt-bubble interactions in spinel-rich taxitic rocks of the Norilsk-Talnakh intrusions, Polar Siberia. *Econ. Geol.* **115**, 1305–1320.

96. Shea T. (2017) Bubble nucleation in magmas: A dominantly heterogeneous process? *J. Volcanol. Geotherm. Res.* **343**, 155–170.

97. Sheets S. A., Oreskes N., Rhodes A. L., Bodnar R. J., and Szabo C. (1997) Fluid inclusion evidence for a hydrothermal origin for magnetite-apatite mineralization at El Laco, Chile: Geological Society of America Abstracts with Programs, 2, A50.

98. Sievwright R. H., Wilkinson J. J., O'Neill H. S. C. and Berry, A. J. (2017) Thermodynamic controls on element partitioning between titanomagnetite and andesitic–dacitic silicate melts. *Contrib. Miner. Petrol.* **172**, 62.

99. Sievwright R. H., O'Neill H. St. C., Tolley J., Wilkinson J. J., and Berry A. J. (2020) Diffusion and partition coefficients of minor and trace elements in magnetite as a function of oxygen fugacity at 1150 ºC. *Contrib. Miner. Petrol.* **175**, 40.

100. Sillitoe R. H. and Burrows D. R. (2002) New field evidence bearing on the origin of the El Laco magnetite deposit, northern Chile: *Econ. Geol.* **97**, 1101–1109.

101. Simon A. C., Pettke T., Candela P. A., Piccoli P. M. and Heinrich, C. A. (2004) Magnetite solubility and iron transport in magmatic-hydrothermal environments. *Geochim. Cosmochim. Acta* **68**, 4905–4914.

102. Simon A. C., Kniping J., Reich M., Barra F., Deditius A. P., Bilenker L., and Childress T., 2018. Kiruna-Type Iron Oxide-Apatite (IOA) and Iron Oxide Copper-Gold (IOCG) Deposits form by a combination of ignous and magmatic-hydrothermal processes: evidence from the Chilean Iron Belt. *SEG Sp. Pub.* **21**, 89–114.

103. Streck M. J. (2008) Mineral textures and zoning as evidence for open system processes. *Rev. Mineral. Geochem.* **69**, 595–622.

104. Tan W., Peng L., He H., Wang C. Y. and Liang, X. (2016) Mineralogy and origin of exsolution in Ti-rich magnetite from diferent magmatic Fe-Ti oxide-bearing intrusions. The *Can. Miner.* **54**, 539–553.

105. Tan W., Wang C. Y., He H., Xing C., Liang X. L. and Dong, H. (2015) Magnetite-rutile symplectite derived from ilmenite-hematite solid solution in the Xinjie Fe-Ti oxidebearing, mafic-ultramafic layered intrusion (SW China) *Am. Mineral.* **100**, 2348–2351.

106. Tanis E. A., Simon A. C., Zhang Y., Chow P., Xiao Y., Hanchar J. M., Tschauner O., Shen, G. (2016) Rutile solubility in NaF-NaCl-KCl-bearing aqueous fluids at 0.5-2.79 GPa and 250–650°C. *Geochim. Cosmochim. Acta* **177**, 170–181.

107. Toplis M. J., and Corgne A. (2002) An experimental study of element partitioning between magnetite, clinopyroxene and iron-bearing silicate liquids with particular emphasis on vanadium. *Contrib. Miner. Petrol.* **144**, 22–37.

108. Tornos F., Velasco, F. and Hanchar J. (2016) Iron-rich melts, magmatic, magnetite, and superheated magmatic-hydrothermal systems: The El Laco deposit, Chile. *Geology* **44**, 427–430.

109. Tornos F., Velasco F. and Hanchar J. M. (2017) The magmatic to magmatic-hydrothermal evolution of the El Laco deposit (Chile) and its implications for the genesis of magnetite-apatite deposits: *Econ. Geol.* **112**, 1595–1628.

110. Turnock A. and Eugster, H. (1962) Fe-Al Oxides: phase relationships below 1,000°C. *J Petrol.* **3**, 533–565.

111. Ubide T. and Kamber B. (2018) Volcanic crystals as time capsules of eruption history. *Nat. Commun.* **9**, 326–326.

112. Ubide T., Mollo, S., Zhao J-X., Nazzari M., and Scarlato P. (2019a) Sector-zoned clinopyroxene as a recorder of magma history, eruption triggers, and ascent rates. *Geochim. Cosmochim. Acta* **251**, 265–283.

113. Ubide T., Caulfield J., Brandt C., Bussweiler Y., Mollo S., Di Stefano F., Nazzari M. and Scarlato, P. (2019b) Deep Magma Storage Revealed by Multi-Method Elemental Mapping of Clinopyroxene Megacrysts at Stromboli Volcano. *Front. Earth Sci.* **7**, 239.

114. Velasco F., Tornos F., and Hanchar J. (2016) Immiscible iron- and silica-rich melts and magnetite geochemistry at the El Laco volcano (northern Chile): Evidence for a magmatic origin for the magnetite deposits: *Ore Geol. Rev.* **79**, 346–366.

115. Vivallo W., Henríquez F., and Espinoza S. (1991) Alteración Hidrotermal en el Complejo Volcánico El Laco, norte de Chile. Congreso Geológico Chileno – Servicio Nacional de Geología y Minería, Chile, 44-47.

116. Vivallo W., Henríquez F., and Espinoza S. (1994) Oxygen and sulfur isotopes in hydrothermally altered rocks and gypsum deposits at El Laco mining district, northern Chile: Departamento de Geología, Universidad de Chile, Comunicaciones, **45**, 93–100.

117. Wang Y-J., Zhu W-G., Huang H-Q., Bai Z-J., Zhong H., Yao J-H., and Fan H-P. (2020) Geochemistry of magnetite from the giant Paleoproterozoic Dahongshan Fe-Cu deposit, SW

China: Constraints on nature of ore-forming fluids and depositional setting. *Ore Geol. Rev.* **118**, 103361.

118. Watenphul A., Schmidt C., and Jahn S. (2014) Cr(III) solubility in aqueous fluids at high pressures and temperatures. *Geochim. Cosmochim. Acta*. **126**, 212-227.

119. Wen G., Li J. W., Hofstra A. H., Koenig A. E., Lowers H. A., and Adams D. (2017) Hydrothermal reequilibration of igneous magnetite in altered granitic plutons and its implications for magnetite classification schemes: Insights from the Handan-Xingtai iron district. North China Craton. *Geochim. Cosmochim. Acta* **213**, 255–270.

120. Wen G., Li J-W., Hofstra A. H., Koenig A. E., and Cui B-Z. (2020) Textures and compositions of clinopyroxene in an Fe skarn with implications for ore-fluid evolution and mineral-fluid REE partitioning. *Geochim. Cosmochim. Acta* **290**, 104-123.

121. Xie Q., Zhang Z., Hou T., Jin Z., and Santosh M. (2017) Geochemistry and oxygen isotope composition of magnetite from the Zhangmatun deposit, North China Craton: Implications for the magmatic-hydrothermal evolution of Cornwall-type iron mineralization. *Ore Geol. Rev.* **88**, 57-70.

122. Xie Q. H., Zhang Z. C., Campos E., Cheng Z. G., Fei X. H., Liu B. X., Qiu Y. Y., Santosh, M., Ke S. and Xu, L. J. (2018) Magnesium isotopic composition of continental arc andesites and the implications: A case study from the El Laco volcanic complex, Chile: *Lithos* **318–319**, 91–103.

123. Xie Q., Zhang Z., Hou T., Cheng Z., Campos E., Wang Z., and Fei X. (2019) New insights for the formation of Kiruna-type iron deposits by immiscible hydrous Fe-P melt and high-temperature hydrothermal processes: Evidence from El Laco deposit: *Econ. Geol*. **114**, 35–46.

124. Xing C-M. and Wang C. Y. (2021) Periodic mixing of magmas recorded by oscillatory zoning of the clinopyroxene macrocrysts from an ultrapotassic lamprophyre dyke. *J Petrol.* **61**, 11-12, 1-26.

125. Yin S., Ma C., and Robinson P. T. (2017) Textures and high field strength elements in hydrothermal magnetite from a skarn system: Implications for coupled dissolution-reprecipitation reactions. *Am. Mineral.* **102**, 1045–1056.

126. Yin S., Wirth R., Ma C. and Xu J. (2019) The role of mineral nanoparticles at a fluid-magnetite interface: Implications for trace-element uptake in hydrothermal systems. *Am. Mineral.* **104**, 1180–1188.

127. Zhang Y., Yu X., Peng Q., Li D., Li X., Shen K., Zhang S. and Shan W. (2020) A Textural and Mineralogical Study of the Shanzhuang Banded Iron Formation, Southeastern Margin of

the North China Craton: Implications for the Overprint History of Hydrothermal Alteration and Supergenesis after Mineralization. *Acta Geologica Sinica*, **94**, 2134-2151.

3.9. FIGURES

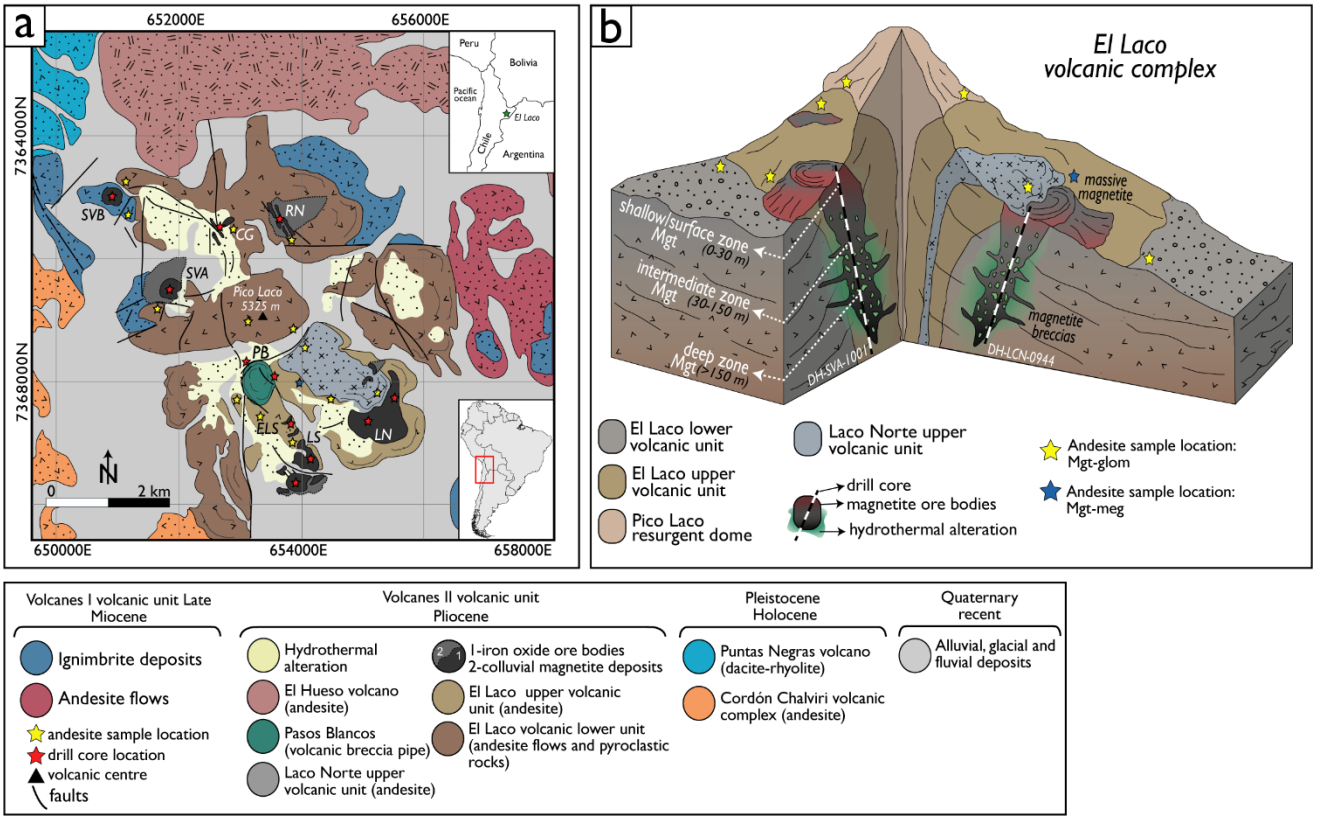

Figure 6: (a) Location and geological map of the El Laco volcanic complex (ELVC). The location of the studied drill cores and surface volcanic rock samples are shown in red and yellow stars, respectively; based on the mapping by the Compañía Minera del Pacífico (CAP Minería). LN: Laco Norte, LS: Laco Sur, ELS: Extensión Laco Sur, PB: Pasos Blancos, SVA: San Vicente Alto, SVB: San Vicente Bajo, CG: Cristales Grandes, RN: Rodados Negros. **(b)** Schematic block diagram of the ELVC showing an idealized architecture of the volcanic complex and its different volcanic units (including illustrative sample location; yellow and blue stars) as well as the configuration and morphology of the associated magnetite-rich ore bodies at depth. An illustrative position of the studied drill cores indicates the different ore zones (e.g., shallow/surface, intermediate and deep zone).

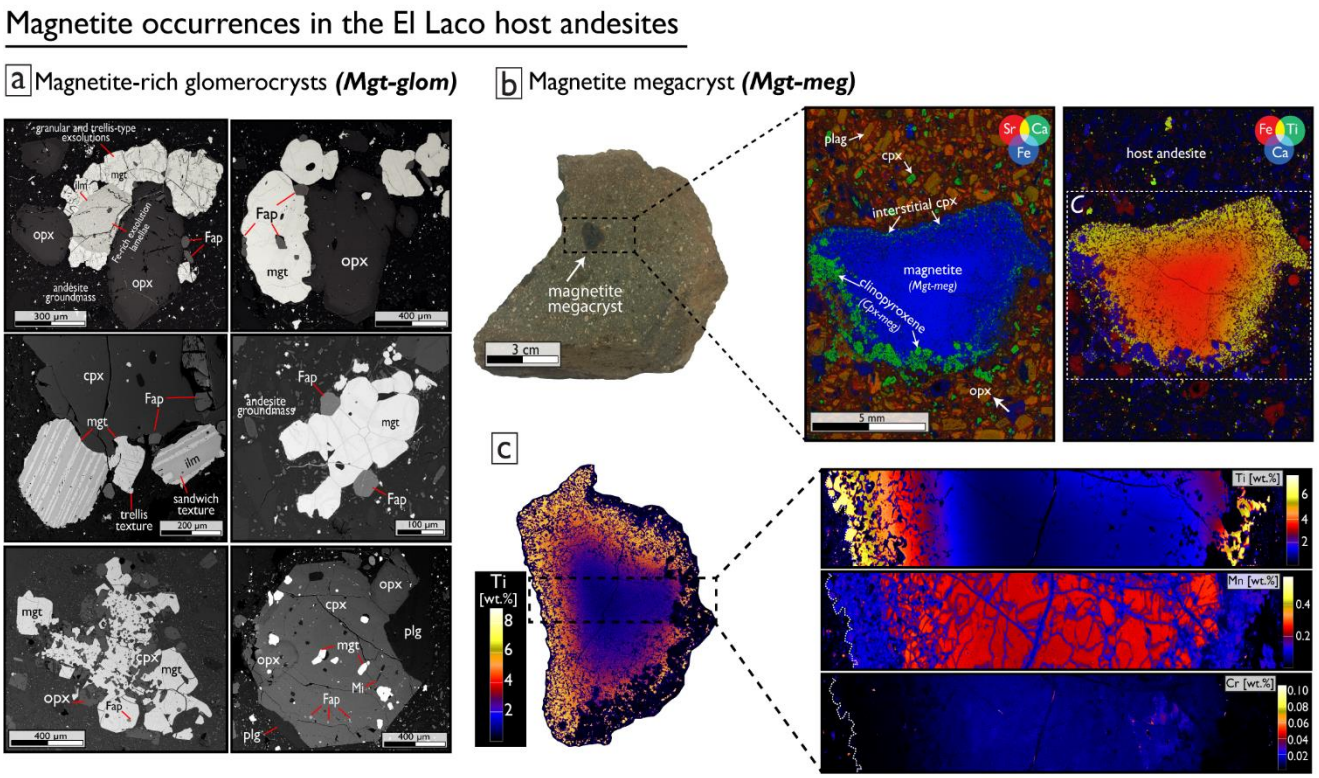

Figure 7: Representative samples of magnetite from the host andesites at ELVC. **(a)** Back-scattered electron (BSE) images of magnetite-rich glomerocrysts (Mgt-glom) showing different types of ilmenite exsolutions and their textural relationship with silicate phases. **(b)** A photograph of a hand-specimen sample and synchrotron µ-XRF three-elemental (RGB) maps of the magnetite megacryst (Mgt-meg) in the matrix of andesite that hosts the mineralization at El Laco. Note abundant clinopyroxene grains associated with the megacryst rims and the core-to-rim Fe and Ti zoning. **(c)** Titanium map of the entire magnetite megacryst, associated with high-resolution Ti, Mn and Cr maps across the megacrysts. Note the core-to-rim heterogeneous distribution of elements: decreasing concentrations of Mn and Cr from core to rim and increasing concentration of Ti towards Mgt-meg rims. Dashed white line in (c) marks the megacryst boundary. mgt: magnetite, ilm: ilmenite, cpx: clinopyroxene, opx: orthopyroxene, Fap: fluorapatite, plg: plagioclase, Mi: melt inclusion.

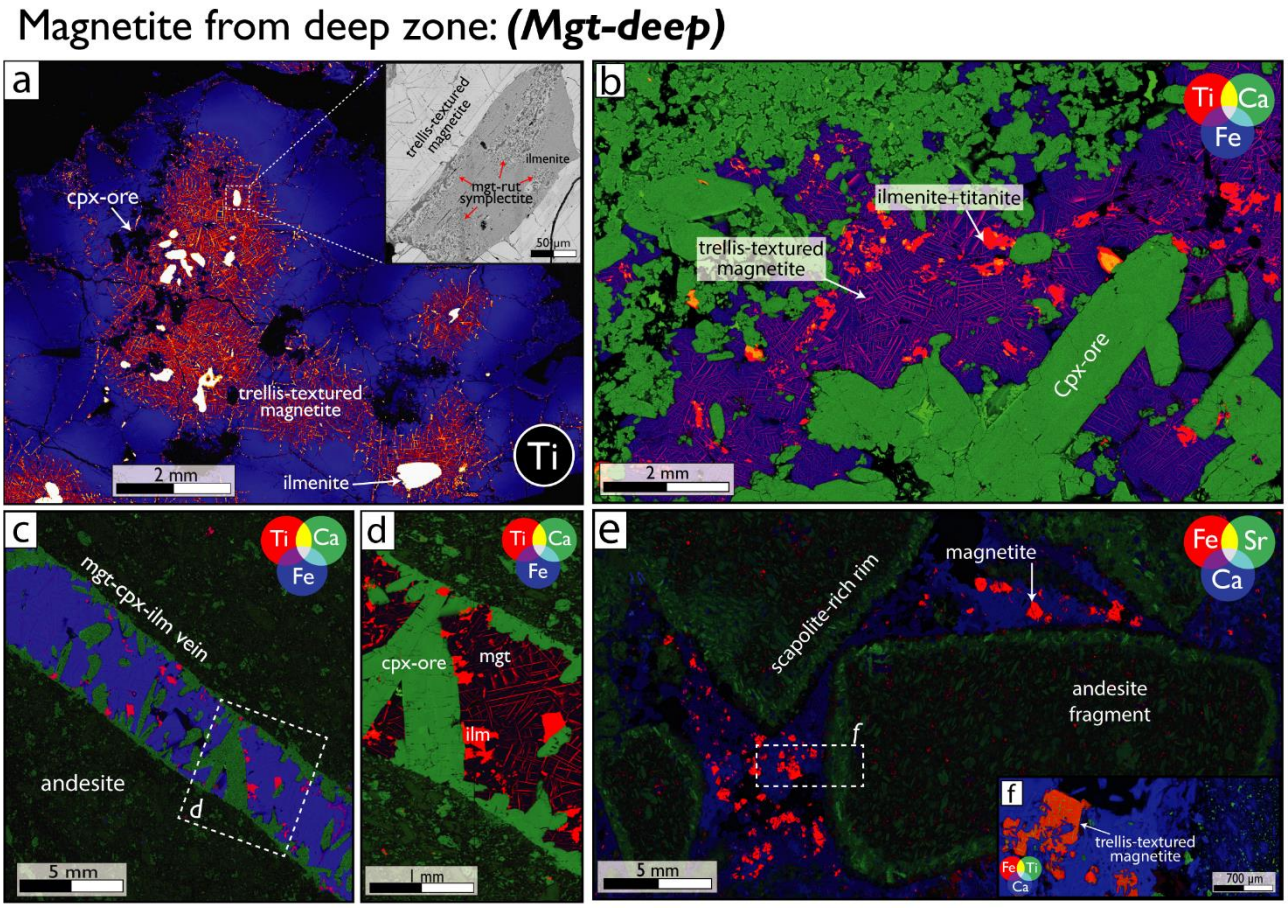

Figure 8: Synchrotron µ-XRF single and three-elemental (RGB) maps of magnetite assemblages in breccias and veinlets from deep levels (> 150 m. Mgt-deep) of the ore bodies. **(a)** A map of Ti distribution in a breccia from Laco Norte ore body showing a matrix consisting mostly of magnetite with minor ilmenite and clinopyroxene. Note the trellis texture associated with magnetite cores and core-to-rim decreasing concentration of Ti in magnetite. The inset in (a) shows a BSE image of an ilmenite grain exhibiting a magnetite-rutile symplectitic intergrowth. **(b)** Ti-Ca-Fe map of a breccia sample from Cristales Grandes ore body showing trellis-textured magnetite with ilmenite and titanite inclusions, and abundant euhedral clinopyroxene. **(c,d)** Low- and high-resolution Ti-Ca-Fe maps of a representative magnetite-clinopyroxene-ilmenite veinlet crosscutting andesite levels below Extensión Laco Sur ore body. **(e)** Fe-Sr-Ca map of a breccia sample from Pasos Blancos ore body showing andesite fragments with rims replaced by scapolite within a matrix consisting of clinopyroxene-scapolite-gypsum and magnetite. **(f)** Close-up view of the clast-matrix contact zone in the breccia. Note the trellis texture in magnetite. Strontium in map (e) was selected to indicate the location of scapolite in the mineral assemblages. Mgt: magnetite, cpx: clinopyroxene, ilm: ilmenite, rut: rutile.

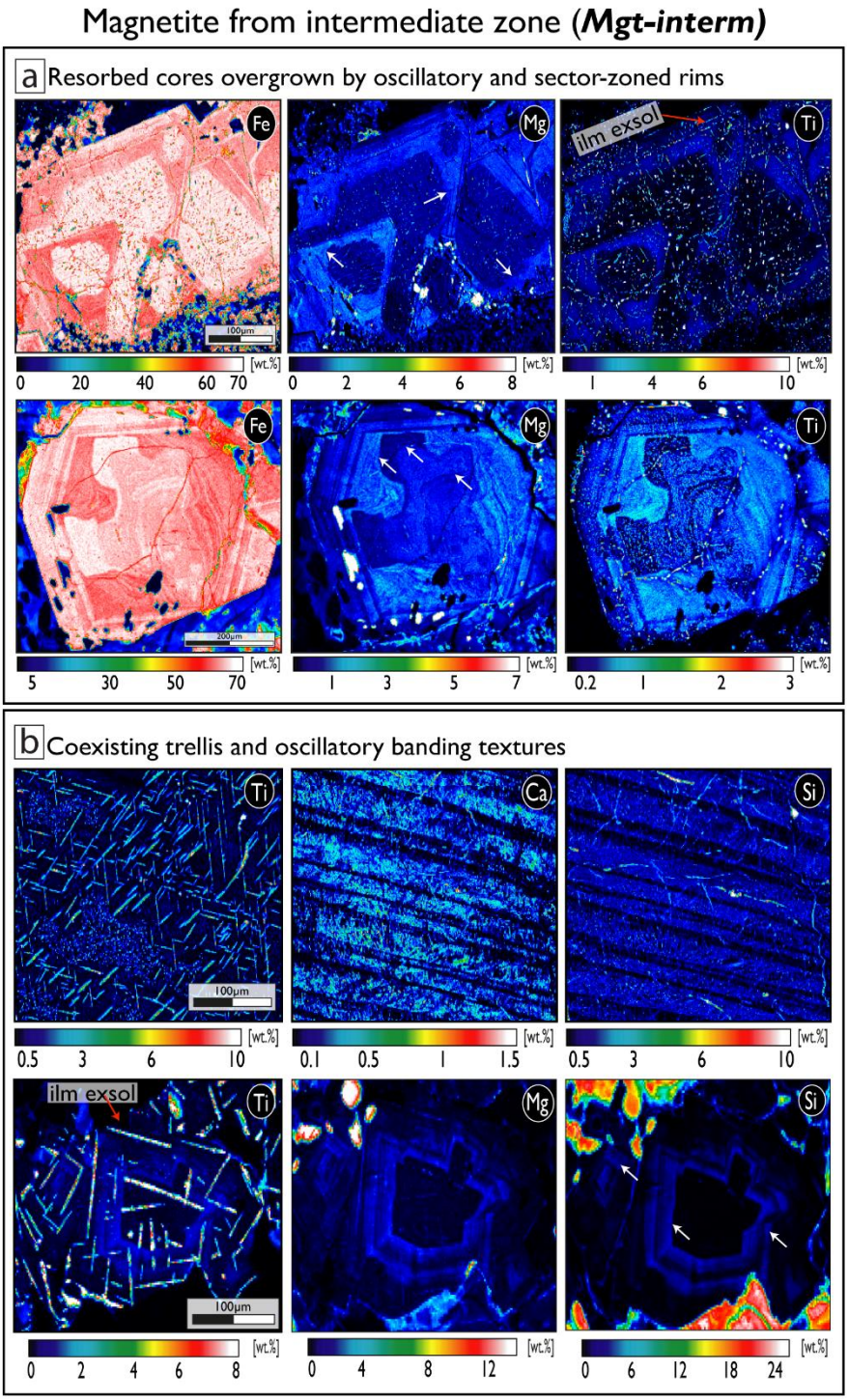

Figure 9: Quantitative WDS maps of selected elements in magnetite grains representative for the intermediate levels (30 – 150 m., Mgt-interm) of the magnetite breccias from Laco Sur and San Vicente Bajo ore bodies. **(a)** Iron, Mg and Ti maps of Mgt-interm grains showing oriented inclusion-rich or oscillatory-zoned cores overgrown by euhedral and oscillatory-zoned rims. Note irregular and sharp resorption surfaces (white arrows) **(b)** Titanium, Ca, Mg and Si maps of Mgt-interm grains showing a microtextural overprinting between oscillatory zoning and ilmenite exsolution lamellae (Ilm exsol).

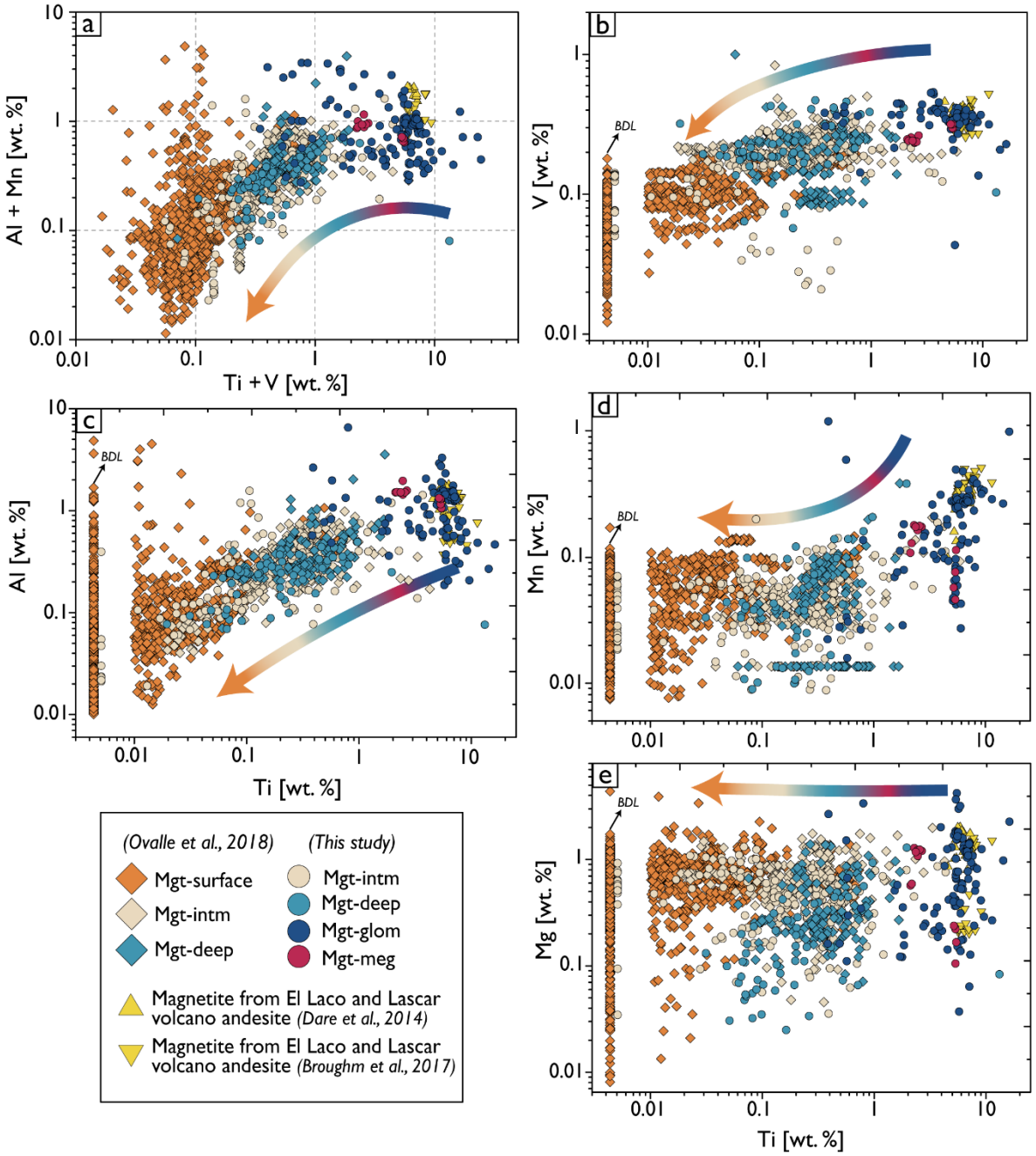

Figure 10: Bivariant plots showing distribution of minor and trace elements (EPMA data) in all magnetite varieties studied at El Laco deposit, including magnetite from the ore bodies at different depth levels (e.g., Mgt-surface, Mgt-interm, and Mgt-deep) as well as the magnetite in the host andesites (e.g., Mgt-glom and Mgt-meg). **(a)** [Ti+V] vs. [Al+Mn] diagram, **(b, c, d, e)** Ti vs. V, Al, Mn, and Mg, respectively. The colored arrow represents a trend of continuous change of the chemical composition from Mgt-glom to Mgt-meg, Mgt-deep, and Mgt-interm to Mgt-surface. Data source: Magnetite EPMA data from drill core and surface samples represented by diamonds (Ovalle et al., 2018), and chemical composition of magnetite from andesite rocks from El Laco and Láscar volcano represented by yellow triangles (Dare et al., 2014 and Broughm et al., 2017, respectively). For data points that were below detection limit (BDL), the half of detection limit was used.

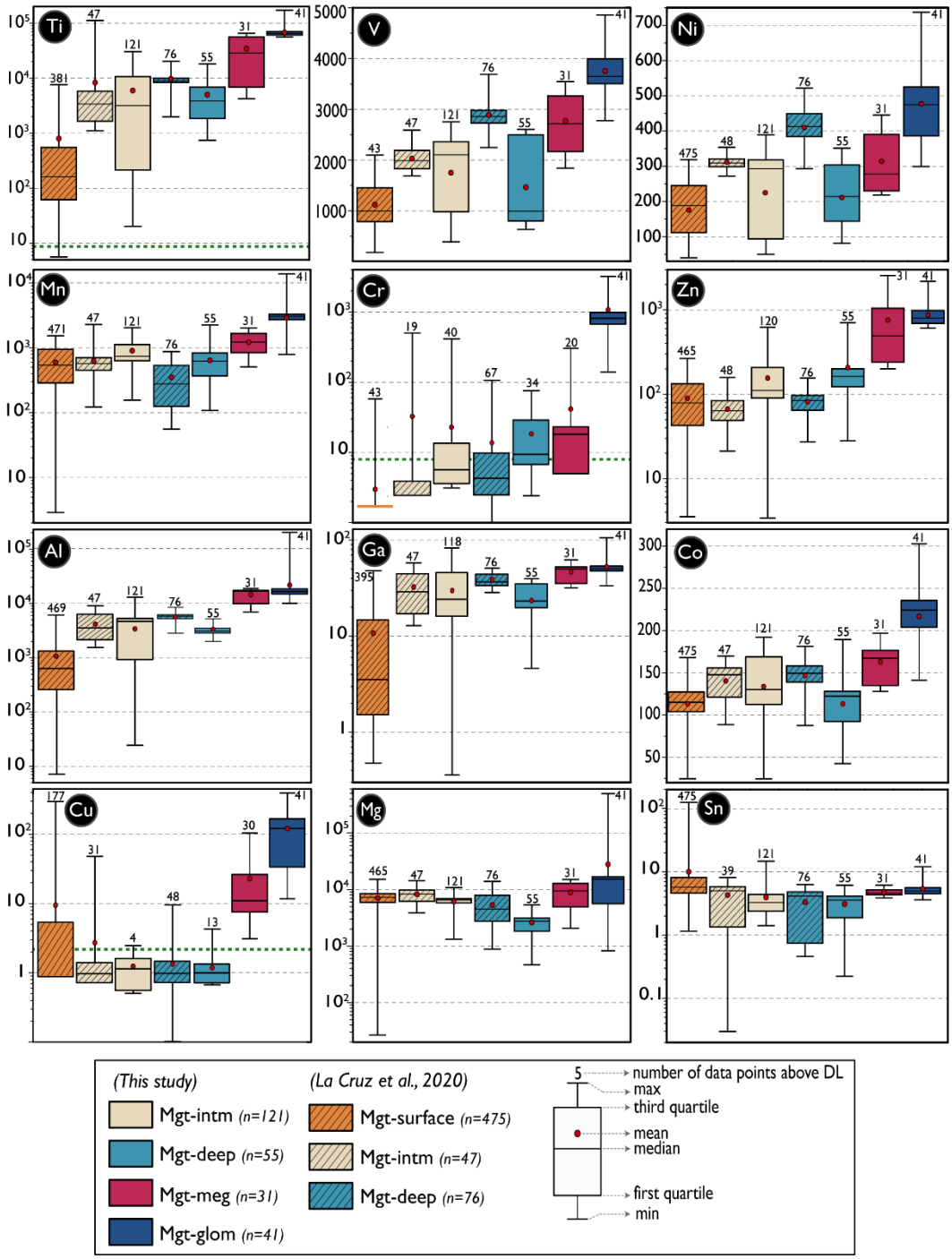

Figure 11: Concentration boxplots for the minor and trace element concentrations determined by LA-ICP-MS from all of the magnetite varieties studied at El Laco deposit (colour coding as in Figure 5). Data in each boxplot are plotted in parts per million (ppm) on a vertical logarithmic scale for all elements with exception of V, Ni and Co. Dashed boxes represent data from drill core and surface samples from El Laco reported by La Cruz et al. (2020). In each boxplot, minimum, mean, median and maximum concentrations are marked, and the number of analyses above detection limit is displayed above the marker of upper quartile. The dashed green line in Ti, Cr and Cu maps marks the median of the detection limit for each element.

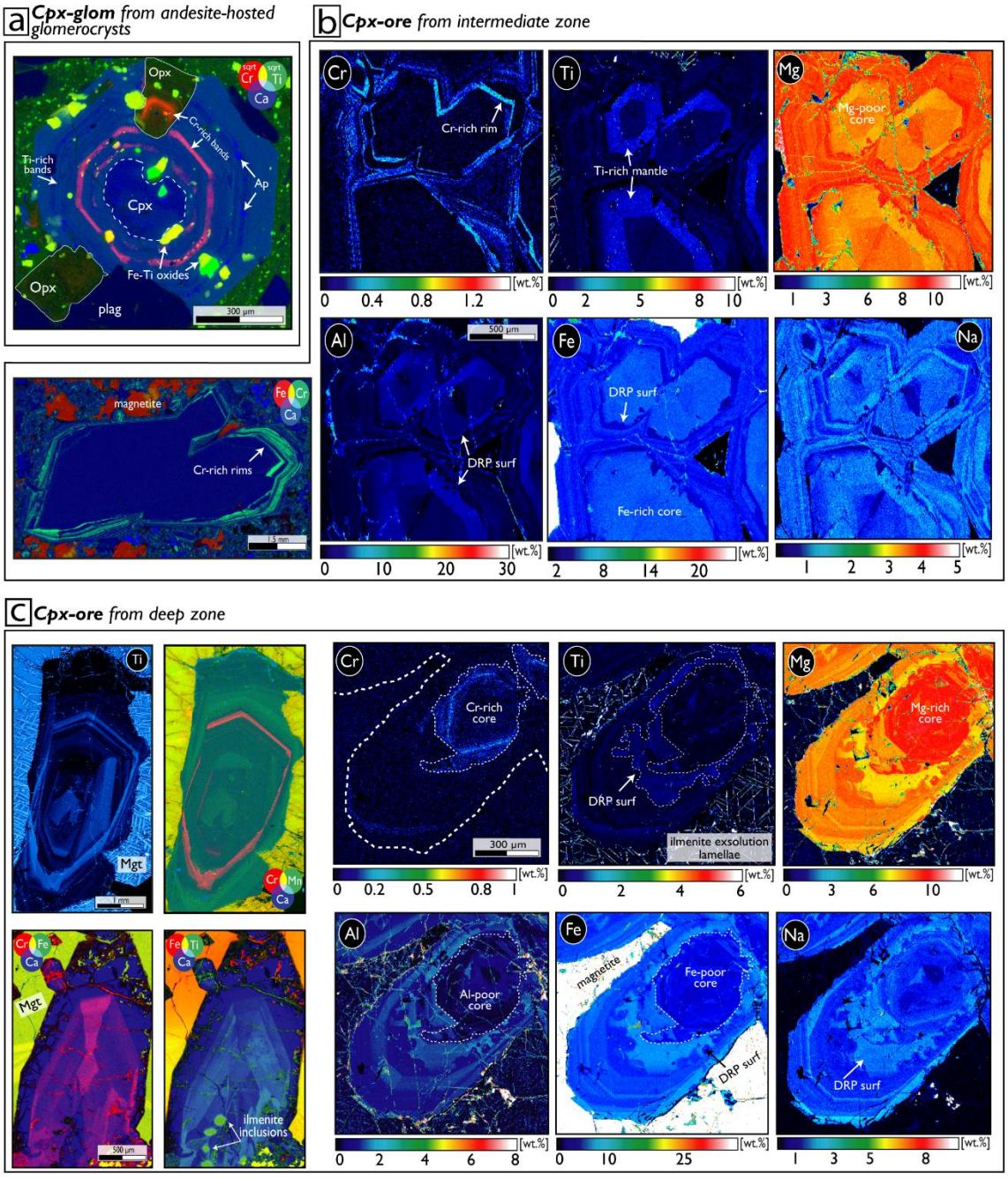

Figure 12: Synchrotron µ-XRF and quantitative WDS maps showing representative clinopyroxene grains from the host andesites (**a**, Cpx-glom) and the ore bodies (Cpx-ore) at deep **(c)** and intermediate **(b)** levels. DRP surf: dissolution-reprecipitation surface, Opx: orthopyroxene; Ap: apatite. (See detailed description in the main text).

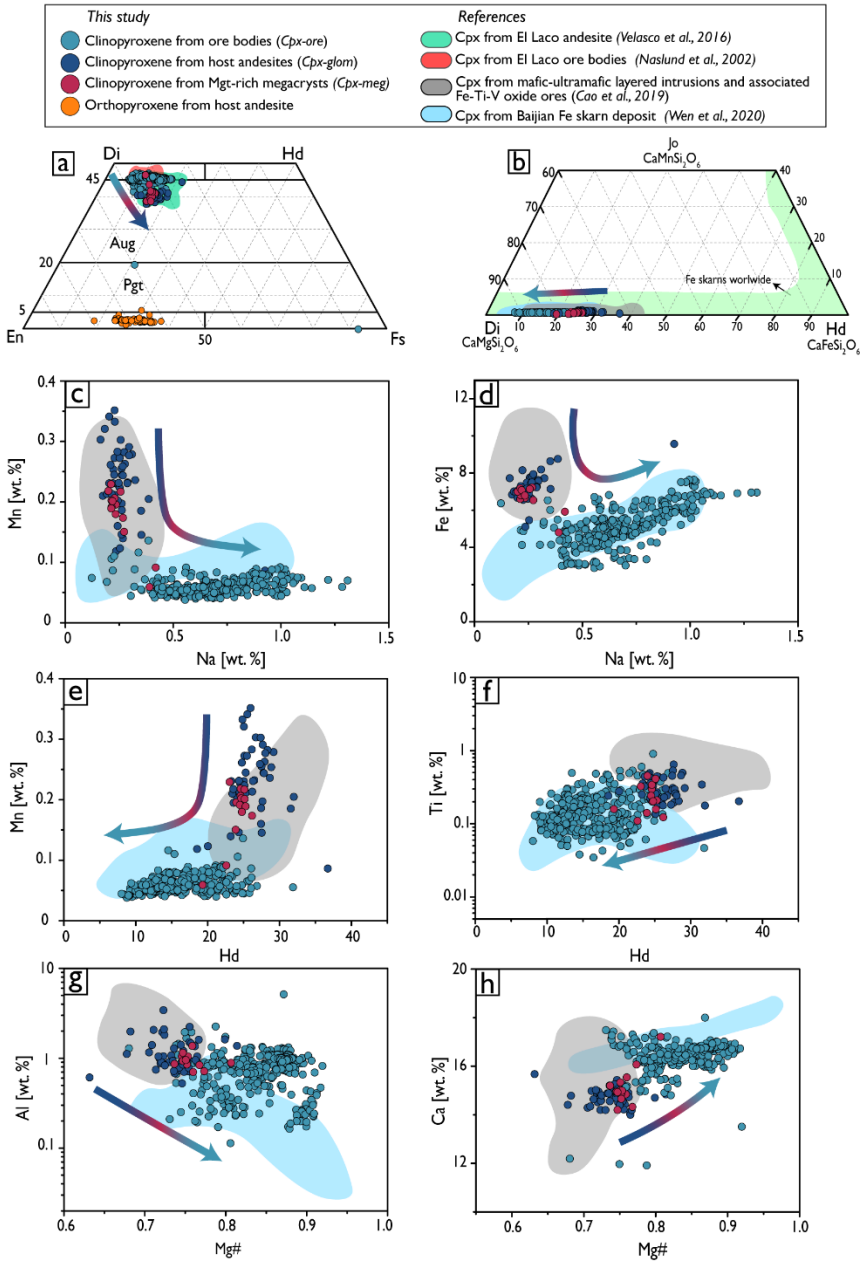

Figure 13: Chemical compositions of clinopyroxene from the ore bodies (Cpx-ore), andesite-hosted glomerocrysts (Cpx-glom) and magnetite-rich megacryst (Cpx-meg). EPMA data are plotted in the wollastonite-enstatite-ferrosilite, and hedenbergite (Hd), johannsenite (Jo), and diopside (Di) ternary plots (**a** and **b**, respectively). **(c-d)** Manganese and Fe concentrations plotted against Na. **(e-f)** Manganese and Ti concentrations plotted against Hd values. **(g-h)** Aluminum and Ca concentrations plotted against #Mg. Colored fields represent clinopyroxene data from the literature used for comparison: green and red fields in (a) correspond to clinopyroxene data from El Laco andesites and ore bodies, respectively (Velasco et al., 2016 and Naslund et al., 2002, respectively). Light green compositional field in (b) for clinopyroxene from Fe-skarn deposits (after Meinert et al., 2005). Grey and light blue fields in b-h correspond to magmatic (Cao et al., 2019) and hydrothermal (Wen et al., 2020) clinopyroxene end members, respectively. The colored arrow represents a trend from Cpx-glom to Cpx-meg to Cpx-ore observed in all plots.

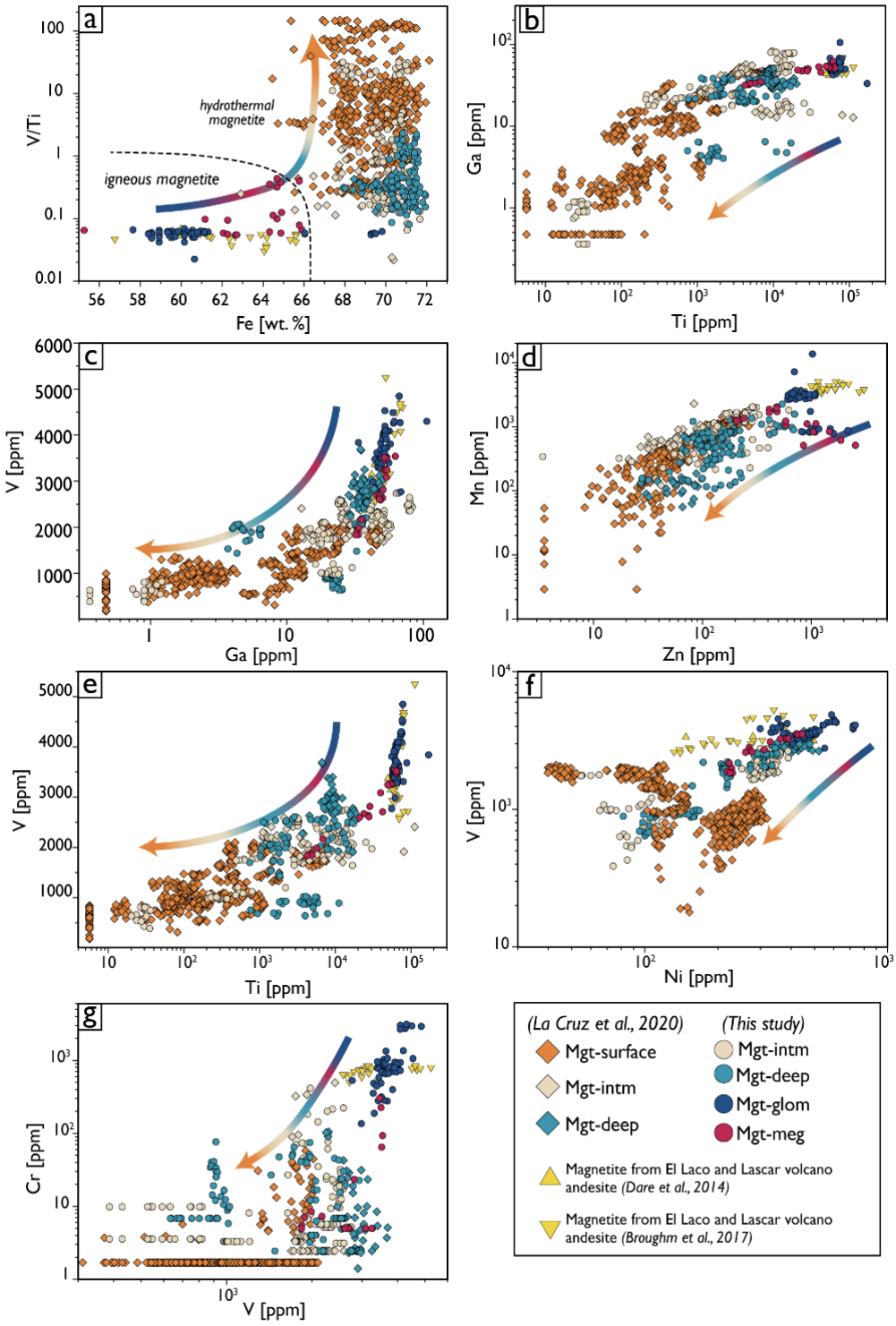

Figure 14: Bivariant trace element plots, based on LA-ICP-MS analyses, for the magnetite types investigated at El Laco (colour coding after Figs. 5 and 6). The discriminant diagram from Wen et al. (2017) for magnetite of magmatic vs. hydrothermal origin is shown in **(a)**. Elemental concentrations in **(b)** Ga vs. Ti, **(c)** V vs. Ga, **(d)** Mn vs. Zn, **(e)** V vs. Ti, **(f)** Cr vs. Ni, and **(g)** Cr vs. V are shown in ppm. A depletion trend for minor and trace elements in magnetite from Mgt-glom to Mgt-surface is represented by the colored arrow. Data source: Magnetite EPMA data from drill core and surface samples (diamonds) are after La Cruz et al. (2020). Data points plotting vertically and horizontally were below detection limits and the half of detection limit was used.

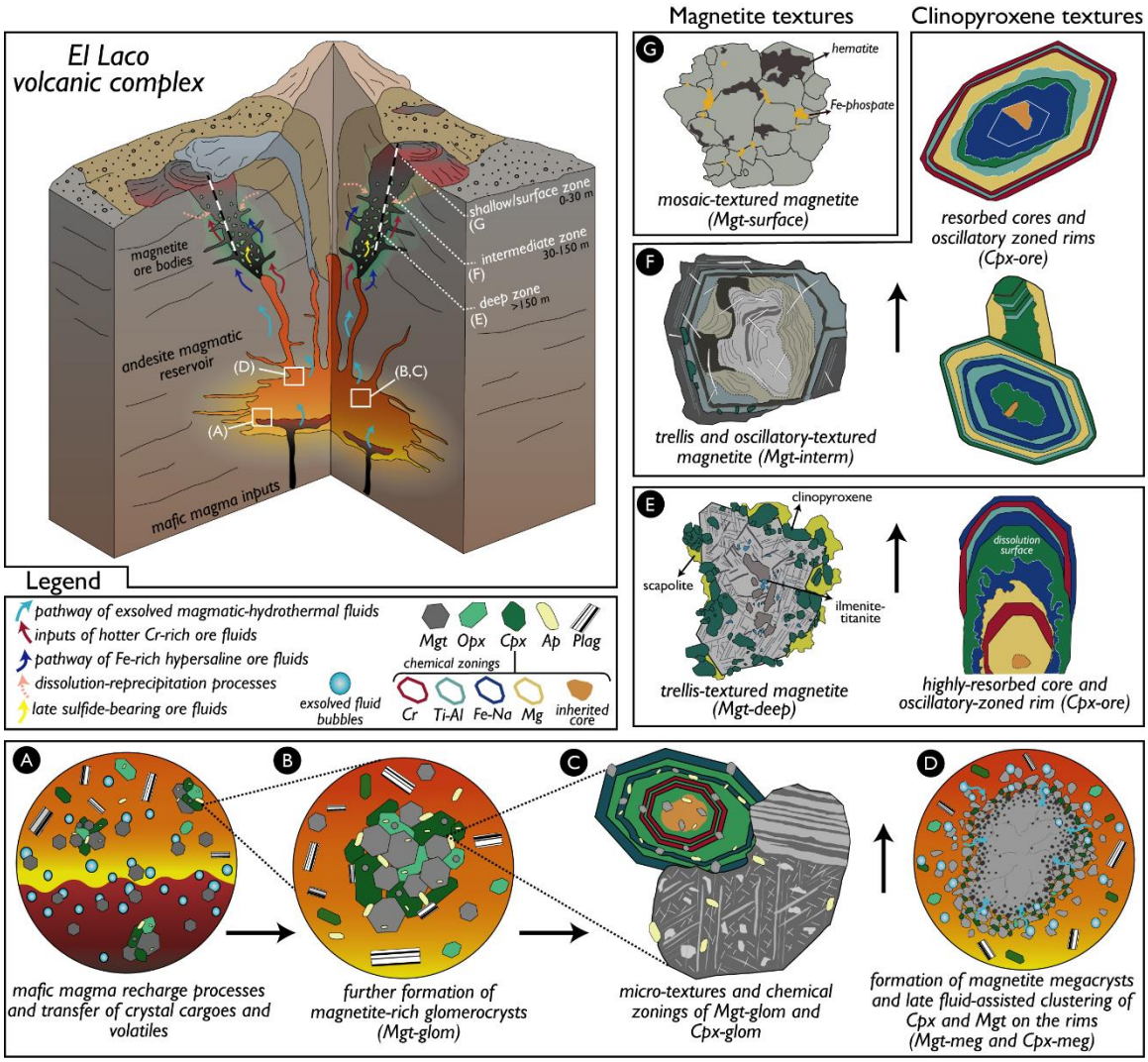

Figure 15: Schematic genetic model for the formation of the El Laco magnetite deposit. The figure illustrates the different types of magmatic and hydrothermal processes taking place in the magma system at depth as well as in the overlying ore-forming hydrothermal system. **(a)** Formation of a magnetite-rich andesite magmatic reservoir by in situ clustering and/or by crystal-volatile transfer from mafic magma through recharge processes resulting in the formation of magnetite-pyroxene glomerocrysts (**b**, Mgt- and Cpx-glom). **(c)** Magma replenishment processes are recorded by clinopyroxene through Cr-rich oscillatory zoning and resorption textures. **(d)** Formation of magnetite megacrysts (Mgt-meg) followed by extensive reaction with high-temperature exsolved fluids promoting partial annealing of the megacryst that results in porosity development and a Ti inverse zoning. Forceful injection of the Fe-rich magmatic-hydrothermal fluids through volcanic collapse-related structures caused continuing ascend of large breccia bodies from depth until reach the surface through fissures and secondary craters. **(e-g)** Magnetite and clinopyroxene (Cpx-ore) from the ore bodies account for highly dynamic crystallization conditions characterized by multiple inputs of magmatic-hydrothermal fluids under variable physicochemical conditions. Both minerals record multiple processes of mineral growth and partial resorption (e.g., dissolution-reprecipitation), marked by complex re-equilibrium processes (e.g., oxy-exsolution of ilmenite exsolution lamellae) and a remarkable trends of compositional depletion from the deeper portions (Mgt-deep, Mgt-interm) towards the surface (Mgt-surface). (See text for detailed discussion).

3.10. TABLES

Table 1: Data summary of EPMA analyses for magnetite types from the different types of occurrence and depth in the ore system

Ore zone/host	Magnetite type	Data source		Fe [wt. %]	Mg [wt. %]	Al [wt. %]	Si [wt. %]	Ti [wt. %]	Ca [wt. %]	V [wt. %]	Cr [wt. %]	Mn [wt. %]	Ni [wt. %]
			MDL	0.02	0.01	0.01	0.01	0.01	0.01	0.01	0.01	0.01	0.01
Surface zone	*Mgt-surface*	Ovalle et al. (2018)	min-max	64.5-72.1	bdl-2.26	bdl-1.71	bdl-1.93	bdl-0.74	bdl-0.57	bdl-0.20	bdl-0.02	bdl-0.17	n.a
			average	***69.3***	***0.65***	***0.13***	***0.34***	***0.09***	***0.12***	***0.09***	***0.01***	***0.06***	
			median	***69.9***	***0.64***	***0.07***	***0.27***	***0.03***	***0.09***	***0.08***	***0.01***	***0.05***	
			N/bdl		1368/70	1368/157	1368/4	1368/724	1368/273	1368/3	1368/1282	1368/356	
Intermediate zone	*Mgt-interm*	Ovalle et al. (2018) and This study	min-max	62.9-71.7	bdl-1.98	bdl-1.57	bdl-2.16	bdl-5.86	bdl-0.84	0.03-0.84	bdl-0.14	bdl-0.21	bdl-0.06
			average	***69.8***	***0.60***	***0.33***	***0.23***	***0.35***	***0.13***	***0.21***	***0.02***	***0.05***	***0.03***
			median	***70.2***	***0.57***	***0.29***	***0.04***	***0.24***	***0.06***	***0.20***	***0.01***	***0.04***	***0.03***
			N/bdl		472/4	472/13	472/6	472/21	472/229	472/0	472/342	472/104	161/28
Deep zone	*Mgt-deep*	Ovalle et al. (2018) and This study	min-max	67.9-71.9	bdl-1.30	0.07-1.29	bdl-0.85	0.02-1.95	bdl-0.29	0.06-0.47	bdl-0.09	bdl-0.38	bdl-0.05
			average	***70.7***	***0.25***	***0.28***	***0.04***	***0.28***	***0.06***	***0.17***	***0.03***	***0.07***	***0.03***
			median	***71.3***	***0.22***	***0.27***	***0.01***	***0.25***	***0.03***	***0.15***	***0.03***	***0.07***	***0.03***
			N/bdl		132/4	132/0	132/5	132/0	132/115	132/0	132/96	132/19	51/3
Andesite-hosted magnetite megacrysts	*Mgt-meg*	This study	min-max	55.3-65.9	0.06-1.28	1.06-1.97	0.03-2.35	2.11-7.10	bdl-0.19	0.23-0.40	0.01-0.13	0.05-0.18	0.03-0.05
			average	***63.2***	***0.71***	***1.43***	***0.22***	***3.90***	***0.06***	***0.29***	***0.07***	***0.12***	***0.03***
			median	***62.7***	***0.59***	***1.44***	***0.04***	***2.66***	***0.03***	***0.26***	***0.06***	***0.11***	***0.03***
			N/bdl		15/0	15/0	15/0	15/0	15/7	15/0	15/8	15/0	15/0
Andesite-hosted magnetite-rich glomerocrysts	*Mgt-glom*	This study	min-max	58.4-69.8	0.04-4.21	0.19-6.55	bdl-3.36	0.38-16.20	bdl-0.55	0.04-0.54	bdl-1.94	0.02-1.19	bdl-0.14
			average	***61.3***	***0.93***	***1.16***	***0.18***	***5.32***	***0.08***	***0.35***	***0.14***	***0.22***	***0.03***
			median	***61.0***	***0.67***	***1.24***	***0.05***	***5.55***	***0.03***	***0.35***	***0.09***	***0.25***	***0.02***
			N/bdl		101/3	101/0	101/0	101/0	101/36	101/0	101/2	101/0	101/3

Magnetite data from Ovalle et al. (2018) are differentiated from the ones from this study in the scatter plots (Fig. 5) and Supplementary Material Appendix 1.
MDL = mean detection limit, N = number of analyses, bdl = number of analyses BDL (below detection limit)
n.a = not analyzed

Table 2: Data summary of LA-ICP-MS analyses for magnetite types from the different types of occurrence and depth in the ore system

Ore zone/host	Magnetite type	Data source		Fe (EPMA) [wt. %]	Mg ppm	Al ppm	Ti ppm	V ppm	Cr ppm	Mn ppm	Co ppm	Ni ppm	Cu ppm	Zn ppm	Ga ppm	Sn ppm
			MDL		1.20	4.60	8.90	1.30	8.00	2.60	1.90	3.00	2.20	5.90	0.82	0.46
Surface zone	*Mgt-surface*	La Cruz et al. (2020)	min-max	64.5-72.1	bdl-14800	bdl-6140	bdl-7650	179-2100	bdl-57.90	7.19-1520	24.70-168	39.90-319	bdl-305	bdl-266	bdl-47.50	1.15-125
			average	***69.3***	***7186***	***1093***	***927***	***1123***	***15.4***	***600***	***113***	***176***	***24***	***91***	***12.7***	***10***
			median	***69.9***	***7310***	***636***	***210.50***	***998***	***9.80***	***557***	***114.70***	***188***	***8.41***	***80.20***	***8.50***	***5.70***
			N/bdl		475/10	475/6	475/63	475/0	475/432	475/4	475/10	475/0	475/296	475/10	475/80	475/0
Intermediate zone	*Mgt-interm*	*La Cruz et al. (2020)* and this study	min-max	62.9-71.7	1326-14240	24.60-13200	20.20-80500	387-2750	bdl-415	122.30-2290	24.60-192	49-390	bdl-48	bdl-622	bdl-83.20	bdl-14.70
			average	***69.8***	***6757***	***3663***	***6001***	***1824***	***55***	***820***	***136***	***249***	***3***	***131***	***31.2***	***4.1***
			median	***70.2***	***6605***	***4560***	***3191.50***	***2059.50***	***19***	***700***	***135.85***	***303.50***	***1.24***	***101.50***	***25.40***	***3.96***
			N/bdl		168/0	168/0	168/0	168/0	168/108	168/0	168/0	168/0	168/133	121/1	121/3	121/8
Deep zone	*Mgt-deep*	*La Cruz et al. (2020)* and this study	min-max	67.9-71.9	468-13900	614-8430	739-24200	633-3690	bdl-105.20	55.60-4990	42.20-189	50.90-521	bdl-15.80	27.20-706	2.95-50.50	bdl-7.90
			average	***70.7***	***3719***	***4213***	***9491***	***2056***	***24.4***	***601***	***123***	***277***	***2.1***	***161***	***27.8***	***3.3***
			median	***71.3***	***2931***	***3690***	***7170***	***2184***	***15.50***	***512***	***125.80***	***292.80***	***1.31***	***115***	***30.80***	***3.74***
			N/bdl		131/0	131/0	131/0	131/0	131/30	131/0	131/0	131/0	131/70	131/0	131/0	131/1
Andesite-hosted magnetite megacrysts	*Mgt-meg*	This study	min-max	55.3-65.9	839-15060	6820-18910	4230-76600	1838-4530	bdl-1058	509-2030	127.7-197	218-525	bdl-104	200-2560	31.9-62.3	3.6-6.19
			average	***62.3***	***8714***	***15242***	***45736***	***3194***	***526***	***1090***	***160***	***355***	***19***	***924***	***48.8***	***4.6***
			median	***62.7***	***9480***	***16620***	***59400***	***3465***	***664***	***934***	***158.2***	***361***	***10.4***	***915***	***51.5***	***4.6***
			N/bdl		31/0	31/0	31/0	31/0	31/11	31/0	31/0	31/0	31/1	31/0	31/0	31/0
Andesite-hosted magnetite-rich glomerocrysts	*Mgt-glom*	This study	min-max	58.4-69.8	7300-515000	10710-195000	55600-172000	2770-4850	135.6-3140	1730-13600	201.8-303	299-737	16.9-381	609-1100	33.4-106	3.7-11.9
			average	***61.4***	***33938***	***22158***	***68932***	***3715***	***1120***	***3447***	***235***	***494***	***149***	***780***	***53***	***5.6***
			median	***61.0***	***16490***	***15590***	***65400***	***3601***	***789***	***3170***	***231***	***480***	***132.80***	***716***	***50***	***5.08***
			N/bdl		41/0	41/0	41/0	41/0	41/0	41/0	41/0	41/0	41/0	41/0	41/0	41/0

Magnetite data from La Cruz et al. (2020) are differentiated from the ones from this study in the scatter plots (Figs. 6 and 9) and Supplementary Material Appendix 2.
MDL = median detecion limit, N = number of analyses. bdl = number of analyses BDL (below detection limit)

Tabla 3: Data summary of EPMA analyses for clinopyroxene from the ore bodies and from the host andesites

Table N°3: Data summary of EPMA analyses for clinopyroxene from the ore bodies and from the host andesites

Ore zone/host	Clinopyroxene type	Data source		Si [wt.%]	Ti [wt.%]	Al [wt.%]	Cr [wt.%]	Fe [wt.%]	Mn [wt.%]	Mg [wt.%]	Ca [wt.%]	Na [wt.%]
			MDL	0.02	0.01	0.01	0.003	0.01	0.01	0.01	0.01	0.004
Ore bodies	*Cpx-ore*	This study	min-max	17-25.93	0.03-0.90	0.11-2.26	bdl-0.48	2.89-7.63	0.04-0.14	6.20-9.83	11.92-18	0.12-1.31
			average	***24.13***	***0.16***	***0.75***	***0.02***	***5.16***	***0.06***	***8.60***	***16.44***	***0.69***
			median	***23.86***	***0.13***	***0.80***	***0.01***	***5.16***	***0.06***	***8.54***	***16.59***	***0.66***
			N/bdl	332/0	332/0	332/0	332/155	332/0	332/0	332/0	332/0	332/0
Clinopyroxene-rimmed magnetite megacrysts	*Cpx-meg*	This study	min-max	24.1-24.9	0.11-0.45	0.70-1.37	bdl-0.01	4.81-7.23	0.06-0.23	8.76-9.53	14.20-17.21	0.20-0.42
			average	***24.48***	***0.24***	***0.95***	***0.01***	***6.67***	***0.18***	***9.06***	***15.15***	***0.26***
			median	***24.50***	***0.21***	***0.94***	***0.01***	***6.81***	***0.19***	***9.1***	***15.0***	***0.23***
			N/bdl	20/0	20/0	20/0	20/13	20/0	20/0	20/0	20/0	20/0
Clinopyroxene from the andesite-hosted magnetite-rich glomerocrysts	*Cpx-glom*	This study	min-max	22.8-24.7	0.14-0.65	0.52-3.43	bdl-0.33	5.11-9.57	0.09-0.35	6.59-9.77	14-15.68	0.16-0.93
			average	***24.13***	***0.31***	***1.18***	***0.04***	***7.24***	***0.23***	***8.81***	***14.72***	***0.26***
			median	***24.2***	***0.28***	***0.99***	***0.01***	***7.14***	***0.23***	***8.8***	***14.7***	***0.25***
			N/bdl	49/0	49/0	49/0	49/2	49/0	49/0	49/0	49/0	49/0

MDL = mean detection limit, N = number of analyses, bdl = number of analyses BDL (below detection limit)

CHAPTER 4: Fluid-assisted assembly of magnetite microparticles: evidence from the giant El Laco iron oxide deposit, Chile

J. Tomás Ovalle[1-2*], Martin Reich[1-2], Fernando Barra[1-2], Adam C. Simon[3], Belinda Godel[4], Margaux Le Vaillant[4], Artur Deditius[5], Gisella Palma[1], Gert Heuser[1,6], Gloria Arancibia[1-2,6], Diego Morata[1-2]

[1]*Department of Geology and Millennium Nucleus for Metal Tracing Along Subduction, FCFM, Universidad de Chile, Santiago, Plaza Ercilla 803, Chile.*

[2]*Andean Geothermal Center of Excellence (CEGA), FCFM, Universidad de Chile, Plaza Ercilla 803, Santiago, Chile*.

[3] *Department of Earth and Environmental Sciences, University of Michigan, 1100 North* 8 *University Avenue, Ann Arbor, MI 48109-1005, USA.*

[4]*Commonwealth Scientific and Industrial Research Organisation (CSIRO) Mineral Resources, 26 Dick Perry Ave, Kensington 6151, Western Australia.*

[5]*School of Engineering and Information Technology, Murdoch University, Murdoch, Australia*

[6]*Departamento de Ingeniería Estructural y Geotécnica, Pontificia Universidad Católica de Chile, Santiago, Chile.*

*Corresponding author: José Tomás Ovalle (joseovalle@ug.uchile.cl)

Article to be submitted

ABSTRACT

The Plio-Pleistocene El Laco iron oxide deposit in northern Chile has attracted significant attention because of its uniquely preserved massive magnetite ore bodies, which bear a remarkable similarity to volcanic products. Outcropping morphologies including lava-like flows and pyroclastic deposits have stimulated controversy, suggesting a volcanogenic origin. To date, the highly vesicular and porous massive magnetite ores have received little attention from a microtextural point of view, limiting our understanding about the role of volcanic-hydrothermal processes on iron mineralization. Here we obtain an unprecedented view of these complex magnetite ores by unraveling their internal structure using a combination of scanning electron microscopy (SEM) and high-resolution X-ray computed tomography (HRXCT). SEM and HRXCT imaging of the samples reveals the presence of abundant magnetite microspheres with diameters ranging from ~100 to ~900 µm, as well as dendritic microstructures that form interconnected networks up to a few millimeters in size. The magnetite microspheres and dendrites occur interspersed within a matrix of variable porosity conformed by

smaller-sized (~2-20 µm) and irregularly-shaped magnetite microparticles. Based on the observed morphologies, which are commonly described in aqueous-phase experimental synthesis of magnetite microspheres, we interpret these occurrences as resulting of precipitation from Fe-rich hydrothermal fluids. We propose that depressurization, cooling and boiling of fluids triggered massive Fe supersaturation, resulting in the nucleation of magnetite microparticles or colloids, followed by self-assembly into larger and more complex aggregates displaying dendritic and spherical morphologies. Our data from El Laco agree with models invoking magmatic-hydrothermal fluids to explain the origin of the deposit, and provide new insights on the potential role of Fe colloids as agents of mineralization in volcanic systems.

4.1. INTRODUCTION

Iron oxide-apatite (IOA) deposits are globally distributed and are economically important sources for iron and strategic elements crucial for modern technologies, such as rare earth elements, cobalt and many others. IOA deposits occurring along the Andean Cordillera comprise massive magnetite ores bodies with morphologies including tabular, stratiform, pegmatitic and also lava-like (Park, 1961; Nyström and Henríquez, 1994; Sillitoe and Burows, 2002; Palma et al., 2020). The Plio-Pleistocene El Laco deposit in the Altiplano of northern Chile is the youngest and one of the most enigmatic IOA deposit on Earth (Fig. 16a, b). El Laco has attracted significant attention because of its uniquely preserved massive magnetite ore bodies, which include remarkable lava-like features with highly vesicular and porous textures, as well as poorly consolidated Fe oxide ash-like deposits. These volcanogenic features have stimulated controversy about their origin, with proposed genetic models involving liquid immiscibility, metasomatic replacement and Fe precipitation from magmatic-hydrothermal fluids as key ore-forming processes (Park, 1961; Nyström and Henríquez, 1994; Rhodes and Oreskes, 1999; Sillitoe and Burrows, 2002; Tornos et al., 2016; Mungall et al., 2018; Ovalle et al., 2018; Bain et al., 2021).

Despite progress on many fronts, microtextural studies of the magnetite ores at El Laco are scarce, and the few ones available have centered on the poorly consolidated (friable), ash-like magnetite horizons at Laco Sur. These locally-stratified, friable materials were described by Henríquez and Martin (1978), Henríquez and Nyström (1998) and Nyström et al. (2016). The cited studies revealed that magnetite in the friable Fe ores at El Laco occurs as spherules formed by aggregates of octahedral magnetite crystals, which were interpreted as a result of growth from hot magmatic gas in a volcanic plume, which was later deposited as ash fall (Nyström et al., 2016). Similar features have been also recognized in IOA deposits in Mexico, such as Cerro de Mercado, La Perla and Peña Colorada (Lyons, 1988; Corona-Esquivel et al., 2010).

Surprisingly, the more widespread and highly vesicular and porous Fe ores at Laco Sur have received little or no attention from a microtextural point of view. These magnetite ores, unlike the pyroclastic-like materials mentioned above, are hard, highly consolidated and display abundant vesicles and dendritic intergrowths (Fig. 16c), suggesting complex processes of crystal growth. To date, the lack of microtextural characterization of these vesicular and porous ores has limited our understanding of the key processes that formed El Laco, and in particular, has obscured the potential role of volcanic-hydrothermal processes on Fe mineralization. On this basis, the complex nature of the samples requires detailed microtextural observations that combine sectional imaging and with volumetric characterization.

In order to fill this gap of knowledge, here we study the vesicular and porous Fe ores at El Laco Sur using a combination of scanning electron microscopy (SEM) and high-resolution X-ray computed tomography (HRXCT). This particular combination of techniques allowed achieving an unprecedented view of the internal structure of the studied samples. In particular, HRXCT has proven key for spatial imaging of complex mineral textures at the micro- and nano-scales, providing 3D data for tracking magma vesiculation mechanisms and ore-forming processes (Gualda and Anderson, 2007; Godel, 2013; Mungall et al., 2015; Sayab et al., 2016; Pleše et al., 2019; Burgisser et al., 2020). Our results at El Laco show an exceptional preservation of complex microtextures configured by the presence of magnetite microspheres, dendritic magnetite aggregates and abundant microparticles. We discuss their significance and implications for the mechanisms of magnetite precipitation during decompression and cooling of Fe-rich fluids in volcanic systems.

4.2. GEOLOGICAL BACKGROUND AND SAMPLES

The Plio-Pleistocene El Laco volcanic complex (ELVC) is located in the Chilean Altiplano at ~5000 m elevation above the sea level (23°48′ S, 67°30′ W; Fig. 16a). The ELVC comprises a composite andesite stratovolcano system formed by several emission centers with variable preserved andesitic to dacitic lava flows, pyroclastic rocks, and volcanic breccias. These are the products of several stages of extensive explosive and effusive volcanic activity developed from the Pliocene to the Pleistocene (5.3 ± 1.9 to 1.6 ± 0.5 Ma; K-Ar; Naranjo et al., 2010). The Fe oxide mineralization at El Laco is estimated at ~733.9 Mt with an average ore grade of 49.2% Fe (CAP Minería 2016 Annual Report) and consists of seven massive magnetite ore bodies emplaced on the flanks of the central volcanic edifice, which are related to subvertical annular collapse structures forming secondary craters, breccia pipes and fissures (Fig. 16b). The ore bodies vary from outcropping Fe-oxide layers resembling lavas, to massive magnetite levels that grade to magnetite-±clinopyroxene-scapolite breccia bodies at depth (Ovalle et al., 2018). Texturally, the outcropping magnetite layers display flow/vesicular textures and crosscutting subvertical degassing structures, including the occurrence of friable pyroclastic-like horizons (Henríquez and Martin 1978; Nyström et al., 2016). Mineralogically, ore bodies at El Laco are largely composed of magnetite (> 90 % modal) with minor diopside, scapolite, apatite, REE-rich phosphates and Fe phosphates. Hematite-goethite alteration formed by supergene oxidation of the original magnetite is widespread.

In this study, we focus on samples collected from the vesicular and porous massive magnetite ore levels that outcrop in the Laco Sur open pit, because they allow to study the magnetite precipitation processes at surface conditions (Fig. 16b). This ore body was partially mined during the 1970s, exposing *ca.* 25 m of the upper portion where levels of massive magnetite occur along with some poorly consolidated (friable) magnetite-(± hematite), pyroclastic-like layers (Nystrom et al., 2016). Macroscopically, the analyzed samples (LS-06A and LS-06B) are hard and consolidated, almost unaltered, and consist of porous aggregates of fine-grained magnetite (Fig. 16c) displaying vesicular and dendritic growth textures, respectively. The samples were cut into thick sections (100 µm) for microanalysis and embedded in epoxy resin blocks for volume scanning.

4.3. METHODS

Observations of polished sections were carried out using a FEI Quanta 250 scanning electron microscope at the Andean Geothermal Center of Excellence (CEGA), Department of Geology,

Universidad de Chile, Santiago. Backscattered-electron (BSE) images were obtained using an accelerating voltage of between 15 and 20 kV, a filament current of 80 µA, a beam intensity of ~1 nA, a spot size of 5µm, and a working distance of 10 mm.

Preliminary 3D scanning of the samples was undertaken using a Bruker Skyscan 1272 micro-CT scanner at the Pontificia Universidad Católica de Chile in Santiago. Detailed 3D characterization of samples was performed using high-resolution X-ray computed tomography (HRXCT) at the Australian Resources Research Centre, CSIRO, Kensington, Western Australia. The high-resolution scans of the samples were carried out using a Zeiss Versa 520 3D X-ray microscope equipped with a large-scale flat panel detector, following the method by Godel et al. (2017). Samples were scanned at a voxel size of 11.8 µm with voltage of 160 kV and power of 10 W. Open pores are defined as pores that are connected in 3D to the outer surface of the samples, while potentially being enclosed within the magnetite if one considers a cross-section; closed pores, on the other hand, are defined as fully enclosed within the magnetite in 3D (Fig. C1). Open and closed pores were segmented from the greyscale volume using CSIRO-image processing workflows (see Fig. C1). Separation between open and closed pores is challenging for the irregularly shaped samples analyzed here, due to difficulties in mathematically defining the optimal sample boundary. Thus, reconstruction of boundaries and separation between pores was carried out using an automated, repeatable and pore-size independent separation algorithm developed for that purpose (Godel et al., 2017). Statistics on the size and morphology of the magnetite pores were then computed according to Godel (2013) and are presented in the results section.

4.4. INTERNAL STRUCTURE

SEM observation of the magnetite samples in Figure 1c reveals the presence of abundant magnetite microspheres (Figs. 17a; C2). Morphologically, the microspheres have diameters ranging from ~300 µm to 1.2 mm and are perfectly rounded, although in cases they can show more irregular shapes (Figs. 17a; b; C2). The microspheres are formed by euhedral magnetite crystals (Figs. 17b; C2), and can be partially to completely filled by octahedral magnetite grains (Fig. 17c). When magnified in Figures 2d-f, the octahedral crystals that form the magnetite microspheres contain micrometer-sized magnetite particles adhered to their surface, and in cases forming micro-botryoidal arrangements of agglomerated microparticles (Fig 17D).

The internal structure of the magnetite samples was reconstructed using HRXCT (Fig. 18). Volumetric imaging of sample LS-06A confirms the presence of magnetite microspheres, which are immersed within a matrix of smaller-sized and irregularly-shaped micrometer-sized magnetite particles (Fig. 18b; e; f). The magnetite microspheres can have a hollow interior structure (Fig. 18c), as observed in the SEM images (Fig. 17a-b; C2), and are present throughout the entire scanned volume, displaying irregular surfaces and sizes that range from ~100 to ~900 µm diameter (Fig. 18f). In addition, the microspheres occur undeformed, with no preferred fabric or orientation (Figs. 18e-f). Volumetric imaging of sample LS-06B show the presence of microspheres as well as dendritic structures (Figs. 18g-l). The magnetite microspheres have diameters of up to ~1.1 mm and coexist with dendritic magnetite aggregates (Figs. 18h; k; l). The latter have variable sizes that are difficult to quantify, but can form interconnected networks of up to a few millimeters in size (Figs. 18k; l).

4.5. FORMATION OF MAGNETITE MICROSPHERES

Microtextural relationships revealed by HRXCT show that the analyzed samples from Laco Sur are characterized by a complex internal structure, defined by magnetite microspheres, dendritic structures, and smaller-sized magnetite microparticles, with variable degrees of porosity (Figs. 18e; f; k; l). The surface roughness of the larger microspheres (Fig. 18f), in addition to the presence of dendrite-like structures (Figs. 18k; l) and aggregates of microparticles (Fig. 3e), strongly suggest that the observed aggregates were formed by assembly of multiple magnetite microparticles.

The occurrence of spherically-shaped Fe oxide particles has been previously reported in different geological materials, including marine sediments, impact-related ejecta and volcanic products (Itambi et al., 2010; Orgeira et al., 2017; Hagstrum et al., 2017; Wu et al., 2013). For example, aggregates of hollow Fe oxide microspheres have been reported as evidence of colloidal transport of Fe during the development of Precambrian iron formations (Ahn and Buseck, 1990). Notably, magnetite spherules have been documented in hydrothermal vents associated with sea-floor volcanism. These records include magnetite-hematite granules in the Earth's oldest hydrothermal vent precipitates in the Nuvvuagittuq belt in Quebec, Canada (Dodd et al., 2017), and magnetite spherules in sediments from the Central Indian Ocean Basin (CIOB) (Iyer et al. 1997; 1999; Amonkar et al., 2021). The magnetite spherules reported at CIOB are interpreted as resulting from hydrovolcanic processes involving Fe-rich hydrothermal emanations. The spherules vary from smooth-surfaced low-crystallinity structures to crystalline particles showing well-developed magnetite crystals and dendritic patterns (Iyer et al. 1999; Amonkar et al., 2021). In these settings, low-crystallinity spherules would have likely formed by rapid quenching processes, whereas well-crystallized spherules would have experienced slower cooling stages leading to the development of euhedral magnetite crystals (Amonkar et al., 2021). However, in addition to these temperature-mediated processes, it is likely that pressure drops related to the activity of these hydrovolcanic systems have also played a key role triggering magnetite precipitation, as demonstrated in magnetite solubility experiments under hydrothermal conditions (Simon et al., 2004).

At Laco Sur, Nystrom et al. (2016) reported magnetite spherules (50-200 µm) in the pyroclastic-like horizons, and proposed that they formed in a Fe-rich volcanic gas plume during eruption. These microspheres are 6 to 8 times smaller in size that the ones described here, and occur within ash-like friable material that is indicative of subaerial conditions of formation and accumulation. Therefore, we argue that the massive, consolidated and highly vesicular samples studied here were formed by a different process than the pyroclastic like-material, most likely mediated by an aqueous fluid.

Magnetite microspheres and dendrites have been synthetized experimentally for technological applications in the fields of material science and biomedicine (Yu, et al., 2006; Hu et al., 2009; Qu et al., 2010; Márquez et al., 2012 Han et al., 2012; Sun et al., 2015; Mandal Goswami, 2016). These experimental studies involve dissolution of $FeCl_3 \cdot 6H_2O$ components and are typically conducted under hydrothermal conditions (e.g., 180 - 250 °C), and therefore provide further insights into the nature of the sample features reported here. All the experiments document a first stage of nucleation of nano- to micro-sized magnetite particles with sub-spherical to irregular shapes, followed by a second stage in which the magnetite particles are self-assembled into either hollow microspheres or dendrites similar to those reported here (see Fig. 3 in Qu et al., 2010a). In particular, the time of hydrothermal reaction or maturation time plays a key role controlling the formation, size and crystallinity of the resulting magnetite microspheres and dendrites (Hu et al., 2009; Qu et al., 2010a; Sun et al., 2015). Importantly, the experiments by Qu et al. (2010a) showed that by increasing the duration of hydrothermal reaction, the hollow magnetite microspheres can evolve into more

crystalline spherical structures formed by multiple octahedral magnetite crystals, similar to those in Figure 17a. Further growth and coarsening of the microspheres is controlled by Ostwald ripening, which involves the dissolution of smaller particles and their subsequent reprecipitation on the energetically favorable surfaces of larger particles (Hu et al., 2010; Qu et al., 2010a, b). Remarkably similar textures to experimental runs in Figure 5 in Qu et al. (2010b) can be observed in the studied samples at Laco Sur, where magnetite microparticles adhered to the octahedral surfaces display botryoidal textures (Figs. 17d-f). A texture that can be also observed at centimeter scale in hand-sample specimens from El Laco that exhibit octahedral magnetite associated to spherical structures (see Fig. C3).

4.6. IMPLICATIONS FOR IRON MINERALIZATION

The microtextures reported here at Laco Sur, in addition to the experimental evidence summarized above, strongly suggest that magnetite precipitated from a Fe-rich hydrothermal fluid. We propose that during ascent to upper volcanic levels, depressurization, cooling and boiling of hydrothermal fluids triggered massive Fe supersaturation resulting in the nucleation of magnetite microparticles or colloids (Fig. 19a). As a result of this continuous process, the once dispersed microparticles aggregated forming clusters (Fig. 19b). During this stage, a series of particle interactions took place, promoting self-assembly into larger and more complex aggregates displaying dendrite-like and semi-spherical morphologies (Fig. 19b). As hydrothermal fluxing proceeded over time, further agglomeration and maturation processes resulted in the evolution of the irregular microparticles and aggregates into more stable and mature magnetite microspheres, which can grow by coalescence or coarsen by further assembly of smaller particles (Fig. 19c). Finally, as degassing of the fluid increased under shallow and/or surface conditions, volatile release led to increased porosity and residual fluids allowed final assemblage and structural maturation of the magnetite microspheres, giving place to the development of aggregates of octahedral magnetite crystals (Fig. 19d). During this final stage, Ostwald ripening may have promoted further coarsening by micro-botryoidal clustering on the octahedral {111} planes of magnetite (Figs. 17f and 19d).

The step-wise process described above may be viewed as an analogue to the well-documented process of silica maturation in sinter deposits (Rodgers et al., 2004; Lynne et al., 2007; Campbell et al., 2015). In these systems, the precipitation of colloidal silica particles as well as their subsequent aggregation and structural transformations are strongly controlled, among other factors, by the degree of undercooling and pH fluctuations of the discharging geothermal fluid, whereas growth and coarsening mechanisms are chemically mediated by Ostwald ripening (Tobler et al., 2009; Sanchez-Yañez et al., 2017). While these aspects should be investigated with detail in future studies, our observations suggest that massive magnetite levels can form by aggregation of magnetite microparticles precipitated from a Fe-rich hydrothermal solution.

Finally, we stress that the data presented here for Laco Sur, which points to a fluid-dominated system, are in agreement with genetic models invoking vapor-rich magmatic-hydrothermal fluids to explain the origin of the deposit (Rhodes and Oreskes, 1999; Sillitoe and Burrows, 2002; Ovalle et al., 2018; La Cruz et al., 2020; Childress et al., 2020). Furthermore, the abundant presence of (colloidal) magnetite microspheres in the outcropping ore bodies at El Laco has important implications for magnetite precipitation in hydrothermal systems. Considering recent evidence suggesting that significant fractions of Fe in hydrothermal plumes exist in the colloidal size range (i.e., Fitzsimmons et al., 2014; Hawkes et al., 2014, 2017; Lough et al., 2019), our data open new avenues of research

aimed at assessing the potential role of Fe colloids as agents of Fe mineralization in volcanic environments.

4.7. ACKNOWLEDGMENTS

The authors acknowledge funding from ANID through Millennium Science Initiative Program grant NCN13_065 “Millennium Nucleus for Metal Tracing Along Subduction”, from FONDAP project 15090013 “Centro de Excelencia en Geotermia de Los Andes, CEGA”, and Fondequip grant EQM 130028 (microCT-PUC). JTO acknowledges funding from Postgraduate Department of the University of Chile. Compañía Minera del Pacífico (CAP Minería) is thanked for providing access to the deposit. J.T. Ovalle thanks financial support provided by ANID/Doctorado Nacional/2017-21170261, through a PhD scholarship.

4.8. REFERENCES

1. Ahn, J.H. and Buseck, P.R., 1990. Hematite nanospheres of possible colloidal origin from a precambrian banded iron formation. Science, 250, 111-113.

2. Amonkar1, A., Iyer, S.D., Babu, E.V.S.S.K., Shailajha, N., Sardar1, A., and Manju, S., 2020, Fluid-driven Hydrovolcanic Activity along Fracture Zones and near Seamounts: Evidence from Deep-sea Fe-rich Spherules, Central Indian Ocean Basin. Acta Geologica Sinica. https://doi.org/10.1111/1755-6724.14697.

3. Bain, W.M., Steele-MacInnis, M., Tornos, F., Hanchar, J.M., Creaser, E.C., and Pietruszka, D.K., 2021 Evidence for iron-rich sulfate melt during magnetite(-apatite) mineralization at El Laco, Chile. Geology. https://doi.org/10.1130/G48861.1

4. Burgisser, A., Arbaret, L., Martel, C., Forien, M., Colombier, M., 2020. The role of oxides in the shallow vesiculation of ascending magmas. Journal Volcano and Geoth Res, 406, 107072.

5. Campbell, K., Lynne, B.Y., Handley, K.M., Jordan, S., Farmer, J.D., Guido, D.M., Foucher, F., Turner, S., and Perry, R.S., 2015 Tracing biosignature preservation of geothermally silicified microbial textures into the geological record. Astrobiology, v. 15, 10, 858-882. DOI: 10.1089/ast.2015.1307.

6. CAP Minería Annual Report 2016 <http://www.capmineria.cl/wp-content/uploads/2017/03/cap_mineria_memoria_2016.pdf >.

7. Corona-Esquivel, R., Martínez-Hernández, E., Henríquez, F., Nyström, J. O. and Tritlla, J. (2010) Palynologic evidence for iron-oxide ash fall at La Perla, an Oligocene Kiruna-type iron ore deposit in northern Mexico. GFF 132, 173–181.

8. Dare, S.A.S., Barnes, S.-J., and Beaudoin, G., 2015. Did the massive magnetite "lava flows" of El Laco (Chile) form by magmatic or hydrothermal processes? New constraints from magnetite composition by LA-ICP-MS: Mineral. Deposita, 50, 607–617.

9. Dodd, M., Papineau, D., Grenne, T., Slack, J.F., Rittner, M., Pirajno, F., O'Neil, J. and Little, C.T.S, 2017. Evidence for early life in Earth's oldest hydrothermal vent precipitates. Nature, 543, 60-64.

10. Fitzsimmons, J.N., Boyle, E.A., and Jenkins, W.J., 2014 Distal transport of dissolved hydrothermal iron in the deep South Pacific Ocean. PNAS, v. 111, p. 16654-16661. https://doi.org/10.1073/pnas.1418778111.

11. Godel, B., 2013. High-Resolution X-Ray Computed Tomography and Its Application to Ore Deposits: From Data Acquisition to Quantitative Three-Dimensional Measurements with Case Studies from Ni-Cu-PGE Deposits. Economic Geology 108(8), 2005-2019.

12. Godel, B., Ellis, B., O'Dea, D., Honeyands, T. and Harvey, T., 2017. Digital rocks for Iron Ore sinters: toward a 3D quantification of sinter textures. Australasian Institute of Mining and Metallurgy, Iron Ore 2017: Building Resilience, 24-26 July 2017, Perth, Australia (Perth, W.A. 24-26 July, 2017), 529-533.

13. Hagstrum, J.T., Firestone, R.B., West, A., Weaver, J.C., and Bunch, T.E., 2017 Impact- related microspherules in Late Pleistocene Alaskan and Yukon "muck" deposits signify recurrent episodes of catastrophic emplacement. Sci. Rep. 7, 16620. https://doi.org/10.1038/s41598-017-16958-2.

14. Hawkes, J.A., Connelly, D.P., Gledhill. M., and Achterberg, E.P., 2013 The stabilisation and transportation of dissolved iron from high temperature hydrothermal vent systems. Earth Planet Sci Lett., v. 375, p.280–290. https://doi.org/10.1016/j.epsl.2013.05.047.

15. Hawkes, J.A., Connelly, D.P., Rijkenberg, M.J.A., and Achterberg, E.P., 2014 The importance of shallow hydrothermal island arc systems in ocean biogeochemistry. Geophys. Res. Lett., v. 41, p. 942–947. https://doi.org/10.1002/2013GL058817.

16. Henriquez, F., and Martin, R.F., 1978, Crystal growth textures in magnetite flows and feeder dykes, El Laco, Chile: Canadian Mineralogist, v. 16, p. 581–589.

17. Henriquez, F. and Nyström, J. O., 1998 Magnetite bombs at El Laco volcano, Chile. GFF, v.120, p.269-271.

18. Hu, M., Ji, R-P., Jiang, J-S., 2010. Hydrothermal synthesis of magnetite crystals: From sheet to pseudo-octahedron. Mater. Res. Bull. 45, 1811–1815.

19. Hu, M., Jiang, J-S., and Li, X., 2009. Surfactant-assisted hydrothermal synthesis of dendritic magnetite microcrystals. Cryst. Growth Des. 9, 2, 820–824.

20. Itambi, A.C., von Dobeneck, T., Dekkers, M.J., 3 and Thomas Frederichs, T., 2010 Magnetic mineral inventory of equatorial Atlantic Ocean marine sediments off Senegal—glacial and interglacial contrast. Geophys. J. Int., 183, 163–177. https://doi.org/10.1111/j.1365-246X.2010.04736.x.

21. Iyer, S.D., Gupta, S.M., Charan, S.N. and Mills, O.P., 1999. Volcanogenic–hydrothermal iron-rich materials from the southern part of the Central Indian Ocean Basin. Marine Geology, 158, 15-25.

22. Iyer, S.D., Prasad, S.M., Gupta, S.M., Charan, S.N., and Mukherjee, A.D., 1997. Hydrovolcanic activity in the Central Indian Ocean Basin. Does nature mimic laboratory experiments? J. Volcanol. Geotherm. Res. 78, 209–220.

23. Lough, A.J.M., Homokyc, W.B., Connelly, D.P., Comer-Warnera, S.A., Nakamurad, K., Abyanehe, M.K., Kauliche, B., and Millsa R.A., 2019 Soluble iron conservation and colloidal iron dynamics in a hydrothermal plume. Chemical Geology, v. 511, p. 225-237. https://doi.org/10.1016/j.chemgeo.2019.01.001.

24. Lynne, B., Campbell, K., James, B., Browne, P., Moore, J., 2007. Tracking crystallinity in siliceous hot-spring deposits. Am. J. Sci. 307, 612-641.

25. Lyons, J. I. Volcanogenic iron oxide deposits, Cerro de Mercado and vicinity Durango, Mexico. Econ. Geol. 83, 1886–1906 (1988).

26. Mandal Goswami, M. 2016 Synthesis of micelles guided magnetite (Fe3O4) hollow spheres and their application for ac magnetic field responsive drug release. Sci. Rep., v. 6, p. 35721. https://doi.org/10.1038/srep35721.

27. Márquez, F., Herrera, G.M., Campo, T., Cotto, M., Ducongé, J., Sanz, J.M., Elizalde, E., Perales, O., and Morant, C., 2012 Preparation of hollow magnetite microspheres and their applications as drugs carriers. Nanoscale Research Letters, v. 7, p. 210. https://doi.org/10.1186/1556-276X-7-210.

28. Mungall, J. E., Long, K., Brenan, J. M., Smythe, D. & Naslund, H. R. Immiscible shoshonitic and Fe-P-oxide melts preserved in unconsolidated tephra at El Laco volcano, Chile. Geology 46, 255–258 (2018).

29. Naranjo, J. A., Henríquez, F. & Nyström, J. O. Subvolcanic contact metasomatism at El Laco Volcanic Complex, Central Andes. Andean Geology 37, 110–120 (2010).

30. Nyström, J.O., Henríquez, F., Naranjo, J.A., and Naslund, H.R., 2016, Magnetite spherules in pyroclastic iron ore at El Laco, Chile: American Mineralogist, v. 101, p. 587–595.

31. Orgeira, M.J., Castro, L.N., Goldmann, G.A., Prezzi, C.B., Sileo, E., Vega, D.R., Franzosi, C., Acevedo, R.D., Martínez, O., Rabassa, J., Ponce, J.F., Tófalo, O.R., 2017 Extraterrestrial microspherules from Bajada del Diablo, Chubut, Argentina. Geoscience Frontiers, v. 8, p. 137-149. https://doi.org/10.1016/j.gsf.2016.01.004.

32. Ovalle, J.T., La Cruz, N.L., Reich, M., Barra, F., Simon, A.C., Konecke, B.A., Rodriguez-Mustafa, M.A., Deditius, A.P., Childress, T.M., and Morata, D., 2018, Formation of massive iron deposits linked to explosive volcanic eruptions: Nature Scientific Reports, v. 8, no. 14855.

33. Palma, G., Barra, F., Reich, M., Simon, A.C., Romero, R., 2020. A review of magnetite geochemistry of Chilean iron oxide-apatite (IOA) deposits and its implications for ore-forming processes. Ore Geol. Rev. 126, 103748.

34. Park, C.R., 1961. A magnetite “flow” in northern Chile: Econ. Geol, 56, 431–441.

35. Paterson, D., de Jonge, M. D., Howard, D.L., Lewis, W., McKinlay, J., Starritt, A., Kusel, M., Ryan, C.G., Kirkham, R., Moorhead, G., and Siddons, D.P., 2011, The X-ray fluorescence microscopy beamline at the Australian Synchrotron: AIP Conference Proceedings, v. 1365, p. 219–222, doi: 10.1063/1.3625343.

36. Pleše, P., Higgins, M.D., Baker, D.R., Lanzafame, G., Kudrna Prašek, M., Mancini, L., and Rooyakkers, S.M., 2019. Production and detachment of oxide crystal shells on bubble walls during experimental vesiculation of andesitic magmas: Contributions to Mineralogy and Petrology, 174, 21.

37. Qu, X-F., Yao, Q-Z., Zhou, G-T., Fu, S-Q., and Jian-Liu Huang, J-L., 2010a Formation of Hollow Magnetite Microspheres and Their Evolution into Durian-like Architectures. J. Phys. Chem. C, 114, 8734–8740.

38. Qu, X-F., Zhou, G-T., Yao, Q-Z., and Fu, S-Q., 2010b. Aspartic-Acid-Assisted Hydrothermal Growth and Properties of Magnetite Octahedrons. J. Phys. Chem. C, 114, 284–289.

39. Rhodes, A.L., and Oreskes, N., 1995, Magnetite deposition at El Laco, Chile: Implications for Fe-oxide formation in magmatic-hydrothermal systems: Giant Ore Deposits Workshop, 2nd, April 25-27, 1995, Queens University, Kingston, Ontario, Canada, Proceedings, p. 582–622.

40. Rodgers, K.A., Browne, P.R.L., Buddle, T.F., Cook, K.L., Greatrex, R.., Hampton, W., Herdianita, N.R., Holland, G.R., Lynne, B.Y., Martin, R., Newton, Z., Pastars, D., Sannazarro, K.L., Teece, C. I., 2004. Silica phases in sinters and residues from geothermal fields of New Zealand. Earth-Sci. Rev. 66, 1-61.

41. Ryan, C.G., Siddons, D.P., Kirkham, R., Li, Z.Y., de Jonge, M.D., Paterson, D.J., Kuczewski, A., Howard, D.L., Dunn, P.A., Falkenberg, G., and others, 2014. Maia X-ray fluorescence imaging: Capturing detail in complex natural samples. Journal of Physics: Conference Series, 499, 012002.

42. Sanchez-Yanez, C., Reich, M., Leisen, M., Morata, D., and Barra, F., 2017. Geochemistry of metals and metalloids in siliceous sinter deposits: Implications for elemental partitioning into silica phases. Applied Geochemistry, 80, 112-133.

43. Sayab, M., Suuronen, J.-P., Moln´ar, F., Villanova, J., Kallonen, A., O’Brien,H., Lahtinen, R. & Lehtonen, M. (2016) Three-dimensional textural and quantitative analyses of orogenic gold at the nanoscale. Geology 44, 739–742.

44. Sillitoe, R.H., and Burrows, D.R., 2002, New field evidence bearing on the origin of the El Laco magnetite deposit, northern Chile: Econ. Geol, 97, 1101–1109.

45. Sun, X., Sun, K., and Liang, Y., 2015. Hydrothermal synthesis of magnetite: investigation of influence of aging time and Mechanism. Micro & Nano Letters, 10, 99–104.

46. Tobler, D.J., Shaw, S. and Benning, L.G., 2009. Quantification of initial steps of nucleation and growth of silica nanoparticles: an in-situ SAXS and DLS study. Geochim. Cosmochim. Acta 73, 5377–5393.

47. Tornos, F., Velasco, F., and Hanchar, J.M., 2016, Iron-rich melts, magmatic magnetite, and superheated hydrothermal systems: The El Laco deposit, Chile: Geology, v. 44, p. 427–430.

48. Wu, Y., Sharma, M., LeCompte, M.A., Demitroff, M.N., and Landis, J.D., 2013 Origin and provenance of spherules and magnetic grains at the Younger Dryas boundary. PNAS, v. 110, p. 3557-3566. https://doi.org/10.1073/pnas.1304059110.

49. Yu, D., Sun, X., Zou, J., Wang, Z., Wang, F., and Tang, K., 2006. Oriented Assembly of Fe3O4 Nanoparticles into Monodisperse Hollow Single-Crystal Microspheres. J. Phys. Chem. B, 110, 21667-21671.

4.9. FIGURES

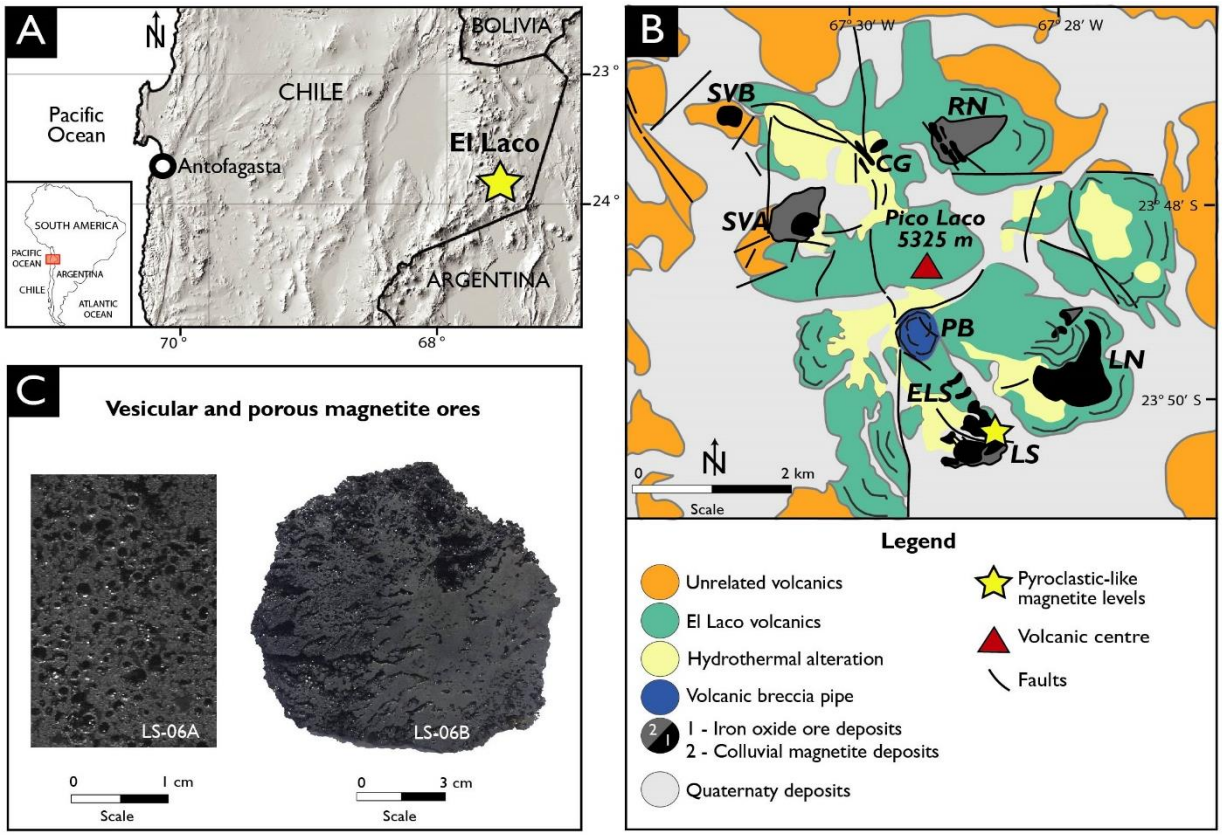

Figure 16: (A) Location of the El Laco volcanic complex (ELVC). **(B)** Simplified geological map of ELVC showing the main volcanic units, iron ore bodies and location of the samples. **(C)** Photos of magnetite samples (LS-06A and LS-06B) representative from vesicular and porous ore levels at Laco Sur.

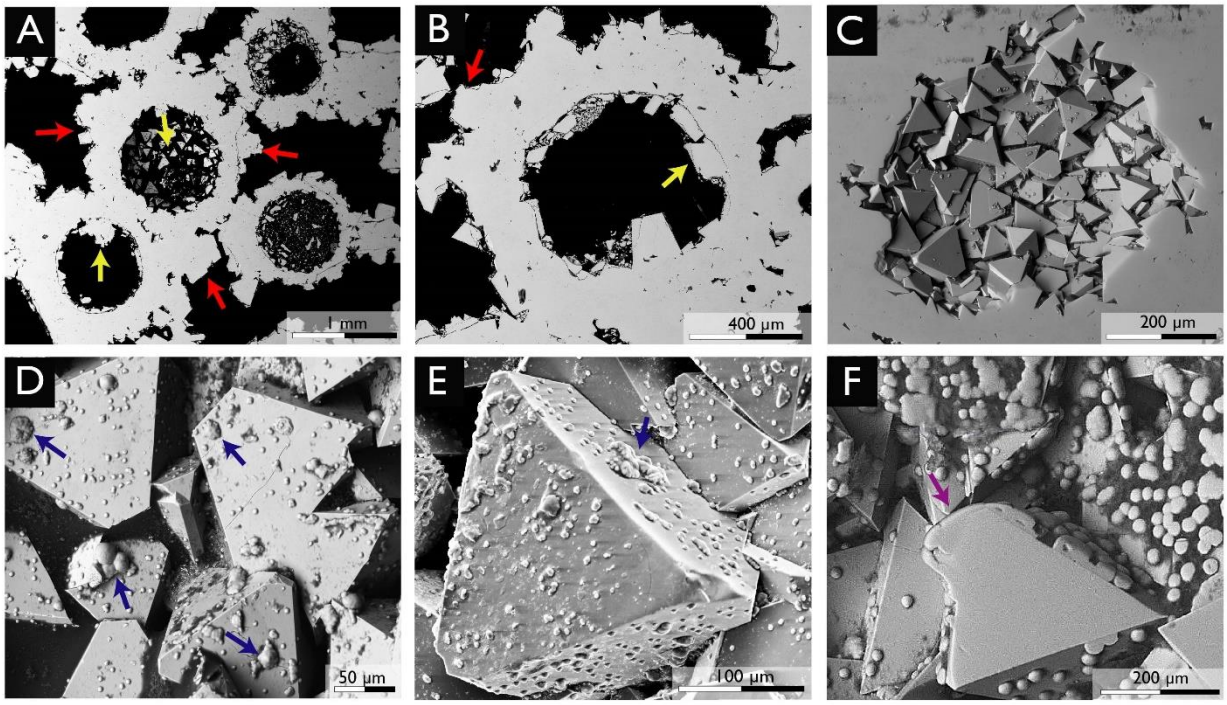

Figure 17: (A-B) SEM images of magnetite microspheres in vesicular and porous ore samples. Note the euhedral magnetite grains growing inward (yellow arrows) and outward (red arrows) from the microsphere surface. **(C-F)** BSE images showing octahedral magnetite crystals that fill some microspheres. Note the spherical magnetite particles attached to octahedral surfaces forming micro-botryoidal (blue arrows). **(F)** BSE image showing a growth surface (purple arrow) product of protracted nucleation of magnetite particles on the octahedral {111} planes of magnetite.

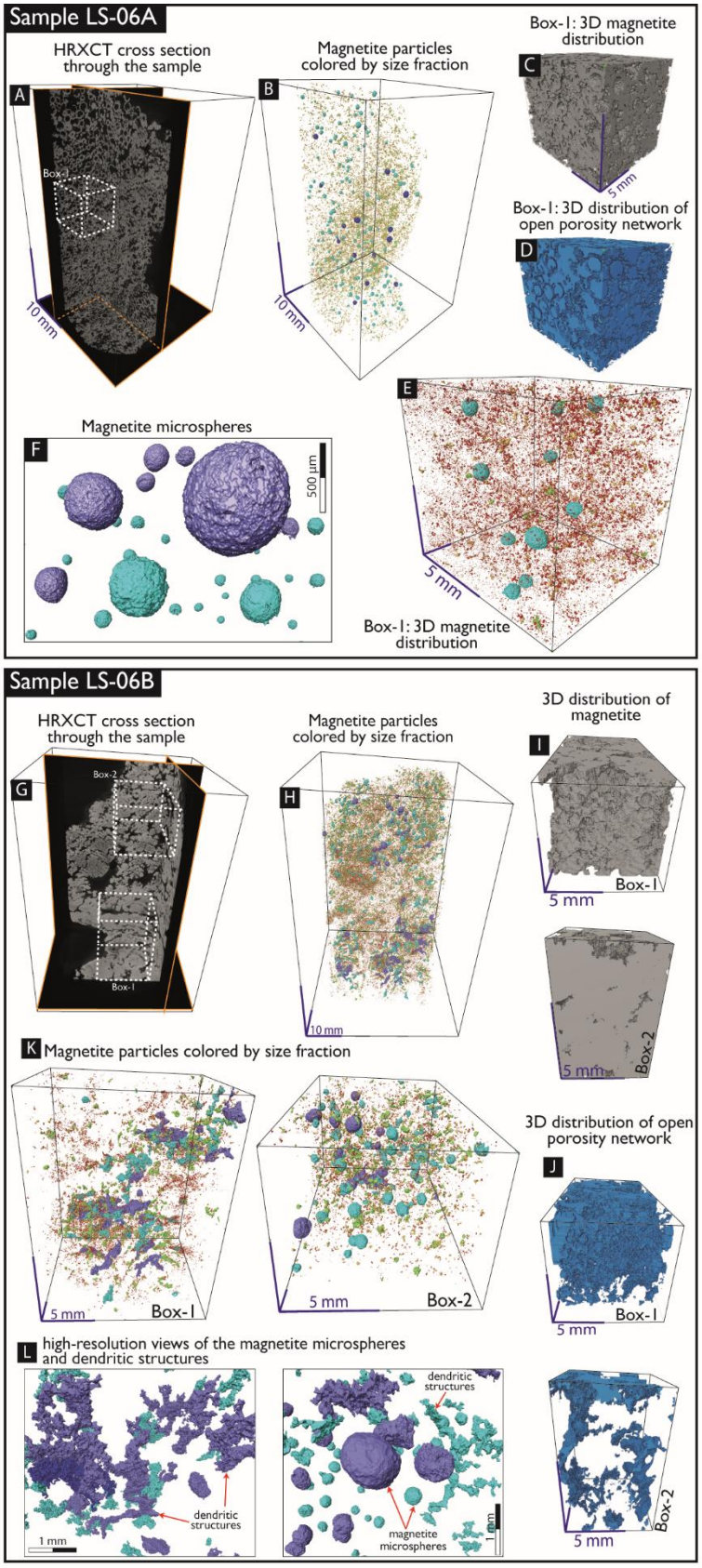

Figure 18: Volumetric imaging of magnetite samples using X-ray computed micro-tomography (HRXCT) data. **(A, E)** HRXCT slices oriented along 3 perpendicular directions through samples LS-06A and LS-06B, showing the location of boxes of interest (dashed lines). **(B, F)** HRXCT reconstructions showing the distribution of the magnetite particles (e.g., micron-sized irregular particles, magnetite microspheres, and dendrite-like structures) colored by size fractions. **(C-D, G-H)** High-resolution views of the magnetite microspheres and dendritic structures (colored by size) in both ore samples.

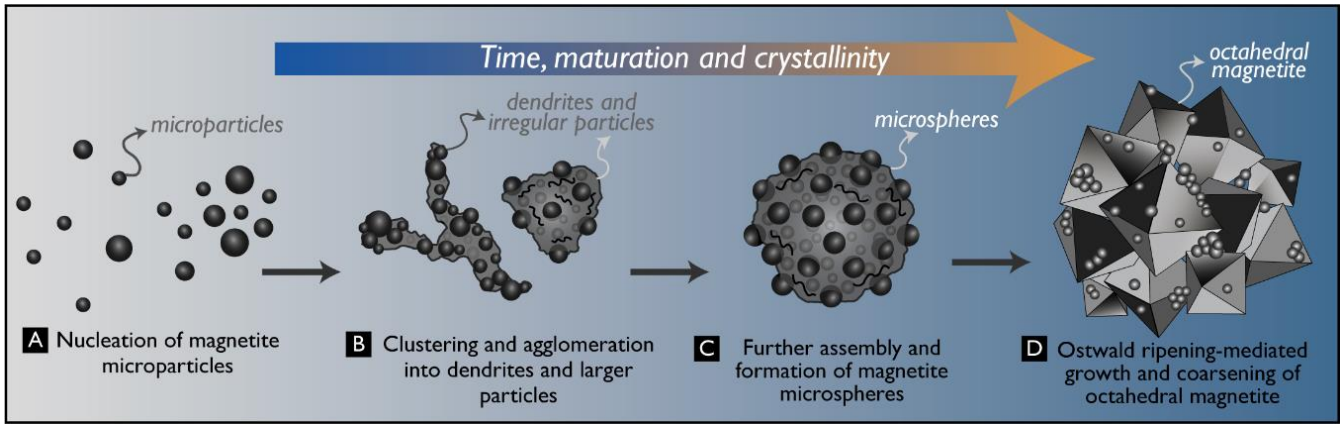

Figure 19: Schematic illustration for the formation of magnetite microspheres and the development of magnetite octahedral crystals at El Laco deposit. **(A)** Decompression, cooling and boiling trigger the supersaturation of a magmatic-hydrothermal fluid with respect to iron, resulting in the nucleation of colloidal magnetite microparticles; **(B)** These amorphous microparticles agglomerate into larger and more complex aggregates particles displaying dendrite-like and semi-spherical morphologies; **(C)** As hydrothermal fluxing proceeds, further agglomeration and maturation processes lead to the formation of magnetite microspheres; **(D)** with prolonged degassing and fluid fluxes, the structural maturation of the microspheres gives place to development of octahedral magnetite crystals. During this stage, Ostwald ripening processes promote the nucleation micro-botryoidal magnetite microparticles on octahedral planes of magnetite allowing them to growth and coarsen.

CHAPTER 5: Conclusions

The results presented in the previous chapters provide new insights on the processes leading to the formation of the Plio-Pleistocene El Laco iron oxide deposit in northern Chile, one of the most peculiar IOA-type mineralization on Earth. The genesis of this deposit has remained elusive over more than a half-century, with several models that have stimulated controversy over the years. Furthermore, this research contributes to a better understanding of how volcanic and hydrothermal processes operate during iron ore formation, and how they can lead to massive IOA-type mineralization in continental volcanic arcs.

The presented work combined fieldwork and drill core logging with a multi-instrumental microanalytical approach for geochemical and microtextural characterization. This approach, which focused primarily on magnetite as a petrogenetic indicator, allowed to constrain the role of the magmatic system, and most importantly, to unravel the key physicochemical processes that led to magnetite precipitation.

One key aspect of this research was the unprecedented access to both surface and drill core samples. This allowed dissecting the El Laco system from its roots to the surface. Observations revealed that the outcropping massive magnetite bodies grade to large magnetite-rich breccia bodies and veinlets towards intermediate and deeper levels of the system. This vertical zoning is characterized by depth-dependent microtextural and geochemical changes that are recorded in magnetite and that reflect the ore-forming conditions during the evolution of the system.

The deeper levels of the El Laco (>150 m depth) are dominated by magmatic-like conditions (>500 °C) in which magnetite displays ilmenite oxy-exsolution textures and high concentrations of Ti, V, Al, Ga, Ni and Cr, spanning compositions from purely igneous to high-temperature hydrothermal magnetite. On the other hand, at intermediate levels the ore bodies (~30-150 m depth) are characterized by magmatic-hydrothermal conditions with intermediate temperatures (~500–300 °C), magnetite microtextures showing abundant re-equilibrium features such as dissolution-reprecipitation textures, minor exsolutions, and oscillatory bands. These textures coupled with decreasing concentrations of key trace elements (Ti, V, Al, Cr, Ni, Mn, Zn, and Ga) point out to hydrothermal fluids as responsible for magnetite growth, and later modification of its primary features. Finally, at shallow levels, the outcropping ore bodies record lower temperatures of magnetite formation (<300 °C), and pervasive replacement of magnetite by supergene oxidation products and development of microporosity. These features, in addition to a highly depleted trace element geochemical signature suggest that magnetite in the outcropping bodies precipitated from a compositionally spent hydrothermal fluid, most likely under subaerial conditions.

Depth-dependent geochemical and microtextural variation trends were also recorded by clinopyroxene, the main silicate phase associated with magnetite in the ore bodies at El Laco. The notorious core-to-rim chemical variations — associated with features such as sector/oscillatory zoning and dissolution-reprecipitation textures — account for multiple stages of growth under highly dynamic physicochemical conditions. In particular, the spatial correspondence between Fe and Na in clinopyroxene, in cases associated with fine Cr layers, suggest growth from hydrothermal fluids with fluctuating salinity, possibly under intermittent boiling conditions.

Observations of andesite host rocks, on the other hand, provided insights into the processes that took place in the magmatic system below the El Laco edifice. Textures and chemical composition of magnetite and clinopyroxene in the andesite rocks allowed determining a purely magmatic origin, providing a framework for assessing the igneous vs. hydrothermal affinities of magnetite in the ore

bodies. Magnetite from the host andesites showed exsolution patterns including trellis- and sandwich-type, which are typically observed in magnetite from volcanic and intrusive rocks. This igneous nature is further supported by its high trace elements contents, particularly of Ti, Cr, Al, and Mn, which can reach concentrations of up to 1-2 orders of magnitude higher than magnetite in the ore bodies. Clinopyroxene in the andesites, like magnetite, revealed distinct compositional differences relative to ore-related clinopyroxene. Textural characteristics include core-to-rim inclusions indicating early magnetite saturation, and Cr-rich oscillations that fingerprint episodic events of hotter and less evolved magma recharges into the El Laco magma reservoir. These chemical differences, particularly those shown for Fe, Ca, Mn, and Na, allowed discerning igneous clinopyroxene in the andesites from hydrothermal clinopyroxene in the ore bodies.

The geochemical trends observed in magnetite and clinopyroxene, varying from trace element-rich varieties in the host andesites to trace element-poor types in the outcropping bodies, is interpreted here as evidence of a transition from purely igneous conditions to a fluid-dominated, cooling magmatic-hydrothermal system. In particular, the systematic trends of progressive depletion in minor and trace elements observed in magnetite from the deeper portions of the El Laco system towards the surface, account for an evolving system that was increasingly influenced by hydrothermal circulation. This interpretation is also supported by the depth-to-surface chemical and textural variations observed in clinopyroxene.

The widespread involvement of Fe-rich hydrothermal fluids during the genesis of El Laco deposit is also supported by HRXCT data of the highly vesicular magnetite samples from Laco Sur. Three-dimensional HRXCT imaging of the internal structure of these samples revealed the presence of magnetite microspheres and dentritic microstructures that suggest a formation by aggregation and self-assembly of multiple smaller-sized magnetite microparticles. Such mechanisms are commonly described in aqueous-phase experimental synthesis of magnetite microspheres and can therefore explain the formation of massive magnetite by aggregation of magnetite microparticles precipitated from Fe-rich hydrothermal fluids. These data are consistent with the depleted geochemical signature of magnetite typical of the outcropping orebodies, and suggest that these levels at Laco Sur may be Fe-rich analogues to sinter deposits. While these aspects must be further investigated, the HRXCT data highlights the potential role of Fe colloids as agents of mineralization in volcanic systems.

In summary, the roots-to-surface study of El Laco presented here reveals that the deposit is the product of a synergistic confluence of common igneous and magmatic-hydrothermal processes, which were enhanced during the evolution of the volcanic system (Fig. 4, chapter II). The proposed genetic model involves a first stage occurring under purely igneous conditions, where early magnetite crystallization promoted volatile exsolution and formation of magnetite-bubble pairs by heterogeneous nucleation processes (Fig. 4a, chapter II). The following fluid-assisted segregation of magnetite-bubble pairs from the magma source formed a magnetite-fluid suspension that accumulate in the uppermost layers of the magma chamber (Fig. 4b, chapter II). In a later stage, the evolving magnetite-bubble suspension is hydraulically injected into the upper volcanic levels through volcanic collapse-related structures, causing extensive brecciation and triggering the development of a shallow magmatic-hydrothermal system (Fig. 4c-d, chapter III). The Fe-rich hydrothermal fluids sourced from the magma migrated upwards precipitating magnetite due to decompression. This magnetite would have a high-temperature, near-igneous geochemical affinity in the deeper levels of the system. As a result of further ascend through fractures and permeable volcanic rocks, depressurization, cooling and boiling processes triggered massive Fe supersaturation of the fluids, which chemically evolved towards more depleted compositions. Therefore, at intermediate to shallower levels, magnetite would

display a hydrothermal signature. Finally, and in the waning stages of activity, magnetite precipitated from aqueous fluids under near-surface and sub-aerial conditions, with precipitation conditions likely governed by nucleation and aggregation of colloidal magnetite microparticles.

Overall, these results provide new evidence that supports volcanic and hydrothermal processes as active agents of metal concentration and IOA-type ore formation in continental arc volcanic systems.

BIBLIOGRAPHY

1. Bain, W.M., Steele-MacInnis, M., Tornos, F., Hanchar, J.M., Creaser, E.C., and Pietruszka, D.K (2021) Evidence for iron-rich sulfate melt during magnetite (-apatite) mineralization at El Laco, Chile. Geology; https://doi.org/10.1130/G48861.1.

2. Barton M. D. (2014) Iron oxide (–Cu–Au–REE–P–Ag–U–Co) systems. In Scott, S.D., ed., Treatise on Geochemistry (second edition, volume 13): Amsterdam, Elsevier, 515–541.

3. Bilenker L.D., Simon A.C., Reich M., Lundstrom C.C., Gajos N., Bindeman I. and Munizaga R. (2016) Fe–O stable isotope pairs elucidate a high-temperature origin of Chilean iron oxide-apatite deposits. Geochim. Cosmochim. Acta 177, 94-104.

4. Boutroy E., Dare S. A. S., Beaudoin G., Barnes S. J., and Lightfoot P. C. (2014) Magnetite composition in Ni-Cu-PGE deposits worldwide: Application to mineral exploration. J. Geochem. Explor. 145, 64-81.

5. Broman C., Nyström J. O., Henriquez F. and Elfman M. (1999) Fluid inclusions in magnetite-apatite ore from a cooling magmatic system at El Laco, Chile: GFF 121, 253–267.

6. Broughm S. G., Hanchar J. M., Tornos F., Westhues A. and Attersley S. (2017) Mineral chemistry of magnetite from magnetite-apatite mineralization and their host rocks: Examples from Kiruna, Sweden, and El Laco, Chile: Miner. Deposita 52, 223–244.

7. CAP Minería Annual Report 2016 <http://www.capmineria.cl/wp-content/uploads/2017/03/cap_mineria_memoria_2016.pdf >.

8. Childress T., Simon A. C., Reich M., Barra F., Bilenker L.D., La Cruz N. L., Bindeman I., and Ovalle J. T. (2020) Triple oxygen, hydrogen, and iron stable isotope signatures indicate a silicate magma source and magmatic-hydrothermal genesis for magnetite orebodies at El Laco, Chile: Econ Geol. 115, 1519–1536.

9. Dare S. A. S., Barnes S.-J., and Beaudoin G. (2012) Variation in trace element content of magnetite crystallized from a fractionating sulfide liquid, Sudbury, Canada: Implications for provenance discrimination: Geochim. Cosmochim. Acta 88, 27–50.

10. Dare S. A. S., Barnes, S-J., Beaudoin G., Méric J., Boutroy E., and Potvin-Doucet, C. (2014) Trace elements in magnetite as petrogenetic indicators. Miner. Deposita 49, 785-796.
11. Dare S., Barnes S. J. and Beaudoin. G. (2015) Did the massive magnetite “lava flows” of El Laco (Chile) form by magmatic or hydrothermal processes? New constraints from magnetite composition LA-ICP-MS. Miner Deposita. 50, 607.

12. Deditius A.P., Reich M., Simon A.C., Suvorova A., Knipping J., Roberts M.P. and Saunders M. (2018) Nanogeochemistry of hydrothermal magnetite. Contrib. Mineral. Petrol. 173, 46.

13. Dupuis C. and Beaudoin G. (2011) Discriminant diagrams for iron oxide trace element fingerprinting of mineral deposit types. Miner. Deposita 46, 319-335.

14. Edmonds M. (2015) Flotation of magmatic minerals. M. Research Focus, Geology 43, 655–656.

15. Frutos J. and Oyarzún M. J. (1975) Tectonic and geochemical evidence concerning the genesis of El Laco magnetite lava flow deposits, Chile. Econ. Geol. 70, 988-990.

16. Gardeweg, M., and Ramírez, C.F., (1985a) Hoja Río Zapaleri, Región de Antofagasta: Santiago, Servicio Nacional de Geología y Minería, p. 89.

17. Henriquez, F., and Martin, R.F., 1978, Crystal growth textures in magnetite flows and feeder dykes, El Laco, Chile: Canadian Mineralogist, v. 16, p. 581–589.

18. Hu H., Lentz D., Li J. W., McCarron T., Zhao X. F., and Hall D., (2015) Reequilibration processes in magnetite from iron skarn deposits. Econ. Geol. 111, 1–8.

19. Hu H., Li J. W., Lentz D., Ren Z., Zhao X., Deng X.D., and Hall D. (2014) Dissolution-reprecipitation process of magnetite from the Chengchao iron deposit: insights into ore genesis and implication for in-situ chemical analysis of magnetite. Ore Geol. Rev. 57, 393–405.

20. Huang X. W. and Beaudoin G. (2019) Textures and chemical compositions of magnetite from iron oxide copper-gold (IOCG) and Kiruna-type iron oxide-apatite (IOA) deposits and their implications for ore genesis and magnetite classification schemes. Econ. Geol. 114, 1–74.

21. Hurwitz S. and Navon O. (1994) Bubble nucleation in rhyolitic melts: Experiments at high pressure, temperature, and water content. Earth Planet. Sci. Lett. 122, 267–280.

22. Knipping J. L., Bilenker L. D., Simon A. C., Reich M., Barra F., Deditius A. P., Wälle M., Heinrich C. A., Holtz F. and Munizaga R. (2015b) Trace elements in magnetite from massive iron oxide-apatite deposits indicate a combined formation by igneous and magmatic-hydrothermal processes. Geochim. Cosmochim. Acta 171, 15-38.

23. Knipping J. L., Bilenker L.D., Simon A.C., Reich M., Barra F., Deditius A. P., Lundstrom C., Bindeman I. and Munizaga R. (2015a) Giant Kiruna-type deposits form by efficient flotation of magmatic magnetite suspensions. Geol. 43, 591-594.

24. Knipping J., L., Fiege A., Simon A.C., Oeser-Rabe M., Reich M. and Bilenker L. (2019a) In-situ iron isotope analyses reveal igneous and magmatic-hydrothermal growth of magnetite at the Los Colorados Kiruna-type iron oxide-apatite deposit, Chile. Am. Mineral. 104, 471–484.

25. Knipping J., Webster J.D., Simon A.C. and Holtz F. (2019b) Accumulation of magnetite by flotation on bubbles during decompression of silicate magma. Sci. Rep. 9, 3852.

26. La Cruz N. L., Ovalle J. T., Simon A. C., Konecke B. A., Barra F., Leisen M., Reich M., and Childress T. M. (2020) The geochemistry of magnetite and apatite from the El Laco iron oxide-apatite deposit, Chile: Implications for ore genesis: Econ. Geol. 115, 1461–1491.

27. Maksaev V., Gardeweg M., Ramírez C. F. and Zentilli M. (1988). Aplicación del método trazas de fisión (fission track) a la datación de cuerpos de magnetita de El Laco e Incahuasi en el altiplano de la Región de Antofagasta. In Congreso Geológico Chileno, No. 5, v. 1: B1-B23.

28. Mungall J. E., Long K., Brenan J. M., Smythe D. and Naslund H. R. (2018) Immiscible shoshonitic and Fe-P-oxide melts preserved in unconsolidated tephra at El Laco volcano, Chile. Geology 46, 255–258.

29. Nadoll P., Angerer T., Mauk J. L., French D. and Walshe J. (2014) The chemistry of hydrothermal magnetite: a review. Ore Geol. Rev. 61, 1-32.

30. Nadoll P., Mauk J.L., Hayes T.S., Koenig A.E. and Box S.E. (2012) Geochemistry of magnetite from hydrothermal ore deposits and host rocks of the Mesoproterozoic Belt Supergroup, USA. Econ. Geol. 107, 1275-1292.

31. Nadoll P., Mauk J.L., Leveille R.A. and Koenig A.E. (2015) Geochemistry of magnetite from porphyry Cu and skarn deposits in the southwestern United States. Miner. Deposita 50, 493-515.

32. Naranjo J.A., Henríquez F. and Nyström J.O. (2010) Subvolcanic contact metasomatism at El Laco volcanic complex, central Andes. Andean Geology, 37, 110-120.

33. Naslund H.R., Henríquez F., Nyström J.O., Vivallo W. and Dobbs F.M. (2002) Magmatic iron ores and associated mineralisation: examples from the Chilean high Andes and coastal Cordillera. In: Hydrothermal Iron Oxide-Copper-Gold: A Global Perspective. T.M. Porter (Ed.), PGC Publishing, Adelaide, Australia, 2, 207-226.

34. Nyström, J. O., Henríquez F., Naranjo J. A., and Nasuland H. R. (2016) Magnetite spherules in pyroclastic iron ore at El Laco, Chile. Am. Min. 101, 587–595.

35. Nyström J. O. and Henríquez F. (1994) Magmatic features of iron ores of the Kiruna-type in Chile and Sweden: ore textures and magnetite geochemistry. Econ. Geol. 89, 820-839.

36. Ovalle J.T., La Cruz N.L., Reich M., Barra F., Simon A.C., Konecke B.A. and Morata D. (2018) Formation of massive iron deposits linked to explosive volcanic eruptions. Sci. Rep. 8, 14855.

37. Palma G., Barra F., Reich M., Simon A. C., Romero R. (2020) A review of magnetite geochemistry of Chilean iron oxide-apatite (IOA) deposits and its implications for ore-forming processes. Ore Geol. Rev. 126, 103748.

38. Park C. R. (1961) A magnetite "flow" in northern Chile: Econ. Geol. 56, 431–441.

39. Rhodes A. L. and Oreskes N. (1995) Magnetite deposition at El Laco, Chile: implications for Fe-oxide formation in magmatic-hydrothermal systems. Giant ore deposits-II: Controls on the scale of orogenic magmatic-hydrothermal mineralization Clark, AH, 582-622.

40. Rhodes A. L. and Oreskes N. (1999) Oxygen isotope composition of magnetite deposits at El Laco, Chile: Evidence of formation from isotopically heavy fluids. Geology and Ore Deposits of the Central Andes, Brian J. Skinner, ed., Society of Economic Geologists Special Publication 7, 333-351.

41. Sheets S. A., Oreskes N., Rhodes A. L., Bodnar R. J., and Szabo C. (1997) Fluid inclusion evidence for a hydrothermal origin for magnetite-apatite mineralization at El Laco, Chile: Geological Society of America Abstracts with Programs, 2, A50.

42. Sillitoe R. H. and Burrows D. R. (2002) New field evidence bearing on the origin of the El Laco magnetite deposit, northern Chile. Econ. Geol. 97, 1101-1109.

43. Simon A. C., Kniping J., Reich M., Barra F., Deditius A. P., Bilenker L. and Childress T. (2018) Kiruna-Type Iron Oxide-Apatite (IOA) and Iron Oxide Copper-Gold (IOCG) Deposits form by a combination of ignous and magmatic-hydrothermal processes:evidence from the Chilean Iron Belt. SEG Special Publications, 21, 89-114.

44. Tornos F., Velasco F. and Hanchar J. M. (2017) The magmatic to magmatic-hydrothermal evolution of the El Laco deposit (Chile) and its implications for the genesis of magnetite-apatite deposits: Econ. Geol. 112, 1595–1628.

45. Tornos F., Velasco F. and Hanchar J.M. (2016) Iron-rich melts, magmatic magnetite, and superheated hydrothermal systems: The El Laco deposit, Chile. Geology 44, 427–430.

46. Velasco F., Tornos F. and Hanchar, J.M. (2016) Immiscible iron-and silica-rich melts and magnetite geochemistry at the El Laco volcano (northern Chile): Evidence for a magmatic origin for the magnetite deposits. Ore Geol. Rev. 79, 346-366.

47. Vivallo W., Henríquez F., and Espinoza S. (1994) Oxygen and sulfur isotopes in hydrothermally altered rocks and gypsum deposits at El Laco mining district, northern Chile: Departamento de Geología, Universidad de Chile, Comunicaciones, 45, 93–100.

48. Wen G., Li J. W., Hofstra A. H., Koenig A. E., Lowers H. A., and Adams D. (2017) Hydrothermal reequilibration of igneous magnetite in altered granitic plutons and its implications for magnetite

classification schemes: Insights from the Handan-Xingtai iron district. North China Craton. Geochim. Cosmochim. Acta 213, 255–270.

49. Williams P.J., Barton M.D., Fontbote L., de Haller A., Johnson D. A., Mark G., Marschik R. and Oliver N. H. S. (2005) Iron oxide-copper-gold deposits: Geology, space-time distribution, and possible modes of origin. Economic Geology 100Th Anniversary Volume 371–406.

50. Xie Q., Zhang Z., Hou T., Cheng Z., Campos E., Wang Z., and Fei X. (2019) New insights for the formation of Kiruna-type iron deposits by immiscible hydrous Fe-P melt and high-temperature hydrothermal processes: Evidence from El Laco deposit: Econ. Geol. 114, 35–46.

ANNEXES

ANNEX A: Supplementary Material for Chapter 2

Formation of massive iron deposits linked to explosive volcanic eruptions

This file includes:

A1. Supplementary Table 1: Summary of EPMA conditions for magnetite analysis.

Supplementary Figures A2-A5

A6. Table showing EPMA data for magnetite from Laco Norte, Laco Sur, Extensión Laco Sur, Pasos Blancos, Rodados Negros, San Vicente Alto y Cristales Grandes.

A1. Supplementary Table 1: Summary of EPMA conditions for magnetite analysis.

Supplementary Table 1: Summary of EPMA conditions for magnetite analysis.

Element/line	Crystal	Standard	Counting time (s)	MDL (wt.%)
Fe Kα	LLIF	USMN Magnetite	20	0.02
Ti Kα	PET	USMN Ilmenite	120	0.01
V Kα	LLIF	V_2O_5	120	0.01
Cr Kα	LLIF	Cr_2O_3	100	0.01
Al Kα	TAP	Jadeite	100	0.01
Mn Kα	LLIF	Rhodonite (BHRH)	100	0.01 - 0.03
Si Kα	LTAP	Wollastonite	100	0.01
Mg Kα	TAP	Geikielite (GEIK)	100	0.01 - 0.02
Ca Kα	PET	Wollastonite	100	0.01
P Kα	LTAP	BaCl	100	0.01 - 0.02

MDL: mean detection limit.

Supplementary Figure A2: This figure is an expanded version of Figure 2 in the main text, where pictures of hand specimens are shown for each sample (Drill core LCN-0944)

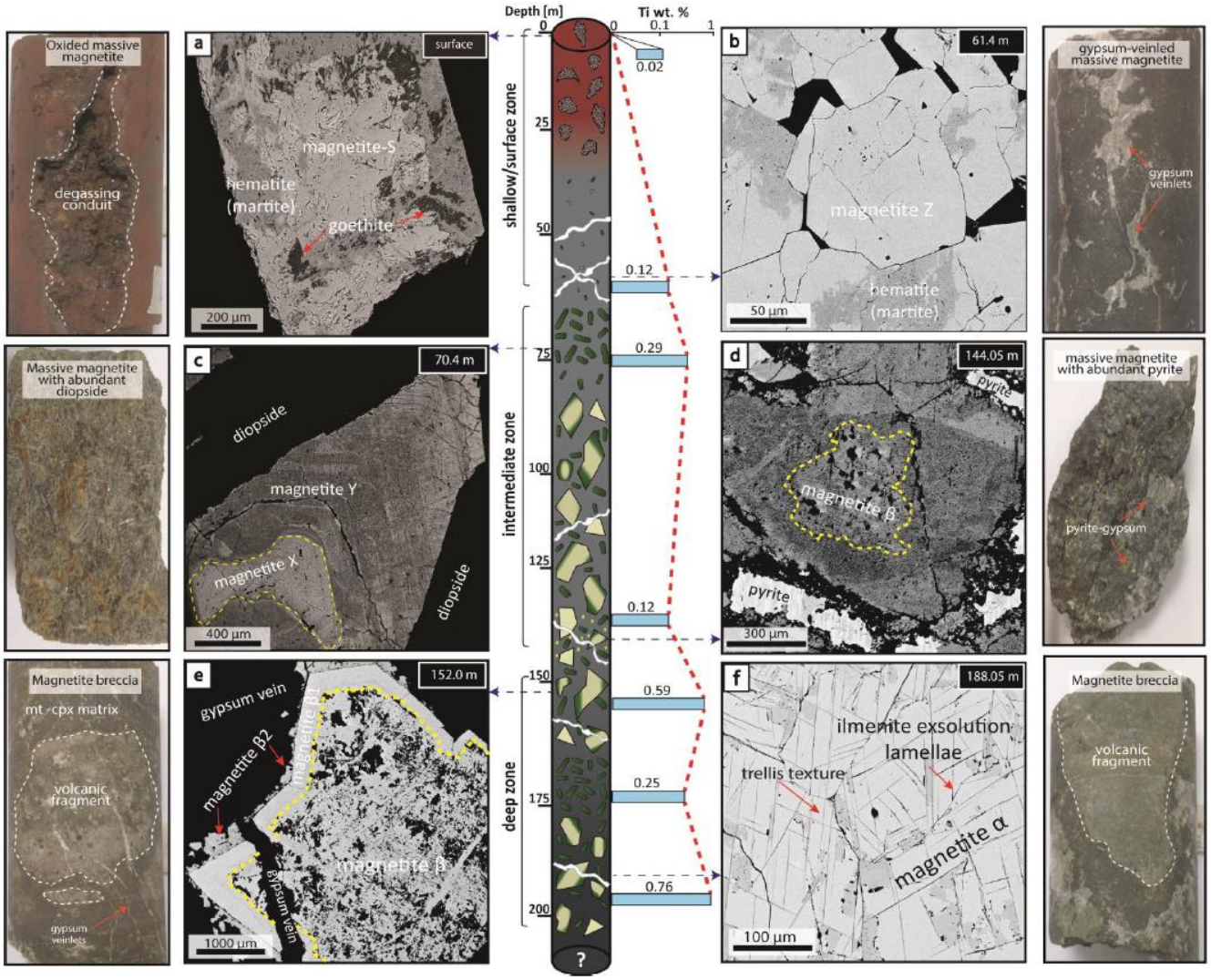

Supplementary Figure A3: Schematic illustration of a representative drill core from Laco Sur showing the morphology and lithological variations of the magnetite ore bodies (drill core LCO-0721A). BSE images of magnetite textural types are shown (center), as well as pictures of hand specimens taken at different depths (left): (a) Euhedral magnetite grain showing inclusion-rich cores surrounded by pristine magnetite rims. Hematite (± goethite) are observed along the grain rims. (b) Coarse magnetite grain containing inclusion-rich cores surrounded by more pristine magnetite rims. (c) Relatively pristine magnetite from the breccia matrix, containing inclusions of scapolite and clinopyroxene. The andesitic fragments are pervasively replaced by fine-grained scapolite. (d) Magnetite from late veins exhibiting crystallographically-controlled, alternating inclusion-rich and inclusion-poor zones (blue arrows). mt: magnetite, cpx: clinopyroxene, scp: scapolite.

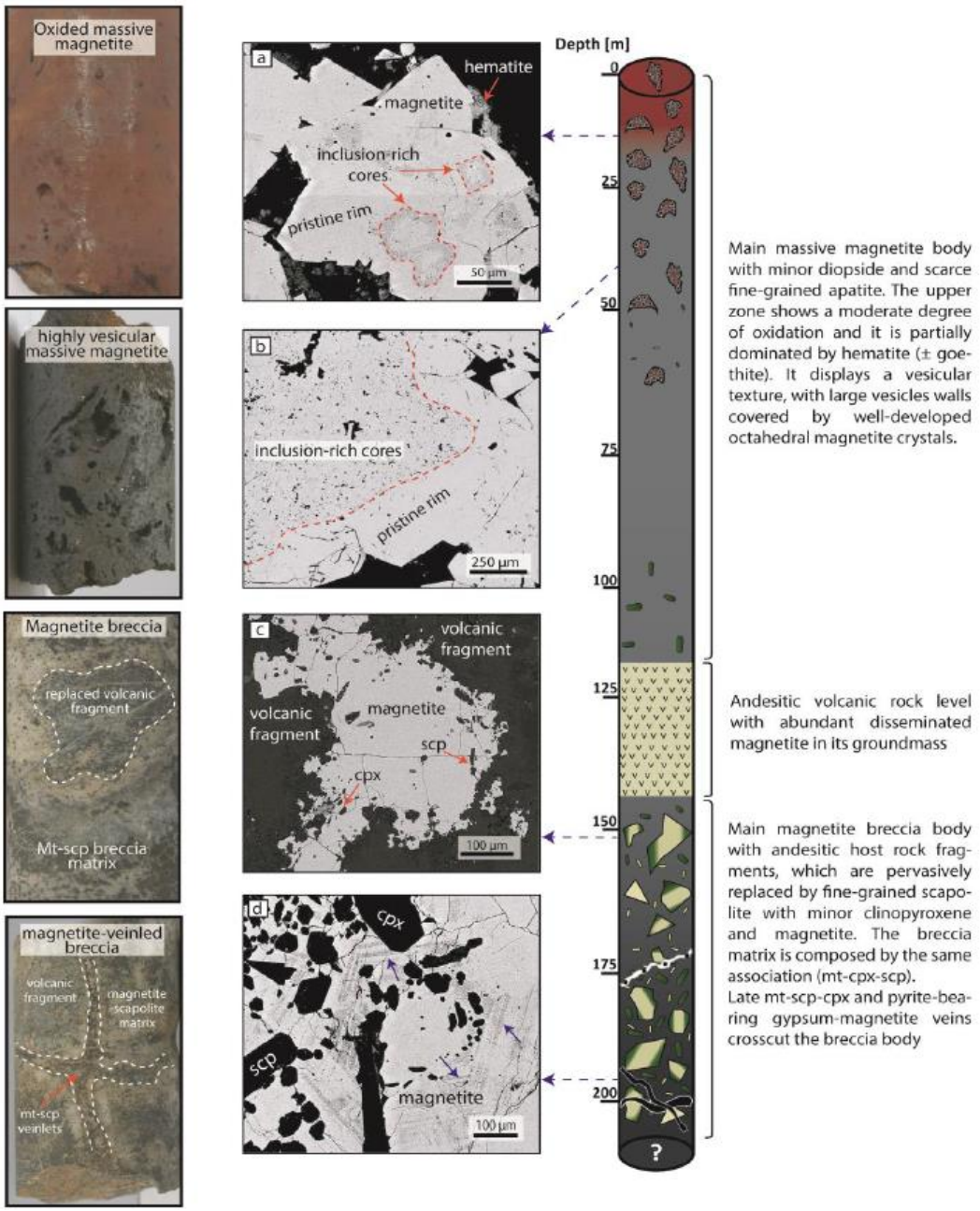

Supplementary Figure A4: Schematic illustration of a representative drill core from Laco Sur showing the morphology and lithological variations of the ore bodies (drill core LCO-0715). BSE images of magnetite textural types are shown (center), as well as pictures of hand specimens taken at different depths (left): (a) Euhedral coarse-grained magnetite grain exhibiting resorbed inclusion-rich cores surrounded by magnetite rims with abundant nano-sized inclusions. (b) Magnetite grain from the breccia matrix containing abundant scapolite and clinopyroxene. (c) Ti-rich magnetite from the breccia matrix, showing well-developed ilmenite exsolution lamellas, which exhibit both trellis and sandwich textures.

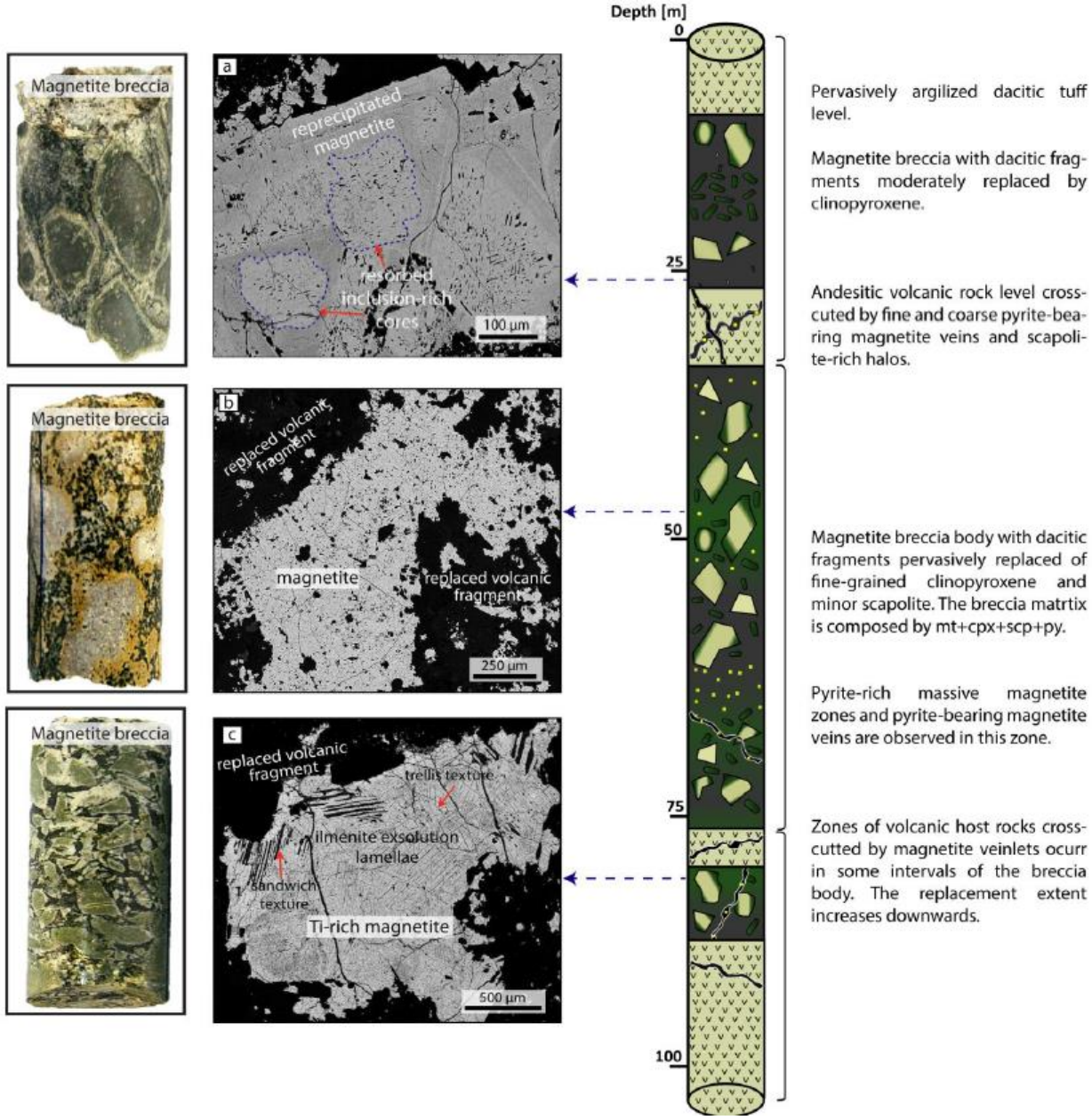

Supplementary Figure A5: Pictures of outcrops and hand samples from the El Laco deposit: (a-c) Outcrop of the Laco Norte ore body. Note the highly vesicular texture. (d-e) Outcrop of the San Vicente Alto ore body. Note the degassing structures including vesicles, pores and rounded structures similar to bubble aggregates (d), and subvertical degassing conduits (e). (f) Massive magnetite outcrop from Laco Norte showing pahoehoe-type flow structures.

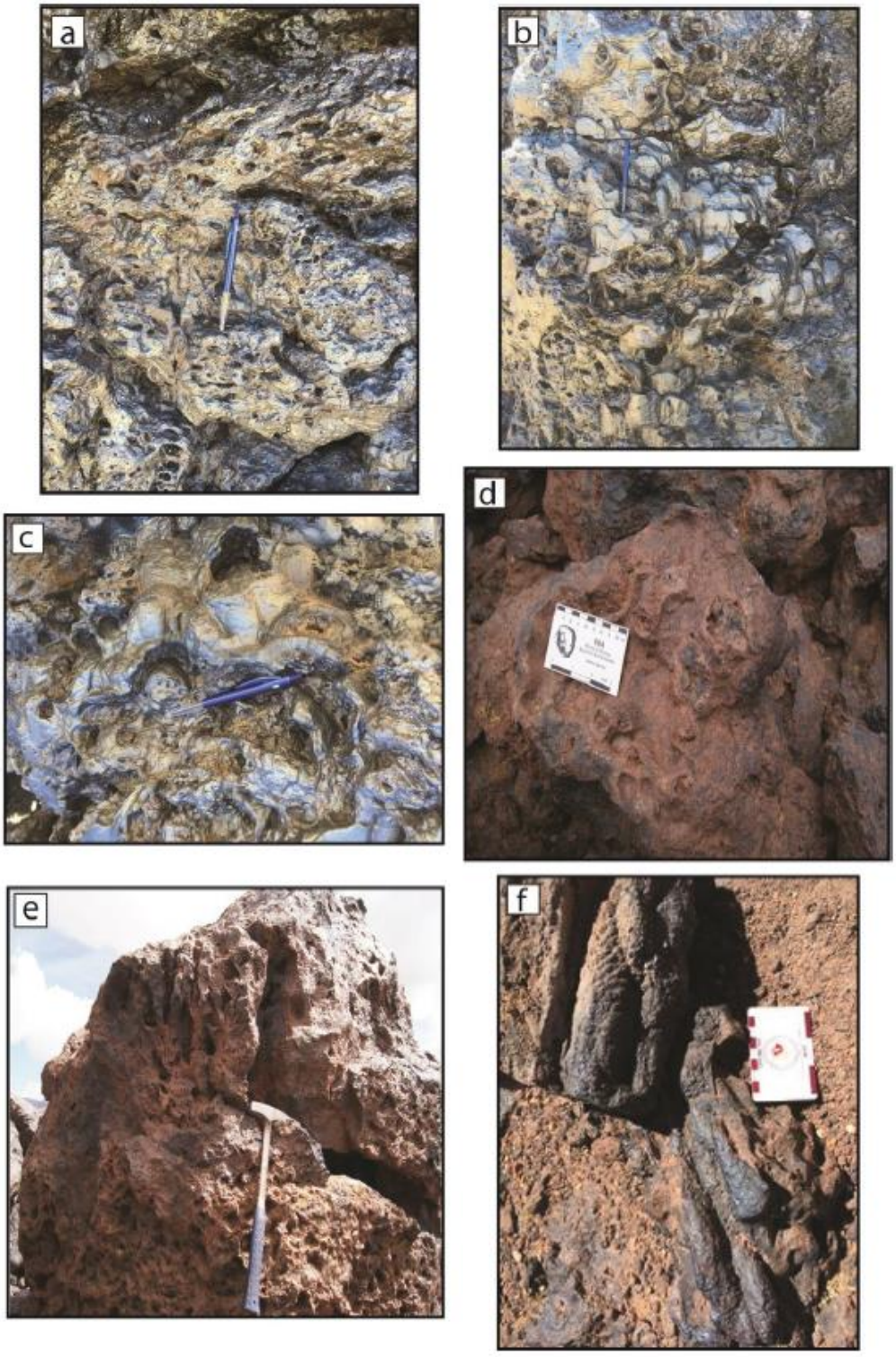

A6. Table showing EPMA data for magnetite from Laco Norte, Laco Sur, Extensión Laco Sur, Pasos Blancos, Rodados Negros, San Vicente Alto y Cristales Grandes.

Sample ID Laco Norte	Mg [wt%]	Al [wt%]	Si [wt%]	Ti [wt%]	Ca [wt%]	P [wt%]	V [wt%]	Cr [wt%]	Fe [wt%]	Mn [wt%]	O [wt%]	Total	Ti+V [wt%]	Al+Mn [wt%]	Sample	Magnetite Type
el 2 grain 1 lower_1	0.94	b.d	0.44	b.d	0.15	b.d	0.07	b.d	70.04	0.03	28.08	99.75	0.07	0.03	Surface	Mt-S
el 2 grain 1 lower_2	1.11	b.d	0.75	b.d	0.28	0.01	0.07	b.d	69.21	0.03	28.21	99.67	0.07	0.03	Surface	Mt-S
el 2 grain 1 lower_3	1.16	0.03	0.90	b.d	0.34	0.01	0.07	b.d	67.79	0.03	27.88	98.21	0.07	0.06	Surface	Mt-S
el 2 grain 1 lower_4	1.20	b.d	1.03	b.d	0.33	0.02	0.06	b.d	68.56	0.03	28.28	99.51	0.07	0.03	Surface	Mt-S
el 2 grain 1 lower_5	1.12	b.d	0.83	b.d	0.29	0.02	0.07	b.d	69.21	0.03	28.28	99.84	0.07	0.03	Surface	Mt-S
el 2 grain 1 lower_6	0.94	0.10	0.46	b.d	0.14	b.d	0.07	b.d	67.45	0.03	27.17	96.36	0.07	0.13	Surface	Mt-S
el 2 grain 1 lower_7	0.81	0.03	0.46	b.d	0.15	b.d	0.08	b.d	69.54	0.03	27.80	98.89	0.08	0.06	Surface	Mt-S
el 2 grain 1 lower_8	0.94	0.01	0.36	b.d	0.13	b.d	0.08	b.d	70.31	0.03	28.12	99.98	0.08	0.04	Surface	Mt-S
el 2 grain 1 lower_9	1.03	0.02	0.50	b.d	0.18	b.d	0.08	b.d	69.76	0.03	28.11	99.70	0.08	0.04	Surface	Mt-S
el 2 grain 1 lower_10	b.d	b.d	0.32	b.d	b.d	b.d	0.08	b.d	68.36	b.d	26.46	95.23	0.09	0.01	Surface	Mt-S
el 2 grain 2 lower_1	0.90	b.d	0.29	b.d	0.11	b.d	0.07	b.d	70.72	0.03	28.16	100.29	0.07	0.04	Surface	Mt-S
el 2 grain 2 lower_2	1.04	b.d	0.38	b.d	0.15	b.d	0.07	b.d	70.32	0.04	28.23	100.24	0.07	0.04	Surface	Mt-S
el 2 grain 2 lower_3	1.21	b.d	0.70	b.d	0.26	0.01	0.07	b.d	69.31	0.03	28.28	99.88	0.08	0.04	Surface	Mt-S
el 2 grain 2 lower_4	0.99	0.28	0.65	b.d	0.25	0.01	0.07	b.d	68.62	0.03	28.00	98.89	0.07	0.31	Surface	Mt-S
el 2 grain 2 lower_5	1.04	b.d	0.70	b.d	0.25	0.01	0.07	b.d	69.53	0.03	28.22	99.85	0.08	0.04	Surface	Mt-S
el 2 grain 2 lower_6	1.02	0.01	0.60	b.d	0.20	b.d	0.07	b.d	69.87	0.03	28.24	100.05	0.07	0.04	Surface	Mt-S
el 2 grain 2 lower_7	0.95	0.01	0.67	b.d	0.24	b.d	0.07	b.d	69.76	0.03	28.20	99.93	0.08	0.04	Surface	Mt-S
el 2 grain 3_1	1.02	0.04	0.52	b.d	0.20	b.d	0.07	b.d	69.73	0.03	28.14	99.75	0.07	0.07	Surface	Mt-S
el 2 grain 3_2	b.d	0.56	0.50	b.d	0.01	0.02	0.07	b.d	67.44	b.d	26.69	95.29	0.07	0.57	Surface	Mt-S
el 2 grain 3_3	1.01	0.01	0.40	b.d	0.14	b.d	0.07	b.d	70.07	0.03	28.13	99.87	0.07	0.04	Surface	Mt-S
el 2 grain 3_4	0.33	0.08	0.58	b.d	0.16	0.01	0.06	b.d	68.34	0.03	27.06	96.66	0.07	0.11	Surface	Mt-S
el 10 rad grain 2 sp 1	0.36	0.42	0.32	b.d	0.10	0.03	0.08	b.d	67.72	b.d	26.90	95.93	0.09	0.42	Surface	Mt-S
el 10 rad grain 2 sp 6	0.29	0.02	0.24	b.d	0.07	0.02	0.08	b.d	68.00	0.03	26.56	95.32	0.09	0.05	Surface	Mt-S
el 10 rad grain 3 sp 2	0.39	0.06	0.84	b.d	0.28	0.02	0.08	b.d	66.68	0.04	26.74	95.13	0.08	0.10	Surface	Mt-S
el 10 rad grain 3 sp 4	0.38	0.03	0.82	b.d	0.27	0.03	0.08	b.d	67.23	0.04	26.91	95.78	0.08	0.07	Surface	Mt-S
el 10 rad grain 3 sp 5	0.09	0.03	0.27	b.d	0.09	0.08	0.08	b.d	68.21	0.03	26.58	95.48	0.09	0.06	Surface	Mt-S
el 10 rad grain 3 sp 6	0.54	0.67	0.75	b.d	0.22	0.05	0.08	b.d	66.31	0.04	27.15	95.81	0.08	0.71	Surface	Mt-S
el 10 core grain 1 sp 1	1.73	0.07	1.74	0.02	0.50	b.d	0.06	b.d	65.99	0.04	28.44	98.59	0.07	0.12	Surface	Mt-S
el 10 core grain 1 sp 2	1.61	0.07	1.85	0.02	0.52	0.01	0.06	b.d	65.72	0.04	28.32	98.22	0.07	0.12	Surface	Mt-S
el 10 core grain 1 sp 3	1.39	0.06	1.26	0.01	0.41	0.01	0.06	b.d	66.07	0.04	27.75	97.07	0.07	0.10	Surface	Mt-S
el 10 core grain 1 sp 4	1.81	0.07	1.78	0.01	0.53	0.02	0.05	b.d	65.95	0.05	28.54	98.81	0.07	0.11	Surface	Mt-S
el 10 core grain 1 sp 5	1.85	0.07	1.87	0.01	0.55	0.01	0.06	b.d	64.73	0.05	28.19	97.39	0.07	0.12	Surface	Mt-S
el 10 core grain 1 sp 6	1.79	0.07	1.88	0.02	0.51	0.01	0.06	b.d	65.67	0.05	28.49	98.57	0.08	0.12	Surface	Mt-S
el 10 core grain 1 sp 7	2.04	0.08	1.65	0.02	0.55	0.01	0.06	b.d	65.52	0.05	28.49	98.46	0.08	0.13	Surface	Mt-S
el 10 core grain 1 sp 8	1.16	0.09	1.52	0.01	0.46	0.02	0.06	b.d	65.29	0.03	27.50	96.15	0.07	0.13	Surface	Mt-S
el 10 core grain 3 sp 1	1.58	0.09	1.90	0.02	0.54	0.02	0.06	b.d	64.92	0.02	28.05	97.20	0.08	0.10	Surface	Mt-S
el 10 core grain 3 sp 2	0.48	0.13	1.06	0.02	0.28	0.02	0.06	b.d	66.36	b.d	26.89	95.31	0.07	0.13	Surface	Mt-S
el 10 core grain 3 sp 3	0.90	0.10	1.42	0.02	0.41	0.01	0.05	b.d	66.41	0.01	27.59	96.93	0.08	0.11	Surface	Mt-S
el 10 core grain 3 sp 4	0.45	0.44	1.30	0.02	0.28	0.04	0.05	b.d	65.59	0.01	27.03	95.21	0.07	0.45	Surface	Mt-S
el 10 core grain 3 sp 5	1.85	0.13	1.93	0.03	0.54	0.01	0.06	b.d	65.40	0.03	28.53	98.50	0.09	0.16	Surface	Mt-S
el 10 core grain 3 sp 6	1.71	0.13	1.82	0.03	0.52	0.01	0.06	b.d	65.33	0.03	28.29	97.93	0.09	0.16	Surface	Mt-S
el 10 core grain 3 sp 7	1.64	0.10	1.73	0.03	0.51	b.d	0.06	b.d	66.40	0.02	28.54	99.03	0.09	0.12	Surface	Mt-S
el 10 core grain 3 sp 8	0.43	0.26	0.92	0.03	0.40	0.05	0.06	b.d	67.39	0.01	27.34	96.88	0.08	0.27	Surface	Mt-S
el 2b sp 1	0.01	0.03	0.23	b.d	b.d	b.d	b.d	b.d	68.68	0.02	26.49	95.46	0.01	0.04	Surface	Mt-S
el 2b bse 1 sp 1	0.01	b.d	0.26	b.d	b.d	b.d	0.07	b.d	68.77	0.05	26.57	95.73	0.07	0.05	Surface	Mt-S
el 2b bse 1 sp 2	0.02	b.d	0.24	b.d	b.d	b.d	0.04	b.d	68.63	0.06	26.50	95.50	0.04	0.07	Surface	Mt-S
el 2b bse 1 sp 3	b.d	b.d	0.23	b.d	b.d	b.d	0.06	b.d	68.52	0.03	26.45	95.29	0.07	0.03	Surface	Mt-S
el 2b bse 2 sp 1	0.03	b.d	0.16	b.d	b.d	0.05	0.05	b.d	69.14	b.d	26.67	96.09	0.05	0.01	Surface	Mt-S
el 2b bse 2 sp 2	b.d	0.01	0.19	b.d	b.d	b.d	0.03	b.d	69.20	b.d	26.67	96.11	0.04	0.01	Surface	Mt-S
el 2b bse 2 sp 3	b.d	b.d	0.19	b.d	b.d	b.d	0.03	b.d	69.42	b.d	26.74	96.39	0.04	0.01	Surface	Mt-S
el 2b bse 3 tran_1	0.01	b.d	0.16	b.d	b.d	b.d	0.03	b.d	69.16	0.03	26.62	96.02	0.04	0.03	Surface	Mt-S
el 2b bse 3 tran_2	b.d	b.d	0.24	b.d	b.d	b.d	0.02	b.d	69.46	b.d	26.80	96.53	0.03	0.01	Surface	Mt-S
el 2b bse 3 tran_3	0.02	b.d	0.28	b.d	b.d	b.d	0.04	b.d	69.05	b.d	26.67	96.06	0.04	0.01	Surface	Mt-S
el 2b bse 3 tran_4	b.d	b.d	0.15	b.d	b.d	b.d	0.05	b.d	69.59	b.d	26.79	96.58	0.06	0.01	Surface	Mt-S
el 2b bse 3 spot 1	0.02	b.d	0.22	b.d	b.d	b.d	0.01	b.d	68.94	0.03	26.58	95.79	0.01	0.03	Surface	Mt-S
el 2b bse 3 spot 2	0.01	b.d	0.25	b.d	b.d	b.d	0.04	b.d	68.75	0.04	26.54	95.63	0.04	0.04	Surface	Mt-S
el 2b bse 4 tran_1	b.d	b.d	0.28	b.d	b.d	b.d	0.03	b.d	68.87	b.d	26.61	95.80	0.04	0.01	Surface	Mt-S
el 2b bse 4 tran_2	b.d	0.01	0.30	b.d	b.d	b.d	0.05	b.d	68.85	b.d	26.63	95.85	0.06	0.01	Surface	Mt-S
el 2b bse 4 tran_3	b.d	b.d	0.19	b.d	b.d	b.d	0.04	b.d	69.09	b.d	26.62	95.95	0.05	0.01	Surface	Mt-S
el 2b bse 4 tran_4	b.d	b.d	0.18	b.d	b.d	b.d	0.04	b.d	68.56	b.d	26.42	95.21	0.05	0.01	Surface	Mt-S
el 2b bse 5 sp 1	b.d	b.d	0.09	b.d	b.d	b.d	0.03	b.d	68.85	b.d	26.45	95.41	0.03	0.01	Surface	Mt-S
el 2b bse 5 sp 2	0.01	b.d	0.08	b.d	b.d	b.d	0.04	b.d	69.55	b.d	26.70	96.38	0.04	0.01	Surface	Mt-S
el 2b bse 5 sp 3	b.d	b.d	0.19	b.d	b.d	b.d	0.05	b.d	68.55	b.d	26.42	95.22	0.06	0.01	Surface	Mt-S
el 2b bse 5 sp 6	0.07	b.d	0.07	b.d	b.d	b.d	0.04	b.d	70.54	b.d	27.13	97.85	0.04	0.01	Surface	Mt-S
el 2b bse 5 sp 7	0.14	0.01	0.24	b.d	0.06	0.04	0.04	b.d	68.75	0.04	26.71	96.03	0.05	0.04	Surface	Mt-S
el 2b bse 5 sp 9	0.12	0.01	0.16	b.d	0.03	0.04	0.04	b.d	69.14	0.05	26.77	96.36	0.04	0.06	Surface	Mt-S
el 2b bse 5 sp 10	0.09	b.d	0.05	b.d	b.d	0.04	0.03	b.d	69.57	0.04	26.81	96.64	0.04	0.05	Surface	Mt-S
el 2b bse 5 sp 11	b.d	b.d	0.15	b.d	b.d	b.d	0.02	b.d	69.61	b.d	26.78	96.56	0.02	0.01	Surface	Mt-S
el 2b bse 6 sp 2	b.d	b.d	0.16	b.d	b.d	b.d	0.03	b.d	68.95	b.d	26.55	95.69	0.03	0.01	Surface	Mt-S
el 2b bse 6 sp 3	b.d	b.d	0.17	b.d	b.d	b.d	0.01	b.d	69.69	b.d	26.83	96.71	0.01	0.01	Surface	Mt-S
el 2b bse 6 sp 4	b.d	b.d	0.11	b.d	b.d	b.d	0.04	b.d	69.45	b.d	26.70	96.30	0.04	0.01	Surface	Mt-S
el 2b bse 6 sp 5	0.02	b.d	0.19	b.d	b.d	b.d	0.05	b.d	69.20	b.d	26.67	96.13	0.05	0.01	Surface	Mt-S
el 2b bse 6 sp 6	0.09	b.d	0.02	b.d	b.d	b.d	0.03	b.d	70.25	b.d	26.99	97.40	0.04	0.01	Surface	Mt-S
el 9 grain 3 tr 2 sp 1	0.09	0.69	0.50	b.d	0.10	0.04	0.08	b.d	67.10	0.02	26.81	95.44	0.08	0.71	Surface	Mt-S
el 9 grain 3 tr 2 sp 2	0.12	0.02	0.55	b.d	0.08	0.02	0.08	b.d	68.08	0.02	26.68	95.65	0.08	0.04	Surface	Mt-S
el 9 grain 3 tr 2 sp 3	0.15	0.02	0.53	b.d	0.10	0.03	0.08	b.d	68.04	0.02	26.69	95.65	0.08	0.04	Surface	Mt-S
el 9 grain 3 tr 2 sp 4	0.05	0.29	0.49	b.d	0.06	0.04	0.07	b.d	67.77	0.02	26.69	95.50	0.08	0.31	Surface	Mt-S

Sample ID Laco Norte	Mg [wt%]	Al [wt%]	Si [wt%]	Ti [wt%]	Ca [wt%]	P [wt%]	V [wt%]	Cr [wt%]	Fe [wt%]	Mn [wt%]	O [wt%]	Total	Ti+V [wt%]	Al+Mn [wt%]	Sample	Magnetite Type
el 9 grain 3 tr 2 sp 5	0.14	0.01	0.56	b.d	0.09	0.01	0.08	b.d	67.77	0.02	26.57	95.26	0.08	0.03	Surface	Mt-S
el 9 grain 3 tr 2 sp 6	0.21	0.02	0.67	b.d	0.15	0.02	0.08	b.d	68.01	0.02	26.86	96.06	0.08	0.05	Surface	Mt-S
el 9 grain 3 tr 2 sp 7	0.07	0.10	0.42	b.d	0.07	0.03	0.08	b.d	68.56	0.02	26.79	96.13	0.08	0.12	Surface	Mt-S
el 9 grain 3 tr 2 sp 8	0.05	0.04	0.46	b.d	0.06	0.01	0.07	b.d	68.28	0.03	26.62	95.62	0.08	0.07	Surface	Mt-S
el 9 grain 3 tr 2 sp 9	0.08	0.04	0.46	b.d	0.07	0.04	0.08	b.d	68.42	0.02	26.72	95.91	0.08	0.06	Surface	Mt-S
el 9 grain 3 tr 2 sp 10	0.04	0.65	0.44	b.d	0.06	0.05	0.08	b.d	68.34	0.02	27.14	96.81	0.08	0.67	Surface	Mt-S
el 9 grain 3 tr 2 sp 11	0.08	0.42	0.48	b.d	0.06	0.04	0.08	b.d	67.78	0.02	26.80	95.75	0.08	0.43	Surface	Mt-S
el 9 grain 3 tr 2 sp 12	0.06	0.06	0.41	b.d	0.05	0.06	0.08	b.d	67.97	0.02	26.53	95.23	0.08	0.08	Surface	Mt-S
el 9 grain 2 sp 1	0.05	0.04	0.56	b.d	0.08	0.03	0.07	b.d	67.76	0.02	26.51	95.10	0.08	0.05	Surface	Mt-S
el 9 grain 2 sp 2	0.08	0.32	0.76	b.d	0.07	0.03	0.07	b.d	67.81	0.02	26.94	96.10	0.07	0.34	Surface	Mt-S
el 9 grain 2 sp 3	0.05	0.11	0.60	b.d	0.06	0.03	0.07	b.d	67.98	0.02	26.68	95.60	0.08	0.12	Surface	Mt-S
el 9 grain 2 sp 7	0.04	0.59	0.56	b.d	0.06	0.04	0.07	b.d	67.55	0.01	26.87	95.80	0.08	0.61	Surface	Mt-S
el 9 grain 2 sp 8	0.03	0.04	0.54	b.d	0.05	0.03	0.07	b.d	68.02	0.02	26.57	95.38	0.07	0.06	Surface	Mt-S
el 9 grain 2 sp 10	0.07	0.02	0.74	b.d	0.08	0.03	0.07	b.d	67.63	0.02	26.60	95.24	0.07	0.04	Surface	Mt-S
el 9 grain 2 sp 11	0.04	0.05	0.61	b.d	0.05	0.02	0.08	b.d	68.08	0.01	26.66	95.61	0.08	0.07	Surface	Mt-S
el 9 grain 2 sp 12	0.05	0.24	0.60	b.d	0.05	0.02	0.07	b.d	68.24	0.03	26.87	96.16	0.08	0.27	Surface	Mt-S
el 9 grain 3 tr 1 sp 2	0.06	0.35	0.54	b.d	0.07	0.03	0.07	b.d	67.67	0.02	26.72	95.54	0.08	0.37	Surface	Mt-S
el 9 grain 3 tr 1 sp 3	0.09	0.10	0.37	b.d	0.08	0.04	0.07	b.d	67.80	0.02	26.47	95.03	0.08	0.12	Surface	Mt-S
el 9 grain 3 tr 1 sp 4	0.04	0.16	0.53	b.d	0.04	0.03	0.07	b.d	68.09	0.02	26.69	95.67	0.08	0.18	Surface	Mt-S
el 9 grain 3 tr 1 sp 5	0.13	0.02	0.55	b.d	0.09	0.02	0.08	b.d	67.68	0.02	26.53	95.12	0.08	0.04	Surface	Mt-S
el 9 grain 3 tr 1 sp 7	0.06	0.30	0.43	b.d	0.06	0.03	0.07	b.d	68.39	0.02	26.87	96.23	0.08	0.32	Surface	Mt-S
el 9 grain 3 tr 1 sp 8	0.05	0.05	0.47	b.d	0.06	0.03	0.08	b.d	68.23	0.02	26.63	95.62	0.08	0.07	Surface	Mt-S
el 9 grain 3 tr 1 sp 9	0.04	0.33	0.48	b.d	0.05	0.03	0.07	b.d	67.54	0.02	26.58	95.14	0.08	0.35	Surface	Mt-S
el 12 rad grain 1 sp 1	0.59	b.d	0.43	b.d	0.10	0.01	0.08	b.d	67.48	0.03	26.75	95.48	0.09	0.03	Surface	Mt-S
el 12 rad grain 1 sp 2	0.60	0.02	0.46	b.d	0.18	0.01	0.09	b.d	67.76	0.04	26.96	96.11	0.09	0.06	Surface	Mt-S
el 12 rad grain 1 sp 3	0.70	1.37	0.97	b.d	0.32	0.03	0.08	b.d	65.36	0.04	27.68	96.55	0.08	1.41	Surface	Mt-S
el 12 rad grain 1 sp 4	0.91	0.19	0.55	b.d	0.23	0.01	0.09	b.d	66.92	0.04	27.14	96.09	0.09	0.23	Surface	Mt-S
el 12 rad grain 1 sp 5	0.25	0.01	0.44	b.d	0.04	b.d	0.09	b.d	68.12	0.02	26.68	95.65	0.09	0.03	Surface	Mt-S
el 12 rad grain 1 sp 6	0.90	b.d	0.62	b.d	0.25	0.01	0.08	b.d	67.52	0.05	27.27	96.69	0.09	0.05	Surface	Mt-S
el 12 rad grain 1 sp 7	0.67	0.22	0.52	b.d	0.18	0.02	0.08	b.d	67.44	0.04	27.11	96.28	0.09	0.26	Surface	Mt-S
el 12 rad grain 1 sp 8	0.63	0.02	0.55	b.d	0.15	0.02	0.08	b.d	67.03	0.04	26.76	95.27	0.09	0.06	Surface	Mt-S
el 12 rad grain 2 sp 1	0.90	0.07	0.76	b.d	0.27	0.02	0.08	b.d	66.43	0.04	27.03	95.61	0.09	0.11	Surface	Mt-S
el 12 rad grain 2 sp 2	0.49	0.01	0.34	b.d	0.10	0.01	0.08	b.d	67.97	0.04	26.81	95.86	0.09	0.05	Surface	Mt-S
el 12 rad grain 2 sp 4	0.82	0.27	0.64	b.d	0.18	0.01	0.09	b.d	67.10	0.04	27.23	96.37	0.09	0.31	Surface	Mt-S
el 12 rad grain 2 sp 5	1.09	0.05	0.45	b.d	0.16	b.d	0.09	b.d	67.33	0.04	27.23	96.44	0.10	0.10	Surface	Mt-S
el 12 rad grain 2 sp 6	1.08	0.01	0.82	b.d	0.31	0.01	0.09	b.d	67.07	0.05	27.46	96.90	0.09	0.05	Surface	Mt-S
el 12 rad grain 2 sp 7	1.15	0.15	0.79	b.d	0.32	0.01	0.08	b.d	66.50	0.04	27.39	96.45	0.09	0.19	Surface	Mt-S
el 11 in grain 2 sp 2	1.00	b.d	0.50	b.d	0.15	b.d	0.05	b.d	68.43	0.02	27.54	97.69	0.05	0.02	Surface	Mt-S
el 11 in grain 2 sp 3	0.92	0.52	0.23	b.d	0.08	0.02	0.06	b.d	67.27	0.02	27.19	96.30	0.06	0.54	Surface	Mt-S
el 11 in grain 2 sp 4	0.92	0.40	0.21	b.d	0.06	0.02	0.06	b.d	67.47	0.03	27.16	96.31	0.06	0.42	Surface	Mt-S
el 11 in grain 2 sp 5	1.07	0.03	0.49	b.d	0.13	b.d	0.05	b.d	69.47	0.03	28.02	99.29	0.06	0.06	Surface	Mt-S
el 8 grain 1 sp 1	0.58	0.05	0.14	b.d	0.01	0.08	0.06	b.d	67.82	b.d	26.72	95.48	0.06	0.06	Surface	Mt-S
el 8 grain 1 sp 2	0.70	0.07	0.03	b.d	b.d	b.d	0.06	b.d	70.61	b.d	27.74	99.20	0.06	0.08	Surface	Mt-S
el 8 grain 1 sp 3	0.63	0.02	0.06	b.d	0.01	0.06	0.06	b.d	70.05	b.d	27.50	98.39	0.06	0.02	Surface	Mt-S
el 8 grain 1 sp 4	1.13	0.04	0.67	b.d	0.19	b.d	0.06	b.d	69.94	0.01	28.41	100.45	0.06	0.05	Surface	Mt-S
el 8 grain 1 sp 5	0.91	0.01	0.35	b.d	0.14	b.d	0.05	b.d	70.69	b.d	28.20	100.36	0.06	0.02	Surface	Mt-S
el 8 grain 1 sp 7	0.60	0.06	0.14	b.d	0.02	0.10	0.06	b.d	68.49	b.d	27.02	96.48	0.06	0.06	Surface	Mt-S
el 8 grain 1 sp 8	1.08	0.31	0.39	b.d	0.22	0.02	0.05	b.d	66.94	b.d	27.25	96.26	0.06	0.31	Surface	Mt-S
el 8 grain 1 sp 9	0.94	0.06	0.31	b.d	0.10	b.d	0.06	b.d	70.46	b.d	28.13	100.06	0.06	0.07	Surface	Mt-S
el 8 grain 1 sp 10	0.60	0.15	0.24	b.d	0.07	b.d	0.05	b.d	70.44	0.01	27.83	99.40	0.06	0.16	Surface	Mt-S
el 8 grain 1 sp 11	0.67	0.01	0.03	b.d	b.d	0.02	0.06	b.d	69.35	b.d	27.20	97.35	0.06	0.01	Surface	Mt-S
el 8 grain 1 sp 12	0.63	0.01	0.08	b.d	0.02	b.d	0.06	b.d	69.88	b.d	27.39	98.07	0.07	0.02	Surface	Mt-S
el 8 grain 1 sp 13	0.77	0.01	0.25	b.d	0.08	b.d	0.06	b.d	70.98	b.d	28.10	100.25	0.06	0.02	Surface	Mt-S
el 8 grain 1 sp 14	0.45	0.10	0.11	b.d	0.03	0.10	0.06	b.d	68.17	b.d	26.79	95.82	0.07	0.10	Surface	Mt-S
el 8 grain 1 sp 15	0.68	0.78	0.04	b.d	0.02	0.03	0.06	b.d	68.65	b.d	27.56	97.82	0.07	0.78	Surface	Mt-S
el 8 grain 2 sp 1	0.98	1.32	0.72	b.d	0.28	0.04	0.05	b.d	64.93	0.02	27.49	95.82	0.05	1.33	Surface	Mt-S
el 8 grain 2 sp 2	1.26	0.01	0.87	b.d	0.30	0.01	0.05	b.d	65.99	0.02	27.20	95.71	0.06	0.03	Surface	Mt-S
el 8 grain 2 sp 4	0.75	0.03	0.15	b.d	0.04	b.d	0.05	b.d	67.98	0.01	26.84	95.85	0.06	0.04	Surface	Mt-S
el 8 grain 2 sp 5	1.30	0.02	0.94	b.d	0.33	b.d	0.05	b.d	66.31	0.02	27.44	96.40	0.05	0.03	Surface	Mt-S
el 8 grain 2 sp 6	1.29	0.25	0.98	b.d	0.39	b.d	0.05	b.d	66.07	0.01	27.58	96.62	0.06	0.26	Surface	Mt-S
el 8 grain 3 sp 1	0.80	0.01	0.28	b.d	0.07	b.d	0.05	b.d	69.77	0.01	27.67	98.66	0.06	0.02	Surface	Mt-S
el 8 grain 3 sp 2	0.77	0.03	0.12	b.d	0.08	b.d	0.06	b.d	70.70	0.01	27.89	99.64	0.06	0.04	Surface	Mt-S
el 8 grain 3 sp 3	0.78	0.02	0.07	b.d	0.02	b.d	0.06	b.d	70.31	b.d	27.68	98.95	0.06	0.03	Surface	Mt-S
el 8 grain 3 sp 4	0.84	0.02	0.19	b.d	0.07	b.d	0.06	b.d	70.32	b.d	27.86	99.36	0.06	0.02	Surface	Mt-S
el 8 grain 3 sp 5	1.09	0.02	0.56	b.d	0.21	0.05	0.06	b.d	68.69	0.01	27.86	98.56	0.06	0.03	Surface	Mt-S
el 8 grain 3 sp 6	0.73	1.23	0.15	b.d	0.09	0.01	0.05	b.d	69.24	0.01	28.29	99.83	0.06	1.24	Surface	Mt-S
el 11 out grain 3 sp 1	1.20	0.02	0.83	b.d	0.28	0.01	0.04	b.d	66.90	0.03	27.46	96.77	0.04	0.05	Surface	Mt-S
el 11 out grain 3 sp 4	1.22	0.01	0.64	b.d	0.24	b.d	0.05	b.d	67.70	0.02	27.62	97.50	0.05	0.03	Surface	Mt-S
el 11 out grain 3 sp 5	1.21	0.09	0.56	b.d	0.22	b.d	0.04	b.d	68.24	0.01	27.80	98.17	0.05	0.10	Surface	Mt-S
el 11 out grain 3 sp 6	1.09	0.14	0.57	b.d	0.20	b.d	0.04	b.d	68.29	0.02	27.76	98.11	0.04	0.16	Surface	Mt-S
el 11out grain 1 tran_1	1.38	0.04	0.93	b.d	0.32	b.d	0.04	b.d	66.64	0.03	27.65	97.04	0.05	0.07	Surface	Mt-S
el 11out grain 1 tran_2	0.76	0.02	0.50	b.d	0.19	0.02	0.04	b.d	66.87	0.02	26.79	95.22	0.04	0.05	Surface	Mt-S
el 11out grain 1 tran_3	0.87	0.03	0.54	b.d	0.14	0.02	0.04	b.d	67.05	0.02	26.95	95.65	0.04	0.05	Surface	Mt-S
el 11out grain 1 tran_4	1.10	0.03	0.80	b.d	0.34	b.d	0.04	b.d	67.54	0.02	27.64	97.50	0.04	0.05	Surface	Mt-S
el 11out grain 1 tran_5	1.38	0.03	0.88	b.d	0.33	b.d	0.04	b.d	68.29	0.02	28.23	99.20	0.05	0.05	Surface	Mt-S
el 11out grain 1 tran_6	1.16	0.48	0.97	b.d	0.34	0.01	0.04	b.d	67.81	0.03	28.28	99.11	0.04	0.51	Surface	Mt-S
el 11out grain 1 tran_7	0.92	0.05	0.87	b.d	0.29	0.01	0.04	b.d	68.83	0.04	28.02	99.07	0.05	0.08	Surface	Mt-S

Sample ID Laco Norte	Mg [wt%]	Al [wt%]	Si [wt%]	Ti [wt%]	Ca [wt%]	P [wt%]	V [wt%]	Cr [wt%]	Fe [wt%]	Mn [wt%]	O [wt%]	Total	Ti+V [wt%]	Al+Mn [wt%]	Sample	Magnetite Type
el 11out grain 1 tran_8	1.31	0.04	0.86	b.d	0.32	0.01	0.04	b.d	68.30	0.04	28.16	99.08	0.04	0.08	Surface	Mt-S
el 11out grain 1 tran_9	1.32	0.01	0.87	b.d	0.33	b.d	0.04	b.d	68.47	0.04	28.22	99.30	0.04	0.05	Surface	Mt-S
el 11out grain 1 tran_10	1.23	b.d	0.82	b.d	0.30	0.01	0.04	b.d	68.63	0.04	28.14	99.20	0.04	0.04	Surface	Mt-S
el 11out grain 1 tran_11	1.02	0.87	0.71	b.d	0.28	0.02	0.04	b.d	67.58	0.03	28.17	98.74	0.04	0.91	Surface	Mt-S
el 11out grain 1 tran_12	1.65	0.02	0.71	b.d	0.28	b.d	0.04	b.d	67.85	0.03	28.13	98.69	0.04	0.05	Surface	Mt-S
el 11out grain 1 tran_13	1.56	0.08	1.03	b.d	0.32	b.d	0.04	b.d	67.30	0.02	28.15	98.51	0.05	0.10	Surface	Mt-S
el 11out grain 1 tran_14	1.37	0.25	0.91	b.d	0.32	b.d	0.05	b.d	66.61	b.d	27.76	97.27	0.05	0.26	Surface	Mt-S
el 11out grain 1 tran_15	1.50	0.03	1.01	b.d	0.32	b.d	0.04	b.d	67.00	b.d	27.92	97.83	0.04	0.03	Surface	Mt-S
el 11 out grain 2 sp 2	1.06	0.02	0.67	b.d	0.33	b.d	0.04	b.d	66.73	0.01	27.18	96.05	0.05	0.03	Surface	Mt-S
el 11 out grain 2 sp 3	1.13	0.01	0.75	b.d	0.30	b.d	0.04	b.d	67.12	0.02	27.43	96.81	0.04	0.03	Surface	Mt-S
el 11 out grain 2 sp 6	1.37	0.04	0.69	b.d	0.28	0.01	0.04	b.d	66.51	0.03	27.37	96.34	0.04	0.07	Surface	Mt-S
el 11 out grain 2 sp 7	1.14	0.01	0.65	b.d	0.28	0.02	0.04	b.d	66.92	0.03	27.29	96.39	0.04	0.04	Surface	Mt-S
el 12 bse 1 spot 1	b.d	0.01	0.44	b.d	0.05	0.02	0.08	b.d	68.39	b.d	26.60	95.61	0.09	0.02	Surface	Mt-S
el 12 bse 1 spot 2	0.01	0.01	0.30	b.d	0.03	0.03	0.09	b.d	68.83	0.05	26.67	96.03	0.09	0.07	Surface	Mt-S
el 12 bse 1 spot 3	b.d	0.01	0.37	b.d	0.04	0.02	0.09	b.d	68.87	0.04	26.74	96.18	0.10	0.05	Surface	Mt-S
el 12 bse 1 spot 4	b.d	0.04	1.03	b.d	0.06	0.05	0.03	b.d	69.05	b.d	27.33	97.59	0.04	0.04	Surface	Mt-S
el 12 bse 1 spot7	0.03	0.02	0.33	b.d	0.03	0.03	0.09	b.d	68.84	0.04	26.71	96.11	0.10	0.06	Surface	Mt-S
el 12 bse 1 spot8	0.01	0.01	0.30	b.d	0.03	0.04	0.09	b.d	68.59	0.17	26.63	95.87	0.09	0.18	Surface	Mt-S
el 12 bse 2 tran_1	0.12	0.01	0.32	b.d	0.02	0.01	0.09	b.d	68.53	0.05	26.64	95.79	0.09	0.06	Surface	Mt-S
el 12 bse 2 tran_2	b.d	b.d	0.34	b.d	0.03	0.02	0.10	b.d	69.00	0.06	26.76	96.31	0.10	0.07	Surface	Mt-S
el 12 bse 2 tran_3	0.03	0.02	0.30	b.d	0.03	0.02	0.10	b.d	69.15	0.04	26.79	96.46	0.10	0.06	Surface	Mt-S
el 12 bse 2 tran_4	0.04	0.01	0.38	b.d	0.06	0.01	0.09	b.d	68.74	0.06	26.72	96.12	0.10	0.07	Surface	Mt-S
el 12 bse 2 tran_5	0.03	0.02	0.29	b.d	0.04	0.02	0.10	b.d	68.93	0.06	26.71	96.19	0.10	0.07	Surface	Mt-S
el 12 bse 2 tran_6	0.05	0.02	0.36	b.d	0.05	0.02	0.09	b.d	68.64	b.d	26.65	95.87	0.10	0.02	Surface	Mt-S
el 12 bse 2 tran_7	b.d	0.01	0.33	b.d	0.03	0.02	0.09	b.d	69.03	0.07	26.77	96.33	0.09	0.08	Surface	Mt-S
el 12 bse 2 tran_8	b.d	0.02	0.35	b.d	0.03	0.02	0.09	b.d	68.72	0.07	26.68	95.98	0.09	0.09	Surface	Mt-S
el 12 bse 2 tran_9	0.05	0.02	0.36	b.d	0.05	0.03	0.10	b.d	68.56	0.06	26.67	95.90	0.10	0.08	Surface	Mt-S
el 12 bse 2 tran_10	0.07	0.02	0.38	b.d	0.07	0.02	0.10	0.00	69.00	0.05	26.86	96.56	0.10	0.07	Surface	Mt-S
el 8 bse 1 tran_1	0.36	b.d	0.38	b.d	0.11	b.d	0.06	b.d	71.43	0.03	28.02	100.38	0.06	0.03	Surface	Mt-S
el 8 bse 1 tran_2	0.56	b.d	0.87	b.d	0.29	b.d	0.06	b.d	70.14	0.05	28.18	100.15	0.06	0.05	Surface	Mt-S
el 8 bse 1 tran_3	0.30	b.d	0.18	b.d	0.09	0.01	0.05	b.d	70.95	0.03	27.61	99.21	0.06	0.03	Surface	Mt-S
el 8 bse 1 tran_4	0.22	b.d	0.20	b.d	0.02	b.d	0.05	b.d	70.72	b.d	27.44	98.67	0.06	0.01	Surface	Mt-S
el 8 bse 1 tran_5	0.30	0.02	0.16	b.d	0.13	b.d	0.05	b.d	72.05	0.03	28.06	100.81	0.06	0.05	Surface	Mt-S
el 8 bse 1 tran_6	0.48	b.d	0.65	b.d	0.23	b.d	0.05	b.d	71.05	0.03	28.24	100.73	0.06	0.04	Surface	Mt-S
el 8 bse 1 tran_7	0.54	b.d	0.93	b.d	0.30	b.d	0.05	b.d	70.28	0.03	28.26	100.40	0.06	0.04	Surface	Mt-S
el 8 bse 1 tran_8	0.26	b.d	0.10	b.d	0.03	0.02	0.06	b.d	70.54	b.d	27.33	98.34	0.06	0.01	Surface	Mt-S
el 8 bse 1 tran_9	0.21	0.01	0.13	b.d	0.02	b.d	0.06	b.d	72.65	b.d	28.12	101.21	0.06	0.01	Surface	Mt-S
el 8 bse 1 tran_10	0.21	b.d	0.02	b.d	b.d	b.d	0.06	b.d	72.56	b.d	27.99	100.83	0.06	0.01	Surface	Mt-S
el 8 bse 1 tran_11	0.34	b.d	0.36	b.d	0.13	b.d	0.06	b.d	70.42	b.d	27.61	98.92	0.06	0.01	Surface	Mt-S
el 8 bse 1 tran_12	0.22	b.d	0.10	b.d	0.02	0.06	0.06	b.d	70.71	b.d	27.41	98.58	0.06	0.01	Surface	Mt-S
el 8 bse 1 tran_13	0.28	b.d	0.10	b.d	0.01	0.03	0.06	b.d	71.05	b.d	27.56	99.10	0.06	0.01	Surface	Mt-S
el 8 bse 1 tran_14	0.23	b.d	0.08	b.d	0.01	0.13	0.06	b.d	69.47	0.02	27.02	97.02	0.06	0.02	Surface	Mt-S
el 8 bse 1 tran_15	0.22	b.d	0.03	b.d	b.d	0.03	0.06	b.d	69.83	0.03	27.00	97.21	0.07	0.03	Surface	Mt-S
el 8 bse 1 tran_16	0.27	b.d	0.11	b.d	0.01	0.05	0.06	b.d	69.25	0.03	26.89	96.67	0.06	0.04	Surface	Mt-S
el 8 bse 1 tran_17	0.17	b.d	0.15	b.d	0.03	0.16	0.06	b.d	69.35	b.d	27.03	96.96	0.06	0.01	Surface	Mt-S
el 8 bse 1 tran_18	0.18	b.d	0.03	b.d	b.d	0.05	0.06	b.d	70.01	b.d	27.04	97.38	0.06	0.01	Surface	Mt-S
el 8 bse 1 tran_19	b.d	b.d	b.d	b.d	b.d	b.d	b.d	b.d	71.12	b.d	27.25	98.39	0.01	0.01	Surface	Mt-S
el 8 bse 1 tran_20	b.d	b.d	0.01	b.d	b.d	b.d	0.04	b.d	70.62	b.d	27.07	97.75	0.04	0.01	Surface	Mt-S
el 8 bse 1 tran_21	0.02	b.d	b.d	b.d	b.d	b.d	0.01	b.d	70.88	b.d	27.15	98.06	0.01	0.01	Surface	Mt-S
el 8 bse 1 tran_22	0.03	0.01	0.08	b.d	0.02	b.d	0.18	b.d	70.34	b.d	27.09	97.75	0.18	0.01	Surface	Mt-S
el 8 bse 1 tran_23	0.03	b.d	b.d	b.d	b.d	b.d	0.01	b.d	70.55	b.d	27.04	97.63	0.02	0.01	Surface	Mt-S
el 8 bse 1 tran_24	0.32	b.d	0.17	b.d	0.03	b.d	0.05	b.d	69.71	b.d	27.11	97.40	0.06	0.01	Surface	Mt-S
el 8 bse 1 tran_25	b.d	b.d	b.d	b.d	b.d	b.d	0.11	0.01	70.65	b.d	27.11	97.89	0.12	0.01	Surface	Mt-S
el 8 bse 1 tran_26	0.03	b.d	0.04	b.d	0.01	b.d	0.05	b.d	70.66	b.d	27.11	97.92	0.06	0.01	Surface	Mt-S
el 8 bse 1 tran_27	0.28	b.d	0.16	b.d	0.15	0.09	0.06	b.d	69.21	0.03	27.06	97.03	0.06	0.03	Surface	Mt-S
el 8 bse 1 tran_28	0.32	b.d	0.04	b.d	b.d	b.d	0.06	b.d	72.27	b.d	28.00	100.70	0.06	0.01	Surface	Mt-S
el 8 bse 1 tran_29	0.42	b.d	0.38	b.d	0.12	b.d	0.06	b.d	70.64	b.d	27.77	99.40	0.06	0.01	Surface	Mt-S
el 8 bse 1 tran_30	0.61	b.d	0.91	b.d	0.29	b.d	0.06	b.d	69.01	b.d	27.81	98.70	0.06	0.01	Surface	Mt-S
el 8 bse 1 tran_31	b.d	b.d	0.04	b.d	0.02	0.35	0.01	b.d	69.59	b.d	27.12	97.13	0.01	0.01	Surface	Mt-S
el 8 bse 1 tran_32	b.d	b.d	0.01	b.d	b.d	b.d	0.06	b.d	70.85	b.d	27.17	98.10	0.07	0.01	Surface	Mt-S
el 8 bse 1 tran_33	0.01	b.d	0.01	b.d	b.d	b.d	0.06	b.d	70.97	b.d	27.20	98.25	0.06	0.01	Surface	Mt-S
el 8 bse 1 tran_34	0.04	b.d	0.03	b.d	b.d	b.d	0.06	b.d	70.64	b.d	27.12	97.89	0.06	0.01	Surface	Mt-S
el 8 bse 1 tran_35	0.05	b.d	0.02	b.d	b.d	b.d	0.09	b.d	70.53	b.d	27.09	97.79	0.10	0.01	Surface	Mt-S
el 8 bse 1 tran_36	0.23	b.d	0.09	b.d	0.01	b.d	0.07	b.d	70.54	b.d	27.29	98.23	0.07	0.01	Surface	Mt-S
el 8 bse 1 tran_37	b.d	b.d	0.09	b.d	b.d	b.d	0.03	b.d	69.99	b.d	26.89	97.02	0.04	0.01	Surface	Mt-S
el 8 bse 1 tran_38	b.d	b.d	0.15	b.d	b.d	b.d	0.04	b.d	69.76	b.d	26.85	96.80	0.04	0.01	Surface	Mt-S
el 8 bse 1 tran_39	b.d	b.d	0.12	b.d	b.d	b.d	0.02	b.d	69.35	b.d	26.66	96.15	0.03	0.01	Surface	Mt-S
el 8 bse 1 tran_40	b.d	b.d	0.18	b.d	b.d	b.d	0.02	b.d	69.65	0.02	26.83	96.70	0.02	0.02	Surface	Mt-S
el 8 bse 1 tran_41	b.d	b.d	0.11	b.d	b.d	b.d	0.03	b.d	69.11	b.d	26.57	95.83	0.04	0.01	Surface	Mt-S
el 8 bse 1 tran_42	b.d	b.d	0.12	b.d	b.d	b.d	0.01	b.d	69.54	b.d	26.73	96.40	0.01	0.01	Surface	Mt-S
el 6 bse 9 sp 1	0.68	b.d	0.70	b.d	0.15	b.d	0.05	b.d	68.87	0.10	27.62	98.17	0.06	0.10	Surface	Mt-S
el 6 bse 9 sp 2	0.45	b.d	0.26	b.d	0.07	b.d	0.05	b.d	69.63	0.09	27.32	97.87	0.06	0.09	Surface	Mt-S
el 6 bse 9 sp 3	0.45	b.d	0.18	b.d	0.04	b.d	0.05	b.d	69.87	0.09	27.34	98.03	0.06	0.09	Surface	Mt-S
el 6 bse 9 sp 3	0.11	b.d	0.22	b.d	0.06	b.d	0.03	b.d	70.19	0.02	27.17	97.80	0.03	0.03	Surface	Mt-S
el 6 bse 9 sp 4	0.09	b.d	0.07	b.d	0.02	b.d	0.02	b.d	70.52	0.03	27.14	97.90	0.03	0.03	Surface	Mt-S
el 6 bse 9 sp 5	0.11	b.d	0.19	b.d	0.04	b.d	0.02	b.d	69.99	0.03	27.06	97.44	0.02	0.04	Surface	Mt-S
el 6 bse 9 sp 6	0.14	b.d	0.25	b.d	0.09	b.d	0.02	b.d	69.81	0.04	27.08	97.43	0.03	0.04	Surface	Mt-S

Sample ID Laco Norte	Mg [wt%]	Al [wt%]	Si [wt%]	Ti [wt%]	Ca [wt%]	P [wt%]	V [wt%]	Cr [wt%]	Fe [wt%]	Mn [wt%]	O [wt%]	Total	Ti+V [wt%]	Al+Mn [wt%]	Sample	Magnetite Type
el 6 bse 9 sp 7	0.11	b.d	0.36	b.d	0.05	b.d	0.02	b.d	69.51	0.03	27.01	97.10	0.02	0.03	Surface	Mt-S
el 6 bse 9 sp 8	0.12	b.d	0.18	b.d	0.05	b.d	0.02	b.d	70.05	0.04	27.09	97.56	0.02	0.04	Surface	Mt-S
el 6 bse 9 sp 9	0.12	b.d	0.17	b.d	0.04	b.d	0.02	b.d	69.68	0.03	26.93	97.00	0.02	0.04	Surface	Mt-S
el 6 bse 9 sp 10	0.12	b.d	0.25	b.d	0.09	b.d	0.02	b.d	69.31	0.03	26.88	96.71	0.02	0.03	Surface	Mt-S
el 6 bse 9 sp 11	0.20	b.d	0.52	b.d	0.20	b.d	0.02	b.d	69.35	0.04	27.23	97.55	0.02	0.04	Surface	Mt-S
el 10 bse 1 light 2	b.d	b.d	0.01	b.d	b.d	b.d	b.d	b.d	71.40	b.d	27.35	98.77	0.01	0.01	Surface	Mt-S
el 10 bse 10 spot 1	0.46	b.d	0.14	b.d	0.03	b.d	0.06	b.d	70.48	0.04	27.53	98.74	0.06	0.04	Surface	Mt-S
el 10 bse 10 spot 2	0.39	0.01	0.29	b.d	0.05	b.d	0.05	b.d	69.06	b.d	27.03	96.88	0.06	0.02	Surface	Mt-S
el 10 bse 10 spot 3	0.45	b.d	0.02	b.d	b.d	b.d	0.05	b.d	71.72	0.05	27.90	100.20	0.05	0.06	Surface	Mt-S
el 10 bse 10 spot 4	0.45	0.01	0.03	b.d	b.d	b.d	0.05	b.d	71.28	0.05	27.75	99.63	0.06	0.06	Surface	Mt-S
el 10 bse 10 spot 5	0.42	b.d	0.08	b.d	0.02	b.d	0.05	b.d	71.70	0.04	27.90	100.22	0.06	0.05	Surface	Mt-S
el 10 bse 10 spot 6	0.43	b.d	0.03	b.d	b.d	b.d	0.05	b.d	71.14	0.07	27.67	99.40	0.05	0.08	Surface	Mt-S
el 10 bse 10 spot 7	0.44	0.01	0.14	b.d	0.02	b.d	0.06	b.d	69.27	b.d	27.03	96.97	0.06	0.02	Surface	Mt-S
el 10 bse 10 spot 8	0.39	b.d	0.03	b.d	b.d	b.d	0.05	b.d	71.41	0.03	27.72	99.62	0.06	0.03	Surface	Mt-S
el 10 bse 10 spot 9	0.56	0.01	0.45	b.d	0.12	b.d	0.04	b.d	70.23	0.08	27.82	99.30	0.04	0.09	Surface	Mt-S
el 10 bse 10 spot 10	0.54	0.07	0.41	b.d	0.11	b.d	0.04	b.d	68.35	0.09	27.09	96.69	0.04	0.16	Surface	Mt-S
el 10 bse 10 spot 11	0.59	b.d	0.43	b.d	0.10	b.d	0.04	b.d	69.99	0.09	27.73	98.98	0.04	0.10	Surface	Mt-S
el 10 bse 10 spot 12	0.52	b.d	0.33	b.d	0.08	b.d	0.04	b.d	70.48	0.08	27.75	99.28	0.04	0.09	Surface	Mt-S
el 10 bse 10 spot 13	0.25	b.d	0.29	b.d	0.06	0.02	0.04	b.d	68.31	0.07	26.65	95.69	0.04	0.07	Surface	Mt-S
el 10 bse 10 spot 14	0.54	b.d	0.40	b.d	0.09	b.d	0.04	b.d	70.27	0.08	27.75	99.16	0.04	0.09	Surface	Mt-S
el 10 bse 10 spot 15	0.36	0.01	0.16	b.d	0.03	b.d	0.04	b.d	70.56	0.07	27.50	98.74	0.05	0.08	Surface	Mt-S
el 10 bse 10 spot 16	0.55	b.d	0.32	b.d	0.08	b.d	0.05	b.d	69.76	0.03	27.49	98.28	0.06	0.04	Surface	Mt-S
el 10 bse 10 spot 17	0.49	0.01	0.18	b.d	0.03	b.d	0.05	b.d	70.41	0.02	27.56	98.76	0.05	0.03	Surface	Mt-S
el 10 bse 10 spot 18	0.47	b.d	0.33	b.d	0.08	b.d	0.05	b.d	70.66	0.06	27.78	99.42	0.05	0.06	Surface	Mt-S
el 10 bse 10 spot 19	0.48	b.d	0.29	b.d	0.08	b.d	0.04	b.d	70.49	0.08	27.70	99.17	0.05	0.08	Surface	Mt-S
el 10 bse 10 spot 20	0.47	b.d	0.31	b.d	0.09	b.d	0.04	b.d	70.09	0.07	27.55	98.63	0.05	0.08	Surface	Mt-S
el 10 bse 10 spot 21	0.42	b.d	0.12	b.d	0.03	b.d	0.05	b.d	70.76	0.06	27.59	99.04	0.06	0.07	Surface	Mt-S
el 10 bse 10 spot 22	0.37	0.01	0.17	b.d	0.03	b.d	0.05	b.d	69.41	0.05	27.07	97.16	0.06	0.06	Surface	Mt-S
el 10 bse 10 spot 23	0.65	0.01	0.68	b.d	0.05	b.d	0.05	b.d	69.74	0.10	27.87	99.16	0.05	0.12	Surface	Mt-S
el 10 bse 10 spot 24	0.52	0.01	0.43	b.d	0.12	b.d	0.04	b.d	69.94	0.08	27.66	98.81	0.05	0.09	Surface	Mt-S
el 10 bse 10 spot 25	0.57	b.d	0.34	b.d	0.08	b.d	0.04	b.d	70.23	0.05	27.70	99.01	0.05	0.06	Surface	Mt-S
el 10 bse 10 spot 26	0.40	0.01	0.14	b.d	0.04	b.d	0.06	b.d	70.18	0.04	27.37	98.24	0.06	0.05	Surface	Mt-S
el 10 bse 10 spot 27	0.41	0.01	0.04	b.d	b.d	b.d	0.06	b.d	68.52	0.03	26.65	95.72	0.06	0.04	Surface	Mt-S
el 10 bse 10 spot 29	0.52	0.01	0.37	b.d	0.08	b.d	0.05	b.d	70.17	0.06	27.68	98.95	0.06	0.07	Surface	Mt-S
el 10 bse 10 spot 31	0.58	b.d	0.49	b.d	0.09	b.d	0.04	b.d	70.04	0.07	27.77	99.08	0.05	0.07	Surface	Mt-S
el 10 bse 10 spot 32	0.51	b.d	0.35	b.d	0.08	b.d	0.04	b.d	70.45	0.05	27.74	99.23	0.05	0.06	Surface	Mt-S
el 10 bse 10 spot 35	0.39	b.d	0.04	b.d	b.d	b.d	0.06	b.d	69.71	0.03	27.09	97.32	0.06	0.03	Surface	Mt-S
el 10 bse 10 spot 36	0.43	0.01	0.04	b.d	b.d	b.d	0.06	b.d	70.84	b.d	27.55	98.94	0.06	0.01	Surface	Mt-S
el 10 bse 10 spot 37	0.52	0.01	0.34	b.d	0.05	b.d	0.04	b.d	70.21	0.07	27.65	98.89	0.05	0.08	Surface	Mt-S
el 10 bse 10 spot 38	0.67	0.02	0.27	b.d	0.06	b.d	0.05	b.d	69.63	0.03	27.50	98.24	0.06	0.05	Surface	Mt-S
el 10 bse 10 spot 39	0.45	b.d	0.25	b.d	0.07	b.d	0.05	b.d	70.79	0.04	27.74	99.38	0.05	0.04	Surface	Mt-S
el 10 bse 10 spot 40	0.38	b.d	0.05	b.d	b.d	0.03	0.05	b.d	70.36	0.02	27.35	98.25	0.06	0.02	Surface	Mt-S
el 10 bse 10 spot 41	0.58	b.d	0.46	b.d	0.07	b.d	0.04	b.d	69.74	0.04	27.60	98.53	0.04	0.05	Surface	Mt-S
el 10 bse 4 spot 11	0.50	b.d	0.31	b.d	0.07	b.d	0.04	b.d	70.79	0.08	27.84	99.64	0.05	0.08	Surface	Mt-S
el 2a sp 1	0.48	b.d	0.33	b.d	0.12	b.d	0.05	b.d	71.22	0.08	28.03	100.30	0.05	0.08	Surface	Mt-S
el 2a sp 2	b.d	b.d	0.09	b.d	b.d	b.d	0.05	b.d	69.42	b.d	26.68	96.25	0.05	0.01	Surface	Mt-S
el 2a sp 3	0.51	b.d	0.76	b.d	0.25	b.d	0.06	b.d	68.87	0.06	27.55	98.07	0.07	0.06	Surface	Mt-S
el 2a bse 1 spot 1	0.46	b.d	0.42	b.d	0.13	b.d	0.06	b.d	69.85	0.07	27.56	98.54	0.06	0.07	Surface	Mt-S
el 2a bse 1 spot 2	0.47	b.d	0.40	b.d	0.12	b.d	0.05	b.d	69.97	0.07	27.60	98.70	0.06	0.08	Surface	Mt-S
el 2a bse 1 spot 3	0.47	b.d	0.41	b.d	0.14	b.d	0.06	b.d	70.32	0.08	27.75	99.21	0.06	0.08	Surface	Mt-S
el 2a bse 1 spot 4	0.46	b.d	0.35	b.d	0.10	b.d	0.06	b.d	70.46	0.08	27.73	99.24	0.06	0.09	Surface	Mt-S
el 2a bse 1 spot 5	0.47	b.d	0.40	b.d	0.13	b.d	0.06	b.d	70.28	0.07	27.72	99.13	0.06	0.07	Surface	Mt-S
el 2a bse 1 spot 6	0.47	b.d	0.40	b.d	0.13	b.d	0.06	b.d	70.38	0.06	27.75	99.24	0.06	0.07	Surface	Mt-S
el 2a bse 1 spot 7	0.46	b.d	0.42	b.d	0.14	b.d	0.06	b.d	70.31	0.07	27.74	99.20	0.06	0.07	Surface	Mt-S
el 2a bse 1 spot 8	0.48	b.d	0.46	b.d	0.15	b.d	0.06	b.d	70.15	0.06	27.73	99.08	0.06	0.07	Surface	Mt-S
el 2a bse 1 spot 9	0.44	b.d	0.33	b.d	0.09	b.d	0.06	b.d	70.15	0.06	27.56	98.70	0.06	0.06	Surface	Mt-S
el 2a bse 1 spot 10	0.43	b.d	0.34	b.d	0.11	b.d	0.05	b.d	70.44	0.07	27.69	99.15	0.06	0.08	Surface	Mt-S
el 2a bse 1 spot 11	0.45	b.d	0.30	b.d	0.09	b.d	0.05	b.d	70.55	0.07	27.71	99.22	0.06	0.07	Surface	Mt-S
el 2a bse 1 spot 12	0.46	b.d	0.40	b.d	0.12	b.d	0.05	b.d	70.51	0.06	27.79	99.40	0.06	0.07	Surface	Mt-S
el 2a bse 1 spot 13	0.46	b.d	0.41	b.d	0.13	b.d	0.06	b.d	70.36	0.07	27.75	99.23	0.06	0.07	Surface	Mt-S
el 2a bse 1 spot 14	0.46	b.d	0.38	b.d	0.12	b.d	0.05	b.d	70.40	0.07	27.74	99.24	0.06	0.07	Surface	Mt-S
el 2a bse 1 spot 15	b.d	b.d	0.10	b.d	b.d	b.d	0.03	b.d	69.16	b.d	26.58	95.88	0.04	0.01	Surface	Mt-S
el 2a bse 1 spot 16	0.45	b.d	0.31	b.d	0.11	b.d	0.06	b.d	70.30	0.07	27.64	98.94	0.06	0.07	Surface	Mt-S
el 2a bse 1 spot 17	0.46	b.d	0.37	b.d	0.10	b.d	0.06	b.d	70.60	0.07	27.80	99.46	0.06	0.07	Surface	Mt-S
el 2a bse 1 spot 18	0.47	b.d	0.35	b.d	0.10	b.d	0.06	b.d	70.44	0.07	27.72	99.20	0.06	0.07	Surface	Mt-S
el 2a bse 1 spot 19	0.01	b.d	0.43	b.d	b.d	b.d	0.06	b.d	68.37	b.d	26.53	95.40	0.06	0.01	Surface	Mt-S
el 2a bse 1 spot 20	0.45	b.d	0.32	b.d	0.10	b.d	0.06	b.d	70.86	0.07	27.85	99.72	0.07	0.08	Surface	Mt-S
el 2a bse 1 spot 21	0.43	b.d	0.25	b.d	0.07	b.d	0.06	b.d	70.76	0.08	27.73	99.39	0.07	0.08	Surface	Mt-S
el 2a bse 1 spot 22	0.44	b.d	0.26	b.d	0.07	b.d	0.06	b.d	70.89	0.07	27.79	99.59	0.07	0.07	Surface	Mt-S
el 2a bse 1 spot 23	0.43	b.d	0.25	b.d	0.08	b.d	0.06	b.d	70.43	0.06	27.61	98.93	0.07	0.07	Surface	Mt-S
el 2a bse 1 spot 24	0.44	b.d	0.28	b.d	0.09	b.d	0.06	b.d	70.60	0.07	27.70	99.24	0.07	0.08	Surface	Mt-S
el 2a bse 1 spot 25	0.41	b.d	0.24	b.d	0.07	b.d	0.06	b.d	70.83	0.06	27.72	99.39	0.07	0.06	Surface	Mt-S
el 2a bse 1 spot 26	0.46	b.d	0.46	b.d	0.15	b.d	0.07	b.d	70.22	0.07	27.75	99.18	0.07	0.07	Surface	Mt-S
el 2a bse 1 spot 27	0.46	b.d	0.39	b.d	0.14	b.d	0.06	b.d	70.43	0.06	27.77	99.32	0.07	0.07	Surface	Mt-S
el 2a bse 1 spot 28	0.44	b.d	0.31	b.d	0.11	b.d	0.07	b.d	70.35	0.07	27.65	99.00	0.07	0.08	Surface	Mt-S
el 2a bse 1 spot 29	0.44	b.d	0.31	b.d	0.10	b.d	0.07	b.d	70.40	0.07	27.66	99.05	0.07	0.07	Surface	Mt-S
el 2a bse 1 spot 30	0.45	b.d	0.42	b.d	0.14	b.d	0.07	b.d	70.18	0.07	27.69	99.03	0.07	0.07	Surface	Mt-S

Sample ID Laco Norte	Mg [wt%]	Al [wt%]	Si [wt%]	Ti [wt%]	Ca [wt%]	P [wt%]	V [wt%]	Cr [wt%]	Fe [wt%]	Mn [wt%]	O [wt%]	Total	Ti+V [wt%]	Al+Mn [wt%]	Sample	Magnetite Type
el 2a bse 1 spot 31	0.46	b.d	0.36	b.d	0.12	b.d	0.06	b.d	70.31	0.08	27.69	99.09	0.07	0.08	Surface	Mt-S
el 2a bse 1 spot 32	0.46	b.d	0.40	b.d	0.13	b.d	0.07	b.d	70.48	0.08	27.80	99.41	0.07	0.09	Surface	Mt-S
el 2a bse 1 spot 33	0.46	b.d	0.35	b.d	0.12	b.d	0.07	b.d	70.62	0.08	27.81	99.53	0.07	0.09	Surface	Mt-S
el 2a bse 1 spot 34	0.47	b.d	0.43	b.d	0.14	b.d	0.06	b.d	69.99	0.09	27.65	98.82	0.06	0.09	Surface	Mt-S
el 2a bse 1 spot 35	0.48	b.d	0.49	b.d	0.17	b.d	0.06	b.d	70.31	0.08	27.84	99.44	0.06	0.08	Surface	Mt-S
el 2a bse 1 spot 36	0.47	b.d	0.44	b.d	0.16	b.d	0.06	b.d	70.25	0.07	27.76	99.21	0.06	0.07	Surface	Mt-S
el 1 bse 2 spot 1	b.d	0.01	0.02	b.d	b.d	b.d	0.10	b.d	71.81	0.07	27.59	99.59	0.10	0.08	Surface	Mt-S
el 1 bse 2 spot 2	b.d	b.d	0.01	b.d	b.d	b.d	0.10	b.d	71.41	b.d	27.40	98.93	0.10	0.01	Surface	Mt-S
el 1 bse 2 spot 3	b.d	0.01	0.12	b.d	0.02	b.d	0.10	b.d	71.14	b.d	27.39	98.78	0.10	0.02	Surface	Mt-S
el 1 bse 2 spot 5	b.d	0.01	0.12	b.d	b.d	b.d	0.11	b.d	71.14	b.d	27.39	98.76	0.11	0.01	Surface	Mt-S
el 1 bse 2 spot 6	b.d	b.d	0.07	b.d	0.02	b.d	0.10	b.d	71.43	b.d	27.45	99.08	0.11	0.01	Surface	Mt-S
el 1 bse 3 spot 1	0.20	0.01	0.30	b.d	0.03	b.d	0.07	b.d	69.02	b.d	26.86	96.50	0.08	0.02	Surface	Mt-S
el 1 bse 3 spot 2	b.d	b.d	0.08	b.d	b.d	0.06	0.09	b.d	70.40	b.d	27.12	97.75	0.09	0.01	Surface	Mt-S
el 1 bse 3 spot 3	b.d	b.d	0.30	b.d	0.01	b.d	0.07	b.d	69.58	b.d	26.91	96.89	0.08	0.01	Surface	Mt-S
el 1 bse 3 spot 4	b.d	b.d	0.17	b.d	b.d	b.d	0.07	b.d	69.50	b.d	26.78	96.53	0.08	0.01	Surface	Mt-S
el 1 bse 3 spot 5	0.46	0.01	0.33	b.d	0.11	0.02	0.07	b.d	68.89	b.d	27.11	97.01	0.08	0.02	Surface	Mt-S
LCN-05_spot1_pt1	0.87	0.17	0.02	0.11	b.d	b.d	0.19	b.d	70.55	b.d	27.99	99.90	0.31	0.17	Drill core	Mt-Z
LCN-05_spot1_pt2	0.89	0.18	0.02	0.12	b.d	b.d	0.19	0.01	70.46	0.04	28.00	99.90	0.31	0.22	Drill core	Mt-Z
LCN-05_spot1_pt3	0.65	0.17	0.02	0.09	b.d	b.d	0.20	b.d	69.78	0.05	27.52	98.47	0.29	0.23	Drill core	Mt-Z
LCN-05_spot1_pt4	0.86	0.14	0.01	0.10	b.d	b.d	0.19	b.d	70.64	b.d	27.98	99.91	0.29	0.14	Drill core	Mt-Z
LCN-05_spo12_pt1	0.86	0.15	0.02	0.11	b.d	b.d	0.19	0.01	70.93	b.d	28.11	100.37	0.30	0.15	Drill core	Mt-Z
LCN-05_spo12_pt2	0.86	0.11	0.02	0.10	b.d	b.d	0.19	b.d	70.74	b.d	28.00	100.01	0.28	0.11	Drill core	Mt-Z
LCN-05_spo12_pt3	0.86	0.13	0.03	0.10	0.05	b.d	0.19	0.01	70.38	b.d	27.92	99.66	0.29	0.13	Drill core	Mt-Z
LCN-05_spo12_pt4	0.85	0.14	0.02	0.11	b.d	b.d	0.19	b.d	70.79	0.03	28.04	100.17	0.30	0.17	Drill core	Mt-Z
LCN-05_spo12_pt5	0.87	0.09	0.03	0.10	0.01	b.d	0.19	b.d	70.84	b.d	28.04	100.16	0.29	0.09	Drill core	Mt-Z
LCN-05_spo10_pt1	0.88	0.18	0.01	0.11	b.d	b.d	0.19	0.01	70.85	b.d	28.12	100.35	0.30	0.18	Drill core	Mt-Z
LCN-05_spo10_pt2	0.38	0.17	0.01	0.11	b.d	b.d	0.20	b.d	69.85	0.04	27.30	98.06	0.30	0.21	Drill core	Mt-Z
LCN-05_spo10_pt3	0.88	0.15	0.01	0.11	b.d	b.d	0.19	0.01	70.76	b.d	28.06	100.16	0.30	0.15	Drill core	Mt-Z
LCN-05_spot8_pt1	0.75	0.19	0.01	0.13	b.d	b.d	0.18	b.d	70.58	0.05	27.92	99.81	0.31	0.24	Drill core	Mt-Z
LCN-05_spot8_pt2	0.62	0.18	0.02	0.13	b.d	b.d	0.18	b.d	70.57	0.05	27.81	99.55	0.31	0.23	Drill core	Mt-Z
LCN-05_spot8_pt3	0.84	0.19	0.01	0.12	b.d	b.d	0.18	b.d	70.49	0.06	27.98	99.89	0.30	0.26	Drill core	Mt-Z
LCN-05_spot8_pt4	0.49	0.19	0.01	0.12	b.d	b.d	0.19	0.01	70.65	0.05	27.73	99.44	0.31	0.24	Drill core	Mt-Z
LCN-05_spot7_pt1	0.72	0.19	0.05	0.13	b.d	b.d	0.19	0.01	67.92	b.d	26.90	96.10	0.32	0.19	Drill core	Mt-Z
LCN-05_spot7_pt2	0.86	0.20	0.01	0.14	b.d	b.d	0.19	0.01	70.71	0.03	28.08	100.23	0.33	0.23	Drill core	Mt-Z
LCN-05_spot7_pt3	0.88	0.21	0.03	0.14	b.d	b.d	0.19	0.01	70.58	b.d	28.06	100.10	0.33	0.21	Drill core	Mt-Z
LCN-05_spot9_pt1	0.87	0.18	0.01	0.12	b.d	b.d	0.19	b.d	70.52	0.05	28.01	99.97	0.31	0.24	Drill core	Mt-Z
LCN-05_spot9_pt2	0.88	0.19	0.01	0.13	b.d	b.d	0.19	0.01	70.54	0.06	28.03	100.03	0.32	0.24	Drill core	Mt-Z
LCN-05_spot9_pt3	0.68	0.18	0.01	0.12	b.d	b.d	0.19	b.d	70.42	b.d	27.78	99.38	0.31	0.18	Drill core	Mt-Z
LCN-05_spot9_pt4	0.10	0.19	0.01	0.11	b.d	b.d	0.19	b.d	70.30	0.03	27.24	98.17	0.30	0.22	Drill core	Mt-Z
LCN-05_spot6_pt1	0.88	0.21	0.01	0.16	b.d	b.d	0.17	b.d	69.51	0.05	27.66	98.66	0.33	0.26	Drill core	Mt-Z
LCN-05_spot6_pt2	0.89	0.22	0.04	0.18	b.d	b.d	0.16	b.d	70.32	0.04	28.00	99.84	0.34	0.25	Drill core	Mt-Z
LCN-05_spot6_pt3	0.42	0.19	0.02	0.15	b.d	b.d	0.18	b.d	69.73	0.05	27.33	98.07	0.33	0.24	Drill core	Mt-Z
LCN-05_spot6_pt4	0.25	0.16	0.02	0.14	0.01	b.d	0.18	b.d	69.46	0.05	27.05	97.32	0.32	0.21	Drill core	Mt-Z
LCN-05_spot5_pt2	0.41	0.19	0.01	0.12	b.d	b.d	0.17	b.d	70.54	0.04	27.61	99.10	0.29	0.23	Drill core	Mt-Z
LCN-05_spot5_pt1	0.48	0.19	0.09	0.17	b.d	0.02	0.18	b.d	67.82	b.d	26.77	95.73	0.35	0.19	Drill core	Mt-Z
LCN-05_spot5_pt3	0.88	0.19	0.02	0.14	b.d	b.d	0.17	b.d	70.03	0.05	27.84	99.31	0.31	0.24	Drill core	Mt-Z
LCN-05_spot4_pt1	0.85	0.16	0.01	0.12	b.d	b.d	0.19	b.d	70.91	0.04	28.11	100.38	0.31	0.20	Drill core	Mt-Z
LCN-05_spot1_pt2	0.49	0.16	0.02	0.12	0.06	0.02	0.19	b.d	70.21	b.d	27.60	98.86	0.31	0.16	Drill core	Mt-Z
LCN-05_spot1_pt3	0.82	0.14	0.01	0.12	b.d	b.d	0.19	0.01	70.47	b.d	27.89	99.66	0.31	0.14	Drill core	Mt-Z
LCN_07_spot_13_1	1.23	0.57	1.06	0.29	0.36	b.d	0.20	0.01	67.10	0.04	28.39	99.25	0.49	0.61	Drill core	Mt-Y
LCN_07_spot_13_2	0.61	0.42	0.05	0.20	b.d	b.d	0.20	b.d	70.45	b.d	27.99	99.93	0.40	0.42	Drill core	Mt-X
LCN_07_spot_13_3	0.57	0.40	0.03	0.19	b.d	b.d	0.20	b.d	70.41	b.d	27.90	99.69	0.39	0.40	Drill core	Mt-X
LCN_07_spot_13_4	0.56	0.36	0.03	0.20	0.04	b.d	0.19	b.d	70.60	0.03	27.97	99.99	0.40	0.39	Drill core	Mt-X
LCN_07_spot_13_5	1.22	0.70	0.69	0.48	0.21	b.d	0.18	b.d	67.91	0.07	28.52	99.99	0.66	0.77	Drill core	Mt-Y
LCN_07_spot_13_6	0.87	0.53	0.12	0.40	0.02	b.d	0.19	0.01	69.63	0.05	28.16	99.97	0.58	0.58	Drill core	Mt-Y
LCN_07_spot_13_7	1.38	0.77	1.04	0.40	0.40	b.d	0.18	b.d	67.32	0.04	28.81	100.35	0.58	0.82	Drill core	Mt-Y
LCN_07_spot_13_8	0.82	0.74	0.06	0.66	0.01	b.d	0.18	0.01	69.05	0.04	28.12	99.68	0.84	0.78	Drill core	Mt-Y
LCN_07_spot_13_9	1.75	0.98	1.52	0.75	0.66	b.d	0.18	b.d	65.17	0.03	29.13	100.16	0.92	1.01	Drill core	Mt-Y
LCN_07_spot_13_10	0.89	0.70	0.37	0.59	0.18	b.d	0.18	b.d	69.01	0.06	28.44	100.44	0.77	0.77	Drill core	Mt-Y
LCN_07_spot_13_11	1.27	0.50	1.06	0.25	0.39	b.d	0.19	b.d	67.28	0.03	28.42	99.39	0.44	0.53	Drill core	Mt-Y
LCN_07_spot_13_12	1.75	0.55	1.53	0.28	0.17	b.d	0.19	0.01	67.12	0.05	29.10	100.76	0.47	0.61	Drill core	Mt-Y
LCN_07_spot_13_13	0.63	0.40	0.04	0.22	b.d	b.d	0.19	b.d	70.65	0.04	28.07	100.22	0.41	0.44	Drill core	Mt-X
LCN_07_spot_13_14	1.32	0.47	1.07	0.23	0.28	b.d	0.19	b.d	68.79	0.04	28.97	101.38	0.42	0.52	Drill core	Mt-Y
LCN_07_spot_13_15	0.64	0.40	0.05	0.22	b.d	b.d	0.19	b.d	70.85	0.04	28.17	100.57	0.41	0.44	Drill core	Mt-X
LCN_07_spot_13_16	0.71	0.47	0.20	0.23	0.06	b.d	0.20	b.d	70.04	0.03	28.13	100.07	0.43	0.50	Drill core	Mt-Y
LCN_07_spot_13_17	1.05	0.57	0.70	0.23	0.20	b.d	0.20	0.01	68.05	0.03	28.20	99.25	0.43	0.60	Drill core	Mt-Y
LCN_07_spot_13_18	0.60	0.42	0.04	0.18	b.d	b.d	0.21	b.d	70.57	b.d	28.02	100.04	0.39	0.42	Drill core	Mt-X
LCN_07_spot_13_19	0.75	0.45	0.02	0.17	b.d	b.d	0.22	0.01	70.49	0.06	28.15	100.31	0.39	0.51	Drill core	Mt-X
LCN_07_spot_2_pt_4	0.63	0.36	0.01	0.19	b.d	b.d	0.19	b.d	70.78	0.03	28.06	100.25	0.38	0.39	Drill core	Mt-X
LCN_07_spot_1_pt_1	0.87	0.55	0.39	0.37	0.20	b.d	0.17	0.01	69.00	0.03	28.21	99.80	0.54	0.59	Drill core	Mt-X
LCN_07_spot_1_pt_2	1.30	0.67	1.07	0.25	0.34	b.d	0.17	b.d	67.55	0.05	28.67	100.08	0.42	0.72	Drill core	Mt-Y
LCN_07_spot_1_pt_3	0.68	0.45	0.18	0.17	0.03	b.d	0.16	b.d	70.19	0.03	28.08	99.98	0.33	0.48	Drill core	Mt-Y
LCN_07_spot_1_pt_10	0.68	0.47	0.11	0.17	0.02	b.d	0.17	b.d	70.30	0.04	28.08	100.03	0.34	0.51	Drill core	Mt-Y
LCN_07_spot_1_pt_4	0.63	0.53	0.09	0.28	b.d	b.d	0.17	b.d	70.07	0.06	28.02	99.85	0.44	0.59	Drill core	Mt-X
LCN_07_spot_1_pt_5	1.32	0.79	1.06	0.41	0.30	b.d	0.17	b.d	66.97	0.05	28.60	99.67	0.58	0.84	Drill core	Mt-Y
LCN_07_spot_1_pt_6	1.40	0.71	1.19	0.34	0.27	b.d	0.17	b.d	66.47	b.d	28.45	98.99	0.51	0.71	Drill core	Mt-Y
LCN_07_spot_1_pt_7	1.36	0.75	1.02	0.38	0.21	b.d	0.17	b.d	67.41	0.06	28.68	100.04	0.55	0.80	Drill core	Mt-Y

Sample ID Laco Norte	Mg [wt%]	Al [wt%]	Si [wt%]	Ti [wt%]	Ca [wt%]	P [wt%]	V [wt%]	Cr [wt%]	Fe [wt%]	Mn [wt%]	O [wt%]	Total	Ti+V [wt%]	Al+Mn [wt%]	Sample	Magnetite Type
LCN_07_spot_1_pt_8	0.59	0.43	0.05	0.17	b.d	b.d	0.18	b.d	70.73	0.04	28.07	100.25	0.34	0.46	Drill core	Mt-X
LCN_07_spot_1_pt_9	0.52	0.40	0.03	0.22	0.03	b.d	0.18	0.01	70.73	0.04	28.01	100.16	0.40	0.44	Drill core	Mt-X
LCN_07_spot_15_pt_1	1.16	0.63	1.57	0.30	0.31	0.00	0.16	b.d	66.12	0.10	28.38	98.73	0.46	0.73	Drill core	Mt-Y
LCN_07_spot_15_pt_2	0.62	0.51	0.02	0.28	b.d	b.d	0.16	b.d	70.57	0.03	28.12	100.32	0.45	0.54	Drill core	Mt-X
LCN_07_spot_15_pt_3	1.01	0.69	0.63	0.40	0.20	b.d	0.16	b.d	68.37	b.d	28.38	99.84	0.57	0.69	Drill core	Mt-Y
LCN_07_spot_15_pt_6	1.34	0.67	1.27	0.41	0.49	b.d	0.17	b.d	66.86	b.d	28.72	99.92	0.57	0.67	Drill core	Mt-Y
LCN_07_spot_15_pt_4	1.19	0.67	0.94	0.36	0.36	b.d	0.16	b.d	67.73	0.04	28.59	100.03	0.52	0.71	Drill core	Mt-Y
LCN_07_spot_15_pt_5	0.96	0.65	0.40	0.63	0.17	b.d	0.17	b.d	68.67	0.06	28.36	100.07	0.80	0.71	Drill core	Mt-Y
LCN_07_spot_16_pt_1	1.11	0.71	1.03	0.37	0.38	b.d	0.16	b.d	67.47	0.03	28.54	99.80	0.53	0.74	Drill core	Mt-Y
LCN_07_spot_16_pt_2	1.04	0.78	0.37	0.40	0.12	b.d	0.16	b.d	69.38	0.06	28.64	100.93	0.56	0.83	Drill core	Mt-X
LCN_07_spot_16_pt_7	1.24	0.86	0.01	0.56	b.d	b.d	0.17	b.d	69.46	0.09	28.65	101.03	0.72	0.95	Drill core	Mt-X
LCN_07_spot_16_pt_8	0.63	0.39	0.01	0.29	b.d	b.d	0.17	b.d	70.69	0.05	28.09	100.32	0.46	0.45	Drill core	Mt-X
LCN_07_spot_16_pt_9	0.87	0.49	0.51	0.21	0.38	b.d	0.17	b.d	69.57	0.04	28.49	100.72	0.38	0.53	Drill core	Mt-Y
LCN_07_spot_16_pt_3	1.55	0.73	1.31	0.33	0.38	b.d	0.17	0.01	66.29	0.05	28.69	99.51	0.50	0.78	Drill core	Mt-Y
LCN_07_spot_16_pt_4	0.65	0.44	0.09	0.26	0.03	b.d	0.18	b.d	70.28	0.03	28.04	100.00	0.44	0.47	Drill core	Mt-Y
LCN_07_spot_16_pt_5	0.50	0.41	0.04	0.20	b.d	b.d	0.19	b.d	70.81	0.03	28.03	100.22	0.39	0.44	Drill core	Mt-X
LCN_07_spot_16_pt_6	0.64	0.51	0.05	0.34	0.01	b.d	0.19	b.d	70.12	0.06	28.05	99.97	0.53	0.57	Drill core	Mt-X
LCN_07_spot_7_pt_1	0.76	0.43	0.26	0.22	0.07	b.d	0.20	b.d	69.69	0.03	28.05	99.71	0.42	0.46	Drill core	Mt-Y
LCN_07_spot_7_pt_2	0.58	0.41	0.03	0.22	b.d	b.d	0.20	b.d	70.64	0.03	28.03	100.13	0.42	0.44	Drill core	Mt-X
LCN_07_spot_7_pt_3	0.49	0.31	0.02	0.18	0.03	b.d	0.20	b.d	70.67	0.03	27.88	99.81	0.38	0.34	Drill core	Mt-X
LCN_07_spot_7_pt_4	0.44	0.18	0.03	0.14	0.05	b.d	0.19	0.01	69.73	b.d	27.36	98.13	0.33	0.18	Drill core	Mt-X
LCN_07_spot_3_pt_1	0.66	0.43	0.08	0.22	0.02	b.d	0.16	0.01	70.37	0.06	28.05	100.03	0.37	0.49	Drill core	Mt-X
LCN_07_spot_3_pt_5	1.32	0.57	1.11	0.30	0.33	b.d	0.16	0.01	67.07	0.06	28.46	99.37	0.45	0.63	Drill core	Mt-Y
LCN_07_spot_3_pt_2	1.30	0.55	1.00	0.29	0.22	b.d	0.18	b.d	67.56	0.04	28.48	99.64	0.48	0.59	Drill core	Mt-Y
LCN_07_spot_3_pt_3	0.65	0.40	0.04	0.25	b.d	b.d	0.19	b.d	70.54	0.03	28.07	100.18	0.44	0.44	Drill core	Mt-X
LCN_07_spot_3_pt_4	0.48	0.34	0.02	0.20	0.04	b.d	0.20	0.01	70.67	b.d	27.90	99.86	0.40	0.34	Drill core	Mt-X
LCN_07_spot_4_pt_1	1.28	0.52	1.16	0.28	0.27	b.d	0.19	0.01	67.38	0.03	28.51	99.63	0.48	0.55	Drill core	Mt-Y
LCN_07_spot_4_pt_2	0.77	0.40	0.24	0.21	0.04	b.d	0.19	b.d	69.93	0.04	28.09	99.91	0.40	0.43	Drill core	Mt-X
LCN_07_spot_4_pt_5	1.30	0.58	1.28	0.26	0.39	b.d	0.19	b.d	66.99	0.04	28.58	99.61	0.45	0.62	Drill core	Mt-Y
LCN_07_spot_4_pt_6	0.54	0.32	0.02	0.17	0.01	b.d	0.20	0.01	70.67	0.04	27.92	99.91	0.37	0.36	Drill core	Mt-X
LCN_07_spot_4_pt_3	0.76	0.42	0.29	0.21	0.04	b.d	0.19	b.d	69.89	0.04	28.12	99.96	0.41	0.45	Drill core	Mt-X
LCN_07_spot_4_pt_4	0.49	0.33	0.01	0.17	0.01	b.d	0.19	0.01	70.97	0.03	27.98	100.19	0.37	0.36	Drill core	Mt-X
LCN_07_spot_6_pt_1	0.81	0.65	1.10	0.36	0.39	b.d	0.17	b.d	66.65	0.09	27.99	98.21	0.53	0.74	Drill core	Mt-Y
LCN_07_spot_6_pt_2	1.14	0.59	1.01	0.33	0.30	b.d	0.16	b.d	67.86	0.04	28.54	99.97	0.49	0.63	Drill core	Mt-Y
LCN_07_spot_6_pt_4	1.36	0.69	1.28	0.30	0.43	b.d	0.17	b.d	66.90	0.04	28.72	99.89	0.46	0.73	Drill core	Mt-Y
LCN_07_spot_6_pt_5	0.89	0.50	0.54	0.35	0.10	b.d	0.17	b.d	68.83	0.06	28.18	99.61	0.52	0.55	Drill core	Mt-Y
LCN_07_spot_6_pt_6	0.56	0.44	0.04	0.24	b.d	b.d	0.18	b.d	70.55	0.03	28.01	100.05	0.42	0.47	Drill core	Mt-Y
LCN_07_spot_6_pt_3	0.56	0.40	0.02	0.22	b.d	b.d	0.20	0.01	70.70	0.03	28.03	100.18	0.42	0.43	Drill core	Mt-X
LCN_07_spot_6_pt_7	0.51	0.34	0.01	0.21	b.d	b.d	0.20	b.d	70.97	0.04	28.02	100.31	0.41	0.38	Drill core	Mt-X
LCN_07_spot_17_pt_1	0.67	0.55	0.03	0.12	b.d	b.d	0.16	b.d	70.91	0.05	28.27	100.76	0.29	0.60	Drill core	Mt-X
LCN_07_spot_17_pt_2	1.32	0.74	1.71	0.30	0.20	b.d	0.17	b.d	65.64	0.08	28.46	98.62	0.47	0.82	Drill core	Mt-Y
LCN_07_spot_17_pt_3	0.55	0.42	0.10	0.31	0.04	b.d	0.17	b.d	70.14	0.03	27.93	99.69	0.48	0.45	Drill core	Mt-X
LCN_07_spot_17_pt_4	0.86	0.61	0.87	0.29	0.32	b.d	0.17	b.d	67.86	0.07	28.21	99.25	0.46	0.68	Drill core	Mt-Y
LCN_07_spot_17_pt_5	0.49	0.43	0.02	0.25	0.02	b.d	0.19	0.01	71.13	0.04	28.17	100.73	0.43	0.47	Drill core	Mt-X
LCN_07_spot_17_pt_6	1.07	0.91	0.03	0.40	b.d	b.d	0.16	b.d	70.32	0.09	28.82	101.80	0.56	1.00	Drill core	Mt-X
LCN_07_spot_17_pt_8	0.58	0.75	0.02	0.24	0.01	b.d	0.17	b.d	70.70	0.01	28.30	100.76	0.40	0.76	Drill core	Mt-X
LCN_07_spot_17_pt_7	1.31	0.70	1.32	0.41	0.45	b.d	0.16	b.d	66.81	0.05	28.73	99.92	0.57	0.75	Drill core	Mt-Y
LCN_07_spot_9_pt_1	1.20	0.48	1.11	0.26	0.32	b.d	0.19	b.d	67.73	0.04	28.52	99.84	0.45	0.52	Drill core	Mt-Y
LCN_07_spot_9_pt_5	0.74	0.32	0.34	0.19	0.12	b.d	0.19	b.d	70.33	0.01	28.25	100.49	0.38	0.34	Drill core	Mt-X
LCN_07_spot_9_pt_2	1.57	0.39	1.38	0.23	0.24	b.d	0.18	b.d	68.01	0.05	29.03	101.07	0.41	0.44	Drill core	Mt-Y
LCN_07_spot_9_pt_3	0.53	0.32	0.03	0.19	b.d	b.d	0.19	b.d	71.01	0.03	28.04	100.34	0.38	0.35	Drill core	Mt-X
LCN_07_spot_9_pt_4	0.52	0.32	0.03	0.19	0.02	b.d	0.18	b.d	70.91	0.01	27.99	100.16	0.37	0.33	Drill core	Mt-X
LCN2-02_spot1_pt_1	b.d	0.13	0.12	0.14	b.d	b.d	0.21	b.d	69.13	0.01	26.75	96.47	0.35	0.14	Drill core	Mt-γ
LCN2-02_spot1_pt_2	b.d	0.10	0.09	0.04	b.d	b.d	0.22	0.01	69.21	0.01	26.70	96.37	0.26	0.11	Drill core	Mt-γ
LCN2-02_spot1_pt_3	b.d	0.19	0.15	0.08	b.d	b.d	0.24	0.01	69.38	0.01	26.90	96.94	0.31	0.21	Drill core	Mt-γ
LCN2-02_spot1_pt_4	b.d	0.10	0.19	0.09	b.d	b.d	0.20	0.01	69.55	0.01	26.92	97.07	0.29	0.12	Drill core	Mt-γ
LCN2-02_spot2_pt_1	0.05	0.42	0.81	0.18	b.d	b.d	0.36	0.01	66.93	0.01	26.79	95.55	0.54	0.43	Drill core	Mt-γ
LCN2-02_spot2_pt_2	0.07	0.08	0.10	0.15	b.d	b.d	0.39	0.01	69.41	0.01	26.95	97.16	0.54	0.09	Drill core	Mt-γ
LCN2-02_spot2_pt_3	0.54	0.18	0.31	0.13	0.06	b.d	0.22	b.d	68.08	0.01	27.04	96.55	0.35	0.20	Drill core	Mt-γ
LCN2-02_spot3_pt_1	0.65	0.18	0.45	0.14	0.08	b.d	0.23	0.01	67.55	0.01	27.05	96.32	0.37	0.19	Drill core	Mt-γ
LCN2-02_spot3_pt_2	0.62	0.18	0.57	0.12	0.01	b.d	0.25	0.01	67.71	0.01	27.15	96.62	0.37	0.20	Drill core	Mt-γ
LCN2-02_spot3_pt_3	0.37	0.20	0.01	0.09	b.d	b.d	0.25	b.d	68.18	0.03	26.69	95.81	0.33	0.23	Drill core	Mt-γ
LCN2-02_spot4_pt_1	0.29	0.27	0.65	0.14	0.02	b.d	0.26	0.01	67.48	0.01	26.92	96.04	0.40	0.29	Drill core	Mt-γ
LCN2-02_spot4_pt_2	0.22	0.18	0.01	0.19	b.d	b.d	0.24	0.01	69.20	0.01	26.96	97.00	0.43	0.19	Drill core	Mt-γ
LCN2-03_spot1_pt1	0.45	0.39	0.01	0.50	0.01	b.d	0.27	0.01	69.34	0.01	27.55	98.54	0.77	0.41	Drill core	Mt-β1
LCN2-03_spot1_pt2	0.80	0.50	0.61	0.71	0.20	b.d	0.26	b.d	68.01	0.01	28.07	99.16	0.97	0.52	Drill core	Mt-β1
LCN2-03_spot1_pt3	0.51	0.46	0.03	0.70	b.d	b.d	0.26	0.01	69.65	0.01	27.86	99.47	0.95	0.47	Drill core	Mt-β1
LCN2-03_spot1_pt4	0.86	0.45	0.33	0.66	0.09	b.d	0.26	b.d	68.66	0.04	28.05	99.40	0.92	0.49	Drill core	Mt-β1
LCN2-03_spot1_pt5	0.88	0.49	0.06	0.71	0.01	b.d	0.27	0.01	68.88	0.06	27.97	99.33	0.98	0.55	Drill core	Mt-β1
LCN2-03_spot1_pt6	0.16	0.26	0.05	0.49	0.34	b.d	0.21	0.01	68.73	0.01	27.13	97.37	0.70	0.28	Drill core	Mt-β1
LCN2-03_spot1_pt7	0.86	0.41	0.29	0.56	0.08	b.d	0.25	0.01	68.63	0.04	27.93	99.07	0.81	0.44	Drill core	Mt-β1
LCN2-03_spot1_pt8	0.25	0.36	0.02	0.57	b.d	b.d	0.27	b.d	69.83	0.01	27.57	98.88	0.84	0.38	Drill core	Mt-β1
LCN2-03_spot4_pt1	0.52	0.41	0.01	0.40	b.d	b.d	0.25	0.01	70.32	0.04	27.95	99.92	0.65	0.45	Drill core	Mt-β
LCN2-03_spot4_pt2	0.62	0.45	0.01	0.52	b.d	b.d	0.25	0.01	70.06	0.04	28.03	100.00	0.77	0.49	Drill core	Mt-β
LCN2-03_spot4_pt3	0.66	0.44	0.02	0.57	b.d	b.d	0.26	0.01	70.20	0.06	28.14	100.34	0.82	0.49	Drill core	Mt-β
LCN2-03_spot4_pt4	0.73	0.43	0.12	0.56	0.07	b.d	0.25	0.01	69.44	0.05	28.01	99.68	0.81	0.48	Drill core	Mt-β1
LCN2-03_spot4_pt5	0.66	0.39	0.01	0.55	b.d	b.d	0.29	0.01	70.07	0.04	28.04	100.06	0.84	0.43	Drill core	Mt-β1

Sample ID Laco Norte	Mg [wt%]	Al [wt%]	Si [wt%]	Ti [wt%]	Ca [wt%]	P [wt%]	V [wt%]	Cr [wt%]	Fe [wt%]	Mn [wt%]	O [wt%]	Total	Ti+V [wt%]	Al+Mn [wt%]	Sample	Magnetite Type
LCN2-03_spot3_pt5	0.67	0.40	0.28	0.08	0.43	b.d	0.25	0.01	68.46	0.01	27.63	98.19	0.32	0.41	Drill core	Mt-β1
LCN2-03_spot3_pt4	0.27	0.30	0.01	0.16	b.d	b.d	0.27	0.01	70.41	0.01	27.56	98.98	0.43	0.31	Drill core	Mt-β1
LCN2-03_spot3_pt3	0.56	0.45	0.01	0.24	0.22	b.d	0.25	0.01	70.01	0.03	27.95	99.74	0.49	0.49	Drill core	Mt-β
LCN2-03_spot3_pt2	0.74	0.45	0.01	0.70	b.d	b.d	0.26	0.01	69.02	0.05	27.82	99.07	0.96	0.50	Drill core	Mt-β
LCN2-03_spot3_pt1	0.55	0.38	0.01	0.55	b.d	b.d	0.26	0.01	70.28	0.05	28.01	100.11	0.82	0.43	Drill core	Mt-β
LCN2-03_spot2_pt1	0.41	0.35	0.02	0.91	b.d	b.d	0.25	0.01	69.68	0.01	27.77	99.39	1.16	0.36	Drill core	Mt-β
LCN2-03_spot2_pt2	0.67	0.58	0.04	0.74	b.d	b.d	0.26	0.01	69.38	0.03	28.03	99.74	0.99	0.62	Drill core	Mt-β
LCN2-03_spot2_pt3	0.71	0.41	0.02	0.52	0.01	b.d	0.26	0.01	69.97	0.03	28.04	99.96	0.78	0.44	Drill core	Mt-β
LCN2-03_spot2_pt4	0.96	0.56	0.17	1.54	0.08	b.d	0.26	0.01	67.91	0.10	28.24	99.83	1.80	0.66	Drill core	Mt-β1
LCN2-03_spot2_pt5	0.47	0.35	0.01	0.56	b.d	b.d	0.28	0.01	70.22	0.01	27.89	99.80	0.84	0.36	Drill core	Mt-β1
LCN2-03_spot2_pt6	0.38	0.07	0.09	0.06	b.d	b.d	0.01	b.d	71.26	0.01	27.70	99.56	0.06	0.08	Drill core	Mt-β2
LCN_16_spot1_pt1	1.34	0.74	1.15	0.41	0.34	b.d	0.20	0.008	68.28	0.04	29.17	101.67	0.61	0.78	Drill core	
LCN_16_spot1_pt2	0.60	0.51	0.03	0.31	b.d	b.d	0.20	b.d	71.13	0.01	28.35	101.13	0.51	0.53	Drill core	
LCN_16_spot2_pt1	1.37	0.73	0.58	0.37	0.11	b.d	0.22	0.009	68.11	0.05	28.57	100.11	0.58	0.78	Drill core	
LCN_16_spot2_pt2	0.90	0.50	0.05	0.23	b.d	b.d	0.21	0.007	70.14	0.07	28.23	100.34	0.44	0.57	Drill core	
LCN_16_spot3_pt1	0.61	0.58	0.51	0.26	0.12	b.d	0.25	0.010	69.75	0.01	28.30	100.37	0.50	0.59	Drill core	
LCN_16_spot3_pt2	0.53	0.43	0.03	0.22	b.d	b.d	0.26	0.009	71.11	0.01	28.20	100.80	0.49	0.45	Drill core	
LCN_16_spot4_pt1	0.93	0.50	0.14	0.33	0.02	b.d	0.21	0.008	70.08	0.01	28.34	100.57	0.54	0.51	Drill core	
LCN_16_spot4_pt2	0.39	0.47	0.12	0.24	0.02	b.d	0.24	0.009	70.90	0.01	28.11	100.49	0.48	0.48	Drill core	
LCN_16_spot6_pt1	0.72	0.43	0.04	0.21	b.d	b.d	0.25	0.008	70.81	0.01	28.24	100.69	0.45	0.44	Drill core	
LCN_16_spot6_pt2	1.39	0.62	1.21	0.27	0.23	b.d	0.24	0.008	67.57	0.01	28.78	100.31	0.51	0.63	Drill core	
LCN_16_spot7_pt1	0.68	0.47	0.22	0.24	0.04	b.d	0.26	0.010	70.14	0.01	28.17	100.23	0.50	0.49	Drill core	
LCN_16_spot7_pt2	0.79	0.42	0.03	0.20	b.d	b.d	0.26	0.008	70.38	0.03	28.14	100.25	0.45	0.45	Drill core	
LCN_16_spot5_pt1	0.78	0.41	0.02	0.23	b.d	b.d	0.26	0.007	70.71	0.04	28.27	100.74	0.49	0.45	Drill core	
LCN_16_spot5_pt2	0.77	0.38	0.02	0.21	b.d	b.d	0.26	0.009	70.70	0.04	28.22	100.63	0.48	0.41	Drill core	
LCN_16_spot5_pt3	0.54	0.38	0.03	0.18	b.d	b.d	0.25	b.d	70.95	0.01	28.08	100.41	0.43	0.39	Drill core	
LCN_16_spot8_pt1	0.83	0.48	0.03	0.20	b.d	b.d	0.24	b.d	70.49	0.05	28.27	100.59	0.44	0.53	Drill core	
LCN_16_spot8_pt2	1.17	0.53	0.55	0.24	0.14	b.d	0.24	b.d	68.64	0.05	28.38	99.94	0.48	0.57	Drill core	
LCN_16_spot8_pt3	0.67	0.41	0.10	0.20	0.04	b.d	0.24	0.011	70.60	0.01	28.17	100.45	0.44	0.43	Drill core	
LCN2-04_spot_1_pt1	0.41	0.61	0.41	0.85	0.16	b.d	0.26	0.008	68.73	0.01	27.98	99.41	1.11	0.62	Drill core	Mt-α
LCN2-04_spot_1_pt2	0.75	0.62	0.96	0.91	0.30	b.d	0.25	0.010	67.35	0.01	28.28	99.42	1.16	0.63	Drill core	Mt-α
LCN2-04_spot_1_pt3	0.33	0.53	0.14	0.72	b.d	b.d	0.27	0.007	69.74	0.01	27.88	99.61	0.99	0.54	Drill core	Mt-α
LCN2-04_spot_1_pt4	0.23	0.44	0.02	0.54	b.d	b.d	0.29	0.008	70.66	0.01	27.92	100.09	0.82	0.46	Drill core	Mt-α
LCN2-04_spot_1_pt5	0.08	0.25	0.02	0.55	b.d	b.d	0.30	0.009	70.79	0.01	27.69	99.69	0.84	0.26	Drill core	Mt-α
LCN2-04_spot_2_pt1	0.70	0.70	0.89	0.93	0.27	b.d	0.25	0.007	66.69	0.01	27.99	98.44	1.18	0.71	Drill core	Mt-α
LCN2-04_spot_2_pt2	0.29	0.57	0.02	0.89	b.d	b.d	0.26	b.d	69.93	0.01	27.93	99.89	1.14	0.58	Drill core	Mt-α
LCN2-04_spot_2_pt3	0.17	0.35	0.01	0.79	0.04	b.d	0.25	b.d	70.33	0.01	27.78	99.73	1.04	0.36	Drill core	Mt-α
LCN2-04_spot_3_pt1	0.30	0.54	0.01	0.51	b.d	b.d	0.25	0.006	70.53	0.01	27.98	100.13	0.77	0.56	Drill core	Mt-α
LCN2-04_spot_3_pt2	0.36	0.62	0.01	0.83	b.d	b.d	0.26	0.009	69.55	0.01	27.86	99.50	1.09	0.64	Drill core	Mt-α
LCN2-04_spot_3_pt3	0.14	0.28	0.03	0.74	0.01	b.d	0.25	0.009	70.42	0.01	27.71	99.59	0.99	0.29	Drill core	Mt-α
LCN2-04_spot_4_pt1	0.59	0.76	0.02	1.50	b.d	b.d	0.25	0.006	68.40	0.01	28.03	99.55	1.75	0.77	Drill core	Mt-α
LCN2-04_spot_4_pt2	0.21	0.42	0.02	0.56	b.d	b.d	0.26	0.008	70.61	0.01	27.86	99.94	0.82	0.43	Drill core	Mt-α
LCN2-04_spot_5_pt1	0.29	0.57	0.01	0.71	b.d	b.d	0.23	0.014	69.50	0.01	27.68	99.02	0.94	0.59	Drill core	Mt-α
LCN2-04_spot_5_pt2	0.27	0.55	0.01	0.73	b.d	b.d	0.24	0.006	70.28	0.01	27.96	100.05	0.97	0.57	Drill core	Mt-α
LCN2-04_spot_5_pt3	0.31	0.78	0.01	0.89	b.d	b.d	0.25	0.008	69.65	0.01	28.00	99.88	1.14	0.79	Drill core	Mt-α
LCN2-04_spot_6_pt2	0.30	0.47	0.01	0.45	b.d	b.d	0.30	0.010	70.83	0.01	28.02	100.39	0.75	0.48	Drill core	Mt-α
LCN2-04_spot_6_pt1	0.33	0.49	0.02	0.70	b.d	b.d	0.24	0.007	70.32	0.01	27.97	100.08	0.94	0.50	Drill core	Mt-α
LCN2-04_spot_6_pt3	0.15	0.21	0.01	0.44	b.d	b.d	0.31	0.007	71.12	0.01	27.80	100.05	0.75	0.22	Drill core	Mt-α
LCN2-04_spot_7_pt1	0.27	0.82	0.01	1.66	b.d	b.d	0.25	0.007	68.82	0.01	28.03	99.87	1.91	0.83	Drill core	Mt-α
LCN2-04_spot_7_pt2	0.07	0.38	0.01	0.79	0.01	b.d	0.25	0.006	70.31	0.01	27.69	99.52	1.04	0.39	Drill core	Mt-α
LCN2-04_spot_9_pt3	0.18	0.44	0.02	0.69	b.d	b.d	0.21	0.012	70.29	0.01	27.77	99.62	0.90	0.46	Drill core	Mt-α
LCN2-04_spot_9_pt2	0.19	0.41	0.02	0.52	b.d	b.d	0.23	0.010	70.50	0.01	27.76	99.65	0.76	0.42	Drill core	Mt-α
LCN2-04_spot_9_pt1	0.12	0.32	0.02	0.72	0.01	b.d	0.27	0.008	70.41	0.01	27.71	99.59	1.00	0.33	Drill core	Mt-α
LCN2-04_spot_8_pt1	0.44	0.67	0.01	1.37	b.d	b.d	0.27	0.008	68.72	0.03	27.91	99.42	1.65	0.70	Drill core	Mt-α
LCN2-04_spot_8_pt2	0.19	0.42	0.02	0.54	b.d	b.d	0.31	0.009	70.49	0.01	27.82	99.81	0.86	0.44	Drill core	Mt-α
LCN2-04_spot_8_pt3	0.12	0.32	0.01	0.38	b.d	b.d	0.32	0.012	71.18	0.01	27.87	100.22	0.70	0.33	Drill core	Mt-α
LCN2-04_spot_8_pt4	0.27	0.48	0.01	0.48	b.d	b.d	0.27	0.010	70.68	0.01	27.95	100.14	0.74	0.49	Drill core	Mt-α

Sample ID Laco Sur	Mg [wt%]	Al [wt%]	Si [wt%]	Ti [wt%]	Ca [wt%]	P [wt%]	V [wt%]	Cr [wt%]	Fe [wt%]	Mn [wt%]	O [wt%]	Total	Ti+V [wt%]	Al+Mn [wt%]	Sample
el-ln-14a-gr-1 sp 5	b.d	0.06	0.11	0.02	b.d	b.d	0.10	b.d	68.37	b.d	26.38	95.03	0.11	0.06	Surface
el-ln-14a-gr-1 sp 6	0.29	0.04	0.03	b.d	b.d	b.d	0.06	b.d	68.63	0.03	26.61	95.70	0.06	0.07	Surface
el-ln-14a-gr-1 sp 8	0.04	0.10	0.09	b.d	b.d	b.d	0.06	b.d	69.00	b.d	26.64	95.92	0.06	0.10	Surface
el-ln-14a-gr-1 sp 9	b.d	0.48	0.11	b.d	b.d	b.d	0.09	b.d	68.55	b.d	26.80	96.03	0.09	0.49	Surface
el-ln-14a-gr-1 sp 10	b.d	0.04	0.06	b.d	b.d	b.d	0.04	b.d	69.10	b.d	26.60	95.84	0.05	0.04	Surface
el-ln-14a-gr-1 sp 11	0.06	0.07	0.09	0.01	b.d	b.d	0.08	b.d	68.51	b.d	26.46	95.28	0.09	0.07	Surface
el-ln-14a-gr-1 sp 12	b.d	0.05	0.12	0.01	b.d	b.d	0.06	b.d	68.43	b.d	26.40	95.07	0.07	0.06	Surface
el-ln-14a-gr-4b sp 1	0.09	0.05	0.02	b.d	b.d	b.d	0.07	b.d	68.55	b.d	26.44	95.24	0.08	0.06	Surface
el-ln-14a-gr-4b sp 2	1.19	0.07	0.19	b.d	0.11	b.d	0.06	b.d	69.47	0.03	27.91	99.04	0.07	0.10	Surface
el-ln-14a-gr-4b sp 3	0.82	0.02	0.08	b.d	0.01	b.d	0.06	b.d	71.20	0.04	28.07	100.29	0.07	0.05	Surface
el-ln-14a-gr-4b sp 4	0.85	0.00	0.23	b.d	0.08	b.d	0.06	b.d	70.71	0.03	28.05	100.01	0.06	0.04	Surface
el-ln-14a-gr-4b sp 5	0.74	0.01	0.01	b.d	b.d	b.d	0.06	b.d	71.41	0.04	28.03	100.30	0.07	0.05	Surface
el-ln-14a-gr-4b sp 6	0.73	0.00	0.01	b.d	b.d	b.d	0.06	b.d	71.51	0.03	28.06	100.41	0.07	0.04	Surface
el-ln-14a-gr-4b sp 7	0.80	0.00	0.02	b.d	b.d	b.d	0.06	b.d	71.18	0.04	27.99	100.09	0.06	0.04	Surface
el-ln-14a-gr-4b sp 8	0.86	0.00	0.22	b.d	0.09	b.d	0.05	b.d	71.00	0.04	28.16	100.42	0.06	0.04	Surface
el-ln-14a-gr-4b sp 9	0.86	0.01	0.22	b.d	0.10	b.d	0.06	b.d	70.83	0.03	28.11	100.22	0.06	0.04	Surface
el-ln-14a-gr-4b sp 10	0.80	0.02	0.20	b.d	0.10	b.d	0.06	b.d	70.63	0.03	27.98	99.82	0.06	0.05	Surface
el-ln-6 sp 1	0.78	0.01	0.31	b.d	0.08	b.d	0.07	b.d	70.76	0.03	28.09	100.14	0.08	0.05	Surface
el-ln-6 sp 2	0.93	0.01	0.42	b.d	0.09	b.d	0.06	b.d	70.52	0.04	28.20	100.26	0.07	0.04	Surface
el-ln-6 sp 3	0.85	0.00	0.44	b.d	0.13	b.d	0.06	b.d	70.42	0.04	28.12	100.04	0.07	0.04	Surface
el-ln-6 sp 4	0.90	0.01	0.59	b.d	0.19	b.d	0.06	b.d	69.88	0.04	28.12	99.79	0.07	0.05	Surface
el-ln-6 sp 5	0.99	0.01	0.62	b.d	0.17	b.d	0.06	b.d	69.92	0.04	28.21	100.01	0.06	0.05	Surface
el-ln-6 sp 6	0.90	0.01	0.62	b.d	0.18	b.d	0.06	b.d	69.91	0.03	28.15	99.87	0.06	0.05	Surface
el-ln-6 sp 7	0.84	0.00	0.44	b.d	0.11	b.d	0.06	b.d	70.43	0.03	28.10	100.01	0.06	0.04	Surface
el-ln-6 sp 8	0.86	0.01	0.52	b.d	0.17	b.d	0.06	b.d	70.51	0.03	28.26	100.42	0.06	0.04	Surface
el-ln-6 sp 9	0.80	0.00	0.34	b.d	0.08	b.d	0.06	b.d	70.60	0.04	28.05	99.98	0.07	0.04	Surface
el-ln-6 sp 10	0.76	0.01	0.26	b.d	0.06	b.d	0.06	b.d	71.00	0.04	28.10	100.30	0.07	0.05	Surface
el-ln-6 sp 11	0.76	0.01	0.11	b.d	0.06	b.d	0.07	b.d	71.17	0.03	28.05	100.26	0.07	0.04	Surface
el-ln-6 sp 12	1.04	0.00	0.68	b.d	0.19	b.d	0.06	b.d	69.77	0.03	28.26	100.04	0.07	0.04	Surface
el 6 out grain 1 bse 1 sp 1	0.82	0.00	0.47	b.d	0.09	b.d	0.06	b.d	68.97	0.04	27.55	98.00	0.06	0.04	Surface
el 6 out grain 1 bse 1 sp 2	0.81	0.00	0.33	b.d	0.07	b.d	0.06	b.d	69.25	0.04	27.53	98.08	0.07	0.04	Surface
el 6 out grain 1 bse 1 sp 3	0.93	0.00	0.43	b.d	0.10	b.d	0.06	b.d	69.05	0.04	27.65	98.26	0.07	0.04	Surface
el 6 out grain 1 bse 1 sp 4	0.99	0.01	0.47	b.d	0.08	b.d	0.06	b.d	69.25	0.04	27.81	98.72	0.06	0.05	Surface
el 6 out grain 1 bse 1 sp 6	0.73	0.00	0.26	b.d	0.04	b.d	0.05	b.d	69.74	0.03	27.57	98.44	0.06	0.04	Surface
el 6 out grain 1 bse 1 sp 7	0.79	0.09	0.28	b.d	0.07	b.d	0.05	b.d	69.39	0.04	27.59	98.30	0.05	0.13	Surface
el 6 out grain 1 bse 1 sp 8	0.89	0.00	0.43	b.d	0.13	b.d	0.05	b.d	69.74	0.04	27.89	99.17	0.05	0.04	Surface
el 6 out grain 1 bse 1 sp 9	0.92	0.00	0.41	b.d	0.09	b.d	0.04	b.d	69.54	0.04	27.80	98.83	0.04	0.04	Surface
el 6 out grain 1 bse 1 sp 10	0.81	0.00	0.25	b.d	0.05	b.d	0.04	b.d	69.46	0.04	27.53	98.19	0.05	0.04	Surface
el 6 out grain 1 bse 1 sp 11	0.95	0.00	0.48	b.d	0.13	b.d	0.04	b.d	69.14	0.04	27.74	98.52	0.04	0.04	Surface
el 6 out grain 1 bse 1 sp 12	0.82	0.02	0.30	b.d	0.12	b.d	0.04	b.d	68.83	0.03	27.38	97.53	0.05	0.05	Surface
el 6 out grain 1 bse 1 sp 13	0.81	0.00	0.26	b.d	0.13	b.d	0.04	b.d	69.97	0.04	27.77	99.01	0.04	0.04	Surface
el 6 out grain 1 bse 1 sp 14	0.72	0.01	0.26	b.d	0.07	b.d	0.03	b.d	69.01	0.04	27.30	97.44	0.04	0.05	Surface
el 6 out grain 1 bse 1 sp 15	0.76	0.01	0.23	b.d	0.05	b.d	0.04	b.d	68.19	0.03	26.98	96.29	0.04	0.04	Surface
el 6 in s grain 3 bse 1 sp 1	0.65	0.07	0.02	0.01	b.d	b.d	0.12	b.d	70.52	0.02	27.68	99.09	0.13	0.09	Surface
el 6 in s grain 3 bse 1 sp 2	0.61	0.08	0.01	0.01	b.d	b.d	0.12	b.d	70.66	0.02	27.70	99.21	0.13	0.09	Surface
el 6 in s grain 3 bse 1 sp 3	0.67	0.06	0.02	b.d	b.d	b.d	0.11	b.d	70.46	0.02	27.66	99.00	0.12	0.08	Surface
el 6 in s grain 3 bse 1 sp 4	0.62	0.06	0.02	0.01	b.d	b.d	0.12	b.d	70.57	0.02	27.66	99.07	0.12	0.08	Surface
el 6 in s grain 3 bse 1 sp 5	0.48	0.73	0.02	0.01	b.d	b.d	0.11	b.d	68.54	0.01	27.28	97.18	0.13	0.74	Surface
el 6 in s grain 3 bse 1 sp 6	0.89	0.08	0.45	b.d	0.16	b.d	0.12	b.d	69.63	0.02	27.96	99.30	0.13	0.09	Surface
el 6 in s grain 3 bse 1 sp 7	0.57	0.20	0.52	0.02	0.16	0.02	0.11	b.d	68.54	0.01	27.40	97.54	0.13	0.21	Surface
el 6 in s grain 3 bse 1 sp 8	1.17	0.08	0.44	0.01	0.10	b.d	0.11	0.02	68.26	0.02	27.63	97.84	0.13	0.10	Surface
el 6 in s grain 3 bse 1 sp 9	0.70	0.08	0.20	b.d	0.11	b.d	0.12	b.d	69.66	0.01	27.59	98.46	0.12	0.09	Surface
el 6 in s grain 3 bse 1 sp 10	0.47	0.53	0.39	0.01	0.06	0.03	0.11	b.d	69.22	0.02	27.70	98.55	0.12	0.55	Surface
el 6 in s grain 3 bse 1 sp 11	0.82	0.08	0.23	0.01	0.01	b.d	0.11	b.d	69.23	0.02	27.48	97.99	0.13	0.10	Surface
el 6 in s grain 3 bse 1 sp 12	0.97	0.08	0.37	0.02	0.08	b.d	0.11	b.d	68.94	0.02	27.66	98.26	0.13	0.10	Surface
el 6 in s grain 3 bse 1 sp 13	0.65	0.07	0.05	0.02	0.02	b.d	0.12	b.d	70.36	0.02	27.63	98.93	0.13	0.08	Surface
el 6 in s grain 3 bse 1 sp 14	0.63	0.06	0.03	0.01	b.d	b.d	0.12	b.d	70.13	0.02	27.51	98.50	0.13	0.07	Surface
el 6 in s grain 3 bse 1 sp 15	0.68	0.07	0.05	b.d	0.02	b.d	0.12	b.d	69.44	b.d	27.35	97.74	0.13	0.08	Surface
el 6 in s grain 3 bse 1 sp 16	0.57	0.20	0.06	b.d	0.02	b.d	0.12	b.d	69.48	0.01	27.34	97.80	0.12	0.21	Surface
el 6 in s grain 3 bse 1 sp 17	0.65	0.09	0.04	0.01	0.05	b.d	0.12	b.d	69.71	0.02	27.41	98.11	0.13	0.12	Surface
el 6 in s grain 3 bse 1 sp 18	0.68	0.08	0.26	b.d	0.09	b.d	0.12	b.d	68.99	0.02	27.36	97.60	0.12	0.10	Surface
el 6 in s grain 3 bse 1 sp 19	0.74	0.09	0.22	b.d	0.09	b.d	0.12	b.d	69.47	0.02	27.56	98.30	0.12	0.10	Surface
el 6 in s grain 3 bse 1 sp 20	0.26	3.98	0.05	0.01	0.10	0.03	0.11	b.d	67.99	0.01	29.54	102.08	0.12	3.99	Surface
el 6 out grain2 sp 1	0.86	0.01	0.40	b.d	0.09	b.d	0.06	b.d	70.80	0.04	28.23	100.49	0.06	0.05	Surface
el 6 out grain2 sp 2	0.91	0.01	0.35	b.d	0.10	b.d	0.06	b.d	70.74	0.03	28.22	100.43	0.06	0.04	Surface
el 6 out grain2 sp 3	0.91	0.00	0.44	b.d	0.13	b.d	0.06	b.d	70.88	0.04	28.36	100.83	0.06	0.04	Surface
el 6 out grain2 sp 4	0.88	0.00	0.42	b.d	0.11	b.d	0.06	b.d	71.01	0.04	28.35	100.87	0.07	0.04	Surface
el 6 out grain2 sp 5	0.92	0.00	0.46	b.d	0.13	b.d	0.06	b.d	70.81	0.04	28.35	100.78	0.06	0.05	Surface
el 6 out grain2 sp 6	0.92	0.01	0.40	b.d	0.16	b.d	0.06	b.d	70.09	0.04	28.05	99.72	0.06	0.05	Surface
el 6 out grain2 sp 7	0.88	0.00	0.43	b.d	0.12	b.d	0.06	b.d	70.92	0.04	28.34	100.79	0.07	0.04	Surface
el 6 out grain2 sp 8	0.84	0.00	0.37	b.d	0.11	b.d	0.06	b.d	70.88	0.04	28.23	100.53	0.06	0.04	Surface
el 6 out grain2 sp 9	0.84	0.01	0.41	b.d	0.12	b.d	0.06	b.d	71.01	0.04	28.32	100.82	0.06	0.05	Surface
el 6 out grain2 sp 10	0.89	0.00	0.50	b.d	0.19	0.01	0.06	b.d	70.70	0.04	28.35	100.75	0.07	0.05	Surface
el 6 out grain2 sp 11	0.94	0.00	0.54	b.d	0.19	b.d	0.06	b.d	70.39	0.04	28.30	100.46	0.06	0.04	Surface
el 6 out grain2 sp 12	0.90	0.00	0.44	b.d	0.13	b.d	0.06	b.d	70.83	0.04	28.33	100.73	0.07	0.04	Surface
els-sample-2-gr-2 sp 1	0.68	0.28	0.02	0.09	b.d	b.d	0.08	b.d	69.83	0.03	27.64	98.67	0.17	0.32	Surface
els-sample-2-gr-2 sp 2	0.83	0.96	0.17	0.11	0.06	0.02	0.08	b.d	68.91	0.03	28.11	99.29	0.19	1.00	Surface

Sample ID Laco Sur	Mg [wt%]	Al [wt%]	Si [wt%]	Ti [wt%]	Ca [wt%]	P [wt%]	V [wt%]	Cr [wt%]	Fe [wt%]	Mn [wt%]	O [wt%]	Total	Ti+V [wt%]	Al+Mn [wt%]	Sample
els-sample-2-gr-2 sp 3	0.76	0.20	0.17	0.10	0.08	b.d	0.08	b.d	70.34	0.04	27.98	99.75	0.18	0.24	Surface
els-sample-2-gr-2 sp 4	0.71	0.24	0.10	0.09	0.03	b.d	0.08	b.d	69.48	0.04	27.56	98.35	0.18	0.28	Surface
els-sample-2-gr-2 sp 5	0.54	0.39	0.04	0.10	b.d	b.d	0.09	b.d	68.74	0.02	27.19	97.11	0.19	0.41	Surface
els-sample-2-gr-1 sp 1	0.83	0.19	0.20	0.09	0.04	b.d	0.07	b.d	70.57	0.04	28.12	100.15	0.16	0.23	Surface
els-sample-2-gr-1 sp 2	0.78	0.20	0.13	0.10	0.05	b.d	0.07	b.d	69.49	0.04	27.63	98.49	0.17	0.24	Surface
els-sample-2-gr-1 sp 3	0.85	0.36	0.03	0.11	0.04	0.01	0.08	b.d	69.35	b.d	27.71	98.54	0.19	0.37	Surface
els-sample-2-gr-1 sp 4	0.28	0.32	0.10	0.09	0.02	b.d	0.08	b.d	68.20	0.03	26.74	95.84	0.17	0.34	Surface
els-sample-2-gr-1 sp 5	0.44	0.20	0.09	0.10	0.01	b.d	0.08	b.d	68.31	0.03	26.83	96.10	0.18	0.23	Surface
els-sample-2-gr-1 sp 6	0.96	0.21	0.27	0.10	0.09	b.d	0.08	b.d	69.94	0.03	28.09	99.77	0.18	0.24	Surface
els-sample-2-gr-1 sp 7	0.72	0.20	0.08	0.10	0.03	b.d	0.08	b.d	70.70	0.04	27.99	99.93	0.17	0.24	Surface
els-sample-2-gr-1 sp 8	0.53	0.20	0.11	0.09	0.05	b.d	0.08	b.d	68.96	0.03	27.18	97.23	0.17	0.24	Surface
shiny mag sp 1	0.90	0.02	0.33	b.d	0.03	b.d	0.08	b.d	70.97	0.01	28.25	100.59	0.08	0.03	Surface
shiny mag sp 2	0.92	0.02	0.79	b.d	0.29	b.d	0.07	b.d	69.12	0.01	28.05	99.27	0.08	0.03	Surface
els-sample-1-gr-2-sp-1-med-	1.01	0.04	1.50	0.01	0.51	0.03	0.10	b.d	67.42	0.03	28.19	98.84	0.11	0.07	Surface
els-sample-1-gr-2-sp-1-high-	0.51	0.03	0.02	b.d	b.d	b.d	0.10	b.d	71.19	0.03	27.78	99.65	0.10	0.06	Surface
els shiny	0.91	0.17	0.43	0.04	0.18	0.01	0.09	b.d	69.56	b.d	28.04	99.43	0.12	0.17	Surface
els-sample-t-5-gr-2 sp 1	0.62	0.03	0.02	b.d	0.02	b.d	0.07	b.d	71.52	0.02	27.99	100.30	0.08	0.04	Surface
els-sample-t-5-gr-2 sp 2	1.05	0.03	0.38	b.d	0.02	b.d	0.08	b.d	70.67	0.02	28.31	100.56	0.09	0.05	Surface
els-sample-t-5-gr-2 sp 3	0.53	0.04	0.01	b.d	0.02	b.d	0.07	b.d	71.69	0.02	27.97	100.36	0.08	0.05	Surface
els-sample-t-5-gr-2 sp 4	0.68	0.03	0.06	b.d	0.01	b.d	0.07	b.d	71.33	0.01	27.99	100.18	0.08	0.04	Surface
els-sample-t-5-gr-2 sp 5	0.58	0.19	0.05	b.d	0.02	b.d	0.08	b.d	71.88	0.01	28.24	101.05	0.08	0.20	Surface
els-sample-t-5-gr-2 sp 6	0.60	0.02	0.01	b.d	b.d	b.d	0.08	b.d	71.37	0.02	27.90	99.99	0.08	0.04	Surface
els-sample-t-5-gr-3-tr-1 sp 1	0.85	0.02	0.29	b.d	0.05	b.d	0.07	b.d	70.61	0.01	28.05	99.95	0.08	0.03	Surface
els-sample-t-5-gr-3-tr-1 sp 2	1.14	0.03	0.58	b.d	0.02	b.d	0.07	b.d	69.73	0.01	28.17	99.75	0.07	0.04	Surface
els-sample-t-5-gr-3-tr-1 sp 3	0.62	0.02	0.01	b.d	0.07	b.d	0.07	b.d	71.23	b.d	27.91	99.92	0.07	0.02	Surface
els-sample-t-5-gr-3-tr-2 sp 1	0.95	0.02	0.40	b.d	0.05	0.02	0.07	b.d	70.28	b.d	28.13	99.92	0.08	0.03	Surface
els-sample-t-5-gr-3-tr-2 sp 2	0.72	0.02	0.29	b.d	0.06	b.d	0.07	b.d	70.70	0.01	27.98	99.86	0.08	0.03	Surface
els-sample-t-5-gr-3-tr-2 sp 3	0.60	0.19	0.04	b.d	0.02	b.d	0.08	b.d	70.46	0.01	27.70	99.09	0.08	0.20	Surface
els-sample-t-5-gr-3-tr-2 sp 4	0.82	0.02	0.26	b.d	0.02	b.d	0.08	b.d	70.76	0.02	28.04	100.01	0.08	0.04	Surface
els-sample-3-gr-3 sp 1	0.94	0.68	0.04	0.02	0.03	b.d	0.09	b.d	69.86	b.d	28.20	99.86	0.12	0.68	Surface
els-sample-3-gr-3 sp 2	0.73	0.34	0.03	0.02	0.02	b.d	0.09	b.d	70.33	b.d	27.91	99.47	0.11	0.34	Surface
els-sample-3-gr-3 sp 3	0.56	0.16	0.01	0.02	b.d	b.d	0.09	b.d	71.17	b.d	27.94	99.96	0.11	0.17	Surface
els-sample-3-gr-3 sp 4	0.77	0.14	0.21	0.03	0.08	b.d	0.09	b.d	70.53	b.d	28.04	99.89	0.11	0.15	Surface
els-sample-3-gr-3 sp 5	0.47	0.19	0.02	0.02	b.d	b.d	0.09	0.01	71.94	b.d	28.18	100.93	0.11	0.20	Surface
els-sample-3-gr-5 sp 1	0.75	0.15	0.10	0.03	0.06	b.d	0.09	b.d	71.21	b.d	28.20	100.59	0.12	0.15	Surface
els-sample-3-gr-5 sp 2	0.71	0.15	0.10	0.03	0.05	b.d	0.09	b.d	70.89	b.d	28.03	100.06	0.12	0.15	Surface
els-sample-3-gr-5 sp 3	0.66	2.31	0.02	0.03	0.07	0.01	0.09	b.d	68.35	b.d	28.67	100.20	0.11	2.31	Surface
els-sample-3-gr-5 sp 4	0.65	0.14	0.10	0.03	0.02	b.d	0.10	b.d	71.22	b.d	28.08	100.33	0.12	0.14	Surface
els-sample-1-gr-2 sp 1	1.06	0.05	1.76	0.02	0.45	0.02	0.10	b.d	68.65	0.04	28.86	100.99	0.12	0.09	Surface
els-sample-1-gr-2 sp 2	0.54	0.04	0.21	0.01	0.05	b.d	0.10	b.d	71.00	0.03	27.89	99.87	0.11	0.07	Surface
els-sample-1-gr-2 sp 3	0.53	0.04	0.02	0.01	b.d	b.d	0.09	b.d	71.48	0.03	27.90	100.10	0.10	0.07	Surface
els-sample-1-gr-2 sp 4	1.15	0.07	2.19	0.02	0.41	0.01	0.09	b.d	67.10	0.03	28.65	99.72	0.11	0.10	Surface
els-sample-1-gr-2 sp 5	0.62	0.04	0.64	0.02	0.33	b.d	0.10	b.d	69.51	0.03	27.87	99.14	0.11	0.07	Surface
els-sample-1-gr-2 sp 6	0.52	0.04	0.02	0.01	b.d	b.d	0.09	b.d	71.57	0.03	27.93	100.21	0.11	0.07	Surface
els-sample-1-gr-2 sp 7	0.52	0.04	0.02	b.d	0.01	b.d	0.09	b.d	71.53	0.03	27.92	100.17	0.10	0.07	Surface
els-sample-1-gr-2 sp 8	0.54	0.05	0.02	0.02	b.d	b.d	0.09	b.d	71.42	0.03	27.90	100.07	0.11	0.08	Surface
els-sample-1-gr-2 sp 9	0.53	0.05	0.01	0.02	b.d	b.d	0.09	b.d	71.12	0.03	27.78	99.64	0.11	0.09	Surface
els-sample-1-gr-2 sp 10	1.03	0.07	1.82	0.03	0.57	0.02	0.08	b.d	66.69	0.03	28.22	98.56	0.11	0.11	Surface
els-sample-1-gr-2 sp 11	0.93	0.06	1.76	0.02	0.43	0.01	0.08	b.d	66.91	0.03	28.06	98.29	0.10	0.10	Surface
els-sample-1-gr-2 sp 12	0.97	0.06	1.64	0.03	0.49	0.02	0.09	b.d	66.89	0.03	28.05	98.27	0.11	0.08	Surface
els-sample-1-gr-2 sp 13	0.53	0.05	0.01	0.03	b.d	b.d	0.09	b.d	71.17	0.03	27.80	99.71	0.12	0.08	Surface
els-sample-1-gr-2 sp 14	0.54	0.05	0.17	0.02	0.04	b.d	0.09	b.d	70.67	0.03	27.75	99.38	0.12	0.09	Surface
els-sample-1-gr-2 sp 15	0.42	0.07	0.02	0.02	b.d	b.d	0.09	b.d	70.10	0.03	27.31	98.05	0.11	0.10	Surface
els-sample-1-gr-2 sp 16	0.53	0.06	0.02	0.02	b.d	b.d	0.10	b.d	71.23	0.03	27.83	99.82	0.12	0.09	Surface
els-sample-t-2-tr-1 sp 1	0.64	0.10	0.02	0.01	b.d	b.d	0.10	b.d	71.21	0.01	27.94	100.02	0.11	0.11	Surface
els-sample-t-2-tr-1 sp 2	1.04	0.12	0.54	0.02	0.20	b.d	0.10	b.d	70.15	0.02	28.40	100.58	0.12	0.14	Surface
els-sample-t-2-tr-1 sp 3	0.65	0.15	0.02	b.d	0.01	b.d	0.10	b.d	70.60	b.d	27.79	99.32	0.11	0.15	Surface
els-sample-t-2-tr-1 sp 4	0.60	0.21	0.13	0.01	0.04	b.d	0.10	b.d	70.87	0.02	27.96	99.95	0.11	0.23	Surface
els-sample-t-2-tr-1 sp 5	0.76	0.13	0.09	b.d	0.03	b.d	0.10	b.d	70.69	0.01	27.94	99.76	0.10	0.15	Surface
els-sample-t-2-tr-1 sp 6	0.74	0.14	0.13	0.01	0.02	b.d	0.10	b.d	70.61	0.02	27.91	99.67	0.11	0.15	Surface
els-sample-t-2-tr-1 sp 7	0.72	0.12	0.16	0.01	b.d	b.d	0.10	b.d	70.81	0.02	27.98	99.91	0.11	0.14	Surface
els-sample-t-2-tr-1 sp 8	0.58	0.21	0.24	0.01	0.10	b.d	0.10	b.d	70.56	0.02	27.94	99.76	0.11	0.23	Surface
els-sample-t-2-tr-1 sp 9	0.70	0.13	0.09	0.01	0.04	b.d	0.10	b.d	70.84	0.02	27.94	99.87	0.11	0.14	Surface
els-sample-t-2-tr-1 sp 10	0.74	0.12	0.14	0.01	0.04	b.d	0.10	b.d	71.32	0.01	28.19	100.67	0.11	0.14	Surface
els-sample-t-2-tr-1 sp 11	0.52	0.47	0.03	b.d	0.02	b.d	0.10	b.d	70.99	0.02	28.06	100.20	0.10	0.48	Surface
els-sample-t-2-tr-1 sp 12	0.73	0.11	0.22	0.01	0.04	b.d	0.10	b.d	70.82	0.02	28.05	100.10	0.11	0.14	Surface
els-sample-t-2-tr-1 sp 13	0.60	0.11	0.03	0.01	0.01	b.d	0.10	0.01	71.76	0.02	28.13	100.78	0.11	0.13	Surface
els-sample-t-2-tr-1 sp 14	0.72	0.13	0.21	0.01	0.04	b.d	0.10	b.d	70.69	0.02	27.99	99.91	0.12	0.15	Surface
els-sample-6-gr-1 sp 1	0.68	0.03	0.10	b.d	0.02	b.d	0.09	b.d	71.30	0.01	28.03	100.26	0.10	0.04	Surface
els-sample-6-gr-1 sp 2	0.63	0.04	0.01	b.d	b.d	b.d	0.08	b.d	71.71	0.03	28.08	100.58	0.09	0.07	Surface
els-sample-6-gr-1 sp 3	1.00	0.04	0.48	b.d	0.05	b.d	0.08	b.d	70.17	0.02	28.18	100.01	0.08	0.06	Surface
els-sample-6-gr-1 sp 4	0.63	0.03	0.10	b.d	b.d	b.d	0.07	b.d	71.56	0.03	28.08	100.51	0.08	0.06	Surface
els-sample-6-gr-1 sp 5	1.41	0.04	1.32	b.d	0.38	0.01	0.09	b.d	67.93	0.03	28.51	99.73	0.09	0.07	Surface
els-sample-6-gr-2 sp 1	0.64	0.04	0.04	b.d	b.d	b.d	0.12	b.d	71.53	0.03	28.05	100.45	0.13	0.07	Surface
els-sample-6-gr-2 sp 2	0.76	0.04	0.09	b.d	b.d	b.d	0.13	b.d	71.48	0.03	28.18	100.70	0.13	0.07	Surface
els-sample-6-gr-2 sp 3	0.64	0.04	0.03	b.d	b.d	b.d	0.12	b.d	72.12	0.03	28.27	101.25	0.13	0.07	Surface
els-sample-6-gr-2 sp 4	0.72	0.04	0.03	b.d	b.d	b.d	0.13	b.d	71.48	0.03	28.10	100.52	0.13	0.07	Surface

Sample ID Laco Sur	Mg [wt%]	Al [wt%]	Si [wt%]	Ti [wt%]	Ca [wt%]	P [wt%]	V [wt%]	Cr [wt%]	Fe [wt%]	Mn [wt%]	O [wt%]	Total	Ti+V [wt%]	Al+Mn [wt%]	Sample
els-sample-6-gr-2 sp 5	0.68	0.04	0.02	b.d	b.d	b.d	0.12	b.d	71.34	0.02	28.00	100.21	0.12	0.06	Surface
els-sample-6-gr-2 sp 6	1.22	0.05	0.87	b.d	0.26	0.02	0.11	b.d	69.22	0.03	28.45	100.23	0.11	0.08	Surface
els-sample-6-gr-2 sp 7	1.18	0.04	0.83	b.d	0.25	0.01	0.09	b.d	69.45	0.02	28.43	100.30	0.10	0.07	Surface
els-sample-6-gr-2 sp 8	0.90	0.06	0.45	0.01	0.18	0.16	0.08	b.d	68.93	0.01	27.86	98.64	0.09	0.07	Surface
els-sample-6-gr-2 sp 9	0.72	0.06	0.26	0.01	0.19	0.05	0.08	b.d	70.02	0.01	27.84	99.25	0.09	0.07	Surface
els-sample-6-gr-2 sp 10	0.92	0.06	0.51	b.d	0.13	b.d	0.09	b.d	70.37	0.02	28.27	100.37	0.09	0.08	Surface
el 14 in grain 1 sp 1	0.64	0.08	0.17	0.02	0.09	b.d	0.11	b.d	69.04	b.d	27.29	97.43	0.13	0.08	Surface
el 14 in grain 1 sp 2	0.79	0.08	0.21	0.02	0.10	b.d	0.10	b.d	70.74	b.d	28.09	100.12	0.12	0.09	Surface
el 14 in grain 1 sp 3	0.75	0.08	0.24	0.02	0.10	b.d	0.11	b.d	70.51	b.d	28.00	99.80	0.13	0.08	Surface
el 14 in grain 1 sp 4	0.78	0.22	0.29	0.02	0.13	b.d	0.10	b.d	69.99	b.d	27.99	99.52	0.12	0.22	Surface
el 14 out grain 1 sp 1	0.82	0.05	0.22	b.d	0.09	b.d	0.07	b.d	70.70	0.03	28.06	100.05	0.08	0.08	Surface
el 14 out grain 1 sp 2	0.79	0.63	0.41	b.d	0.12	0.01	0.08	b.d	69.10	0.03	28.04	99.21	0.08	0.67	Surface
el 14 out grain 1 sp 3	0.53	0.17	0.09	b.d	0.01	b.d	0.08	b.d	68.20	0.02	26.80	95.90	0.08	0.19	Surface
el 14 out grain 1 sp 4	0.34	0.06	0.18	b.d	b.d	0.01	0.09	b.d	68.12	0.01	26.58	95.39	0.09	0.07	Surface
el 14 out grain 1 sp 8	0.45	0.07	0.16	b.d	0.01	0.01	0.09	b.d	67.79	0.02	26.55	95.15	0.09	0.09	Surface
el 3 ox grain 1 bse 1 sp 1	b.d	0.20	0.03	b.d	b.d	b.d	0.09	b.d	71.95	b.d	27.81	100.08	0.09	0.21	Surface
el 3 ox grain 1 bse 1 sp 2	0.48	0.07	0.74	0.01	0.26	0.03	0.09	b.d	68.84	b.d	27.58	98.09	0.10	0.07	Surface
el 3 ox grain 1 bse 1 sp 3	0.46	0.04	0.51	0.01	0.17	b.d	0.09	b.d	70.82	b.d	28.07	100.18	0.10	0.05	Surface
el 3 ox grain 1 bse 1 sp 4	0.21	0.05	0.27	0.01	0.09	b.d	0.09	b.d	71.10	b.d	27.74	99.56	0.10	0.06	Surface
el 3 ox grain 1 bse 1 sp 5	0.18	0.05	0.24	b.d	0.06	b.d	0.09	b.d	71.65	b.d	27.89	100.16	0.09	0.05	Surface
el 3 ox grain 1 bse 1 sp 6	0.24	0.13	0.60	0.01	0.18	0.02	0.09	b.d	70.04	b.d	27.73	99.03	0.10	0.13	Surface
el 3 ox grain 1 bse 1 sp 7	0.04	0.05	0.20	b.d	0.06	0.03	0.09	b.d	70.39	b.d	27.27	98.11	0.09	0.05	Surface
el 3 ox grain 1 bse 1 sp 8	0.16	0.04	0.40	0.01	0.14	b.d	0.08	b.d	71.25	b.d	27.86	99.95	0.10	0.04	Surface
el 3 ox grain 1 bse 1 sp 9	0.01	0.04	0.19	0.01	0.03	0.07	0.09	b.d	69.28	b.d	26.84	96.57	0.10	0.04	Surface
el 3 ox grain 3 bse 1 sp 1	0.36	0.06	0.19	0.04	0.03	0.03	0.09	b.d	68.96	b.d	27.00	96.76	0.13	0.07	Surface
el 3 ox grain 3 bse 1 sp 2	0.14	0.15	0.02	0.02	0.02	0.03	0.09	b.d	69.58	b.d	26.97	97.01	0.11	0.15	Surface
el 3 ox grain 3 bse 1 sp 3	0.53	1.17	0.36	0.03	0.04	0.03	0.09	b.d	68.35	b.d	27.92	98.51	0.12	1.17	Surface
el 3 ox grain 3 bse 1 sp 4	0.51	0.22	0.41	0.04	0.05	b.d	0.09	b.d	70.56	b.d	28.02	99.89	0.12	0.22	Surface
el 3 ox grain 3 bse 1 sp 5	0.65	0.32	0.53	0.05	0.05	0.01	0.08	b.d	69.39	b.d	27.87	98.95	0.12	0.33	Surface
el 3 ox grain 2 bse 1 sp 1	0.04	0.42	0.20	0.01	0.06	0.08	0.08	b.d	68.16	b.d	26.76	95.80	0.09	0.42	Surface
el 3 ox grain 2 bse 1 sp 2	b.d	0.07	0.15	0.02	0.02	0.03	0.08	b.d	70.44	b.d	27.24	98.07	0.10	0.08	Surface
el 3 ox grain 2 bse 1 sp 3	0.04	1.24	0.35	b.d	0.11	0.16	0.07	b.d	66.86	b.d	27.17	96.00	0.08	1.24	Surface
el 3 ox grain 2 bse 1 sp 4	0.15	0.08	0.35	0.02	0.08	0.01	0.08	b.d	70.47	b.d	27.53	98.77	0.10	0.08	Surface
el 3 ox grain 2 bse 1 sp 5	0.12	0.04	0.38	0.06	0.10	0.05	0.08	b.d	69.04	b.d	27.01	96.87	0.14	0.04	Surface
el 3 ox grain 2 bse 1 sp 6	0.13	0.04	0.31	0.03	0.08	0.01	0.08	b.d	69.88	b.d	27.22	97.77	0.12	0.04	Surface
el 3 ox grain 2 bse 1 sp 7	0.23	0.04	0.33	0.03	0.02	b.d	0.08	b.d	70.90	b.d	27.69	99.32	0.11	0.05	Surface
el 3 ox grain 2 bse 1 sp 8	0.09	0.05	0.23	0.02	0.05	0.05	0.08	b.d	69.20	b.d	26.90	96.67	0.10	0.05	Surface
el 3 clean grain 1 bse 1 sp 1	0.90	0.04	0.46	b.d	0.13	b.d	0.08	b.d	70.35	b.d	28.22	100.18	0.09	0.05	Surface
el 3 clean grain 1 bse 1 sp 2	1.22	0.17	0.77	b.d	0.27	0.01	0.08	b.d	69.43	b.d	28.56	100.52	0.08	0.18	Surface
el 3 clean grain 1 bse 1 sp 3	1.19	0.07	0.58	b.d	0.09	b.d	0.08	b.d	69.87	b.d	28.38	100.26	0.08	0.08	Surface
el 3 clean grain 1 bse 1 sp 4	1.27	0.03	0.98	b.d	0.32	0.01	0.08	b.d	68.91	0.01	28.44	100.05	0.09	0.04	Surface
el 3 clean grain 1 bse 1 sp 5	1.08	0.04	0.52	b.d	0.11	b.d	0.08	b.d	69.77	b.d	28.19	99.79	0.09	0.05	Surface
el 3 clean grain 1 bse 1 sp 6	1.41	0.04	0.91	b.d	0.20	0.01	0.08	b.d	68.82	b.d	28.46	99.92	0.09	0.04	Surface
el 3 clean grain 1 bse 1 sp 7	1.18	0.04	0.69	b.d	0.20	0.02	0.08	b.d	69.35	b.d	28.31	99.87	0.09	0.04	Surface
el 3 clean grain 1 bse 1 sp 8	1.19	0.07	0.82	b.d	0.18	0.01	0.08	b.d	68.55	0.01	28.06	98.96	0.08	0.08	Surface
el 3 clean grain 1 bse 1 sp 9	0.91	0.04	0.34	b.d	0.14	b.d	0.08	b.d	70.35	b.d	28.14	99.99	0.08	0.04	Surface
el 3 clean grain 1 bse 1 sp 10	1.12	0.03	0.61	b.d	0.18	b.d	0.08	b.d	69.56	b.d	28.24	99.82	0.09	0.04	Surface
el 3 clean grain 1 bse 1 sp 11	0.83	0.05	0.38	b.d	0.09	b.d	0.08	b.d	69.50	b.d	27.75	98.67	0.08	0.05	Surface
el 3 clean grain 1 bse 1 sp 12	0.66	0.28	0.13	b.d	0.02	b.d	0.08	b.d	69.87	b.d	27.71	98.75	0.09	0.29	Surface
el 3 clean grain 2 bse 1 sp 1	1.12	0.08	0.46	b.d	0.10	b.d	0.08	b.d	70.26	b.d	28.38	100.47	0.09	0.08	Surface
el 3 clean grain 2 bse 1 sp 2	1.35	0.66	0.89	b.d	0.21	0.02	0.08	b.d	66.99	b.d	28.19	98.38	0.08	0.66	Surface
el 3 clean grain 2 bse 1 sp 3	1.17	4.85	1.09	b.d	0.27	0.01	0.08	b.d	64.90	b.d	30.73	103.09	0.08	4.86	Surface
el 3 clean grain 2 bse 1 sp 4	0.70	0.03	0.01	b.d	b.d	b.d	0.08	b.d	71.33	b.d	28.01	100.16	0.09	0.03	Surface
el 3 clean grain 2 bse 1 sp 5	0.79	0.03	0.28	b.d	0.09	b.d	0.09	b.d	71.05	b.d	28.23	100.55	0.09	0.04	Surface
el 3 clean grain 2 bse 1 sp 6	0.66	0.34	0.68	0.01	0.15	0.01	0.08	b.d	69.22	b.d	27.98	99.14	0.09	0.34	Surface
el 3 clean grain 2 bse 1 sp 7	1.12	0.19	0.64	b.d	0.16	b.d	0.08	b.d	69.18	0.01	28.20	99.58	0.09	0.20	Surface
el 3 clean grain 3 bse 1 sp 1	1.18	0.03	0.57	b.d	0.08	b.d	0.08	b.d	70.56	b.d	28.60	101.10	0.09	0.03	Surface
el 3 clean grain 3 bse 1 sp 2	0.73	0.64	0.16	b.d	0.05	0.02	0.08	b.d	70.16	b.d	28.20	100.04	0.08	0.64	Surface
el 3 clean grain 3 bse 1 sp 3	1.31	0.05	0.76	b.d	0.09	0.01	0.08	b.d	69.34	b.d	28.40	100.03	0.09	0.05	Surface
el 3 clean grain 3 bse 1 sp 4	1.03	0.03	0.58	b.d	0.12	b.d	0.08	b.d	70.04	b.d	28.30	100.18	0.09	0.03	Surface
el 3 clean grain 3 bse 1 sp 5	1.28	0.87	0.81	b.d	0.11	0.01	0.09	b.d	69.59	b.d	29.18	101.94	0.09	0.88	Surface
el 3 clean grain 3 bse 1 sp 6	0.84	0.02	0.44	b.d	0.14	0.03	0.09	b.d	69.98	b.d	28.03	99.56	0.09	0.03	Surface
el 3 clean grain 3 bse 1 sp 7	1.21	0.03	0.77	b.d	0.18	0.01	0.08	b.d	69.62	b.d	28.46	100.35	0.09	0.03	Surface
el 3 clean grain 3 bse 1 sp 8	0.89	0.04	0.43	b.d	0.13	b.d	0.08	b.d	70.39	b.d	28.21	100.17	0.09	0.04	Surface
el 3 clean grain 3 bse 1 sp 9	0.78	0.03	0.15	b.d	0.04	b.d	0.08	b.d	71.20	b.d	28.15	100.44	0.09	0.04	Surface
el 3 clean grain 3 bse 1 sp 10	1.22	0.18	0.29	b.d	0.14	b.d	0.08	b.d	69.89	0.01	28.27	100.07	0.09	0.18	Surface
el 5 out grain 2 bse 1 sp 1	0.67	0.45	0.07	b.d	0.04	b.d	0.10	b.d	67.80	0.02	27.00	96.14	0.10	0.48	Surface
el 5 out grain 2 bse 1 sp 2	0.80	0.04	0.32	b.d	0.01	b.d	0.10	b.d	68.98	0.03	27.43	97.71	0.10	0.07	Surface
el 5 out grain 2 bse 1 sp 3	0.70	0.02	0.09	b.d	0.03	b.d	0.10	b.d	69.90	0.03	27.50	98.37	0.10	0.05	Surface
el 5 out grain 2 bse 1 sp 5	0.79	0.03	0.10	b.d	0.02	b.d	0.10	b.d	69.56	0.03	27.47	98.11	0.11	0.06	Surface
el 5 out grain 2 bse 1 sp 6	0.79	0.02	0.08	b.d	0.04	b.d	0.10	b.d	69.52	0.03	27.44	98.03	0.11	0.05	Surface
el 5 out grain 2 bse 1 sp 7	0.82	0.02	0.13	b.d	0.03	b.d	0.11	b.d	69.73	0.03	27.57	98.43	0.11	0.05	Surface
el 5 out grain 2 bse 1 sp 8	0.64	0.07	0.51	b.d	0.09	b.d	0.11	b.d	69.09	0.01	27.54	98.06	0.11	0.08	Surface
el 5 out grain 2 bse 1 sp 9	0.82	0.03	0.20	b.d	0.06	b.d	0.11	b.d	69.21	0.01	27.46	97.90	0.11	0.04	Surface
el 5 out grain 2 bse 1 sp 11	0.85	0.02	0.38	b.d	0.15	b.d	0.10	b.d	68.50	0.01	27.39	97.41	0.11	0.03	Surface
el 5 out grain 2 bse 1 sp 12	0.77	0.10	0.62	b.d	0.20	b.d	0.10	b.d	68.02	0.01	27.39	97.21	0.10	0.11	Surface
el 5 out grain 2 bse 1 sp 13	0.67	1.43	0.23	b.d	0.14	0.03	0.09	b.d	66.41	0.01	27.44	96.45	0.10	1.44	Surface

Sample ID Laco Sur	Mg [wt%]	Al [wt%]	Si [wt%]	Ti [wt%]	Ca [wt%]	P [wt%]	V [wt%]	Cr [wt%]	Fe [wt%]	Mn [wt%]	O [wt%]	Total	Ti+V [wt%]	Al+Mn [wt%]	Sample
el 5 out grain 2 bse 1 sp 14	0.80	0.09	0.26	b.d	0.10	b.d	0.10	b.d	68.08	0.02	27.11	96.56	0.10	0.11	Surface
el 5 out grain 2 bse 1 sp 15	0.85	0.03	0.36	b.d	0.13	b.d	0.10	b.d	68.55	0.02	27.38	97.42	0.10	0.05	Surface
el 5 out grain 2 bse 1 sp 16	0.87	0.18	0.35	b.d	0.15	b.d	0.10	b.d	68.03	0.02	27.32	97.00	0.10	0.20	Surface
el 5 out grain 3 bse 1 sp 1	1.14	0.09	0.60	0.01	0.13	b.d	0.10	b.d	69.64	0.03	28.28	100.02	0.11	0.12	Surface
el 5 out grain 3 bse 1 sp 2	0.82	0.17	0.22	b.d	0.09	0.05	0.10	b.d	69.33	0.02	27.69	98.51	0.11	0.20	Surface
el 5 out grain 3 bse 1 sp 3	0.50	0.29	0.40	0.01	0.16	0.20	0.10	b.d	66.61	0.02	26.81	95.08	0.11	0.31	Surface
el 5 out grain 3 bse 1 sp 4	1.17	0.10	1.02	0.01	0.22	b.d	0.10	b.d	68.08	0.03	28.09	98.83	0.12	0.13	Surface
el 5 out grain 3 bse 1 sp 5	1.28	3.06	0.86	0.01	0.20	0.01	0.10	b.d	64.91	0.03	29.17	99.61	0.11	3.09	Surface
el 5 out grain 3 bse 1 sp 6	0.99	0.11	0.85	0.01	0.23	b.d	0.11	b.d	68.90	0.04	28.14	99.38	0.12	0.15	Surface
el 5 out grain 3 bse 1 sp 7	1.39	0.26	0.49	0.01	0.17	b.d	0.11	b.d	66.89	0.04	27.53	96.89	0.12	0.30	Surface
el 5 out grain 3 bse 1 sp 8	0.92	0.21	0.79	0.01	0.18	b.d	0.11	b.d	68.32	0.04	27.86	98.44	0.12	0.25	Surface
el 5 out grain 3 bse 1 sp 9	0.86	0.06	0.34	b.d	0.07	b.d	0.11	b.d	70.51	0.03	28.13	100.11	0.11	0.10	Surface
el 5 out grain 3 bse 1 sp 10	0.76	0.72	0.53	0.01	0.18	0.09	0.11	b.d	67.54	0.03	27.71	97.68	0.12	0.75	Surface
el 5 out grain 3 bse 1 sp 11	0.83	0.33	0.73	0.01	0.19	b.d	0.11	b.d	69.04	0.03	28.11	99.39	0.12	0.36	Surface
el 5 out grain 3 bse 1 sp 12	0.94	0.08	0.41	b.d	0.06	b.d	0.10	b.d	69.96	0.04	28.04	99.62	0.11	0.11	Surface
el 5 out grain 3 bse 1 sp 13	0.98	0.07	0.48	b.d	0.13	b.d	0.11	b.d	69.76	0.04	28.09	99.65	0.12	0.11	Surface
el 5 out grain 3 bse 1 sp 14	0.85	0.16	0.62	b.d	0.15	b.d	0.11	b.d	69.13	0.02	27.91	98.95	0.11	0.18	Surface
el 5 out grain 3 bse 1 sp 15	0.84	0.74	0.45	b.d	0.16	b.d	0.11	b.d	69.06	0.03	28.23	99.62	0.11	0.78	Surface
el 5 out grain 3 bse 1 sp 16	0.91	1.68	0.25	b.d	0.11	b.d	0.10	b.d	68.13	0.04	28.48	99.69	0.11	1.71	Surface
el 5 out grain 3 bse 1 sp 17	0.89	0.07	0.58	b.d	0.17	b.d	0.11	b.d	69.70	0.03	28.09	99.64	0.11	0.10	Surface
el 5 out grain 3 bse 1 sp 18	1.11	0.07	0.73	b.d	0.22	b.d	0.11	b.d	69.07	0.03	28.18	99.53	0.11	0.10	Surface
el 5 out grain 3 bse 1 sp 19	0.95	0.42	0.87	0.01	0.22	b.d	0.11	b.d	69.07	0.03	28.42	100.11	0.12	0.45	Surface
el 5 out grain 3 bse 1 sp 20	0.97	0.16	0.73	b.d	0.22	0.01	0.10	b.d	68.49	0.02	27.89	98.59	0.11	0.18	Surface
el 5 in grain 3 bse 1 sp 1	0.76	0.07	0.03	0.01	b.d	b.d	0.10	b.d	71.72	0.01	28.23	100.93	0.11	0.08	Surface
el 5 in grain 3 bse 1 sp 2	0.72	0.07	0.03	0.01	b.d	b.d	0.10	b.d	71.54	0.01	28.12	100.61	0.11	0.08	Surface
el 5 in grain 3 bse 1 sp 3	0.85	0.90	0.02	0.01	b.d	b.d	0.10	b.d	69.52	0.01	28.11	99.52	0.11	0.91	Surface
el 5 in grain 3 bse 1 sp 4	0.68	0.28	0.14	b.d	0.02	0.01	0.10	b.d	68.96	b.d	27.39	97.58	0.10	0.28	Surface
el 5 in grain 3 bse 1 sp 5	0.64	0.10	0.07	0.02	0.01	0.03	0.09	b.d	68.95	b.d	27.16	97.07	0.11	0.11	Surface
el 5 in grain 3 bse 1 sp 6	1.08	0.19	0.42	0.02	0.14	0.02	0.09	b.d	70.01	b.d	28.35	100.32	0.11	0.20	Surface
el 5 in grain 3 bse 1 sp 7	0.87	0.18	0.62	0.02	0.10	b.d	0.10	b.d	69.83	0.01	28.17	99.89	0.12	0.19	Surface
el 5 in grain 3 bse 1 sp 8	0.52	0.17	0.07	0.01	0.03	0.03	0.09	b.d	69.71	b.d	27.41	98.04	0.10	0.17	Surface
el 5 in grain2 bse 1 sp 1	0.65	0.18	0.02	0.01	b.d	b.d	0.10	b.d	70.51	b.d	27.78	99.24	0.11	0.19	Surface
el 5 in grain2 bse 1 sp 2	0.77	0.10	0.02	0.01	0.01	b.d	0.09	b.d	70.75	0.01	27.87	99.64	0.11	0.11	Surface
el 5 in grain2 bse 1 sp 3	0.70	0.07	0.03	0.01	b.d	b.d	0.10	b.d	71.40	0.01	28.05	100.36	0.11	0.08	Surface
el 5 in grain2 bse 1 sp 4	0.71	0.08	0.01	0.01	b.d	b.d	0.09	b.d	71.47	b.d	28.11	100.48	0.10	0.08	Surface
el 5 in grain2 bse 1 sp 5	0.73	0.22	0.02	0.01	b.d	b.d	0.09	b.d	70.80	b.d	27.99	99.87	0.11	0.22	Surface
el 5 in grain2 bse 1 sp 6	0.51	0.29	0.06	0.01	b.d	0.01	0.09	b.d	70.09	b.d	27.60	98.66	0.10	0.29	Surface
el 5 in grain2 bse 1 sp 8	0.67	0.07	0.04	0.01	0.01	0.09	0.09	b.d	69.49	b.d	27.43	97.92	0.10	0.08	Surface
el 5 in grain 1 bse 1 sp 1	0.60	4.52	0.23	0.01	b.d	b.d	0.10	b.d	69.67	b.d	31.01	106.14	0.11	4.52	Surface
el 5 in grain 1 bse 1 sp 2	0.69	0.36	0.03	0.01	b.d	0.01	0.09	b.d	70.04	0.01	27.75	99.00	0.11	0.37	Surface
el 5 in grain 1 bse 1 sp 3	0.71	0.11	0.01	0.01	b.d	b.d	0.10	b.d	71.28	0.01	28.03	100.25	0.11	0.12	Surface
el 5 in grain 1 bse 1 sp 4	0.80	0.16	0.06	0.02	0.01	b.d	0.09	b.d	69.62	0.02	27.55	98.33	0.11	0.18	Surface
el 5 in grain 1 bse 1 sp 5	0.68	0.72	0.02	0.01	0.02	b.d	0.09	b.d	71.42	0.01	28.54	101.51	0.10	0.73	Surface
el 5 in grain 1 bse 1 sp 6	0.67	0.07	0.17	0.02	0.02	b.d	0.09	b.d	70.73	b.d	27.92	99.70	0.11	0.08	Surface
el 5 in grain 1 bse 1 sp 7	0.80	0.18	0.06	0.02	0.03	0.01	0.10	b.d	70.23	b.d	27.83	99.23	0.11	0.18	Surface
el 5 in grain 1 bse 1 sp 8	0.56	3.08	0.02	0.01	0.03	0.04	0.09	b.d	70.66	b.d	30.09	104.59	0.10	3.09	Surface
el 5 in grain 1 bse 1 sp 9	0.71	0.07	0.02	0.02	b.d	b.d	0.10	b.d	71.52	0.01	28.10	100.55	0.11	0.09	Surface
el 7 ox grain2 sp 1	1.19	0.01	0.56	b.d	0.19	b.d	0.06	b.d	68.30	0.04	27.75	98.12	0.06	0.05	Surface
el 7 ox grain2 sp 2	1.40	0.51	0.56	b.d	0.20	0.01	0.06	b.d	68.64	0.03	28.45	99.86	0.06	0.54	Surface
el 7 ox grain2 sp 3	1.16	0.01	0.53	b.d	0.19	b.d	0.05	b.d	68.17	0.02	27.64	97.78	0.06	0.03	Surface
el 7 ox grain2 sp 4	1.10	0.00	0.58	b.d	0.20	b.d	0.06	b.d	69.17	0.04	28.01	99.16	0.06	0.04	Surface
el 7 ox grain2 sp 5	1.09	0.00	0.50	b.d	0.21	b.d	0.06	b.d	69.44	0.04	28.05	99.40	0.06	0.04	Surface
el 7 ox grain2 sp 6	0.87	0.00	0.25	b.d	0.03	b.d	0.06	b.d	68.60	0.04	27.26	97.12	0.07	0.05	Surface
el 7 ox grain2 sp 7	0.60	1.37	0.24	b.d	0.10	0.02	0.06	b.d	70.06	0.04	28.68	101.16	0.06	1.40	Surface
el 7 ox grain2 sp 8	0.63	0.02	0.14	b.d	0.02	b.d	0.06	b.d	69.39	0.02	27.26	97.54	0.06	0.04	Surface
el 7 ox grain2 tr 2 sp 1	0.77	0.29	0.44	b.d	0.19	0.02	0.06	b.d	67.31	0.03	27.13	96.24	0.06	0.33	Surface
el 7 ox grain2 tr 2 sp 2	1.10	0.13	0.59	b.d	0.21	b.d	0.06	b.d	68.85	0.04	28.01	98.99	0.06	0.17	Surface
el 7 ox grain2 tr 2 sp 3	1.25	0.01	0.63	b.d	0.20	b.d	0.06	b.d	67.89	0.04	27.70	97.79	0.06	0.05	Surface
el 7 ox grain2 tr 2 sp 4	1.10	0.01	0.57	b.d	0.20	b.d	0.06	b.d	67.92	0.04	27.53	97.43	0.07	0.05	Surface
el 7 ox grain2 tr 2 sp 5	0.39	3.63	0.31	b.d	0.16	0.51	0.05	b.d	64.01	0.03	28.69	97.78	0.06	3.66	Surface
el 7 ox grain2 tr 2 sp 6	1.31	0.00	0.69	b.d	0.23	b.d	0.06	b.d	67.99	0.04	27.85	98.18	0.06	0.05	Surface
el 7 ox grain2 tr 2 sp 7	0.47	0.00	0.29	b.d	0.06	0.07	0.06	b.d	68.35	0.03	26.93	96.26	0.06	0.03	Surface
el 7 ox grain2 tr 2 sp 8	1.39	0.01	0.80	b.d	0.30	b.d	0.06	b.d	68.50	0.05	28.25	99.36	0.06	0.06	Surface
el 7 ox grain2 tr 2 sp 9	1.41	0.01	0.81	b.d	0.29	b.d	0.06	b.d	68.55	0.05	28.27	99.44	0.06	0.05	Surface
el 7 ox grain2 tr 2 sp 10	0.99	0.01	0.54	b.d	0.19	0.02	0.06	b.d	67.80	0.04	27.37	97.02	0.06	0.06	Surface
el c out grain 1 sp 2	0.07	1.71	0.38	0.01	0.04	0.06	0.09	b.d	67.77	b.d	27.78	97.92	0.10	1.72	Surface
el c out grain 1 sp 3	0.05	0.44	0.63	b.d	0.07	0.08	0.08	b.d	67.08	b.d	26.72	95.16	0.08	0.44	Surface
el c out grain 1 sp 5	0.12	0.12	0.10	b.d	0.04	0.05	0.10	b.d	68.60	b.d	26.66	95.79	0.10	0.12	Surface
el b out grain 1 sp 2	b.d	0.03	0.03	b.d	b.d	b.d	0.02	b.d	69.44	b.d	26.69	96.21	0.03	0.03	Surface
el b out grain 1 sp 3	b.d	0.13	0.04	b.d	b.d	b.d	0.01	b.d	69.11	b.d	26.64	95.94	0.02	0.13	Surface
el b out grain 1 sp 4	0.02	0.06	0.03	b.d	b.d	b.d	0.01	b.d	68.96	b.d	26.52	95.60	0.02	0.06	Surface
el b out grain 1 sp 5	b.d	1.27	0.03	b.d	0.01	0.01	0.02	b.d	68.17	b.d	27.17	96.68	0.02	1.27	Surface
el b out grain 1 sp 6	b.d	0.78	0.03	b.d	b.d	b.d	0.02	b.d	68.99	b.d	27.11	96.93	0.03	0.78	Surface
el b out grain 1 sp 7	b.d	0.22	0.03	b.d	b.d	b.d	0.02	b.d	69.02	b.d	26.68	95.98	0.03	0.23	Surface
el b out grain 1 sp 8	0.03	0.02	0.05	b.d	b.d	b.d	0.02	b.d	68.72	b.d	26.42	95.25	0.03	0.02	Surface
el b out grain 3 sp 6	0.06	0.06	0.06	b.d	b.d	b.d	0.03	b.d	68.95	b.d	26.58	95.74	0.03	0.06	Surface
el b out grain 3 sp 7	b.d	0.22	0.05	b.d	0.04	b.d	0.02	b.d	68.63	b.d	26.56	95.53	0.03	0.22	Surface

Sample ID Laco Sur	Mg [wt%]	Al [wt%]	Si [wt%]	Ti [wt%]	Ca [wt%]	P [wt%]	V [wt%]	Cr [wt%]	Fe [wt%]	Mn [wt%]	O [wt%]	Total	Ti+V [wt%]	Al+Mn [wt%]	Sample
el b out grain 3 sp 8	b.d	0.43	0.05	b.d	0.01	b.d	0.02	b.d	68.30	b.d	26.58	95.39	0.03	0.44	Surface
el c in grain 3 sp 1	0.19	0.08	0.10	b.d	0.02	0.06	0.08	b.d	68.14	b.d	26.50	95.16	0.08	0.09	Surface
el c in grain 3 sp 2	0.31	0.09	0.08	b.d	0.02	0.02	0.08	b.d	69.20	b.d	26.96	96.77	0.09	0.10	Surface
el c in grain 3 sp 4	0.12	0.61	0.04	b.d	0.02	0.05	0.08	b.d	68.48	b.d	26.93	96.32	0.09	0.61	Surface
el c in grain 3 sp 5	0.22	0.10	0.11	b.d	0.04	0.07	0.08	b.d	68.12	b.d	26.57	95.29	0.08	0.10	Surface
el c in grain 3 sp 6	0.35	1.10	0.08	0.01	0.03	0.06	0.08	b.d	67.15	b.d	27.07	95.93	0.09	1.10	Surface
el c in grain 2 sp 1	0.22	0.17	0.05	b.d	0.03	0.04	0.08	b.d	69.09	b.d	26.91	96.58	0.09	0.17	Surface
el c in grain 2 sp 3	0.22	0.06	0.04	0.01	b.d	0.01	0.09	b.d	69.03	b.d	26.75	96.21	0.10	0.06	Surface
el c in grain 2 sp 4	0.22	0.07	0.02	b.d	b.d	b.d	0.08	b.d	69.40	b.d	26.90	96.69	0.09	0.07	Surface
el c in grain 2 sp 5	0.14	0.08	0.09	b.d	0.03	0.09	0.08	b.d	68.24	b.d	26.53	95.27	0.09	0.08	Surface
el c out grain 3 sp 1	0.04	0.08	0.08	b.d	0.04	0.01	0.10	b.d	69.89	b.d	26.98	97.21	0.10	0.08	Surface
el c out grain 3 sp 2	0.02	0.18	0.06	b.d	0.06	0.01	0.10	b.d	69.55	b.d	26.92	96.90	0.10	0.19	Surface
el c out grain 3 sp 3	0.07	0.12	0.20	0.01	0.05	0.07	0.09	b.d	68.25	b.d	26.58	95.44	0.10	0.12	Surface
el 15 porous sp 1	1.00	0.14	0.64	0.01	0.22	b.d	0.08	b.d	68.50	0.02	27.83	98.44	0.10	0.16	Surface
el 15 porous sp 2	0.65	0.16	0.02	0.01	b.d	b.d	0.09	b.d	71.11	0.02	27.95	100.00	0.10	0.18	Surface
el 15 porous sp 3	0.81	0.16	0.03	0.02	b.d	b.d	0.09	b.d	70.57	0.01	27.91	99.60	0.11	0.18	Surface
el 15 porous sp 4	0.76	0.23	0.09	0.02	0.06	b.d	0.09	b.d	70.65	0.02	28.01	99.93	0.11	0.25	Surface
el 14 in sp 2	0.65	0.09	0.03	0.01	0.02	b.d	0.10	b.d	70.23	b.d	27.61	98.76	0.12	0.10	Surface
el 3a bse 1 high z	0.32	0.00	0.02	b.d	0.01	b.d	0.08	b.d	70.71	b.d	27.42	98.56	0.08	0.01	Surface
el 3a bse 1 regular z	0.88	0.02	1.03	b.d	0.17	b.d	0.09	b.d	68.62	0.03	27.96	98.79	0.09	0.05	Surface
el 3a bse 2 sp 1 reg Z	0.07	0.03	0.43	b.d	b.d	0.05	0.09	b.d	68.21	b.d	26.64	95.52	0.09	0.04	Surface
el 3a bse 2 sp 1 high Z	0.22	0.03	0.18	0.01	b.d	0.05	0.07	b.d	70.80	0.03	27.52	98.91	0.08	0.05	Surface
el 3a bse 1 sp 1	0.26	0.03	0.02	0.01	b.d	b.d	0.08	b.d	70.91	b.d	27.46	98.76	0.09	0.03	Surface
el 3a bse 1 sp 2	0.65	0.03	0.76	b.d	0.16	0.01	0.08	b.d	68.57	b.d	27.55	97.80	0.08	0.03	Surface
el 3a bse 1 sp 3	0.34	0.02	0.27	b.d	0.10	0.05	0.08	b.d	68.33	b.d	26.82	96.01	0.08	0.02	Surface
el 3a bse 1 sp 4	0.55	0.02	0.41	b.d	0.11	b.d	0.08	b.d	68.89	b.d	27.29	97.34	0.08	0.02	Surface
el 3a bse 1 sp 5	0.34	0.03	0.01	b.d	0.01	b.d	0.08	b.d	70.66	b.d	27.43	98.56	0.08	0.03	Surface
el 3a bse 1 sp 6	0.29	0.03	0.04	b.d	0.02	b.d	0.08	b.d	69.01	0.08	26.78	96.33	0.08	0.11	Surface
el 3a bse 1 sp 7	0.36	0.03	0.04	b.d	0.03	b.d	0.08	b.d	71.00	b.d	27.61	99.15	0.09	0.03	Surface
el 3a bse 1 sp 8	0.35	0.03	0.01	b.d	0.01	b.d	0.08	b.d	71.11	b.d	27.61	99.20	0.08	0.03	Surface
el 3a bse 1 sp 9	0.47	0.04	0.34	b.d	0.18	0.02	0.08	b.d	69.75	b.d	27.56	98.44	0.08	0.04	Surface
el 3a bse 1 sp 10	0.34	0.02	0.01	b.d	b.d	b.d	0.08	b.d	70.87	b.d	27.51	98.82	0.08	0.02	Surface
el 3a bse 1 sp 11	0.35	0.02	0.01	0.01	b.d	b.d	0.08	b.d	71.31	b.d	27.68	99.47	0.09	0.02	Surface
el 6 bse 1 sp 1	0.40	0.02	0.02	b.d	b.d	b.d	0.06	b.d	71.67	0.05	27.85	100.07	0.06	0.07	Surface
el 6 bse 1 sp 2	0.42	0.02	0.02	b.d	b.d	b.d	0.06	b.d	71.66	0.07	27.87	100.12	0.06	0.08	Surface
el 6 bse 1 sp 3	0.40	0.02	0.02	b.d	b.d	b.d	0.06	b.d	71.77	0.07	27.90	100.24	0.07	0.08	Surface
el 6 bse 1 sp 4	0.44	0.01	0.02	b.d	b.d	b.d	0.06	b.d	71.68	0.07	27.88	100.16	0.06	0.08	Surface
el 6 bse 1 sp 5	0.41	0.02	0.01	b.d	b.d	b.d	0.06	b.d	71.83	0.06	27.91	100.30	0.06	0.08	Surface
el 6 bse 1 sp 6	0.41	0.02	0.02	b.d	b.d	b.d	0.05	b.d	71.71	0.06	27.88	100.15	0.06	0.08	Surface
el 6 bse 1 sp 7	0.41	0.02	0.02	b.d	b.d	b.d	0.06	b.d	71.84	0.05	27.93	100.34	0.07	0.07	Surface
el 6 bse 2 sp 1	0.52	0.00	0.23	b.d	0.04	b.d	0.03	b.d	71.56	0.08	28.07	100.53	0.03	0.08	Surface
el 6 bse 2 sp 2	0.53	0.00	0.23	b.d	0.04	b.d	0.02	b.d	71.57	0.08	28.08	100.55	0.03	0.08	Surface
el 6 bse 2 sp 3	0.46	0.00	0.13	b.d	0.02	b.d	0.02	b.d	71.87	0.08	28.05	100.65	0.03	0.09	Surface
el 6 bse 2 sp 4	0.45	0.00	0.17	b.d	0.02	b.d	0.03	b.d	71.64	0.08	27.98	100.38	0.03	0.09	Surface
el 6 bse 2 sp 5	0.49	0.00	0.16	b.d	0.03	b.d	0.02	b.d	71.69	0.08	28.03	100.51	0.03	0.09	Surface
el 6 bse 2 sp 6	0.49	0.00	0.14	b.d	0.03	b.d	0.03	b.d	71.97	0.08	28.12	100.86	0.04	0.09	Surface
el 6 bse 2 sp 7	0.47	0.00	0.18	b.d	0.04	b.d	0.03	b.d	71.88	0.08	28.11	100.80	0.03	0.09	Surface
el 6 bse 2 sp 8	0.48	0.00	0.14	b.d	0.03	b.d	0.03	b.d	71.90	0.09	28.10	100.77	0.04	0.09	Surface
el 6 bse 2 sp 9	0.50	0.00	0.20	b.d	0.04	b.d	0.03	b.d	71.84	0.08	28.14	100.83	0.04	0.08	Surface
el 6 bse 2 sp 10	0.47	0.00	0.22	b.d	0.04	b.d	0.03	b.d	71.70	0.09	28.08	100.64	0.04	0.10	Surface
el 6 bse 3 sp 1	0.85	0.14	0.95	0.03	0.26	b.d	0.09	b.d	69.50	0.07	28.36	100.23	0.11	0.21	Surface
el 6 bse 3 sp 2	0.72	0.15	0.81	0.03	0.18	b.d	0.08	b.d	69.59	0.07	28.14	99.77	0.11	0.22	Surface
el 6 bse 3 sp 3	0.69	0.15	0.78	0.03	0.16	b.d	0.08	b.d	70.02	0.07	28.24	100.21	0.11	0.21	Surface
el 6 bse 3 sp 4	0.63	0.15	0.74	0.03	0.19	b.d	0.08	b.d	70.10	0.05	28.21	100.18	0.12	0.20	Surface
el 6 bse 3 sp 5	0.67	0.16	0.97	0.02	0.24	b.d	0.08	b.d	69.25	0.05	28.12	99.56	0.10	0.21	Surface
el 6 bse 3 sp 6	0.74	0.11	0.77	0.02	0.18	b.d	0.08	b.d	69.86	0.04	28.18	99.98	0.10	0.15	Surface
el 6 bse 3 sp 7	0.47	0.10	0.40	0.02	0.16	0.02	0.07	b.d	70.37	0.02	27.85	99.49	0.10	0.12	Surface
el 6 bse 4 transect 1 sp 1	0.81	0.22	1.14	0.07	0.30	b.d	0.12	b.d	68.50	0.05	28.20	99.41	0.18	0.27	Surface
el 6 bse 4 transect 1 sp 2	0.44	0.24	0.64	0.05	0.07	0.02	0.11	b.d	69.69	0.04	27.84	99.15	0.16	0.27	Surface
el 6 bse 4 transect 1 sp 3	0.44	0.13	0.17	0.03	0.06	b.d	0.13	b.d	71.56	0.05	28.10	100.67	0.16	0.18	Surface
el 6 bse 4 transect 1 sp 4	0.39	0.13	0.02	0.03	b.d	b.d	0.13	b.d	71.85	0.06	28.03	100.64	0.16	0.18	Surface
el 6 bse 4 transect 1 sp 5	0.42	0.13	0.06	0.03	b.d	b.d	0.13	b.d	71.73	0.05	28.04	100.58	0.16	0.18	Surface
el 6 bse 4 transect 1 sp 6	0.54	0.26	0.90	0.06	0.14	b.d	0.12	b.d	68.93	0.04	27.89	98.88	0.18	0.30	Surface
el 6 bse 4 transect 1 sp 7	0.42	0.12	0.04	0.03	b.d	b.d	0.12	b.d	71.38	0.03	27.87	100.01	0.16	0.15	Surface
el 6 bse 4 transect 1 sp 8	0.39	0.12	0.02	b.d	b.d	b.d	0.13	b.d	71.57	0.03	27.90	100.16	0.13	0.15	Surface
el 6 bse 4 transect 2 sp 1	0.40	0.12	0.02	0.04	b.d	b.d	0.13	b.d	71.82	0.06	28.02	100.61	0.17	0.18	Surface
el 6 bse 4 transect 2 sp 2	0.41	0.11	0.02	0.04	b.d	b.d	0.13	b.d	71.75	0.06	28.00	100.53	0.18	0.18	Surface
el 6 bse 4 transect 2 sp 3	0.39	0.11	0.02	0.03	b.d	b.d	0.12	b.d	71.28	0.04	27.79	99.79	0.16	0.15	Surface
el 6 bse 4 transect 2 sp 4	0.41	0.11	0.01	0.03	b.d	b.d	0.12	b.d	71.71	0.07	27.97	100.42	0.15	0.17	Surface
el 6 bse 4 transect 2 sp 5	0.51	0.11	0.30	0.04	0.12	b.d	0.12	b.d	71.67	0.06	28.31	101.23	0.16	0.17	Surface
el 6 bse 4 transect 2 sp 6	0.42	0.11	0.10	0.04	0.05	b.d	0.12	b.d	71.23	0.06	27.88	100.00	0.16	0.17	Surface
el 6 bse 4 transect 2 sp 7	0.49	0.11	0.26	0.03	0.10	b.d	0.12	b.d	70.73	0.06	27.90	99.79	0.15	0.17	Surface
el 6 bse 4 transect 2 sp 8	0.45	0.11	0.21	0.03	0.03	b.d	0.12	b.d	71.19	0.04	27.95	100.13	0.15	0.15	Surface
el 6 bse 4 transect 2 sp 9	0.45	0.10	0.15	0.03	0.04	b.d	0.12	b.d	71.48	0.05	28.02	100.44	0.15	0.16	Surface
el 6 bse 4 transect 2 sp 10	0.49	0.11	0.26	0.03	0.11	b.d	0.12	b.d	70.99	0.05	28.00	100.16	0.15	0.16	Surface
el 6 bse 9 sp 1	0.53	0.00	0.29	b.d	0.04	b.d	0.05	b.d	70.61	0.09	27.78	99.39	0.05	0.09	Surface
el 6 bse 9 sp 2	0.52	0.01	0.27	b.d	0.04	b.d	0.04	b.d	70.69	0.09	27.78	99.44	0.05	0.11	Surface

Sample ID Laco Sur	Mg [wt%]	Al [wt%]	Si [wt%]	Ti [wt%]	Ca [wt%]	P [wt%]	V [wt%]	Cr [wt%]	Fe [wt%]	Mn [wt%]	O [wt%]	Total	Ti+V [wt%]	Al+Mn [wt%]	Sample
el 6 bse 9 sp 3	0.52	0.00	0.31	b.d	0.07	b.d	0.05	b.d	70.51	0.09	27.76	99.32	0.05	0.09	Surface
el 6 bse 9 sp 4	0.59	0.00	0.39	b.d	0.11	b.d	0.06	b.d	70.17	0.09	27.77	99.18	0.06	0.09	Surface
el 6 bse 9 sp 5	0.54	0.00	0.39	b.d	0.10	b.d	0.06	b.d	70.09	0.09	27.69	98.95	0.06	0.09	Surface
el 6 bse 9 sp 6	0.55	0.00	0.35	b.d	0.09	b.d	0.06	b.d	70.04	0.09	27.65	98.82	0.06	0.09	Surface
el 6 bse 9 sp 7	0.59	0.00	0.47	b.d	0.14	b.d	0.06	b.d	69.86	0.08	27.73	98.94	0.06	0.09	Surface
el 6 bse 9 sp 8	0.55	0.00	0.34	b.d	0.09	b.d	0.06	b.d	69.83	0.09	27.56	98.52	0.06	0.10	Surface
el 6 bse 9 sp 9	0.53	0.00	0.35	b.d	0.07	b.d	0.06	b.d	69.57	0.08	27.44	98.10	0.07	0.08	Surface
el 6 bse 9 sp 10	0.54	0.00	0.35	b.d	0.08	b.d	0.06	b.d	69.99	0.08	27.62	98.73	0.06	0.09	Surface
el 6 bse 9 sp 11	0.56	0.00	0.37	b.d	0.08	b.d	0.06	b.d	69.71	0.08	27.54	98.41	0.07	0.09	Surface
el 6 bse 9 sp 12	0.56	0.00	0.35	b.d	0.05	b.d	0.05	b.d	69.42	0.08	27.39	97.90	0.06	0.08	Surface
el 6 bse 5 sp 1	0.54	0.01	0.31	b.d	0.12	b.d	0.05	b.d	71.57	0.08	28.20	100.87	0.05	0.08	Surface
el 6 bse 5 sp 2	0.63	0.01	0.53	b.d	0.17	b.d	0.05	b.d	70.85	0.07	28.20	100.51	0.06	0.08	Surface
el 6 bse 5 sp 3	0.58	0.01	0.44	b.d	0.14	b.d	0.05	b.d	70.87	0.08	28.08	100.24	0.05	0.09	Surface
el 6 bse 5 sp 4	0.57	0.01	0.44	b.d	0.15	b.d	0.05	b.d	71.23	0.09	28.22	100.76	0.05	0.10	Surface
el 6 bse 5 sp 5	0.58	0.01	0.47	b.d	0.16	b.d	0.05	b.d	71.02	0.08	28.18	100.56	0.06	0.09	Surface
el 6 bse 6 transect 1 sp 1	0.50	0.07	0.67	b.d	0.19	b.d	0.08	b.d	70.55	0.06	28.15	100.28	0.08	0.14	Surface
el 6 bse 6 transect 1 sp 2	0.46	0.07	0.66	0.02	0.19	b.d	0.08	b.d	70.38	0.05	28.04	99.96	0.10	0.12	Surface
el 6 bse 6 transect 1 sp 3	0.45	0.07	0.53	b.d	0.15	b.d	0.08	b.d	70.87	0.04	28.08	100.26	0.08	0.10	Surface
el 6 bse 6 transect 1 sp 4	0.40	0.06	0.44	b.d	0.15	b.d	0.07	b.d	71.12	0.03	28.06	100.34	0.08	0.09	Surface
el 6 bse 6 transect 2 sp 1	0.23	0.10	0.09	b.d	0.03	0.02	0.07	b.d	70.60	b.d	27.45	98.60	0.08	0.11	Surface
el 6 bse 6 transect 2 sp 2	0.47	0.07	0.61	b.d	0.17	b.d	0.08	b.d	70.86	0.06	28.18	100.50	0.08	0.13	Surface
el 6 bse 6 transect 2 sp 3	0.53	0.07	0.65	b.d	0.20	b.d	0.07	b.d	70.57	0.07	28.17	100.34	0.08	0.14	Surface
el 6 bse 6 transect 2 sp 4	0.57	0.07	0.78	0.02	0.21	b.d	0.07	b.d	70.31	0.08	28.21	100.32	0.09	0.15	Surface
el 6 bse 6 transect 2 sp 5	0.59	0.07	0.83	b.d	0.27	b.d	0.07	b.d	70.02	0.06	28.19	100.10	0.07	0.13	Surface
el 6 bse 6 transect 2 sp 6	0.50	0.07	0.58	0.02	0.18	b.d	0.08	b.d	70.78	0.04	28.15	100.39	0.09	0.11	Surface
el 6 bse 8 sp 1	0.47	0.00	0.33	b.d	0.08	b.d	0.04	b.d	71.12	0.09	27.96	100.09	0.04	0.09	Surface
el 6 bse 8 sp 2	0.57	0.00	0.50	b.d	0.13	b.d	0.04	b.d	70.53	0.09	27.98	99.85	0.04	0.10	Surface
el 6 bse 8 sp 3	0.46	0.01	0.27	b.d	0.07	b.d	0.04	b.d	71.18	0.09	27.93	100.06	0.05	0.10	Surface
el 6 bse 8 sp 4	0.57	0.01	0.45	b.d	0.12	b.d	0.04	b.d	70.87	0.08	28.07	100.21	0.04	0.09	Surface
el 6 bse 8 sp 5	0.48	0.01	0.29	b.d	0.10	b.d	0.04	b.d	71.20	0.08	27.98	100.17	0.04	0.09	Surface
el 6 bse 7 sp 1	0.44	0.00	0.14	b.d	0.02	b.d	0.04	b.d	72.15	0.09	28.15	101.02	0.05	0.09	Surface
el 6 bse 7 sp 2	0.44	0.01	0.16	b.d	0.03	b.d	0.04	b.d	71.33	0.08	27.86	99.96	0.05	0.09	Surface
el 6 bse 7 sp 3	0.46	0.00	0.17	b.d	0.03	b.d	0.04	b.d	72.14	0.09	28.19	101.10	0.04	0.09	Surface
el 6 bse 7 sp 4	0.51	0.00	0.18	b.d	0.04	b.d	0.04	b.d	72.07	0.08	28.22	101.13	0.04	0.09	Surface
el 6 bse 7 sp 5	0.52	0.00	0.24	b.d	0.06	b.d	0.03	b.d	71.83	0.09	28.20	100.98	0.04	0.09	Surface
el 6 bse 7 sp 6	0.46	0.00	0.14	b.d	0.03	b.d	0.03	b.d	72.12	0.07	28.15	101.01	0.04	0.08	Surface
el 6 bse 7 sp 7	0.49	0.00	0.22	b.d	0.05	b.d	0.03	b.d	71.88	0.09	28.17	100.94	0.03	0.09	Surface
el 6 bse 7 sp 8	0.52	0.01	0.22	b.d	0.04	b.d	0.03	b.d	71.92	0.08	28.21	101.03	0.03	0.09	Surface
el 6 bse 7 sp 9	0.51	0.00	0.22	b.d	0.05	b.d	0.03	b.d	71.53	0.09	28.05	100.49	0.03	0.09	Surface
el 6 bse 7 sp 10	0.47	0.01	0.21	b.d	0.05	b.d	0.03	b.d	71.61	0.09	28.04	100.49	0.03	0.10	Surface
el 3a bse 2 transect 1 sp 1	0.05	0.03	0.15	b.d	0.07	0.03	0.08	b.d	68.88	b.d	26.65	95.93	0.09	0.03	Surface
el 3a bse 2 transect 1 sp 2	0.01	0.03	0.11	b.d	0.02	0.02	0.09	b.d	69.34	b.d	26.73	96.34	0.09	0.03	Surface
el 3a bse 2 transect 1 sp 3	0.06	0.03	0.22	b.d	0.04	b.d	0.08	b.d	69.48	b.d	26.91	96.83	0.09	0.03	Surface
el 3a bse 2 transect 2 sp 1	0.02	0.03	0.04	b.d	b.d	0.06	0.09	b.d	69.67	b.d	26.88	96.80	0.10	0.04	Surface
el 3a bse 2 transect 2 sp 2	b.d	0.03	0.06	b.d	b.d	b.d	0.10	b.d	70.02	b.d	26.96	97.17	0.11	0.03	Surface
el 3a bse 2 transect 2 sp 3	0.05	0.05	1.31	0.02	b.d	0.04	0.14	b.d	68.11	b.d	27.26	96.97	0.16	0.05	Surface
el 3a bse 2 transect 2 sp 4	0.10	0.03	0.14	b.d	b.d	0.05	0.10	b.d	69.55	b.d	26.96	96.92	0.11	0.04	Surface
el 3a bse 2 transect 2 sp 5	0.10	0.03	0.04	b.d	b.d	0.02	0.09	b.d	70.54	b.d	27.22	98.04	0.09	0.04	Surface
el 3a bse 2 transect 2 sp 6	0.15	0.03	0.09	b.d	b.d	b.d	0.08	b.d	72.39	b.d	27.99	100.72	0.08	0.03	Surface
el 3a bse 2 transect 2 sp 7	0.08	0.03	0.10	b.d	0.01	b.d	0.08	b.d	72.28	b.d	27.89	100.48	0.08	0.04	Surface
el 3a bse 2 transect 2 sp 8	0.04	0.04	0.10	0.01	0.01	b.d	0.08	b.d	72.41	b.d	27.91	100.61	0.10	0.05	Surface
el 3a bse 3 transect sp 1	0.02	0.03	0.26	b.d	0.05	0.10	0.08	b.d	68.81	b.d	26.76	96.10	0.08	0.03	Surface
el 3a bse 3 transect sp 2	0.01	0.03	0.05	b.d	0.01	0.04	0.09	b.d	69.44	b.d	26.76	96.44	0.09	0.04	Surface
el 3a bse 3 transect sp 3	b.d	0.04	0.44	0.01	b.d	0.05	0.11	b.d	69.16	b.d	26.98	96.79	0.13	0.04	Surface
el 3a bse 3 transect sp 4	b.d	0.05	2.69	b.d	b.d	0.05	0.15	b.d	65.64	b.d	27.37	95.96	0.16	0.05	Surface
el 3a bse 3 transect sp 5	b.d	0.03	0.04	b.d	b.d	0.01	0.09	b.d	70.00	b.d	26.94	97.12	0.09	0.04	Surface
el 3a bse 3 transect sp 6	0.02	0.03	0.17	0.01	0.02	0.12	0.08	b.d	69.17	b.d	26.85	96.48	0.10	0.04	Surface
el 3a bse 4 sp 1	0.02	0.02	0.10	0.02	0.04	0.06	0.08	b.d	70.19	b.d	27.11	97.65	0.11	0.03	Surface
el 3a bse 4 sp 2	0.04	0.02	0.17	0.02	0.06	0.07	0.08	b.d	69.61	b.d	26.98	97.05	0.10	0.03	Surface
el 3a bse 4 sp 3	0.04	0.03	0.09	0.02	0.03	0.04	0.08	b.d	70.40	b.d	27.18	97.92	0.10	0.03	Surface
el 3a bse 4 sp 4	b.d	0.02	0.05	0.01	b.d	0.09	0.08	b.d	70.17	b.d	27.08	97.50	0.09	0.02	Surface
el 3a bse 4 sp 5	b.d	0.02	0.03	0.01	b.d	0.01	0.08	b.d	71.35	b.d	27.42	98.92	0.09	0.02	Surface
el 3a bse 5 sp 1	0.52	0.04	0.36	0.01	0.02	b.d	0.09	b.d	71.07	b.d	28.03	100.14	0.10	0.05	Surface
el 3a bse 5 sp 2	0.67	0.06	0.78	0.01	0.20	b.d	0.09	b.d	69.73	b.d	28.07	99.61	0.10	0.06	Surface
el 3a bse 5 sp 3	0.42	0.05	0.19	b.d	0.01	b.d	0.09	b.d	71.39	b.d	27.94	100.09	0.10	0.06	Surface
el 3a bse 5 sp 4	0.54	0.06	0.41	0.01	0.15	b.d	0.10	b.d	70.63	b.d	28.01	99.92	0.12	0.06	Surface
el 3a bse 5 sp 5	0.47	0.06	0.26	0.01	0.05	b.d	0.10	b.d	71.21	b.d	28.00	100.17	0.11	0.07	Surface
el 3a bse 6 sp 1	0.57	0.06	0.58	0.01	0.21	0.05	0.12	b.d	68.66	0.08	27.48	97.82	0.13	0.14	Surface
el 3a bse 6 sp 2	0.56	0.05	0.57	b.d	0.15	0.05	0.11	b.d	68.33	0.07	27.31	97.21	0.12	0.13	Surface
el 3a bse 6 sp 3	0.66	0.06	0.64	0.01	0.22	0.03	0.11	b.d	69.22	0.08	27.79	98.82	0.12	0.14	Surface
el 3a bse 6 sp 4	0.69	0.06	0.68	0.01	0.26	0.05	0.11	b.d	68.46	0.07	27.61	98.00	0.12	0.13	Surface
el 3a bse 6 sp 5	0.64	0.06	0.77	0.01	0.23	0.02	0.11	b.d	68.82	0.08	27.73	98.48	0.12	0.14	Surface
el 3a bse 6 sp 6	0.64	0.05	0.60	b.d	0.14	0.07	0.11	b.d	68.97	0.08	27.66	98.33	0.12	0.13	Surface
el 3a bse 6 sp 7	0.57	0.05	0.94	b.d	0.09	0.02	0.11	b.d	68.72	0.08	27.68	98.27	0.11	0.13	Surface
el 3a bse 6 sp 8	0.56	0.05	0.33	b.d	0.26	0.07	0.11	b.d	68.28	0.07	27.18	96.91	0.12	0.12	Surface
el 3a bse 7 sp 1	0.30	0.03	0.01	b.d	b.d	b.d	0.08	b.d	72.04	b.d	27.93	100.38	0.09	0.03	Surface
el 3a bse 7 sp 2	0.41	0.03	0.24	b.d	0.09	b.d	0.08	b.d	71.23	b.d	27.93	100.02	0.08	0.03	Surface

Sample ID Laco Sur	Mg [wt%]	Al [wt%]	Si [wt%]	Ti [wt%]	Ca [wt%]	P [wt%]	V [wt%]	Cr [wt%]	Fe [wt%]	Mn [wt%]	O [wt%]	Total	Ti+V [wt%]	Al+Mn [wt%]	Sample
el 3a bse 7 sp 3	0.41	0.03	0.22	b.d	0.07	b.d	0.08	b.d	71.36	b.d	27.95	100.12	0.08	0.03	Surface
el 3a bse 7 sp 4	0.29	0.04	0.08	b.d	b.d	b.d	0.08	b.d	71.55	b.d	27.80	99.83	0.09	0.04	Surface
el 3a bse 7 sp 5	0.49	0.03	0.36	b.d	0.05	b.d	0.08	b.d	71.18	b.d	28.05	100.25	0.09	0.03	Surface
el 3a bse 7 sp 6	0.59	0.03	0.48	b.d	0.15	0.02	0.08	b.d	70.00	b.d	27.83	99.17	0.09	0.03	Surface
el 3a bse 7 sp 7	0.45	0.03	0.35	b.d	0.14	b.d	0.08	b.d	71.10	b.d	28.02	100.18	0.09	0.03	Surface
el 3a bse 7 sp 8	0.43	0.03	0.23	b.d	0.03	b.d	0.08	b.d	71.48	b.d	28.01	100.29	0.09	0.03	Surface
el 3a bse 7 sp 1 high z	0.36	0.02	0.01	b.d	b.d	b.d	0.08	b.d	71.84	b.d	27.91	100.23	0.09	0.02	Surface
el 3a bse 8 sp 1	0.69	0.03	0.68	b.d	0.17	b.d	0.09	b.d	69.71	0.02	27.94	99.31	0.09	0.05	Surface
el 3a bse 8 sp 2	0.73	0.03	0.72	b.d	0.24	0.01	0.08	b.d	69.28	0.02	27.88	99.00	0.09	0.05	Surface
el 3a bse 8 sp 3	0.56	0.02	0.38	b.d	0.16	0.02	0.09	b.d	68.91	0.02	27.29	97.44	0.09	0.05	Surface
el 3a bse 8 sp 4	0.51	0.03	0.29	b.d	0.10	b.d	0.08	b.d	70.81	b.d	27.90	99.73	0.09	0.03	Surface
el 3a bse 8 sp 5	0.46	0.03	0.15	b.d	0.02	b.d	0.08	b.d	71.24	0.02	27.84	99.85	0.09	0.05	Surface
el 3a bse 8 sp 6	0.87	0.03	1.07	0.01	0.36	0.02	0.08	b.d	68.44	0.03	28.01	98.93	0.09	0.06	Surface
el 3a bse 8 sp 7	0.53	0.02	0.42	b.d	0.09	0.01	0.08	b.d	68.11	0.03	26.95	96.25	0.09	0.05	Surface
el 3a bse 8 sp 8	0.49	0.03	0.47	b.d	0.37	0.02	0.08	b.d	68.96	0.02	27.43	97.87	0.08	0.05	Surface
el 3a bse 8 sp 9	0.58	0.03	0.76	b.d	0.25	0.03	0.08	b.d	68.19	b.d	27.42	97.35	0.09	0.03	Surface
el 3a bse 9 sp 1	0.37	0.02	0.21	b.d	0.05	b.d	0.08	b.d	71.19	b.d	27.83	99.76	0.08	0.03	Surface
el 3a bse 9 sp 2	0.82	0.03	1.06	b.d	0.29	0.01	0.08	b.d	68.94	b.d	28.14	99.38	0.08	0.04	Surface
el 3a bse 9 sp 3	0.70	0.03	1.08	b.d	0.32	0.02	0.08	b.d	68.45	0.02	27.87	98.58	0.08	0.05	Surface
el 3a bse 9 sp 4	0.35	0.02	0.01	b.d	0.01	b.d	0.09	b.d	71.35	b.d	27.70	99.54	0.09	0.03	Surface
el 3a bse 9 sp 5	0.35	0.02	0.13	b.d	0.05	b.d	0.08	b.d	70.94	b.d	27.66	99.24	0.08	0.03	Surface
el 3a bse 9 sp 6	0.50	0.03	0.63	b.d	0.22	0.03	0.08	b.d	68.01	b.d	27.17	96.69	0.08	0.03	Surface
el 3a bse 9 sp 7	0.61	0.03	0.89	b.d	0.21	0.02	0.08	b.d	68.54	b.d	27.65	98.03	0.08	0.04	Surface
el 3a bse 9 sp 8	0.60	0.03	0.59	b.d	0.14	b.d	0.08	b.d	70.38	b.d	28.05	99.86	0.08	0.03	Surface
el 3a bse11 transect sp 1	0.40	0.03	0.30	0.01	0.07	b.d	0.09	b.d	71.20	b.d	27.95	100.06	0.10	0.04	Surface
el 3a bse11 transect sp 2	0.53	0.04	0.51	b.d	0.15	0.01	0.09	b.d	69.60	0.03	27.64	98.60	0.10	0.07	Surface
el 3a bse11 transect sp 3	0.51	0.05	0.43	0.01	0.12	b.d	0.09	b.d	70.56	b.d	27.93	99.69	0.10	0.05	Surface
el 3a bse11 transect sp 4	0.72	0.05	1.07	0.02	0.34	0.02	0.09	b.d	69.18	0.02	28.17	99.68	0.11	0.07	Surface
el 3a bse11 transect sp 5	0.80	0.05	1.13	0.01	0.35	0.02	0.09	b.d	68.81	0.03	28.15	99.42	0.10	0.08	Surface
el 3a bse11 transect sp 6	0.72	0.05	1.03	0.01	0.34	0.01	0.09	b.d	68.97	0.02	28.06	99.31	0.10	0.07	Surface
el 3a bse11 transect sp 7	0.65	0.04	0.78	0.01	0.19	b.d	0.09	b.d	69.62	b.d	27.99	99.36	0.10	0.05	Surface
el 7 bse 2 spot 1	0.89	0.00	0.71	b.d	0.26	b.d	0.07	b.d	68.47	0.09	27.72	98.23	0.07	0.10	Surface
el 7 bse 2 spot 4	0.86	0.01	0.72	b.d	0.27	b.d	0.07	b.d	68.84	0.10	27.85	98.73	0.08	0.11	Surface
el 15 bse 1 sp 1	0.75	0.24	0.60	0.04	0.17	b.d	0.10	b.d	69.38	0.04	28.00	99.32	0.15	0.28	Surface
el 15 bse 1 sp 2	0.48	0.23	0.10	0.04	0.01	b.d	0.11	b.d	70.49	b.d	27.74	99.20	0.15	0.24	Surface
el 15 bse 1 transect sp 1	0.55	0.28	0.24	0.08	0.06	b.d	0.10	b.d	70.45	0.04	27.95	99.76	0.18	0.32	Surface
el 15 bse 1 transect sp 2	0.42	0.29	0.14	0.07	0.03	b.d	0.11	b.d	70.83	0.05	27.89	99.82	0.18	0.35	Surface
el 15 bse 1 transect sp 3	0.64	0.36	0.33	0.08	0.11	b.d	0.10	b.d	70.19	b.d	28.10	99.92	0.19	0.36	Surface
el 15 bse 1 transect sp 4	b.d	0.27	0.03	0.04	b.d	b.d	0.10	b.d	71.29	b.d	27.63	99.36	0.14	0.28	Surface
el 15 bse 1 transect sp 5	0.46	0.28	0.02	0.05	b.d	b.d	0.11	b.d	71.10	b.d	27.94	99.95	0.16	0.28	Surface
el 15 bse 1 transect 2 sp 1	0.52	0.30	0.07	0.05	b.d	b.d	0.10	b.d	71.06	0.06	28.01	100.16	0.16	0.35	Surface
el 15 bse 1 transect 2 sp 2	0.91	0.31	0.78	0.06	0.17	b.d	0.10	b.d	68.37	0.06	27.96	98.72	0.16	0.37	Surface
el 15 bse 1 transect 2 sp 3	0.61	0.29	0.21	0.06	0.06	b.d	0.10	b.d	70.36	0.06	27.95	99.71	0.16	0.36	Surface
el 15 bse 1 transect 2 sp 4	0.61	0.32	0.29	0.06	0.16	b.d	0.10	0.01	69.73	b.d	27.85	99.13	0.16	0.33	Surface
el 15 bse 1 transect 2 sp 5	0.72	0.30	0.47	0.06	0.16	b.d	0.10	b.d	69.48	0.05	27.96	99.29	0.15	0.35	Surface
el 15 bse 3 transect 1 sp 1	0.35	0.27	0.07	0.06	0.01	b.d	0.10	b.d	70.57	0.04	27.64	99.10	0.16	0.31	Surface
el 15 bse 3 transect 1 sp 2	0.47	0.26	0.02	0.05	0.01	b.d	0.11	b.d	71.29	0.06	27.98	100.23	0.15	0.32	Surface
el 15 bse 3 transect 1 sp 3	0.52	0.30	0.22	0.06	0.07	b.d	0.10	b.d	70.59	0.05	27.98	99.90	0.17	0.35	Surface
el 15 bse 3 transect 1 sp 4	0.52	0.28	0.06	0.05	0.02	b.d	0.11	b.d	70.78	b.d	27.90	99.71	0.16	0.28	Surface
el 15 bse 3 transect 1 sp 5	0.11	0.26	0.04	0.05	b.d	b.d	0.11	0.01	71.19	0.05	27.65	99.48	0.16	0.31	Surface
el 15 bse 3 spot 1	0.41	0.31	0.03	0.06	b.d	b.d	0.10	b.d	70.63	b.d	27.75	99.28	0.16	0.32	Surface
el 15 bse 3 spot 2	0.55	0.26	0.30	0.05	0.13	b.d	0.10	b.d	69.79	b.d	27.76	98.94	0.15	0.26	Surface
el 15 bse 4 transect sp 1	0.49	0.29	0.03	0.04	b.d	b.d	0.10	b.d	71.10	0.10	27.97	100.11	0.14	0.39	Surface
el 15 bse 4 transect sp 2	0.53	0.26	0.07	0.04	0.03	b.d	0.10	b.d	71.06	0.11	28.01	100.20	0.15	0.36	Surface
el 15 bse 4 transect sp 3	0.66	0.28	0.43	0.06	0.21	b.d	0.10	b.d	69.71	0.09	27.99	99.52	0.16	0.37	Surface
el 15 bse 4 transect sp 4	0.71	0.28	0.39	0.05	0.12	b.d	0.10	b.d	70.05	0.09	28.08	99.87	0.15	0.37	Surface
el 15 bse 4 spot 1	0.50	0.26	0.10	0.05	0.03	b.d	0.10	b.d	70.87	0.08	27.93	99.92	0.15	0.34	Surface
el 15 bse 4 spot 2	0.50	0.25	0.02	0.04	b.d	b.d	0.10	b.d	71.15	0.06	27.95	100.07	0.14	0.31	Surface
el 15 bse 5 transect sp 1	0.66	0.18	0.41	0.03	0.14	b.d	0.11	b.d	69.55	b.d	27.80	98.88	0.13	0.19	Surface
el 15 bse 5 transect sp 2	0.23	0.14	0.68	0.01	0.10	b.d	0.11	b.d	68.23	0.05	27.04	96.60	0.12	0.19	Surface
el 15 bse 5 transect sp 3	0.41	0.16	0.09	0.03	b.d	b.d	0.11	b.d	69.50	b.d	27.23	97.52	0.13	0.17	Surface
el 15 bse 5 transect sp 4	0.34	0.15	0.02	0.02	b.d	b.d	0.10	b.d	70.22	b.d	27.38	98.23	0.12	0.16	Surface
el 15 bse 5 transect sp 5	0.54	0.17	0.04	0.02	b.d	b.d	0.10	b.d	70.74	0.05	27.77	99.43	0.12	0.22	Surface
el 15 bse 5 transect sp 6	0.08	0.15	0.21	0.02	0.03	b.d	0.09	b.d	68.69	0.06	26.70	96.03	0.12	0.20	Surface
el 15 bse 5 transect sp 7	0.37	0.16	0.01	0.02	b.d	b.d	0.10	b.d	71.20	b.d	27.78	99.64	0.12	0.16	Surface
el 15 bse 6 transect sp 1	0.47	0.33	0.03	0.08	b.d	b.d	0.10	b.d	70.43	b.d	27.75	99.18	0.18	0.33	Surface
el 15 bse 6 transect sp 2	0.46	0.33	0.07	0.07	b.d	b.d	0.10	b.d	70.32	0.05	27.70	99.10	0.17	0.38	Surface
el 15 bse 6 transect sp 3	0.51	0.29	0.06	0.07	b.d	b.d	0.10	b.d	70.94	b.d	27.96	99.91	0.17	0.29	Surface
el 15 bse 6 transect sp 4	0.39	0.23	0.46	0.07	b.d	b.d	0.09	0.01	69.90	0.05	27.70	98.90	0.16	0.29	Surface
el 15 bse 1 transect sp 1	0.26	0.29	0.02	0.10	0.10	b.d	0.09	b.d	71.45	b.d	27.96	100.26	0.18	0.30	Surface
el 15 bse 1 transect sp 2	0.27	0.30	0.05	0.10	0.08	b.d	0.08	b.d	71.07	0.05	27.82	99.82	0.18	0.35	Surface
el 15 bse 1 transect sp 3	0.24	0.28	0.02	0.08	0.32	0.01	0.07	0.01	70.52	b.d	27.68	99.23	0.15	0.28	Surface
el c - b bse 1 transect sp 1	0.18	0.06	0.13	b.d	0.04	0.02	0.12	b.d	68.19	b.d	26.50	95.22	0.12	0.06	Surface
el c - b bse 1 transect sp 2	0.23	0.06	0.10	b.d	0.03	0.02	0.12	b.d	68.12	b.d	26.49	95.16	0.12	0.06	Surface
el c - b bse 1 transect sp 3	0.23	0.05	0.02	b.d	0.01	b.d	0.12	b.d	71.59	b.d	27.73	99.76	0.12	0.06	Surface
el c - b bse 2 transect sp 1	0.23	0.06	0.08	0.01	0.06	b.d	0.12	b.d	69.14	b.d	26.87	96.57	0.13	0.06	Surface
el c - b bse 2 transect sp 2	0.24	0.05	0.09	b.d	0.11	b.d	0.11	b.d	69.13	b.d	26.91	96.64	0.12	0.06	Surface

Sample ID Laco Sur	Mg [wt%]	Al [wt%]	Si [wt%]	Ti [wt%]	Ca [wt%]	P [wt%]	V [wt%]	Cr [wt%]	Fe [wt%]	Mn [wt%]	O [wt%]	Total	Ti+V [wt%]	Al+Mn [wt%]	Sample
el c - b bse 2 transect sp 3	0.24	0.06	0.13	b.d	0.04	b.d	0.11	b.d	68.65	b.d	26.71	95.93	0.12	0.06	Surface
el c - b bse 2 transect sp 4	0.32	0.05	0.25	0.01	0.02	0.01	0.11	b.d	70.63	b.d	27.61	99.02	0.12	0.06	Surface
el c - b bse 2 transect sp 5	0.19	0.06	0.19	b.d	0.04	b.d	0.11	0.01	68.67	b.d	26.72	95.98	0.11	0.06	Surface
el c - b bse 2 transect sp 6	0.20	0.06	0.16	b.d	0.03	0.03	0.11	b.d	68.35	b.d	26.61	95.55	0.12	0.06	Surface
el c - b bse 2 transect sp 7	0.25	0.06	0.12	b.d	0.03	0.02	0.12	b.d	68.60	b.d	26.70	95.88	0.13	0.06	Surface
el c - b bse 3 transect sp 1	0.14	0.06	0.15	0.01	0.03	0.05	0.11	b.d	68.44	b.d	26.60	95.59	0.12	0.06	Surface
el c - b bse 3 transect sp 2	0.26	0.05	0.06	b.d	0.01	b.d	0.11	b.d	68.92	b.d	26.77	96.19	0.12	0.06	Surface
el c - b bse 3 transect sp 3	0.16	0.06	0.03	b.d	0.01	b.d	0.12	b.d	70.30	b.d	27.19	97.88	0.13	0.06	Surface
el c - b bse 3 transect sp 4	0.16	0.06	0.15	0.01	0.02	b.d	0.11	b.d	68.91	b.d	26.74	96.16	0.12	0.06	Surface
el c - b bse 3 transect sp 5	0.26	0.06	0.11	b.d	0.02	b.d	0.12	b.d	69.81	b.d	27.16	97.53	0.13	0.06	Surface
el c - b bse 3 transect sp 6	0.17	0.06	0.09	b.d	b.d	0.03	0.11	b.d	68.83	b.d	26.70	95.99	0.11	0.06	Surface
el c - b bse 3 transect sp 7	0.18	0.05	0.09	b.d	0.02	0.02	0.11	b.d	68.50	b.d	26.58	95.56	0.12	0.06	Surface
el c - b bse 3 transect sp 8	0.18	0.06	0.20	b.d	0.06	0.03	0.11	b.d	68.74	b.d	26.78	96.15	0.11	0.06	Surface
el c - b bse4 transect sp 1	0.22	0.07	0.14	b.d	0.02	0.01	0.11	b.d	68.03	b.d	26.48	95.09	0.12	0.07	Surface
el c - b bse4 transect sp 2	0.19	0.07	0.23	b.d	0.02	0.03	0.11	b.d	68.53	b.d	26.71	95.88	0.11	0.07	Surface
el c - b bse4 transect sp 3	0.13	0.06	0.17	0.02	0.01	0.02	0.11	b.d	68.34	b.d	26.52	95.38	0.13	0.06	Surface
el c - b bse4 transect sp 4	0.26	0.07	0.24	0.01	0.03	0.01	0.12	b.d	68.39	b.d	26.72	95.84	0.13	0.07	Surface
el c - b bse4 transect sp 5	0.20	0.06	0.12	b.d	0.02	0.02	0.11	b.d	68.60	b.d	26.66	95.80	0.12	0.07	Surface
el c - b bse4 transect sp 6	0.23	0.06	0.08	b.d	0.01	b.d	0.12	0.01	71.08	b.d	27.59	99.17	0.12	0.06	Surface
el 14 bse 5 sp 1	0.33	0.08	0.20	0.01	0.10	b.d	0.10	b.d	69.12	b.d	27.06	97.00	0.11	0.08	Surface
el 14 bse 2 sp 1	0.03	0.01	0.07	b.d	b.d	b.d	0.06	b.d	68.94	b.d	26.53	95.63	0.06	0.01	Surface
el 14 bse 4 sp 7	0.32	0.08	0.04	0.03	b.d	b.d	0.11	b.d	70.26	b.d	27.34	98.18	0.13	0.08	Surface
el 14 bse 5 sp 3	0.40	0.09	0.21	0.02	0.09	b.d	0.10	b.d	71.76	b.d	28.15	100.81	0.13	0.09	Surface
el 14 bse 1 transect 1 mag	0.42	0.03	0.20	b.d	0.10	b.d	0.06	b.d	71.72	0.08	28.10	100.72	0.06	0.12	Surface
el 14 bse 1 transect 1 mag	0.42	0.04	0.15	b.d	0.04	b.d	0.06	b.d	71.56	0.08	27.96	100.31	0.06	0.12	Surface
el 14 bse 1 transect 1 mag	0.46	0.04	0.24	b.d	0.11	b.d	0.06	b.d	71.71	0.09	28.16	100.87	0.06	0.13	Surface
el 14 bse 1 transect 1 mag	0.42	0.03	0.20	b.d	0.12	b.d	0.06	b.d	71.90	0.08	28.17	100.99	0.06	0.11	Surface
el 14 bse 1 transect 1 mag	0.38	0.03	0.06	b.d	0.02	b.d	0.06	b.d	71.64	0.09	27.88	100.17	0.07	0.12	Surface
el 14 bse 1 transect 1 mag	0.44	0.04	0.23	b.d	0.08	b.d	0.06	b.d	71.68	0.09	28.11	100.73	0.06	0.13	Surface
el 14 bse 1 transect 1 mag	0.46	0.03	0.27	b.d	0.11	b.d	0.06	b.d	71.35	0.08	28.04	100.39	0.06	0.12	Surface
el 14 bse 1 transect 1 mag	0.45	0.04	0.29	b.d	0.12	b.d	0.06	b.d	71.49	0.08	28.12	100.65	0.07	0.13	Surface
el 14 bse 1 transect 1 hem	b.d	0.06	0.12	b.d	b.d	b.d	0.01	b.d	69.18	b.d	26.68	96.06	0.02	0.07	Surface
el 14 bse 1 transect 1 hem	b.d	0.07	0.13	b.d	b.d	b.d	0.06	b.d	68.40	b.d	26.42	95.08	0.06	0.08	Surface
el 14 bse 1 transect 1 hem	b.d	0.07	0.16	b.d	b.d	b.d	0.08	b.d	68.91	b.d	26.64	95.86	0.08	0.08	Surface
el 14 bse 1 transect 1 hem	0.04	0.08	0.10	b.d	b.d	b.d	0.07	b.d	69.10	b.d	26.68	96.07	0.08	0.08	Surface
el 14 bse 2 transect 1 mag	0.43	0.07	0.33	b.d	0.08	b.d	0.08	b.d	71.05	0.07	27.97	100.09	0.08	0.15	Surface
el 14 bse 2 transect 1 mag	0.47	0.07	0.47	b.d	0.15	b.d	0.08	b.d	70.94	0.07	28.10	100.35	0.09	0.14	Surface
el 14 bse 2 transect 1 mag	0.47	0.05	0.54	b.d	0.13	b.d	0.07	b.d	70.50	0.06	27.95	99.78	0.08	0.11	Surface
el 14 bse 2 transect 1 mag	0.44	0.04	0.50	b.d	0.18	b.d	0.08	b.d	71.04	0.08	28.12	100.47	0.08	0.12	Surface
el 14 bse 2 transect 1 mag	0.52	0.03	0.57	b.d	0.16	b.d	0.07	b.d	70.49	0.07	28.01	99.92	0.07	0.09	Surface
el 14 bse 2 transect 1 mag	0.41	0.04	0.43	b.d	0.18	b.d	0.07	b.d	71.39	0.07	28.18	100.77	0.08	0.11	Surface
el 14 bse 2 transect 1 mag	0.50	0.00	0.56	b.d	0.18	b.d	0.07	b.d	70.73	0.06	28.06	100.17	0.07	0.06	Surface
el 14 bse 2 transect 1 mag	0.25	0.00	0.26	b.d	0.09	b.d	0.07	b.d	70.71	0.07	27.57	99.03	0.08	0.07	Surface
el 14 bse 2 transect 1 mag	0.46	0.00	0.35	b.d	0.14	b.d	0.07	b.d	71.37	0.07	28.10	100.57	0.07	0.08	Surface
el 14 bse 2 transect 1 mag	0.15	0.01	0.19	b.d	0.05	b.d	0.06	b.d	71.13	0.03	27.55	99.18	0.07	0.05	Surface
el 14 bse 2 sp 2	b.d	0.02	0.08	b.d	b.d	b.d	0.06	b.d	69.22	b.d	26.65	96.03	0.07	0.02	Surface
el 14 bse 2 sp 3	0.01	0.03	0.09	b.d	b.d	b.d	0.06	b.d	68.70	b.d	26.46	95.35	0.07	0.03	Surface
el 14 bse 2 sp 4	0.02	0.04	0.14	b.d	b.d	b.d	0.07	b.d	68.97	b.d	26.62	95.87	0.08	0.05	Surface
el 14 bse 2 sp 5	0.27	0.04	0.03	b.d	b.d	b.d	0.07	b.d	70.97	0.05	27.50	98.93	0.07	0.09	Surface
el 14 bse 3 sp 1	0.45	0.10	0.41	0.01	0.15	b.d	0.09	b.d	70.75	0.02	27.96	99.95	0.10	0.12	Surface
el 14 bse 3 sp 2	0.47	0.10	0.43	b.d	0.12	b.d	0.09	b.d	70.84	0.06	28.04	100.14	0.10	0.16	Surface
el 14 bse 3 sp 3	0.48	0.09	0.48	b.d	0.18	b.d	0.09	b.d	70.71	0.06	28.06	100.15	0.09	0.16	Surface
el 14 bse 3 sp 4	0.46	0.09	0.45	b.d	0.18	b.d	0.09	b.d	70.61	0.06	27.97	99.90	0.09	0.15	Surface
el 14 bse 3 sp 5	0.37	0.09	0.43	b.d	0.15	b.d	0.08	b.d	69.86	0.07	27.59	98.64	0.09	0.16	Surface
el 14 bse 3 sp 6	0.42	0.10	0.33	b.d	0.14	b.d	0.09	b.d	71.23	0.07	28.07	100.44	0.09	0.16	Surface
el 14 bse 4 sp 1	0.31	0.07	0.06	0.02	b.d	b.d	0.10	b.d	68.82	b.d	26.78	96.15	0.12	0.08	Surface
el 14 bse 4 sp 3	0.27	0.08	0.08	0.02	b.d	b.d	0.10	b.d	68.40	b.d	26.61	95.57	0.12	0.08	Surface
el 14 bse 4 sp 4	0.35	0.08	0.29	0.02	0.15	b.d	0.11	b.d	71.27	b.d	28.01	100.29	0.13	0.08	Surface
el 14 bse 4 sp 5	0.17	0.07	0.04	b.d	b.d	0.02	0.10	b.d	69.28	b.d	26.84	96.53	0.10	0.07	Surface
el 14 bse 4 sp 6	0.45	0.09	0.33	0.03	0.07	b.d	0.11	b.d	69.75	b.d	27.51	98.34	0.14	0.09	Surface
el 14 bse 4 sp 9	0.47	0.07	0.36	0.02	0.07	b.d	0.10	b.d	70.76	b.d	27.92	99.76	0.12	0.08	Surface
el 14 bse 4 sp 10	0.48	0.08	0.41	0.02	0.08	b.d	0.10	b.d	71.32	b.d	28.19	100.67	0.12	0.08	Surface
el 14 bse 5 transect 1 sp 1	0.52	0.09	0.62	0.02	0.25	b.d	0.10	b.d	70.35	b.d	28.12	100.07	0.12	0.09	Surface
el 14 bse 5 transect 1 sp 2	0.32	0.07	0.01	0.02	b.d	b.d	0.10	b.d	71.89	b.d	27.93	100.35	0.12	0.08	Surface
el 14 bse 5 transect 1 sp 3	0.31	0.07	0.02	0.02	b.d	b.d	0.10	b.d	71.15	b.d	27.65	99.33	0.12	0.08	Surface
el 14 bse 5 transect 1 sp 4	0.32	0.06	0.01	0.02	0.01	b.d	0.10	b.d	72.04	b.d	27.98	100.55	0.12	0.06	Surface
el 14 bse 5 transect 2 sp 1	0.32	0.03	0.02	0.02	0.06	b.d	0.10	b.d	71.98	b.d	27.96	100.50	0.12	0.04	Surface
el 14 bse 5 transect 2 sp 2	0.33	0.07	0.01	0.02	0.03	b.d	0.10	b.d	71.85	b.d	27.93	100.35	0.12	0.08	Surface
el 14 bse 5 transect 2 sp 3	0.33	0.07	0.01	0.02	0.02	b.d	0.10	b.d	72.20	b.d	28.06	100.82	0.12	0.08	Surface
el 14 bse 5 transect 2 sp 4	0.32	0.07	0.01	0.02	b.d	b.d	0.10	b.d	72.19	b.d	28.05	100.76	0.12	0.08	Surface
el 14 bse 5 transect 2 sp 5	0.32	0.08	0.01	0.02	b.d	b.d	0.10	b.d	72.03	b.d	27.99	100.55	0.12	0.08	Surface
el 14 bse 5 transect 2 sp 6	0.32	0.07	0.01	b.d	b.d	b.d	0.10	b.d	71.78	b.d	27.89	100.18	0.11	0.07	Surface
el 14 bse 5 transect 2 sp 7	0.36	0.10	0.32	0.03	0.08	b.d	0.10	b.d	71.27	b.d	28.01	100.26	0.13	0.10	Surface
el 14 bse 5 transect 2 sp 8	0.14	0.08	0.14	0.02	0.04	b.d	0.10	b.d	69.57	b.d	27.00	97.08	0.12	0.09	Surface
el 14 bse 5 sp 2	0.09	0.07	0.26	0.02	0.05	0.01	0.10	b.d	69.25	b.d	26.93	96.78	0.12	0.07	Surface
el 14 bse 5 sp 4	0.10	0.11	0.35	0.03	0.09	0.03	0.09	b.d	68.70	b.d	26.87	96.38	0.12	0.11	Surface
el 14 high z	0.39	0.00	0.05	b.d	0.02	b.d	0.06	b.d	71.86	0.09	27.93	100.40	0.06	0.09	Surface

Sample ID Laco Sur	Mg [wt%]	Al [wt%]	Si [wt%]	Ti [wt%]	Ca [wt%]	P [wt%]	V [wt%]	Cr [wt%]	Fe [wt%]	Mn [wt%]	O [wt%]	Total	Ti+V [wt%]	Al+Mn [wt%]	Sample
el 14 int z	b.d	0.07	0.20	b.d	b.d	b.d	0.08	b.d	68.76	b.d	26.61	95.73	0.09	0.08	Surface
LS-3B1_spot1_pt1	1.22	0.23	0.80	0.37	0.07	0.02	0.10	b.d	68.99	b.d	28.51	100.31	0.47	0.23	Surface
LS-3B1_spot1_pt2	0.41	0.23	0.03	0.30	b.d	b.d	0.10	b.d	70.67	b.d	27.74	99.48	0.40	0.23	Surface
LS-3B1_spot1_pt3	0.72	0.27	0.18	0.22	0.03	b.d	0.10	b.d	70.69	0.04	28.15	100.39	0.31	0.31	Surface
LS-3B1_spot1_pt4	0.89	0.29	0.46	0.24	0.17	b.d	0.10	b.d	69.77	b.d	28.25	100.18	0.34	0.29	Surface
LS-3B1_spot1_pt5	0.59	0.24	0.02	0.21	b.d	b.d	0.10	b.d	71.18	b.d	28.05	100.38	0.31	0.24	Surface
LS-3B1_spot1_pt6	0.88	0.31	0.48	0.28	0.31	b.d	0.10	b.d	68.72	b.d	27.96	99.05	0.38	0.31	Surface
LS-3B1_spot1_pt7	0.55	0.23	0.02	0.26	b.d	b.d	0.10	b.d	71.02	b.d	27.97	100.15	0.36	0.23	Surface
LS-3B1_spot2_pt1	0.81	0.26	0.34	0.09	0.10	b.d	0.10	b.d	70.20	0.03	28.13	100.05	0.19	0.29	Surface
LS-3B1_spot2_pt2	0.82	0.26	0.34	0.09	0.09	b.d	0.09	b.d	70.37	b.d	28.19	100.26	0.18	0.26	Surface
LS-3B1_spot2_pt3	0.58	0.24	0.02	0.08	b.d	b.d	0.10	b.d	71.04	b.d	27.93	99.99	0.18	0.24	Surface
LS-3B1_spot2_pt4	0.57	0.25	0.01	0.08	b.d	b.d	0.10	b.d	71.45	b.d	28.08	100.55	0.19	0.25	Surface
LS-3B1_spot2_pt5	0.56	0.26	0.02	0.09	b.d	b.d	0.10	b.d	71.28	b.d	28.02	100.32	0.18	0.26	Surface
LS-3B1_spot3_pt1	0.62	0.26	0.03	0.05	0.03	b.d	0.10	b.d	70.71	b.d	27.86	99.65	0.15	0.26	Surface
LS-3B1_spot3_pt2	0.62	0.28	0.02	0.05	b.d	b.d	0.10	b.d	71.42	0.03	28.13	100.65	0.15	0.31	Surface
LS-3B1_spot3_pt3	0.61	0.28	0.02	0.05	b.d	b.d	0.10	b.d	71.13	b.d	28.01	100.20	0.15	0.28	Surface
LS-3B1_spot3_pt4	0.86	0.28	0.55	0.05	0.18	b.d	0.10	b.d	69.93	0.03	28.27	100.25	0.14	0.32	Surface
LS-3B1_spot3_pt5	0.62	0.25	0.02	0.05	0.04	b.d	0.10	b.d	71.11	b.d	28.00	100.17	0.15	0.25	Surface
LS-3B1_spot3_pt6	0.66	0.28	0.05	0.05	0.07	b.d	0.10	b.d	70.78	b.d	27.98	99.97	0.15	0.28	Surface
LS-3B1_spot3_pt7	0.60	0.26	0.02	0.05	b.d	b.d	0.11	b.d	71.07	b.d	27.95	100.05	0.16	0.26	Surface
LS-3B1_spot4_pt1	0.63	0.28	0.07	0.05	0.04	b.d	0.10	b.d	70.94	b.d	28.01	100.12	0.15	0.28	Surface
LS-3B1_spot4_pt2	0.60	0.26	0.02	0.05	b.d	b.d	0.10	b.d	71.30	0.03	28.05	100.41	0.15	0.28	Surface
LS-3B1_spot4_pt3	0.61	0.30	0.08	0.06	0.02	b.d	0.10	b.d	71.03	b.d	28.04	100.24	0.16	0.30	Surface
LS-3B1_spot5_pt1	0.96	0.28	0.52	0.06	0.09	b.d	0.10	b.d	70.25	0.03	28.42	100.71	0.16	0.31	Surface
LS-3B1_spot5_pt2	0.60	0.26	0.01	0.05	b.d	b.d	0.10	b.d	71.37	0.04	28.07	100.50	0.15	0.29	Surface
LS-3B1_spot5_pt3	0.89	0.29	0.50	0.06	0.18	b.d	0.11	b.d	70.04	b.d	28.31	100.37	0.16	0.29	Surface
LS-3B1_spot5_pt4	0.61	0.27	0.01	0.06	b.d	b.d	0.10	b.d	71.19	b.d	28.03	100.28	0.16	0.27	Surface
LS-3B1_spot5_pt5	0.76	0.37	0.33	0.07	0.04	b.d	0.10	b.d	70.29	0.04	28.17	100.18	0.17	0.41	Surface
LS-3B1_spot5_pt6	0.71	0.31	0.03	0.07	b.d	b.d	0.10	b.d	70.94	b.d	28.06	100.23	0.17	0.31	Surface
LS-3B1_spot5_pt7	1.29	0.32	1.21	0.07	0.40	0.01	0.10	b.d	67.92	0.03	28.56	99.90	0.17	0.35	Surface
LCO2-02_spot_3_pt_1	0.82	0.09	0.15	0.04	0.01	b.d	0.22	b.d	70.38	b.d	27.91	99.63	0.27	0.09	Drill core
LCO2-02_spot_3_pt_2	0.74	0.10	0.01	0.05	b.d	b.d	0.23	0.01	70.99	b.d	27.97	100.10	0.28	0.10	Drill core
LCO2-02_spot_3_pt_3	0.74	0.10	0.01	0.06	b.d	b.d	0.22	b.d	71.05	b.d	28.00	100.19	0.27	0.10	Drill core
LCO2-02_spot_3_pt_4	0.71	0.09	0.01	0.06	b.d	b.d	0.22	b.d	70.86	b.d	27.88	99.82	0.27	0.09	Drill core
LCO2-02_spot_3_pt_6	0.76	0.11	0.07	0.06	0.01	b.d	0.22	0.01	70.80	0.03	27.99	100.06	0.28	0.14	Drill core
LCO2-02_spot_3_pt_5	1.03	0.12	0.57	0.06	0.21	b.d	0.23	b.d	69.38	b.d	28.16	99.76	0.29	0.12	Drill core
LCO2-02_spot_4_pt_1	1.31	0.07	1.06	0.03	0.35	0.01	0.21	b.d	68.36	b.d	28.43	99.82	0.24	0.07	Drill core
LCO2-02_spot_4_pt_2	1.01	0.07	0.49	0.04	0.13	b.d	0.20	0.01	69.85	b.d	28.17	99.96	0.24	0.07	Drill core
LCO2-02_spot_4_pt_3	0.73	0.06	0.04	0.03	0.01	b.d	0.21	b.d	70.91	b.d	27.91	99.89	0.23	0.06	Drill core
LCO2-02_spot_4_pt_4	0.73	0.05	0.01	0.02	b.d	b.d	0.21	0.01	71.05	b.d	27.94	100.03	0.23	0.05	Drill core
LCO2-02_spot_5_pt_1	0.36	0.04	0.03	0.03	0.01	0.01	0.21	0.01	70.29	b.d	27.36	98.33	0.23	0.04	Drill core
LCO2-02_spot_5_pt_2	0.71	0.04	0.02	0.02	b.d	b.d	0.21	b.d	70.98	b.d	27.88	99.87	0.23	0.04	Drill core
LCO2-02_spot_5_pt_3	0.74	0.05	0.01	0.02	b.d	b.d	0.21	b.d	71.17	b.d	27.98	100.19	0.23	0.05	Drill core
LCO2-02_spot_5_pt_5	0.75	0.05	0.01	0.02	b.d	b.d	0.20	0.01	71.07	b.d	27.94	100.05	0.23	0.05	Drill core
LCO2-02_spot_5_pt_4	0.64	0.05	0.05	0.02	0.01	b.d	0.21	b.d	70.63	b.d	27.72	99.34	0.24	0.05	Drill core
LCO2-02_spot_6_pt_3	1.29	0.07	0.75	0.05	0.11	b.d	0.20	b.d	69.51	0.03	28.49	100.51	0.25	0.10	Drill core
LCO2-02_spot_6_pt_4	0.73	0.04	0.01	0.03	b.d	b.d	0.20	b.d	71.24	b.d	28.00	100.26	0.24	0.04	Drill core
LCO2-02_spot_6_pt_5	0.73	0.04	0.01	0.03	b.d	b.d	0.20	b.d	71.14	b.d	27.95	100.11	0.23	0.04	Drill core
LCO2-02_spot_6_pt_1	0.73	0.04	0.35	0.03	b.d	b.d	0.20	b.d	70.72	b.d	28.05	100.12	0.23	0.04	Drill core
LCO2-02_spot_6_pt_2	0.74	0.05	0.01	0.04	b.d	b.d	0.20	b.d	71.04	b.d	27.94	100.02	0.24	0.05	Drill core
LCO2-02_spot_1_pt_5	0.67	0.09	0.01	0.04	b.d	b.d	0.20	0.01	71.06	0.03	27.93	100.05	0.24	0.12	Drill core
LCO2-02_spot_1_pt_4	0.73	0.09	0.01	0.04	b.d	b.d	0.20	0.01	70.99	0.03	27.95	100.05	0.24	0.13	Drill core
LCO2-02_spot_1_pt_3	0.72	0.08	0.01	0.03	b.d	b.d	0.19	b.d	70.94	b.d	27.89	99.87	0.23	0.08	Drill core
LCO2-02_spot_1_pt_2	0.70	0.07	0.02	0.03	b.d	b.d	0.18	b.d	71.99	0.03	28.28	101.29	0.20	0.10	Drill core
LCO2-02_spot_1_pt_1	0.58	0.07	0.06	0.03	b.d	b.d	0.17	b.d	71.02	b.d	27.83	99.78	0.21	0.07	Drill core
LCO2-02_spot_2_pt_4	0.72	0.07	0.02	0.03	b.d	b.d	0.22	0.01	71.00	b.d	27.92	99.98	0.24	0.07	Drill core
LCO2-02_spot_2_pt_3	1.32	0.08	1.11	0.03	0.33	b.d	0.21	b.d	68.20	b.d	28.39	99.67	0.24	0.08	Drill core
LCO2-02_spot_2_pt_2	0.74	0.08	0.05	0.02	b.d	b.d	0.22	b.d	71.27	b.d	28.07	100.44	0.24	0.08	Drill core
LCO2-02_spot_2_pt_1	1.33	0.09	1.03	0.03	0.30	b.d	0.21	b.d	68.50	b.d	28.45	99.94	0.24	0.09	Drill core
LCO2-02_spot_2_pt_6	0.74	0.07	0.01	0.02	b.d	b.d	0.21	b.d	71.14	b.d	27.99	100.19	0.24	0.07	Drill core
LCO2-02_spot_2_pt_5	1.48	0.08	1.37	0.03	0.45	0.01	0.21	b.d	67.61	b.d	28.61	99.85	0.24	0.08	Drill core
LCO2-06_spot1_pt1	0.25	0.29	0.02	0.35	b.d	b.d	0.23	0.01	71.12	0.04	27.91	100.23	0.58	0.33	Drill core
LCO2-06_spot1_pt2	0.18	0.27	0.02	0.35	b.d	b.d	0.24	0.02	71.03	0.04	27.80	99.96	0.59	0.31	Drill core
LCO2-06_spot1_pt3	0.17	0.24	0.02	0.42	b.d	b.d	0.25	0.02	71.14	b.d	27.82	100.06	0.66	0.24	Drill core
LCO2-06_spot2_pt1	0.09	0.26	0.02	0.30	0.01	b.d	0.26	0.01	71.40	b.d	27.82	100.18	0.56	0.26	Drill core
LCO2-06_spot2_pt2	0.11	0.25	0.02	0.30	b.d	b.d	0.25	0.01	71.10	b.d	27.71	99.75	0.55	0.25	Drill core
LCO2-06_spot3_pt1	0.09	0.29	0.02	0.47	b.d	b.d	0.26	0.01	70.76	0.04	27.69	99.64	0.74	0.33	Drill core
LCO2-06_spot3_pt2	0.19	0.25	0.02	0.36	0.01	b.d	0.26	0.01	70.88	b.d	27.73	99.72	0.63	0.25	Drill core
LCO2-06_spot3_pt3	0.12	0.26	0.03	0.32	0.02	b.d	0.26	0.01	71.36	b.d	27.86	100.24	0.58	0.26	Drill core
LCO2-06_spot4_pt1	0.16	0.25	0.02	0.39	b.d	b.d	0.23	0.01	70.85	b.d	27.68	99.57	0.61	0.25	Drill core
LCO2-06_spot4_pt2	0.14	0.33	0.05	0.33	0.01	b.d	0.22	b.d	70.62	b.d	27.64	99.34	0.55	0.33	Drill core
LCO2-06_spot6_pt1	0.70	0.14	b.d	0.15	b.d	b.d	0.49	0.01	70.92	0.04	28.10	100.55	0.63	0.18	Drill core
LCO2-06_spot6_pt2	0.73	0.15	b.d	0.20	b.d	b.d	0.38	0.01	70.57	0.04	27.98	100.06	0.57	0.19	Drill core
LCO2-06_spot6_pt3	0.36	0.17	0.02	0.29	b.d	b.d	0.21	0.01	71.19	0.04	27.89	100.18	0.51	0.21	Drill core
LCO2-06_spot7_pt1	0.88	0.21	0.02	0.34	b.d	b.d	0.27	0.01	70.47	0.05	28.15	100.39	0.61	0.26	Drill core
LCO2-06_spot7_pt2	0.46	0.22	0.01	0.34	b.d	b.d	0.27	0.01	70.96	0.05	27.98	100.31	0.61	0.27	Drill core
LCO2-06_spot7_pt3	0.13	0.24	0.01	0.39	0.01	b.d	0.22	b.d	70.83	0.04	27.65	99.53	0.62	0.28	Drill core

Sample ID Laco Sur	Mg [wt%]	Al [wt%]	Si [wt%]	Ti [wt%]	Ca [wt%]	P [wt%]	V [wt%]	Cr [wt%]	Fe [wt%]	Mn [wt%]	O [wt%]	Total	Ti+V [wt%]	Al+Mn [wt%]	Sample
LCO2-06_spot5_pt1	0.54	0.22	0.02	0.43	b.d	b.d	0.27	0.01	70.45	0.06	27.90	99.90	0.70	0.28	Drill core
LCO2-06_spot5_pt2	0.52	0.20	0.02	0.33	b.d	b.d	0.27	0.01	71.07	0.06	28.06	100.54	0.60	0.26	Drill core
LCO2-06_spot5_pt3	0.28	0.27	0.05	0.40	b.d	b.d	0.30	0.01	70.68	0.04	27.81	99.84	0.71	0.30	Drill core
LCO2-07_spot1_pt1	0.46	0.42	0.02	0.44	b.d	b.d	0.32	0.02	69.87	0.04	27.79	99.39	0.76	0.46	Drill core
LCO2-07_spot1_pt2	0.87	0.37	0.33	1.36	0.08	b.d	0.31	0.01	67.43	0.07	27.87	98.69	1.67	0.44	Drill core
LCO2-07_spot1_pt3	0.60	0.31	0.03	0.40	b.d	b.d	0.32	0.01	69.79	0.05	27.79	99.30	0.72	0.37	Drill core
LCO2-07_spot1_pt4	0.57	0.35	0.01	0.43	0.12	b.d	0.30	0.01	69.10	0.05	27.58	98.52	0.73	0.39	Drill core
LCO2-07_spot1_pt5	0.78	0.30	0.02	0.42	b.d	b.d	0.29	0.01	68.95	0.05	27.60	98.41	0.70	0.35	Drill core
LCO2-07_spot2_pt1	0.51	0.31	0.16	0.49	0.02	b.d	0.25	0.01	70.10	0.08	27.95	99.87	0.74	0.39	Drill core
LCO2-07_spot2_pt2	0.51	0.27	0.19	0.33	0.01	b.d	0.23	0.01	70.28	0.06	27.93	99.82	0.55	0.34	Drill core
LCO2-07_spot2_pt3	0.49	0.35	0.69	0.50	0.26	b.d	0.21	b.d	68.71	0.04	27.94	99.20	0.71	0.39	Drill core
LCO2-07_spot2_pt4	0.23	0.17	0.05	0.33	0.05	b.d	0.20	b.d	70.99	0.03	27.76	99.82	0.54	0.20	Drill core
LCO2-07_spot3_pt1	0.64	0.33	0.20	0.46	0.05	b.d	0.28	0.01	69.94	0.09	28.08	100.08	0.74	0.42	Drill core
LCO2-07_spot3_pt2	0.39	0.24	0.01	0.41	0.06	b.d	0.25	0.01	70.01	0.06	27.63	99.08	0.66	0.29	Drill core
LCO2-07_spot3_pt3	0.22	0.17	0.02	0.43	0.11	b.d	0.22	0.01	69.71	0.06	27.33	98.28	0.66	0.23	Drill core
LCO2-07_spot4_pt1	1.03	0.32	0.86	0.36	0.80	b.d	0.26	b.d	68.52	0.10	28.71	100.95	0.62	0.41	Drill core
LCO2-07_spot4_pt2	0.50	0.20	0.01	0.33	0.01	b.d	0.24	0.01	70.33	0.08	27.75	99.46	0.57	0.27	Drill core
LCO2-07_spot4_pt3	0.57	0.24	0.02	0.42	b.d	b.d	0.24	b.d	70.73	0.12	28.05	100.38	0.66	0.36	Drill core
LCO2-07_spot4_pt4	0.52	0.26	0.54	0.39	0.28	b.d	0.22	b.d	69.46	0.05	28.03	99.74	0.61	0.30	Drill core
LCO2-07_spot4_pt5	0.11	0.24	0.13	0.35	0.13	b.d	0.22	b.d	70.49	0.03	27.64	99.34	0.57	0.27	Drill core
LCO2-07_spot4_pt6	0.69	0.26	0.01	0.37	b.d	b.d	0.28	0.01	70.57	0.08	28.09	100.37	0.65	0.34	Drill core
LCO2-07_spot4_pt7	0.65	0.24	0.29	0.41	0.09	b.d	0.26	0.01	69.43	0.07	27.87	99.32	0.66	0.31	Drill core
LCO2-07_spot4_pt8	0.16	0.21	0.01	0.37	0.10	b.d	0.23	b.d	71.21	0.04	27.84	100.16	0.60	0.25	Drill core
LCO2-07_spot5_pt1	0.74	0.25	0.01	0.33	b.d	b.d	0.28	0.01	69.97	0.07	27.88	99.55	0.61	0.32	Drill core
LCO2-07_spot5_pt2	0.60	0.25	0.23	0.51	0.12	b.d	0.25	b.d	69.66	0.07	27.94	99.64	0.75	0.33	Drill core
LCO2-07_spot5_pt3	0.60	0.49	0.93	0.56	0.29	b.d	0.30	0.01	67.86	0.04	28.10	99.19	0.86	0.53	Drill core
LCO2-07_spot5_pt4	0.38	0.29	0.06	0.44	b.d	b.d	0.30	0.01	70.51	0.05	27.88	99.92	0.74	0.34	Drill core
LCO2-07_spot6_pt1	0.79	0.31	0.01	0.39	b.d	b.d	0.29	0.01	69.54	0.06	27.83	99.23	0.68	0.37	Drill core
LCO2-07_spot6_pt2	0.09	0.16	0.01	0.29	0.01	b.d	0.19	b.d	70.06	b.d	27.20	98.02	0.48	0.16	Drill core
LCO2-07_spot6_pt3	0.59	0.37	0.03	0.46	b.d	b.d	0.32	0.01	69.75	0.06	27.83	99.41	0.77	0.43	Drill core
LCO2-07_spot6_pt4	0.75	0.40	0.43	0.40	0.12	b.d	0.31	0.01	68.36	0.05	27.80	98.62	0.72	0.45	Drill core
LCO2-07_spot6_pt5	0.76	0.41	0.01	0.67	b.d	b.d	0.32	0.01	69.06	0.09	27.86	99.20	0.99	0.50	Drill core
LCO2-07_spot6_pt6	0.40	0.37	0.15	0.55	0.05	b.d	0.32	0.01	70.10	0.05	27.96	99.96	0.87	0.42	Drill core
LCO2-07_spot6_pt7	0.96	0.48	0.97	0.67	0.34	b.d	0.31	0.01	66.60	0.07	28.05	98.47	0.99	0.55	Drill core
LCO3_10_spot3_pt1	0.42	0.25	0.02	0.11	b.d	b.d	0.29	0.01	71.45	b.d	28.05	100.60	0.40	0.25	Drill core
LCO3_10_spot3_pt2	1.07	0.61	1.13	0.71	0.31	b.d	0.30	0.01	67.18	b.d	28.55	99.86	1.01	0.61	Drill core
LCO3_10_spot3_pt3	0.51	0.37	0.22	0.30	0.04	b.d	0.35	0.01	70.26	b.d	28.05	100.13	0.66	0.37	Drill core
LCO3_10_spot4_pt1	0.21	0.40	0.02	0.14	b.d	b.d	0.84	0.04	70.86	b.d	28.01	100.51	0.97	0.40	Drill core
LCO3_10_spot4_pt2	1.60	0.87	2.16	0.92	0.53	b.d	0.50	0.02	63.73	0.05	29.01	99.39	1.42	0.92	Drill core
LCO3_10_spot4_pt3	1.17	0.76	1.56	0.66	0.37	b.d	0.48	0.02	65.66	0.03	28.60	99.30	1.14	0.79	Drill core
LCO3_10_spot4_pt4	0.35	0.30	0.12	0.17	0.02	b.d	0.37	0.01	71.11	b.d	28.04	100.48	0.54	0.30	Drill core
LCO3_10_spot6_pt1	0.39	0.28	0.01	0.12	b.d	b.d	0.24	b.d	71.44	b.d	28.02	100.50	0.36	0.28	Drill core
LCO3_10_spot6_pt2	0.88	0.65	0.77	0.71	0.16	b.d	0.24	0.01	67.97	b.d	28.33	99.71	0.94	0.65	Drill core
LCO3_10_spot6_pt3	0.11	0.40	0.17	0.14	0.03	b.d	0.27	0.01	70.88	b.d	27.81	99.82	0.41	0.40	Drill core
LCO3_10_spot7_pt1	0.51	0.38	0.02	0.15	b.d	b.d	0.25	0.01	71.54	0.03	28.27	101.16	0.40	0.41	Drill core
LCO3_10_spot7_pt2	0.87	0.81	0.88	0.38	0.24	b.d	0.30	0.01	68.17	b.d	28.55	100.22	0.68	0.81	Drill core
LCO3_10_spot7_pt3	0.53	0.37	0.19	0.14	0.04	b.d	0.32	0.01	70.29	b.d	27.97	99.87	0.46	0.37	Drill core
LCO3_10_spot2_pt1	0.67	0.58	0.40	0.26	0.05	b.d	0.16	0.01	70.23	b.d	28.38	100.72	0.42	0.58	Drill core
LCO3_10_spot2_pt2	1.14	0.81	1.99	0.38	0.46	b.d	0.30	0.01	65.39	b.d	28.67	99.15	0.68	0.81	Drill core
LCO3_10_spot2_pt3	0.20	0.35	0.13	0.33	0.02	b.d	0.35	0.01	70.73	b.d	27.88	100.00	0.68	0.35	Drill core
LCO3_10_spot2_pt4	0.37	0.59	0.41	0.43	0.06	b.d	0.37	0.01	69.31	b.d	27.96	99.53	0.80	0.59	Drill core
LCO3_10_spot5_pt1	0.62	0.51	0.02	0.22	b.d	b.d	0.29	0.01	71.17	b.d	28.37	101.21	0.51	0.51	Drill core
LCO3_10_spot5_pt2	0.89	0.53	0.86	0.78	0.26	b.d	0.29	0.01	67.83	0.03	28.39	99.87	1.07	0.56	Drill core
LCO3_10_spot5_pt3	0.51	0.24	0.04	0.17	0.02	b.d	0.29	0.01	71.44	b.d	28.17	100.91	0.46	0.24	Drill core
LCO3-13_spot1_pt1	0.42	0.35	0.17	0.19	0.02	0.00	0.27	0.02	70.96	0.00	28.10	100.50	0.46	0.35	Drill core
LCO3-13_spot1_pt2	0.27	0.38	0.09	0.12	0.02	0.00	0.27	0.02	70.82	0.00	27.84	99.84	0.39	0.38	Drill core
LCO3-13_spot2_pt1	0.69	0.62	0.04	0.68	0.00	0.00	0.35	0.02	70.13	0.00	28.37	100.90	1.04	0.62	Drill core
LCO3-13_spot2_pt2	0.53	0.30	0.04	0.16	0.00	0.00	0.36	0.03	70.80	0.00	28.01	100.23	0.52	0.30	Drill core
LCO3-13_spot3_pt1	0.58	0.35	0.14	0.21	0.02	0.00	0.28	0.01	70.43	0.00	28.03	100.06	0.50	0.35	Drill core
LCO3-13_spot3_pt2	0.46	0.24	0.12	0.12	0.02	0.00	0.27	0.03	70.76	0.00	27.91	99.93	0.39	0.24	Drill core
LCO3-13_spot5_pt1	0.62	0.40	0.03	0.36	0.00	0.00	0.32	0.01	70.32	0.00	28.05	100.13	0.68	0.40	Drill core
LCO3-13_spot5_pt2	0.72	0.34	0.08	0.29	0.03	0.00	0.30	0.01	70.31	0.03	28.11	100.22	0.59	0.37	Drill core
LCO3-13_spot4_pt1	0.36	0.19	0.02	0.12	0.01	0.00	0.28	0.01	71.20	0.00	27.86	100.05	0.40	0.19	Drill core
LCO3-13_spot4_pt2	0.48	0.67	0.02	0.50	0.00	0.00	0.28	0.01	70.15	0.00	28.10	100.21	0.78	0.67	Drill core
LCO3-13_spot6_pt1	0.74	0.65	0.13	0.39	0.01	0.00	0.28	0.01	69.63	0.06	28.18	100.09	0.67	0.71	Drill core
LCO3-13_spot6_pt2	1.31	0.68	1.21	0.69	0.29	0.00	0.29	0.01	66.45	0.06	28.60	99.60	0.97	0.74	Drill core
LCO3-13_spot6_pt3	0.87	0.58	1.08	0.54	0.18	0.00	0.25	0.01	67.29	0.00	28.19	98.99	0.79	0.58	Drill core
LCO3-13_spot6_pt4	0.28	0.61	0.37	0.82	0.09	0.00	0.26	0.01	69.39	0.00	28.03	99.85	1.08	0.61	Drill core
LCO3-13_spot7_pt1	0.49	0.20	0.09	0.38	0.01	0.00	0.28	0.01	70.34	0.04	27.84	99.69	0.66	0.25	Drill core
LCO3-13_spot7_pt2	0.66	0.53	0.01	0.33	0.00	0.00	0.29	0.02	70.18	0.00	28.09	100.11	0.62	0.53	Drill core
LCO3-13_spot8_pt1	0.61	0.45	0.02	0.26	0.00	0.00	0.29	0.01	70.27	0.00	28.00	99.93	0.55	0.45	Drill core
LCO3-13_spot8_pt2	0.29	0.23	0.03	0.16	0.00	0.00	0.27	0.01	71.20	0.00	27.85	100.05	0.43	0.23	Drill core
LCO3-13_spot9_pt1	0.96	0.49	0.03	0.99	0.00	0.00	0.31	0.01	69.16	0.10	28.28	100.32	1.30	0.59	Drill core
LCO3-13_spot9_pt2	0.59	0.48	0.01	0.37	0.00	0.00	0.32	0.01	70.36	0.04	28.10	100.28	0.69	0.52	Drill core
LCO3-13_spot9_pt3	0.76	0.68	0.02	0.20	0.00	0.00	0.31	0.01	70.42	0.03	28.36	100.79	0.51	0.71	Drill core
LCO3-13_spot10_pt1	0.64	0.71	0.04	1.29	0.03	0.00	0.29	0.01	68.81	0.05	28.17	100.03	1.58	0.76	Drill core
LCO3-18_spot_3_pt1	0.96	0.17	0.02	4.27	0.00	0.00	0.19	0.08	65.23	0.17	27.99	99.10	4.46	0.35	Drill core

Sample ID Laco Sur	Mg [wt%]	Al [wt%]	Si [wt%]	Ti [wt%]	Ca [wt%]	P [wt%]	V [wt%]	Cr [wt%]	Fe [wt%]	Mn [wt%]	O [wt%]	Total	Ti+V [wt%]	Al+Mn [wt%]	Sample
LCO3-18_spot_3_pt2	0.90	0.46	1.08	0.28	0.22	0.00	0.16	0.01	67.03	0.04	27.91	98.09	0.45	0.50	Drill core
LCO3-18_spot_3_pt3	0.49	0.17	0.12	0.25	0.03	0.00	0.17	0.01	71.15	0.04	28.06	100.51	0.43	0.22	Drill core
LCO3-18_spot_3_pt4	0.45	0.21	0.03	0.13	0.00	0.00	0.18	0.01	71.38	0.04	28.00	100.42	0.30	0.24	Drill core
LCO3-18_spot_3_pt5	1.98	0.35	1.26	3.33	0.38	0.00	0.18	0.02	63.06	0.21	28.91	99.67	3.51	0.56	Drill core
LCO3-18_spot_4_pt1	1.01	0.22	0.51	2.34	0.20	0.00	0.18	0.01	67.12	0.14	28.36	100.09	2.52	0.35	Drill core
LCO3-18_spot_4_pt2	1.69	0.39	1.27	1.61	0.26	0.00	0.17	0.02	65.56	0.10	28.77	99.85	1.78	0.50	Drill core
LCO3-18_spot_5_pt1	0.35	0.19	0.02	5.86	0.02	0.00	0.20	0.03	62.92	0.09	27.26	96.94	6.06	0.29	Drill core
LCO3-18_spot_5_pt2	1.28	0.47	1.28	0.42	0.19	0.00	0.16	0.01	66.68	0.04	28.31	98.84	0.58	0.51	Drill core
LCO3-18_spot_5_pt3	0.45	0.20	0.03	0.45	0.00	0.00	0.18	0.01	70.94	0.04	27.97	100.26	0.62	0.24	Drill core
LCO3-18_spot_6_pt1	0.33	0.20	0.02	0.66	0.00	0.00	0.21	0.05	70.38	0.04	27.75	99.63	0.87	0.23	Drill core
LCO3-18_spot_6_pt3	0.72	0.29	0.68	0.24	0.13	0.00	0.16	0.00	68.80	0.03	27.92	98.97	0.41	0.33	Drill core
LCO3-18_spot_6_pt2	0.71	0.29	0.64	0.23	0.13	0.00	0.17	0.00	69.03	0.03	27.96	99.18	0.40	0.32	Drill core
LCO3-18_spot_6_pt4	0.63	0.28	0.48	1.23	0.13	0.00	0.17	0.00	67.82	0.04	27.75	98.55	1.40	0.32	Drill core
LCO3-18_spot_6_pt5	0.42	0.18	0.04	0.95	0.00	0.00	0.18	0.00	69.63	0.04	27.65	99.08	1.12	0.23	Drill core
LCO3-18_spot_7_pt1	0.24	0.23	0.18	0.68	0.00	0.00	0.18	0.03	70.30	0.00	27.77	99.61	0.86	0.23	Drill core
LCO3-18_spot_7_pt2	0.62	0.27	0.67	0.27	0.14	0.00	0.17	0.00	69.59	0.00	28.11	99.83	0.44	0.27	Drill core
LCO3-18_spot_7_pt3	0.75	0.21	0.07	2.76	0.00	0.00	0.18	0.00	67.54	0.11	28.02	99.64	2.94	0.31	Drill core
LCO3-18_spot_9_pt1	1.20	0.41	1.08	1.28	0.43	0.00	0.20	0.01	64.69	0.05	27.81	97.15	1.48	0.46	Drill core
LCO3-18_spot_9_pt2	0.54	0.25	0.09	0.08	0.01	0.00	0.23	0.01	71.07	0.05	28.04	100.37	0.31	0.29	Drill core
LCO3-18_spot_9_pt3	0.05	0.24	0.08	0.35	0.02	0.00	0.18	0.00	70.87	0.04	27.62	99.45	0.53	0.28	Drill core
LCO3-18_spot_1_pt1	0.48	0.24	0.02	0.15	0.01	0.00	0.21	0.01	71.23	0.04	28.02	100.42	0.36	0.28	Drill core
LCO3-18_spot_1_pt2	0.88	0.42	0.52	0.25	0.05	0.00	0.21	0.00	68.81	0.04	28.02	99.19	0.46	0.46	Drill core
LCO3-18_spot_11_pt1	0.62	0.29	0.04	0.09	0.01	0.00	0.22	0.01	70.07	0.03	27.72	99.11	0.31	0.32	Drill core
LCO3-18_spot_11_pt2	0.62	0.33	0.19	0.29	0.03	0.00	0.22	0.00	70.08	0.05	27.97	99.78	0.51	0.38	Drill core
LCO3-18_spot_11_pt3	0.81	0.45	0.40	0.22	0.06	0.00	0.20	0.01	69.18	0.04	28.03	99.40	0.42	0.50	Drill core
LCO3-18_spot_12_pt1	0.92	0.40	0.75	0.25	0.08	0.00	0.25	0.01	68.73	0.05	28.23	99.68	0.49	0.45	Drill core
LCO3-18_spot_12_pt2	0.48	0.24	0.03	0.16	0.02	0.00	0.25	0.01	70.95	0.03	27.94	100.11	0.41	0.28	Drill core
LCO3-18_spot_12_pt3	0.50	0.20	0.04	0.06	0.00	0.00	0.21	0.00	71.41	0.03	28.02	100.47	0.26	0.24	Drill core
LCO3-18_spot_12_pt4	0.45	0.28	0.14	0.30	0.01	0.00	0.19	0.01	70.96	0.04	28.06	100.44	0.49	0.32	Drill core
LCO3-18_spot_13_pt1	0.49	0.22	0.03	0.10	0.03	0.00	0.22	0.01	70.81	0.04	27.85	99.80	0.32	0.26	Drill core
LCO3-18_spot_13_pt2	0.47	0.24	0.04	0.08	0.01	0.00	0.22	0.01	70.47	0.04	27.69	99.26	0.30	0.28	Drill core
LCO3-18_spot_13_pt3	0.49	0.23	0.03	0.08	0.00	0.00	0.21	0.00	71.22	0.05	27.97	100.27	0.28	0.28	Drill core
LCO3-18_spot_2_pt1	0.34	0.38	0.23	0.70	0.02	0.00	0.20	0.01	69.78	0.03	27.84	99.53	0.89	0.41	Drill core
LCO3-18_spot_2_pt2	0.73	0.32	0.60	0.18	0.14	0.00	0.18	0.00	69.70	0.07	28.23	100.15	0.36	0.39	Drill core
LCO3-18_spot_2_pt3	0.47	0.22	0.01	0.10	0.00	0.00	0.20	0.00	71.55	0.05	28.08	100.68	0.30	0.27	Drill core

Sample ID San Vicente Alto	Mg [wt%]	Al [wt%]	Si [wt%]	Ti [wt%]	Ca [wt%]	P [wt%]	V [wt%]	Cr [wt%]	Fe [wt%]	Mn [wt%]	O [wt%]	Total	Ti+V [wt%]	Al+Mn [wt%]	Sample
el va 1-1a sp 2	0.81	0.03	0.44	0.01	0.10	b.d	0.10	b.d	68.25	0.06	27.29	97.09	0.11	0.09	Surface
el va 1-1a sp 3	0.98	0.04	0.51	0.01	0.11	b.d	0.11	b.d	67.81	0.06	27.33	96.96	0.12	0.10	Surface
el va 1-1b1	1.02	0.05	0.69	0.01	0.16	b.d	0.10	b.d	67.39	0.06	27.37	96.85	0.12	0.11	Surface
el va 1-1b2	0.82	0.05	0.59	0.02	0.12	b.d	0.10	b.d	67.81	0.05	27.26	96.82	0.12	0.11	Surface
el va 1-1b3	0.86	0.06	0.94	0.02	0.16	b.d	0.10	b.d	67.02	0.05	27.29	96.50	0.12	0.11	Surface
el va 1-1b4	0.88	0.05	0.51	0.02	0.12	b.d	0.10	b.d	67.69	0.05	27.21	96.62	0.12	0.10	Surface
el va 1-1b5	0.78	0.05	0.41	0.01	0.08	b.d	0.10	b.d	67.29	0.02	26.86	95.60	0.11	0.07	Surface
el va 1-1b6	0.88	0.04	0.51	0.01	0.05	b.d	0.10	b.d	67.50	0.04	27.09	96.21	0.11	0.08	Surface
el va 1-1b7	0.80	0.05	0.43	0.01	0.04	b.d	0.10	b.d	67.64	0.04	27.01	96.11	0.11	0.08	Surface
el-va-sample-5-point	1.20	0.01	0.73	b.d	0.24	b.d	0.07	b.d	69.51	0.06	28.38	100.21	0.07	0.07	Surface
el-va-sample-1-gr-2-high-z	1.00	0.04	0.88	0.02	0.17	b.d	0.08	b.d	69.01	0.07	28.12	99.39	0.10	0.11	Surface
el-va-sample-5-t-1 sp 1	0.75	0.04	0.30	b.d	0.08	b.d	0.08	b.d	70.28	0.06	27.90	99.49	0.09	0.10	Surface
el-va-sample-5-t-1 sp 2	0.73	0.00	0.20	b.d	0.06	b.d	0.07	b.d	70.57	0.06	27.87	99.57	0.08	0.07	Surface
el-va-sample-5-t-1 sp 3	0.75	0.01	0.18	b.d	0.06	b.d	0.07	b.d	70.60	0.07	27.89	99.64	0.08	0.08	Surface
el-va-sample-5-t-1 sp 4	0.76	0.00	0.28	b.d	0.07	b.d	0.06	b.d	70.14	0.06	27.80	99.19	0.07	0.07	Surface
el-va-sample-5-t-1 sp 5	0.84	0.00	0.32	b.d	0.05	b.d	0.06	b.d	70.25	0.07	27.93	99.52	0.07	0.07	Surface
el-va-sample-5-t-1 sp 6	0.76	0.00	0.29	b.d	0.12	b.d	0.07	b.d	70.18	0.07	27.85	99.34	0.08	0.07	Surface
el-va-sample-5-t-2 sp 1	0.82	0.00	0.29	b.d	0.07	b.d	0.08	b.d	70.36	0.06	27.94	99.62	0.08	0.06	Surface
el-va-sample-5-t-2 sp 2	1.03	0.02	0.73	b.d	0.26	b.d	0.08	b.d	69.18	0.07	28.13	99.50	0.08	0.09	Surface
el-va-sample-5-t-2 sp 3	0.82	0.01	0.36	b.d	0.15	b.d	0.08	b.d	70.52	0.07	28.11	100.11	0.09	0.08	Surface
el-va-sample-5-t-2 sp 4	0.69	0.00	0.25	b.d	0.10	b.d	0.07	b.d	70.27	0.06	27.78	99.23	0.08	0.07	Surface
el-va-sample-5-t-3 sp 1	0.68	0.01	0.06	b.d	0.07	0.01	0.08	b.d	70.91	0.07	27.87	99.76	0.09	0.08	Surface
el-va-sample-5-t-3 sp 2	0.75	0.01	0.21	b.d	0.01	b.d	0.08	b.d	70.84	0.06	27.99	99.96	0.09	0.07	Surface
el-va-sample-5-t-3 sp 3	0.62	0.01	0.02	b.d	b.d	b.d	0.09	b.d	71.10	0.05	27.83	99.72	0.09	0.06	Surface
el-va-sample-5-t-3 sp 4	0.67	0.01	0.03	b.d	0.26	0.12	0.08	b.d	70.49	0.07	27.91	99.63	0.09	0.08	Surface
el-va-sample-5-t-3 sp 5	0.65	0.02	0.02	b.d	b.d	b.d	0.08	b.d	71.23	0.07	27.92	99.98	0.09	0.08	Surface
el-va-sample-5-t-3 sp 6	0.60	0.00	0.02	b.d	b.d	b.d	0.08	b.d	71.17	0.05	27.83	99.76	0.09	0.06	Surface
el-va-sample-1-gr-8 sp 1	0.89	0.18	0.50	0.02	0.12	b.d	0.10	b.d	68.58	0.05	27.66	98.11	0.11	0.24	Surface
el-va-sample-1-gr-8 sp 2	0.87	0.07	0.44	0.02	0.07	b.d	0.09	b.d	68.31	0.05	27.37	97.29	0.11	0.12	Surface
el-va-sample-1-gr-8 sp 3	0.91	0.08	0.49	0.01	0.10	b.d	0.09	b.d	67.77	0.06	27.26	96.76	0.11	0.14	Surface
el-va-sample-1-gr-8 sp 4	0.80	0.09	0.43	0.02	0.05	b.d	0.10	b.d	67.90	0.06	27.16	96.61	0.12	0.15	Surface
el-va-sample-1-gr-8 sp 5	1.06	0.07	0.64	0.02	0.19	b.d	0.10	b.d	67.95	0.06	27.62	97.70	0.11	0.12	Surface

Sample ID San Vicente Alto	Mg [wt%]	Al [wt%]	Si [wt%]	Ti [wt%]	Ca [wt%]	P [wt%]	V [wt%]	Cr [wt%]	Fe [wt%]	Mn [wt%]	O [wt%]	Total	Ti+V [wt%]	Al+Mn [wt%]	Sample
el-va-sample-1-gr-8 sp 6	0.99	0.06	0.58	0.02	0.13	b.d	0.10	b.d	67.80	0.06	27.41	97.14	0.11	0.12	Surface
el-va-sample-1-gr-8 sp 7	0.71	0.19	0.19	0.02	0.09	b.d	0.09	b.d	68.97	0.06	27.41	97.73	0.11	0.24	Surface
el-va-sample-1-gr-8 sp 8	0.65	0.23	0.68	0.01	0.03	b.d	0.10	b.d	67.49	0.05	27.15	96.39	0.11	0.28	Surface
el-va-sample-1-gr-2 sp 1	0.72	0.04	0.85	b.d	0.08	b.d	0.10	b.d	67.91	0.04	27.39	97.14	0.10	0.09	Surface
el-va-sample-1-gr-2 sp 1	1.02	0.05	0.76	b.d	0.08	b.d	0.10	b.d	68.68	0.05	27.88	98.61	0.10	0.09	Surface
el-va-sample-1-gr-2 sp 2	0.79	0.07	0.60	b.d	0.09	b.d	0.09	b.d	68.25	0.05	27.42	97.38	0.10	0.13	Surface
el-va-sample-1-gr-2 sp 3	1.00	0.06	0.68	0.02	0.22	b.d	0.10	b.d	68.40	0.06	27.78	98.32	0.11	0.12	Surface
el-va-sample-1-gr-2 sp 4	0.95	0.13	0.55	0.02	0.19	b.d	0.10	b.d	66.50	0.06	26.96	95.45	0.11	0.19	Surface
el-va-sample-1-gr-2 sp 5	1.03	0.07	1.03	0.02	0.12	b.d	0.09	b.d	67.88	0.06	27.84	98.15	0.12	0.13	Surface
el-va-sample-1-gr-2 sp 6	0.87	0.05	0.51	0.02	0.13	b.d	0.10	b.d	68.74	0.05	27.61	98.08	0.12	0.10	Surface
el-va-sample-2-gr-4 sp 1	0.77	0.05	0.25	0.02	0.06	b.d	0.08	b.d	70.44	0.06	27.93	99.66	0.11	0.11	Surface
el-va-sample-2-gr-4 sp 2	0.19	0.07	0.34	0.02	0.05	b.d	0.09	0.01	67.74	b.d	26.49	95.00	0.11	0.07	Surface
el-va-sample-2-gr-4 sp 4	0.15	0.06	0.17	0.02	b.d	b.d	0.09	b.d	68.25	0.03	26.47	95.24	0.11	0.09	Surface
el-va-sample-2-gr-4 sp 7	0.08	0.09	0.11	0.02	b.d	b.d	0.09	b.d	68.27	0.03	26.40	95.09	0.10	0.12	Surface
el-va-sample-2-gr-4 sp 8	0.24	0.12	0.28	0.02	0.02	0.14	0.09	b.d	68.13	0.03	26.79	95.84	0.11	0.15	Surface
el-va-sample-2-gr-4 sp 9	0.23	0.04	0.17	0.02	0.01	b.d	0.08	b.d	68.28	0.03	26.52	95.37	0.10	0.07	Surface
el-va-sample-2-gr-4 sp 10	0.79	0.04	0.31	0.02	0.08	b.d	0.08	b.d	70.37	0.06	27.97	99.71	0.10	0.10	Surface
el-va-sample-2-gr-3 sp 1	0.70	0.06	0.51	0.01	0.10	b.d	0.08	b.d	70.18	0.05	27.99	99.69	0.10	0.11	Surface
el-va-sample-2-gr-3 sp 2	0.21	0.06	0.26	0.01	b.d	b.d	0.09	b.d	68.01	0.02	26.49	95.14	0.10	0.08	Surface
el-va-sample-2-gr-3 sp 4	0.04	0.09	0.25	0.02	b.d	b.d	0.09	b.d	68.12	b.d	26.43	95.03	0.11	0.09	Surface
el-va-sample-2-gr-3 sp 6	0.30	0.05	0.14	0.02	0.01	0.03	0.09	b.d	68.65	0.04	26.75	96.08	0.10	0.09	Surface
el-va-sample-2-gr-3 sp 7	0.87	0.06	0.55	0.01	0.15	b.d	0.08	b.d	69.93	0.05	28.11	99.82	0.10	0.11	Surface
el-va-sample-4-gr-9 sp 1	0.54	0.06	0.05	b.d	b.d	0.04	0.09	b.d	68.28	0.04	26.78	95.88	0.10	0.10	Surface
el-va-sample-4-gr-9 sp 2	0.59	0.03	0.04	b.d	0.01	0.08	0.10	b.d	68.29	0.05	26.84	96.01	0.10	0.08	Surface
el-va-sample-4-gr-9 sp 3	0.51	0.15	0.03	b.d	0.01	0.05	0.09	b.d	69.02	0.05	27.10	97.01	0.09	0.20	Surface
el-va-sample-4-gr-9 sp 4	0.57	0.14	0.06	b.d	0.01	0.06	0.09	b.d	67.79	0.05	26.71	95.48	0.10	0.18	Surface
el-va-sample-4-gr-9 sp 5	0.55	0.06	0.06	b.d	0.02	0.12	0.09	b.d	68.12	0.04	26.82	95.87	0.09	0.10	Surface
el-va-sample-4-gr-5-mottled	0.24	0.04	0.08	0.02	0.01	0.04	0.08	b.d	68.26	0.01	26.49	95.28	0.10	0.05	Surface
el-va-sample-4-gr-5-mottled	0.52	0.08	0.06	0.02	b.d	0.07	0.09	b.d	68.53	0.03	26.91	96.31	0.11	0.11	Surface
el-va-sample-4-gr-5-tr sp 1	0.58	0.06	0.05	0.02	0.01	0.03	0.07	b.d	68.44	0.05	26.84	96.13	0.09	0.10	Surface
el-va-sample-4-gr-5-tr sp 2	0.35	0.17	0.10	0.01	0.01	0.07	0.06	b.d	68.27	0.03	26.74	95.82	0.08	0.20	Surface
el-va-sample-4-gr-5-tr sp 3	0.28	0.16	0.14	0.02	0.03	0.12	0.08	b.d	67.78	0.02	26.60	95.24	0.10	0.18	Surface
el-va-sample-4-gr-5-tr sp 4	0.44	0.11	0.10	0.01	0.02	0.09	0.08	b.d	68.62	b.d	26.97	96.45	0.09	0.11	Surface
el-va-sample-4-gr-5-tr sp 5	0.41	0.45	0.17	0.01	0.05	0.22	0.08	b.d	67.69	0.04	27.06	96.17	0.09	0.49	Surface
el-va-sample-4-gr-5-tr sp 6	0.45	0.04	0.09	0.01	0.01	0.11	0.08	b.d	68.19	0.02	26.74	95.74	0.09	0.06	Surface
el-va-sample-3-gr-4 sp 1	0.74	0.08	0.92	0.02	0.15	b.d	0.09	b.d	67.08	0.03	27.20	96.31	0.11	0.11	Surface
el-va-sample-3-gr-4 sp 2	0.88	0.09	0.97	0.02	0.15	b.d	0.09	b.d	67.07	0.05	27.37	96.70	0.11	0.14	Surface
el-va-sample-3-gr-4 sp 3	0.77	0.14	0.87	0.03	0.12	b.d	0.10	b.d	67.56	0.06	27.42	97.08	0.12	0.20	Surface
el-va-sample-3-gr-4 sp 4	0.81	0.07	0.65	0.03	0.13	b.d	0.09	b.d	67.62	0.03	27.24	96.68	0.12	0.10	Surface
el-va-sample-3-gr-2sp 1	0.94	0.09	0.64	0.03	0.15	b.d	0.09	b.d	67.69	0.04	27.41	97.09	0.12	0.13	Surface
el-va-sample-3-gr-2sp 2	0.84	0.09	0.45	0.04	0.13	b.d	0.09	b.d	68.27	0.05	27.39	97.35	0.13	0.14	Surface
el-va-sample-3-gr-2sp 3	0.97	0.19	0.86	0.05	0.26	b.d	0.09	b.d	67.12	0.05	27.53	97.12	0.14	0.24	Surface
el-va-sample-3-gr-2sp 4	1.12	0.11	0.95	0.04	0.31	b.d	0.09	b.d	66.96	0.06	27.63	97.27	0.13	0.17	Surface
el-va-sample-3-gr-2sp 5	0.83	0.09	0.71	0.03	0.14	b.d	0.09	b.d	67.93	0.06	27.46	97.34	0.12	0.14	Surface
el-va-sample-3-gr-2sp 6	0.83	0.08	0.49	0.03	0.09	b.d	0.09	b.d	68.52	0.04	27.48	97.66	0.12	0.12	Surface
el-va-sample-3-gr-5 sp 1	0.87	0.13	0.61	0.03	0.14	b.d	0.10	b.d	68.10	0.06	27.51	97.55	0.13	0.19	Surface
el-va-sample-3-gr-5 sp 2	0.82	0.08	0.73	0.03	0.09	b.d	0.10	b.d	68.26	0.06	27.56	97.74	0.13	0.14	Surface
el-va-sample-3-gr-5 sp 3	1.02	0.09	0.85	0.03	0.18	b.d	0.10	b.d	67.75	0.06	27.69	97.78	0.13	0.15	Surface
el-va-sample-3-gr-5 sp 4	0.84	0.08	0.56	0.03	0.15	b.d	0.10	0.01	68.13	0.06	27.42	97.36	0.12	0.14	Surface
el-va-sample-3-gr-5 sp 5	1.14	0.12	0.51	0.02	0.14	b.d	0.10	0.01	68.02	0.06	27.63	97.75	0.12	0.18	Surface
el-va-sample-3-gr-5 sp 6	0.74	0.09	0.93	0.03	0.08	b.d	0.09	b.d	67.78	0.05	27.46	97.27	0.13	0.15	Surface
el-va-sample-3-gr-5 sp 7	0.63	0.22	1.19	0.02	0.06	b.d	0.10	b.d	67.22	0.05	27.44	96.95	0.13	0.28	Surface
el-va-sample-3-gr-5 sp 8	0.94	0.10	1.17	0.03	0.21	b.d	0.10	b.d	66.93	0.06	27.57	97.11	0.13	0.16	Surface
el-va-sample-3-gr-5 sp 9	0.76	0.10	0.97	0.03	0.09	b.d	0.10	b.d	67.74	0.06	27.51	97.35	0.12	0.15	Surface
el-va-sample-t-1gr-1 sp 7	0.19	0.08	0.26	0.01	b.d	0.06	0.08	b.d	68.29	b.d	26.68	95.64	0.09	0.08	Surface
el-va-sample-t-1gr-1 sp 8	3.90	0.07	0.37	0.01	b.d	b.d	0.09	b.d	67.72	b.d	29.75	101.92	0.11	0.08	Surface
el-va-sample-t-1gr-4 sp 1	0.87	0.03	0.70	b.d	0.19	b.d	0.10	b.d	69.52	0.05	28.06	99.51	0.10	0.08	Surface
el-va-sample-t-1gr-4 sp 3	0.79	0.03	0.59	b.d	0.18	b.d	0.10	b.d	69.98	0.05	28.09	99.80	0.10	0.08	Surface
el-va-sample-t-1gr-4 sp 6	0.09	0.05	0.39	b.d	b.d	b.d	0.10	b.d	67.94	0.02	26.46	95.05	0.10	0.07	Surface
el-va-sample-t-1gr-4 sp 8	0.64	0.03	0.48	b.d	0.13	b.d	0.09	b.d	69.60	0.04	27.70	98.72	0.10	0.07	Surface

Sample ID Rodados Negros	Mg [wt%]	Al [wt%]	Si [wt%]	Ti [wt%]	Ca [wt%]	P [wt%]	V [wt%]	Cr [wt%]	Fe [wt%]	Mn [wt%]	O [wt%]	Total	Ti+V [wt%]	Al+Mn [wt%]	Sample
rnc-sample-1-gr-3 sp 1	0.68	0.08	1.09	0.05	0.34	b.d	0.14	b.d	66.54	0.08	26.74	95.74	0.18	0.16	Surface
rnc-sample-1-gr-3 sp 2	0.76	0.07	0.46	0.05	0.14	b.d	0.15	0.01	70.46	0.07	27.64	99.80	0.19	0.14	Surface
rnc-sample-1-gr-3 sp 3	0.64	0.07	0.34	0.04	0.12	b.d	0.15	b.d	70.56	0.07	27.57	99.55	0.19	0.14	Surface
rnc-sample-1-gr-3 sp 4	0.65	0.06	0.36	0.04	0.15	b.d	0.15	0.01	70.73	0.07	27.65	99.86	0.18	0.13	Surface
rnc-sample-1-gr-3 sp 5	0.65	0.06	0.35	0.04	0.12	b.d	0.15	b.d	70.63	0.07	27.60	99.69	0.19	0.13	Surface
rnc-sample-1-gr-3 sp 6	1.06	0.06	0.39	0.04	0.14	b.d	0.14	b.d	70.73	0.07	27.72	100.33	0.18	0.13	Surface
rnc-sample-1-gr-2 sp 1	0.73	0.05	0.44	0.04	0.16	b.d	0.13	b.d	70.21	0.08	27.52	99.35	0.16	0.13	Surface
rnc-sample-1-gr-2 sp 2	0.81	0.05	0.32	0.03	0.10	b.d	0.13	b.d	70.79	0.08	27.63	99.95	0.16	0.13	Surface
rnc-sample-1-gr-2 sp 3	0.60	0.06	0.17	0.03	0.07	b.d	0.13	b.d	71.06	0.07	27.58	99.77	0.17	0.13	Surface
rnc-sample-1-gr-2 sp 4	0.78	0.06	0.50	0.04	0.17	b.d	0.14	b.d	70.05	0.08	27.53	99.33	0.18	0.13	Surface
rnc-sample-1-gr-2 sp 5	0.78	0.06	0.52	0.04	0.19	b.d	0.13	b.d	70.18	0.07	27.60	99.57	0.17	0.13	Surface
rnc-sample-1-gr-2 sp 6	1.00	0.09	0.77	0.04	0.25	b.d	0.13	b.d	69.41	0.08	27.59	99.37	0.17	0.17	Surface
rnc-sample-1-gr-2 sp 7	0.80	0.07	0.55	0.04	0.23	b.d	0.14	b.d	69.88	0.07	27.55	99.33	0.18	0.14	Surface
rnc-sample-1-gr-2 sp 8	0.86	0.08	0.74	0.05	0.27	b.d	0.13	0.01	69.26	0.08	27.48	98.95	0.18	0.16	Surface
rnc-sample-1-gr-2 sp 9	0.82	0.05	0.54	0.04	0.21	b.d	0.14	b.d	69.72	0.08	27.46	99.06	0.18	0.13	Surface
rnc-sample-1-gr-2 sp 10	0.86	0.06	0.73	0.04	0.28	b.d	0.13	b.d	68.96	0.08	27.36	98.50	0.18	0.13	Surface
rnc-sample-1-gr-2 sp 11	0.73	0.06	0.50	0.04	0.19	b.d	0.13	b.d	70.03	0.07	27.52	99.26	0.17	0.13	Surface
rnc-sample-2-gr-2 sp 1	1.96	0.33	1.22	0.12	0.20	b.d	0.12	b.d	68.15	0.08	27.77	99.95	0.24	0.41	Surface
rnc-sample-2-gr-2 sp 2	1.08	0.28	0.52	0.13	0.23	b.d	0.13	b.d	69.42	0.08	27.60	99.48	0.26	0.36	Surface
rnc-sample-2-gr-2 sp 3	0.93	0.26	0.20	0.13	0.05	b.d	0.13	b.d	69.94	0.09	27.42	99.14	0.26	0.35	Surface
rnc-sample-2-gr-2 sp 4	0.87	0.26	0.12	0.12	0.03	b.d	0.13	0.01	70.23	0.09	27.44	99.29	0.25	0.35	Surface
rnc-sample-2-gr-2 sp 5	1.23	0.29	0.49	0.17	0.09	b.d	0.14	0.01	69.29	0.08	27.49	99.27	0.30	0.38	Surface
rnc-sample-2-gr-2 sp 6	1.02	0.26	0.49	0.13	0.20	b.d	0.14	b.d	69.64	0.08	27.61	99.57	0.27	0.34	Surface
rnc-sample-2-gr-2 sp 7	1.08	0.30	0.44	0.17	0.15	b.d	0.14	b.d	69.65	0.08	27.62	99.64	0.30	0.39	Surface
rnc-sample-2-gr-2 sp 8	0.85	0.29	0.10	0.16	0.04	b.d	0.14	0.01	70.28	0.09	27.49	99.43	0.30	0.37	Surface
rnc-sample-2-gr-4sp 1	0.79	0.12	0.02	0.06	0.00	b.d	0.13	b.d	70.77	0.08	27.42	99.38	0.19	0.20	Surface
rnc-sample-2-gr-4sp 2	0.78	0.11	0.02	0.06	0.00	b.d	0.13	b.d	70.63	0.08	27.36	99.17	0.19	0.19	Surface
rnc-sample-2-gr-4sp 3	0.83	0.11	0.04	0.05	0.00	b.d	0.12	b.d	70.64	0.08	27.38	99.26	0.17	0.19	Surface
rnc-sample-2-gr-4sp 4	0.77	0.10	0.04	0.05	0.00	b.d	0.12	b.d	70.77	0.08	27.41	99.34	0.17	0.18	Surface
rnc-sample-2-gr-4sp 5	0.79	0.09	0.05	0.04	0.00	b.d	0.12	b.d	70.54	0.08	27.32	99.03	0.16	0.17	Surface
rnc-sample-2-gr-4sp 6	0.72	0.08	0.02	0.03	0.00	b.d	0.12	b.d	70.80	0.07	27.37	99.22	0.15	0.15	Surface
rnc-sample-2-gr-4sp 7	0.76	0.07	0.02	0.03	0.00	b.d	0.13	b.d	70.75	0.08	27.35	99.19	0.16	0.15	Surface
rnc-sample-2-gr-4sp 8	0.87	0.06	0.14	0.03	0.02	b.d	0.13	0.01	70.15	0.08	27.22	98.70	0.15	0.14	Surface
rnc-sample-2-gr-4sp 9	0.95	0.06	0.28	0.02	0.03	b.d	0.14	b.d	69.67	0.07	27.15	98.37	0.16	0.13	Surface
rnc-sample-2-gr-4sp 10	1.02	0.07	0.26	0.02	0.07	b.d	0.13	b.d	69.48	0.07	27.10	98.22	0.15	0.14	Surface
rnc-sample-3-gr-4 sp 1	0.60	0.14	0.04	0.07	0.00	b.d	0.09	b.d	70.30	0.13	27.27	98.65	0.16	0.28	Surface
rnc-sample-3-gr-4 sp 2	0.59	0.13	0.05	0.07	0.00	b.d	0.10	b.d	70.22	0.13	27.25	98.55	0.17	0.26	Surface
rnc-sample-3-gr-4 sp 3	0.59	0.14	0.03	0.07	0.00	b.d	0.10	b.d	70.25	0.14	27.25	98.56	0.16	0.27	Surface
rnc-sample-3-gr-4 sp 4	0.62	0.13	0.04	0.06	0.00	b.d	0.10	b.d	70.11	0.14	27.20	98.40	0.16	0.27	Surface
rnc-sample-3-gr-4 sp 5	0.63	0.14	0.05	0.06	0.00	b.d	0.10	b.d	70.17	0.14	27.23	98.52	0.16	0.28	Surface
rnc-sample-3-gr-4 sp 6	0.61	0.13	0.05	0.06	0.00	b.d	0.10	b.d	70.08	0.14	27.19	98.34	0.16	0.27	Surface
rnc-sample-3-gr-4 sp 7	0.60	0.14	0.04	0.05	0.00	b.d	0.10	b.d	70.21	0.13	27.23	98.51	0.16	0.27	Surface
rnc-sample-3-gr-4 sp 8	0.60	0.13	0.04	0.05	0.00	b.d	0.10	b.d	70.40	0.13	27.29	98.74	0.15	0.26	Surface
rnc-sample-3-gr-2-t-1 sp 1	0.65	0.11	0.03	0.08	0.00	b.d	0.08	b.d	71.01	0.13	27.52	99.61	0.16	0.24	Surface
rnc-sample-3-gr-2-t-1 sp 2	0.65	0.10	0.02	0.08	0.00	b.d	0.08	b.d	71.03	0.14	27.51	99.60	0.16	0.24	Surface
rnc-sample-3-gr-2-t-1 sp 3	0.64	0.10	0.01	0.08	0.00	b.d	0.07	b.d	71.19	0.14	27.56	99.78	0.15	0.24	Surface
rnc-sample-3-gr-2-t-1 sp 4	0.61	0.09	0.01	0.07	0.00	b.d	0.07	b.d	71.18	0.14	27.54	99.72	0.14	0.23	Surface
rnc-sample-3-gr-2-t-1 sp 5	0.61	0.08	0.01	0.07	0.00	b.d	0.07	b.d	71.14	0.14	27.52	99.63	0.13	0.22	Surface
rnc-sample-3-gr-2-t-1 sp 6	0.62	0.07	0.02	0.06	0.00	b.d	0.06	b.d	71.07	0.14	27.48	99.52	0.12	0.21	Surface
rnc-sample-3-gr-2-t-1 sp 7	0.63	0.07	0.02	0.05	0.00	b.d	0.06	b.d	71.16	0.14	27.51	99.64	0.12	0.21	Surface
rnc-sample-3-gr-2-t-1 sp 8	0.64	0.09	0.04	0.06	0.00	b.d	0.06	b.d	71.01	0.14	27.49	99.51	0.12	0.23	Surface
rnc-sample-3-gr-2-t-1 sp 9	0.61	0.06	0.03	0.05	0.00	b.d	0.06	b.d	70.94	0.13	27.42	99.31	0.11	0.19	Surface
rnc-sample-3-gr-2-t-2 sp 1	0.62	0.07	0.02	0.07	0.00	b.d	0.07	b.d	71.29	0.13	27.57	99.84	0.13	0.21	Surface
rnc-sample-3-gr-2-t-2 sp 2	0.63	0.08	0.04	0.06	0.00	b.d	0.07	b.d	71.22	0.14	27.57	99.81	0.12	0.22	Surface
rnc-sample-3-gr-2-t-2 sp 3	0.63	0.06	0.03	0.06	0.00	b.d	0.07	b.d	71.13	0.14	27.52	99.64	0.13	0.20	Surface
rnc-sample-3-gr-2-t-2 sp 4	0.66	0.06	0.05	0.05	0.00	b.d	0.06	b.d	70.98	0.13	27.47	99.47	0.12	0.19	Surface
rnc-sample-3-gr-2-t-2 sp 5	0.64	0.05	0.06	0.05	0.00	b.d	0.06	b.d	71.13	0.13	27.52	99.66	0.11	0.19	Surface
rnc-sample-3-gr-2-t-2 sp 6	0.65	0.04	0.05	0.04	0.00	b.d	0.06	b.d	70.99	0.13	27.44	99.40	0.10	0.18	Surface
rnc-sample-4-gr-3 sp 1	0.86	0.03	0.42	0.00	0.14	b.d	0.14	b.d	70.01	0.07	27.40	99.07	0.14	0.10	Surface
rnc-sample-4-gr-3 sp 2	0.65	0.02	0.23	0.01	0.08	b.d	0.14	b.d	70.70	0.06	27.46	99.36	0.16	0.08	Surface
rnc-sample-4-gr-3 sp 3	0.71	0.02	0.32	0.01	0.10	b.d	0.14	b.d	70.23	0.07	27.37	98.97	0.15	0.09	Surface
rnc-sample-4-gr-3 sp 4	0.63	0.02	0.25	0.02	0.09	b.d	0.14	b.d	70.37	0.07	27.35	98.93	0.16	0.08	Surface
rnc-sample-4-gr-3 sp 5	0.75	0.02	0.40	0.01	0.10	b.d	0.14	b.d	69.73	0.07	27.24	98.46	0.15	0.09	Surface
rnc-sample-4-gr-3 sp 6	0.66	0.02	0.23	0.02	0.08	b.d	0.14	b.d	70.18	0.07	27.26	98.65	0.15	0.08	Surface
rnc-sample-4-gr-3 sp 7	0.73	0.02	0.37	0.02	0.12	b.d	0.14	b.d	69.92	0.06	27.30	98.67	0.16	0.08	Surface
rnc-sample-4-gr-3 sp 8	0.74	0.02	0.30	0.00	0.09	b.d	0.14	0.01	70.09	0.06	27.28	98.74	0.15	0.08	Surface
rnc-sample-4-gr-3 sp 9	4.37	0.05	4.24	0.00	0.06	b.d	0.12	0.01	61.04	0.09	27.32	97.31	0.13	0.14	Surface
rnc-sample-4-gr-3 sp 10	0.74	0.02	0.38	0.01	0.11	b.d	0.14	0.01	69.64	0.07	27.19	98.31	0.16	0.09	Surface
rnc-sample-4-gr-1 sp 1	0.88	0.02	0.42	0.01	0.13	b.d	0.14	b.d	70.32	0.07	27.52	99.52	0.15	0.10	Surface
rnc-sample-4-gr-1 sp 2	0.79	0.01	0.42	0.01	0.11	b.d	0.14	b.d	70.08	0.07	27.40	99.03	0.16	0.08	Surface
rnc-sample-4-gr-1 sp 3	0.60	0.01	0.15	0.01	0.06	b.d	0.14	b.d	70.54	0.07	27.31	98.90	0.16	0.08	Surface
rnc-sample-4-gr-1 sp 4	0.79	0.02	0.42	0.01	0.12	b.d	0.14	0.01	69.88	0.07	27.32	98.77	0.15	0.08	Surface
rnc-sample-4-gr-1 sp 5	0.66	0.02	0.29	0.01	0.10	b.d	0.14	b.d	70.02	0.06	27.25	98.55	0.15	0.08	Surface
rnc-sample-4-gr-1 sp 6	0.84	0.02	0.47	0.00	0.13	b.d	0.14	b.d	69.69	0.07	27.30	98.66	0.14	0.08	Surface
rnc-sample-4-gr-1 sp 7	0.87	0.01	0.57	0.01	0.15	b.d	0.14	b.d	69.34	0.07	27.26	98.42	0.15	0.08	Surface
rnc-sample-4-gr-1 sp 8	0.60	0.02	0.25	0.01	0.08	b.d	0.14	b.d	69.61	0.06	27.05	97.82	0.15	0.08	Surface
rnc-sample-4-gr-1 sp 9	0.68	0.02	0.26	0.01	0.10	b.d	0.14	b.d	69.90	0.06	27.19	98.37	0.16	0.08	Surface

Sample ID Rodados Negros	Mg [wt%]	Al [wt%]	Si [wt%]	Ti [wt%]	Ca [wt%]	P [wt%]	V [wt%]	Cr [wt%]	Fe [wt%]	Mn [wt%]	O [wt%]	Total	Ti+V [wt%]	Al+Mn [wt%]	Sample
rnc-sample-4-gr-1 sp 10	0.80	0.02	0.48	0.01	0.14	b.d	0.14	b.d	69.16	0.07	27.11	97.93	0.15	0.09	Surface
rnc-sample-4-gr-1 sp 11	0.68	0.02	0.35	0.02	0.11	b.d	0.14	b.d	69.44	0.07	27.09	97.93	0.16	0.09	Surface
rnc-sample-7-gr-4 sp 1	0.83	0.08	0.14	0.00	0.01	b.d	0.09	b.d	70.93	0.10	27.52	99.70	0.09	0.18	Surface
rnc-sample-7-gr-4 sp 2	0.84	0.08	0.13	0.01	0.02	b.d	0.09	b.d	71.20	0.10	27.61	100.08	0.10	0.18	Surface
rnc-sample-7-gr-4 sp 3	0.74	0.07	0.02	0.00	0.00	b.d	0.09	b.d	71.31	0.10	27.55	99.88	0.10	0.17	Surface
rnc-sample-7-gr-4 sp 4	0.68	0.11	0.02	0.00	0.00	b.d	0.09	b.d	71.54	0.10	27.66	100.21	0.10	0.21	Surface
rnc-sample-7-gr-4 sp 5	0.72	0.08	0.02	0.00	0.00	b.d	0.09	b.d	71.30	0.10	27.55	99.87	0.10	0.18	Surface
rnc-sample-7-gr-4 sp 6	0.75	0.08	0.02	0.00	0.00	b.d	0.09	b.d	71.25	0.10	27.54	99.84	0.10	0.18	Surface
rnc-sample-7-gr-4 sp 7	0.99	0.07	0.22	0.00	0.01	b.d	0.09	b.d	70.86	0.10	27.57	99.92	0.10	0.18	Surface
rnc-sample-7-gr-4 sp 8	0.79	0.07	0.08	0.00	0.00	b.d	0.09	b.d	70.95	0.10	27.47	99.55	0.09	0.17	Surface
rnc-sample-7-gr-4 sp 9	0.88	0.07	0.23	0.00	0.04	b.d	0.09	b.d	70.48	0.10	27.42	99.29	0.09	0.17	Surface
rnc-sample-7-gr-4 sp 10	0.77	0.07	0.05	0.00	0.02	b.d	0.09	b.d	71.08	0.10	27.49	99.66	0.09	0.17	Surface
rnc-sample-7-gr-1 sp 1	0.71	0.22	0.02	0.05	0.00	b.d	0.10	b.d	70.83	0.10	27.51	99.56	0.16	0.32	Surface
rnc-sample-7-gr-1 sp 2	0.70	0.22	0.02	0.05	0.00	b.d	0.09	b.d	70.95	0.10	27.55	99.69	0.15	0.32	Surface
rnc-sample-7-gr-1 sp 3	0.71	0.21	0.02	0.05	0.00	b.d	0.09	b.d	70.77	0.10	27.47	99.43	0.14	0.31	Surface
rnc-sample-7-gr-1 sp 4	0.70	0.18	0.03	0.04	0.00	b.d	0.09	b.d	70.88	0.10	27.50	99.54	0.14	0.28	Surface
rnc-sample-7-gr-1 sp 5	0.69	0.17	0.03	0.04	0.00	b.d	0.09	b.d	70.62	0.10	27.38	99.12	0.13	0.26	Surface
rnc-sample-7-gr-1 sp 6	0.71	0.16	0.04	0.04	0.00	b.d	0.09	b.d	70.77	0.10	27.44	99.34	0.13	0.26	Surface
rnc-sample-7-gr-1 sp 7	0.81	0.15	0.17	0.02	0.01	b.d	0.09	b.d	70.20	0.09	27.31	98.86	0.12	0.24	Surface
rnc-sample-7-gr-1 sp 8	0.72	0.13	0.03	0.02	0.00	b.d	0.09	b.d	70.62	0.10	27.35	99.07	0.12	0.23	Surface
rnc-sample-7-gr-1 sp 9	0.87	0.12	0.02	0.02	0.00	b.d	0.09	b.d	70.65	0.10	27.37	99.24	0.11	0.22	Surface
rnc-sample-7-gr-1 sp 10	0.67	0.11	0.02	0.01	0.00	b.d	0.09	b.d	70.66	0.10	27.33	98.99	0.10	0.20	Surface
rn-d-gr-2 sp 1	0.71	0.04	0.03	0.00	0.00	b.d	0.10	b.d	70.90	0.11	27.38	99.27	0.10	0.15	Surface
rn-d-gr-2 sp 2	0.84	0.04	0.16	0.00	0.00	b.d	0.09	b.d	70.57	0.10	27.37	99.18	0.10	0.14	Surface
rn-d-gr-2 sp 3	0.76	0.04	0.06	0.00	0.00	b.d	0.11	b.d	70.81	0.10	27.38	99.25	0.11	0.14	Surface
rn-d-gr-2 sp 4	0.70	0.04	0.02	0.00	0.00	b.d	0.11	b.d	71.00	0.10	27.42	99.39	0.11	0.15	Surface
rn-d-gr-2 sp 5	0.76	0.04	0.09	0.00	0.00	b.d	0.11	b.d	70.91	0.11	27.44	99.46	0.11	0.15	Surface
rn-d-gr-2 sp 6	0.80	0.04	0.18	0.00	0.03	b.d	0.11	b.d	70.49	0.10	27.36	99.12	0.11	0.15	Surface
rn-d-gr-2 sp 7	0.79	0.04	0.15	b.d	0.03	b.d	0.11	b.d	70.60	0.10	27.39	99.21	0.11	0.15	Surface
rn-d-gr-2 sp 8	0.74	0.04	0.11	b.d	b.d	b.d	0.11	b.d	70.70	0.11	27.39	99.20	0.12	0.15	Surface
rn-d-gr-2 sp 9	0.82	0.05	0.17	0.01	0.02	b.d	0.11	b.d	70.49	0.11	27.36	99.14	0.12	0.16	Surface
rn-d-gr-2 sp 10	0.77	0.05	0.16	0.01	0.01	b.d	0.11	b.d	70.60	0.10	27.38	99.19	0.12	0.15	Surface
rn-d-gr-2 sp 11	0.91	0.05	0.31	0.01	0.01	b.d	0.11	b.d	70.22	0.11	27.37	99.10	0.12	0.16	Surface
rn-d-gr-2 sp 12	1.00	0.06	0.31	b.d	0.03	b.d	0.11	0.01	70.45	0.12	27.50	99.57	0.12	0.18	Surface
rn-d-gr-2 sp 13	0.85	0.05	0.26	b.d	0.04	b.d	0.12	0.01	70.75	0.10	27.55	99.74	0.12	0.16	Surface
rn-d-gr-2 sp 14	0.68	0.05	0.02	b.d	b.d	b.d	0.11	b.d	70.97	0.10	27.42	99.36	0.12	0.15	Surface
rn-d-gr-2 sp 15	0.71	0.05	0.02	b.d	b.d	b.d	0.10	b.d	71.16	0.10	27.49	99.64	0.11	0.15	Surface
rn-d-gr-2 sp 16	0.71	0.04	0.02	b.d	b.d	b.d	0.11	b.d	70.92	0.09	27.39	99.29	0.11	0.14	Surface
rn-d-gr-3 sp 1	0.68	0.07	0.04	0.04	b.d	b.d	0.10	b.d	70.71	0.11	27.35	99.09	0.14	0.18	Surface
rn-d-gr-3 sp 2	0.72	0.10	0.06	0.03	b.d	b.d	0.07	b.d	70.52	0.10	27.31	98.91	0.10	0.20	Surface
rn-d-gr-3 sp 3	0.73	0.06	0.05	0.03	b.d	b.d	0.05	b.d	70.89	0.11	27.40	99.32	0.08	0.16	Surface
rn-d-gr-3 sp 4	0.73	0.04	0.03	0.01	b.d	b.d	0.05	b.d	70.99	0.11	27.41	99.37	0.06	0.15	Surface
rn-d-gr-3 sp 5	0.70	0.03	0.02	0.01	b.d	b.d	0.05	b.d	71.36	0.10	27.53	99.80	0.07	0.13	Surface
rn-d-gr-3 sp 6	0.65	0.03	0.02	b.d	b.d	b.d	0.06	b.d	71.15	0.10	27.44	99.46	0.07	0.13	Surface
rn-d-gr-3 sp 7	0.95	0.03	0.23	b.d	0.01	b.d	0.06	b.d	70.84	0.11	27.53	99.77	0.07	0.13	Surface
rn-d-gr-3 sp 8	0.69	0.03	0.03	b.d	b.d	b.d	0.06	b.d	71.47	0.10	27.58	99.95	0.06	0.13	Surface
rn-d-gr-3 sp 9	0.68	0.02	0.04	b.d	b.d	b.d	0.04	b.d	71.55	0.10	27.60	100.02	0.05	0.12	Surface
rn-d-gr-3 sp 10	0.68	0.02	0.03	b.d	b.d	b.d	0.03	b.d	71.44	0.09	27.54	99.84	0.03	0.11	Surface
rn-d-gr-3 sp 11	0.69	0.03	0.02	b.d	b.d	b.d	0.03	b.d	71.49	0.09	27.56	99.91	0.03	0.12	Surface
rn-d-gr-3 sp 12	0.74	0.09	0.06	0.01	b.d	b.d	0.03	b.d	69.76	0.09	26.98	97.76	0.04	0.18	Surface
rn-d-gr-1 sp 1	0.62	0.02	0.03	b.d	b.d	b.d	0.03	b.d	70.97	0.08	27.35	99.10	0.04	0.10	Surface
rn-d-gr-1 sp 2	0.71	0.04	0.03	0.01	b.d	b.d	0.08	b.d	71.14	0.06	27.44	99.52	0.09	0.10	Surface
rn-d-gr-1 sp 3	0.74	0.02	0.03	0.02	b.d	b.d	0.09	b.d	71.15	0.06	27.44	99.55	0.11	0.09	Surface
rn-d-gr-1 sp 4	0.71	0.05	0.04	0.03	b.d	b.d	0.08	b.d	71.14	0.08	27.48	99.61	0.10	0.13	Surface
rn-d-gr-1 sp 5	0.71	0.06	0.06	0.03	0.01	b.d	0.10	b.d	71.01	0.08	27.45	99.50	0.13	0.14	Surface
rn-d-gr-1 sp 6	0.73	0.06	0.06	0.03	b.d	b.d	0.11	0.01	71.05	0.09	27.48	99.61	0.14	0.14	Surface
rn-d-gr-1 sp 7	0.66	0.05	0.06	0.03	0.01	b.d	0.12	b.d	70.89	0.09	27.41	99.32	0.15	0.14	Surface
rn-d-gr-1 sp 8	0.74	0.06	0.08	0.03	b.d	b.d	0.11	b.d	70.95	0.09	27.46	99.52	0.14	0.15	Surface
rn-d-gr-1 sp 9	0.72	0.05	0.05	0.03	b.d	b.d	0.09	b.d	70.95	0.09	27.43	99.43	0.12	0.15	Surface
rn-d-gr-1 sp 10	0.78	0.05	0.10	0.03	b.d	b.d	0.08	b.d	70.92	0.09	27.45	99.50	0.11	0.14	Surface
rn-d-gr-1 sp 11	0.69	0.05	0.03	0.03	b.d	b.d	0.07	b.d	71.50	0.07	27.59	100.03	0.10	0.12	Surface
rn-d-gr-1 sp 12	0.75	0.05	0.02	0.02	b.d	b.d	0.06	b.d	71.17	0.09	27.48	99.64	0.08	0.14	Surface
rn-d-gr-1 sp 13	0.75	0.04	0.13	0.02	b.d	b.d	0.06	b.d	70.87	0.09	27.43	99.38	0.08	0.13	Surface
rn-d-gr-1 sp 14	0.69	0.03	0.02	0.02	b.d	b.d	0.05	b.d	71.31	0.09	27.50	99.72	0.07	0.12	Surface

Sample ID Cristales Grandes	Mg [wt%]	Al [wt%]	Si [wt%]	Ti [wt%]	Ca [wt%]	P [wt%]	V [wt%]	Cr [wt%]	Fe [wt%]	Mn [wt%]	O [wt%]	Total	Ti+V [wt%]	Al+Mn [wt%]	Sample
cg-mag-mt-sample-1-gr-7 sp 1	1.28	0.06	0.50	0.03	0.19	b.d	0.16	0.01	69.77	0.05	27.47	99.53	0.20	0.12	Surface
cg-mag-mt-sample-1-gr-7 sp 2	1.53	0.06	0.89	0.04	0.27	b.d	0.17	b.d	68.57	0.05	27.39	98.95	0.20	0.11	Surface
cg-mag-mt-sample-1-gr-7 sp 3	1.26	0.06	0.51	0.03	0.19	b.d	0.17	b.d	69.49	0.05	27.39	99.17	0.21	0.12	Surface
cg-mag-mt-sample-1-gr-7 sp 4	1.33	0.12	0.49	0.04	0.26	b.d	0.17	b.d	69.27	0.05	27.37	99.11	0.20	0.17	Surface
cg-mag-mt-sample-1-gr-7 sp 5	1.25	0.06	0.54	0.04	0.23	b.d	0.17	0.01	69.79	0.05	27.53	99.68	0.21	0.11	Surface
cg-mag-mt-sample-1-gr-7 sp 6	1.28	0.06	0.58	0.04	0.22	b.d	0.17	b.d	69.31	0.06	27.38	99.10	0.21	0.11	Surface
cg-mag-mt-sample-1-gr-7 sp 7	1.31	0.06	0.58	0.03	0.24	b.d	0.17	0.01	69.37	0.05	27.41	99.23	0.20	0.11	Surface
cg-mag-mt-sample-1-gr-7 sp 8	3.39	0.05	1.88	0.03	0.24	b.d	0.16	b.d	68.98	0.06	28.51	103.30	0.19	0.11	Surface
cg-mag-mt-sample-1-gr-7 sp 9	1.24	0.06	0.51	0.03	0.20	b.d	0.17	0.01	69.47	0.06	27.37	99.12	0.20	0.12	Surface
cg-mag-mt-sample-1-gr-7 sp 10	1.25	0.06	0.51	0.03	0.18	b.d	0.17	0.01	69.65	0.05	27.43	99.34	0.20	0.11	Surface
cg-mag-mt-sample-1-gr-5 sp 1	1.25	0.06	0.50	0.04	0.19	b.d	0.17	0.01	69.52	0.05	27.37	99.15	0.21	0.11	Surface
cg-mag-mt-sample-1-gr-5 sp 2	1.29	0.06	0.57	0.03	0.20	b.d	0.17	b.d	69.39	0.05	27.39	99.14	0.20	0.11	Surface
cg-mag-mt-sample-1-gr-5 sp 3	1.24	0.06	0.60	0.04	0.24	b.d	0.17	b.d	69.28	0.05	27.39	99.06	0.21	0.11	Surface
cg-mag-mt-sample-1-gr-5 sp 4	1.22	0.05	0.48	0.04	0.26	b.d	0.16	b.d	69.30	0.05	27.31	98.90	0.20	0.11	Surface
cg-mag-mt-sample-1-gr-5 sp 5	1.11	0.05	0.33	0.04	0.15	b.d	0.16	b.d	69.87	0.05	27.33	99.09	0.19	0.10	Surface
cg-mag-mt-sample-1-gr-5 sp 6	1.15	0.06	0.38	0.03	0.15	b.d	0.16	b.d	69.74	0.05	27.33	99.05	0.19	0.11	Surface
cg-mag-mt-sample-1-gr-5 sp 7	1.18	0.06	0.33	0.03	0.12	b.d	0.16	0.01	69.96	0.05	27.36	99.26	0.20	0.11	Surface
cg-mag-mt-sample-1-gr-5 sp 8	1.25	0.06	0.56	0.03	0.22	b.d	0.16	b.d	69.49	0.06	27.42	99.25	0.19	0.12	Surface
cg-mag-mt-sample-1-gr-5 sp 9	0.76	0.09	0.40	0.07	b.d	b.d	0.12	b.d	69.11	b.d	27.03	97.59	0.19	0.10	Surface
cg-mag-mt-sample-1-gr-5 sp 10	1.20	0.05	0.42	0.03	0.15	b.d	0.14	b.d	69.76	0.05	27.37	99.19	0.18	0.11	Surface
cg-mag-mt-sample-5-gr-1 sp 1	0.75	0.12	0.19	0.03	0.03	b.d	0.18	0.01	70.39	0.09	27.39	99.18	0.21	0.21	Surface
cg-mag-mt-sample-5-gr-1 sp 2	0.83	0.12	0.22	0.04	0.05	b.d	0.18	b.d	70.48	0.09	27.47	99.49	0.22	0.21	Surface
cg-mag-mt-sample-5-gr-1 sp 3	0.77	0.16	0.04	0.03	b.d	b.d	0.19	b.d	70.78	0.09	27.45	99.50	0.22	0.25	Surface
cg-mag-mt-sample-5-gr-1 sp 4	0.91	0.31	0.36	0.03	0.02	b.d	0.18	0.01	69.53	0.09	27.35	98.78	0.21	0.40	Surface
cg-mag-mt-sample-5-gr-1 sp 5	0.69	0.09	0.17	0.03	0.03	b.d	0.18	0.01	70.31	0.08	27.31	98.92	0.22	0.17	Surface
cg-mag-mt-sample-5-gr-1 sp 6	0.74	0.12	0.05	0.03	b.d	b.d	0.18	b.d	70.85	0.09	27.46	99.52	0.21	0.21	Surface
cg-mag-mt-sample-5-gr-1 sp 7	0.71	0.11	0.07	0.03	0.02	b.d	0.18	0.01	70.83	0.09	27.44	99.49	0.22	0.20	Surface
cg-mag-mt-sample-5-gr-1 sp 8	0.77	0.12	0.10	0.03	0.01	b.d	0.19	b.d	70.55	0.09	27.38	99.24	0.22	0.21	Surface
cg-mag-mt-sample-5-gr-1 sp 9	0.91	0.13	0.26	0.04	0.06	b.d	0.18	b.d	70.49	0.09	27.53	99.68	0.22	0.22	Surface
cg-mag-mt-sample-5-gr-1 sp 10	0.89	0.12	0.30	0.04	0.05	b.d	0.18	0.01	70.34	0.09	27.48	99.51	0.22	0.21	Surface
cg-mag-mt-sample-5-gr-4 sp 1	0.86	0.09	0.44	0.03	0.15	b.d	0.15	b.d	70.16	0.09	27.54	99.52	0.18	0.19	Surface
cg-mag-mt-sample-5-gr-4 sp 2	0.94	0.10	0.48	0.02	0.16	b.d	0.15	b.d	69.98	0.09	27.52	99.44	0.17	0.20	Surface
cg-mag-mt-sample-5-gr-4 sp 3	1.08	0.11	0.45	0.03	0.17	b.d	0.15	b.d	70.05	0.10	27.56	99.69	0.18	0.21	Surface
cg-mag-mt-sample-5-gr-4 sp 4	0.89	0.10	0.47	0.02	0.20	b.d	0.15	b.d	70.10	0.09	27.57	99.60	0.17	0.19	Surface
cg-mag-mt-sample-5-gr-4 sp 5	1.05	0.11	0.52	0.03	0.18	b.d	0.15	b.d	69.98	0.10	27.59	99.70	0.17	0.21	Surface
cg-mag-mt-sample-5-gr-4 sp 6	0.60	0.22	0.71	0.02	0.12	0.02	0.15	0.01	69.13	0.09	27.40	98.49	0.17	0.32	Surface
cg-mag-mt-sample-5-gr-4 sp 7	0.99	0.11	0.46	0.02	0.19	b.d	0.15	b.d	69.90	0.10	27.50	99.42	0.17	0.20	Surface
cg-mag-mt-sample-5-gr-4 sp 8	0.88	0.10	0.45	0.03	0.16	b.d	0.15	b.d	70.05	0.10	27.52	99.45	0.18	0.20	Surface
cg-mag-mt-sample-5-gr-4 sp 9	0.82	0.10	0.21	0.02	0.03	b.d	0.16	b.d	70.79	0.10	27.54	99.77	0.18	0.20	Surface
cg-mag-mt-sample-5-gr-4 sp 10	0.86	0.09	0.25	0.02	0.05	b.d	0.15	b.d	70.52	0.09	27.47	99.50	0.17	0.18	Surface
cg-mag-mt-sample-4-gr-3 sp 1	0.76	0.07	0.23	0.02	0.04	b.d	0.14	b.d	70.70	0.09	27.49	99.54	0.16	0.16	Surface
cg-mag-mt-sample-4-gr-3 sp 2	0.63	0.15	0.26	0.01	0.02	b.d	0.14	b.d	70.49	0.09	27.46	99.25	0.15	0.24	Surface
cg-mag-mt-sample-4-gr-3 sp 3	1.03	0.07	0.49	0.02	0.10	b.d	0.14	b.d	70.12	0.09	27.53	99.59	0.16	0.16	Surface
cg-mag-mt-sample-4-gr-3 sp 4	0.78	0.07	0.30	0.02	0.09	b.d	0.14	b.d	70.26	0.09	27.39	99.13	0.16	0.15	Surface
cg-mag-mt-sample-4-gr-3 sp 5	0.76	0.06	0.21	0.01	0.03	b.d	0.13	b.d	70.73	0.09	27.46	99.49	0.15	0.15	Surface
cg-mag-mt-sample-4-gr-3 sp 6	0.84	0.08	0.22	0.01	0.04	b.d	0.14	b.d	70.44	0.08	27.38	99.23	0.15	0.16	Surface
cg-mag-mt-sample-4-gr-3 sp 7	0.82	0.07	0.27	b.d	0.07	b.d	0.14	b.d	70.35	0.09	27.40	99.21	0.14	0.16	Surface
cg-mag-mt-sample-4-gr-3 sp 8	0.86	0.06	0.39	b.d	0.10	b.d	0.14	b.d	70.08	0.09	27.41	99.13	0.14	0.15	Surface
cg-mag-mt-sample-4-gr-2 sp 1	0.68	0.15	0.12	0.12	0.03	b.d	0.15	b.d	70.71	0.09	27.50	99.55	0.28	0.24	Surface
cg-mag-mt-sample-4-gr-2 sp 2	1.02	0.17	0.82	0.12	0.15	b.d	0.15	0.01	70.30	0.10	28.00	100.84	0.27	0.27	Surface
cg-mag-mt-sample-4-gr-2 sp 3	1.02	0.16	0.70	0.12	0.24	b.d	0.15	0.01	69.51	0.09	27.65	99.65	0.27	0.26	Surface
cg-mag-mt-sample-4-gr-2 sp 4	0.79	0.15	0.38	0.11	0.13	b.d	0.14	b.d	70.32	0.10	27.62	99.74	0.25	0.25	Surface
cg-mag-mt-sample-4-gr-2 sp 5	0.81	0.16	0.41	0.11	0.20	b.d	0.14	b.d	69.93	0.09	27.53	99.38	0.25	0.25	Surface
cg-mag-mt-sample-4-gr-2 sp 6	0.61	0.15	0.02	0.09	b.d	b.d	0.14	b.d	71.37	0.09	27.64	100.11	0.24	0.24	Surface
cg-mag-mt-sample-4-gr-2 sp 7	0.95	0.16	0.53	0.10	0.19	b.d	0.14	b.d	69.86	0.09	27.60	99.63	0.24	0.25	Surface
cg-mag-mt-sample-4-gr-2 sp 8	0.99	0.15	0.64	0.10	0.22	b.d	0.13	b.d	69.09	0.10	27.41	98.83	0.23	0.25	Surface
cg-mag-mt-sample-4-gr-2 sp 9	1.19	0.65	0.47	0.10	0.22	b.d	0.14	b.d	68.63	0.10	27.52	99.00	0.23	0.75	Surface
cg-mag-mt-sample-4-gr-2 sp 10	1.01	0.15	0.65	0.08	0.28	b.d	0.14	0.01	69.54	0.10	27.61	99.57	0.22	0.25	Surface
cg-mag-mt-sample-3-gr-2 sp 1	0.61	0.30	0.38	0.43	0.22	b.d	0.18	b.d	69.73	0.08	27.68	99.60	0.60	0.37	Surface
cg-mag-mt-sample-3-gr-2 sp 2	0.60	0.35	0.23	0.47	0.15	b.d	0.18	b.d	69.19	0.09	27.38	98.63	0.64	0.44	Surface
cg-mag-mt-sample-3-gr-2 sp 3	0.15	0.30	0.14	0.45	0.02	b.d	0.18	0.01	68.67	0.10	26.94	96.97	0.63	0.40	Surface
cg-mag-mt-sample-3-gr-2 sp 4	0.69	0.39	0.29	0.54	0.08	b.d	0.18	0.01	67.10	0.09	26.66	96.02	0.72	0.48	Surface
cg-mag-mt-sample-3-gr-2 sp 5	0.49	0.33	0.03	0.44	b.d	b.d	0.18	0.01	70.47	0.07	27.60	99.62	0.62	0.40	Surface
cg-mag-mt-sample-3-gr-2 sp 6	0.45	0.37	0.26	0.51	0.16	b.d	0.19	0.01	68.00	0.08	26.96	96.99	0.70	0.45	Surface
cg-mag-mt-sample-3-gr-2 sp 7	0.43	0.41	0.21	0.52	0.07	b.d	0.19	b.d	69.85	0.09	27.63	99.41	0.71	0.50	Surface
cg-mag-mt-sample-3-gr-2 sp 8	0.58	0.39	0.21	0.57	0.03	b.d	0.18	b.d	68.83	0.09	27.24	98.12	0.75	0.48	Surface
cg-mag-mt-sample-3-gr-2 sp 9	0.50	0.30	0.22	0.49	0.04	b.d	0.18	b.d	70.01	0.07	27.58	99.39	0.66	0.37	Surface
cg-mag-mt-sample-3-gr-8 sp 1	0.43	0.35	0.10	0.61	0.03	b.d	0.17	0.01	69.17	0.06	27.23	98.16	0.78	0.41	Surface
cg-mag-mt-sample-3-gr-8 sp 2	0.52	0.29	0.30	0.35	0.15	b.d	0.17	0.01	69.16	0.06	27.29	98.30	0.51	0.35	Surface
cg-mag-mt-sample-3-gr-8 sp 3	0.49	0.29	0.09	0.52	0.04	b.d	0.17	0.01	70.40	0.10	27.64	99.74	0.68	0.39	Surface
cg-mag-mt-sample-3-gr-8 sp 4	0.53	0.35	0.07	0.56	0.03	b.d	0.17	0.01	70.06	0.08	27.55	99.42	0.73	0.43	Surface
cg-mag-mt-sample-3-gr-8 sp 5	0.22	0.41	0.13	0.52	0.01	b.d	0.17	0.01	68.48	0.08	26.97	97.00	0.69	0.49	Surface
cg-mag-mt-sample-3-gr-8 sp 6	0.69	0.40	0.80	0.44	0.18	b.d	0.16	0.01	66.45	0.07	26.81	96.02	0.61	0.47	Surface
cg-mag-mt-sample-3-gr-8 sp 7	0.75	0.39	0.82	0.43	0.24	b.d	0.16	b.d	68.56	0.07	27.66	99.10	0.59	0.47	Surface
cg-mag-mt-sample-3-gr-8 sp 8	0.50	0.40	0.60	0.43	0.22	b.d	0.16	b.d	68.73	0.07	27.52	98.65	0.60	0.48	Surface
cg-mag-mt-sample-2-gr-4 sp 1	1.23	0.08	0.53	0.06	0.23	b.d	0.18	b.d	69.62	0.05	27.50	99.49	0.24	0.14	Surface
cg-mag-mt-sample-2-gr-4 sp 2	1.49	0.09	0.89	0.07	0.30	b.d	0.18	0.01	68.50	0.05	27.41	98.99	0.25	0.15	Surface

Sample ID Cristales Grandes	Mg [wt%]	Al [wt%]	Si [wt%]	Ti [wt%]	Ca [wt%]	P [wt%]	V [wt%]	Cr [wt%]	Fe [wt%]	Mn [wt%]	O [wt%]	Total	Ti+V [wt%]	Al+Mn [wt%]	Sample
cg-mag-mt-sample-2-gr-4 sp 3	1.21	0.10	0.44	0.07	0.16	b.d	0.18	0.01	69.50	0.05	27.35	99.07	0.25	0.15	Surface
cg-mag-mt-sample-2-gr-4 sp 4	1.69	0.09	1.40	0.07	0.21	b.d	0.17	0.01	66.92	0.05	27.18	97.79	0.24	0.15	Surface
cg-mag-mt-sample-2-gr-4 sp 5	1.31	0.41	0.56	0.06	0.24	b.d	0.19	b.d	68.65	0.05	27.42	98.89	0.25	0.46	Surface
cg-mag-mt-sample-2-gr-4 sp 6	1.38	0.11	0.75	0.07	0.31	b.d	0.18	0.01	68.42	0.05	27.27	98.53	0.24	0.16	Surface
cg-mag-mt-sample-2-gr-4 sp 7	1.25	0.11	0.60	0.06	0.23	b.d	0.18	b.d	68.84	0.05	27.26	98.57	0.24	0.16	Surface
cg-mag-mt-sample-2-gr-4 sp 8	1.49	0.11	0.89	0.07	0.31	b.d	0.18	0.01	68.23	0.05	27.33	98.67	0.24	0.16	Surface
cg-mag-mt-sample-2-gr-4 sp 9	1.52	0.10	1.01	0.07	0.42	b.d	0.18	b.d	67.65	0.06	27.27	98.29	0.25	0.16	Surface
cg-mag-mt-sample-2-gr-4 sp 10	1.22	0.11	0.55	0.07	0.24	b.d	0.18	b.d	69.34	0.06	27.43	99.21	0.25	0.17	Surface
cg-mag-mt-sample-2-gr-7 sp 1	1.34	0.14	0.79	0.09	0.34	b.d	0.17	b.d	68.57	0.06	27.42	98.92	0.27	0.20	Surface
cg-mag-mt-sample-2-gr-7 sp 2	1.34	0.14	0.74	0.10	0.32	b.d	0.18	b.d	68.81	0.05	27.47	99.14	0.28	0.19	Surface
cg-mag-mt-sample-2-gr-7 sp 3	1.47	0.15	0.87	0.09	0.38	b.d	0.18	b.d	68.40	0.05	27.47	99.07	0.27	0.20	Surface
cg-mag-mt-sample-2-gr-7 sp 4	1.46	0.14	0.86	0.09	0.34	b.d	0.18	b.d	68.51	0.06	27.47	99.11	0.27	0.20	Surface
cg-mag-mt-sample-2-gr-7 sp 5	1.37	0.14	0.89	0.10	0.37	b.d	0.18	b.d	68.24	0.06	27.39	98.73	0.28	0.19	Surface
cg-mag-mt-sample-2-gr-7 sp 6	1.62	0.14	1.11	0.09	0.39	b.d	0.18	0.01	67.37	0.06	27.26	98.21	0.27	0.20	Surface
cg-mag-mt-sample-2-gr-7 sp 7	1.37	0.13	0.81	0.10	0.33	b.d	0.18	b.d	68.28	0.06	27.32	98.57	0.28	0.18	Surface
cg-mag-mt-sample-2-gr-7 sp 8	1.40	0.13	0.86	0.10	0.38	b.d	0.18	0.01	68.00	0.06	27.29	98.43	0.28	0.19	Surface
cg-mag-mt-sample-2-gr-7 sp 9	1.42	0.14	0.93	0.09	0.41	b.d	0.18	b.d	67.87	0.05	27.31	98.41	0.27	0.19	Surface
cg-mag-mt-sample-2-gr-7 sp 10	2.26	0.13	0.91	0.09	0.37	0.01	0.19	b.d	68.08	0.06	27.45	99.55	0.28	0.19	Surface
cg-sample-3-gr-6 sp 1	0.87	0.33	0.75	0.26	0.31	b.d	0.17	b.d	68.98	0.06	27.70	99.44	0.44	0.39	Surface
cg-sample-3-gr-6 sp 2	0.80	0.35	0.57	0.28	0.22	b.d	0.17	b.d	68.99	0.08	27.54	98.99	0.45	0.43	Surface
cg-sample-3-gr-6 sp 3	0.90	0.40	1.06	0.36	0.18	b.d	0.17	b.d	67.68	0.09	27.48	98.32	0.53	0.49	Surface
cg-sample-3-gr-6 sp 4	0.67	0.81	0.57	0.32	0.15	b.d	0.17	b.d	68.26	0.08	27.59	98.62	0.49	0.89	Surface
cg-sample-3-gr-6 sp 5	1.00	0.38	1.15	0.38	0.34	b.d	0.17	b.d	67.63	0.10	27.62	98.77	0.55	0.47	Surface
cg-sample-3-gr-1 sp 1	0.56	0.25	0.34	0.25	0.07	b.d	0.16	0.01	70.26	0.07	27.63	99.59	0.41	0.32	Surface
cg-sample-3-gr-1 sp 2	0.31	0.23	0.20	0.17	0.02	b.d	0.16	b.d	68.33	0.02	26.67	96.12	0.34	0.26	Surface
cg-sample-3-gr-1 sp 3	0.54	0.64	0.32	0.35	0.09	b.d	0.18	0.01	68.11	0.09	27.16	97.47	0.52	0.72	Surface
cg-sample-3-gr-1 sp 4	0.56	0.52	0.20	0.35	0.05	b.d	0.16	b.d	69.58	0.08	27.51	99.01	0.51	0.60	Surface
cg-sample-3-gr-1 sp 5	0.92	0.47	0.19	0.33	0.19	b.d	0.16	b.d	68.34	0.07	27.10	97.77	0.49	0.54	Surface
cg-sample-3-gr-1 sp 6	0.68	0.35	0.34	0.46	0.16	b.d	0.17	b.d	69.59	0.07	27.62	99.45	0.63	0.42	Surface
cg-sample-3-gr-1 sp 7	0.62	0.39	0.42	0.50	0.20	b.d	0.17	b.d	70.01	0.08	27.91	100.30	0.67	0.47	Surface
cg-sample-3-gr-1 sp 8	0.51	0.53	0.46	0.50	0.33	b.d	0.17	b.d	66.80	0.07	26.87	96.24	0.67	0.60	Surface
cg-sample-3-gr-4 sp 1	0.69	0.42	0.42	0.56	0.21	b.d	0.17	0.01	68.63	0.09	27.44	98.62	0.73	0.51	Surface
cg-sample-3-gr-4 sp 2	0.50	0.31	0.31	0.25	0.06	b.d	0.16	0.01	67.84	0.04	26.71	96.18	0.41	0.35	Surface
cg-sample-3-gr-4 sp 3	0.36	0.40	0.51	0.46	0.14	b.d	0.17	0.01	68.37	0.07	27.26	97.74	0.63	0.47	Surface
cg-sample-3-gr-4 sp 4	0.61	0.37	0.44	0.51	0.17	b.d	0.16	b.d	68.25	0.09	27.22	97.81	0.67	0.45	Surface
cg-sample-3-gr-4 sp 5	0.68	0.35	0.35	0.52	0.10	b.d	0.16	b.d	69.94	0.08	27.75	99.93	0.68	0.43	Surface
cg-sample-3-gr-4 sp 6	0.24	0.34	0.44	0.55	0.17	b.d	0.16	b.d	66.81	0.07	26.61	95.40	0.71	0.42	Surface
cg-sample-3-gr-4 sp 7	0.81	0.42	0.70	0.49	0.19	b.d	0.17	0.01	68.95	0.08	27.75	99.57	0.66	0.50	Surface
cg-sample-3-gr-4 sp 8	0.58	0.34	0.06	0.46	0.02	b.d	0.17	b.d	69.73	0.08	27.37	98.81	0.63	0.42	Surface
cg-sample-3-gr-7-tr-1 sp 1	0.46	0.35	0.38	0.42	0.05	b.d	0.18	b.d	67.21	0.08	26.64	95.77	0.60	0.43	Surface
cg-sample-3-gr-7-tr-1 sp 2	1.24	0.39	0.54	0.42	0.22	b.d	0.17	b.d	68.61	0.08	27.52	99.20	0.59	0.47	Surface
cg-sample-3-gr-7-tr-1 sp 3	0.22	0.39	0.65	0.37	0.09	b.d	0.17	b.d	66.92	0.08	26.74	95.63	0.54	0.47	Surface
cg-sample-3-gr-7-tr-1 sp 4	b.d	0.34	0.25	0.43	0.03	b.d	0.17	0.01	67.96	0.07	26.76	96.02	0.60	0.41	Surface
cg-sample-3-gr-7-tr-1 sp 5	0.71	0.34	0.27	0.43	0.22	b.d	0.18	0.01	69.88	0.09	27.70	99.82	0.61	0.43	Surface
cg-sample-3-gr-7-tr-1 sp 6	0.56	0.48	0.08	0.44	0.03	b.d	0.18	0.01	69.54	0.08	27.41	98.79	0.62	0.55	Surface
cg-sample-3-gr-7-tr-1 sp 7	0.67	0.58	0.35	0.47	0.25	b.d	0.19	b.d	69.15	0.04	27.68	99.36	0.66	0.62	Surface
cg-sample-3-gr-7-tr-1 sp 8	0.55	1.06	0.16	0.49	0.31	b.d	0.18	b.d	69.14	0.07	27.96	99.93	0.67	1.14	Surface
cg-sample-3-gr-7-tr-1 sp 9	0.55	0.33	0.22	0.48	0.08	b.d	0.18	b.d	69.86	0.07	27.57	99.34	0.66	0.40	Surface
cg-sample-3-gr-7-tr-1 sp 10	0.45	0.36	0.10	0.54	0.05	b.d	0.19	b.d	68.10	0.06	26.83	96.70	0.74	0.42	Surface
cg-sample-3-gr-7-tr-2 sp 1	0.69	0.34	0.34	0.33	0.12	b.d	0.17	b.d	68.22	0.08	27.01	97.30	0.50	0.42	Surface
cg-sample-3-gr-7-tr-2 sp 2	0.56	0.30	0.31	0.33	0.06	b.d	0.16	b.d	67.67	0.04	26.69	96.13	0.50	0.35	Surface
cg-sample-3-gr-7-tr-2 sp 3	0.44	0.47	0.45	0.33	0.08	b.d	0.16	b.d	67.04	0.05	26.68	95.71	0.49	0.52	Surface
cg-sample-3-gr-7-tr-2 sp 5	0.52	0.31	0.22	0.43	0.09	b.d	0.18	0.01	68.93	0.05	27.16	97.90	0.60	0.37	Surface
cg-sample-3-gr-7-tr-2 sp 6	0.41	0.46	0.53	0.49	0.18	b.d	0.17	0.01	68.68	0.08	27.50	98.52	0.67	0.54	Surface
cg-sample-3-gr-7-tr-2 sp 7	0.79	0.46	0.35	0.64	0.05	b.d	0.18	b.d	69.11	0.10	27.59	99.29	0.83	0.56	Surface
cg-sample-3-gr-7-tr-2 sp 8	1.37	0.37	1.50	0.61	0.49	b.d	0.18	0.01	65.89	0.07	27.43	97.92	0.79	0.44	Surface
cg-sample-3-gr-7-tr-2 sp 9	0.66	0.40	0.56	0.61	0.22	b.d	0.18	0.01	68.59	0.10	27.55	98.88	0.80	0.50	Surface
cg-sample-3-gr-7-tr-2 sp 10	0.59	0.43	0.66	0.55	0.25	b.d	0.18	b.d	68.49	0.09	27.59	98.83	0.73	0.51	Surface
cg-sample-3-gr-7-tr-2 sp 11	0.70	0.40	0.35	0.56	0.11	b.d	0.18	0.01	69.19	0.09	27.53	99.11	0.74	0.48	Surface
cg-sample-3-gr-7-tr-2 sp 12	0.70	0.35	0.47	0.53	0.27	b.d	0.17	0.01	68.58	0.08	27.43	98.59	0.70	0.43	Surface
cg-sample-3-gr-9 sp 1	0.69	0.33	0.14	0.53	0.09	b.d	0.18	0.01	69.11	0.08	27.27	98.44	0.71	0.41	Surface
cg-sample-3-gr-9 sp 2	0.91	0.52	0.79	0.66	0.23	b.d	0.19	0.01	65.55	0.07	26.71	95.62	0.84	0.59	Surface
cg-sample-3-gr-9 sp 3	0.58	0.41	0.18	0.67	0.04	b.d	0.20	0.01	67.88	0.09	26.92	96.97	0.87	0.50	Surface
cg-sample-3-gr-9 sp 4	0.49	0.40	0.10	0.62	0.05	b.d	0.20	0.01	69.18	0.09	27.31	98.43	0.81	0.48	Surface
cg-sample-3-gr-9 sp 5	0.79	0.53	0.62	0.73	0.16	b.d	0.19	0.01	67.25	0.12	27.24	97.64	0.93	0.65	Surface
cg-sample-3-gr-9 sp 6	0.87	0.51	0.70	0.70	0.30	b.d	0.19	b.d	67.62	0.10	27.49	98.48	0.90	0.61	Surface
cg-sample-3-gr-9 sp 7	0.57	0.43	0.24	0.56	0.08	b.d	0.20	0.01	67.30	0.10	26.73	96.20	0.76	0.53	Surface
cg-sample-3-gr-9 sp 8	0.68	0.50	0.60	0.62	0.24	b.d	0.19	0.01	67.94	0.09	27.43	98.29	0.81	0.59	Surface
cg-sample-3-gr-9 sp 9	0.87	0.52	0.60	0.66	0.17	b.d	0.18	0.01	67.83	0.10	27.41	98.35	0.84	0.62	Surface
cg-sample-3-gr-9 sp 10	0.58	0.44	0.37	0.56	0.14	b.d	0.19	0.01	68.13	0.11	27.20	97.73	0.75	0.55	Surface
cg-sample-3-gr-9 sp 11	0.44	0.44	0.37	0.67	0.07	b.d	0.19	0.01	68.74	0.15	27.43	98.49	0.85	0.58	Surface
cg-sample-3-gr-9 sp 12	0.55	0.38	0.14	0.42	0.07	b.d	0.18	0.01	68.97	0.08	27.18	97.99	0.61	0.45	Surface
cg-mount-3-gr-1 sp 1	0.39	0.21	0.02	0.06	b.d	b.d	0.08	b.d	71.44	0.10	27.66	99.96	0.14	0.31	Surface
cg-mount-3-gr-1 sp 2	0.42	0.51	0.01	0.04	0.02	b.d	0.07	b.d	72.06	0.09	28.11	101.33	0.11	0.61	Surface
cg-mount-3-gr-1 sp 3	0.61	0.16	0.03	0.03	0.03	b.d	0.07	b.d	71.36	0.09	27.61	99.99	0.10	0.25	Surface
cg-mount-3-gr-1 sp 4	0.63	0.15	0.02	0.03	b.d	b.d	0.08	b.d	71.51	0.09	27.65	100.15	0.10	0.23	Surface
cg-mount-3-gr-1 sp 5	0.74	0.14	0.03	0.02	b.d	b.d	0.07	b.d	71.18	0.09	27.53	99.79	0.09	0.23	Surface

Sample ID Cristales Grandes	Mg [wt%]	Al [wt%]	Si [wt%]	Ti [wt%]	Ca [wt%]	P [wt%]	V [wt%]	Cr [wt%]	Fe [wt%]	Mn [wt%]	O [wt%]	Total	Ti+V [wt%]	Al+Mn [wt%]	Sample
cg-mount-3-gr-1 sp 6	1.29	0.38	0.32	0.01	0.05	b.d	0.08	b.d	69.50	0.08	27.38	99.10	0.10	0.47	Surface
cg-mount-3-gr-1 sp 7	0.79	0.10	0.02	0.01	b.d	b.d	0.09	b.d	71.42	0.08	27.58	100.08	0.10	0.18	Surface
cg-mount-3-gr-1 sp 8	0.77	0.10	0.01	b.d	0.01	b.d	0.09	b.d	71.63	0.08	27.66	100.34	0.10	0.17	Surface
cg-mount-3-gr-1 sp 9	1.05	0.13	0.48	b.d	0.09	b.d	0.09	b.d	69.34	0.08	27.24	98.50	0.09	0.21	Surface
cg-mount-3-gr-1 sp 10	0.97	0.13	0.28	0.01	b.d	b.d	0.09	b.d	70.69	0.07	27.55	99.79	0.10	0.20	Surface
cg-mount-3-gr-1 sp 11	0.84	0.17	0.05	b.d	0.02	b.d	0.09	b.d	70.64	0.08	27.38	99.26	0.10	0.25	Surface
cg-mount-3-gr-1 sp 12	0.73	0.12	0.01	0.01	b.d	b.d	0.09	b.d	71.10	0.07	27.47	99.60	0.10	0.19	Surface
cg-mount-3-gr-1 sp 13	0.85	0.13	0.08	0.02	0.02	b.d	0.09	b.d	71.03	0.08	27.52	99.81	0.11	0.21	Surface
cg-mount-3-gr-1 sp 14	0.71	0.13	0.01	0.01	b.d	b.d	0.10	b.d	71.15	0.07	27.50	99.70	0.11	0.21	Surface
cg-mount-3-gr-2 sp 1	1.19	0.10	0.62	b.d	0.01	b.d	0.08	b.d	69.86	0.08	27.50	99.44	0.08	0.18	Surface
cg-mount-3-gr-2 sp 2	0.64	0.41	0.06	b.d	0.01	b.d	0.07	b.d	70.60	0.07	27.53	99.39	0.07	0.49	Surface
cg-mount-3-gr-2 sp 3	0.77	0.08	0.02	b.d	b.d	b.d	0.07	b.d	71.15	0.08	27.46	99.62	0.07	0.15	Surface
cg-mount-3-gr-2 sp 4	0.80	0.07	0.02	0.01	b.d	b.d	0.07	b.d	71.06	0.07	27.42	99.53	0.08	0.15	Surface
cg-mount-3-gr-2 sp 5	0.74	0.07	0.02	b.d	b.d	b.d	0.07	b.d	71.28	0.08	27.50	99.74	0.07	0.14	Surface
cg-mount-3-gr-2 sp 6	0.85	0.14	0.06	b.d	b.d	b.d	0.07	b.d	70.06	0.08	27.14	98.40	0.07	0.22	Surface
cg-mount-3-gr-2 sp 7	0.73	0.05	0.02	b.d	b.d	b.d	0.06	b.d	71.37	0.08	27.52	99.83	0.07	0.13	Surface
cg-mount-3-gr-2 sp 8	0.30	0.08	0.06	b.d	0.01	0.02	0.06	b.d	70.75	0.06	27.27	98.61	0.06	0.14	Surface
cg-mount-3-gr-2 sp 9	1.74	0.07	0.36	b.d	b.d	b.d	0.05	b.d	68.19	0.08	26.70	97.18	0.05	0.15	Surface
cg-mount-3-gr-2 sp 10	0.79	0.06	0.04	b.d	b.d	b.d	0.04	b.d	71.38	0.08	27.54	99.93	0.05	0.13	Surface
cg-mount-3-gr-2 sp 11	0.79	0.08	0.02	0.01	b.d	b.d	0.04	b.d	71.45	0.07	27.56	100.01	0.05	0.15	Surface
cg-mount-3-gr-2 sp 12	0.76	0.12	0.07	0.02	b.d	b.d	0.04	b.d	71.07	0.08	27.49	99.66	0.07	0.20	Surface
cg-mount-3-gr-2 sp 13	0.75	0.18	0.01	0.03	b.d	b.d	0.06	b.d	71.24	0.07	27.56	99.91	0.09	0.25	Surface
cg-mount-3-gr-2 sp 14	0.80	0.20	0.04	0.04	b.d	b.d	0.05	b.d	70.89	0.07	27.47	99.57	0.09	0.27	Surface

Sample ID Ext. Laco Sur	Mg [wt%]	Al [wt%]	Si [wt%]	Ti [wt%]	Ca [wt%]	P [wt%]	V [wt%]	Cr [wt%]	Fe [wt%]	Mn [wt%]	O [wt%]	Total	Ti+V [wt%]	Al+Mn [wt%]	Sample
ELS-16_spot1_pt_1	0.24	0.27	0.02	0.28	b.d	b.d	0.14	b.d	71.70	0.04	28.02	100.70	0.41	0.31	Drill core
ELS-16_spot1_pt_2	0.21	0.21	0.01	0.19	b.d	b.d	0.15	b.d	71.43	0.05	27.81	100.05	0.33	0.26	Drill core
ELS-16_spot1_pt_3	0.21	0.22	0.01	0.13	b.d	b.d	0.13	0.01	72.05	0.04	28.02	100.81	0.27	0.25	Drill core
ELS-16_spot1_pt_4	0.16	0.21	0.01	0.09	b.d	b.d	0.13	b.d	71.50	0.04	27.74	99.89	0.22	0.25	Drill core
ELS-16_spot2_pt_1	0.10	0.22	0.01	0.14	b.d	b.d	0.14	0.01	71.90	0.04	27.87	100.42	0.28	0.26	Drill core
ELS-16_spot2_pt_2	0.16	0.98	0.01	0.38	b.d	b.d	0.14	b.d	71.12	0.07	28.34	101.19	0.52	1.05	Drill core
ELS-16_spot2_pt_3	0.77	3.55	0.01	1.70	b.d	b.d	0.14	b.d	65.85	0.38	29.61	102.01	1.84	3.94	Drill core
ELS-16_spot3_pt_1	1.08	2.03	0.02	0.89	b.d	b.d	0.12	b.d	68.54	0.20	29.27	102.14	1.01	2.23	Drill core
ELS-16_spot3_pt_2	0.48	1.03	0.02	0.25	b.d	b.d	0.12	0.01	70.76	0.07	28.47	101.20	0.37	1.10	Drill core
ELS-16_spot3_pt_3	0.13	0.20	0.01	0.20	b.d	b.d	0.15	b.d	71.79	0.05	27.88	100.42	0.35	0.26	Drill core
ELS-16_spot5_pt_1	0.18	0.37	0.01	0.24	b.d	b.d	0.14	0.01	71.67	0.04	28.02	100.69	0.39	0.41	Drill core
ELS-16_spot5_pt_2	0.32	1.29	0.01	0.25	b.d	b.d	0.15	0.01	70.25	0.07	28.34	100.68	0.39	1.35	Drill core
ELS-16_spot5_pt_3	0.14	0.21	0.01	0.10	b.d	b.d	0.14	0.01	71.64	0.04	27.79	100.08	0.23	0.25	Drill core
ELS-16_spot6_pt_1	0.20	0.36	b.d	0.31	b.d	b.d	0.15	b.d	71.17	0.08	27.87	100.14	0.46	0.43	Drill core
ELS-16_spot6_pt_2	0.13	1.03	0.01	0.42	b.d	b.d	0.14	b.d	70.96	0.10	28.33	101.12	0.56	1.13	Drill core
ELS-16_spot6_pt_3	0.19	0.47	0.01	0.34	b.d	b.d	0.16	0.01	71.35	0.08	28.05	100.65	0.50	0.55	Drill core
ELS-16_spot4_pt_2	0.11	0.26	0.01	0.09	b.d	b.d	0.14	0.01	71.76	0.04	27.84	100.26	0.23	0.30	Drill core
ELS-16_spot4_pt_3	0.33	0.86	0.01	0.38	b.d	b.d	0.14	0.01	70.37	0.10	28.13	100.35	0.52	0.96	Drill core
ELS-16_spot4_pt_1	0.12	0.22	0.01	0.13	b.d	b.d	0.12	0.01	72.00	0.04	27.91	100.56	0.25	0.26	Drill core
ELS-23_spot1_pt1	0.27	0.24	0.01	0.11	b.d	b.d	0.24	0.01	71.53	b.d	27.91	100.31	0.34	0.24	Drill core
ELS-23_spot1_pt2	0.26	0.23	0.01	0.10	b.d	b.d	0.24	0.01	71.46	b.d	27.86	100.17	0.33	0.23	Drill core
ELS-23_spot1_pt3	0.25	0.22	0.02	0.12	b.d	b.d	0.23	0.01	71.44	b.d	27.85	100.13	0.35	0.22	Drill core
ELS-23_spot1_pt4	0.25	0.22	0.01	0.08	b.d	b.d	0.23	0.01	71.44	b.d	27.84	100.10	0.32	0.22	Drill core
ELS-23_spot2_pt1	0.25	0.28	0.01	0.18	b.d	b.d	0.25	b.d	71.43	b.d	27.91	100.30	0.43	0.28	Drill core
ELS-23_spot2_pt2	0.25	0.28	0.01	0.09	b.d	b.d	0.24	0.01	71.37	0.03	27.88	100.17	0.34	0.31	Drill core
ELS-23_spot3_pt1	0.28	0.28	0.01	0.10	b.d	b.d	0.23	0.01	71.29	b.d	27.85	100.05	0.33	0.28	Drill core
ELS-23_spot3_pt2	0.33	0.22	0.02	0.78	b.d	b.d	0.24	0.01	70.54	0.06	27.90	100.09	1.02	0.28	Drill core
ELS-23_spot3_pt3	0.27	0.26	0.01	0.10	b.d	b.d	0.24	0.01	71.31	0.03	27.85	100.07	0.34	0.29	Drill core
ELS-23_spot3_pt4	0.58	0.35	0.45	0.15	0.14	b.d	0.24	0.01	70.18	0.03	28.18	100.30	0.39	0.37	Drill core
ELS-23_spot3_pt5	0.26	0.25	0.01	0.18	b.d	b.d	0.23	b.d	71.65	b.d	27.99	100.59	0.42	0.25	Drill core
ELS-23_spot4_pt1	0.21	0.32	0.08	0.16	0.02	b.d	0.42	0.01	70.92	b.d	27.84	99.98	0.58	0.32	Drill core
ELS-23_spot4_pt2	0.28	0.36	0.01	0.12	0.03	b.d	0.42	0.01	70.85	b.d	27.84	99.92	0.54	0.36	Drill core

Sample ID Pasos Blancos	Mg [wt%]	Al [wt%]	Si [wt%]	Ti [wt%]	Ca [wt%]	P [wt%]	V [wt%]	Cr [wt%]	Fe [wt%]	Mn [wt%]	O [wt%]	Total	Ti+V [wt%]	Al+Mn [wt%]	Sample
EPI-26_spot1_pt1	0.22	0.28	0.01	0.31	b.d	b.d	0.10	b.d	71.46	0.07	27.92	100.36	0.41	0.35	Drill core
EPI-26_spot1_pt2	0.21	0.28	0.02	0.29	b.d	b.d	0.10	b.d	71.48	0.06	27.92	100.35	0.38	0.35	Drill core
EPI-26_spot1_pt3	0.22	0.27	0.01	0.38	b.d	b.d	0.11	b.d	71.47	0.08	27.95	100.48	0.49	0.34	Drill core
EPI-26_spot4_pt1	0.23	0.28	0.02	0.32	b.d	b.d	0.10	b.d	71.39	0.07	27.91	100.31	0.42	0.35	Drill core
EPI-26_spot4_pt2	0.22	0.27	0.02	0.29	b.d	b.d	0.10	b.d	71.43	0.09	27.91	100.33	0.40	0.36	Drill core
EPI-26_spot4_pt3	0.22	0.27	0.01	0.29	b.d	b.d	0.10	0.01	71.55	0.05	27.94	100.45	0.39	0.32	Drill core
EPI-26_spot3_pt1	0.20	0.28	0.01	0.33	b.d	b.d	0.10	b.d	71.43	0.09	27.91	100.35	0.43	0.37	Drill core
EPI-26_spot3_pt2	0.20	0.32	0.02	0.36	b.d	b.d	0.10	b.d	71.32	0.08	27.91	100.29	0.46	0.39	Drill core
EPI-26_spot3_pt3	0.20	0.28	0.02	0.36	b.d	b.d	0.10	b.d	71.51	0.09	27.97	100.53	0.46	0.37	Drill core
EPI-26_spot3_pt4	0.20	0.28	0.01	0.36	b.d	b.d	0.10	b.d	71.41	0.07	27.92	100.37	0.46	0.36	Drill core
EPI-26_spot2_pt4	0.20	0.29	0.02	0.34	b.d	b.d	0.10	b.d	71.08	0.07	27.79	99.89	0.45	0.36	Drill core
EPI-26_spot2_pt3	0.19	0.29	0.02	0.35	b.d	b.d	0.10	b.d	71.28	0.08	27.87	100.18	0.45	0.37	Drill core
EPI-26_spot2_pt2	0.21	0.30	0.01	0.33	b.d	b.d	0.10	b.d	71.54	0.08	27.97	100.53	0.43	0.37	Drill core
EPI-26_spot5_pt1	0.20	0.23	0.02	0.38	0.01	b.d	0.10	b.d	71.22	0.09	27.82	100.07	0.47	0.32	Drill core
EPI-26_spot5_pt2	0.19	0.24	0.01	0.35	b.d	b.d	0.10	b.d	71.32	0.09	27.83	100.12	0.45	0.33	Drill core
EPI-26_spot5_pt3	0.18	0.20	0.01	0.33	b.d	b.d	0.10	b.d	71.32	0.09	27.79	100.03	0.43	0.29	Drill core
EPI-26_spot7_pt1	0.20	0.23	0.02	0.56	b.d	b.d	0.10	b.d	71.21	0.10	27.90	100.32	0.67	0.33	Drill core
EPI-26_spot7_pt2	0.19	0.24	0.01	0.31	b.d	b.d	0.10	b.d	71.44	0.07	27.86	100.23	0.41	0.32	Drill core
EPI-26_spot7_pt3	0.21	0.26	0.02	0.65	b.d	b.d	0.10	b.d	70.98	0.14	27.90	100.25	0.75	0.40	Drill core
EPI-26_spot8_pt1	0.17	0.21	0.01	0.48	b.d	b.d	0.11	0.01	71.13	0.11	27.79	100.00	0.58	0.31	Drill core
EPI-26_spot8_pt2	0.16	0.20	0.01	0.26	b.d	b.d	0.10	0.01	71.72	0.06	27.89	100.41	0.36	0.26	Drill core
EPI-26_spot8_pt3	0.16	0.20	0.01	0.29	b.d	b.d	0.11	0.01	71.58	0.10	27.86	100.30	0.39	0.29	Drill core
EPI-28_spot1_pt_1	0.28	0.29	0.02	0.29	b.d	b.d	0.09	b.d	71.23	0.08	27.89	100.17	0.38	0.37	Drill core
EPI-28_spot1_pt_2	0.30	0.36	0.01	0.55	b.d	b.d	0.09	0.01	70.96	0.07	27.98	100.33	0.64	0.43	Drill core
EPI-28_spot1_pt_3	0.28	0.31	0.01	0.48	b.d	b.d	0.09	b.d	71.18	0.08	27.96	100.38	0.56	0.38	Drill core
EPI-28_spot4_pt_1	0.28	0.31	0.02	0.44	b.d	b.d	0.09	0.01	71.26	0.09	27.99	100.47	0.52	0.39	Drill core
EPI-28_spot4_pt_2	0.37	0.42	0.01	0.67	b.d	b.d	0.09	0.01	70.66	0.11	28.04	100.37	0.76	0.53	Drill core
EPI-28_spot4_pt_3	0.27	0.30	0.01	0.35	b.d	b.d	0.09	b.d	71.51	0.07	28.02	100.63	0.44	0.37	Drill core
EPI-28_spot8_pt_1	0.29	0.28	0.01	0.31	b.d	b.d	0.08	b.d	71.28	0.06	27.90	100.22	0.40	0.34	Drill core
EPI-28_spot8_pt_2	0.31	0.30	0.01	0.37	0.01	b.d	0.09	0.01	71.26	0.07	27.97	100.39	0.45	0.37	Drill core
EPI-28_spot8_pt_3	0.27	0.27	0.01	0.29	b.d	b.d	0.09	b.d	71.41	0.07	27.93	100.35	0.38	0.34	Drill core
EPI-28_spot8_pt_4	0.31	0.32	0.01	0.37	0.01	b.d	0.09	b.d	71.28	0.06	27.99	100.44	0.45	0.38	Drill core
EPI-28_spot7_pt_1	0.36	0.35	0.02	0.85	b.d	b.d	0.09	0.01	70.37	0.12	27.95	100.12	0.94	0.47	Drill core
EPI-28_spot7_pt_2	0.27	0.29	0.01	0.27	b.d	b.d	0.09	0.01	71.68	0.05	28.04	100.71	0.36	0.34	Drill core
EPI-28_spot7_pt_3	0.31	0.32	0.01	0.31	b.d	b.d	0.09	b.d	71.32	0.07	27.99	100.42	0.40	0.40	Drill core
EPI-28_spot6_pt_1	0.25	0.30	0.02	0.35	b.d	b.d	0.09	b.d	71.32	0.07	27.93	100.32	0.44	0.37	Drill core
EPI-28_spot6_pt_2	0.33	0.35	0.02	0.42	b.d	b.d	0.09	b.d	71.35	0.08	28.09	100.74	0.51	0.43	Drill core
EPI-28_spot6_pt_3	0.33	0.33	0.01	0.32	0.01	b.d	0.09	b.d	71.42	0.09	28.06	100.66	0.41	0.42	Drill core
EPI-28_spot6_pt_4	0.26	0.29	0.01	0.30	b.d	b.d	0.10	0.01	71.44	0.06	27.96	100.42	0.39	0.34	Drill core
EPI-28_spot5_pt_1	0.19	0.26	0.02	0.23	b.d	b.d	0.08	0.01	71.93	0.06	28.02	100.80	0.31	0.31	Drill core
EPI-28_spot5_pt_2	0.21	0.27	0.01	0.43	b.d	b.d	0.08	b.d	71.68	0.07	28.04	100.78	0.51	0.34	Drill core
EPI-28_spot5_pt_3	0.18	0.27	0.02	0.29	b.d	b.d	0.08	0.01	71.94	0.06	28.05	100.90	0.37	0.33	Drill core
EPI-28_spot3_pt_1	0.25	0.28	0.02	0.26	b.d	b.d	0.09	0.01	71.80	0.07	28.06	100.82	0.36	0.34	Drill core
EPI-28_spot3_pt_2	0.24	0.26	0.02	0.25	b.d	b.d	0.09	0.01	71.89	0.05	28.05	100.85	0.34	0.31	Drill core
EPI-28_spot3_pt_3	0.22	0.28	0.02	0.23	0.09	b.d	0.09	0.01	71.48	0.05	27.94	100.41	0.32	0.33	Drill core
EPI-28_spot2_pt_1	0.28	0.27	0.01	0.30	b.d	b.d	0.10	b.d	71.66	0.05	28.03	100.69	0.40	0.32	Drill core
EPI-28_spot2_pt_2	0.33	0.30	0.01	0.51	b.d	b.d	0.10	b.d	71.13	0.08	28.00	100.46	0.61	0.38	Drill core
EPI-28_spot2_pt_3	0.30	0.28	0.01	0.36	b.d	b.d	0.09	b.d	71.37	0.07	27.98	100.46	0.45	0.34	Drill core

ANNEX B: Supplementary Material for Chapter 3

Magmatic-hydrothermal evolution of the El Laco iron deposit revealed by trace element geochemistry and high-resolution chemical mapping of magnetite assemblages

This file includes:

Supplementary Figures B1-B9

B10. Supplementary Table 1: Sample descriptions and and geographic location of the different volcanic units studied.

B11. Analytical conditions for EPMA analyses of pyroxenes and Fe-Ti oxides from El Laco deposit.

B12. EPMA data of magnetite from El Laco ore bodies and host andesites.

B13. EPMA data of pyroxene from El Laco ore bodies and host andesites.

B14. LA-ICP-MS data of magnetite from El Laco ore bodies and host andesites.

Supplementary Figure B1: Photographs of the andesite samples from the units that host the different ore bodies at El Laco volcanic complex associated with back-scattered electron (BSE) images of magnetite-rich glomerocrysts. mgt: magnetite, ilm: ilmenite, cpx: clinopyroxene, opx: orthopyroxene, Fap: fluorapatite, plg: plagioclase.

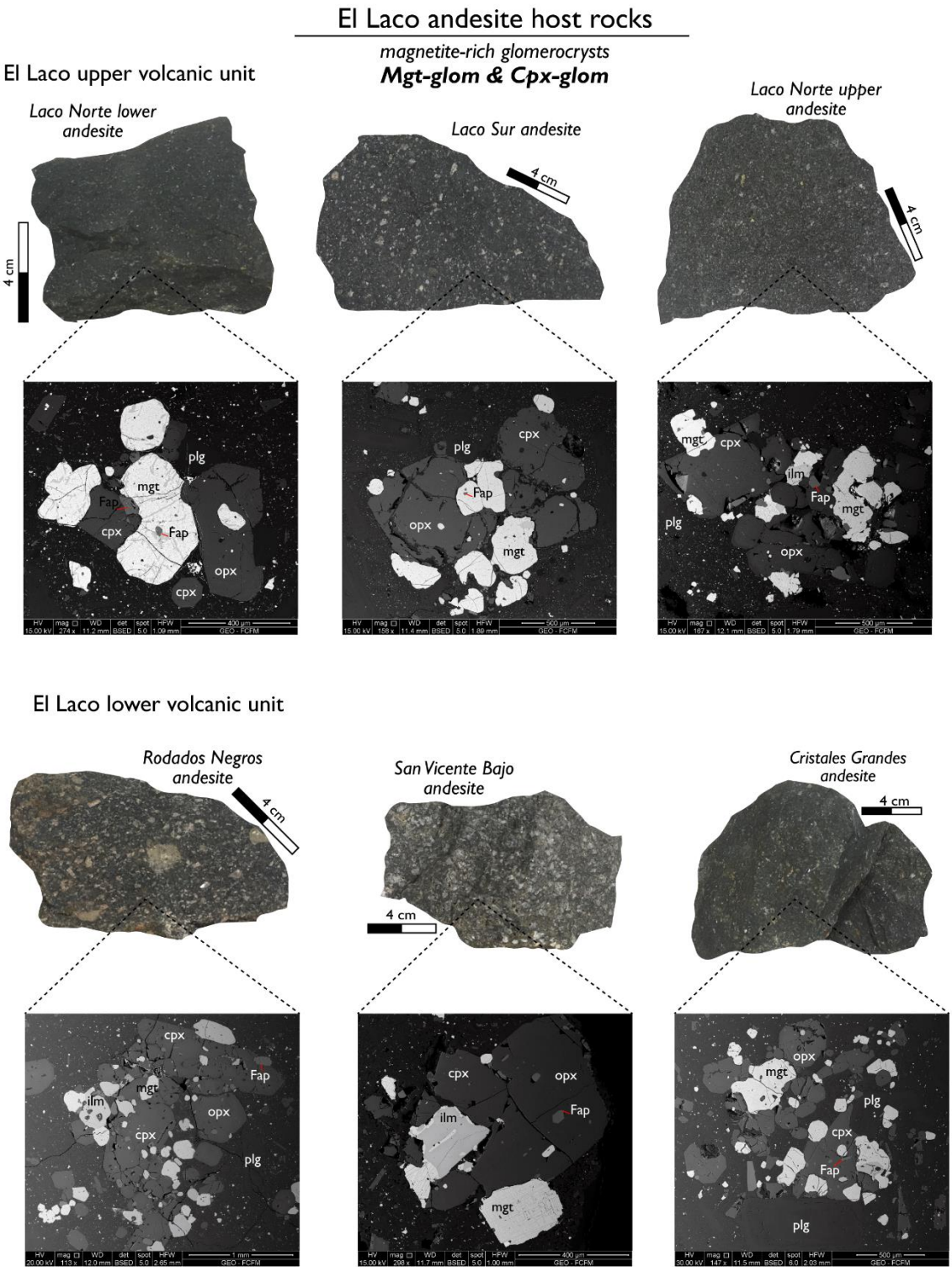

Supplementary Figure B2: Photographs of the drill core samples from the El Laco magnetite ore bodies. (a) SVA-1001 drill core from San Vicente Alto ore body. (b) EPI-0702 drill core from Cristales Grandes ore body. (c) EPI-0808 drill core from Rodados Negros ore body. Photographs display the transition from massive magnetite at surface/shallow depths to magnetite breccias at depth; some host veinlets.

Supplementary Figure B3: Photographs of the drill core samples from the El Laco magnetite ore bodies. (a) SVA-1010 drill core from San Vicente Alto ore body. (b) SVB-1004 drill core from San Vicente Bajo ore body. (c) SVB-1002 drill core from San Vicente Alto ore body. The examples show the transition from massive magnetite at surface/shallow depths to magnetite breccias at depth.

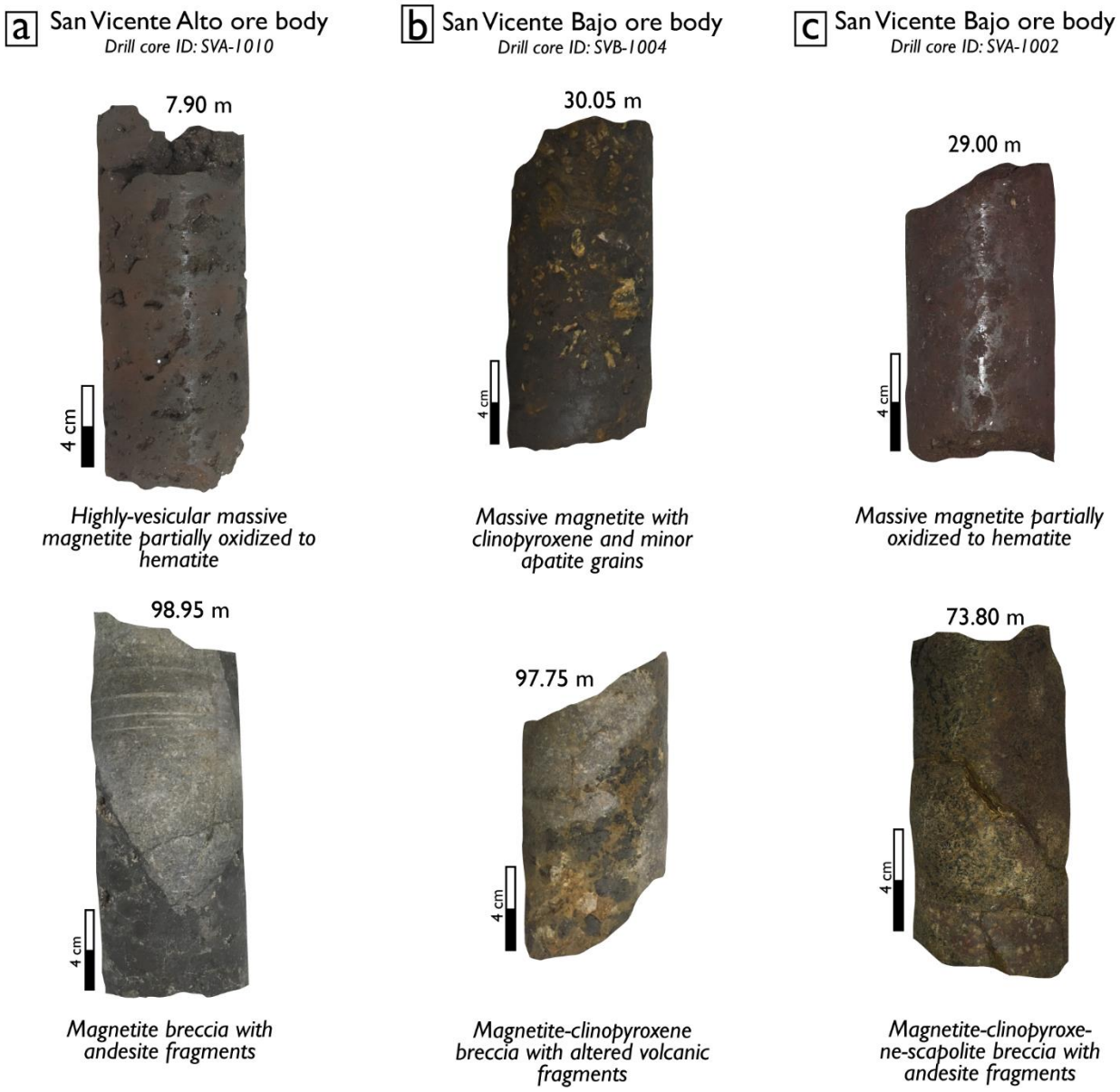

Supplementary Figure B4: Synchrotron three-elemental (RGB) μ-XRF maps and BSE images iron ore samples from the deep zone (Mgt-deep; breccias and veinlets) at El Laco. (a,d, f) Whole-thin section photographs of the different types of breccias and crosscutting veinlets (f). (b) Ca-Ti-Fe map of a breccia sample from Laco Norte ore body showing trellis textured magnetite and ilmenite grains, which are also shown in BSE images (c,d). (e) K-Ca-Fe map of breccia sample from Pasos Blancos ore body. (g) Ti-Ca-Fe map of a breccia sample crosscut by a magnetite-clinopyroxene veinlet from Pasos Blancos ore body. Note that the trellis texture in magnetite in the veinlet. mgt: magnetite, cpx: clinopyroxene, ilm: ilmenite, gyp: gypsum, rut: rutile.

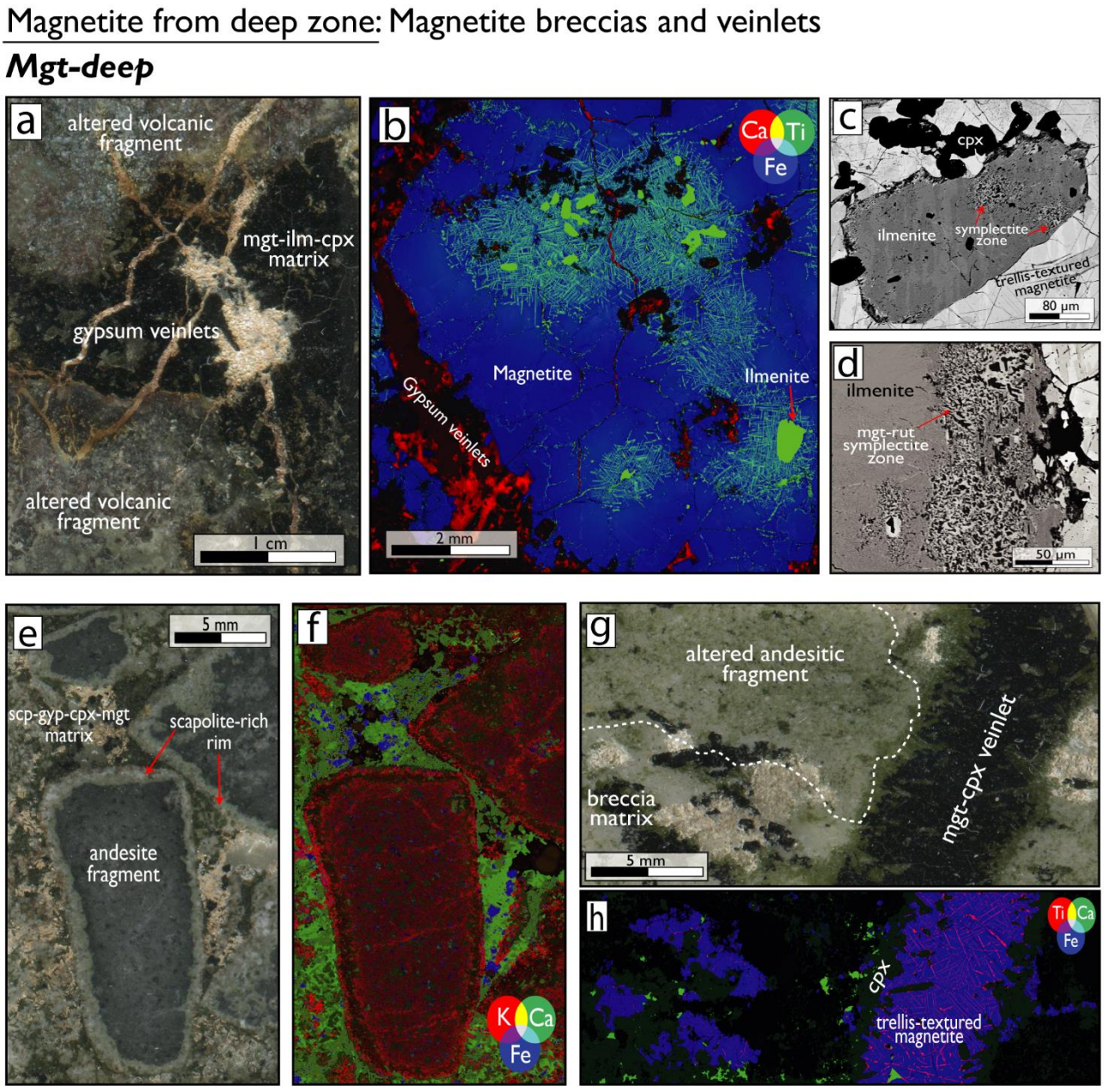

Supplementary Figure B5: Synchrotron single and three-elemental (RGB) μ-XRF maps of iron ore samples from deep zone (Mgt-deep; veinlets) from El Laco. (a,e) Whole-thin section photographs of the different type of veinlets observed in drill core samples from Extensión Laco Sur ore body. (b,c) Ti-Ca-Fe and Mn maps of magnetite-clinopyroxene-ilmenite veinlets crosscutting andesite horizons. (f,g,i) Sr-Ti-Ca maps showing the textural relationships between magnetite, ilmenite, clinopyroxene and scapolite. Note the symplectitic-like intergrowth between titanite, ilmenite and clinopyroxene in (h). Note the trellis texture displayed by magnetite in (j). tit: titanite, scp: scapolite.

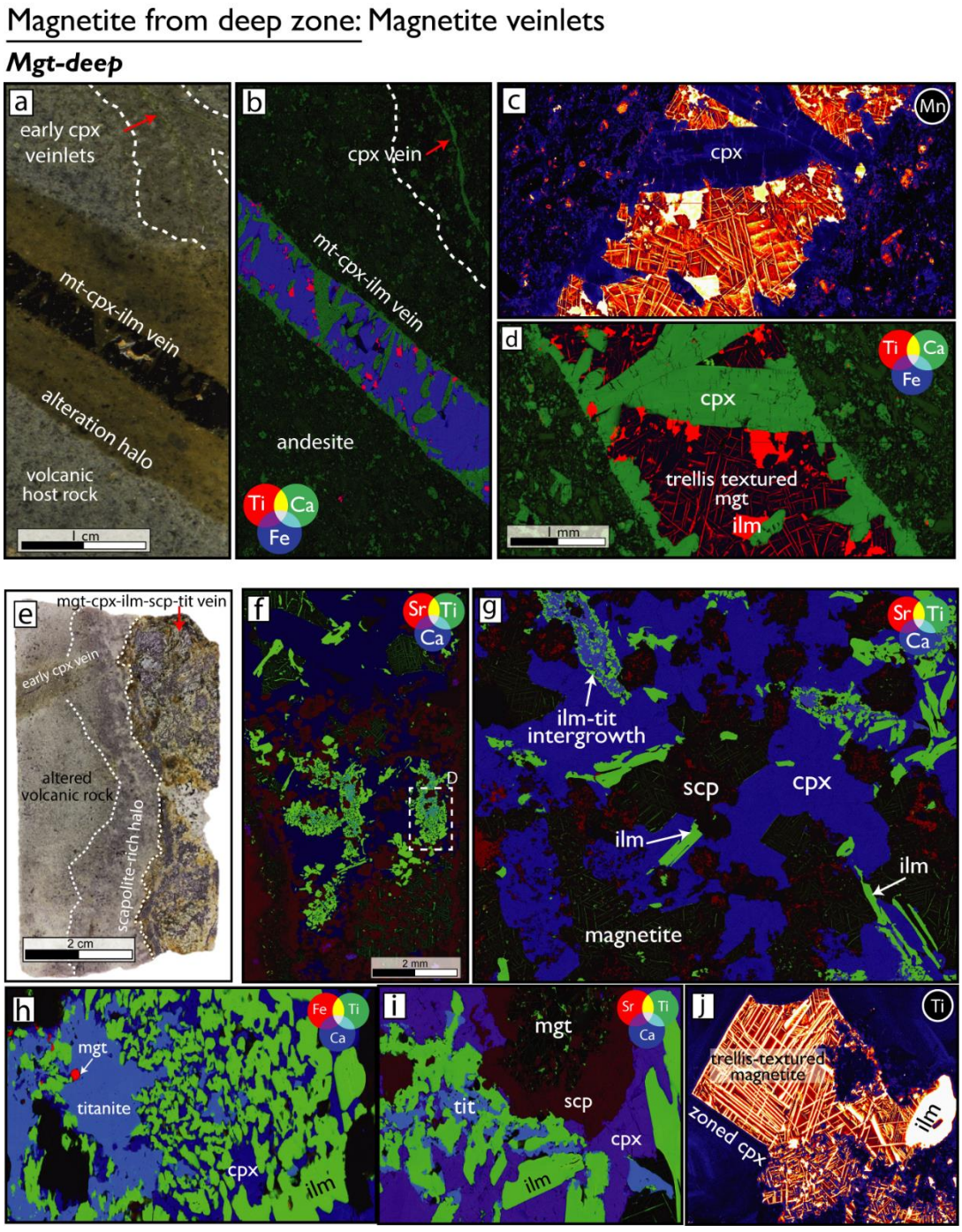

Supplementary Figure B6: Quantitative WDS maps of magnetite grains representative for deep (Mgt-deep: a) and intermediate (Mgt-interm: b) zones of the El Laco ore bodies (breccias).

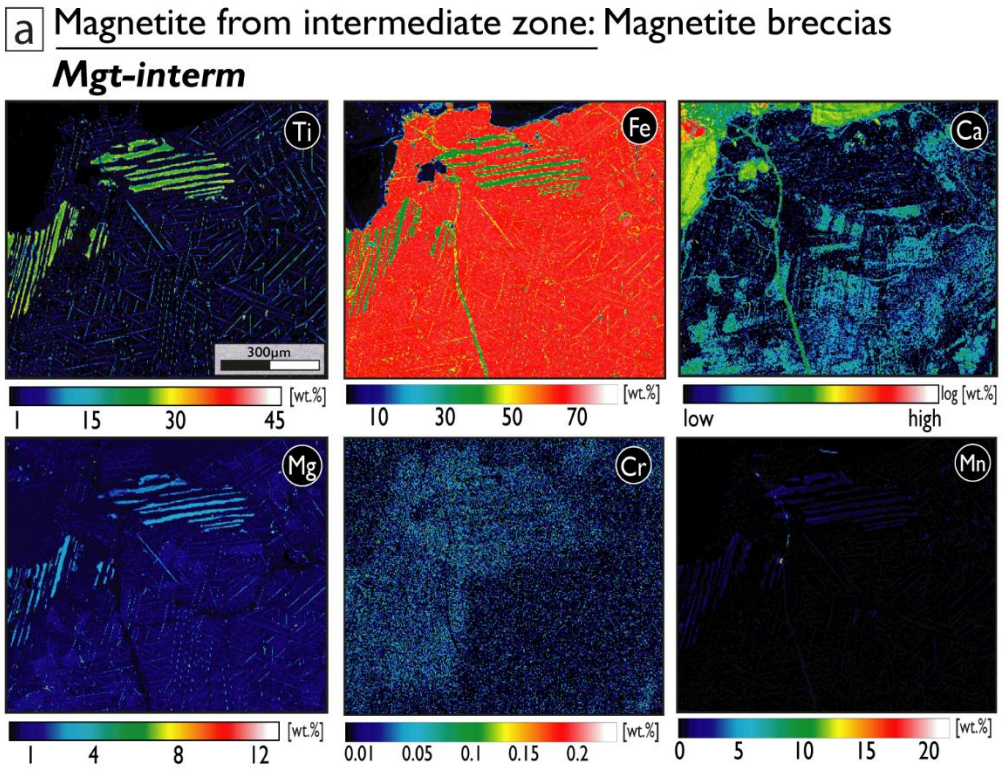

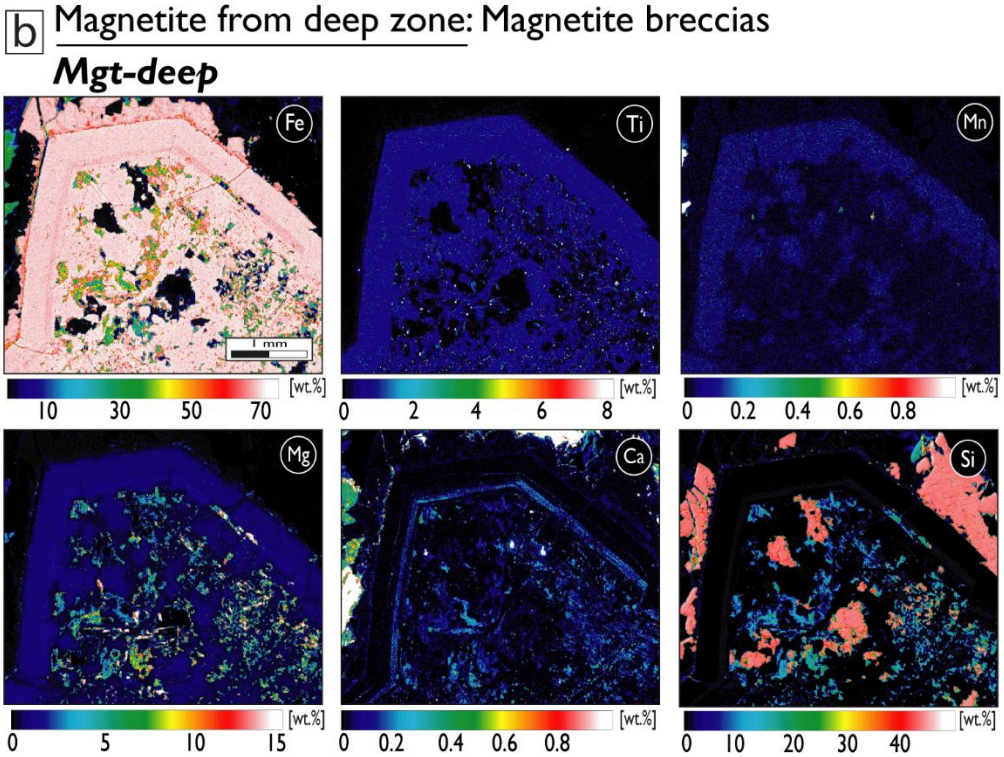

Supplementary Figure B7: Synchrotron single and three-elemental (RGB) µ-XRF and quantitative WDS maps of clinopyroxene grains from drill core samples from Laco Norte (a) and San Vicente Alto (b) ore bodies.

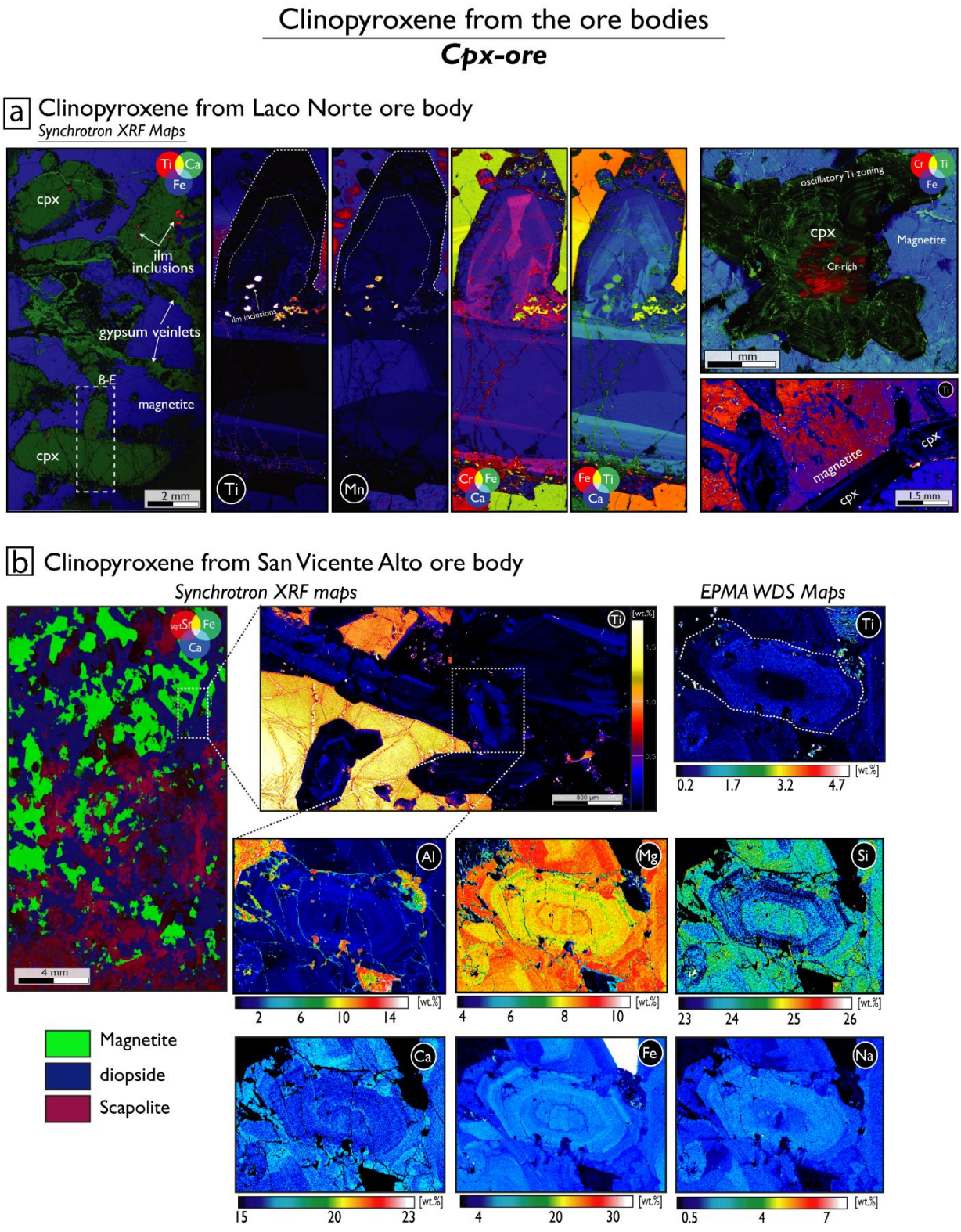

Supplementary Figure B8: Backscattered-electron (BSE) images and SEM EDS spectra of scapolite-bearing ore samples from El Laco deposit.

Marialitic (Na-rich) Scapolite from El Laco ore bodies

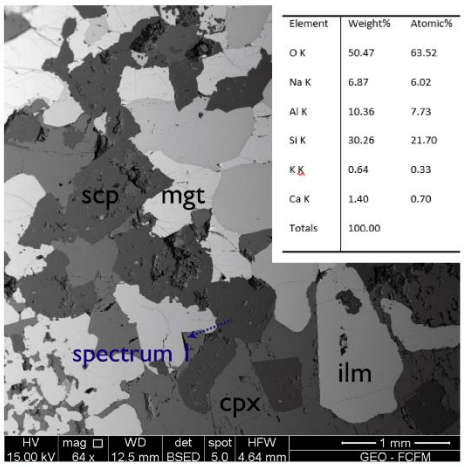

Element	Weight%	Atomic%
O K	50.47	63.52
Na K	6.87	6.02
Al K	10.36	7.73
Si K	30.26	21.70
K K	0.64	0.33
Ca K	1.40	0.70
Totals	100.00	

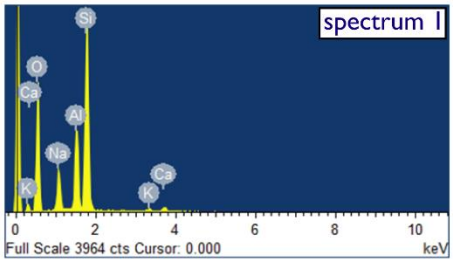

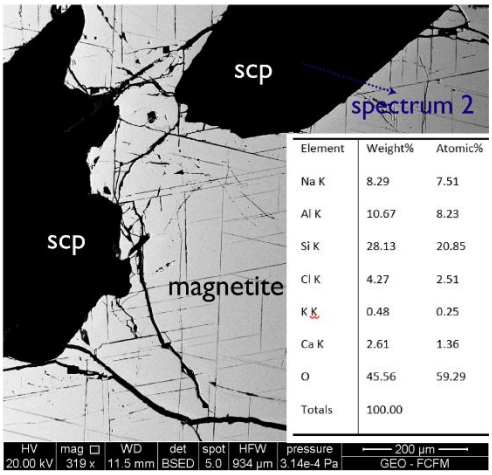

Element	Weight%	Atomic%
Na K	8.29	7.51
Al K	10.67	8.23
Si K	28.13	20.85
Cl K	4.27	2.51
K K	0.48	0.25
Ca K	2.61	1.36
O	45.56	59.29
Totals	100.00	

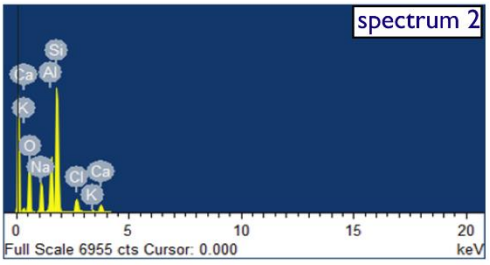

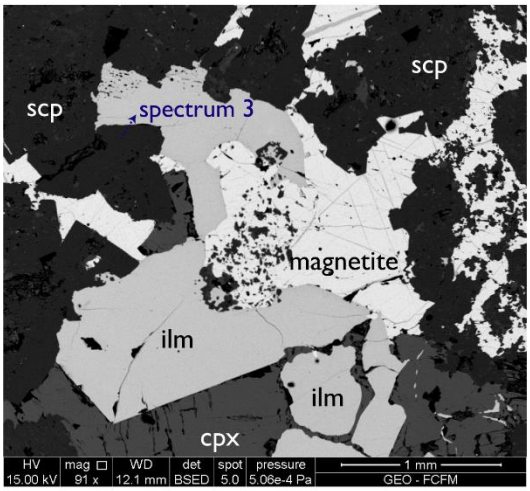

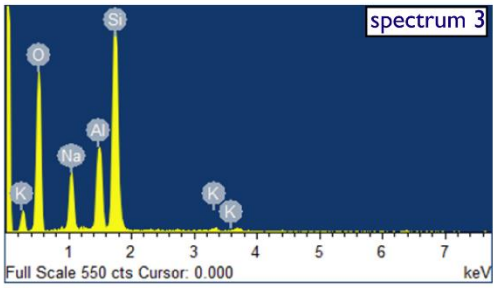

Element	Weight%	Atomic%
O K	50.36	63.16
Na K	7.84	6.84
Al K	10.32	7.68
Si K	30.59	21.86
K K	0.89	0.46
Totals	100.00	

Supplementary Figure B9: Backscattered-electron (BSE) images and SEM EDS spectra of oriented fluid inclusions hosted by magnetite from deep levels of the El Laco ore bodies.

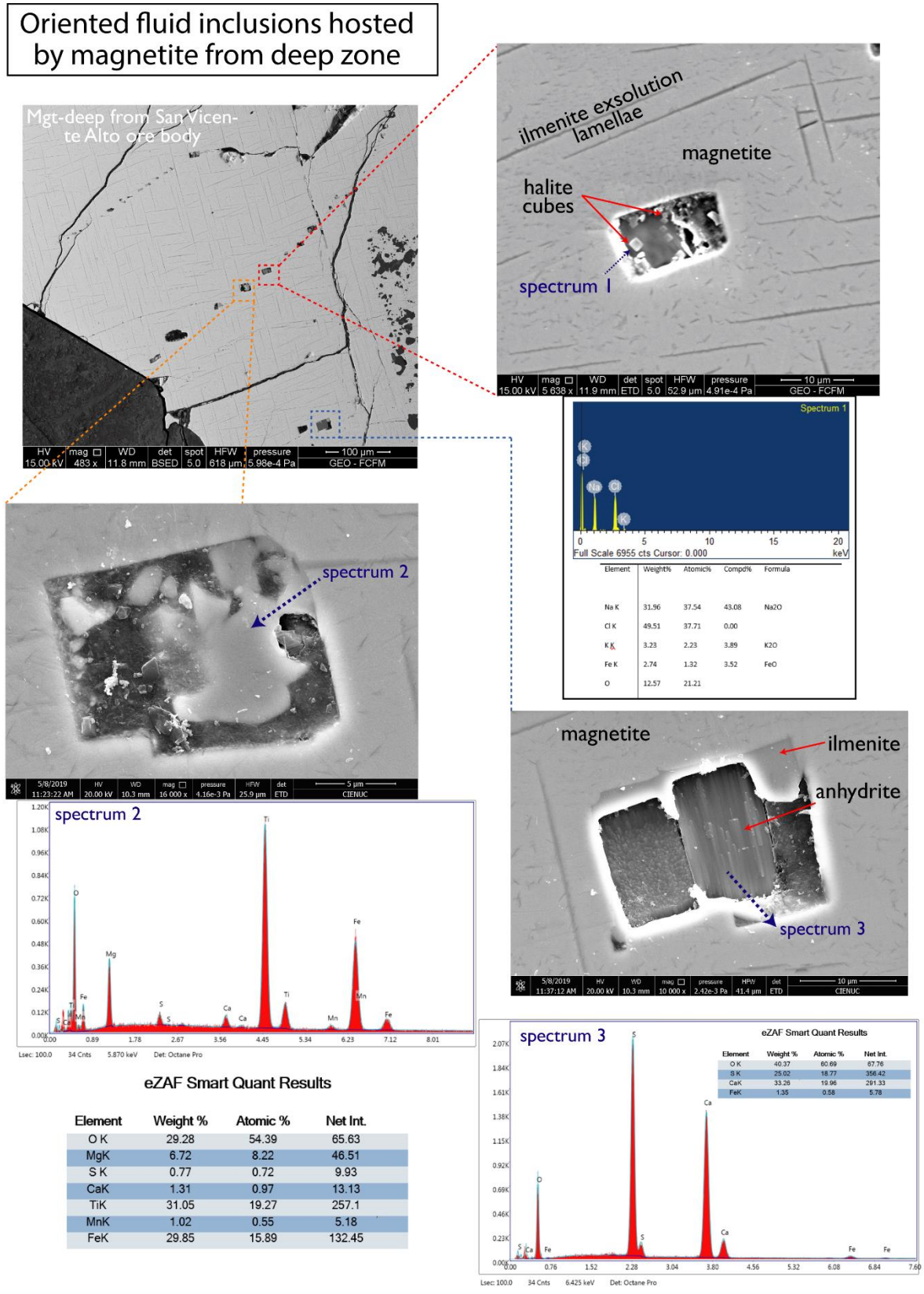

B10. Supplementary Table 1: Sample descriptions and and geographic location of the different volcanic units studied.

Sample #	Description	mineralogy	volcanic form	host - ore body	volcanic unit	WGS-84 North	WGS-84 East
AILN-02	fine-grained porphyrytic dark grey andesite	plag, cpx, opx, mgt, amph, apa	lava flow	Laco Norte	Laco Norte lower andesites	7364210	653591
ALS-01	coarse-grained porphyrytic dark grey andesite	plag, cpx, opx, mgt, apa	lava flow	Laco Sur	Lower andesites	7363197	653444
ACG-03	fine-grained porphyrytic dark grey andesite	plag, cpx, opx, mgt, apa	lava flow	Cristales Grandes	El Laco volcanic centre	7366158	652624
ASLN-06	coarse-grained porphyrytic light grey andesite	plag, cpx, opx, mgt, amph, apa	lava flow	Laco Norte	Laco Norte Upper andesites	7364717	654046
ASSVB-03	fine-grained porphyrytic light grey tuff	plag, cpx, opx, mgt, apa	pyroclastic level	San Vicente Bajo	El Laco volcanic centre	7367247	651319
PL-05	coarse-grained porphyrytic dark grey andesite	plag, cpx, opx, mgt, apa	lava flow	San Vicente Alto	El Laco volcanic centre	7365223	651793
PL-02	fine-grained porphyrytic dark grey andesite	plag, cpx, opx, mgt, amph, apa	extrusive dome	Barren	El Laco volcanic centre	7364377	653321
BxVRN-01b	polymictic volcanic breccia	plag, cpx, opx, mgt, apa	volcanic breccia	Rodados Negros	El Laco volcanic centre	7366372	653788
ACUM-01a	coarse-grained porphyrytic greenish andesite	plag, cpx, opx, mgt, apa	lava flow	Laco Norte	Lower andesites	7363855	653877

plag: plagioclase; cpx: clinopyroxene; opx: orthopyroxene; mgt: magnetite: amph: amphibole; apa: apatite

B11. Analytical conditions for EPMA analyses of pyroxenes and Fe-Ti oxides from El Laco deposit.

Pyroxene

Instrument	Intensity Correction	Accelerating Voltage (kV)	Beam Current (nA)	Beam Size (µm)
Cameca SX100, EMAL/U. Michigan	ZAF (Armstrong-Love/Scott)	15	40	2

Element	Peak Counting Time (s)*	Analyzing Crystal	Calibration Standard	MDL Oxide [wt.%]
Si Kα	10	TAP	FeSiO3, Synthetic	0.016 (0.02)
Ti Kα	100	PET	TiO2, Synthetic	0.007 (0.01)
Al Kα	60	TAP	Anorthite, Great Sitkin (NMNH 137041)	0.006 (0.01)
Cr Kα	120	LPET	Cr2O3, Synthetic	0.003
Fe Kα	30	LLiF	Hematite, Harvard (H92649)	0.010
Mn Kα	90	LLiF	Rhodonite, Broken Hill	0.006 (0.01)
Mg Kα	20	LTAP	Forsterite Olivine, Synthetic	0.007 (0.01)
Ca Kα	20	PET	Wollastonite, ANU	0.009 (0.01)
Na Kα	60	LTAP	Albite, Harvard (H131705)	0.004

Fe-Ti Oxides

Instrument	Intensity Correction	Accelerating Voltage (kV)	Beam Current (nA)	Beam Size (µm)
Cameca SX100, EMAL/U. Michigan	X-PHI (Merlet)	20	30	Focused

Element-Line	Peak Counting Time (s)**	Analyzing Crystal	Calibration Standard	MDL [wt.%]
Si Kα	100	LTAP	Wollastonite, ANU	0.008 (0.01)
Mg Kα	100	LTAP	MgO, Synthetic	0.010
Al Kα	100	LTAP	Al2O3, Synthetic	0.009 (0.01)
Ti Kα	120	PET	Ilmenite, USSR (NMNH 96189)	0.010
Cr Kα	100	PET	Cr2O3 (Synthetic)	0.012 (0.01)
V Kα	120	LLiF	V2O5 (Synthetic)	0.006 (0.01)
Mn Kα	100	LLiF	MnFe2O4 (Synthetic)	0.008 (0.01)
Fe Kα	20	LLiF	Magnetite, Minas Gerais (NMNH 114887)	0.015 (0.02)
Ni Kα	100	LLiF	Ni2SiO4 (Synthetic)	0.008 (0.01)
Ca Kα	100	PET	Wollastonite, ANU	0.005 (0.01)

B12. EPMA data for magnetite from El Laco ore bodies and host andesites.

Magnetite EPMA data from El Laco deposit: Intermediate zone														
Sample - spot	Ore body	Drill core	Source	Mg [wt. %]	Al [wt. %]	Si [wt. %]	Ti [wt. %]	Ca [wt. %]	V [wt. %]	Cr [wt. %]	Fe [wt. %]	Mn [wt. %]	Ni [wt. %]	O [wt. %]	Total
CG02_Area2_1	Cristales Grandes	EPI-0702	This study	1.24	0.11	0.89	0.09	0.27	0.16	b.d	68.7	0.07	0.01	28.6	100.2
CG02_Area2_2	Cristales Grandes	EPI-0702	This study	0.97	0.11	0.53	0.05	0.22	0.17	b.d	69.7	0.06	b.d	28.3	100.2
CG02_Area2_3	Cristales Grandes	EPI-0702	This study	1.04	0.10	0.58	0.04	0.23	0.16	b.d	69.5	0.06	b.d	28.3	100.1
CG02_Area2_4	Cristales Grandes	EPI-0702	This study	0.81	0.17	0.46	0.05	0.18	0.16	b.d	69.6	0.03	b.d	28.1	99.6
CG02_Area2_5	Cristales Grandes	EPI-0702	This study	0.94	0.11	0.60	0.06	0.22	0.16	b.d	69.4	0.05	b.d	28.2	99.8
CG02_Area3_1	Cristales Grandes	EPI-0702	This study	0.48	0.11	0.06	0.01	0.01	0.10	b.d	70.8	0.04	b.d	27.7	99.4
CG02_Area3_2	Cristales Grandes	EPI-0702	This study	0.01	0.10	0.31	0.02	b.d	0.11	b.d	68.5	b.d	b.d	26.6	95.8
CG02_Area3_3	Cristales Grandes	EPI-0702	This study	0.82	0.12	0.39	0.03	0.05	0.09	b.d	70.1	0.07	b.d	28.1	99.8
CG02_Area3_4	Cristales Grandes	EPI-0702	This study	0.09	0.12	0.18	0.03	0.02	0.10	b.d	68.3	b.d	b.d	26.5	95.4
CG02_Area4_1	Cristales Grandes	EPI-0702	This study	0.65	0.09	0.04	0.02	b.d	0.10	b.d	70.9	0.06	b.d	27.9	99.8
CG02_Area4_2	Cristales Grandes	EPI-0702	This study	0.71	0.09	0.12	0.03	0.01	0.09	b.d	70.7	0.06	b.d	27.9	99.9
CG02_Area4_3	Cristales Grandes	EPI-0702	This study	0.76	0.13	0.20	0.06	0.03	0.10	b.d	70.3	0.07	b.d	28.0	99.7
CG02_Area4_4	Cristales Grandes	EPI-0702	This study	0.07	0.09	0.06	0.06	0.01	0.18	b.d	69.3	0.01	b.d	26.8	96.6
CG17_Area2_1	Cristales Grandes	EPI-0702	This study	0.86	1.42	0.17	3.67	b.d	0.14	b.d	64.4	0.19	0.03	28.4	99.4
CG17_Area2_2	Cristales Grandes	EPI-0702	This study	0.17	0.13	0.02	0.04	b.d	0.16	b.d	71.6	0.01	0.03	27.7	100.0
CG17_Area2_4	Cristales Grandes	EPI-0702	This study	0.23	0.31	0.02	0.07	b.d	0.17	b.d	71.2	0.02	0.03	27.8	100.0
CG17_Area2_5	Cristales Grandes	EPI-0702	This study	0.08	0.11	0.59	0.27	0.05	0.17	b.d	68.1	b.d	0.02	27.0	96.4
CG17_Area3_1	Cristales Grandes	EPI-0702	This study	0.49	0.86	0.01	0.13	b.d	0.19	b.d	70.1	0.03	0.03	28.1	100.0
CG17_Area3_3	Cristales Grandes	EPI-0702	This study	0.22	0.17	0.81	0.89	0.02	0.13	b.d	68.1	0.02	0.03	27.6	98.0
CG17_Area3_4	Cristales Grandes	EPI-0702	This study	0.28	0.34	0.02	0.25	0.02	0.15	b.d	70.5	0.01	0.03	27.7	99.4
CG17_Area3_5	Cristales Grandes	EPI-0702	This study	0.76	0.83	0.53	4.34	0.21	0.12	b.d	62.1	0.11	0.02	27.7	96.8
CG17_Area4_1	Cristales Grandes	EPI-0702	This study	0.60	1.57	0.02	0.11	b.d	0.15	0.04	69.2	0.03	0.03	28.4	100.2
CG17_Area4_2	Cristales Grandes	EPI-0702	This study	0.31	0.40	0.04	0.99	0.02	0.14	0.03	70.0	0.03	0.03	27.9	100.0
CG17_Area4_3	Cristales Grandes	EPI-0702	This study	0.20	0.14	0.03	3.31	0.01	0.14	0.03	67.2	0.06	0.02	27.6	98.8
CG17_Area4_4	Cristales Grandes	EPI-0702	This study	0.54	1.17	0.02	0.11	b.d	0.15	0.09	69.0	0.03	0.03	28.0	99.2
CG02_Area2a_1	Cristales Grandes	EPI-0702	This study	0.97	0.11	0.57	0.04	0.22	0.16	b.d	69.6	0.06	b.d	28.3	100.1
CG02_Area2a_2	Cristales Grandes	EPI-0702	This study	0.99	0.11	0.59	0.08	0.22	0.16	b.d	69.5	0.06	b.d	28.3	100.1
CG02_Area2a_3	Cristales Grandes	EPI-0702	This study	0.63	0.16	0.56	0.13	0.23	0.16	b.d	69.6	b.d	b.d	28.1	99.6
CG02_Area3a_1	Cristales Grandes	EPI-0702	This study	0.54	0.12	0.02	0.02	b.d	0.10	b.d	71.1	0.06	b.d	27.8	99.8
CG02_Area3a_2	Cristales Grandes	EPI-0702	This study	0.55	0.14	0.02	0.04	b.d	0.15	b.d	70.8	0.06	0.01	27.8	99.6
CG02_Area3a_3	Cristales Grandes	EPI-0702	This study	0.15	0.21	0.01	0.08	b.d	0.19	b.d	71.5	b.d	0.01	27.8	100.1
CG02_Area5_1	Cristales Grandes	EPI-0702	This study	1.07	0.06	0.26	0.02	0.05	0.13	b.d	70.1	0.05	b.d	28.1	99.9
CG02_Area5_2	Cristales Grandes	EPI-0702	This study	1.09	0.06	0.24	0.02	0.07	0.13	b.d	70.1	0.06	b.d	28.2	100.0
CG02_Area5_3	Cristales Grandes	EPI-0702	This study	1.05	0.07	0.15	0.03	0.02	0.12	b.d	70.3	0.06	b.d	28.1	100.0
CG32_Area5_1	Cristales Grandes	EPI-0702	This study	0.03	0.23	0.01	0.05	b.d	0.19	b.d	71.5	b.d	0.02	27.7	99.8
CG32_Area5_2	Cristales Grandes	EPI-0702	This study	0.03	0.25	b.d	0.10	b.d	0.19	b.d	71.4	b.d	0.02	27.6	99.7
CG32_Area5_3	Cristales Grandes	EPI-0702	This study	0.03	0.15	0.01	0.08	b.d	0.19	b.d	71.7	b.d	0.02	27.7	99.9
CG32_Area6_1	Cristales Grandes	EPI-0702	This study	0.05	0.25	0.01	0.07	b.d	0.19	b.d	71.0	b.d	0.02	27.5	99.2
CG32_Area6_2	Cristales Grandes	EPI-0702	This study	0.05	0.24	0.01	0.07	b.d	0.19	b.d	71.0	b.d	0.02	27.5	99.1
CG32_Area6_3	Cristales Grandes	EPI-0702	This study	0.06	0.24	0.01	0.13	b.d	0.19	b.d	70.7	b.d	0.02	27.4	98.9
CG32_Area7_1	Cristales Grandes	EPI-0702	This study	0.06	0.25	0.01	0.09	b.d	0.19	b.d	71.6	b.d	0.02	27.7	100.0
CG32_Area7_2	Cristales Grandes	EPI-0702	This study	0.07	0.27	0.01	0.19	b.d	0.18	b.d	71.5	0.01	0.03	27.8	100.1
CG32_Area7_3	Cristales Grandes	EPI-0702	This study	0.11	0.37	0.01	0.20	b.d	0.19	b.d	71.2	0.01	0.02	27.8	100.0
CG17_Area5_1	Cristales Grandes	EPI-0702	This study	0.18	0.08	0.02	0.04	b.d	0.19	b.d	71.7	0.02	0.03	27.8	100.1
CG17_Area5_2	Cristales Grandes	EPI-0702	This study	0.19	0.10	0.02	0.04	b.d	0.18	b.d	71.6	0.02	0.03	27.8	100.1
CG17_Area5_3	Cristales Grandes	EPI-0702	This study	0.30	0.46	0.02	0.07	b.d	0.17	b.d	70.9	0.02	0.03	27.9	99.9
CG17_Area6_1	Cristales Grandes	EPI-0702	This study	0.23	0.13	0.02	0.07	b.d	0.19	b.d	71.3	0.03	0.03	27.7	99.7
CG17_Area6_2	Cristales Grandes	EPI-0702	This study	0.22	0.11	0.02	0.09	b.d	0.20	b.d	71.4	0.03	0.02	27.7	99.9
CG17_Area6_3	Cristales Grandes	EPI-0702	This study	0.20	0.10	0.02	0.06	b.d	0.19	b.d	71.2	0.03	0.03	27.6	99.6
CG17_Area7_1	Cristales Grandes	EPI-0702	This study	0.54	0.46	0.35	0.08	0.15	0.15	b.d	70.4	0.03	0.03	28.3	100.6
CG17_Area7_2	Cristales Grandes	EPI-0702	This study	0.46	0.61	0.08	0.65	0.03	0.15	b.d	69.8	0.04	0.03	28.0	100.0
cg-08 area 2 sp 2	Cristales Grandes	EPI-0702	This study	0.06	0.16	b.d	0.61	0.02	0.13	0.07	71.1	0.02	0.03	27.7	100.0
cg-08 area 2 sp 3	Cristales Grandes	EPI-0702	This study	0.04	0.08	0.02	0.39	0.07	0.14	0.14	70.6	0.03	0.02	27.5	99.1
cg-08 area 2 sp 4	Cristales Grandes	EPI-0702	This study	0.09	0.17	0.01	0.26	b.d	0.16	0.08	71.7	0.02	0.03	27.9	100.4
cg-08 area 2 sp 5	Rodados Negros	EPI-0808	This study	0.69	0.23	0.03	0.07	b.d	0.16	b.d	69.8	0.06	0.03	27.6	98.7
cg-08 area 2 sp 6	Rodados Negros	EPI-0808	This study	1.10	0.31	0.75	0.06	0.21	0.16	b.d	67.9	0.07	0.03	28.1	98.8
cg-08 area 2 sp 7	Rodados Negros	EPI-0808	This study	1.31	0.34	1.02	0.07	0.27	0.16	b.d	67.4	0.07	0.02	28.4	99.2
cg-08 area 2 sp 8	Rodados Negros	EPI-0808	This study	0.75	0.24	0.05	0.04	0.01	0.15	b.d	69.9	0.06	0.02	27.7	99.0
cg-08 area 2 sp 9	Rodados Negros	EPI-0808	This study	0.62	0.16	0.04	0.07	b.d	0.17	b.d	69.5	0.05	0.02	27.4	98.1
cg-08 area 2 sp 10	Rodados Negros	EPI-0808	This study	0.71	0.19	0.05	0.07	b.d	0.16	b.d	69.9	0.07	0.02	27.7	98.9
cg-08 area 2 sp 11	Rodados Negros	EPI-0808	This study	0.20	0.37	1.24	0.08	0.11	0.16	b.d	66.2	0.01	0.01	27.1	95.6
cg-08 area 2 sp 12	Rodados Negros	EPI-0808	This study	0.68	0.23	0.04	0.06	b.d	0.15	b.d	70.2	0.08	0.02	27.8	99.3
cg-08 area 2 sp 13	Rodados Negros	EPI-0808	This study	0.60	0.14	0.07	0.11	b.d	0.16	b.d	70.2	0.06	0.03	27.7	99.1
cg-08 area 2 sp 14	Rodados Negros	EPI-0808	This study	0.64	bdl	0.01	bdl	b.d	0.08	b.d	71.1	0.05	0.01	27.8	99.7
cg-08 area 2 sp 15	Rodados Negros	EPI-0808	This study	0.03	bdl	0.11	bdl	b.d	0.07	b.d	69.5	b.d	b.d	26.7	96.5
cg-08 area 2 sp 16	Rodados Negros	EPI-0808	This study	0.78	bdl	0.29	bdl	0.08	0.08	b.d	70.5	0.05	0.01	28.0	99.9
cg-08 area 2 sp 17	Rodados Negros	EPI-0808	This study	0.75	bdl	0.25	bdl	0.06	0.08	b.d	70.7	0.06	0.01	28.0	99.9
cg-08 area 2 sp 18	Rodados Negros	EPI-0808	This study	0.64	bdl	0.02	bdl	b.d	0.07	b.d	70.6	0.05	0.01	27.6	99.1
cg-08 area 2 sp 19	Rodados Negros	EPI-0808	This study	0.62	0.05	0.02	bdl	b.d	0.05	b.d	71.0	0.07	0.01	27.8	99.7
cg-08 area 2 sp 20	Rodados Negros	EPI-0808	This study	0.93	0.03	0.57	bdl	0.21	0.06	b.d	69.3	0.07	0.01	28.0	99.2
cg-08 area 2 sp 21	Rodados Negros	EPI-0808	This study	0.63	0.05	0.02	bdl	b.d	0.06	b.d	70.8	0.06	0.01	27.7	99.4
cg-08 area 2 sp 22	Rodados Negros	EPI-0808	This study	0.63	bdl	0.02	bdl	b.d	0.06	b.d	71.0	0.07	0.01	27.8	99.6
rn-07- area 1 sp 1	Rodados Negros	EPI-0808	This study	0.66	0.46	0.02	0.27	b.d	0.24	b.d	69.6	0.07	0.02	27.8	99.2
rn-07- area 1 sp 2	Rodados Negros	EPI-0808	This study	0.73	0.61	0.01	0.30	b.d	0.23	b.d	69.3	0.07	0.03	27.9	99.3
rn-07- area 1 sp 3	Rodados Negros	EPI-0808	This study	0.66	0.48	0.03	0.27	b.d	0.23	b.d	69.7	0.08	0.03	27.9	99.4
rn-07- area 1 sp 4	Rodados Negros	EPI-0808	This study	0.66	0.52	0.01	0.30	b.d	0.23	b.d	69.8	0.08	0.03	28.0	99.7

Magnetite EPMA data from El Laco deposit: Intermediate zone

Sample - spot	Ore body	Drill core	Source	Mg [wt. %]	Al [wt. %]	Si [wt. %]	Ti [wt. %]	Ca [wt. %]	V [wt. %]	Cr [wt. %]	Fe [wt. %]	Mn [wt. %]	Ni [wt. %]	O [wt. %]	Total
rn-07- area 1 sp 5	Rodados Negros	EPI-0808	This study	0.59	0.40	0.02	0.25	b.d	0.23	b.d	69.8	0.06	0.03	27.8	99.2
rn-07- area 1 sp 6	Rodados Negros	EPI-0808	This study	0.54	0.41	0.03	0.25	0.02	0.23	b.d	69.9	0.08	0.02	27.8	99.3
rn-07- area 1 sp 7	Rodados Negros	EPI-0808	This study	0.24	0.31	0.02	0.17	b.d	0.08	b.d	70.3	0.09	0.01	27.5	98.8
rn-07- area 1 sp 8	Rodados Negros	EPI-0808	This study	0.15	0.22	0.12	0.35	0.03	0.08	b.d	70.6	0.11	0.01	27.6	99.4
rn-07- area 1 sp 9	Rodados Negros	EPI-0808	This study	0.17	0.24	0.08	0.11	0.03	0.08	b.d	70.7	0.08	b.d	27.6	99.2
sva 1 - 14 area 8 sp 1	San Vicente Alto	SVA-1001	This study	0.11	0.24	0.01	0.70	0.02	0.19	0.11	70.9	0.03	0.03	27.9	100.2
sva 1 - 14 area 8 sp 3	San Vicente Alto	SVA-1001	This study	0.15	0.36	0.01	0.86	0.06	0.19	0.09	70.1	0.03	0.03	27.8	99.7
sva 1 - 14 area 5 sp 1	San Vicente Alto	SVA-1001	This study	0.49	0.66	0.02	0.43	b.d	0.20	b.d	69.9	0.06	0.04	28.0	99.9
sva 1 - 14 area 5 sp 2	San Vicente Alto	SVA-1001	This study	0.42	0.49	0.01	0.44	b.d	0.20	b.d	70.6	0.05	0.03	28.1	100.4
sva 1 - 14 area 5 sp 3	San Vicente Alto	SVA-1001	This study	0.67	0.91	0.01	0.41	b.d	0.20	b.d	70.4	0.08	0.03	28.5	101.3
sva 1 - 14 area 5 sp 4	San Vicente Alto	SVA-1001	This study	0.35	0.19	0.01	0.24	b.d	0.19	b.d	70.5	0.05	0.04	27.7	99.3
sva 1 - 14 area 10 sp 1	San Vicente Alto	SVA-1001	This study	0.50	0.39	0.01	0.74	b.d	0.22	b.d	69.3	0.08	0.03	27.7	99.1
sva 1 - 14 area 10 sp 2	San Vicente Alto	SVA-1001	This study	0.58	0.31	0.02	0.48	b.d	0.21	b.d	70.4	0.14	0.04	28.1	100.3
sva 1 - 14 area 10 sp 3	San Vicente Alto	SVA-1001	This study	0.57	0.45	0.01	0.58	b.d	0.22	b.d	69.9	0.08	0.03	28.0	99.9
sva 1 - 14 area 10 sp 4	San Vicente Alto	SVA-1001	This study	0.54	0.44	0.01	0.30	b.d	0.22	b.d	70.7	0.12	0.03	28.1	100.6
sva 1 - 14 area 3 sp 1	San Vicente Alto	SVA-1001	This study	0.50	0.39	0.01	0.44	b.d	0.21	b.d	70.0	0.11	0.03	27.9	99.7
sva 1 - 14 area 3 sp 2	San Vicente Alto	SVA-1001	This study	0.38	0.34	0.02	0.66	0.03	0.20	b.d	69.2	0.04	0.03	27.5	98.5
sva 1 - 14 area 3 sp 3	San Vicente Alto	SVA-1001	This study	0.51	0.36	0.02	0.53	b.d	0.21	0.04	69.9	0.07	0.03	27.8	99.5
SVA1-09b_Area2_1	San Vicente Alto	SVA-1001	This study	0.13	0.40	0.01	1.21	0.23	0.21	0.04	69.4	0.07	b.d	27.7	99.5
SVA1-09b_Area2_4	San Vicente Alto	SVA-1001	This study	0.24	0.16	0.13	0.27	0.05	0.02	b.d	70.8	0.07	b.d	27.7	99.5
SVA1-09b_Area2_5	San Vicente Alto	SVA-1001	This study	0.19	0.17	0.15	0.36	0.06	0.02	b.d	70.5	0.07	0.01	27.6	99.2
SVA1-09b_Area2_8	San Vicente Alto	SVA-1001	This study	1.01	1.20	0.23	0.09	0.15	0.05	b.d	70.0	0.20	0.03	29.0	102.0
SVA1-09b_Area5_1	San Vicente Alto	SVA-1001	This study	0.17	0.20	0.08	0.12	0.04	0.04	b.d	70.5	0.05	0.02	27.5	98.8
SVA1-09b_Area5_2	San Vicente Alto	SVA-1001	This study	0.16	0.11	0.04	0.26	0.02	0.02	b.d	71.4	0.06	b.d	27.7	99.9
SVA1-09b_Area5_3	San Vicente Alto	SVA-1001	This study	0.40	0.23	0.48	0.50	0.18	0.05	b.d	68.9	0.07	b.d	27.7	98.6
SVA1-09b_Area5_5	San Vicente Alto	SVA-1001	This study	0.16	0.13	0.06	0.08	0.09	0.04	b.d	70.8	0.04	b.d	27.5	99.0
SVA1-09b_Area5_6	San Vicente Alto	SVA-1001	This study	0.17	0.12	0.07	0.07	0.20	0.03	b.d	69.6	0.03	0.01	27.1	97.4
SVA1-09b_Area5_7	San Vicente Alto	SVA-1001	This study	0.22	0.12	0.11	0.22	0.22	0.03	b.d	70.3	0.05	b.d	27.5	98.8
SVA1-09b_Area5_9	San Vicente Alto	SVA-1001	This study	0.18	0.11	0.10	0.43	0.15	0.03	b.d	70.6	0.07	0.01	27.6	99.4
SVA1-09b_Area6_2	San Vicente Alto	SVA-1001	This study	0.25	0.18	0.22	0.27	0.10	0.04	b.d	70.0	0.05	b.d	27.5	98.8
SVA1-08_Area2_1	San Vicente Alto	SVA-1001	This study	0.91	0.43	0.83	0.32	0.32	0.23	b.d	68.5	0.04	0.03	28.5	100.2
SVA1-08_Area2_2	San Vicente Alto	SVA-1001	This study	0.52	0.36	0.31	0.26	0.13	0.23	b.d	69.7	0.04	0.03	28.0	99.6
SVA1-08_Area2_3	San Vicente Alto	SVA-1001	This study	0.37	0.31	b.d	0.20	b.d	0.23	b.d	70.5	0.02	0.03	27.7	99.5
SVA1-08_Area2_4	San Vicente Alto	SVA-1001	This study	0.38	0.30	0.01	0.20	0.01	0.23	b.d	70.7	0.01	0.03	27.8	99.7
SVA1-08_Area3_1	San Vicente Alto	SVA-1001	This study	0.83	0.27	1.42	0.28	0.84	0.22	b.d	66.5	0.01	0.02	28.4	98.8
SVA1-08_Area3_2	San Vicente Alto	SVA-1001	This study	0.38	0.28	0.06	0.27	0.29	0.24	b.d	69.8	0.01	0.01	27.7	99.1
SVA1-08_Area3_3	San Vicente Alto	SVA-1001	This study	0.32	0.17	0.02	0.24	0.18	0.24	b.d	69.2	0.02	0.01	27.2	97.8
SVA1-08_Area4_1	San Vicente Alto	SVA-1001	This study	0.46	0.43	0.02	0.43	0.06	0.23	b.d	69.6	0.03	0.03	27.7	99.0
SVA1-08_Area4_2	San Vicente Alto	SVA-1001	This study	0.39	0.25	0.01	0.17	0.09	0.22	b.d	70.3	0.03	0.03	27.7	99.3
SVA1-08_Area4_3	San Vicente Alto	SVA-1001	This study	0.47	0.31	b.d	0.30	0.13	0.23	b.d	70.0	0.03	0.03	27.7	99.3
SVA1-08_Area4_4	San Vicente Alto	SVA-1001	This study	0.49	0.35	0.01	0.36	b.d	0.24	b.d	69.2	0.02	0.03	27.5	98.2
SVA1-11_Area2_1	San Vicente Alto	SVA-1001	This study	0.38	0.23	0.01	0.28	b.d	0.21	b.d	71.0	0.04	0.03	27.9	100.2
SVA1-11_Area2_2	San Vicente Alto	SVA-1001	This study	0.79	0.75	0.01	1.02	b.d	0.21	b.d	68.6	0.10	0.03	28.1	99.7
SVA1-11_Area2_3	San Vicente Alto	SVA-1001	This study	0.47	0.49	0.03	0.43	b.d	0.21	b.d	70.4	0.04	0.03	28.0	100.2
SVA1-11_Area2_4	San Vicente Alto	SVA-1001	This study	0.42	0.40	0.01	0.34	b.d	0.21	b.d	70.5	0.04	0.03	27.9	99.9
SVA1-11_Area4_1	San Vicente Alto	SVA-1001	This study	0.46	0.32	0.02	0.50	b.d	0.22	0.04	70.0	0.07	0.03	27.8	99.5
SVA1-11_Area4_2	San Vicente Alto	SVA-1001	This study	0.54	0.45	0.01	0.42	b.d	0.21	0.03	70.2	0.06	0.03	28.0	100.1
SVA1-11_Area4_3	San Vicente Alto	SVA-1001	This study	0.36	0.57	0.58	0.38	0.04	0.20	0.03	69.0	0.05	0.03	28.0	99.4
SVA1-11_Area4_4	San Vicente Alto	SVA-1001	This study	0.53	0.43	0.02	0.68	0.02	0.21	b.d	69.5	0.05	0.03	27.8	99.3
SVA1-11_Area7_1	San Vicente Alto	SVA-1001	This study	0.38	0.22	0.01	0.16	b.d	0.20	b.d	70.2	0.03	0.03	27.5	98.8
SVA1-11_Area7_2	San Vicente Alto	SVA-1001	This study	0.48	0.46	0.01	0.63	b.d	0.20	b.d	68.9	0.03	0.03	27.5	98.3
SVA1-11_Area7_3	San Vicente Alto	SVA-1001	This study	0.46	0.45	0.01	0.54	b.d	0.22	b.d	69.9	0.03	0.04	27.8	99.6
SVA1-11_Area7_4	San Vicente Alto	SVA-1001	This study	0.70	0.62	0.02	1.19	b.d	0.21	b.d	67.6	0.09	0.03	27.6	98.1
sva1 - 04 area 3 sp 4	San Vicente Alto	SVA-1001	This study	0.58	0.02	0.05	bdl	0.01	0.14	b.d	68.4	0.04	0.03	26.8	96.1
sva1 - 04 area 3 sp 5	San Vicente Alto	SVA-1001	This study	0.09	bdl	0.15	bdl	0.09	0.12	b.d	70.4	0.02	0.02	27.3	98.3
sva1 - 04 area 3 sp 6	San Vicente Alto	SVA-1001	This study	0.54	bdl	0.05	bdl	0.02	0.14	b.d	68.0	0.03	0.03	26.6	95.4
sva1 - 04 area 2 sp 1	San Vicente Alto	SVA-1001	This study	0.63	0.02	0.22	bdl	0.05	0.14	b.d	68.3	0.02	0.02	27.0	96.5
sva1 - 04 area 2 sp 2	San Vicente Alto	SVA-1001	This study	0.55	0.02	0.07	bdl	0.02	0.13	b.d	68.2	0.02	0.03	26.7	95.9
sva1 - 04 area 2 sp 3	San Vicente Alto	SVA-1001	This study	0.59	0.02	0.09	bdl	0.03	0.14	b.d	68.7	0.02	0.03	27.0	96.6
sva1 - 04 area 2 sp 4	San Vicente Alto	SVA-1001	This study	0.48	bdl	0.06	bdl	0.02	0.14	b.d	68.5	0.03	0.03	26.8	96.1
sva1 - 04 area 2 sp 5	San Vicente Alto	SVA-1001	This study	0.53	bdl	0.08	bdl	0.03	0.14	b.d	68.0	0.02	0.03	26.6	95.6
sva1 - 04 area 1 sp 1	San Vicente Alto	SVA-1001	This study	0.39	0.02	0.12	0.01	0.07	0.13	b.d	67.9	0.02	0.03	26.6	95.3
sva1 - 04 area 1 sp 2	San Vicente Alto	SVA-1001	This study	0.38	0.40	0.04	bdl	0.02	0.14	b.d	67.7	0.02	0.03	26.7	95.5
sva1 - 04 area 1 sp 3	San Vicente Alto	SVA-1001	This study	0.57	bdl	0.10	bdl	0.04	0.14	b.d	68.1	0.03	0.03	26.7	95.8
sva1 - 04 area 1 sp 4	San Vicente Alto	SVA-1001	This study	0.51	bdl	0.05	bdl	0.01	0.14	b.d	68.1	0.02	0.02	26.6	95.6
sva1 - 04 area 1 sp 7	San Vicente Alto	SVA-1001	This study	0.51	bdl	0.04	bdl	0.02	0.14	b.d	68.5	0.02	0.03	26.7	96.1
svb 06 Area 1 sp 1	San Vicente Bajo	SVB-1003	This study	0.46	0.23	0.02	0.22	b.d	0.22	b.d	70.6	0.09	0.03	27.8	99.8
svb 06 Area 1 sp 2	San Vicente Bajo	SVB-1003	This study	0.40	0.20	0.03	0.13	b.d	0.23	b.d	70.9	0.05	0.03	27.8	99.9
svb 06 Area 1 sp 3	San Vicente Bajo	SVB-1003	This study	0.06	0.18	0.03	0.10	b.d	0.28	b.d	68.7	0.03	0.02	26.7	96.1
svb 06 Area 1 sp 4	San Vicente Bajo	SVB-1003	This study	0.44	0.21	0.03	0.13	b.d	0.23	b.d	70.5	0.10	0.03	27.7	99.5
svb 06 Area 2 sp 1	San Vicente Bajo	SVB-1003	This study	0.47	0.57	0.01	0.17	b.d	0.24	b.d	70.5	0.05	0.03	28.0	100.2
svb 06 Area 2 sp 2	San Vicente Bajo	SVB-1003	This study	0.37	0.35	0.02	0.16	b.d	0.25	b.d	70.4	0.06	0.03	27.8	99.5
svb 06 Area 2 sp 3	San Vicente Bajo	SVB-1003	This study	0.39	0.34	0.01	0.15	b.d	0.23	0.03	70.7	0.06	0.03	27.8	99.8
svb 06 Area 3 sp 1	San Vicente Bajo	SVB-1003	This study	0.46	0.59	0.01	0.14	b.d	0.26	b.d	70.4	0.05	0.04	28.0	100.0
svb 06 Area 3 sp 2	San Vicente Bajo	SVB-1003	This study	0.30	0.29	0.02	0.13	b.d	0.25	b.d	70.6	0.05	0.03	27.7	99.4
svb 06 Area 3 sp 3	San Vicente Bajo	SVB-1003	This study	0.34	0.38	0.01	0.14	b.d	0.24	b.d	70.5	0.04	0.03	27.7	99.5

Magnetite EPMA data from El Laco deposit: Intermediate zone

Sample - spot	Ore body	Drill core	Source	Mg [wt. %]	Al [wt. %]	Si [wt. %]	Ti [wt. %]	Ca [wt. %]	V [wt. %]	Cr [wt. %]	Fe [wt. %]	Mn [wt. %]	Ni [wt. %]	O [wt. %]	Total
svb 06 Area 4 sp 1	San Vicente Bajo	SVB-1003	This study	0.45	0.39	0.01	0.33	b.d	0.26	b.d	70.2	0.06	0.03	27.8	99.7
svb 06 Area 4 sp 2	San Vicente Bajo	SVB-1003	This study	0.20	0.27	0.08	0.29	b.d	0.25	b.d	68.1	0.03	0.03	26.8	96.1
svb 06 Area 4 sp 3	San Vicente Bajo	SVB-1003	This study	0.44	0.36	0.02	0.14	b.d	0.26	b.d	70.5	0.06	0.03	27.8	99.7
svb 06 Area 4 sp 4	San Vicente Bajo	SVB-1003	This study	0.59	0.22	0.02	0.30	b.d	0.25	b.d	70.6	0.10	0.03	28.0	100.2
svb 03 area 4 sp 1	San Vicente Bajo	SVB-1003	This study	0.23	0.25	0.06	0.32	0.01	0.21	b.d	70.1	0.06	0.03	27.5	98.9
svb 03 area 4 sp 2	San Vicente Bajo	SVB-1003	This study	0.31	0.26	0.05	0.46	b.d	0.23	b.d	70.5	0.09	0.03	27.8	99.8
svb 03 area 4 sp 3	San Vicente Bajo	SVB-1003	This study	0.34	0.37	0.03	0.85	b.d	0.22	b.d	69.7	0.07	0.03	27.8	99.5
svb 03 area 4 sp 4	San Vicente Bajo	SVB-1003	This study	0.19	0.19	0.07	0.13	0.04	0.23	b.d	70.9	0.02	0.03	27.7	99.6
svb 03 area 4 sp 5	San Vicente Bajo	SVB-1003	This study	0.39	0.17	0.22	0.21	0.09	0.21	b.d	70.2	0.08	0.03	27.8	99.5
svb 03 area 4 sp 6	San Vicente Bajo	SVB-1003	This study	0.32	0.20	0.25	0.34	0.11	0.22	b.d	70.3	0.03	0.02	27.9	99.7
svb 03 area 4 sp 7	San Vicente Bajo	SVB-1003	This study	0.36	0.18	0.23	0.25	0.11	0.20	b.d	70.5	0.06	0.03	27.9	99.9
svb 03 area 4 sp 8	San Vicente Bajo	SVB-1003	This study	0.30	0.17	0.18	0.20	0.06	0.21	b.d	70.7	0.06	0.03	27.8	99.8
svb 11 t area 4 sp 1	San Vicente Bajo	SVB-1003	This study	0.40	0.56	0.03	0.32	b.d	0.23	b.d	70.1	0.02	0.03	27.9	99.7
svb 11 t area 4 sp 2	San Vicente Bajo	SVB-1003	This study	0.32	0.39	0.02	0.31	b.d	0.24	b.d	70.3	0.01	0.03	27.8	99.5
svb 11 t area 4 sp 3	San Vicente Bajo	SVB-1003	This study	0.80	1.19	0.02	1.94	b.d	0.22	b.d	67.6	0.11	0.03	28.5	100.5
svb 11 t area 1sp 1	San Vicente Bajo	SVB-1003	This study	0.18	0.28	0.01	0.21	b.d	0.23	b.d	71.5	0.01	0.04	27.9	100.4
svb 11 t area 1sp 2	San Vicente Bajo	SVB-1003	This study	0.23	0.28	0.01	0.59	b.d	0.22	b.d	71.2	0.04	0.03	28.0	100.7
svb 11 t area 1sp 3	San Vicente Bajo	SVB-1003	This study	0.20	0.46	0.02	0.36	b.d	0.21	b.d	70.6	b.d	0.03	27.8	99.8
svb 11 t area 1sp 4	San Vicente Bajo	SVB-1003	This study	0.45	0.41	0.05	2.27	b.d	0.21	b.d	67.2	0.06	0.03	27.6	98.3
svb 11 t area 2 sp 1	San Vicente Bajo	SVB-1003	This study	0.24	0.50	0.04	0.96	0.03	0.29	b.d	66.7	0.03	0.03	26.7	95.6
svb 11 t area 2 sp 2	San Vicente Bajo	SVB-1003	This study	0.28	0.41	0.02	0.72	0.01	0.33	0.03	67.9	0.04	0.04	27.1	96.9
svb 11 t area 2 sp 3	San Vicente Bajo	SVB-1003	This study	0.15	0.11	0.01	0.12	b.d	0.28	b.d	68.7	b.d	0.03	26.7	96.2
svb 08 area 1 sp 1	San Vicente Bajo	SVB-1003	This study	0.40	0.42	0.01	0.53	b.d	0.24	b.d	70.1	0.05	0.03	27.9	99.8
svb 08 area 1 sp 2	San Vicente Bajo	SVB-1003	This study	0.38	0.41	0.01	0.51	b.d	0.25	b.d	70.1	0.03	0.03	27.8	99.7
svb 08 area 1 sp 3	San Vicente Bajo	SVB-1003	This study	0.36	0.39	0.01	0.48	b.d	0.24	b.d	70.1	0.04	0.03	27.8	99.5
svb 08 area 1 sp 6	San Vicente Bajo	SVB-1003	This study	0.29	0.33	0.04	0.25	b.d	0.24	b.d	67.8	0.11	0.06	26.7	95.9
svb 08 area 5a sp 1	San Vicente Bajo	SVB-1003	This study	0.40	0.37	0.01	0.48	b.d	0.28	0.03	70.3	0.06	0.03	27.9	100.0
svb 08 area 5a sp 2	San Vicente Bajo	SVB-1003	This study	0.16	0.30	0.03	0.44	b.d	0.29	b.d	67.7	0.09	0.02	26.6	95.7
svb 08 area 5b sp 1	San Vicente Bajo	SVB-1003	This study	0.43	0.38	0.02	0.51	b.d	0.28	b.d	70.1	0.04	0.03	27.9	99.7
svb 08 area 5b sp 2	San Vicente Bajo	SVB-1003	This study	0.09	0.33	0.02	0.40	b.d	0.25	b.d	67.8	0.03	0.01	26.6	95.7
svb 08 area 4 sp 1	San Vicente Bajo	SVB-1003	This study	0.24	0.36	0.06	0.37	b.d	0.24	b.d	68.9	b.d	0.03	27.2	97.5
svb 08 area 4 sp 2	San Vicente Bajo	SVB-1003	This study	0.29	0.39	0.02	0.48	b.d	0.22	b.d	69.4	0.01	0.04	27.4	98.3
svb 08 area 4 sp 3	San Vicente Bajo	SVB-1003	This study	0.42	0.28	0.02	0.23	b.d	0.24	b.d	70.1	0.03	0.03	27.6	99.1
svb 08 area 4 sp 4	San Vicente Bajo	SVB-1003	This study	0.26	0.43	0.01	0.41	b.d	0.23	b.d	70.2	0.01	0.04	27.7	99.3
svb 08 area 4 sp 5	San Vicente Bajo	SVB-1003	This study	0.33	0.42	0.02	0.51	b.d	0.24	b.d	70.1	0.02	0.03	27.8	99.6

Magnetite EPMA data from El Laco deposit: Deep zone

Sample - spot	Ore body	Drill core	Source	Mg [wt. %]	Al [wt. %]	Si [wt. %]	Ti [wt. %]	Ca [wt. %]	V [wt. %]	Cr [wt. %]	Fe [wt. %]	Mn [wt. %]	Ni [wt. %]	O [wt. %]	Total
CG23_Area1_1	Cristales Grandes	EPI-0702	This study	b.d	0.08	0.01	0.02	b.d	0.32	0.03	69.2	b.d	0.01	26.7	96.4
CG23_Area1_2	Cristales Grandes	EPI-0702	This study	0.21	0.29	0.02	0.13	0.02	0.23	0.04	70.8	0.04	0.04	27.7	99.6
CG23_Area1_3	Cristales Grandes	EPI-0702	This study	0.20	0.09	0.02	0.07	0.02	0.23	0.03	71.3	0.03	0.03	27.7	99.8
CG23_Area2_1	Cristales Grandes	EPI-0702	This study	0.10	0.11	0.01	0.05	b.d	0.22	b.d	71.5	0.04	0.04	27.7	99.8
CG23_Area2_2	Cristales Grandes	EPI-0702	This study	0.20	0.13	0.29	0.22	0.02	0.32	0.03	68.3	b.d	b.d	26.9	96.5
CG23_Area2_4	Cristales Grandes	EPI-0702	This study	0.24	0.27	0.01	0.08	b.d	0.22	b.d	71.0	0.04	0.03	27.7	99.6
CG23_Area2_5	Cristales Grandes	EPI-0702	This study	0.42	0.30	0.40	0.15	0.03	0.28	b.d	67.8	0.01	0.01	27.1	96.6
CG32_Area1_1	Cristales Grandes	EPI-0702	This study	0.09	0.27	0.01	0.14	b.d	0.19	b.d	71.2	b.d	0.02	27.7	99.6
CG32_Area1_3	Cristales Grandes	EPI-0702	This study	0.10	0.30	0.01	0.13	b.d	0.18	b.d	70.5	0.01	0.02	27.5	98.8
CG32_Area1_4	Cristales Grandes	EPI-0702	This study	0.07	0.26	0.01	0.09	b.d	0.18	b.d	70.9	0.01	0.02	27.5	99.1
CG32_Area1_5	Cristales Grandes	EPI-0702	This study	0.07	0.24	0.02	0.10	0.01	0.18	b.d	70.7	b.d	0.02	27.4	98.8
CG32_Area3_1	Cristales Grandes	EPI-0702	This study	0.06	0.23	0.01	0.08	b.d	0.16	b.d	71.6	b.d	0.02	27.7	99.9
CG32_Area3_3	Cristales Grandes	EPI-0702	This study	0.07	0.22	0.01	0.06	b.d	0.14	b.d	70.8	b.d	0.02	27.4	98.8
CG32_Area4_1	Cristales Grandes	EPI-0702	This study	0.05	0.24	0.01	0.07	b.d	0.18	b.d	71.6	0.01	0.02	27.7	100.0
CG32_Area4_2	Cristales Grandes	EPI-0702	This study	0.07	0.32	b.d	0.52	b.d	0.18	b.d	71.0	0.04	0.02	27.8	100.0
CG32_Area4_3	Cristales Grandes	EPI-0702	This study	0.03	0.23	0.01	0.26	b.d	0.18	b.d	71.4	0.01	0.02	27.7	100.0
CG23_Area3_1	Cristales Grandes	EPI-0702	This study	b.d	0.07	b.d	0.07	b.d	0.18	b.d	69.5	b.d	0.01	26.7	96.6
CG23_Area3_2	Cristales Grandes	EPI-0702	This study	b.d	0.08	0.01	0.09	b.d	0.19	b.d	69.4	b.d	0.02	26.7	96.6
CG23_Area3_3	Cristales Grandes	EPI-0702	This study	b.d	0.08	b.d	0.04	b.d	0.19	b.d	69.4	b.d	0.03	26.7	96.5
CG23_Area5_1	Cristales Grandes	EPI-0702	This study	0.11	0.10	0.01	0.24	b.d	0.19	b.d	71.6	0.04	0.03	27.8	100.1
CG23_Area5_2	Cristales Grandes	EPI-0702	This study	0.13	0.09	0.01	0.03	b.d	0.19	b.d	71.6	0.03	0.03	27.7	99.9
CG23_Area5_4	Cristales Grandes	EPI-0702	This study	0.11	0.09	0.02	0.07	b.d	0.20	b.d	71.6	0.04	0.04	27.7	100.0
CG23_Area6_1	Cristales Grandes	EPI-0702	This study	0.03	0.09	0.21	0.16	b.d	0.20	0.09	70.9	0.03	0.03	27.6	99.4
CG23_Area6_2	Cristales Grandes	EPI-0702	This study	0.08	0.10	0.02	0.06	b.d	0.20	0.08	71.5	0.03	0.03	27.7	99.9
CG23_Area6_3	Cristales Grandes	EPI-0702	This study	0.11	0.11	0.02	0.07	b.d	0.20	0.08	71.4	0.04	0.03	27.7	99.8
CG23_Area6_4	Cristales Grandes	EPI-0702	This study	0.13	0.24	0.01	0.07	b.d	0.20	0.07	71.1	0.04	0.03	27.7	99.7
cg-28 area 1 sp 1	Cristales Grandes	EPI-0702	This study	0.31	0.18	0.02	0.06	b.d	0.16	b.d	71.2	0.09	0.03	27.8	99.8
cg-28 area 1 sp 2	Cristales Grandes	EPI-0702	This study	0.30	0.17	0.01	0.04	b.d	0.16	b.d	71.2	0.09	0.03	27.8	99.9
cg-28 area 1 sp 3	Cristales Grandes	EPI-0702	This study	0.31	0.16	0.02	0.03	b.d	0.17	b.d	71.2	0.10	0.03	27.8	99.9
cg-28 area 1 sp 4	Cristales Grandes	EPI-0702	This study	0.33	0.21	0.02	0.04	b.d	0.16	b.d	71.2	0.10	0.03	27.8	100.0
cg-28 area 2 sp 1	Cristales Grandes	EPI-0702	This study	0.13	0.14	0.02	0.03	b.d	0.17	b.d	71.4	0.07	0.02	27.6	99.7
cg-28 area 2 sp 2	Cristales Grandes	EPI-0702	This study	0.11	0.12	0.02	0.05	b.d	0.17	b.d	71.6	0.06	0.02	27.7	99.9
cg-28 area 2 sp 3	Cristales Grandes	EPI-0702	This study	0.20	0.14	0.02	0.03	b.d	0.17	b.d	71.3	0.09	0.02	27.7	99.7
cg-28 area 2 sp 4	Cristales Grandes	EPI-0702	This study	0.22	0.14	0.01	0.03	b.d	0.17	b.d	71.6	0.09	0.03	27.8	100.3
cg-28 area 2 sp 5	Rodados Negros	EPI-0808	This study	0.16	0.19	0.01	0.07	b.d	0.06	b.d	70.9	0.10	b.d	27.5	99.1
cg-28 area 2 sp 6	Rodados Negros	EPI-0808	This study	0.19	0.14	0.01	0.20	b.d	0.06	b.d	71.1	0.12	b.d	27.7	99.6
cg-28 area 2 sp 7	Rodados Negros	EPI-0808	This study	0.27	0.28	0.01	0.17	b.d	0.07	b.d	70.8	0.10	0.01	27.7	99.5
rn 10 area 4 sp 1	Rodados Negros	EPI-0808	This study	0.40	0.21	0.02	0.32	b.d	0.47	0.04	70.0	0.07	0.03	27.7	99.4
rn 10 area 4 sp 2	Rodados Negros	EPI-0808	This study	0.72	0.43	0.85	0.60	0.29	0.46	0.04	67.0	0.09	0.04	28.1	98.7
rn 10 area 4 sp 3	Rodados Negros	EPI-0808	This study	0.49	0.27	0.11	0.47	0.05	0.39	0.03	69.3	0.10	0.04	27.7	99.1
rn 10 area 4 sp 4	Rodados Negros	EPI-0808	This study	1.30	0.25	0.02	1.95	b.d	0.42	0.03	67.1	0.38	0.04	28.2	99.7
rn 10 area 4 sp 5	Rodados Negros	EPI-0808	This study	0.56	0.30	0.02	0.80	b.d	0.37	0.03	68.9	0.16	0.04	27.7	99.0
rn 10 area 4 sp 6	Rodados Negros	EPI-0808	This study	0.39	0.37	0.02	0.29	b.d	0.41	0.03	69.9	0.07	0.05	27.7	99.3
rn 10 area 4 sp 7	Rodados Negros	EPI-0808	This study	0.49	0.44	0.22	0.46	0.03	0.42	0.03	69.1	0.10	0.05	27.9	99.2
rn 10 area 4 sp 8	Rodados Negros	EPI-0808	This study	0.31	0.24	0.01	0.13	b.d	0.43	0.04	70.4	0.04	0.04	27.7	99.4
rn 10 area 4 sp 9	Rodados Negros	EPI-0808	This study	0.93	0.50	0.62	0.97	0.16	0.39	0.03	66.7	0.21	0.04	28.1	98.7
rn 10 area 4 sp 10	Rodados Negros	EPI-0808	This study	0.45	0.35	0.02	0.59	b.d	0.34	0.03	69.9	0.14	0.04	27.9	99.8
rn 10 area 4 sp 11	Rodados Negros	EPI-0808	This study	0.44	0.33	0.09	0.44	0.04	0.31	b.d	69.5	0.14	0.05	27.7	99.2
ELS 28 _Area 7_ sp 1	Extensión Laco Sur	ELS-0901	This study	0.29	0.32	0.02	0.21	b.d	0.24	b.d	71.1	0.03	0.03	27.9	100.2
ELS 28 _Area 4 sp1 mag	Extensión Laco Sur	ELS-0901	This study	0.15	0.18	0.01	0.20	b.d	0.17	0.03	71.4	0.02	0.04	27.8	100.1
ELS 28 _Area 4 sp 5 mag	Extensión Laco Sur	ELS-0901	This study	0.15	0.15	0.02	0.41	b.d	0.16	0.03	71.2	0.02	0.03	27.8	100.0
ELS 28 _Area 3 sp 2	Extensión Laco Sur	ELS-0901	This study	0.23	0.25	0.02	0.20	b.d	0.20	0.03	71.3	0.02	0.03	27.9	100.2
ELS 28 _Area 5 mag sp 1	Extensión Laco Sur	ELS-0901	This study	0.15	0.16	0.01	0.25	b.d	0.17	0.03	71.4	0.02	0.03	27.8	100.1
LCN-2-04 Area 4 sp 3	Laco Norte	LCN-0944	This study	0.07	0.36	b.d	0.72	b.d	0.21	0.08	70.3	b.d	0.04	27.7	99.5

Magnetite EPMA data from El Laco host andesites: Magnetite megacrysts

Sample - spot	Type	Host	Mg [wt. %]	Al [wt. %]	Si [wt. %]	Ti [wt. %]	Ca [wt. %]	V [wt. %]	Cr [wt. %]	Fe [wt. %]	Mn [wt. %]	Ni [wt. %]	O [wt. %]	Total
Acum 01 a area 8 sp 1 mag	Mgt-meg	Magnetite megacryst Laco Norte lower andesite	1.02	1.29	0.05	5.36	0.02	0.34	0.11	61.3	0.10	0.03	28.0	97.7
Acum 01 a area 8 sp 3 mag	Mgt-meg	Magnetite megacryst Laco Norte lower andesite	0.06	1.36	0.33	7.10	0.02	0.40	0.13	59.3	0.10	0.03	27.6	96.5
Acum 01 a area 8 sp 4 mag	Mgt-meg	Magnetite megacryst Laco Norte lower andesite	0.39	1.44	0.04	5.85	b.d	0.36	0.11	61.1	0.08	0.04	27.7	97.2
Acum 01 a area 4.1 sp 1 mag	Mgt-meg	Magnetite megacryst Laco Norte lower andesite	0.17	1.06	0.06	5.41	0.03	0.30	0.03	62.7	0.11	0.04	27.6	97.5
Acum 01 a area 4.1 sp 2 mag	Mgt-meg	Magnetite megacryst Laco Norte lower andesite	0.11	1.16	0.06	5.32	0.19	0.30	0.04	62.1	0.08	0.04	27.4	96.8
Acum 01 a area 4.1 sp 3 mag	Mgt-meg	Magnetite megacryst Laco Norte lower andesite	0.22	1.30	0.07	5.32	0.01	0.32	0.04	62.3	0.05	0.04	27.7	97.4
Acum 01 a area 4.1 sp 4 mag	Mgt-meg	Magnetite megacryst Laco Norte lower andesite	0.24	1.32	0.03	5.15	0.02	0.32	0.06	62.7	0.06	0.05	27.8	97.8
Acum 01 a area 4.2 sp 1 mag	Mgt-meg	Magnetite megacryst Laco Norte lower andesite	1.28	1.52	0.04	2.27	b.d	0.26	b.d	64.9	0.18	0.03	28.4	98.9
Acum 01 a area 4.2 sp 2 mag	Mgt-meg	Magnetite megacryst Laco Norte lower andesite	1.20	1.57	0.04	2.66	b.d	0.26	b.d	64.3	0.17	0.03	28.3	98.6
Acum 01 a area 4.2 sp 4 mag	Mgt-meg	Magnetite megacryst Laco Norte lower andesite	0.57	1.51	0.04	2.11	b.d	0.25	b.d	65.9	0.11	0.03	28.0	98.6
Acum 01 a area 4.2 sp 5 mag	Mgt-meg	Magnetite megacryst Laco Norte lower andesite	0.59	1.52	0.04	2.17	b.d	0.24	b.d	65.8	0.13	0.03	28.0	98.6
Acum 01 a area 4.4 sp 1 mag	Mgt-meg	Magnetite megacryst Laco Norte lower andesite	1.23	1.97	2.35	2.45	0.04	0.23	b.d	61.2	0.17	0.03	29.5	99.2
Acum 01 a area 4.4 sp 2 mag	Mgt-meg	Magnetite megacryst Laco Norte lower andesite	1.08	1.44	0.07	2.45	0.14	0.24	b.d	64.7	0.16	0.03	28.2	98.6
Acum 01 a area 4.4 sp 3 mag	Mgt-meg	Magnetite megacryst Laco Norte lower andesite	1.24	1.51	0.04	2.55	b.d	0.24	b.d	64.5	0.18	0.03	28.3	98.6
Acum 01 a area 4.4 sp 4 mag	Mgt-meg	Magnetite megacryst Laco Norte lower andesite	1.18	1.52	0.04	2.35	b.d	0.24	b.d	64.9	0.17	0.03	28.3	98.8

Magnetite EPMA data from El Laco host andesites: Magnetite glomerocrysts

Sample - spot	Type	Host	Si [wt. %]	Mg [wt. %]	Al [wt. %]	Ti [wt. %]	Cr [wt. %]	V [wt. %]	Mn [wt. %]	Fe [wt. %]	Ni [wt. %]	Ca [wt. %]	O [wt. %]	Total
acg 03 area 8 sp 3	Mgt-glom	Cristales Grandes	0.02	0.04	0.19	5.73	0.07	0.42	0.23	64.4	0.02	b.d	27.7	98.9
acg 03 area 1 sp 1	Mgt-glom	Cristales Grandes	0.02	0.16	0.85	1.85	0.08	0.44	0.08	68.1	0.03	b.d	27.9	99.6
acg 03 area 1 sp 2	Mgt-glom	Cristales Grandes	0.02	0.12	0.63	1.77	0.08	0.45	0.15	68.3	0.03	b.d	27.8	99.4
acg 03 area 1 sp 3	Mgt-glom	Cristales Grandes	0.01	0.27	0.49	11.33	0.09	0.32	0.29	57.2	0.02	0.02	27.9	98.0
acg 03 area 1 sp 4	Mgt-glom	Cristales Grandes	0.03	0.12	0.75	1.71	0.10	0.45	0.11	68.0	0.03	b.d	27.8	99.1
acg 03 area 1 sp 5	Mgt-glom	Cristales Grandes	0.03	0.41	0.61	9.00	0.08	0.33	0.35	60.0	0.03	b.d	28.1	99.0
acg 03 area 1 sp 6	Mgt-glom	Cristales Grandes	0.02	0.15	0.62	5.56	0.08	0.38	0.27	63.8	0.02	b.d	27.8	98.8
acg 03 area 1 sp 7	Mgt-glom	Cristales Grandes	0.02	0.18	0.21	6.22	0.08	0.37	0.48	62.5	0.02	0.02	27.4	97.5
ASSVB 03 area 8 sp 2	Mgt-glom	San Vicente Bajo	0.26	0.35	0.55	3.65	0.10	0.52	0.13	63.4	0.03	0.02	27.2	96.3
ASSVB 03 area 8 sp 3	Mgt-glom	San Vicente Bajo	0.12	0.22	0.59	3.60	0.11	0.54	0.10	64.1	0.03	b.d	27.2	96.6
ASSVB 03 area 8 sp 4	Mgt-glom	San Vicente Bajo	0.04	0.25	0.64	2.85	0.24	0.44	0.15	66.0	0.03	b.d	27.6	98.4
ASSVB 03 area 8 sp 5	Mgt-glom	San Vicente Bajo	0.04	0.31	0.61	3.45	0.13	0.39	0.21	65.0	0.03	0.03	27.5	97.9
ASSVB 03 area 7 sp 2	Mgt-glom	San Vicente Bajo	0.53	0.21	0.92	4.04	0.12	0.46	0.11	61.9	0.04	0.04	27.2	95.6
ASSVB 03 area 7 sp 3	Mgt-glom	San Vicente Bajo	0.25	1.30	1.15	4.91	0.16	0.33	0.28	61.1	0.04	0.03	28.2	97.7
ASSVB 03 area 7 sp 4	Mgt-glom	San Vicente Bajo	0.44	0.60	0.67	6.02	0.18	0.41	0.30	59.4	0.02	0.01	27.2	95.3
ASSVB 03 area 7 sp 5	Mgt-glom	San Vicente Bajo	0.06	0.24	0.74	2.76	0.12	0.39	0.11	65.6	0.03	0.03	27.5	97.6
ASSVB 03 area 7 sp 6	Mgt-glom	San Vicente Bajo	0.02	0.21	0.68	3.42	0.10	0.53	0.10	64.6	0.03	b.d	27.3	97.1
als 01 area 5 sp 4 mag	Mgt-glom	Laco Sur	0.01	0.31	0.33	5.91	0.06	0.31	0.12	64.6	0.02	b.d	28.1	99.8
als 01 area 5 sp 5 mag	Mgt-glom	Laco Sur	b.d	0.24	0.30	7.81	0.06	0.31	0.23	62.0	0.03	b.d	27.9	98.9
als 01 area 5 sp 6 mag	Mgt-glom	Laco Sur	0.03	0.14	0.37	5.92	0.10	0.38	0.22	64.1	0.02	b.d	27.9	99.2
als 01 area 5 sp 7 mag	Mgt-glom	Laco Sur	0.02	0.13	0.32	7.21	0.09	0.35	0.28	62.0	0.02	0.01	27.6	98.1
als 01 area 2 sp 1 mag	Mgt-glom	Laco Sur	1.03	0.66	1.91	5.39	0.13	0.33	0.49	57.5	0.02	0.23	28.0	95.7
als 01 area 2 sp 2 mag	Mgt-glom	Laco Sur	0.02	0.14	0.63	4.52	0.15	0.40	0.18	64.8	0.02	b.d	27.7	98.6
als 01 area 2 sp 3 mag	Mgt-glom	Laco Sur	0.04	0.19	0.58	3.71	0.15	0.41	0.16	66.2	0.02	b.d	27.9	99.4
als 01 area 2 sp 4 mag	Mgt-glom	Laco Sur	0.02	0.24	1.09	3.82	0.15	0.40	0.17	64.9	0.02	0.01	27.9	98.8
als 01 area 2 sp 6 mag	Mgt-glom	Laco Sur	3.36	3.00	1.07	5.68	0.12	0.34	0.38	53.1	0.01	0.10	29.9	97.1
als 01 area 5 sp 8 mag r	Mgt-glom	Laco Sur	0.11	0.29	0.21	9.60	0.07	0.37	0.34	57.9	0.01	0.10	27.3	96.4
AILN-02_Area3_2	Mgt-glom	Laco Norte lower andesite	1.74	0.87	0.92	4.26	0.09	0.40	0.10	61.7	0.03	0.05	28.9	99.1
AILN-02_Area5_2	Mgt-glom	Laco Norte lower andesite	0.03	0.16	0.77	0.49	0.34	0.37	0.03	69.3	0.04	0.01	27.8	99.4
AILN-02_Area5_3	Mgt-glom	Laco Norte lower andesite	0.03	0.16	0.57	0.38	0.41	0.38	0.02	69.4	0.04	0.01	27.7	99.2
AILN-02_Area5_4	Mgt-glom	Laco Norte lower andesite	0.64	0.20	0.36	1.84	0.51	0.31	0.18	66.0	0.04	0.06	27.6	97.8
AILN-02_Area5_5	Mgt-glom	Laco Norte lower andesite	0.02	0.11	0.49	0.57	0.34	0.38	0.03	69.8	0.04	0.02	27.8	99.7
AILN-02_Area6_1	Mgt-glom	Laco Norte lower andesite	0.02	0.36	1.24	1.80	0.12	0.37	0.03	68.1	0.05	b.d	28.4	100.5
AILN-02_Area6_2	Mgt-glom	Laco Norte lower andesite	0.02	0.35	1.34	0.76	0.14	0.36	0.03	69.1	0.05	b.d	28.4	100.6
AILN-02_Area6_4	Mgt-glom	Laco Norte lower andesite	0.02	0.30	1.07	0.58	0.12	0.38	0.03	69.7	0.04	b.d	28.3	100.6
AILN-02_Area6_5	Mgt-glom	Laco Norte lower andesite	0.05	0.17	0.78	5.96	0.14	0.31	0.03	61.2	0.04	0.07	27.1	95.8
AILN-02_Area6_6	Mgt-glom	Laco Norte lower andesite	0.03	0.36	1.01	2.79	0.12	0.35	0.15	65.8	0.04	b.d	27.8	98.5
Asln cum area 6 sp 1	Mgt-glom	Laco Norte upper andesite	0.05	1.54	1.42	5.47	0.11	0.30	0.30	60.7	0.04	0.05	28.5	98.5
Asln cum area 6 sp 2	Mgt-glom	Laco Norte upper andesite	0.03	2.02	2.06	3.93	0.43	0.38	0.31	60.2	0.05	0.12	28.7	98.3
Asln cum area 6 sp 3	Mgt-glom	Laco Norte upper andesite	0.06	1.59	1.53	6.16	0.13	0.35	0.30	59.4	0.04	0.15	28.5	98.3
Asln cum area 6 sp 4	Mgt-glom	Laco Norte upper andesite	0.03	1.84	1.45	5.32	0.11	0.35	0.25	60.3	0.05	0.10	28.6	98.5
Asln cum area 6 sp 5	Mgt-glom	Laco Norte upper andesite	1.97	1.69	2.91	5.19	0.34	0.29	0.27	56.0	0.05	0.55	30.0	99.3
Asln cum area 6 sp 6	Mgt-glom	Laco Norte upper andesite	0.12	1.43	0.97	7.03	0.18	0.35	0.34	58.4	0.03	0.10	28.0	97.0
Asln cum area 1 sp 1	Mgt-glom	Laco Norte upper andesite	0.04	1.80	1.58	5.38	0.11	0.32	0.27	60.6	0.05	b.d	28.7	98.8
Asln cum area 1 sp 2	Mgt-glom	Laco Norte upper andesite	0.07	1.82	1.60	5.60	0.11	0.33	0.29	58.6	0.05	b.d	28.1	96.6
Asln cum area 1 sp 3	Mgt-glom	Laco Norte upper andesite	0.04	1.55	1.48	5.42	0.11	0.31	0.27	60.4	0.06	0.02	28.4	98.1

Magnetite EPMA data from El Laco host andesites: Magnetite glomerocrysts

Sample - spot	Type	Host	Si [wt. %]	Mg [wt. %]	Al [wt. %]	Ti [wt. %]	Cr [wt. %]	V [wt. %]	Mn [wt. %]	Fe [wt. %]	Ni [wt. %]	Ca [wt. %]	O [wt. %]	Total
Asln cum area 1 sp 4	Mgt-glom	Laco Norte upper andesite	0.17	1.80	1.54	5.65	0.08	0.33	0.28	58.9	0.05	b.d	28.3	97.2
Asln cum area 1 sp 5	Mgt-glom	Laco Norte upper andesite	0.05	1.66	1.35	5.55	0.10	0.32	0.28	61.0	0.05	0.01	28.6	99.0
Asln cum area 1 sp 6	Mgt-glom	Laco Norte upper andesite	0.67	1.08	0.81	7.59	0.06	0.30	0.40	56.7	0.02	0.52	27.9	96.1
Asln cum area 9 sp 3	Mgt-glom	Laco Norte upper andesite	0.39	0.86	0.70	7.78	0.03	0.30	0.41	57.3	0.03	0.21	27.5	95.5
Asln cum area 9 sp 4	Mgt-glom	Laco Norte upper andesite	0.05	4.21	3.30	5.50	0.87	0.21	0.25	52.8	0.11	0.15	29.6	97.1
Asln cum area 9 sp 5	Mgt-glom	Laco Norte upper andesite	0.06	3.67	2.74	5.37	1.94	0.25	0.24	53.0	0.14	0.21	29.3	97.0
Asln cum area 9 sp 6	Mgt-glom	Laco Norte upper andesite	0.04	3.20	2.32	5.87	0.79	0.30	0.27	54.8	0.12	0.18	28.9	96.9
Asln cum area 9 sp 7	Mgt-glom	Laco Norte upper andesite	0.23	0.82	0.79	8.32	0.08	0.35	0.38	56.6	0.03	0.13	27.3	95.1
BxVRN-01b_Area1_1	Mgt-glom	Rodados Negros	0.13	0.37	1.36	5.27	0.07	0.32	0.05	61.8	0.02	0.01	27.7	97.1
BxVRN-01b_Area1_2	Mgt-glom	Rodados Negros	0.06	0.68	1.31	5.37	0.07	0.33	0.08	61.2	0.02	0.01	27.7	96.9
BxVRN-01b_Area1_3	Mgt-glom	Rodados Negros	0.07	0.72	1.31	5.37	0.07	0.34	0.05	61.4	0.02	0.01	27.8	97.2
BxVRN-01b_Area1_4	Mgt-glom	Rodados Negros	0.04	0.37	1.35	5.39	0.07	0.33	0.04	61.8	0.02	b.d	27.7	97.1
BxVRN-01b_Area1_5	Mgt-glom	Rodados Negros	0.06	0.54	1.40	5.55	0.06	0.34	0.06	61.5	0.02	0.02	27.8	97.4
BxVRN-01b_Area1_6	Mgt-glom	Rodados Negros	0.06	0.42	1.34	5.34	0.07	0.33	0.08	61.9	0.02	0.01	27.7	97.4
BxVRN-01b_Area1.1_sp 1	Mgt-glom	Rodados Negros	0.04	0.42	1.39	5.22	0.07	0.33	0.06	62.0	0.02	0.10	27.8	97.5
BxVRN-01b_Area1.1_sp 2	Mgt-glom	Rodados Negros	0.15	0.45	1.27	5.07	0.07	0.33	0.04	61.9	0.02	0.03	27.7	97.0
BxVRN-01b_Area1.1_sp 3	Mgt-glom	Rodados Negros	0.03	1.25	1.67	4.49	0.07	0.37	0.20	61.4	0.03	0.11	28.3	98.0
BxVRN-01b_Area1.1_sp 4	Mgt-glom	Rodados Negros	0.04	0.42	1.50	4.63	0.07	0.35	0.09	62.9	0.02	0.03	27.9	98.0
BxVRN-01b_Area1.1_sp 5	Mgt-glom	Rodados Negros	0.05	0.51	1.28	1.53	0.12	0.37	0.07	66.9	0.01	0.08	28.0	99.0
BxVRN-01b_Area1.1_sp 6	Mgt-glom	Rodados Negros	0.05	0.77	1.33	5.42	0.08	0.34	0.07	61.7	0.02	0.02	28.0	97.9
BxVRN-01b_Area1.1_sp 7	Mgt-glom	Rodados Negros	0.11	0.40	1.40	5.11	0.08	0.33	0.05	62.4	0.03	0.06	27.9	98.0
PL-02_Area1_1	Mgt-glom	Pico Laco dome	0.14	1.32	1.35	6.53	0.12	0.34	0.27	58.9	0.02	0.02	28.1	97.1
PL-02_Area1_2	Mgt-glom	Pico Laco dome	0.03	1.35	1.39	6.30	0.14	0.34	0.27	60.2	0.02	b.d	28.4	98.5
PL-02_Area1_3	Mgt-glom	Pico Laco dome	0.05	1.25	1.33	6.34	0.14	0.34	0.27	60.2	0.02	0.03	28.4	98.4
PL-02_Area1_4	Mgt-glom	Pico Laco dome	0.04	1.23	1.24	7.02	0.06	0.34	0.30	60.1	0.02	0.01	28.5	98.9
PL-02_Area1_5	Mgt-glom	Pico Laco dome	0.04	1.26	1.27	6.29	0.07	0.33	0.27	60.4	0.01	0.02	28.3	98.4
PL-02_Area1_6	Mgt-glom	Pico Laco dome	0.04	1.27	1.26	6.74	0.07	0.34	0.29	59.7	0.02	0.02	28.3	98.1
PL-02_Area2_1	Mgt-glom	Pico Laco dome	0.04	1.39	1.40	7.15	0.09	0.35	0.30	59.3	0.02	0.02	28.6	98.7
PL-02_Area2_2	Mgt-glom	Pico Laco dome	0.04	1.44	1.27	7.13	0.11	0.35	0.30	59.8	0.01	b.d	28.6	99.1
PL-02_Area2_3	Mgt-glom	Pico Laco dome	0.04	1.43	1.26	7.10	0.10	0.35	0.30	59.1	0.02	b.d	28.4	98.1
PL-02_Area2_4	Mgt-glom	Pico Laco dome	0.05	1.40	1.30	7.05	0.09	0.35	0.30	59.5	0.02	0.06	28.5	98.6
PL-02_Area2_5	Mgt-glom	Pico Laco dome	0.72	0.78	1.76	6.88	0.05	0.33	0.28	56.8	0.02	0.20	27.9	95.8
PL-02_Area5_1	Mgt-glom	Pico Laco dome	0.04	1.19	1.38	6.51	0.03	0.36	0.27	60.2	0.02	b.d	28.4	98.5
PL-02_Area5_2	Mgt-glom	Pico Laco dome	0.04	1.19	1.37	6.46	0.04	0.36	0.26	60.4	0.02	b.d	28.4	98.6
PL-02_Area5_3	Mgt-glom	Pico Laco dome	0.05	1.19	1.43	6.66	0.03	0.37	0.27	58.7	0.02	b.d	27.9	96.7
PL-02_Area5_4	Mgt-glom	Pico Laco dome	0.09	1.19	1.57	6.77	0.04	0.37	0.29	58.2	0.02	b.d	27.9	96.6
PL-02_Area5_5	Mgt-glom	Pico Laco dome	0.06	0.94	1.29	7.35	0.04	0.38	0.28	58.6	0.02	0.02	27.9	96.9
PL-02_Area5_6	Mgt-glom	Pico Laco dome	0.32	1.05	1.53	6.76	0.04	0.37	0.28	58.3	0.02	0.01	28.0	96.8
PL-02_Area5_7	Mgt-glom	Pico Laco dome	0.05	1.09	1.54	6.92	0.04	0.38	0.28	58.4	0.02	b.d	27.9	96.6
PL-02_Area8_2	Mgt-glom	Pico Laco dome	0.14	2.27	0.47	16.20	b.d	0.23	0.99	49.1	0.01	0.01	28.9	98.3
pl 05 area 6 sp 1	Mgt-glom	Pico Laco dome	b.d	1.51	0.82	0.56	0.08	0.33	0.59	67.6	0.05	b.d	28.5	100.2
pl 05 area 6 sp 2	Mgt-glom	Pico Laco dome	0.03	0.51	0.50	7.96	0.08	0.37	0.08	58.8	b.d	0.01	27.1	95.5
pl 05 area 6 sp 3	Mgt-glom	Pico Laco dome	0.11	0.58	0.54	6.16	0.07	0.34	0.14	61.1	0.01	b.d	27.4	96.4
pl 05 area 6b sp 3	Mgt-glom	Pico Laco dome	b.d	1.26	0.41	9.11	b.d	0.14	0.32	56.8	0.01	b.d	27.4	95.5
pl 05 area 6c sp 1	Mgt-glom	Pico Laco dome	0.01	0.98	0.27	14.24	0.04	0.21	0.26	52.0	0.01	0.02	27.5	95.5
pl 05 area 7 sp 1	Mgt-glom	Pico Laco dome	0.06	0.66	0.57	6.94	0.06	0.37	0.13	59.7	0.01	b.d	27.2	95.8
pl 05 area 7 sp 2	Mgt-glom	Pico Laco dome	0.39	3.38	6.55	0.80	0.07	0.14	0.14	59.0	0.04	0.02	31.6	102.1
pl 05 area 7 sp 3	Mgt-glom	Pico Laco dome	0.05	0.59	0.53	8.11	0.07	0.36	0.14	58.2	0.01	b.d	27.1	95.1
pl 05 area 7 sp 4	Mgt-glom	Pico Laco dome	0.01	2.68	2.64	0.39	0.08	0.31	1.19	64.1	0.09	b.d	29.8	101.3
pl 05 area 7 sp 5	Mgt-glom	Pico Laco dome	0.06	0.77	0.84	5.61	0.05	0.04	0.25	60.3	0.03	0.01	27.1	95.1
pl 05 area 7 sp 6	Mgt-glom	Pico Laco dome	0.03	1.05	1.29	3.32	0.10	0.31	0.26	63.6	0.02	0.21	28.2	98.5
pl 05 area 2 sp 5	Mgt-glom	Pico Laco dome	0.28	0.52	0.68	6.20	0.10	0.32	0.18	59.7	b.d	0.02	27.1	95.1
pl 05 area 10b sp 1	Mgt-glom	Pico Laco dome	0.04	0.53	0.55	5.99	0.07	0.27	0.04	60.4	0.01	0.21	27.0	95.1
pl 05 area 10b sp 3	Mgt-glom	Pico Laco dome	0.07	0.67	1.98	0.58	0.07	0.42	0.02	65.2	b.d	0.08	27.6	96.7
pl 05 area 10b sp 5	Mgt-glom	Pico Laco dome	0.08	0.58	0.63	1.61	0.04	0.21	0.08	65.4	0.03	0.04	27.0	95.7

B13. EPMA data of pyroxene from El Laco ore bodies and host andesites.

Clinopyroxene EPMA data from El Laco deposit: Ore-related clinopyroxene

Sample spot	Type	Ore body	Drill core	Si [wt.%]	Ti [wt.%]	Al [wt.%]	Cr [wt.%]	Fe [wt.%]	Mn [wt.%]	Mg [wt.%]	Ca [wt.%]	Na [wt.%]	Total	Dp	Hd	Joh	#Mg	Fs	Wo	En
LCN2-04_A_Px_01	Cpx-ore	Laco Norte	LCN-0944	25.4	0.15	0.43	0.03	4.17	0.06	9.6	16.6	0.43	100.6	83.81	15.98	0.22	0.84	9.01	44.36	46.63
LCN2-04_A_Px_01	Cpx-ore	Laco Norte	LCN-0944	25.3	0.24	0.57	0.06	4.54	0.06	9.4	16.3	0.52	100.7	82.40	17.36	0.25	0.83	9.89	43.84	46.28
LCN2-04_A_Px_01	Cpx-ore	Laco Norte	LCN-0945	25.3	0.24	0.56	0.06	3.99	0.05	9.5	16.5	0.53	100.4	84.27	15.52	0.21	0.84	8.71	44.64	46.66
LCN2-04_A_Px_01	Cpx-ore	Laco Norte	LCN-0946	25.7	0.11	0.32	0.03	3.83	0.06	9.8	16.7	0.40	100.9	85.23	14.56	0.21	0.85	8.23	44.27	47.50
LCN2-04_A_Px_01	Cpx-ore	Laco Norte	LCN-0947	25.5	0.16	0.48	0.04	3.78	0.05	9.6	16.8	0.47	100.9	85.21	14.61	0.18	0.85	8.14	44.93	46.93
LCN2-04_A_Px_01	Cpx-ore	Laco Norte	LCN-0948	25.2	0.20	0.61	0.07	4.00	0.05	9.4	16.5	0.57	100.2	84.20	15.61	0.19	0.84	8.73	44.72	46.54
LCN2-04_A_Px_01	Cpx-ore	Laco Norte	LCN-0949	25.5	0.15	0.49	0.02	3.87	0.05	9.6	16.7	0.47	100.7	84.91	14.91	0.19	0.85	8.36	44.61	47.03
LCN2-04_B_Px_02	Cpx-ore	Laco Norte	LCN-0950	25.4	0.20	0.65	0.06	4.09	0.05	9.4	16.4	0.59	100.7	83.87	15.93	0.20	0.84	8.95	44.48	46.56
LCN2-04_B_Px_02	Cpx-ore	Laco Norte	LCN-0951	25.3	0.14	0.49	0.02	3.92	0.05	9.6	16.5	0.48	100.0	84.63	15.18	0.19	0.85	8.52	44.53	46.94
LCN2-04_B_Px_02	Cpx-ore	Laco Norte	LCN-0952	25.6	0.15	0.55	0.02	4.17	0.05	9.6	16.6	0.52	101.3	83.85	15.97	0.17	0.84	8.98	44.40	46.63
LCN2-04_B_Px_02	Cpx-ore	Laco Norte	LCN-0953	25.2	0.20	0.53	0.05	4.38	0.06	9.5	16.3	0.50	100.4	83.06	16.72	0.22	0.83	9.50	43.92	46.58
LCN2-04_B_Px_02	Cpx-ore	Laco Norte	LCN-0954	25.5	0.18	0.49	0.06	4.34	0.06	9.6	16.1	0.52	100.7	83.34	16.43	0.23	0.84	9.43	43.42	47.16
LCN2-04_B_Px_02	Cpx-ore	Laco Norte	LCN-0955	25.4	0.23	0.53	0.04	4.16	0.05	9.5	16.5	0.52	100.7	83.75	16.06	0.19	0.84	9.04	44.35	46.61
LCN2-04_B_Px_02	Cpx-ore	Laco Norte	LCN-0956	25.3	0.24	0.65	0.04	4.30	0.06	9.5	16.4	0.53	100.9	83.26	16.52	0.22	0.83	9.33	44.26	46.41
LCN2-04_B_Px_02	Cpx-ore	Laco Norte	LCN-0957	25.0	0.07	0.83	0.00	5.57	0.06	8.9	15.6	0.76	100.0	78.43	21.33	0.24	0.79	12.32	42.90	44.78
LCN2-04_C_Px_03	Cpx-ore	Laco Norte	LCN-0958	25.5	0.12	0.41	0.03	3.71	0.04	9.6	16.7	0.47	100.4	85.39	14.44	0.17	0.86	8.05	44.87	47.07
LCN2-04_C_Px_03	Cpx-ore	Laco Norte	LCN-0959	25.2	0.24	0.66	0.07	4.22	0.05	9.4	16.5	0.59	100.7	83.40	16.41	0.19	0.84	9.18	44.68	46.14
LCN2-04_C_Px_03	Cpx-ore	Laco Norte	LCN-0960	25.7	0.13	0.40	0.02	4.57	0.05	9.8	15.3	0.42	100.1	82.87	16.95	0.18	0.83	10.02	41.50	48.48
LCN2-04_C_Px_03	Cpx-ore	Laco Norte	LCN-0961	25.7	0.10	0.24	0.03	4.22	0.07	9.8	16.2	0.42	100.6	83.92	15.82	0.26	0.84	9.12	43.29	47.59
LCN2-04_C_Px_03	Cpx-ore	Laco Norte	LCN-0962	25.2	0.06	0.62	0.00	6.10	0.09	9.4	15.0	0.50	100.2	77.60	22.09	0.32	0.78	13.33	40.49	46.18
ELS-28_A_Px_01	Cpx-ore	Extensión Laco Sur	ELS-0901	25.7	0.13	0.27	0.01	5.37	0.06	9.4	15.7	0.59	101.1	79.89	19.90	0.21	0.80	11.64	42.13	46.23
ELS-28_A_Px_01	Cpx-ore	Extensión Laco Sur	ELS-0901	25.5	0.13	0.31	0.01	5.38	0.05	9.4	15.8	0.57	100.7	79.82	19.99	0.20	0.80	11.63	42.38	45.99
ELS-28_A_Px_01	Cpx-ore	Extensión Laco Sur	ELS-0901	25.4	0.12	0.31	0.01	5.44	0.06	9.4	15.8	0.58	100.6	79.59	20.20	0.21	0.80	11.75	42.44	45.81
ELS-28_A_Px_01	Cpx-ore	Extensión Laco Sur	ELS-0901	25.4	0.12	0.37	0.00	5.21	0.05	9.2	16.3	0.58	100.7	80.01	19.82	0.18	0.80	11.25	43.73	45.02
ELS-28_B_Px_02	Cpx-ore	Extensión Laco Sur	ELS-0901	25.5	0.10	0.28	0.00	5.07	0.04	9.4	16.4	0.51	100.9	80.83	19.01	0.17	0.81	10.82	43.55	45.62
ELS-28_B_Px_02	Cpx-ore	Extensión Laco Sur	ELS-0901	25.5	0.12	0.38	0.01	5.29	0.04	9.1	16.1	0.59	100.8	79.67	20.16	0.17	0.80	11.47	43.57	44.96
ELS-28_B_Px_02	Cpx-ore	Extensión Laco Sur	ELS-0901	25.5	0.11	0.34	0.01	5.06	0.04	9.2	16.0	0.61	100.5	80.55	19.28	0.17	0.81	11.01	43.39	45.60
ELS-28_B_Px_02	Cpx-ore	Extensión Laco Sur	ELS-0901	25.6	0.13	0.31	0.01	5.09	0.05	9.3	16.0	0.64	100.8	80.55	19.25	0.19	0.81	11.06	43.13	45.81
ELS-28_B_Px_02	Cpx-ore	Extensión Laco Sur	ELS-0901	25.7	0.14	0.32	0.01	4.99	0.04	9.3	16.1	0.66	101.1	80.79	19.05	0.16	0.81	10.84	43.56	45.59
ELS-28_C_Px_03	Cpx-ore	Extensión Laco Sur	ELS-0901	25.3	0.19	0.42	0.01	5.32	0.05	9.3	15.8	0.62	100.3	79.83	19.97	0.20	0.80	11.57	42.65	45.78
ELS-28_C_Px_03	Cpx-ore	Extensión Laco Sur	ELS-0901	25.5	0.14	0.32	0.01	5.23	0.05	9.3	15.9	0.60	100.7	80.20	19.61	0.19	0.80	11.32	42.85	45.84
ELS-28_C_Px_03	Cpx-ore	Extensión Laco Sur	ELS-0901	25.5	0.18	0.36	0.01	5.35	0.05	9.3	15.7	0.65	100.7	79.87	19.95	0.18	0.80	11.59	42.41	46.00
ELS-28_C_Px_03	Cpx-ore	Extensión Laco Sur	ELS-0901	25.0	0.29	0.52	0.01	6.02	0.05	8.9	15.3	0.73	100.0	77.05	22.76	0.19	0.77	13.27	42.19	44.55
ELS-28_C_Px_03	Cpx-ore	Extensión Laco Sur	ELS-0901	25.5	0.19	0.45	0.01	5.32	0.04	9.1	15.9	0.69	101.0	79.60	20.24	0.16	0.80	11.59	43.17	45.24
ELS-28_D_Px_04	Cpx-ore	Extensión Laco Sur	ELS-0901	25.4	0.13	0.32	0.01	5.16	0.05	9.3	16.1	0.63	100.7	80.29	19.53	0.18	0.80	11.17	43.35	45.49
ELS-28_D_Px_04	Cpx-ore	Extensión Laco Sur	ELS-0901	25.6	0.14	0.35	0.00	5.38	0.04	9.1	16.1	0.60	100.9	79.32	20.52	0.15	0.79	11.68	43.50	44.82
ELS-28_D_Px_04	Cpx-ore	Extensión Laco Sur	ELS-0901	25.5	0.14	0.37	0.01	5.39	0.05	9.1	16.0	0.64	100.9	79.40	20.43	0.18	0.80	11.69	43.27	45.04
ELS-28_E_Px_05	Cpx-ore	Extensión Laco Sur	ELS-0901	25.4	0.19	0.46	0.01	5.59	0.05	9.0	15.9	0.70	100.8	78.62	21.20	0.18	0.79	12.17	43.08	44.75
ELS-28_E_Px_05	Cpx-ore	Extensión Laco Sur	ELS-0901	25.4	0.19	0.42	0.01	5.32	0.05	9.1	15.9	0.63	100.5	79.44	20.38	0.18	0.80	11.64	43.36	44.99
ELS-28_E_Px_05	Cpx-ore	Extensión Laco Sur	ELS-0901	25.4	0.11	0.11	0.01	5.22	0.06	9.5	16.2	0.32	100.4	80.39	19.39	0.22	0.81	11.17	43.05	45.78
ELS-28_E_Px_05	Cpx-ore	Extensión Laco Sur	ELS-0901	25.5	0.14	0.46	0.01	5.25	0.05	9.2	15.9	0.69	101.0	79.90	19.89	0.21	0.80	11.44	43.08	45.48
ELS-28_E_Px_05	Cpx-ore	Extensión Laco Sur	ELS-0901	25.3	0.21	0.42	0.01	5.49	0.05	9.2	15.7	0.64	100.6	79.23	20.58	0.19	0.79	11.94	42.51	45.55
LCN-07_A_Px_01	Cpx-ore	Laco Norte	LCN-0944	25.9	0.06	0.17	0.01	4.05	0.05	9.7	16.7	0.50	101.2	84.38	15.45	0.17	0.85	8.68	44.46	46.86
LCN-07_A_Px_01	Cpx-ore	Laco Norte	LCN-0944	25.9	0.05	0.19	0.00	4.00	0.05	9.6	16.5	0.52	100.8	84.43	15.37	0.19	0.85	8.67	44.30	47.03
LCN-07_A_Px_01	Cpx-ore	Laco Norte	LCN-0944	25.7	0.09	0.20	0.01	4.90	0.06	9.4	16.4	0.42	101.0	81.26	18.50	0.24	0.81	10.54	43.78	45.68
LCN-07_A_Px_01	Cpx-ore	Laco Norte	LCN-0944	25.4	0.16	0.26	0.01	6.23	0.08	9.3	15.0	0.58	100.3	77.10	22.61	0.30	0.77	13.61	40.55	45.83
LCN-07_A_Px_01	Cpx-ore	Laco Norte	LCN-0944	25.4	0.36	0.23	0.00	5.33	0.06	9.3	15.5	0.65	100.3	79.77	19.99	0.24	0.80	11.70	42.14	46.15
LCN-07_A_Px_01	Cpx-ore	Laco Norte	LCN-0944	25.4	0.41	0.28	0.01	5.44	0.07	9.2	15.4	0.68	100.3	79.32	20.43	0.25	0.80	11.98	42.06	45.96
LCN-07_A_Px_01	Cpx-ore	Laco Norte	LCN-0944	25.2	0.20	0.23	0.01	6.46	0.09	9.2	14.9	0.56	100.0	76.27	23.39	0.34	0.77	14.14	40.40	45.46
LCN-07_A_Px_01	Cpx-ore	Laco Norte	LCN-0944	25.4	0.40	0.24	0.00	5.41	0.06	9.3	15.5	0.67	100.4	79.55	20.21	0.23	0.80	11.85	42.06	46.09
LCN-07_A_Px_01	Cpx-ore	Laco Norte	LCN-0944	25.5	0.30	0.36	0.01	6.35	0.05	8.4	15.4	0.99	100.7	74.97	24.82	0.21	0.75	14.24	43.10	42.66
LCN-07_A_Px_01	Cpx-ore	Laco Norte	LCN-0944	25.9	0.13	0.24	0.00	4.89	0.05	9.5	16.1	0.56	101.4	81.46	18.36	0.19	0.82	10.56	43.05	46.39
LCN-07_B_Px_02	Cpx-ore	Laco Norte	LCN-0944	25.5	0.35	0.37	0.01	6.01	0.06	8.7	15.4	0.94	100.9	76.60	23.18	0.22	0.77	13.39	42.78	43.83
LCN-07_B_Px_02	Cpx-ore	Laco Norte	LCN-0944	25.2	0.48	0.41	0.01	5.97	0.07	8.8	15.2	0.87	100.3	76.85	22.90	0.26	0.77	13.38	42.22	44.40
LCN-07_B_Px_02	Cpx-ore	Laco Norte	LCN-0944	25.7	0.20	0.29	0.01	5.18	0.06	9.3	15.8	0.69	101.1	80.22	19.57	0.21	0.80	11.30	42.85	45.84
LCN-07_B_Px_02	Cpx-ore	Laco Norte	LCN-0944	25.1	0.53	0.53	0.01	5.92	0.06	8.8	15.1	0.91	100.3	77.15	22.61	0.24	0.77	13.24	42.05	44.71
LCN-07_B_Px_02	Cpx-ore	Laco Norte	LCN-0944	25.5	0.30	0.24	0.01	5.56	0.05	9.1	16.0	0.60	101.0	78.79	21.02	0.19	0.79	12.07	43.10	44.83
LCN-07_B_Px_02	Cpx-ore	Laco Norte	LCN-0944	25.1	0.44	0.33	0.01	5.42	0.07	9.2	15.3	0.67	99.7	79.32	20.43	0.25	0.80	11.98	42.08	45.94
LCN-07_C_Px_03	Cpx-ore	Laco Norte	LCN-0944	25.2	0.22	0.23	0.01	6.59	0.08	9.1	15.0	0.58	100.3	75.70	24.01	0.30	0.76	14.40	40.74	44.86
LCN-07_C_Px_03	Cpx-ore	Laco Norte	LCN-0944	25.4	0.17	0.25	0.00	6.17	0.08	9.4	14.9	0.59	100.4	77.41	22.29	0.30	0.78	13.46	40.41	46.13
LCN-07_C_Px_03	Cpx-ore	Laco Norte	LCN-0944	25.3	0.21	0.30	0.01	6.31	0.08	9.2	15.1	0.64	100.6	76.70	23.01	0.29	0.77	13.76	40.96	45.28
LCN-07_C_Px_03	Cpx-ore	Laco Norte	LCN-0944	25.6	0.38	0.28	0.01	5.27	0.07	9.3	15.4	0.70	100.6	79.86	19.89	0.25	0.80	11.66	42.14	46.21
LCN-07_C_Px_03	Cpx-ore	Laco Norte	LCN-0944	25.2	0.53	0.29	0.01	6.11	0.07	9.1	14.8	0.79	100.1	82.20	17.61	0.18	0.82	10.05	43.53	46.42
CG-08_A_Px_01	Cpx-ore	Cristales Grandes	EPI-0702	24.5	0.49	1.44	0.02	5.08	0.06	8.4	16.9	0.47	100.6	77.15	22.61	0.25	0.77	13.53	40.78	45.68
CG-08_A_Px_01	Cpx-ore	Cristales Grandes	EPI-0702	24.9	0.21	0.91	0.01	5.06	0.07	8.7	17.0	0.37	100.7	79.47	20.24	0.29	0.80	11.06	46.11	42.83
CG-08_A_Px_01	Cpx-ore	Cristales Grandes	EPI-0702	25.7	0.14	0.21	0.04	4.13	0.09	9.2	17.5	0.22	101.1	83.20	16.45	0.35	0.83	8.99	46.49	44.52
CG-08_A_Px_01	Cpx-ore	Cristales Grandes	EPI-0702	25.7	0.13	0.48	0.10	3.66	0.05	9.6	17.1	0.41	101.4	85.50	14.32	0.18	0.86	7.90	45.54	46.56
CG-08_B_Px_02	Cpx-ore	Cristales Grandes	EPI-0702	25.0	0.32	0.53	0.04	4.93	0.11	8.9	17.1	0.21	100.6	80.13	19.44	0.42	0.80	10.75	45.87	43.38
CG-08_B_Px_02	Cpx-ore	Cristales Grandes	EPI-0702	25.2	0.30	0.85	0.48	3.44	0.05	9.0	16.8	0.65	100.5	85.40	14.39	0.22	0.86	7.77	46.79	45.44
CG-08_B_Px_02	Cpx-ore	Cristales Grandes	EPI-0702	23.7	0.90	1.95	0.02	5.11	0.06	8.1	16.8	0.50	100.3	78.33	21.42	0.25	0.79	11.48	47.03	41.49
CG-08_B_Px_02	Cpx-ore	Cristales Grandes	EPI-0702	25.2	0.26	0.88	0.02	4.22	0.05	9.1	16.8	0.52	100.9	82.99	16.82	0.18	0.83	9.25	45.62	45.13
CG-08_B_Px_02	Cpx-ore	Cristales Grandes	EPI-0702	25.3	0.26	0.81	0.04	4.11	0.07	9.0	17.2	0.46	101.0	83.04	16.67	0.29	0.83	9.04	46.70	44.26
CG-08_B_Px_02	Cpx-ore	Cristales Grandes	EPI-0702	25.1	0.29	1.09	0.01	4.15	0.05	9.0	17.4	0.36	101.4	82.99	16.79	0.22	0.83	9.03	46.93	44.04
CG-08_B_Px_02	Cpx-ore	Cristales Grandes	EPI-0702	24.4	0.49	1.39	0.12	4.43	0.05	8.7	17.1	0.44	100.5	81.65	18.13	0.21	0.82	9.77	46.77	43.47
CG-08_B_Px_02	Cpx-ore	Cristales Grandes	EPI-0702	25.4	0.21	0.67	0.15	3.58	0.05	9.3	17.3	0.41	101.0	85.35	14.45	0.21	0.86	7.82	46.61	45.57
CG-08_B_Px_02	Cpx-ore	Cristales Grandes	EPI-0702	25.0	0.30	0.52	0.04	4.87	0.11	9.0	17.2	0.23	100.6	80.48	19.08	0.44	0.81	10.59	45.75	43.66
CG-08_C_Px_03	Cpx-ore	Cristales Grandes	EPI-0702	24.5	0.46	1.34	0.04	5.05	0.07	8.5	16.9	0.45	100.7	79.20	20.52	0.29	0.79	11.18	46.28	42.55
CG-08_C_Px_03	Cpx-ore	Cristales Grandes	EPI-0702	24.5	0.45	1.31	0.04	5.01	0.07	8.5	17.0	0.43	100.6	79.28	20.46	0.27	0.79	11.07	46.58	42.35
CG-08_C_Px_03	Cpx-ore	Cristales Grandes	EPI-0702	25.3	0.26	0.96	0.06	3.95	0.06	9.0	17.2	0.50	101.2	83.67	16.10	0.24	0.84	8.70	46.72	44.57
CG-08_C_Px_03	Cpx-ore	Cristales Grandes	EPI-0702	25.3	0.15	0.58	0.01	4.69	0.05	9.0	17.0	0.48	101.2	81.36	18.44	0.20	0.82	10.12	45.68	44.19
CG-08_C_Px_03	Cpx-ore	Cristales Grandes	EPI-0702	24.2	0.47	1.73	0.03	5.24	0.07	8.3	16.7	0.49	100.6	78.19	21.51	0.30	0.78	11.70	46.34	41.96
CG-08_C_Px_03	Cpx-ore	Cristales Grandes	EPI-0702	25.2	0.43	0.99	0.05	3.61	0.04	9.3	17.3	0.42	101.4	85.30	14.52	0.18	0.85	7.86	46.52	45.62
CG-08_D_Px_04	Cpx-ore	Cristales Grandes	EPI-0702	25.1	0.23	0.88	0.02	4.41	0.05	8.9	17.0	0.52	100.8	82.11	17.71	0.18	0.82	9.64	46.11	44.25
CG-08_D_Px_04	Cpx-ore	Cristales Grandes	EPI-0702	25.2	0.28	0.91	0.02	3.64	0.05	9.2	17.4	0.42	100.9	84.99	14.81	0.20	0.85	7.97	46.93	45.11
CG-08_D_Px_04	Cpx-ore	Cristales Grandes	EPI-0702	24.0	0.60	1.67	0.02	5.26	0.07	8.3	16.9	0.43	100.4	78.01	21.68	0.31	0.78	11.74	46.61	41.65
CG-08_D_Px_04	Cpx-ore	Cristales Grandes	EPI-0702	25.1	0.29	0.80	0.09	4.37	0.07	8.9	17.2	0.41	100.9	82.15	17.57	0.28	0.82	9.55	46.46	43.98
CG-08_D_Px_04	Cpx-ore	Cristales Grandes	EPI-0702	25.9	0.06	0.25	0.13	3.35	0.06	9.5	17.3	0.43	101.1	86.33	13.44	0.23	0.87	7.33	46.43	46.25
CG-08_D_Px_04	Cpx-ore	Cristales Grandes	EPI-0702	25.7	0.13	0.44	0.03	3.83	0.04	9.5	17.1	0.41	101.3	84.91	14.92	0.17	0.85	8.21	45.60	46.19
SVA1-14_A_Px_01_1	Cpx-ore	San Vicente Alto	SVA-1001	25.4	0.11	0.28	0.00	5.37	0.09	8.9	16.8	0.32	100.7	78.79	20.86	0.35	0.79	11.68	44.93	43.39
SVA1-14_A_Px_01_2	Cpx-ore	San Vicente Alto	SVA-1001	24.9	0.24	0.90	0.00	6.01	0.08	8.5	16.2	0.58	100.8	76.24	23.46	0.30	0.76	13.24	44.27	42.49
SVA1-14_A_Px_01_3	Cpx-ore	San Vicente Alto	SVA-1001	24.6	0.24	1.14	0.01	5.99	0.06	8.4	16.3	0.64	100.6	76.04	23.73	0.23	0.76	13.20	44.91	41.89
SVA1-14_A_Px_01_4	Cpx-ore	San Vicente Alto	SVA-1001	25.1	0.17	0.75	0.00	5.46	0.06	8.7	16.4	0.57	100.6	78.33	21.42	0.25	0.79	12.00	44.62	43.38
SVA1-14_A_Px_01_5	Cpx-ore	San Vicente Alto	SVA-1001	25.3	0.16	0.62	0.01	4.77	0.06	9.0	16.7	0.53	100.9	81.07	18.69	0.23	0.81	10.39	45.12	44.50
SVA1-14_A_Px_01_6	Cpx-ore	San Vicente Alto	SVA-1001	25.6	0.14	0.49	0.01	4.50	0.05	9.2	16.9	0.54	101.4	82.16	17.64	0.20	0.82	9.76	45.30	44.94
SVA1-14_A_Px_01_7	Cpx-ore	San Vicente Alto	SVA-1001	25.4	0.09	0.39	0.00	4.84	0.07	9.1	16.6	0.42	100.6	80.98	18.75	0.26	0.81	10.53	44.63	44.84
SVA1-14_A_Px_01_8	Cpx-ore	San Vicente Alto	SVA-1001	25.2	0.09	0.39	0.00	4.82	0.06	9.1	16.7	0.43	100.2	81.02	18.72	0.25	0.81	10.45	44.92	44.62

Clinopyroxene EPMA data from El Laco deposit: Ore-related clinopyroxene

Sample spot	Type	Ore body	Drill core	Si [wt.%]	Ti [wt.%]	Al [wt.%]	Cr [wt.%]	Fe [wt.%]	Mn [wt.%]	Mg [wt.%]	Ca [wt.%]	Na [wt.%]	Total	Dp	Hd	Joh	#Mg	Fs	Wo	En
SVA1-14_A_Px_01_9	Cpx-ore	San Vicente Alto	SVA-1001	24.9	0.07	0.82	0.01	5.41	0.06	8.8	16.5	0.52	100.5	78.63	21.12	0.25	0.79	11.79	44.82	43.38
SVA1-14_A_Px_01_10	Cpx-ore	San Vicente Alto	SVA-1001	25.5	0.05	0.62	0.00	4.50	0.05	9.1	17.0	0.48	101.1	82.03	17.76	0.21	0.82	9.77	45.63	44.60
SVA1-14_A_Px_01_11	Cpx-ore	San Vicente Alto	SVA-1001	25.4	0.03	0.63	0.00	4.97	0.05	9.1	16.8	0.51	101.3	80.47	19.31	0.21	0.81	10.73	45.02	44.24
SVA1-14_A_Px_01_12	Cpx-ore	San Vicente Alto	SVA-1001	24.5	0.35	1.21	0.01	5.99	0.06	8.3	16.3	0.68	100.5	75.82	23.94	0.24	0.76	13.29	45.03	41.68
SVA1-14_A_Px_01_13	Cpx-ore	San Vicente Alto	SVA-1001	25.4	0.13	0.62	0.01	4.94	0.05	8.9	16.7	0.57	101.1	80.38	19.41	0.21	0.81	10.75	45.20	44.05
SVA1-14_A_Px_01_14	Cpx-ore	San Vicente Alto	SVA-1001	25.5	0.16	0.60	0.00	4.65	0.05	9.1	16.7	0.56	101.2	81.51	18.31	0.18	0.82	10.12	45.24	44.64
SVA1-14_A_Px_01_15	Cpx-ore	San Vicente Alto	SVA-1001	24.9	0.27	0.86	0.00	5.09	0.05	8.8	16.7	0.58	100.6	79.60	20.19	0.21	0.80	11.15	45.35	43.50
SVA1-14_A_Px_01_16	Cpx-ore	San Vicente Alto	SVA-1001	24.9	0.09	0.94	0.00	5.52	0.05	8.6	16.7	0.55	100.6	77.90	21.88	0.21	0.78	12.06	45.42	42.52
SVA1-14_A_Px_01_17	Cpx-ore	San Vicente Alto	SVA-1001	24.9	0.10	1.06	0.00	5.56	0.05	8.5	16.6	0.59	100.8	77.73	22.06	0.21	0.78	12.17	45.37	42.46
SVA1-14_B_Px_02_1	Cpx-ore	San Vicente Alto	SVA-1001	24.2	0.48	1.30	0.01	6.50	0.06	7.9	16.0	0.80	100.2	74.27	25.48	0.24	0.74	14.56	44.88	40.56
SVA1-14_B_Px_02_1	Cpx-ore	San Vicente Alto	SVA-1001	24.8	0.27	0.86	0.01	6.13	0.07	8.4	16.1	0.64	100.5	75.64	24.07	0.28	0.76	13.55	44.36	42.09
SVA1-14_B_Px_02_1	Cpx-ore	San Vicente Alto	SVA-1001	24.9	0.14	0.93	0.00	5.52	0.05	8.6	16.6	0.59	100.7	77.99	21.80	0.21	0.78	12.05	45.24	42.71
SVA1-14_B_Px_02_1	Cpx-ore	San Vicente Alto	SVA-1001	25.4	0.14	0.49	0.01	4.58	0.05	9.2	16.8	0.53	100.8	81.93	17.86	0.21	0.82	9.92	45.08	44.99
SVA1-14_B_Px_02_2	Cpx-ore	San Vicente Alto	SVA-1001	24.4	0.25	1.23	0.01	6.56	0.06	8.0	16.0	0.80	100.3	73.98	25.77	0.24	0.74	14.66	44.68	40.67
SVA1-14_B_Px_02_2	Cpx-ore	San Vicente Alto	SVA-1001	25.1	0.22	0.82	0.00	5.09	0.05	8.8	16.6	0.60	100.8	79.67	20.14	0.19	0.80	11.13	45.25	43.61
SVA1-14_B_Px_02_2	Cpx-ore	San Vicente Alto	SVA-1001	24.2	0.34	1.11	0.01	6.82	0.08	8.1	16.0	0.62	99.9	72.84	26.85	0.31	0.73	15.16	44.19	40.65
SVA1-14_B_Px_02_2	Cpx-ore	San Vicente Alto	SVA-1001	25.6	0.11	0.37	0.01	4.38	0.05	9.2	16.8	0.39	100.8	82.63	17.16	0.21	0.83	9.52	45.17	45.31
SVA1-14_B_Px_03	Cpx-ore	San Vicente Alto	SVA-1001	24.8	0.06	0.80	0.00	6.72	0.08	8.3	16.3	0.56	100.6	73.61	26.06	0.33	0.74	14.70	44.30	41.00
SVA1-14_B_Px_03	Cpx-ore	San Vicente Alto	SVA-1001	25.1	0.04	0.34	0.01	6.53	0.12	8.5	16.5	0.34	100.6	74.48	25.07	0.45	0.75	14.20	44.35	41.45
SVA1-14_B_Px_03	Cpx-ore	San Vicente Alto	SVA-1001	25.0	0.04	0.83	0.00	6.16	0.07	8.4	16.2	0.65	100.6	75.55	24.17	0.27	0.76	13.60	44.38	42.02
SVA1-14_B_Px_03	Cpx-ore	San Vicente Alto	SVA-1001	24.9	0.25	1.04	0.00	6.03	0.06	8.3	16.3	0.74	100.9	75.73	24.03	0.24	0.76	13.37	44.92	41.71
SVA1-14_B_Px_03	Cpx-ore	San Vicente Alto	SVA-1001	24.9	0.22	1.05	0.01	6.23	0.06	8.2	16.2	0.74	101.1	75.01	24.76	0.23	0.75	13.79	44.82	41.39
SVA1-14_B_Px_03	Cpx-ore	San Vicente Alto	SVA-1001	24.5	0.25	1.20	0.01	6.54	0.06	8.0	16.0	0.79	100.3	73.94	25.83	0.24	0.74	14.58	44.62	40.81
SVA1-14_B_Px_03	Cpx-ore	San Vicente Alto	SVA-1001	24.4	0.49	1.33	0.00	6.50	0.06	8.0	16.2	0.75	100.7	73.67	26.10	0.23	0.74	14.48	45.02	40.51
SVA1-14_B_Px_03	Cpx-ore	San Vicente Alto	SVA-1001	24.5	0.36	1.23	0.01	6.56	0.06	8.0	16.0	0.80	100.6	73.73	26.04	0.23	0.74	14.62	44.74	40.63
SVA1-14_B_Px_03	Cpx-ore	San Vicente Alto	SVA-1001	25.0	0.22	0.88	0.01	5.42	0.05	8.6	16.5	0.65	100.7	78.33	21.45	0.22	0.79	11.91	45.03	43.06
CG-28_T8	Cpx-ore	Cristales Grandes	EPI-0702	24.1	0.10	0.39	bdl	3.92	0.05	9.3	16.6	0.55	97.8	87.90	11.87	0.22	0.88	9.39	44.81	45.79
CG-28_T8	Cpx-ore	Cristales Grandes	EPI-0702	24.0	0.09	0.46	bdl	4.10	0.05	9.2	16.5	0.57	97.6	86.83	12.96	0.21	0.87	9.86	44.68	45.45
CG-28_T8	Cpx-ore	Cristales Grandes	EPI-0702	23.9	0.09	0.50	bdl	4.23	0.06	9.1	16.5	0.56	97.5	86.58	13.18	0.24	0.87	10.19	44.68	45.13
CG-28_T8	Cpx-ore	Cristales Grandes	EPI-0702	23.9	0.08	0.50	bdl	4.20	0.05	9.1	16.4	0.59	97.4	86.78	12.99	0.23	0.87	10.16	44.80	45.04
CG-28_T8	Cpx-ore	Cristales Grandes	EPI-0702	23.8	0.14	0.88	bdl	4.31	0.05	8.8	16.2	0.82	97.5	87.24	12.54	0.22	0.87	10.61	44.97	44.42
CG-28_T8	Cpx-ore	Cristales Grandes	EPI-0702	23.7	0.11	0.87	bdl	4.25	0.05	8.8	16.2	0.85	97.5	88.90	10.90	0.20	0.89	10.42	44.99	44.59
CG-28_T8	Cpx-ore	Cristales Grandes	EPI-0702	24.2	0.08	0.32	0.01	3.03	0.05	9.7	16.8	0.48	97.5	90.59	9.19	0.22	0.91	7.26	45.16	47.58
CG-28_T8	Cpx-ore	Cristales Grandes	EPI-0702	24.2	0.09	0.35	0.01	3.07	0.05	9.7	16.7	0.51	97.4	90.38	9.43	0.19	0.91	7.37	44.93	47.71
CG-28_T8	Cpx-ore	Cristales Grandes	EPI-0702	24.2	0.11	0.44	bdl	3.25	0.04	9.6	16.6	0.56	97.5	89.83	10.00	0.17	0.90	7.80	45.02	47.18
CG-28_T8	Cpx-ore	Cristales Grandes	EPI-0702	24.1	0.11	0.43	0.01	3.16	0.04	9.6	16.7	0.55	97.4	90.36	9.48	0.16	0.91	7.60	45.22	47.18
CG-28_T8	Cpx-ore	Cristales Grandes	EPI-0702	24.2	0.13	0.41	0.01	2.99	0.04	9.7	16.7	0.56	97.4	91.09	8.74	0.18	0.91	7.19	45.06	47.76
CG-28_T8	Cpx-ore	Cristales Grandes	EPI-0702	24.2	0.12	0.39	0.02	2.89	0.04	9.7	16.7	0.56	97.5	91.07	8.77	0.16	0.91	6.93	45.15	47.91
CG-28_T8	Cpx-ore	Cristales Grandes	EPI-0702	24.1	0.13	0.47	0.02	2.98	0.04	9.6	16.7	0.58	97.5	91.55	8.27	0.18	0.92	7.17	45.27	47.56
CG-28_T8	Cpx-ore	Cristales Grandes	EPI-0702	24.3	0.11	0.31	0.02	3.10	0.05	9.7	16.6	0.51	97.5	89.73	10.08	0.19	0.90	7.44	44.82	47.74
CG-28_T8	Cpx-ore	Cristales Grandes	EPI-0702	24.4	0.07	0.21	bdl	3.02	0.04	9.8	16.8	0.42	97.5	88.97	10.87	0.17	0.89	7.20	44.99	47.81
CG-28_T8	Cpx-ore	Cristales Grandes	EPI-0702	24.4	0.07	0.20	0.01	3.01	0.05	9.8	16.8	0.40	97.5	89.08	10.73	0.19	0.89	7.17	44.99	47.85
CG-28_T8	Cpx-ore	Cristales Grandes	EPI-0702	24.2	0.08	0.27	bdl	3.13	0.05	9.7	16.7	0.46	97.2	89.29	10.49	0.22	0.89	7.51	45.07	47.42
CG-28_T8	Cpx-ore	Cristales Grandes	EPI-0702	24.3	0.09	0.27	bdl	3.16	0.05	9.7	16.7	0.44	97.4	88.52	11.28	0.20	0.89	7.58	44.83	47.59
CG-28_T8	Cpx-ore	Cristales Grandes	EPI-0702	24.3	0.08	0.27	bdl	3.16	0.05	9.7	16.7	0.45	97.3	88.52	11.27	0.21	0.89	7.58	44.92	47.50
CG-28_T8	Cpx-ore	Cristales Grandes	EPI-0702	24.3	0.10	0.27	0.01	3.16	0.05	9.7	16.7	0.48	97.6	89.72	10.06	0.21	0.90	7.57	44.89	47.55
CG-28_T8	Cpx-ore	Cristales Grandes	EPI-0702	24.3	0.08	0.26	0.01	3.15	0.05	9.7	16.7	0.46	97.5	89.24	10.57	0.19	0.89	7.53	44.92	47.56
CG-28_T8	Cpx-ore	Cristales Grandes	EPI-0702	24.3	0.08	0.26	bdl	3.21	0.05	9.7	16.8	0.44	97.6	89.22	10.59	0.19	0.89	7.65	44.90	47.45
CG-28_T8	Cpx-ore	Cristales Grandes	EPI-0702	24.4	0.09	0.23	bdl	3.11	0.05	9.8	16.8	0.45	97.7	88.57	11.21	0.22	0.89	7.45	44.87	47.68
CG-28_T8	Cpx-ore	Cristales Grandes	EPI-0702	24.3	0.09	0.24	0.02	3.12	0.06	9.8	16.8	0.43	97.6	89.62	10.15	0.23	0.90	7.44	44.90	47.66
CG-28_T8	Cpx-ore	Cristales Grandes	EPI-0702	24.3	0.10	0.26	0.02	3.11	0.05	9.8	16.9	0.45	97.7	90.20	9.58	0.21	0.90	7.40	45.09	47.52
CG-28_T8	Cpx-ore	Cristales Grandes	EPI-0702	24.1	0.11	0.34	0.03	3.51	0.05	9.3	16.8	0.65	97.7	90.38	9.40	0.22	0.91	8.43	45.43	46.14
CG-28_T8	Cpx-ore	Cristales Grandes	EPI-0702	24.4	0.08	0.17	0.07	3.35	0.04	9.5	16.7	0.69	97.9	89.79	10.02	0.19	0.90	8.06	45.21	46.73
CG-28_T8	Cpx-ore	Cristales Grandes	EPI-0702	24.2	0.09	0.30	0.02	3.42	0.04	9.4	16.6	0.72	97.6	90.60	9.21	0.19	0.91	8.26	45.02	46.72
CG-28_T8	Cpx-ore	Cristales Grandes	EPI-0702	24.3	0.08	0.23	0.04	3.28	0.04	9.5	16.7	0.68	97.7	90.69	9.13	0.18	0.91	7.88	45.07	47.05
CG-28_T8	Cpx-ore	Cristales Grandes	EPI-0702	24.4	0.08	0.23	0.07	3.37	0.05	9.5	16.5	0.74	98.0	90.60	9.19	0.21	0.91	8.12	44.75	47.13
CG-28_T8	Cpx-ore	Cristales Grandes	EPI-0702	24.5	0.07	0.20	0.14	3.36	0.05	9.4	16.4	0.80	97.8	89.80	9.99	0.21	0.90	8.17	44.86	46.96
CG-28_T8	Cpx-ore	Cristales Grandes	EPI-0702	15.8	0.06	0.82	0.10	4.14	0.04	5.1	13.5	0.30	70.0	91.63	8.02	0.35	0.92	13.65	50.97	35.38
CG-28_T8	Cpx-ore	Cristales Grandes	EPI-0702	24.4	0.10	0.24	0.06	3.03	0.04	9.5	16.8	0.70	97.7	90.75	9.08	0.18	0.91	7.32	45.58	47.10
CG-28_T8	Cpx-ore	Cristales Grandes	EPI-0702	24.3	0.08	0.20	0.05	3.20	0.06	9.5	16.7	0.56	97.4	88.55	11.22	0.23	0.89	7.75	45.24	47.02
CG-28_T8	Cpx-ore	Cristales Grandes	EPI-0702	23.0	0.18	1.30	bdl	5.96	0.05	7.9	16.0	1.00	98.0	86.71	13.04	0.25	0.87	14.67	45.00	40.33
CG-28_T8	Cpx-ore	Cristales Grandes	EPI-0702	23.0	0.18	1.24	0.01	5.91	0.05	8.0	16.0	0.97	97.9	86.48	13.29	0.23	0.87	14.52	44.83	40.65
CG-28_T8	Cpx-ore	Cristales Grandes	EPI-0702	23.0	0.19	1.26	bdl	5.94	0.05	7.9	16.0	1.00	97.7	86.76	13.00	0.24	0.87	14.64	44.91	40.45
CG-28_T8	Cpx-ore	Cristales Grandes	EPI-0702	23.0	0.22	1.27	bdl	5.90	0.05	7.9	16.0	0.97	97.8	86.84	12.93	0.23	0.87	14.51	45.02	40.47
CG-28_T8	Cpx-ore	Cristales Grandes	EPI-0702	23.1	0.18	1.32	bdl	5.98	0.06	8.1	15.9	0.99	98.5	87.51	12.22	0.27	0.88	14.61	44.14	41.25
CG-28_T8	Cpx-ore	Cristales Grandes	EPI-0702	23.0	0.19	1.27	bdl	5.98	0.05	7.9	16.0	1.03	98.0	87.02	12.73	0.25	0.87	14.71	44.88	40.41
CG-28_T8	Cpx-ore	Cristales Grandes	EPI-0702	23.1	0.19	1.27	bdl	5.94	0.05	7.9	16.1	0.97	98.0	86.23	13.55	0.22	0.86	14.58	45.00	40.42
CG-28_T8	Cpx-ore	Cristales Grandes	EPI-0702	23.1	0.18	1.24	bdl	5.84	0.05	7.9	16.1	0.98	98.0	86.93	12.81	0.26	0.87	14.35	45.06	40.59
CG-28_T8	Cpx-ore	Cristales Grandes	EPI-0702	23.0	0.19	1.23	bdl	5.85	0.04	7.9	16.1	0.98	97.9	87.32	12.47	0.22	0.88	14.37	45.02	40.61
CG-28_T8	Cpx-ore	Cristales Grandes	EPI-0702	23.2	0.21	1.05	0.01	5.39	0.04	8.1	16.7	0.78	98.0	86.12	13.68	0.20	0.86	13.12	46.18	40.70
CG-28_T8	Cpx-ore	Cristales Grandes	EPI-0702	23.0	0.20	1.22	bdl	5.88	0.04	8.0	16.1	1.00	97.9	87.81	11.97	0.22	0.88	14.40	44.99	40.60
CG-28_T8	Cpx-ore	Cristales Grandes	EPI-0702	23.1	0.29	1.08	bdl	5.68	0.05	8.1	16.2	0.89	98.0	86.25	13.51	0.24	0.86	13.89	45.05	41.06
CG-28_T8	Cpx-ore	Cristales Grandes	EPI-0702	23.5	0.13	0.70	bdl	4.95	0.06	8.6	16.9	0.45	97.8	84.19	15.56	0.25	0.84	11.89	45.66	42.45
CG-28_T8	Cpx-ore	Cristales Grandes	EPI-0702	23.3	0.14	0.91	bdl	5.55	0.06	8.2	16.3	0.84	97.9	86.41	13.33	0.26	0.87	13.49	44.95	41.56
CG-28_T8	Cpx-ore	Cristales Grandes	EPI-0702	24.3	0.05	0.17	0.03	3.91	0.05	9.1	16.8	0.68	97.9	87.53	12.27	0.20	0.88	9.39	45.56	45.05
CG-28_T8	Cpx-ore	Cristales Grandes	EPI-0702	23.4	0.08	0.67	bdl	6.41	0.07	7.8	16.3	0.88	98.1	82.40	17.26	0.34	0.83	15.61	45.07	39.33
CG-28_T8	Cpx-ore	Cristales Grandes	EPI-0702	23.5	0.06	0.70	bdl	6.42	0.09	7.8	16.4	0.88	98.6	82.32	17.27	0.41	0.83	15.61	45.07	39.32
CG-28_T8	Cpx-ore	Cristales Grandes	EPI-0702	23.5	0.09	0.67	bdl	6.28	0.07	7.9	16.3	0.87	98.1	82.37	17.31	0.32	0.83	15.31	44.98	39.71
CG-28_T8	Cpx-ore	Cristales Grandes	EPI-0702	24.3	0.06	0.16	0.05	3.84	0.06	9.1	16.7	0.71	97.8	87.66	12.09	0.25	0.88	9.29	45.56	45.14
CG-28_T8	Cpx-ore	Cristales Grandes	EPI-0702	23.5	0.23	0.87	0.01	5.21	0.05	8.4	16.2	0.96	98.2	88.35	11.42	0.23	0.89	12.69	44.99	42.31
CG-28_T8	Cpx-ore	Cristales Grandes	EPI-0702	23.6	0.26	0.90	0.05	4.10	0.05	8.8	16.5	0.77	97.7	89.20	10.58	0.22	0.89	10.03	45.65	44.32
CG-28_T8	Cpx-ore	Cristales Grandes	EPI-0702	24.3	0.05	0.19	0.05	3.71	0.05	9.2	16.8	0.65	97.9	87.80	11.97	0.23	0.88	8.95	45.58	45.47
CG-28_T8	Cpx-ore	Cristales Grandes	EPI-0702	23.1	0.18	0.96	0.01	6.65	0.07	7.5	16.3	0.90	98.0	81.33	18.32	0.35	0.82	16.35	45.50	38.16
CG-28_T8	Cpx-ore	Cristales Grandes	EPI-0702	22.9	0.18	1.12	bdl	6.71	0.08	7.4	16.3	0.95	98.2	82.78	16.82	0.40	0.83	16.50	45.64	37.87
CG-28_T8	Cpx-ore	Cristales Grandes	EPI-0702	22.8	0.23	1.31	0.01	6.78	0.08	7.4	16.3	0.94	98.3	82.66	16.95	0.39	0.83	16.70	45.64	37.66
CG-28_T8	Cpx-ore	Cristales Grandes	EPI-0702	22.9	0.21	1.26	bdl	6.61	0.07	7.4	16.3	0.93	98.0	82.12	17.54	0.34	0.82	16.36	45.78	37.86
CG-28_T9	Cpx-ore	Cristales Grandes	EPI-0702	23.5	0.11	0.77	bdl	4.46	0.05	8.7	16.9	0.55	97.4	87.24	12.54	0.22	0.87	10.75	46.10	43.15
CG-28_T9	Cpx-ore	Cristales Grandes	EPI-0702	23.5	0.11	0.82	bdl	4.54	0.06	8.7	16.9	0.57	97.6	87.42	12.32	0.26	0.88	10.97	45.99	43.04
CG-28_T9	Cpx-ore	Cristales Grandes	EPI-0702	23.4	0.13	0.86	bdl	4.63	0.06	8.6	16.9	0.58	97.7	87.59	12.15	0.26	0.88	11.16	46.05	42.79
CG-28_T9	Cpx-ore	Cristales Grandes	EPI-0702	23.4	0.13	0.87	bdl	4.57	0.05	8.6	16.8	0.59	97.4	87.69	12.06	0.24	0.88	11.07	46.13	42.80
CG-28_T9	Cpx-ore	Cristales Grandes	EPI-0702	23.4	0.13	0.87	bdl	4.61	0.05	8.6	16.8	0.61	97.5	87.41	12.38	0.21	0.88	11.13	46.07	42.80
CG-28_T9	Cpx-ore	Cristales Grandes	EPI-0702	23.4	0.14	0.89	bdl	4.69	0.06	8.6	16.9	0.61	97.8	87.86	11.88	0.26	0.88	11.31	46.05	42.64
CG-28_T9	Cpx-ore	Cristales Grandes	EPI-0702	23.5	0.14	0.89	bdl	4.63	0.05	8.6	16.8	0.61	97.7	87.02	12.75	0.23	0.87	11.20	46.04	42.77
CG-28_T9	Cpx-ore	Cristales Grandes	EPI-0702	23.5	0.13	0.87	bdl	4.53	0.05	8.8	16.9	0.60	98.1	89.17	10.60	0.23	0.89	10.83	45.66	43.51
CG-28_T9	Cpx-ore	Cristales Grandes	EPI-0702	23.6	0.06	0.74	bdl	4.65	0.05	8.6	16.9	0.58	97.7	86.92	12.84	0.24	0.87	11.20	46.06	42.74
CG-28_T9	Cpx-ore	Cristales Grandes	EPI-0702	23.4	0.08	0.93	bdl	4.98	0.05	8.4	16.8	0.62	97.9	86.34	13.43	0.23	0.87	12.02	45.92	42.06

Clinopyroxene EPMA data from El Laco deposit: Ore-related clinopyroxene

Sample spot	Type	Ore body	Drill core	Si [wt.%]	Ti [wt.%]	Al [wt.%]	Cr [wt.%]	Fe [wt.%]	Mn [wt.%]	Mg [wt.%]	Ca [wt.%]	Na [wt.%]	Total	Dp	Hd	Joh	#Mg	Fs	Wo	En
CG-28_T9	Cpx-ore	Cristales Grandes	EPI-0702	23.2	0.10	1.03	bdl	5.16	0.06	8.3	16.8	0.63	97.9	86.75	13.00	0.26	0.87	12.46	45.93	41.61
CG-28_T9	Cpx-ore	Cristales Grandes	EPI-0702	23.2	0.12	1.06	bdl	5.29	0.06	8.3	16.7	0.64	97.7	86.23	13.48	0.29	0.86	12.81	45.83	41.36
CG-28_T9	Cpx-ore	Cristales Grandes	EPI-0702	23.0	0.13	1.10	bdl	5.25	0.05	8.2	16.7	0.64	97.5	86.40	13.37	0.23	0.87	12.74	46.11	41.15
CG-28_T9	Cpx-ore	Cristales Grandes	EPI-0702	23.2	0.12	1.07	bdl	5.19	0.06	8.3	16.8	0.60	97.8	85.75	13.98	0.28	0.86	12.56	45.99	41.45
CG-28_T9	Cpx-ore	Cristales Grandes	EPI-0702	23.2	0.13	1.06	bdl	5.03	0.05	8.4	16.8	0.58	97.8	86.32	13.44	0.23	0.87	12.15	45.96	41.89
CG-28_T9	Cpx-ore	Cristales Grandes	EPI-0702	23.2	0.12	1.07	bdl	5.11	0.06	8.4	16.8	0.60	97.8	87.03	12.70	0.27	0.87	12.32	45.97	41.70
CG-28_T9	Cpx-ore	Cristales Grandes	EPI-0702	23.1	0.16	1.08	bdl	5.07	0.06	8.3	16.8	0.60	97.6	86.71	13.02	0.27	0.87	12.29	46.01	41.70
CG-28_T9	Cpx-ore	Cristales Grandes	EPI-0702	23.2	0.17	1.10	bdl	5.08	0.06	8.3	16.7	0.65	97.6	86.19	13.54	0.27	0.86	12.38	46.03	41.59
CG-28_T9	Cpx-ore	Cristales Grandes	EPI-0702	23.2	0.19	1.09	bdl	5.06	0.06	8.4	16.7	0.67	97.9	87.28	12.46	0.26	0.88	12.27	45.91	41.82
CG-28_T9	Cpx-ore	Cristales Grandes	EPI-0702	23.2	0.15	1.09	bdl	5.17	0.05	8.2	16.7	0.68	97.7	86.44	13.32	0.23	0.87	12.57	46.21	41.21
CG-28_T9	Cpx-ore	Cristales Grandes	EPI-0702	23.1	0.16	1.08	bdl	5.23	0.05	8.3	16.8	0.67	98.0	87.64	12.11	0.25	0.88	12.60	45.90	41.49
CG-28_T9	Cpx-ore	Cristales Grandes	EPI-0702	23.1	0.17	1.10	bdl	5.27	0.06	8.3	16.7	0.70	97.9	87.44	12.28	0.28	0.88	12.75	45.84	41.41
CG-28_T9	Cpx-ore	Cristales Grandes	EPI-0702	23.1	0.16	1.06	bdl	5.19	0.05	8.3	16.7	0.70	97.7	87.64	12.12	0.23	0.88	12.56	46.01	41.43
CG-28_T9	Cpx-ore	Cristales Grandes	EPI-0702	23.2	0.15	1.04	bdl	5.06	0.05	8.3	16.8	0.66	97.7	87.11	12.66	0.23	0.87	12.24	46.09	41.67
CG-28_T9	Cpx-ore	Cristales Grandes	EPI-0702	23.3	0.16	1.01	bdl	4.99	0.06	8.4	16.8	0.69	97.9	88.16	11.57	0.27	0.88	12.07	46.03	41.91
CG-28_T9	Cpx-ore	Cristales Grandes	EPI-0702	23.3	0.15	0.96	bdl	4.81	0.06	8.5	16.8	0.65	97.7	88.19	11.52	0.29	0.88	11.65	46.14	42.20
CG-28_T9	Cpx-ore	Cristales Grandes	EPI-0702	23.4	0.18	0.88	bdl	4.43	0.05	8.7	16.9	0.64	97.7	89.40	10.37	0.23	0.90	10.69	46.08	43.23
CG-28_T9	Cpx-ore	Cristales Grandes	EPI-0702	23.3	0.09	0.87	bdl	6.01	0.06	8.0	16.3	1.01	98.4	88.47	11.24	0.29	0.89	14.53	45.07	40.40
CG-28_T9	Cpx-ore	Cristales Grandes	EPI-0702	23.2	0.08	0.89	bdl	6.37	0.07	7.7	16.4	0.89	98.2	84.52	15.14	0.34	0.85	15.47	45.46	39.06
CG-28_T9	Cpx-ore	Cristales Grandes	EPI-0702	23.3	0.09	0.86	bdl	6.27	0.07	7.9	16.5	0.78	98.4	83.25	16.40	0.35	0.84	15.17	45.45	39.38
CG-28_T9	Cpx-ore	Cristales Grandes	EPI-0702	23.3	0.09	0.85	bdl	5.53	0.06	8.1	16.7	0.69	97.8	84.71	14.99	0.30	0.85	13.42	45.93	40.66
CG-28_T9	Cpx-ore	Cristales Grandes	EPI-0702	23.3	0.09	0.85	bdl	5.34	0.06	8.3	16.8	0.65	98.0	85.93	13.79	0.28	0.86	12.85	45.94	41.20
CG-28_T9	Cpx-ore	Cristales Grandes	EPI-0702	23.3	0.30	1.02	0.04	4.92	0.05	8.4	16.6	0.72	97.9	86.96	12.80	0.23	0.87	11.98	45.92	42.11
CG-28_T9	Cpx-ore	Cristales Grandes	EPI-0702	23.2	0.29	1.00	0.04	4.90	0.05	8.3	16.7	0.72	97.8	86.99	12.76	0.25	0.87	11.95	46.16	41.88
CG-28_T9	Cpx-ore	Cristales Grandes	EPI-0702	23.3	0.25	0.93	0.02	4.89	0.05	8.4	16.7	0.72	97.7	87.32	12.44	0.24	0.88	11.89	45.94	42.17
CG-28_T9	Cpx-ore	Cristales Grandes	EPI-0702	23.4	0.25	0.85	0.02	4.79	0.05	8.4	16.7	0.75	97.9	87.32	12.47	0.21	0.88	11.64	45.99	42.37
CG-28_T9	Cpx-ore	Cristales Grandes	EPI-0702	23.5	0.23	0.87	0.03	4.82	0.05	8.4	16.8	0.71	98.0	86.93	12.85	0.22	0.87	11.67	46.05	42.28
CG-28_T9	Cpx-ore	Cristales Grandes	EPI-0702	23.4	0.23	0.88	0.03	4.73	0.05	8.5	16.8	0.70	97.9	87.17	12.60	0.22	0.87	11.48	46.07	42.45
CG-28_T9	Cpx-ore	Cristales Grandes	EPI-0702	23.4	0.25	0.87	0.03	4.85	0.05	8.4	16.7	0.70	97.9	86.88	12.88	0.24	0.87	11.76	45.98	42.26
CG-28_T9	Cpx-ore	Cristales Grandes	EPI-0702	23.5	0.22	0.83	0.01	5.01	0.04	8.4	16.6	0.72	98.0	85.76	14.06	0.18	0.86	12.15	45.78	42.08
CG-28_T9	Cpx-ore	Cristales Grandes	EPI-0702	23.3	0.15	0.85	bdl	5.98	0.06	7.9	16.5	0.87	98.3	84.39	15.30	0.30	0.85	14.57	45.52	39.92
CG-28_T9	Cpx-ore	Cristales Grandes	EPI-0702	23.3	0.15	0.84	bdl	6.16	0.06	7.8	16.4	0.90	98.3	83.94	15.79	0.27	0.84	15.00	45.50	39.51
CG-28_T9	Cpx-ore	Cristales Grandes	EPI-0702	23.3	0.14	0.84	bdl	6.05	0.05	7.9	16.4	0.89	98.3	84.58	15.18	0.24	0.85	14.70	45.35	39.96
CG-28_T9	Cpx-ore	Cristales Grandes	EPI-0702	23.4	0.12	0.80	bdl	5.55	0.06	8.3	16.5	0.82	98.2	86.54	13.17	0.28	0.87	13.43	45.21	41.35
CG-28_T9	Cpx-ore	Cristales Grandes	EPI-0702	24.0	0.09	1.21	bdl	6.96	0.07	7.8	15.5	1.31	100.8	82.70	16.97	0.33	0.83	17.01	43.14	39.84
CG-28_T9	Cpx-ore	Cristales Grandes	EPI-0702	22.9	0.11	1.00	bdl	6.96	0.06	7.5	15.9	1.28	98.3	89.20	10.49	0.31	0.89	17.01	44.77	38.21
CG-28_T9	Cpx-ore	Cristales Grandes	EPI-0702	22.9	0.14	1.02	bdl	6.91	0.07	7.5	16.0	1.22	98.4	87.23	12.40	0.37	0.88	16.95	44.81	38.24
CG-28_T9	Cpx-ore	Cristales Grandes	EPI-0702	23.0	0.12	1.00	bdl	6.79	0.06	7.6	16.1	1.14	98.4	87.81	11.90	0.29	0.88	16.51	44.74	38.74
CG-28_T9	Cpx-ore	Cristales Grandes	EPI-0702	23.0	0.11	0.99	bdl	6.81	0.06	7.6	16.1	1.11	98.4	87.06	12.64	0.30	0.87	16.54	44.80	38.66
CG-28_T9	Cpx-ore	Cristales Grandes	EPI-0702	23.0	0.10	0.99	bdl	6.94	0.07	7.5	16.2	1.09	98.6	85.94	13.69	0.37	0.86	16.88	44.96	38.16
CG-28_T10	Cpx-ore	Cristales Grandes	EPI-0702	23.1	0.21	1.11	bdl	6.15	0.08	7.7	16.4	0.94	98.3	84.90	14.71	0.39	0.85	15.09	45.76	39.15
CG-28_T10	Cpx-ore	Cristales Grandes	EPI-0702	25.0	0.15	0.87	0.02	5.31	0.08	9.0	18.0	0.70	104.6	86.53	13.11	0.36	0.87	12.06	46.13	41.82
CG-28_T10	Cpx-ore	Cristales Grandes	EPI-0702	23.1	0.18	1.10	0.01	5.95	0.08	7.8	16.4	0.91	97.9	85.23	14.38	0.39	0.86	14.65	45.84	39.51
CG-28_T10	Cpx-ore	Cristales Grandes	EPI-0702	23.1	0.21	1.07	bdl	5.85	0.06	7.8	16.4	0.90	97.9	85.07	14.63	0.30	0.85	14.37	45.82	39.80
CG-28_T10	Cpx-ore	Cristales Grandes	EPI-0702	23.1	0.21	1.07	bdl	6.07	0.08	7.8	16.4	0.93	98.3	84.92	14.70	0.38	0.85	14.90	45.74	39.36
CG-28_T10	Cpx-ore	Cristales Grandes	EPI-0702	23.1	0.22	1.09	bdl	5.93	0.08	7.7	16.4	0.90	98.1	84.19	15.42	0.39	0.85	14.64	45.92	39.44
CG-28_T10	Cpx-ore	Cristales Grandes	EPI-0702	23.2	0.21	1.06	0.01	5.91	0.08	7.8	16.5	0.86	98.1	83.90	15.73	0.38	0.84	14.54	45.87	39.59
CG-28_T10	Cpx-ore	Cristales Grandes	EPI-0702	23.2	0.18	1.06	0.01	5.68	0.08	7.9	16.5	0.88	98.2	85.47	14.16	0.37	0.86	13.96	45.90	40.14
CG-28_T10	Cpx-ore	Cristales Grandes	EPI-0702	23.2	0.19	1.06	0.00	5.61	0.08	7.9	16.5	0.85	97.9	84.96	14.67	0.37	0.85	13.82	46.17	40.01
CG-28_T10	Cpx-ore	Cristales Grandes	EPI-0702	23.2	0.19	1.09	0.01	5.65	0.07	7.9	16.6	0.90	98.3	86.10	13.56	0.34	0.86	13.84	46.02	40.14
CG-28_T10	Cpx-ore	Cristales Grandes	EPI-0702	23.3	0.20	0.99	bdl	5.51	0.07	8.0	16.6	0.85	98.2	85.72	13.96	0.32	0.86	13.47	46.07	40.47
CG-28_T10	Cpx-ore	Cristales Grandes	EPI-0702	23.2	0.17	1.00	bdl	5.51	0.07	8.0	16.7	0.81	98.1	86.31	13.35	0.34	0.87	13.43	46.18	40.39
CG-28_T10	Cpx-ore	Cristales Grandes	EPI-0702	23.2	0.20	0.99	bdl	5.35	0.07	8.0	16.5	0.88	97.6	86.20	13.49	0.31	0.86	13.21	46.05	40.74
CG-28_T10	Cpx-ore	Cristales Grandes	EPI-0702	23.3	0.19	1.00	bdl	5.28	0.07	8.1	16.6	0.83	98.0	86.43	13.26	0.32	0.87	12.93	46.03	41.04
CG-28_T10	Cpx-ore	Cristales Grandes	EPI-0702	23.3	0.18	1.00	bdl	5.20	0.06	8.1	16.7	0.81	98.0	86.64	13.06	0.30	0.87	12.70	46.17	41.13
CG-28_T10	Cpx-ore	Cristales Grandes	EPI-0702	23.3	0.21	0.98	0.01	5.10	0.07	8.2	16.7	0.81	98.1	87.08	12.61	0.32	0.87	12.44	46.25	41.30
CG-28_T10	Cpx-ore	Cristales Grandes	EPI-0702	23.4	0.20	0.95	bdl	5.16	0.07	8.2	16.7	0.78	98.1	86.49	13.18	0.33	0.87	12.59	45.99	41.41
CG-28_T10	Cpx-ore	Cristales Grandes	EPI-0702	23.4	0.17	0.91	bdl	4.99	0.07	8.3	16.6	0.78	97.9	87.14	12.55	0.31	0.87	12.18	45.94	41.88
CG-28_T10	Cpx-ore	Cristales Grandes	EPI-0702	23.5	0.18	0.88	bdl	4.97	0.07	8.3	16.7	0.78	98.0	86.61	13.09	0.30	0.87	12.12	45.99	41.89
CG-28_T10	Cpx-ore	Cristales Grandes	EPI-0702	23.5	0.16	0.85	0.01	4.77	0.07	8.4	16.7	0.74	97.8	87.33	12.33	0.33	0.88	11.63	46.05	42.32
CG-28_T10	Cpx-ore	Cristales Grandes	EPI-0702	23.5	0.15	0.81	0.01	4.84	0.06	8.4	16.8	0.75	98.1	87.75	11.95	0.30	0.88	11.73	46.04	42.22
CG-28_T10	Cpx-ore	Cristales Grandes	EPI-0702	23.4	0.12	0.70	0.01	6.54	0.08	7.7	16.5	0.87	98.6	82.56	17.05	0.40	0.83	15.86	45.46	38.69
CG-28_T10	Cpx-ore	Cristales Grandes	EPI-0702	23.6	0.12	0.79	bdl	6.52	0.08	7.6	16.4	0.82	98.7	77.65	22.00	0.35	0.78	16.02	45.70	38.29
CG-28_T10	Cpx-ore	Cristales Grandes	EPI-0702	23.5	0.12	0.70	bdl	5.77	0.07	8.2	16.6	0.77	98.6	84.70	14.99	0.30	0.85	13.87	45.27	40.85
CG-28_T10	Cpx-ore	Cristales Grandes	EPI-0702	17.0	0.08	2.26	0.01	6.37	0.07	6.2	11.9	0.12	77.7	78.43	21.16	0.41	0.79	19.42	41.35	39.24
CG-28_T10	Cpx-ore	Cristales Grandes	EPI-0702	24.1	0.12	0.81	bdl	6.47	0.08	8.1	16.4	0.88	100.6	80.48	19.16	0.36	0.81	15.50	44.49	40.00
CG-28_T10	Cpx-ore	Cristales Grandes	EPI-0702	23.7	0.11	0.71	bdl	4.37	0.05	8.8	17.1	0.54	98.0	87.37	12.39	0.24	0.88	10.46	46.18	43.36
CG-28_T10	Cpx-ore	Cristales Grandes	EPI-0702	23.7	0.12	0.72	bdl	4.28	0.05	8.8	17.0	0.56	97.9	88.23	11.53	0.24	0.88	10.26	46.11	43.63
CG-28_T10	Cpx-ore	Cristales Grandes	EPI-0702	23.8	0.14	0.69	0.01	4.13	0.04	8.9	17.0	0.60	98.1	87.74	12.07	0.19	0.88	9.92	46.09	43.99
CG-28_T10	Cpx-ore	Cristales Grandes	EPI-0702	22.4	0.11	1.95	0.01	5.50	0.14	8.0	12.0	0.39	91.0	74.53	24.91	0.56	0.75	15.83	37.83	46.33
CG-28_T10	Cpx-ore	Cristales Grandes	EPI-0702	23.9	0.20	0.69	0.03	3.85	0.04	9.1	16.9	0.68	98.3	90.83	8.99	0.18	0.91	9.22	45.86	44.92
CG-28_T10	Cpx-ore	Cristales Grandes	EPI-0702	23.9	0.18	0.66	0.02	3.84	0.04	9.0	17.0	0.62	98.2	89.34	10.47	0.19	0.90	9.21	46.13	44.66
CG-28_T10	Cpx-ore	Cristales Grandes	EPI-0702	23.6	0.16	0.75	0.01	4.56	0.05	8.7	16.8	0.66	98.1	88.39	11.38	0.23	0.89	10.95	45.74	43.31
CG-28_T10	Cpx-ore	Cristales Grandes	EPI-0702	23.6	0.06	0.80	bdl	4.73	0.06	8.6	16.9	0.67	98.2	88.12	11.61	0.27	0.88	11.38	45.96	42.67
CG-28_T10	Cpx-ore	Cristales Grandes	EPI-0702	23.4	0.08	0.95	bdl	4.90	0.06	8.5	16.9	0.70	98.3	88.56	11.14	0.30	0.89	11.80	46.01	42.19
CG-28_T10	Cpx-ore	Cristales Grandes	EPI-0702	23.4	0.10	0.97	bdl	4.87	0.06	8.5	16.8	0.65	98.0	86.98	12.75	0.27	0.87	11.79	45.97	42.24
CG-28_T10	Cpx-ore	Cristales Grandes	EPI-0702	23.5	0.10	0.94	bdl	4.78	0.07	8.5	16.9	0.65	98.0	87.43	12.25	0.32	0.88	11.58	46.20	42.22
CG-28_T10	Cpx-ore	Cristales Grandes	EPI-0702	23.5	0.08	0.94	bdl	4.77	0.06	8.5	16.9	0.64	98.0	87.45	12.27	0.27	0.88	11.50	46.16	42.34
CG-28_T10	Cpx-ore	Cristales Grandes	EPI-0702	23.4	0.09	0.98	bdl	4.72	0.06	8.5	16.9	0.63	97.9	87.91	11.83	0.26	0.88	11.40	46.13	42.47
CG-28_T10	Cpx-ore	Cristales Grandes	EPI-0702	23.5	0.09	1.00	bdl	4.79	0.06	8.7	16.8	0.64	98.4	89.18	10.55	0.27	0.89	11.46	45.62	42.92
CG-28_T10	Cpx-ore	Cristales Grandes	EPI-0702	23.4	0.11	0.99	bdl	4.76	0.06	8.5	16.9	0.67	98.1	88.03	11.71	0.27	0.88	11.48	46.17	42.35
CG-28_T10	Cpx-ore	Cristales Grandes	EPI-0702	23.4	0.11	0.98	bdl	4.81	0.06	8.5	16.8	0.65	98.2	87.86	11.88	0.27	0.88	11.58	45.96	42.46
CG-28_T10	Cpx-ore	Cristales Grandes	EPI-0702	23.6	0.12	1.06	bdl	4.82	0.06	8.9	16.6	0.72	99.1	89.95	9.79	0.26	0.90	11.47	44.80	43.73
CG-28_T10	Cpx-ore	Cristales Grandes	EPI-0702	23.6	0.14	0.99	bdl	4.69	0.06	8.5	16.8	0.71	98.3	87.53	12.19	0.29	0.88	11.37	45.99	42.64
CG-28_T10	Cpx-ore	Cristales Grandes	EPI-0702	23.4	0.12	0.99	bdl	4.89	0.06	8.5	16.8	0.71	98.2	87.94	11.77	0.29	0.88	11.83	45.98	42.19
CG-28_T10	Cpx-ore	Cristales Grandes	EPI-0702	23.5	0.11	0.97	bdl	4.81	0.06	8.5	16.8	0.69	98.2	87.55	12.17	0.28	0.88	11.64	46.08	42.28
CG-28_T10	Cpx-ore	Cristales Grandes	EPI-0702	23.4	0.13	0.96	bdl	4.82	0.06	8.5	16.8	0.72	98.1	88.85	10.88	0.27	0.89	11.63	46.08	42.29
CG-28_T10	Cpx-ore	Cristales Grandes	EPI-0702	23.4	0.13	0.97	bdl	4.86	0.05	8.4	16.8	0.70	98.0	87.38	12.39	0.23	0.88	11.76	46.04	42.20
CG-28_T10	Cpx-ore	Cristales Grandes	EPI-0702	23.5	0.11	0.95	bdl	4.80	0.05	8.5	16.8	0.69	98.0	87.35	12.42	0.22	0.88	11.61	46.04	42.34
CG-28_T10	Cpx-ore	Cristales Grandes	EPI-0702	23.5	0.13	0.94	bdl	4.84	0.06	8.5	16.7	0.87	98.3	90.34	9.37	0.29	0.91	11.73	45.88	42.38
CG-28_T11	Cpx-ore	Cristales Grandes	EPI-0702	23.6	0.13	0.91	bdl	4.81	0.05	8.5	16.9	0.65	98.6	86.79	12.97	0.24	0.87	11.56	46.06	42.38
CG-28_T11	Cpx-ore	Cristales Grandes	EPI-0702	23.9	0.11	0.68	bdl	4.20	0.06	8.9	17.0	0.62	98.4	88.33	11.42	0.26	0.89	10.08	46.00	43.93
CG-28_T11	Cpx-ore	Cristales Grandes	EPI-0702	23.7	0.10	0.74	bdl	5.56	0.06	8.2	16.4	1.01	98.6	87.04	12.66	0.30	0.87	13.52	45.37	41.10
CG-28_T11	Cpx-ore	Cristales Grandes	EPI-0702	23.7	0.07	0.69	bdl	5.35	0.07	8.4	16.8	0.75	98.7	85.70	14.00	0.30	0.86	12.85	45.65	41.50
CG-28_T11	Cpx-ore	Cristales Grandes	EPI-0702	23.9	0.09	0.68	bdl	4.93	0.06	8.6	16.8	0.69	98.7	86.12	13.61	0.27	0.86	11.82	45.70	42.48
CG-28_T11	Cpx-ore	Cristales Grandes	EPI-0702	23.8	0.06	0.63	bdl	5.36	0.06	8.3	16.8	0.75	98.6	84.90	14.85	0.25	0.85	12.89	45.68	41.43

Clinopyroxene EPMA data from El Laco deposit: Ore-related clinopyroxene

Sample spot	Type	Ore body	Drill core	Si [wt.%]	Ti [wt.%]	Al [wt.%]	Cr [wt.%]	Fe [wt.%]	Mn [wt.%]	Mg [wt.%]	Ca [wt.%]	Na [wt.%]	Total	Dp	Hd	Joh	#Mg	Fs	Wo	En
CG-28_T11	Cpx-ore	Cristales Grandes	EPI-0702	23.7	0.19	0.78	bdl	4.56	0.05	8.6	16.9	0.69	98.4	87.65	12.13	0.22	0.88	10.98	46.12	42.90
CG-28_T11	Cpx-ore	Cristales Grandes	EPI-0702	23.8	0.08	0.64	bdl	5.11	0.07	8.5	16.7	0.74	98.6	85.62	14.07	0.31	0.86	12.32	45.59	42.09
CG-28_T11	Cpx-ore	Cristales Grandes	EPI-0702	23.8	0.24	0.75	0.04	4.62	0.05	8.6	16.8	0.73	98.5	86.78	12.98	0.24	0.87	11.16	45.83	43.00
CG-28_T11	Cpx-ore	Cristales Grandes	EPI-0702	23.7	0.21	0.76	0.05	4.65	0.05	8.6	16.8	0.73	98.4	86.67	13.08	0.24	0.87	11.26	45.90	42.84
CG-28_T11	Cpx-ore	Cristales Grandes	EPI-0702	23.8	0.19	0.76	0.02	4.78	0.05	8.6	16.7	0.75	98.6	85.99	13.77	0.24	0.86	11.56	45.74	42.70
CG-28_T11	Cpx-ore	Cristales Grandes	EPI-0702	23.8	0.17	0.75	0.01	5.06	0.06	8.4	16.7	0.79	98.8	86.03	13.72	0.26	0.86	12.21	45.71	42.08
CG-28_T11	Cpx-ore	Cristales Grandes	EPI-0702	23.9	0.08	0.62	bdl	5.24	0.05	8.4	16.7	0.80	98.9	85.49	14.28	0.23	0.86	12.58	45.52	41.90
CG-28_T11	Cpx-ore	Cristales Grandes	EPI-0702	23.5	0.08	0.82	bdl	6.21	0.06	7.8	16.4	1.01	98.7	84.44	15.25	0.31	0.85	15.14	45.46	39.41
CG-28_T11	Cpx-ore	Cristales Grandes	EPI-0702	23.4	0.08	0.81	0.01	7.33	0.08	7.3	16.3	1.01	99.2	79.73	19.88	0.39	0.80	17.85	45.21	36.94
CG-28_T11	Cpx-ore	Cristales Grandes	EPI-0702	23.3	0.09	0.87	bdl	7.28	0.08	7.3	16.3	1.02	99.1	80.35	19.25	0.40	0.81	17.76	45.19	37.05
CG-28_T11	Cpx-ore	Cristales Grandes	EPI-0702	23.2	0.07	0.89	bdl	7.58	0.08	7.1	16.2	1.02	99.0	78.66	20.93	0.41	0.79	18.54	45.23	36.23
CG-28_T11	Cpx-ore	Cristales Grandes	EPI-0702	23.3	0.07	0.86	bdl	7.56	0.08	7.2	16.2	1.03	99.2	78.93	20.68	0.40	0.79	18.44	45.09	36.47
CG-28_T11	Cpx-ore	Cristales Grandes	EPI-0702	23.2	0.08	0.87	bdl	7.63	0.08	7.1	16.2	1.01	98.8	77.60	22.02	0.37	0.78	18.74	45.25	36.01
CG-28_T11	Cpx-ore	Cristales Grandes	EPI-0702	23.3	0.08	0.88	bdl	7.63	0.09	7.1	16.2	1.02	99.2	77.83	21.74	0.43	0.78	18.70	45.19	36.11
CG-28_T11	Cpx-ore	Cristales Grandes	EPI-0702	23.3	0.08	0.87	bdl	7.63	0.09	7.1	16.2	1.00	99.0	77.46	22.10	0.44	0.78	18.72	45.26	36.02
CG-28_T11	Cpx-ore	Cristales Grandes	EPI-0702	23.3	0.08	0.83	bdl	7.52	0.09	7.1	16.3	0.98	98.9	77.73	21.84	0.43	0.78	18.43	45.37	36.20
CG-28_T11	Cpx-ore	Cristales Grandes	EPI-0702	23.3	0.09	0.81	bdl	7.51	0.09	7.2	16.3	0.96	98.9	77.43	22.15	0.42	0.78	18.39	45.31	36.30
CG-28_T11	Cpx-ore	Cristales Grandes	EPI-0702	23.4	0.08	0.75	bdl	7.01	0.08	7.4	16.4	0.91	98.8	79.45	20.17	0.38	0.80	17.08	45.34	37.58
CG-28_T11	Cpx-ore	Cristales Grandes	EPI-0702	23.5	0.09	0.74	bdl	6.48	0.07	7.7	16.6	0.84	98.9	81.39	18.29	0.33	0.82	15.69	45.62	38.69
CG-28_T11	Cpx-ore	Cristales Grandes	EPI-0702	6.0	0.88	2.56	bdl	5.11	0.03	1.3	8.4	0.00	41.6	120.86	-22.19	1.33	1.22	28.43	55.74	15.83
CG-28_T11	Cpx-ore	Cristales Grandes	EPI-0702	23.7	0.08	0.68	bdl	6.14	0.07	7.9	16.6	0.82	98.9	80.80	18.89	0.31	0.81	14.92	45.67	39.41
CG-28_T11	Cpx-ore	Cristales Grandes	EPI-0702	23.3	0.12	0.98	0.01	6.91	0.08	7.4	16.2	1.05	98.8	82.13	17.50	0.37	0.82	16.93	45.30	37.77
CG-28_T11	Cpx-ore	Cristales Grandes	EPI-0702	23.3	0.09	0.96	bdl	7.02	0.07	7.4	16.2	1.07	98.9	81.84	17.82	0.34	0.82	17.17	45.17	37.65
CG-28_T11	Cpx-ore	Cristales Grandes	EPI-0702	23.4	0.08	0.80	bdl	6.85	0.07	7.6	16.3	1.08	99.1	83.02	16.62	0.36	0.83	16.67	45.10	38.23
CG-28_T11	Cpx-ore	Cristales Grandes	EPI-0702	23.5	0.09	0.88	bdl	6.86	0.08	7.5	16.3	1.02	99.0	81.02	18.60	0.37	0.81	16.78	45.24	37.98
CG-28_T11	Cpx-ore	Cristales Grandes	EPI-0702	23.4	0.09	0.85	bdl	6.75	0.07	7.6	16.3	1.03	98.8	82.34	17.31	0.35	0.83	16.47	45.16	38.36
CG-28_T11	Cpx-ore	Cristales Grandes	EPI-0702	23.4	0.09	0.85	bdl	6.75	0.07	7.5	16.3	0.98	98.8	81.45	18.21	0.34	0.82	16.48	45.33	38.19
CG-28_T11	Cpx-ore	Cristales Grandes	EPI-0702	24.0	0.10	0.89	bdl	6.80	0.08	7.6	16.3	1.00	100.2	78.11	21.54	0.35	0.78	16.58	44.94	38.48
CG-28_T11	Cpx-ore	Cristales Grandes	EPI-0702	23.5	0.10	0.79	bdl	6.59	0.07	7.6	16.4	1.01	98.9	82.49	17.19	0.33	0.83	16.07	45.34	38.59
CG-28_T11	Cpx-ore	Cristales Grandes	EPI-0702	23.5	0.07	0.69	bdl	6.44	0.08	7.7	16.5	0.88	98.6	81.40	18.22	0.38	0.82	15.68	45.47	38.85
CG-28_T11	Cpx-ore	Cristales Grandes	EPI-0702	24.0	0.07	0.71	bdl	6.29	0.07	7.9	16.5	0.88	99.8	80.36	19.32	0.32	0.81	15.21	45.23	39.56
CG-28_T11	Cpx-ore	Cristales Grandes	EPI-0702	19.2	0.05	1.28	bdl	6.02	0.06	6.2	12.2	0.35	80.2	67.86	31.87	0.27	0.68	18.55	42.27	39.18
CG-28_T11	Cpx-ore	Cristales Grandes	EPI-0702	16.0	0.05	5.13	bdl	6.88	0.07	9.1	5.4	0.19	77.8	86.91	12.80	0.29	0.87	21.44	19.43	59.13
CG-28_T11	Cpx-ore	Cristales Grandes	EPI-0702	23.8	0.09	0.79	bdl	6.00	0.07	8.0	16.5	0.90	99.2	83.09	16.59	0.32	0.83	14.54	45.39	40.07
CG-28_T11	Cpx-ore	Cristales Grandes	EPI-0702	23.6	0.07	0.79	bdl	6.16	0.06	7.9	16.4	0.97	98.7	83.95	15.76	0.29	0.84	14.98	45.26	39.75
CG-28_T11	Cpx-ore	Cristales Grandes	EPI-0702	23.6	0.08	0.73	bdl	5.91	0.06	8.0	16.3	0.93	98.4	83.40	16.31	0.28	0.84	14.44	45.30	40.27
CG-28_T11	Cpx-ore	Cristales Grandes	EPI-0702	23.8	0.09	0.67	bdl	5.87	0.06	8.0	16.5	0.91	98.8	83.74	15.96	0.29	0.84	14.24	45.43	40.33
CG-28_T11	Cpx-ore	Cristales Grandes	EPI-0702	23.7	0.08	0.71	bdl	5.89	0.05	8.0	16.5	0.93	98.6	83.95	15.82	0.24	0.84	14.32	45.50	40.18
CG-28_T11	Cpx-ore	Cristales Grandes	EPI-0702	23.7	0.07	0.70	bdl	6.00	0.06	8.0	16.5	0.89	98.8	82.60	17.13	0.27	0.83	14.57	45.32	40.11
CG-28_T11	Cpx-ore	Cristales Grandes	EPI-0702	23.7	0.08	0.72	bdl	5.86	0.06	8.0	16.6	0.84	98.6	82.93	16.81	0.25	0.83	14.22	45.62	40.16
CG-28_T11	Cpx-ore	Cristales Grandes	EPI-0702	23.7	0.08	0.68	bdl	5.56	0.07	8.2	16.7	0.75	98.6	83.35	16.35	0.30	0.84	13.46	45.78	40.76
CG-28_T11	Cpx-ore	Cristales Grandes	EPI-0702	23.8	0.08	0.67	bdl	5.46	0.06	8.2	16.7	0.71	98.6	82.90	16.81	0.28	0.83	13.21	45.72	41.07
CG-28_T11	Cpx-ore	Cristales Grandes	EPI-0702	23.8	0.09	0.68	bdl	5.46	0.06	8.2	16.8	0.64	98.6	82.38	17.35	0.26	0.83	13.15	45.92	40.92
CG-28_T11	Cpx-ore	Cristales Grandes	EPI-0702	23.5	0.08	0.79	bdl	6.50	0.07	7.8	16.2	1.06	99.0	84.78	14.91	0.31	0.85	15.77	44.91	39.32

Clinopyroxene EPMA data from El Laco host andesites

Sample Name	Type	Volcanic	Si [wt.%]	Ti [wt.%]	Al [wt.%]	Cr [wt.%]	Fe [wt.%]	Mn [wt.%]	Mg [wt.%]	Ca [wt.%]	Na [wt.%]	Total	Dp	Hd	Joh	#Mg	Fs	Wo	En
ASLN-06_A_Px_Phen_01	Cpx-glom	Laco Norte upper andesite	24.04	0.44	1.36	0.01	6.56	0.19	9.15	14.90	0.23	99.78	75.65	23.64	0.71	0.76	14.53	40.32	45.15
ASLN-06_A_Px_Phen_01	Cpx-glom	Laco Norte upper andesite	24.19	0.20	0.61	0.00	9.57	0.09	6.59	15.68	0.93	99.79	62.94	36.70	0.36	0.63	21.62	44.37	34.00
ASLN-06_C_Px_GC_01	Cpx-glom	Laco Norte upper andesite	24.73	0.14	0.52	0.01	6.85	0.27	8.81	15.43	0.23	99.80	73.85	25.13	1.01	0.75	15.29	41.51	43.19
ASLN-06_C_Px_GC_01	Cpx-glom	Laco Norte upper andesite	24.22	0.26	0.99	0.03	7.69	0.26	8.55	14.76	0.28	99.62	71.14	27.90	0.97	0.72	17.25	40.25	42.51
ASLN-06_C_Px_GC_01	Cpx-glom	Laco Norte upper andesite	24.33	0.31	1.05	0.00	7.62	0.25	8.68	14.77	0.26	100.09	71.61	27.46	0.93	0.72	17.01	40.07	42.92
AILN-02_A_Px_Phen_01	Cpx-glom	Laco Norte lower andesite	23.39	0.65	1.95	0.02	7.50	0.20	8.47	14.67	0.26	99.64	71.62	27.64	0.74	0.72	16.89	40.51	42.61
AILN-02_A_Px_Phen_01	Cpx-glom	Laco Norte lower andesite	23.85	0.49	1.51	bdl	6.82	0.20	9.16	14.50	0.24	99.53	74.98	24.31	0.71	0.76	15.16	39.43	45.41
AILN-02_A_Px_Phen_01	Cpx-glom	Laco Norte lower andesite	24.08	0.47	1.46	0.01	6.83	0.20	9.28	14.42	0.24	100.00	75.16	24.12	0.72	0.76	15.14	39.06	45.80
AILN-02_A_Px_Phen_01	Cpx-glom	Laco Norte lower andesite	24.52	0.35	0.93	0.00	6.84	0.21	9.67	14.11	0.17	99.87	75.83	23.44	0.73	0.76	15.04	37.78	47.18
ACUMt-01a_B_Px_Phen_01	Cpx-glom	Laco Norte lower andesite	24.64	0.21	0.71	bdl	6.73	0.23	9.04	15.24	0.21	99.99	74.80	24.35	0.84	0.75	14.89	40.89	44.21
ACUMt-01a_B_Px_Phen_01	Cpx-glom	Laco Norte lower andesite	24.26	0.35	1.05	0.00	6.81	0.23	9.65	14.00	0.20	99.38	75.85	23.34	0.80	0.76	15.06	37.64	47.30
PL-01_E_Px_Phen_01	Cpx-glom	Pico Laco dome	24.48	0.22	0.73	bdl	7.09	0.34	8.89	15.00	0.20	99.69	73.24	25.52	1.24	0.74	15.95	40.40	43.65
PL-01_E_Px_Phen_01	Cpx-glom	Pico Laco dome	24.37	0.24	0.76	0.00	7.01	0.32	9.02	14.76	0.18	99.27	73.79	25.05	1.16	0.75	15.76	39.85	44.39
PL-01_F_Px_GC_02	Cpx-glom	Pico Laco dome	22.83	0.53	3.43	0.08	7.14	0.15	8.13	14.20	0.35	99.54	71.90	27.54	0.57	0.72	16.64	40.80	42.57
PL-01_F_Px_GC_02	Cpx-glom	Pico Laco dome	23.94	0.31	1.16	0.05	8.19	0.28	8.54	14.29	0.31	99.47	69.83	29.17	1.01	0.71	18.39	39.05	42.56
PL-01_F_Px_GC_02	Cpx-glom	Pico Laco dome	24.46	0.20	0.68	0.00	7.21	0.35	8.83	14.83	0.23	99.39	72.74	25.98	1.28	0.74	16.31	40.14	43.54
PL-01_F_Px_GC_02	Cpx-glom	Pico Laco dome	24.54	0.21	0.71	0.02	6.86	0.33	8.92	15.18	0.23	99.83	73.94	24.84	1.22	0.75	15.42	40.84	43.74
PL-01_F_Px_GC_02	Cpx-glom	Pico Laco dome	24.19	0.24	0.91	0.00	7.72	0.30	9.11	14.20	0.16	99.39	72.24	26.70	1.06	0.73	17.16	38.17	44.67
PL-02_F_Px_Phen_01	Cpx-glom	Pico Laco dome	24.38	0.25	1.60	0.14	6.60	0.14	9.48	14.19	0.27	100.42	76.29	23.21	0.50	0.77	14.58	38.53	46.90
PL-02_F_Px_Phen_01	Cpx-glom	Pico Laco dome	23.69	0.42	2.23	0.25	6.66	0.15	8.98	14.22	0.26	99.89	75.13	24.32	0.54	0.76	15.05	39.49	45.47
PL-02_F_Px_Phen_01	Cpx-glom	Pico Laco dome	23.70	0.50	1.40	0.01	8.15	0.25	8.64	14.35	0.22	99.71	70.24	28.85	0.91	0.71	18.15	39.01	42.84
PL-02_G_Px_GC_01	Cpx-glom	Pico Laco dome	23.89	0.18	1.12	0.01	8.76	0.20	8.03	14.41	0.39	99.05	67.26	31.98	0.76	0.68	19.69	39.85	40.46
PL-02_G_Px_GC_01	Cpx-glom	Pico Laco dome	23.40	0.34	1.98	0.01	8.65	0.19	7.83	14.78	0.35	99.90	67.74	31.55	0.71	0.68	19.41	40.99	39.59
PL-02_G_Px_GC_01	Cpx-glom	Pico Laco dome	23.88	0.40	1.21	bdl	7.04	0.23	9.09	14.51	0.22	99.05	74.14	25.02	0.83	0.75	15.67	39.38	44.95
PL-02_G_Px_GC_01	Cpx-glom	Pico Laco dome	24.25	0.36	0.99	0.01	6.95	0.21	9.29	14.56	0.19	99.59	74.81	24.43	0.76	0.75	15.33	39.15	45.52
PL-02_G_Px_GC_01	Cpx-glom	Pico Laco dome	23.81	0.45	1.41	0.00	7.03	0.21	8.93	14.70	0.23	99.33	73.89	25.34	0.77	0.74	15.66	40.02	44.32
PL-02_G_Px_GC_01	Cpx-glom	Pico Laco dome	24.01	0.32	0.95	0.00	6.66	0.22	9.32	14.73	0.20	98.90	75.65	23.56	0.78	0.76	14.70	39.61	45.69
PL-02_G_Px_GC_01	Cpx-glom	Pico Laco dome	24.06	0.29	0.86	0.00	7.76	0.30	8.83	14.69	0.26	99.50	71.54	27.37	1.08	0.72	17.21	39.51	43.27
PL-02_G_Px_GC_01	Cpx-glom	Pico Laco dome	24.22	0.33	0.99	0.00	6.98	0.26	9.14	14.40	0.21	99.13	74.29	24.77	0.94	0.75	15.66	39.12	45.23
ALS-01_A_Px_GC_01	Cpx-glom	Laco Sur	24.30	0.27	0.89	0.01	7.09	0.24	9.02	14.89	0.23	99.65	73.82	25.30	0.89	0.74	15.69	40.06	44.25
ALS-01_A_Px_GC_01	Cpx-glom	Laco Sur	23.30	0.46	2.07	0.33	7.72	0.24	8.09	14.98	0.32	100.03	70.43	28.66	0.91	0.71	17.51	41.57	40.92
ALS-01_D_Px_GC_02	Cpx-glom	Laco Sur	23.96	0.30	0.91	0.01	7.73	0.24	8.67	14.62	0.26	98.92	71.36	27.75	0.89	0.72	17.25	39.78	42.97
ALS-01_D_Px_GC_02	Cpx-glom	Laco Sur	24.10	0.26	0.88	0.01	7.84	0.24	8.75	14.52	0.27	99.25	71.30	27.83	0.88	0.72	17.41	39.35	43.24
ACG-03_D_Px_Phen_01	Cpx-glom	Cristales Grandes	24.46	0.20	0.91	0.00	7.63	0.29	8.57	14.96	0.30	100.12	71.27	27.67	1.07	0.72	17.08	40.55	42.37
ACG-03_D_Px_Phen_01	Cpx-glom	Cristales Grandes	23.75	0.45	1.82	0.01	7.48	0.16	8.57	14.59	0.24	99.79	71.99	27.42	0.59	0.72	16.75	40.20	43.05
ACG-03_D_Px_Phen_01	Cpx-glom	Cristales Grandes	23.57	0.45	2.10	0.06	7.45	0.19	8.51	14.57	0.26	99.92	71.87	27.44	0.70	0.72	16.80	40.30	42.90
ACG-03_D_Px_Phen_01	Cpx-glom	Cristales Grandes	24.46	0.20	0.75	bdl	7.94	0.28	8.64	14.64	0.27	99.85	70.64	28.34	1.02	0.71	17.73	39.62	42.65
ACG-03_E_Px_GC_02	Cpx-glom	Cristales Grandes	24.35	0.24	1.05	0.01	7.57	0.28	8.37	15.02	0.30	99.86	70.94	28.03	1.04	0.72	17.11	41.13	41.76
ACG-03_E_Px_GC_02	Cpx-glom	Cristales Grandes	24.45	0.18	0.83	0.00	7.50	0.26	8.63	14.81	0.27	99.55	71.79	27.26	0.95	0.72	16.84	40.33	42.83
ACG-03_E_Px_GC_02	Cpx-glom	Cristales Grandes	24.00	0.43	1.28	0.01	7.30	0.21	8.88	14.56	0.21	99.54	73.04	26.19	0.78	0.74	16.28	39.64	44.09
ACG-03_E_Px_GC_02	Cpx-glom	Cristales Grandes	24.71	0.18	0.79	0.01	6.96	0.27	8.79	15.26	0.25	100.24	73.53	25.46	1.01	0.74	15.57	41.17	43.25
ACG-03_E_Px_GC_02	Cpx-glom	Cristales Grandes	24.56	0.18	0.72	0.00	7.16	0.28	8.72	15.20	0.24	99.84	72.82	26.14	1.05	0.74	16.02	41.06	42.92
ASSVB-03_A_Px_Phen_01	Cpx-glom	San Vicente Bajo	24.42	0.24	1.37	0.28	5.11	0.12	9.77	14.84	0.24	99.66	81.04	18.52	0.43	0.81	11.32	40.31	48.38
ASSVB-03_A_Px_Phen_01	Cpx-glom	San Vicente Bajo	24.12	0.28	1.62	0.27	5.47	0.12	9.49	14.70	0.25	99.35	79.52	20.02	0.46	0.80	12.22	40.33	47.45
ASSVB-03_D_Px_GC_01	Cpx-glom	San Vicente Bajo	24.28	0.30	1.07	0.01	7.26	0.23	8.69	14.88	0.29	99.76	72.65	26.49	0.86	0.73	16.26	40.56	43.18
ASSVB-03_E_Px_GC_02	Cpx-glom	San Vicente Bajo	24.39	0.25	0.89	0.01	6.71	0.23	8.92	15.09	0.25	99.46	74.64	24.52	0.84	0.75	14.99	40.91	44.10
ASSVB-03_E_Px_GC_02	Cpx-glom	San Vicente Bajo	24.35	0.26	0.85	0.01	6.89	0.22	8.88	15.05	0.25	99.40	74.07	25.10	0.83	0.75	15.35	40.79	43.86
ASSVB-03_E_Px_GC_02	Cpx-glom	San Vicente Bajo	24.39	0.22	0.78	0.01	6.62	0.23	8.89	14.96	0.25	98.88	74.79	24.35	0.86	0.75	14.92	40.83	44.26
ASSVB-03_E_Px_GC_02	Cpx-glom	San Vicente Bajo	24.17	0.23	0.94	0.01	7.23	0.23	8.73	14.88	0.29	99.15	72.83	26.32	0.85	0.73	16.16	40.53	43.31

Clinopyroxene EPMA data from El Laco host andesites

Sample Name	Type	Volcanic	Si [wt.%]	Ti [wt.%]	Al [wt.%]	Cr [wt.%]	Fe [wt.%]	Mn [wt.%]	Mg [wt.%]	Ca [wt.%]	Na [wt.%]	Total	Dp	Hd	Joh	#Mg	Fs	Wo	En
ACUMt-01a_A1_Cum_Px_01	Cpx-meg	Mgt megacrysts LN low and	24.1	0.45	1.37	0.01	6.67	0.20	9.1	14.8	0.23	99.92	75.32	23.97	0.71	0.76	14.77	40.16	45.07
ACUMt-01a_A1_Cum_Px_01	Cpx-meg	Mgt megacrysts LN low and	24.6	0.32	0.84	bdl	6.61	0.23	9.5	14.3	0.21	99.59	76.13	23.06	0.81	0.77	14.67	38.56	46.77
ACUMt-01a_A1_Cum_Px_01	Cpx-meg	Mgt megacrysts LN low and	24.2	0.30	1.00	bdl	6.81	0.21	9.0	14.9	0.23	99.20	74.66	24.59	0.75	0.75	15.12	40.32	44.56
ACUMt-01a_A1_Cum_Px_01	Cpx-meg	Mgt megacrysts LN low and	24.5	0.20	0.99	bdl	6.83	0.20	9.0	15.0	0.21	99.93	74.59	24.67	0.74	0.75	15.11	40.53	44.35
ACUMt-01a_A1_Cum_Px_01	Cpx-meg	Mgt megacrysts LN low and	24.4	0.24	1.04	bdl	6.81	0.19	9.1	15.0	0.21	99.91	74.81	24.49	0.70	0.75	15.02	40.38	44.60
ACUMt-01a_A2_Cum_Px_02	Cpx-meg	Mgt megacrysts LN low and	24.5	0.12	0.86	0.00	7.23	0.17	8.8	15.2	0.27	100.01	73.18	26.18	0.64	0.74	15.85	40.91	43.25
ACUMt-01a_A2_Cum_Px_02	Cpx-meg	Mgt megacrysts LN low and	24.8	0.16	0.89	bdl	4.81	0.06	8.8	17.2	0.39	100.50	80.47	19.29	0.24	0.81	10.46	46.45	43.09
ACUMt-01a_A2_Cum_Px_02	Cpx-meg	Mgt megacrysts LN low and	24.7	0.11	0.72	bdl	5.92	0.09	8.8	16.1	0.42	99.68	77.05	22.59	0.35	0.77	12.95	43.57	43.48
ACUMt-01a_A3_Cum_Px_03	Cpx-meg	Mgt megacrysts LN low and	24.6	0.34	0.85	0.01	7.00	0.22	9.3	14.7	0.20	100.21	74.63	24.60	0.78	0.75	15.41	39.26	45.33
ACUMt-01a_A3_Cum_Px_03	Cpx-meg	Mgt megacrysts LN low and	24.5	0.21	1.05	bdl	7.18	0.19	9.2	15.0	0.21	100.67	74.05	25.27	0.68	0.75	15.61	39.83	44.55
ACUMt-01a_A3_Cum_Px_03	Cpx-meg	Mgt megacrysts LN low and	24.5	0.16	0.93	bdl	7.08	0.20	9.1	14.9	0.22	100.10	74.14	25.14	0.72	0.75	15.52	40.00	44.48
ACUMt-01a_A4_Cum_Px_04	Cpx-meg	Mgt megacrysts LN low and	24.4	0.41	1.15	0.00	7.15	0.22	9.2	14.2	0.26	100.03	74.12	25.11	0.77	0.75	15.91	38.51	45.57
ACUMt-01a_A4_Cum_Px_04	Cpx-meg	Mgt megacrysts LN low and	24.2	0.20	0.95	bdl	6.79	0.18	8.9	15.3	0.23	99.48	74.56	24.77	0.67	0.75	14.93	41.33	43.75
ACUMt-01a_A4_Cum_Px_04	Cpx-meg	Mgt megacrysts LN low and	24.8	0.14	0.70	bdl	6.54	0.15	9.0	15.5	0.27	100.25	75.54	23.90	0.56	0.76	14.27	41.65	44.08

Clinopyroxene EPMA data from El Laco host andesites

Sample Name	Type	Volcanic	Si [wt.%]	Ti [wt.%]	Al [wt.%]	Cr [wt.%]	Fe [wt.%]	Mn [wt.%]	Mg [wt.%]	Ca [wt.%]	Na [wt.%]	Total
ASLN-06_A_Px_Phen_01	Opx-glom	Laco Norte upper andesite	25.5	0.14	0.46	bdl	12.1	0.34	16.3	1.07	0.02	100.11
ASLN-06_A_Px_Phen_01	Opx-glom	Laco Norte upper andesite	25.4	0.14	0.53	bdl	11.6	0.35	15.9	1.27	0.03	99.27
ASLN-06_A_Px_Phen_01	Opx-glom	Laco Norte upper andesite	24.8	0.26	0.98	bdl	11.8	0.34	15.6	1.66	0.02	99.10
ASLN-06_A_Px_Phen_01	Opx-glom	Laco Norte upper andesite	24.7	0.20	0.60	0.00	15.0	0.41	14.2	1.07	0.02	99.33
ASLN-06_C_Px_GC_01	Opx-glom	Laco Norte upper andesite	24.3	0.16	1.22	0.24	16.1	0.48	13.5	0.94	0.03	99.85
ASLN-06_C_Px_GC_01	Opx-glom	Laco Norte upper andesite	24.6	0.12	0.60	0.03	16.4	0.45	13.8	0.86	0.02	99.80
ASLN-06_C_Px_GC_01	Opx-glom	Laco Norte upper andesite	24.6	0.11	0.71	0.01	16.1	0.47	13.8	0.91	0.02	99.78
ASLN-06_C_Px_GC_01	Opx-glom	Laco Norte upper andesite	24.9	0.12	0.48	0.00	16.3	0.46	13.9	0.89	0.02	100.36
ASLN-06_D_Px_GC_02	Opx-glom	Laco Norte upper andesite	25.2	0.13	0.48	bdl	13.6	0.37	15.3	0.94	0.01	99.78
ASLN-06_D_Px_GC_02	Opx-glom	Laco Norte upper andesite	25.0	0.17	0.72	bdl	13.9	0.36	15.1	0.93	0.02	99.75
ASLN-06_D_Px_GC_02	Opx-glom	Laco Norte upper andesite	25.2	0.19	0.60	bdl	13.8	0.35	15.2	1.00	0.02	100.21
ASLN-06_D_Px_GC_02	Opx-glom	Laco Norte upper andesite	25.1	0.18	0.61	0.00	13.6	0.36	15.2	0.97	0.02	99.86
ASLN-06_D_Px_GC_02	Opx-glom	Laco Norte upper andesite	25.1	0.10	0.60	bdl	13.7	0.34	15.5	0.78	0.02	99.83
ASLN-06_D_Px_GC_02	Opx-glom	Laco Norte upper andesite	25.2	0.08	0.64	0.01	13.0	0.34	15.9	0.66	0.01	99.74
ASLN-06_D_Px_GC_02	Opx-glom	Laco Norte upper andesite	25.5	0.07	0.43	bdl	13.8	0.35	15.8	0.48	0.01	100.71
ASLN-06_D_Px_GC_02	Opx-glom	Laco Norte upper andesite	24.7	0.21	0.92	0.01	14.1	0.34	14.9	1.08	0.02	99.69
ASLN-06_D_Px_GC_02	Opx-glom	Laco Norte upper andesite	25.0	0.21	0.78	bdl	12.1	0.34	15.8	1.20	0.02	99.12
AILN-02_A_Px_Phen_01	Opx-glom	Laco Norte lower andesite	25.6	0.15	0.40	bdl	12.2	0.32	16.2	1.08	0.02	100.10
AILN-02_A_Px_Phen_01	Opx-glom	Laco Norte lower andesite	25.6	0.08	0.23	bdl	13.9	0.50	15.5	0.68	0.01	100.50
AILN-02_E_Px_GC_01	Opx-glom	Laco Norte lower andesite	24.8	0.15	0.51	bdl	14.9	0.39	14.5	1.09	0.02	99.70
AILN-02_E_Px_GC_01	Opx-glom	Laco Norte lower andesite	25.2	0.16	0.54	bdl	12.2	0.35	15.9	1.03	0.02	99.16

Clinopyroxene EPMA data from El Laco host andesites

Sample Name	Type	Volcanic	Si [wt.%]	Ti [wt.%]	Al [wt.%]	Cr [wt.%]	Fe [wt.%]	Mn [wt.%]	Mg [wt.%]	Ca [wt.%]	Na [wt.%]	Total
AILN-02_E_Px_GC_01	Opx-glom	Laco Norte lower andesite	25.5	0.14	0.41	bdl	12.1	0.34	16.2	1.09	0.02	100.10
AILN-02_E_Px_GC_01	Opx-glom	Laco Norte lower andesite	24.8	0.15	0.47	bdl	15.4	0.38	14.3	1.09	0.02	99.70
AILN-02_E_Px_GC_01	Opx-glom	Laco Norte lower andesite	24.8	0.22	0.67	bdl	15.4	0.38	14.3	1.10	0.02	100.13
AILN-02_E_Px_GC_01	Opx-glom	Laco Norte lower andesite	25.0	0.14	0.47	bdl	15.0	0.39	14.6	1.10	0.02	100.05
AILN-02_E_Px_GC_01	Opx-glom	Laco Norte lower andesite	25.1	0.18	0.65	bdl	11.9	0.33	16.2	1.19	0.02	99.50
AILN-02_A_Px_GC_02	Opx-glom	Laco Norte lower andesite	24.9	0.11	0.49	bdl	16.4	0.60	13.8	0.75	0.01	100.24
AILN-02_A_Px_GC_02	Opx-glom	Laco Norte lower andesite	25.1	0.23	0.63	bdl	12.8	0.41	15.6	1.20	0.02	99.90
AILN-02_A_Px_GC_02	Opx-glom	Laco Norte lower andesite	24.6	0.10	0.42	bdl	16.6	0.59	13.6	1.08	0.02	99.88
AILN-02_A_Px_GC_02	Opx-glom	Laco Norte lower andesite	24.9	0.11	0.43	bdl	17.0	0.59	13.6	0.75	0.01	100.46
AILN-02_A_Px_GC_02	Opx-glom	Laco Norte lower andesite	24.7	0.12	0.50	bdl	16.6	0.61	13.7	0.77	0.01	100.01
AILN-02_A_Px_GC_02	Opx-glom	Laco Norte lower andesite	25.1	0.22	0.81	bdl	12.2	0.35	15.9	1.21	0.02	99.84
AILN-02_A_Px_GC_02	Opx-glom	Laco Norte lower andesite	25.1	0.20	0.79	bdl	12.1	0.34	16.0	1.12	0.02	99.71
ACUMt-01a_B_Px_Phen_0	Opx-glom	Laco Norte lower andesite	25.4	0.15	0.43	bdl	11.9	0.35	16.3	1.06	0.02	99.64
ACUMt-01a_B_Px_Phen_0	Opx-glom	Laco Norte lower andesite	24.9	0.19	0.55	bdl	14.9	0.40	14.5	1.11	0.02	100.03
ACUMt-01a_B_Px_Phen_0	Opx-glom	Laco Norte lower andesite	25.5	0.14	0.42	bdl	11.8	0.34	16.2	1.05	0.01	99.59
ACUMt-01a_C_Px_GC_01	Opx-glom	Laco Norte lower andesite	24.9	0.14	0.49	0.01	15.0	0.45	14.4	1.01	0.02	99.63
ACUMt-01a_C_Px_GC_01	Opx-glom	Laco Norte lower andesite	24.8	0.09	0.70	0.15	15.6	0.42	14.1	0.90	0.02	100.04
ACUMt-01a_C_Px_GC_01	Opx-glom	Laco Norte lower andesite	24.4	0.10	1.04	0.30	16.1	0.42	13.8	0.87	0.02	100.27
ACUMt-01a_C_Px_GC_01	Opx-glom	Laco Norte lower andesite	24.8	0.14	0.55	0.02	15.6	0.43	14.2	0.98	0.01	100.01
ACUMt-01a_C_Px_GC_01	Opx-glom	Laco Norte lower andesite	25.0	0.16	0.51	bdl	15.0	0.44	14.6	1.05	0.02	100.28
ACUMt-01a_A2_Cum_Px_	Cpx-meg	Mgt megacrysts Laco Norte lower andesite	24.2	0.31	1.22	0.01	11.7	0.33	13.7	4.19	0.10	98.93
ACUMt-01a_A2_Cum_Px_	Cpx-meg	Mgt megacrysts Laco Norte lower andesite	25.5	0.16	0.47	bdl	11.9	0.33	16.2	1.11	0.02	99.83
ACUMt-01a_A3_Cum_Px_	Cpx-meg	Mgt megacrysts Laco Norte lower andesite	24.3	0.20	1.51	0.06	14.1	0.30	14.7	1.14	0.02	99.69
ACUMt-01a_A4_Cum_Px_	Cpx-meg	Mgt megacrysts Laco Norte lower andesite	25.3	0.17	0.57	bdl	12.1	0.33	16.3	1.02	0.02	99.98
ACUMt-01a_A4_Cum_Px_	Cpx-meg	Mgt megacrysts Laco Norte lower andesite	24.9	0.13	0.48	0.00	14.5	0.40	14.6	1.13	0.02	99.49
ACUMt-01a_A4_Cum_Px_	Cpx-meg	Mgt megacrysts Laco Norte lower andesite	25.4	0.16	0.47	bdl	12.0	0.34	16.2	1.06	0.02	99.68
PL-01_E_Px_Phen_01	Opx-glom	Pico Laco dome	25.0	0.11	0.46	bdl	14.5	0.50	14.8	0.83	0.01	99.60
PL-01_E_Px_Phen_01	Opx-glom	Pico Laco dome	25.2	0.12	0.37	bdl	13.6	0.46	15.1	1.06	0.01	99.51
PL-01_E_Px_Phen_01	Opx-glom	Pico Laco dome	24.9	0.11	0.26	bdl	15.4	0.65	14.2	0.91	0.01	99.51
PL-01_E_Px_Phen_01	Opx-glom	Pico Laco dome	24.8	0.15	0.83	bdl	14.3	0.51	14.5	0.98	0.02	99.42
PL-01_G_Px_Phen_02	Opx-glom	Pico Laco dome	24.9	0.12	0.76	bdl	12.7	0.28	15.6	1.06	0.01	99.11
PL-01_G_Px_Phen_02	Opx-glom	Pico Laco dome	24.8	0.11	0.54	bdl	14.8	0.53	14.4	0.92	0.01	99.34
PL-01_G_Px_Phen_02	Opx-glom	Pico Laco dome	24.3	0.14	0.43	bdl	15.7	0.64	13.7	1.66	0.02	98.98
PL-01_G_Px_Phen_02	Opx-glom	Pico Laco dome	24.8	0.11	0.38	bdl	15.5	0.61	14.1	0.92	0.02	99.37
PL-01_D_Px_GC_01	Opx-glom	Pico Laco dome	24.2	0.11	0.91	0.12	16.2	0.79	13.6	0.73	0.02	99.28
PL-01_D_Px_GC_01	Opx-glom	Pico Laco dome	24.3	0.08	0.82	0.35	15.9	0.83	13.7	0.73	0.02	99.50
PL-01_D_Px_GC_01	Opx-glom	Pico Laco dome	24.2	0.14	2.05	0.03	12.7	0.21	15.5	0.82	0.02	99.54
PL-01_D_Px_GC_01	Opx-glom	Pico Laco dome	24.6	0.11	1.36	0.22	13.1	0.23	15.4	0.81	0.02	99.47
PL-01_D_Px_GC_01	Opx-glom	Pico Laco dome	24.4	0.16	0.67	0.05	15.9	0.53	13.9	1.00	0.02	99.46
PL-01_D_Px_GC_01	Opx-glom	Pico Laco dome	24.2	0.11	1.20	0.22	15.8	0.38	13.8	0.92	0.03	99.45
PL-02_F_Px_Phen_01	Opx-glom	Pico Laco dome	24.4	0.15	1.95	0.03	13.3	0.23	15.0	1.11	0.03	100.10
PL-02_F_Px_Phen_01	Opx-glom	Pico Laco dome	24.0	0.16	2.33	0.03	13.6	0.23	14.9	1.07	0.03	100.26
PL-02_F_Px_Phen_01	Opx-glom	Pico Laco dome	24.8	0.15	1.72	0.14	12.0	0.21	16.0	0.98	0.02	100.36
PL-02_F_Px_Phen_01	Opx-glom	Pico Laco dome	24.9	0.22	0.65	bdl	14.9	0.44	14.4	1.16	0.02	100.07
PL-02_F_Px_Phen_01	Opx-glom	Pico Laco dome	25.1	0.16	0.64	0.01	14.0	0.37	15.0	0.96	0.01	100.01
PL-02_F_Px_Phen_01	Opx-glom	Pico Laco dome	24.5	0.14	1.89	0.03	13.2	0.23	15.3	0.96	0.03	100.19
PL-02_F_Px_Phen_01	Opx-glom	Pico Laco dome	24.7	0.12	1.34	0.02	13.1	0.24	15.4	1.07	0.02	99.70
PL-02_F_Px_Phen_01	Opx-glom	Pico Laco dome	25.0	0.16	1.50	0.14	12.0	0.22	16.1	1.01	0.02	100.61
PL-02_F_Px_Phen_01	Opx-glom	Pico Laco dome	25.0	0.19	0.61	bdl	14.6	0.41	14.6	1.10	0.02	99.88
PL-02_F_Px_Phen_01	Opx-glom	Pico Laco dome	24.5	0.21	1.27	0.06	14.7	0.36	14.3	1.29	0.02	100.06
PL-02_F_Px_Phen_01	Opx-glom	Pico Laco dome	24.6	0.13	1.81	0.03	13.2	0.24	15.3	1.01	0.02	100.48
PL-02_F_Px_Phen_01	Opx-glom	Pico Laco dome	24.8	0.15	1.46	0.16	12.0	0.22	16.1	0.98	0.02	100.22
PL-02_G_Px_GC_01	Opx-glom	Pico Laco dome	24.1	0.13	1.07	0.00	16.5	0.34	13.7	0.78	0.03	99.22
PL-02_G_Px_GC_01	Opx-glom	Pico Laco dome	24.6	0.20	0.78	bdl	13.2	0.34	15.3	1.01	0.02	98.75
PL-02_G_Px_GC_01	Opx-glom	Pico Laco dome	24.6	0.18	0.57	bdl	15.4	0.49	14.3	0.96	0.02	99.55
ALS-01_A_Px_Phen_01	Opx-glom	Laco Sur	24.9	0.16	0.83	0.02	12.8	0.27	15.7	1.11	0.02	99.67
ALS-01_A_Px_Phen_01	Opx-glom	Laco Sur	25.0	0.19	0.53	bdl	14.5	0.37	14.5	1.13	0.01	99.48
ALS-01_A_Px_Phen_01	Opx-glom	Laco Sur	25.0	0.12	0.38	bdl	15.2	0.45	14.6	0.86	0.01	99.96
ALS-01_A_Px_Phen_01	Opx-glom	Laco Sur	24.7	0.21	0.85	0.00	14.2	0.34	14.8	1.18	0.02	99.77
ALS-01_A_Px_Phen_01	Opx-glom	Laco Sur	24.8	0.15	0.43	bdl	15.2	0.47	14.4	0.89	0.02	99.51
ALS-01_A_Px_Phen_01	Opx-glom	Laco Sur	24.7	0.20	0.95	bdl	15.3	0.44	14.1	1.03	0.02	100.21
ALS-01_A_Px_Phen_01	Opx-glom	Laco Sur	25.2	0.15	0.41	bdl	14.6	0.39	14.7	1.12	0.04	100.38
ALS-01_A_Px_GC_01	Opx-glom	Laco Sur	24.9	0.13	0.68	0.05	14.5	0.40	14.1	2.21	0.04	100.51
ALS-01_A_Px_GC_01	Opx-glom	Laco Sur	24.8	0.16	0.47	bdl	15.1	0.46	14.6	0.91	0.01	99.79
ALS-01_A_Px_GC_01	Opx-glom	Laco Sur	24.8	0.14	0.67	0.05	15.4	0.46	14.5	0.86	0.02	100.16
ALS-01_A_Px_GC_01	Opx-glom	Laco Sur	25.0	0.16	0.51	bdl	15.3	0.45	14.5	0.89	0.01	100.44
ALS-01_D_Px_GC_02	Opx-glom	Laco Sur	24.8	0.14	0.41	bdl	15.4	0.47	14.2	0.97	0.02	99.28
ALS-01_D_Px_GC_02	Opx-glom	Laco Sur	24.8	0.14	0.43	0.00	15.9	0.46	14.3	0.97	0.02	100.40
ALS-01_D_Px_GC_02	Opx-glom	Laco Sur	24.7	0.14	0.44	bdl	15.9	0.46	14.3	0.94	0.02	100.08
ALS-01_D_Px_GC_02	Opx-glom	Laco Sur	24.8	0.14	0.42	bdl	16.0	0.46	14.2	0.95	0.02	100.22
ACG-03_D_Px_Phen_01	Opx-glom	Cristales Grandes	24.5	0.12	0.50	bdl	17.6	0.56	13.0	0.87	0.02	99.70

Clinopyroxene EPMA data from El Laco host andesites

Sample Name	Type	Volcanic	Si [wt.%]	Ti [wt.%]	Al [wt.%]	Cr [wt.%]	Fe [wt.%]	Mn [wt.%]	Mg [wt.%]	Ca [wt.%]	Na [wt.%]	Total
ACG-03_D_Px_Phen_01	Opx-glom	Cristales Grandes	24.7	0.16	1.04	bdl	14.0	0.31	14.8	0.96	0.02	99.50
ACG-03_D_Px_Phen_01	Opx-glom	Cristales Grandes	25.1	0.18	0.56	bdl	13.7	0.35	15.1	1.05	0.02	99.48
ACG-03_A_Px_GC_01	Opx-glom	Cristales Grandes	25.0	0.10	0.38	bdl	16.3	0.56	13.9	0.75	0.01	100.11
ACG-03_A_Px_GC_01	Opx-glom	Cristales Grandes	24.9	0.10	0.38	bdl	16.7	0.55	13.8	0.82	0.01	100.25
ACG-03_A_Px_GC_01	Opx-glom	Cristales Grandes	25.0	0.09	0.40	bdl	15.5	0.47	14.3	0.96	0.01	100.16
ACG-03_A_Px_GC_01	Opx-glom	Cristales Grandes	24.7	0.11	0.38	bdl	16.9	0.55	13.6	0.80	0.02	99.84
ACG-03_A_Px_GC_01	Opx-glom	Cristales Grandes	24.9	0.09	0.38	bdl	16.3	0.56	13.9	0.77	0.01	100.03
ACG-03_A_Px_GC_01	Opx-glom	Cristales Grandes	25.1	0.16	0.48	bdl	14.5	0.38	14.8	0.99	0.01	99.95
ACG-03_E_Px_GC_02	Opx-glom	Cristales Grandes	24.9	0.17	0.55	bdl	14.1	0.38	14.8	1.00	0.01	99.24
ACG-03_E_Px_GC_02	Opx-glom	Cristales Grandes	24.8	0.10	0.46	bdl	16.4	0.56	13.8	0.77	0.02	99.95
ACG-03_E_Px_GC_02	Opx-glom	Cristales Grandes	24.8	0.09	0.39	bdl	16.4	0.56	13.8	0.75	0.01	99.78
ASSVB-03_A_Px_Phen_01	Opx-glom	San Vicente Bajo	24.8	0.13	0.46	bdl	15.0	0.46	14.5	0.85	0.01	99.11
ASSVB-03_A_Px_Phen_01	Opx-glom	San Vicente Bajo	25.1	0.12	1.39	0.44	9.1	0.17	17.3	0.97	0.02	99.12
ASSVB-03_A_Px_Phen_01	Opx-glom	San Vicente Bajo	25.0	0.10	0.43	bdl	15.4	0.46	14.4	0.85	0.01	99.94
ASSVB-03_D_Px_GC_01	Opx-glom	San Vicente Bajo	24.9	0.11	0.48	bdl	15.3	0.45	14.4	0.83	0.02	99.62
ASSVB-03_D_Px_GC_01	Opx-glom	San Vicente Bajo	24.8	0.12	0.51	0.00	15.1	0.46	14.4	0.83	0.02	99.38
ASSVB-03_D_Px_GC_01	Opx-glom	San Vicente Bajo	25.07	0.14	0.47	bdl	15.14	0.46	13.87	0.78	0.02	98.96
ASSVB-03_D_Px_GC_01	Opx-glom	San Vicente Bajo	24.80	0.13	0.47	bdl	15.11	0.45	14.45	0.84	0.02	99.33
ASSVB-03_D_Px_GC_01	Opx-glom	San Vicente Bajo	24.90	0.14	0.48	bdl	15.02	0.45	14.59	0.85	0.01	99.72
ASSVB-03_E_Px_GC_02	Opx-glom	San Vicente Bajo	24.72	0.12	0.42	bdl	15.51	0.48	14.25	0.85	0.01	99.29
ASSVB-03_E_Px_GC_02	Opx-glom	San Vicente Bajo	24.86	0.11	0.37	bdl	15.17	0.46	14.53	0.77	0.01	99.37
ASSVB-03_E_Px_GC_02	Opx-glom	San Vicente Bajo	24.94	0.12	0.43	bdl	15.01	0.44	14.58	0.88	0.01	99.68

B14. LA-ICP-MS data of magnetite from El Laco ore bodies and host andesites.

Magnetite LA-ICP-MS data from El Laco deposit: Intermediate zone			Detection limits in ppm											
			Average	1.53	5.90	12.98	1.60	9.87	3.10	2.44	3.71	3.91	7.52	1.67	0.55
			Median	1.20	4.60	8.90	1.30	8.00	2.60	1.90	3.00	2.20	5.90	0.82	0.46
Sample	**Ore body**	**Drill core**	**Fe (EPMA) [wt. %]**	**Mg ppm**	**Al ppm**	**Ti ppm**	**V ppm**	**Cr ppm**	**Mn ppm**	**Co ppm**	**Ni ppm**	**Cu ppm**	**Zn ppm**	**Ga ppm**	**Sn ppm**
CG02_1	Cristales Grandes	EPI-0702	68.7	7090	1739	1513	1749	BDL	264.2	24.6	83	BDL	90.3	27.0	10.35
CG02_2	Cristales Grandes	EPI-0702	69.66	9530	1426	907	1778	BDL	631	84.8	64.9	BDL	90.9	23.4	13.2
CG02_3	Cristales Grandes	EPI-0702	69.45	10230	1190	621	1767	BDL	689	96.6	55.2	BDL	82.8	22.2	13.87
CG02_4	Cristales Grandes	EPI-0702	69.56	9910	1304	783	1759	BDL	675	86.4	59.9	BDL	90.1	22.7	13.37
CG02_5	Cristales Grandes	EPI-0702	69.37	9950	1204	638	1744	BDL	525.3	65.2	54.6	BDL	89.0	22.2	14.04
CG02_6	Cristales Grandes	EPI-0702	69.66	9960	1109	532	1746	BDL	666	92.5	49	BDL	88.3	20.8	14.7
CG02_7	Cristales Grandes	EPI-0702	69.56	10830	1101	491	1743	BDL	675	92.2	49.3	BDL	81.4	19.7	14.46
CG02_8	Cristales Grandes	EPI-0702	70.81	3940	979	215	1076	BDL	376	65.5	67.8	BDL	55.0	24.2	5.68
CG02_9	Cristales Grandes	EPI-0702	70.09	6830	859	210	982	BDL	662	114.3	65.3	BDL	82.5	21.4	5.59
CG02_10	Cristales Grandes	EPI-0702	70.81	7100	1004	301	978	BDL	691	111.6	71.5	BDL	93.3	22.0	6.06
CG02_11	Cristales Grandes	EPI-0702	70.09	7020	1135	369	977	BDL	696	110.6	76.2	BDL	94.0	22.7	5.49
CG02_12	Cristales Grandes	EPI-0702	70.45	7000	1052	285	981	BDL	700	112.7	71.7	BDL	88.9	23.8	5.43
CG02_13	Cristales Grandes	EPI-0702	70.45	3880	1735	793	1123	BDL	360.7	50.4	103.8	BDL	106.5	30.1	4.87
CG02_14	Cristales Grandes	EPI-0702	70.92	7660	1323	480	1049	BDL	675	107.9	94.6	BDL	86.7	20.4	5.18
CG02_15	Cristales Grandes	EPI-0702	70.73	7840	997	279	994	BDL	676	109.6	70	BDL	89.2	19.4	5.8
CG02_16	Cristales Grandes	EPI-0702	70.3	7720	1468	599	1086	BDL	687	109.7	96.7	BDL	86.3	22.3	4.93
CG02_17	Cristales Grandes	EPI-0702	70.92	7580	1423	519	1205	BDL	718	112.2	106.7	BDL	93.5	21.8	4.45
CG02_18	Cristales Grandes	EPI-0702	70.73	7680	935	228	1001	BDL	684	109.5	72.4	BDL	88.7	18.1	5.46
CG02_19	Cristales Grandes	EPI-0702	70.72	7710	994	269	1011	BDL	712	106.2	85.9	BDL	98.0	17.8	5.57
RN03_1	Rodados Negros	EPI-0808	71.06	7150	42	26.5	809	BDL	613	130.5	104.9	BDL	81.3	1.2	4.47
RN03_2	Rodados Negros	EPI-0808	69.51	8450	44.1	33.2	749	BDL	622	118.6	112.1	BDL	80.1	1.0	4.07
RN03_3	Rodados Negros	EPI-0808	70.48	6860	43	32.3	809	BDL	558	123.6	117.8	BDL	78.9	0.9	3.95
RN03_4	Rodados Negros	EPI-0808	70.66	6660	40.2	30.1	820	BDL	593	125.4	105	BDL	78.6	1.2	3.97
RN03_5	Rodados Negros	EPI-0808	70.63	8600	41.1	36	745	BDL	653	118.7	98.5	BDL	86.9	1.1	4.11
RN03_6	Rodados Negros	EPI-0808	71.0	7510	40.6	30.3	804	BDL	581	122	107.6	BDL	73.0	0.9	3.96
RN03_7	Rodados Negros	EPI-0808	69.3	6530	34.4	30.1	593	BDL	594	121.6	93.7	BDL	78.0	1.1	3.8
RN03_8	Rodados Negros	EPI-0808	70.8	6860	27.1	25.3	542	BDL	724	121.5	84	BDL	101.7	0.8	4.31
RN03_9	Rodados Negros	EPI-0808	71.0	7060	25	29.6	429	BDL	708	119.7	84.6	BDL	105.3	0.9	4.74
RN03_10	Rodados Negros	EPI-0808	71.1	6870	25.3	23.7	548	BDL	700	119.9	88.2	BDL	101.5	1.2	4.24
RN03_11	Rodados Negros	EPI-0808	69.5	6700	24.6	35.2	387	BDL	712	118.4	74.1	BDL	109.8	BDL	5.07
RN03_12	Rodados Negros	EPI-0808	70.5	7840	155	27.3	527	BDL	744	117.6	88.1	BDL	105.1	BDL	4.62
RN03_13	Rodados Negros	EPI-0808	70.7	6720	650	31.8	632	BDL	637	113.1	84.5	BDL	105.0	BDL	6.17
RN03_14	Rodados Negros	EPI-0808	70.6	6330	97	20.2	633	BDL	655	105.2	78.9	BDL	106.0	1.0	4.22
RN03_15	Rodados Negros	EPI-0808	71.0	6850	81	23.4	658	BDL	721	123.1	81.8	BDL	108.6	0.7	4.38
SVA1_04_1	San Vicente Alto	SVA-1001	67.9	7150	42	26.5	809	BDL	613	130.5	104.9	BDL	81.3	1.2	4.47
SVA1_04_2	San Vicente Alto	SVA-1001	67.7	8450	44.1	33.2	749	BDL	622	118.6	112.1	BDL	80.1	1.0	4.07
SVA1_04_3	San Vicente Alto	SVA-1001	68.1	6860	43	32.3	809	BDL	558	123.6	117.8	BDL	78.9	0.9	3.95
SVA1_04_4	San Vicente Alto	SVA-1001	68.1	6660	40.2	30.1	820	BDL	593	125.4	105	BDL	78.6	1.2	3.97
SVA1_04_5	San Vicente Alto	SVA-1001	67.9	8600	41.1	36	745	BDL	653	118.7	98.5	BDL	86.9	1.1	4.11
SVA1_04_6	San Vicente Alto	SVA-1001	68.3	7510	40.6	30.3	804	BDL	581	122	107.6	BDL	73.0	0.9	3.96
SVA1_04_7	San Vicente Alto	SVA-1001	68.2	6530	34.4	30.1	593	BDL	594	121.6	93.7	BDL	78.0	1.1	3.8
SVA1_04_8	San Vicente Alto	SVA-1001	68.7	6860	27.1	25.3	542	BDL	724	121.5	84	BDL	101.7	0.8	4.31
SVA1_04_9	San Vicente Alto	SVA-1001	68.5	7060	25	29.6	429	BDL	708	119.7	84.6	BDL	105.3	0.9	4.74
SVA1_04_10	San Vicente Alto	SVA-1001	68.0	6870	25.3	23.7	548	BDL	700	119.9	88.2	BDL	101.5	1.2	4.24
SVA1_04_11	San Vicente Alto	SVA-1001	67.4	6700	24.6	35.2	387	BDL	712	118.4	74.1	BDL	109.8	0.9	5.07
SVA1_04_12	San Vicente Alto	SVA-1001	67.9	7840	155	27.3	527	BDL	744	117.6	88.1	BDL	105.1	0.9	4.62
SVA1_04_13	San Vicente Alto	SVA-1001	68.3	6720	650	31.8	632	BDL	637	113.1	84.5	BDL	105.0	0.9	6.17
SVA1_04_14	San Vicente Alto	SVA-1001	67.9	6330	97	20.2	633	BDL	655	105.2	78.9	BDL	106.0	1.0	4.22
RN07_1	Rodados Negros	EPI-0808	69.6	5030	4676	2908	2530	12.2	776	95.9	282	BDL	106.7	23.6	3.12
RN07_2	Rodados Negros	EPI-0808	69.3	5770	5650	3162	2514	32.1	741	113.8	319	BDL	106.1	25.0	2.88
RN07_3	Rodados Negros	EPI-0808	69.7	6440	5325	3062	2568	21.7	1043	134.7	304	BDL	141.6	25.2	3.01
RN07_4	Rodados Negros	EPI-0808	69.8	4020	5024	3091	2492	11.9	425	65.3	323	BDL	100.1	24.3	3.39
RN07_5	Rodados Negros	EPI-0808	69.8	6490	5235	3074	2604	20.7	1074	136.6	306	BDL	131.1	24.4	3.27
RN07_6	Rodados Negros	EPI-0808	69.9	6540	5485	3081	2521	28.9	1011	140.4	316	BDL	111.4	25.3	2.98
RN07_7	Rodados Negros	EPI-0808	69.7	6520	5892	3196	2427	3.12	898	136.9	302.7	BDL	102.6	24.9	3.08
RN07_8	Rodados Negros	EPI-0808	69.7	7730	5880	3310	2508	14.4	1032	142.8	305	BDL	110.8	26.1	3.14
RN07_9	Rodados Negros	EPI-0808	69.7	6129	5618	3175	2535	12.5	896	130.4	310	BDL	127.2	25.0	3.3
RN07_10	Rodados Negros	EPI-0808	69.9	5810	4990	2857	2518	3.12	765	116.8	283.9	BDL	126.1	25.1	3.34
RN07_11	Rodados Negros	EPI-0808	69.6	6350	5221	3051	2574	17.4	1034	140.8	312.2	BDL	122.9	25.4	3.38
RN07_12	Rodados Negros	EPI-0808	69.3	6200	5548	3127	2507	16.3	949	135.8	302.5	BDL	106.8	24.0	3.19
RN07_13	Rodados Negros	EPI-0808	69.7	6554	5779	3187	2517	20.3	966	145.2	310	BDL	101.3	23.9	3.49
RN07_14	Rodados Negros	EPI-0808	69.8	5790	4627	2824	2590	3.12	900	134	293.5	BDL	130.3	24.1	3.35
RN07_15	Rodados Negros	EPI-0808	69.8	6488	5662	3204	2564	20.8	1063	145.8	315	BDL	117.0	25.1	3.4

Magnetite LA-ICP-MS data from El Laco deposit: Intermediate zone			Detection limits in ppm											
			Average	1.53	5.90	12.98	1.60	9.87	3.10	2.44	3.71	3.91	7.52	1.67	0.55
			Median	1.20	4.60	8.90	1.30	8.00	2.60	1.90	3.00	2.20	5.90	0.82	0.46
Sample	**Ore body**	**Drill core**	**Fe (EPMA) [wt. %]**	**Mg ppm**	**Al ppm**	**Ti ppm**	**V ppm**	**Cr ppm**	**Mn ppm**	**Co ppm**	**Ni ppm**	**Cu ppm**	**Zn ppm**	**Ga ppm**	**Sn ppm**
RN07_16	Rodados Negros	EPI-0808	69.9	6161	5741	3222	2569	19.1	841	127.6	308	BDL	140.0	24.8	3.11
CG08_1	Cristales Grandes	EPI-0702	70.6	2630	4530	2830	1752	70.8	470	175.7	289	BDL	402.0	18.0	1.94
CG08_4	Cristales Grandes	EPI-0702	71.7	2460	3660	16900	1641	BDL	1250	182	277	BDL	252.0	17.2	2.59
CG08_5	Cristales Grandes	EPI-0702	70.6	1998	4110	2860	1645	27.1	463	169.8	282	BDL	336.0	17.9	2.75
CG08_7	Cristales Grandes	EPI-0702	71.7	2820	4630	14500	1878	72	1120	192	276	BDL	445.0	20.1	3.1
CG08_8	Cristales Grandes	EPI-0702	70.6	3000	4590	14800	1843	74	1110	180	283	BDL	427.0	18.6	4.4
CG08_9	Cristales Grandes	EPI-0702	71.0	2490	4510	11700	2099	144	890	175.5	283	BDL	405.0	18.4	2.98
CG08_12	Cristales Grandes	EPI-0702	71.0	3070	4880	25500	2102	35	1820	187.8	272	BDL	622.0	19.0	4.41
CG08_13	Cristales Grandes	EPI-0702	71.0	3460	3520	30400	1971	415	2000	172.8	251	BDL	315.0	14.8	3.71
CG08_14	Cristales Grandes	EPI-0702	71.0	2410	3090	15300	1925	183	1140	172.9	267	BDL	245.0	17.1	2.25
CG08_18	Cristales Grandes	EPI-0702	71.1	1410	3976	2200	1199	BDL	227.3	176.1	292	BDL	274.0	16.2	2.42
SVA1_11_1	San Vicente Alto	SVA-1001	70.2	5180	13200	9250	2360	216	786	147.9	334	BDL	159.0	51.7	2.55
SVA1_11_2	San Vicente Alto	SVA-1001	69.0	5870	4800	10030	2329	BDL	900	164.5	302	BDL	146.4	45.8	2.38
SVA1_11_3	San Vicente Alto	SVA-1001	69.5	6180	4710	10160	2316	BDL	1055	158.6	305	BDL	137.0	45.5	2.13
SVA1_11_4	San Vicente Alto	SVA-1001	70.2	6320	5420	10090	2334	BDL	918	166.8	328	BDL	142.0	46.1	2.48
SVA1_11_5	San Vicente Alto	SVA-1001	69.0	6190	5010	9720	2308	BDL	927	160.5	306	BDL	121.9	45.9	2.16
SVA1_11_6	San Vicente Alto	SVA-1001	69.5	6520	4870	11380	2247	23.7	1043	165.1	313	BDL	122.9	44.3	2.24
SVA1_11_7	San Vicente Alto	SVA-1001	69.6	6450	4960	10660	2275	77	1025	162.8	313	BDL	128.2	44.6	2.25
SVA1_11_8	San Vicente Alto	SVA-1001	69.6	6210	4950	10720	2285	103	923	166	315	1.61	132.1	44.8	2.44
SVA1_11_9	San Vicente Alto	SVA-1001	70.2	6000	4760	9510	2329	9.3	961	161.1	310	BDL	147.0	46.1	2.15
SVA1_11_10	San Vicente Alto	SVA-1001	68.9	5860	4980	14150	2271	61.1	816	170.9	321	1.32	169.0	49.2	2.24
SVA1_11_11	San Vicente Alto	SVA-1001	69.9	6770	5020	15840	2275	BDL	1140	167.4	327	1.31	128.0	47.3	2.53
SVA1_11_12	San Vicente Alto	SVA-1001	69.5	6150	4700	14400	2247	BDL	1022	177.8	322	1.27	137.0	45.4	2.15
SVA1_11_13	San Vicente Alto	SVA-1001	70.2	5560	5420	11270	2326	BDL	622	170.3	322	BDL	169.0	46.1	2.05
SVB_11_1	San Vicente Bajo	SVB-1003	70.6	3303	5380	10880	2382	21.5	389	104.1	331	BDL	257.0	80.5	1.41
SVB_11_2	San Vicente Bajo	SVB-1003	70.1	3874	5310	13730	2361	23.2	629	108.8	333	BDL	290.0	78.2	1.74
SVB_11_3	San Vicente Bajo	SVB-1003	70.3	3158	5430	9690	2439	17.8	397	106.2	357	BDL	223.0	83.2	1.69
SVB_11_4	San Vicente Bajo	SVB-1003	71.2	2196	4920	9290	2498	18.9	217	89	362	BDL	132.0	80.6	1.94
SVB_11_5	San Vicente Bajo	SVB-1003	70.6	3960	6830	10810	2362	13.5	227	79.7	390	BDL	43.3	80.1	2.82
SVB_11_7	San Vicente Bajo	SVB-1003	70.1	6530	5230	17590	2474	10.6	1329	162.1	347	BDL	267.0	77.6	1.96
SVB_11_8	San Vicente Bajo	SVB-1003	70.1	6200	5140	14660	2471	6.5	1200	160.6	335	BDL	218.0	75.9	1.59
SVB_11_9	San Vicente Bajo	SVB-1003	70.3	6840	5220	18600	2580	223	1420	164.3	360	BDL	208.0	79.3	2.49
SVB_11_10	San Vicente Bajo	SVB-1003	71.2	6610	5270	16160	2500	9.6	1185	159.1	342	BDL	244.0	77.8	2.36
SVB_11_11	San Vicente Bajo	SVB-1003	70.6	1450	9060	15860	2646	BDL	341	86.6	389	BDL	BDL	79.0	1.76
SVB_11_12	San Vicente Bajo	SVB-1003	70.1	1612	8460	13870	2746	BDL	322	47.9	299	BDL	17.2	63.8	3.1
SVB_11_13	San Vicente Bajo	SVB-1003	71.2	1326	3400	12100	2734	BDL	156.2	46.4	325	BDL	37.3	63.1	3.95
SVB_11_14	San Vicente Bajo	SVB-1003	70.3	2540	5630	11260	2750	BDL	285	41.5	317	BDL	22.4	66.0	3.3
SVA1_14_1	San Vicente Alto	SVA-1001	70.9	6240	4860	5540	2458	BDL	1970	168.4	343	BDL	298.0	41.7	2.29
SVA1_14_2	San Vicente Alto	SVA-1001	70.1	6040	5080	5730	2377	BDL	1325	175.3	303	BDL	275.0	40.6	1.82
SVA1_14_3	San Vicente Alto	SVA-1001	69.9	6400	5260	6790	2277	BDL	1786	173	314	BDL	267.0	43.6	2.38
SVA1_14_4	San Vicente Alto	SVA-1001	70.6	6410	5300	7000	2251	25.8	1995	170.3	313	BDL	286.0	44.0	1.8
SVA1_14_5	San Vicente Alto	SVA-1001	70.4	6000	5390	7180	2262	201	1184	175.1	336	BDL	287.0	48.1	2.5
SVA1_14_6	San Vicente Alto	SVA-1001	70.5	5950	5270	6950	2234	BDL	1517	175.8	321	BDL	257.0	42.5	1.95
SVA1_14_7	San Vicente Alto	SVA-1001	69.3	5820	5220	7130	2215	BDL	1698	166.8	317	BDL	246.0	45.3	1.75
SVA1_14_8	San Vicente Alto	SVA-1001	70.4	5810	5190	7390	2316	BDL	1426	174.6	326	BDL	236.0	45.9	2.71
SVA1_14_9	San Vicente Alto	SVA-1001	69.9	7130	5720	17290	2059	BDL	2040	175.1	338	BDL	289.0	57.1	3.19
SVA1_14_10	San Vicente Alto	SVA-1001	70.7	6700	5780	16170	2092	BDL	1505	178	346	BDL	257.0	54.0	2.79
SVA1_14_11	San Vicente Alto	SVA-1001	70.0	6880	5980	14670	2052	BDL	1519	180.9	333	BDL	240.0	55.5	2.42
SVA1_14_12	San Vicente Alto	SVA-1001	69.2	5380	5250	12610	2118	BDL	1529	180	322	BDL	331.0	52.0	3.02
SVA1_14_13	San Vicente Alto	SVA-1001	69.9	5060	5060	11600	2163	BDL	1417	174	331	BDL	301.0	50.9	2.87
SVA1_14_14	San Vicente Alto	SVA-1001	70.9	6290	5830	9390	2278	BDL	1626	177.3	329	BDL	248.0	51.5	2.14
SVA1_14_15	San Vicente Alto	SVA-1001	70.1	6630	5690	9090	2226	BDL	1544	174	312	BDL	199.0	50.4	2.42
SVA1_14_16	San Vicente Alto	SVA-1001	69.9	6920	5820	10020	2162	BDL	1604	170.1	315	BDL	161.0	51.1	2.27
SVA1_14_17	San Vicente Alto	SVA-1001	70.4	6730	5680	10720	2119	BDL	1635	169.4	329	BDL	177.0	51.6	2.32
SVA1_14_18	San Vicente Alto	SVA-1001	69.9	6700	5530	10070	2162	BDL	1585	170.3	315	BDL	166.0	51.3	2.12
SVA1_14_19	San Vicente Alto	SVA-1001	70.7	6600	5450	8570	2252	BDL	1664	174.9	318	BDL	206.0	48.6	1.97
SVA1_14_20	San Vicente Alto	SVA-1001	70.0	5990	5210	7580	2249	BDL	1383	157	291	BDL	205.0	46.6	2.82
SVA1_14_21	San Vicente Alto	SVA-1001	69.2	6300	5440	9360	2149	BDL	1162	167.8	304	BDL	184.0	49.6	2.39

Magnetite LA-ICP-MS data from El Laco deposit: Deep zone			Detection limits in ppm											
			Average	1.53	5.90	12.98	1.60	9.87	3.10	2.44	3.71	3.91	7.52	1.67	0.55
			Median	1.20	4.60	8.90	1.30	8.00	2.60	1.90	3.00	2.20	5.90	0.82	0.46
Sample	**Ore body**	**Drill core**	**Fe (EPMA) [wt. %]**	**Mg ppm**	**Al ppm**	**Ti ppm**	**V ppm**	**Cr ppm**	**Mn ppm**	**Co ppm**	**Ni ppm**	**Cu ppm**	**Zn ppm**	**Ga ppm**	**Sn ppm**
RN16_1	Rodados Negros	EPI-0808	70.9	2450	3660	5100	802	BDL	1360	171	98	BDL	283	23.7	3.1
RN16_2	Rodados Negros	EPI-0808	71.1	2390	3610	11200	890	14.3	2250	158.8	81.5	2.9	541	23.4	4.54
RN16_3	Rodados Negros	EPI-0808	70.8	2476	3900	3400	914	12.1	977	175.8	98.9	2.62	666	24.6	3.92
RN16_4	Rodados Negros	EPI-0808	70.3	1829	3290	1970	930	BDL	755	166.5	111	BDL	416	23.4	3.2
RN16_5	Rodados Negros	EPI-0808	70.6	2630	3490	2000	880	BDL	994	178	110.1	BDL	571	24.1	2.88
RN16_6	Rodados Negros	EPI-0808	70.7	2920	3930	1830	916	BDL	815	185.6	108	BDL	459	23.6	3
RN16_7	Rodados Negros	EPI-0808	70.9	2950	3600	3830	863	BDL	1044	189	105.2	BDL	546	23	3.18
RN16_8	Rodados Negros	EPI-0808	71.1	2740	3770	2230	928	BDL	895	175.4	110	4.3	689	24.6	4.3
RN16_9	Rodados Negros	EPI-0808	70.8	1720	2300	940	682	BDL	1205	100.9	103.6	BDL	82	21.7	1.83
RN16_10	Rodados Negros	EPI-0808	70.3	1990	3020	1760	690	BDL	1099	113.8	98	BDL	351	23.2	2.12
RN16_11	Rodados Negros	EPI-0808	70.6	2510	3150	4000	640	BDL	1280	126	100	BDL	413	25.4	4.2
RN16_12	Rodados Negros	EPI-0808	70.7	2540	3120	5390	666	BDL	1800	124	102	BDL	473	25.3	4.19
RN16_13	Rodados Negros	EPI-0808	70.9	4690	3960	35100	633	BDL	4990	127.7	108	9.5	580	23.2	7.9
RN16_14	Rodados Negros	EPI-0808	71.1	2310	3430	1690	634	BDL	998	116.5	110	BDL	502	24.1	2.79
RN16_15	Rodados Negros	EPI-0808	70.8	2280	3690	1530	693	BDL	1064	118.4	95	BDL	477	23.1	2.9
RN16_16	Rodados Negros	EPI-0808	70.3	2572	3750	7950	682	BDL	1567	125.8	104	BDL	706	23.2	6.12
RN16_17	Rodados Negros	EPI-0808	70.6	1830	2450	760	754	BDL	1250	113.9	105	BDL	182	21.6	0.91
EPI28_1	Pasos Blancos	EPI-0916	71.3	2783	3220	5370	885	40.4	942	128.8	160	BDL	194	20.4	4.12
EPI28_2	Pasos Blancos	EPI-0916	70.4	2710	3120	4300	876	34	810	123	155.4	BDL	182	19.2	3.48
EPI28_3	Pasos Blancos	EPI-0916	71.7	2656	3132	3504	902	41	786	128.3	155.8	BDL	164	19.98	3.74
EPI28_4	Pasos Blancos	EPI-0916	71.3	2805	3261	4940	885	35.7	897	124.2	158.4	BDL	197	20.76	3.51
EPI28_5	Pasos Blancos	EPI-0916	71.3	2846	3166	3510	918	33.6	739	117	139.5	BDL	158	20.43	3.8
EPI28_6	Pasos Blancos	EPI-0916	71.4	2890	3085	4210	920	29.6	791	118.5	121.9	BDL	148.8	19.22	3.71
EPI28_7	Pasos Blancos	EPI-0916	71.4	2880	3044	4510	929	29.3	874	124.6	146.5	BDL	185	20.5	3.82
EPI28_8	Pasos Blancos	EPI-0916	71.4	2875	3066	4500	919	25.3	813	123.8	151.7	BDL	167	20.06	3.98
EPI28_9	Pasos Blancos	EPI-0916	71.9	3113	3376	5910	899	19.2	871	116	132.9	1.34	220	20.2	4.16
EPI28_10	Pasos Blancos	EPI-0916	71.7	5380	3160	30420	885	37.8	2014	116.4	139	4.5	160	17.8	6.57
EPI28_11	Pasos Blancos	EPI-0916	71.9	3000	3335	3950	918	76.4	679	112.4	151.2	BDL	155	19.8	3.56
EPI28_12	Pasos Blancos	EPI-0916	71.8	2976	3571	5280	956	13.6	948	127.4	162.6	BDL	192	21.2	3.99
EPI28_13	Pasos Blancos	EPI-0916	71.9	2868	3530	3950	976	BDL	822	126.7	158.1	BDL	194	21.03	3.78
EPI28_14	Pasos Blancos	EPI-0916	71.5	2901	3570	4341	992	12.3	855	128.1	163.5	BDL	186	20.93	3.73
EPI28_15	Pasos Blancos	EPI-0916	71.7	2832	3488	3790	979	16.5	775	122.5	168	3.1	176	21.1	3.61
EPI28_16	Pasos Blancos	EPI-0916	71.1	3155	3161	5720	1007	8.8	834	122	146.4	1.31	182	20.3	4.13
EPI28_17	Pasos Blancos	EPI-0916	71.4	3123	3155	5450	1013	5.8	822	122.1	143.8	BDL	180	20.06	4.49
EPI28_18	Pasos Blancos	EPI-0916	71.3	2960	3160	3788	1017	9.5	704	121.9	135.4	BDL	155.2	20.1	3.84
EPI28_19	Pasos Blancos	EPI-0916	71.3	3010	2952	4110	1025	9.9	737	121.2	138.3	BDL	163	20.6	3.97
CG32_1	Cristales Grandes	EPI-0702	71.2	988	3260	1463	2062	BDL	108.1	79.5	222.3	1.99	130	4.5	0.96
CG32_2	Cristales Grandes	EPI-0702	70.5	959	3076	1113	2023	BDL	115.8	81.7	218.5	BDL	109	4.37	0.79
CG32_3	Cristales Grandes	EPI-0702	70.9	1096	3310	1440	1971	BDL	136.9	92.1	225	BDL	200	3.99	0.85
CG32_4	Cristales Grandes	EPI-0702	70.7	1038	3511	1363	2050	BDL	121.8	82.3	216.7	BDL	180	4.16	0.86
CG32_5	Cristales Grandes	EPI-0702	71.6	786	2950	1750	2061	12.2	154	75.2	211	BDL	99	4.38	0.62
CG32_6	Cristales Grandes	EPI-0702	70.8	1077	3240	2190	1991	BDL	123	73.6	214	BDL	148	4.03	0.78
CG32_7	Cristales Grandes	EPI-0702	70.7	1143	3055	1790	1972	12.1	157	73.2	208	BDL	99.8	4.71	0.62
CG32_8	Cristales Grandes	EPI-0702	71.6	1231	3590	1850	1435	26.9	161	76.3	218	1.78	228	4.31	0.99
CG32_9	Cristales Grandes	EPI-0702	70.8	1073	3500	1408	1532	47.5	191.5	70	219	BDL	222	3.7	1.04
CG32_10	Cristales Grandes	EPI-0702	71.6	612	2438	1890	1711	52.2	198	55.5	218	BDL	50	5.15	0.47
CG32_11	Cristales Grandes	EPI-0702	70.8	647	3290	1525	1726	64.8	210.7	42.2	225	BDL	174	5.32	1.03
CG32_12	Cristales Grandes	EPI-0702	70.8	601	2743	739	1700	49	144.4	50.6	218	BDL	74.1	5	BDL
CG32_13	Cristales Grandes	EPI-0702	71.6	613	2795	7790	1965	75.2	415	48.3	220	BDL	70.9	6.47	0.84
CG32_14	Cristales Grandes	EPI-0702	71.0	608	2830	1790	1891	42.2	220	45.9	223	BDL	102	5.49	0.94
CG32_15	Cristales Grandes	EPI-0702	71.4	1067	3080	11000	1925	44.1	622	55.1	222	4.3	228	4.85	1.31
CG32_16	Cristales Grandes	EPI-0702	71.6	994	3260	14950	1954	51.6	510	59.2	210	3.8	159	4.75	1.45
CG32_17	Cristales Grandes	EPI-0702	71.0	783	2829	16960	1913	39.4	804	48	210	3.8	113	6.25	1.44
CG32_18	Cristales Grandes	EPI-0702	71.4	468	2682	1047	1970	47.5	146	47.2	214	BDL	32	6.35	0.71
CG32_19	Cristales Grandes	EPI-0702	70.8	1080	2740	1020	1826	41	156	53.5	210	BDL	27.9	6.38	0.47

Magnetite LA-ICP-MS data from El Laco host andesite			Detection limits in ppm											
			Average	1.53	5.90	12.98	1.60	9.87	3.10	2.44	3.71	3.91	7.52	1.67	0.55
			Median	1.20	4.60	8.90	1.30	8.00	2.60	1.90	3.00	2.20	5.90	0.82	0.46
Sample	Volcanic	Type	Fe (EPMA) [wt. %]	Mg ppm	Al ppm	Ti ppm	V ppm	Cr ppm	Mn ppm	Co ppm	Ni ppm	Cu ppm	Zn ppm	Ga ppm	Sn ppm
ASLN_CUM_1	Laco Norte upper andesite	Mgt-glom	60.6	18190	17980	57300	3553	815	2929	228.5	499	119.7	851	52.7	5.03
ASLN_CUM_2	Laco Norte upper andesite	Mgt-glom	58.6	18330	17760	57600	3392	789	2980	225.7	488	76.9	637	47.7	3.91
ASLN_CUM_3	Laco Norte upper andesite	Mgt-glom	59.6	18440	17550	57800	3490	761	3017	220.6	507	83.8	614	47.6	4.21
ASLN_CUM_4	Laco Norte upper andesite	Mgt-glom	59.7	17450	16150	57200	3438	764	3021	225.1	472	118.6	645	46.6	4.29
ASLN_CUM_5	Laco Norte upper andesite	Mgt-glom	58.9	17270	15700	58100	3442	587	2936	226.5	480	165.1	642	48	4.78
ASLN_CUM_6	Laco Norte upper andesite	Mgt-glom	61.0	17900	17500	60500	3601	867	3150	235.9	465	194.4	691	49.6	4.3
ASLN_CUM_7	Laco Norte upper andesite	Mgt-glom	60.6	17620	16100	62800	4043	754	3236	245.1	722	134	699	51.1	5.08
ASLN_CUM_8	Laco Norte upper andesite	Mgt-glom	59.6	16910	15570	61000	3830	702	3180	235.9	722	90.6	671	48.6	4.84
ASLN_CUM_9	Laco Norte upper andesite	Mgt-glom	58.9	17020	15430	61800	3962	691	3192	239.6	721	114.7	728	51.5	4.75
ASLN_CUM_10	Laco Norte upper andesite	Mgt-glom	61.0	17810	15800	65200	4095	729	3270	248.3	737	116.9	741	52	4.74
ASLN_CUM_11	Laco Norte upper andesite	Mgt-glom	58.6	14940	11370	62800	3480	941	3240	204	372	117.4	716	44.1	4.72
ASLN_CUM_12	Laco Norte upper andesite	Mgt-glom	59.6	15340	22100	65800	3577	1023	3260	213.2	386	138.3	703	50	5.26
ASLN_CUM_13	Laco Norte upper andesite	Mgt-glom	58.9	14280	11100	65400	3584	953	3209	214	372	113.1	683	46.6	5.63
ASLN_CUM_14	Laco Norte upper andesite	Mgt-glom	59.6	16340	12410	70000	3557	712	2681	231.1	463	201.8	640	48.2	5.56
ASLN_CUM_15	Laco Norte upper andesite	Mgt-glom	58.9	17230	12650	79600	3310	188	3170	236	471	238	1074	49.3	6.1
ASLN_CUM_16	Laco Norte upper andesite	Mgt-glom	60.2	14830	13460	88200	3680	278	3010	235.2	503	252	805	50.2	6.52
ASLN_CUM_17	Laco Norte upper andesite	Mgt-glom	58.4	14530	13200	60000	3420	280	2672	215.8	429	98.8	609	46.9	5.33
ASLN_CUM_18	Laco Norte upper andesite	Mgt-glom	59.7	15530	14440	63200	3582	285	2847	234.2	488	116.6	638	50.5	4.67
ASLN_CUM_19	Laco Norte upper andesite	Mgt-glom	58.9	15110	14090	59100	3510	316	2690	220	474	110.3	723	48.4	4.95
ASLN_CUM_20	Laco Norte upper andesite	Mgt-glom	60.6	16490	15690	70100	3500	487	3588	224.4	441	159.2	701	49.1	4.99
ASLN_CUM_21	Laco Norte upper andesite	Mgt-glom	58.6	14730	14390	61800	2982	135.6	3120	204.4	408	132.8	615	42.7	4.21
ASLN_CUM_22	Laco Norte upper andesite	Mgt-glom	59.6	15730	15590	66700	3296	486	3414	218.9	454	165.8	702	46.6	4.79
ASLN_CUM_23	Laco Norte upper andesite	Mgt-glom	59.7	15770	14960	66400	3372	443	3371	219.5	449	140.6	669	49.4	4.74
ASLN_CUM_24	Laco Norte upper andesite	Mgt-glom	58.9	15770	15130	65100	3281	354	3334	223.9	426	132.3	652	48.3	5.01
ASLN_CUM_25	Laco Norte upper andesite	Mgt-glom	60.7	222000	26800	172000	3840	396	7180	228	299	49	700	33.4	8.5
ASLN_CUM_26	Laco Norte upper andesite	Mgt-glom	60.2	17750	16800	55600	3810	827	2710	243	503	16.9	890	57.3	3.7
ASLN_CUM_27	Laco Norte upper andesite	Mgt-glom	59.4	21570	16490	72400	4192	1357	3105	221	386	32.8	875	52.2	6.8
ASLN_CUM_28	Laco Norte upper andesite	Mgt-glom	60.3	22250	18630	62000	3730	818	3037	231	491	95.7	1090	54.1	8.1
ASLN_CUM_29	Laco Norte upper andesite	Mgt-glom	60.1	18260	18310	60300	3400	960	3360	231	398	132.9	888	55.8	5.8
ASLN_CUM_30	Laco Norte upper andesite	Mgt-glom	60.7	515000	100600	55600	2770	529	13600	303	551	176	1030	68.3	7
ASLN_CUM_31	Laco Norte upper andesite	Mgt-glom	60.2	16370	15130	68300	3643	1341	3640	207.6	337	149.3	800	50.3	5.6
ASLN_CUM_32	Laco Norte upper andesite	Mgt-glom	59.4	15650	14320	68600	3620	907	3670	201.8	331	132.6	716	45.7	4.26
ASLN_CUM_33	Laco Norte upper andesite	Mgt-glom	69.3	8120	10820	75800	4260	2730	3160	274	565	254	870	60.4	6.7
ASLN_CUM_34	Laco Norte upper andesite	Mgt-glom	69.4	16900	14330	73200	4270	2790	3280	274	615	287	1100	67.6	9
ASLN_CUM_35	Laco Norte upper andesite	Mgt-glom	66.0	14900	13520	72600	4090	3032	3005	263	542	228	744	56.2	5.58
ASLN_CUM_36	Laco Norte upper andesite	Mgt-glom	69.3	9310	10710	75200	4090	2670	2840	266	546	211	785	54.8	5.6
ASLN_CUM_37	Laco Norte upper andesite	Mgt-glom	69.4	17500	16480	77200	4490	2970	2800	282	601	381	976	60	5.2
ASLN_CUM_38	Laco Norte upper andesite	Mgt-glom	69.8	45900	19900	78600	4850	2930	3170	260	588	171	1060	66.5	6.7
ASLN_CUM_39	Laco Norte upper andesite	Mgt-glom	69.5	7300	195000	75500	4300	3120	1730	246	588	122	986	106	11.9
ASLN_CUM_40	Laco Norte upper andesite	Mgt-glom	66.0	16110	23200	74000	4300	3140	3200	259	608	247	961	61.2	4.5
ASLN_CUM_41	Laco Norte upper andesite	Mgt-glom	58.4	12990	11300	65800	3688	1063	3318	206.4	345	99.9	678	48.6	5.34
ACUMT01a_1	Mgt megacryst, LN low and	Mgt-meg	59.3	11100	17780	59500	3570	692	817	156.2	489	7.4	966	49.5	4.19
ACUMT01a_2	Mgt megacryst, LN low and	Mgt-meg	60.5	11680	18560	62600	3580	665	826	165.3	508	11.6	838	51.7	3.89
ACUMT01a_3	Mgt megacryst, LN low and	Mgt-meg	60.6	12150	18430	61100	3516	690	841	170.9	508	14	816	54	4.03
ACUMT01a_4	Mgt megacryst, LN low and	Mgt-meg	60.8	8490	18450	60800	3630	657	845	158.7	506	8.7	966	51.8	3.6
ACUMT01a_5	Mgt megacryst, LN low and	Mgt-meg	61.2	9670	18910	63900	3720	663	852	158.8	525	7.1	1044	52	3.96
ACUMT01a_6	Mgt megacryst, LN low and	Mgt-meg	61.1	11370	17130	64800	3990	881	823	154.5	362	5.6	1086	50.5	4.47
ACUMT01a_7	Mgt megacryst, LN low and	Mgt-meg	59.9	11280	16900	64200	3980	924	939	157.8	364	31.4	1014	50.8	4.64
ACUMT01a_8	Mgt megacryst, LN low and	Mgt-meg	61.3	8900	17130	67400	4094	931	906	153.6	363	31.9	1092	52.7	4.75
ACUMT01a_9	Mgt megacryst, LN low and	Mgt-meg	59.3	6810	16420	63400	3916	947	925	153.9	337	6.1	1177	50.3	4.63
ACUMT01a_10	Mgt megacryst, LN low and	Mgt-meg	61.1	5840	16620	66000	3980	892	934	149.6	361	5.2	1500	52.8	4.69
ACUMT01a_11	Mgt megacryst, LN low and	Mgt-meg	57.7	3130	15510	59400	3910	795	783	158.2	354	25	1614	53.6	5.55
ACUMT01a_12	Mgt megacryst, LN low and	Mgt-meg	59.3	839	9620	76600	4530	1058	872	141.3	355	10.2	2182	52.1	6.19
ACUMT01a_16	Mgt megacryst, LN low and	Mgt-meg	62.7	2287	15490	63900	3465	304	842	175.8	422	BDL	1473	52.1	5.8
ACUMT01a_17	Mgt megacryst, LN low and	Mgt-meg	62.1	2480	16430	60800	3540	93	511	197	421	9.9	2560	62.3	6.1
ACUMT01a_18	Mgt megacryst, LN low and	Mgt-meg	62.3	2073	16200	63000	3496	225	611	176.8	429	3.1	1874	53.9	5.7
ACUMT01a_19	Mgt megacryst, LN low and	Mgt-meg	62.7	3270	16610	64100	3515	64.8	1118	186.7	445	26.8	1108	51.9	5.51
ACUMT01a_20	Mgt megacryst, LN low and	Mgt-meg	64.9	7250	14360	55900	3252	BDL	1110	175.7	381	5.3	915	51.5	5.1
ACUMT01a_21	Mgt megacryst, LN low and	Mgt-meg	64.3	6210	16030	53800	3261	BDL	827	165.6	390	104	1047	52.9	4.55
ACUMT01a_22	Mgt megacryst, LN low and	Mgt-meg	55.3	4920	14220	42270	2709	BDL	509	143.4	311	10.6	850	45.9	3.82
ACUMT01a_23	Mgt megacryst, LN low and	Mgt-meg	65.9	12840	17000	49500	3244	BDL	1061	196.8	362	24.5	586	54	3.94
ACUMT01a_24	Mgt megacryst, LN low and	Mgt-meg	65.8	15060	16630	39700	3084	BDL	1226	187.7	329	26.1	584	53.6	4.6
ACUMT01a_25	Mgt megacryst, LN low and	Mgt-meg	61.2	11230	17570	27300	2638	BDL	1711	156.9	272	45.6	488	50.2	3.96
ACUMT01a_26	Mgt megacryst, LN low and	Mgt-meg	64.7	14260	18510	28600	2815	23.5	2030	173.5	270	11	483	50.7	5.15
ACUMT01a_27	Mgt megacryst, LN low and	Mgt-meg	64.5	13520	17170	23910	2671	BDL	1871	167.1	269	26.3	413	47.6	4.28
ACUMT01a_28	Mgt megacryst, LN low and	Mgt-meg	64.9	11800	16900	20920	2593	BDL	1669	148.7	260	13.2	413	48.6	4.3
ACUMT01a_29	Mgt megacryst, LN low and	Mgt-meg	62.3	14030	17840	27980	2611	BDL	1956	168.8	277	60	483	47.5	4.58
ACUMT01a_30	Mgt megacryst, LN low and	Mgt-meg	64.3	9960	8380	5660	1987	8.5	1268	130.9	228	6.6	221	33.6	4.45
ACUMT01a_31	Mgt megacryst, LN low and	Mgt-meg	64.7	9740	9680	6840	2165	7.3	1363	135.1	223	7.5	241	35.3	4.36
ACUMT01a_32	Mgt megacryst, LN low and	Mgt-meg	65.8	9480	7660	4780	1879	7.1	1269	129.1	218	9.7	200	32.5	4.55
ACUMT01a_33	Mgt megacryst, LN low and	Mgt-meg	64.9	9450	7530	4920	1840	BDL	1258	128.4	230	3.12	216	33.5	4.46
ACUMT01a_34	Mgt megacryst, LN low and	Mgt-meg	64.7	9020	6820	4230	1838	BDL	1225	127.7	224	8.31	206	31.9	4.23

ANNEX C: Supplementary Material for Chapter 4

Fluid-assisted assembly of magnetite microparticles: evidence from the giant El Laco iron oxide deposit, Chile

This file includes:

Supplementary Figures C1-C3

Supplementary Figure C1: Examples of reconstructed (A) and segmented slices (B) virtually cut through sample LS06A. Grey: magnetite; Blue: open pores; Red: closed pores.

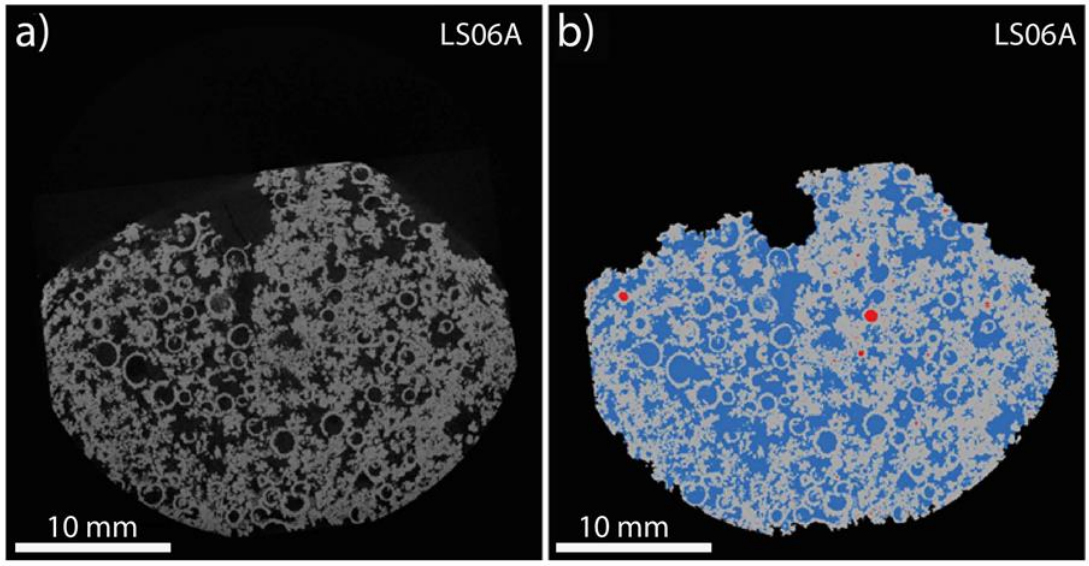

Supplementary Figure C2: (A-B) SEM images of magnetite microspheres in vesicular and porous ore samples. Note the euhedral magnetite grains growing inward from the microsphere surface.

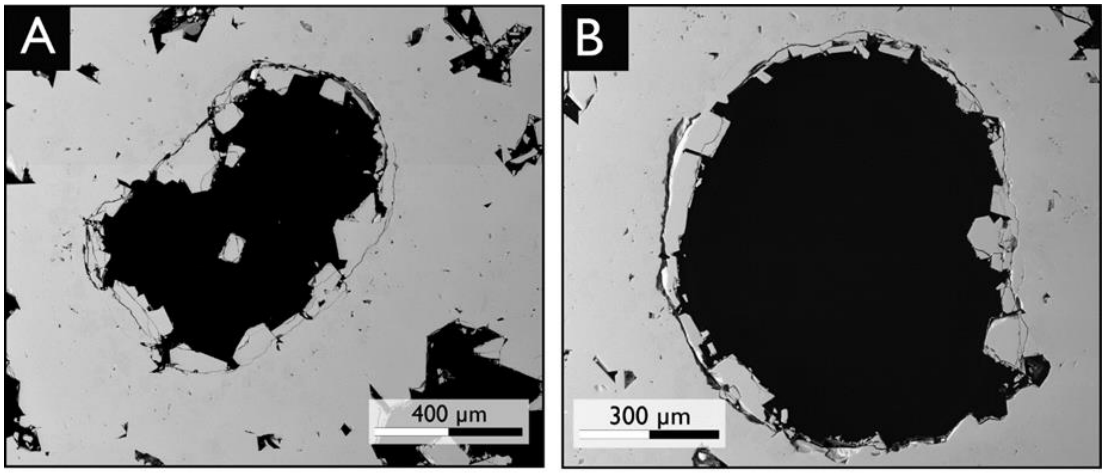

Supplementary Figure C3: (A-C) Hand-sample ore specimen from Laco Norte ore body showing centimetre-scale well-developed octahedral magnetite associated with abundant spherical structures formed by magnetite.